frontiers | Research Topics

Image-based computational approaches for personalized cardiovascular medicine: Improving clinical applicability and reliability through medical imaging and experimental data

Edited by
Selene Pirola, Amirhossein Arzani, Claudio Chiastra and Francesco Sturla

Published in
Frontiers in Medical Technology
Frontiers in Bioengineering and Biotechnology
Frontiers in Cardiovascular Medicine

ISSN 1664-8714
ISBN 978-2-8325-2957-7
DOI 10.3389/978-2-8325-2957-7

About Frontiers

Frontiers is more than just an open access publisher of scholarly articles: it is a pioneering approach to the world of academia, radically improving the way scholarly research is managed. The grand vision of Frontiers is a world where all people have an equal opportunity to seek, share and generate knowledge. Frontiers provides immediate and permanent online open access to all its publications, but this alone is not enough to realize our grand goals.

Frontiers journal series

The Frontiers journal series is a multi-tier and interdisciplinary set of open-access, online journals, promising a paradigm shift from the current review, selection and dissemination processes in academic publishing. All Frontiers journals are driven by researchers for researchers; therefore, they constitute a service to the scholarly community. At the same time, the *Frontiers journal series* operates on a revolutionary invention, the tiered publishing system, initially addressing specific communities of scholars, and gradually climbing up to broader public understanding, thus serving the interests of the lay society, too.

Dedication to quality

Each Frontiers article is a landmark of the highest quality, thanks to genuinely collaborative interactions between authors and review editors, who include some of the world's best academicians. Research must be certified by peers before entering a stream of knowledge that may eventually reach the public - and shape society; therefore, Frontiers only applies the most rigorous and unbiased reviews. Frontiers revolutionizes research publishing by freely delivering the most outstanding research, evaluated with no bias from both the academic and social point of view. By applying the most advanced information technologies, Frontiers is catapulting scholarly publishing into a new generation.

What are Frontiers Research Topics?

Frontiers Research Topics are very popular trademarks of the *Frontiers journals series*: they are collections of at least ten articles, all centered on a particular subject. With their unique mix of varied contributions from Original Research to Review Articles, Frontiers Research Topics unify the most influential researchers, the latest key findings and historical advances in a hot research area.

Find out more on how to host your own Frontiers Research Topic or contribute to one as an author by contacting the Frontiers editorial office: frontiersin.org/about/contact

Image-based computational approaches for personalized cardiovascular medicine: Improving clinical applicability and reliability through medical imaging and experimental data

Topic editors

Selene Pirola — Delft University of Technology, Netherlands
Amirhossein Arzani — The University of Utah, United States
Claudio Chiastra — Polytechnic University of Turin, Italy
Francesco Sturla — IRCCS San Donato Polyclinic, Italy

Citation

Pirola, S., Arzani, A., Chiastra, C., Sturla, F., eds. (2023). *Image-based computational approaches for personalized cardiovascular medicine: Improving clinical applicability and reliability through medical imaging and experimental data*. Lausanne: Frontiers Media SA. doi: 10.3389/978-2-8325-2957-7

Table of contents

frontiers | Frontiers in Medical Technology

TYPE Editorial
PUBLISHED 23 June 2023
DOI 10.3389/fmedt.2023.1222837

OPEN ACCESS

EDITED BY
Stephane Avril,
Institut Mines-Télécom, France

REVIEWED BY
Emanuele Gasparotti,
Gabriele Monasterio Tuscany Foundation (CNR), Italy
Elena S. Di Martino,
University of Calgary, Canada

*CORRESPONDENCE
Francesco Sturla
✉ francesco.sturla@grupposandonato.it

†These authors have contributed equally to this work

RECEIVED 15 May 2023
ACCEPTED 15 June 2023
PUBLISHED 23 June 2023

CITATION
Pirola S, Arzani A, Chiastra C and Sturla F (2023) Editorial: Image-based computational approaches for personalized cardiovascular medicine: improving clinical applicability and reliability through medical imaging and experimental data.
Front. Med. Technol. 5:1222837.
doi: 10.3389/fmedt.2023.1222837

Editorial: Image-based computational approaches for personalized cardiovascular medicine: improving clinical applicability and reliability through medical imaging and experimental data

Selene Pirola[1†], Amirhossein Arzani[2†], Claudio Chiastra[3†] and Francesco Sturla[4,5*†]

[1]Department of Biomechanical Engineering, Delft University of Technology, Delft, Netherlands, [2]Department of Mechanical Engineering and Scientific Computing and Imaging Institute, The University of Utah, Salt Lake City, UT, United States, [3]PoliTo[BIO]Med Lab, Department of Mechanical and Aerospace Engineering, Politecnico di Torino, Torino, Italy, [4]3D and Computer Simulation Laboratory, IRCCS Policlinico San Donato, San Donato Milanese, Italy, [5]Department of Electronics, Information and Bioengineering, Politecnico di Milano, Milano, Italy

KEYWORDS

computational modeling, cardiovascular biomechanics, patient-specific models, surgical planning, diagnosis, cardiovascular imaging

Editorial on the Research Topic
Image-based computational approaches for personalized cardiovascular medicine: improving clinical applicability and reliability through medical imaging and experimental data

Computational analysis is frequently integrated with medical imaging to develop novel and personalized solutions for the diagnosis, prognosis, and treatment of cardiovascular disease. Despite the significant increase in computational capabilities and the emergence of novel technologies that automate and accelerate workflows, the personalization of cardiovascular computational modeling remains a challenge with several unresolved issues. Multimodality cardiovascular imaging, including echocardiography, cardiac magnetic resonance (CMR), and cardiac computed tomography (CT), has significantly evolved in recent decades, enabling accurate and three-dimensional (3D) representation of cardiovascular anatomy. Furthermore, to account for the complexity of cardiovascular anatomy and function, mechanical properties of cardiovascular tissues and model boundary conditions should be prescribed on a patient-specific basis. However, obtaining these data directly from *in vivo* imaging can be challenging and may require additional imaging and a dedicated framework for data elaboration. In particular, model assumptions and simplifications may be necessary to avoid the use of invasive diagnostic imaging or to reduce the computational burden of numerical simulations.

The studies collected in this Research Topic address several key issues related to patient-specific cardiovascular modeling, with a specific focus on several aspects of the workflow limiting the clinical translation of computational analysis.

Two works in the present article collection focus on the segmentation and reconstruction of patient-specific geometries of blood vessels from clinical imaging. A trained deep learning-based approach was applied by Abdolmanafi et al. to achieve a fully automated segmentation of abdominal aortic aneurysm (AAA) tissues from CT, including arterial wall and lumen, intraluminal thrombus (ILT), and calcification. The automated segmentation showed very good agreement with the manual ground-truth segmentation, thus expediting the segmentation process and reducing inter- and intra-operator variability. An automated and user-friendly approach was proposed by Warren et al. to generate patient-specific 3D models of atherosclerotic coronary arteries by combining virtual histology-intravascular ultrasound (VH-IVUS) and angiography data. Leveraging an automated meshing algorithm for volumetric reconstruction of the arterial network, the program enables finite element (FE) analysis of stresses and strains across the arterial wall to facilitate the biomechanical assessment of atherosclerotic plaque stability. Notably, mechanical properties can be assigned to arterial tissues according to their specific VH-IVUS color-coded value.

Computational advances in cardiovascular biomechanics are possible by combining imaging with clinical data. Fruelund et al. proposed a novel non-invasive electrocardiographic imaging (ECGi) method based on a 12-lead inverse ECG algorithm that accurately reconstructed a 3D electrical ventricular activation map during right ventricle (RV) pacing and effectively identified the initial site of activation in relation to ventricular anatomy. When validated against the true CT-based RV pacing site, the reconstructed ventricular activation model could extend the clinical applicability of 12-lead ECG-based methods and overcome more complex ECGi methods requiring a dense array of electrodes. A new approach was proposed by Celi et al. to estimate the local distribution of aortic stiffness by combining *in vivo* dynamic knowledge of arterial morphology with clinical records of systemic pressure. To achieve this, a novel mesh-morphing approach based on radial basis function interpolation was applied to ECG-gated aortic CT images to map the aortic luminal surface over the cardiac cycle. A novel methodology to characterize the mechanical properties of AAA was proposed by Jansen et al. using non-ECG-gated freehand two-dimensional (2D) ultrasound imaging: a dedicated framework was established to semi-automatically segment and register probe-tracked images of the aorta at different phases of the cardiac cycle. Local aortic compliance and distensibility were subsequently computed using measured brachial pulse pressure values.

The promising results of the inverse modeling approaches developed in the last two studies and their application to real patient-specific cases suggest that the availability of time-resolved *in vivo* imaging can yield additional quantitative parameters of vessel wall biomechanics beyond 3D model geometry, such as regional characterization of deformation and stiffness. Using four-dimensional (4D) CT image data, Peng et al. showed that incorporating the aortic wall movement into the CFD analysis of AAA does not considerably alter the overall aortic flow field and wall shear stress distribution, as predicted by assuming rigid walls. However, it reveals greater blood stagnation in AAA, which may trigger ILT formation. Therefore, dedicated processing of *in vivo* images can help to configure boundary conditions that are relevant to the clinical goals of patient-specific CFD analysis. Using CFD analysis, Canè et al. examined how the interplay between left ventricular (LV) wall torsion and vortex guidance by the mitral valve (MV) affects intraventricular hemodynamics by combining patient-specific 3D models of the beating LV endocardium and patient-inspired MV leaflet kinematics through overset meshes. LV torsion significantly impacted the evaluation of blood stasis and residence time, and MV enhanced the inlet jet propagation toward the LV apex and apical washout.

Computational modeling can also be used to reproduce pathological cardiovascular conditions and investigate the severity of disease and the mechanisms of disease progression. In this context, Jafarinia et al. optimized an existing phenomenological shear-driven thrombosis model to predict thrombus formation in the false lumen (FL) of type B aortic dissection (TBAD) using a limited number of parameters. When tested on a real TBAD case reconstructed from CT, the prediction of FL status was in excellent agreement with the 3-year follow-up CT scan in terms of thrombus location and volume. The improved model also reduced computational time by ~65%, making it more feasible for clinical use. Weissmann et al. developed a pre-clinical FE model of heart failure with preserved left ventricular ejection fraction (HFpEF) using CMR data and intracardiac pressures from swine heart models subjected to pressure overload. Different HFpEF phenotypes were studied, evaluating changes in mechanical properties. An isotropic change in myocardial passive behavior was observed, the magnitude of which was heavily dependent on the degree of hypertrophy. Moreover, hypertrophy emerged as an initial compensatory response to HFpEF, with myocardial thickening enabling a steady transition in passive properties while maintaining tissue incompressibility.

Kohli et al. showed that CFD analysis also has the potential to predict the outcome of clinical procedures, thereby improving patient safety. Specifically, they assessed the impact of a catheter-based laceration of the anterior mitral leaflet to prevent LV outflow obstruction (LAMPOON) on the hemodynamic outcomes of transcatheter mitral valve replacement (TMVR). In a quantitative comparison with a virtual simulation of TMVR without LAMPOON, the LAMPOON procedure achieved a critical increment in the outflow area that was effective in improving LV outflow hemodynamics, particularly in subjects with a small neo-LV outflow tract.

To tackle the scarcity of clinical measurements, personalized computational simulations can still be performed by appropriately calibrating the model parameters. To this end, Shen et al. satisfactorily reproduced the cerebral hemodynamics in the circle of Willis (CoW) in patients with acute subarachnoid aneurysmal hemorrhage by calibrating the parameters of a block diagram hydraulic model with transcranial Doppler flow velocity

measurements of CoW vessels. Tanade et al. focused on the numerical quantification of fractional flow reserve (FFR) in coronary arteries, demonstrating that streamlined models can be defined that minimize the set of required patient-specific inputs while also achieving good agreement with gold standard invasive FFR measurements. The proposed approach offers a flexible framework that can expedite the data collection and simulation pipeline, also enabling the analysis of cases with missing data.

When patient-specific boundary conditions are not available for CFD analysis, Tricarico et al. proposed a pipeline to non-invasively estimate the parameters of three-element Windkessel (WK3) models for the hemodynamic assessment of the aortic arch arteries. A set of normalized WK3 parameters was defined based on ultrasound-derived patient-specific flow rates and intra-operatively measured pressure waveforms. When patient-specific flow rate and pressure waveforms are not available, these normalized parameters can be combined with readily available vessel diameter, brachial blood pressure, and heart rate data to obtain patient-specific WK3 parameters. Bhardwaj et al. developed an *in vitro* anatomical cerebrovascular model to study the mechanism of acute ischemic stroke (AIS). The experimental model was used to benchmark corresponding CFD predictions, which proved to be in relatively close agreement with experimental measurements for both normal and stroke conditions in terms of pressure and flow rate. This represents an important milestone toward validating a computational AIS model, providing additional insights into the dynamics of embolus migration and lodging in the brain, which are difficult aspects to measure *in vivo*.

The final step of a computational workflow involves the post-processing and visualization of relevant data. However, results are often viewed on a 2D display and as static images. To address these limitations, Venn et al. developed a semi-automated workflow for more enhanced and interactive viewing of CFD results in an immersive virtual environment (IVE). The increasing popularity of virtual and augmented reality IVEs is expected to provide more detailed insights from biomedical CFD simulations and also promote greater collaboration between bioengineers and clinicians.

The studies collected in this Research Topic share the common goal of advancing the personalization of cardiovascular computational modeling: model reliability can be improved by combining cardiovascular imaging with clinical data while increasing the usability of computational analysis in real clinical settings by minimizing computational effort.

Author contributions

All authors listed have made a substantial, direct, and intellectual contribution to the work and approved it for publication. All authors contributed to the article and approved the submitted version.

Funding

AA acknowledges support from the National Science Foundation (2247173, 2246911, 2205265, 2246916). SP acknowledges the support from the Delft Technology Fellowship. IRCCS Policlinico San Donato is a clinical research hospital partially funded by the Italian Ministry of Health.

Conflict of interest

The authors declare that the research was conducted in the absence of any commercial or financial relationships that could be construed as a potential conflict of interest.

Publisher's note

frontiers | Frontiers in Cardiovascular Medicine

ORIGINAL RESEARCH
published: 09 June 2022
doi: 10.3389/fcvm.2022.869259

Assessing the Hemodynamic Impact of Anterior Leaflet Laceration in Transcatheter Mitral Valve Replacement: An *in silico* Study

Keshav Kohli[1], Zhenglun Alan Wei[1,2], Vahid Sadri[1], Andrew W. Siefert[1], Philipp Blanke[3], Emily Perdoncin[4], Adam B. Greenbaum[4], Jaffar M. Khan[5], Robert J. Lederman[5], Vasilis C. Babaliaros[4], Ajit P. Yoganathan[1] and John N. Oshinski[1,6]*

[1] Wallace H. Coulter Department of Biomedical Engineering at the Georgia Institute of Technology and Emory University, Atlanta, GA, United States, [2] Department of Biomedical Engineering, University of Massachusetts Lowell, Lowell, MA, United States, [3] Department of Radiology, St. Paul's Hospital, The University of British Columbia, Vancouver, BC, Canada, [4] Structural Heart and Valve Center, Emory University Hospital, Atlanta, GA, United States, [5] Cardiovascular Branch, Division of Intramural Research, National Heart Lung and Blood Institute, National Institutes of Health, Bethesda, MD, United States, [6] Department of Radiology and Imaging Science, Emory University School of Medicine, Atlanta, GA, United States

OPEN ACCESS

Edited by:
Amirhossein Arzani, Northern Arizona University, United States

Reviewed by:
Zahra K. Motamed, McMaster University, Canada
Wenbin Mao, University of South Florida, United States

***Correspondence:**
Keshav Kohli
keshavkohli@gmail.com

Specialty section:
This article was submitted to Cardiovascular Imaging, a section of the journal Frontiers in Cardiovascular Medicine

Received: *04 February 2022*
Accepted: *22 April 2022*
Published: *09 June 2022*

Citation:
Kohli K, Wei ZA, Sadri V, Siefert AW, Blanke P, Perdoncin E, Greenbaum AB, Khan JM, Lederman RJ, Babaliaros VC, Yoganathan AP and Oshinski JN (2022) Assessing the Hemodynamic Impact of Anterior Leaflet Laceration in Transcatheter Mitral Valve Replacement: An in silico Study. Front. Cardiovasc. Med. 9:869259. doi: 10.3389/fcvm.2022.869259

Background: A clinical study comparing the hemodynamic outcomes of transcatheter mitral valve replacement (TMVR) with vs. without Laceration of the Anterior Mitral leaflet to Prevent Outflow Obstruction (LAMPOON) has never been designed nor conducted.

Aims: To quantify the hemodynamic impact of LAMPOON in TMVR using patient-specific computational (*in silico*) models.

Materials: Eight subjects from the LAMPOON investigational device exemption trial were included who had acceptable computed tomography (CT) data for analysis. All subjects were anticipated to be at prohibitive risk of left ventricular outflow tract (LVOT) obstruction from TMVR, and underwent successful LAMPOON immediately followed by TMVR. Using post-procedure CT scans, two 3D anatomical models were created for each subject: (1) TMVR with LAMPOON (performed procedure), and (2) TMVR without LAMPOON (virtual control). A validated computational fluid dynamics (CFD) paradigm was then used to simulate the hemodynamic outcomes for each condition.

Results: LAMPOON exposed on average 2 ± 0.6 transcatheter valve cells (70 ± 20 mm^2 total increase in outflow area) which provided an additional pathway for flow into the LVOT. As compared to TMVR without LAMPOON, TMVR with LAMPOON resulted in lower peak LVOT velocity, lower peak LVOT gradient, and higher peak LVOT effective orifice area by 0.4 ± 0.3 m/s (14 ± 7% improvement, p = 0.006), 7.6 ± 10.9 mmHg (31 ± 17% improvement, p = 0.01), and 0.2 ± 0.1 cm^2 (17 ± 9% improvement, p = 0.002), respectively.

Conclusion: This was the first study to permit a quantitative, patient-specific comparison of LVOT hemodynamics following TMVR with and without LAMPOON.

The LAMPOON procedure achieved a critical increment in outflow area which was effective for improving LVOT hemodynamics, particularly for subjects with a small neo-left ventricular outflow tract (neo-LVOT).

Keywords: transcatheter mitral valve replacement (TMVR), LAMPOON, left ventricular outflow tract obstruction, neo-LVOT, computational fluid dynamics (CFD), computed tomography (CT), personalized computational modeling

INTRODUCTION

Left ventricular outflow tract (LVOT) obstruction is a prevalent and potentially fatal complication of transcatheter mitral valve replacement (TMVR) caused by displacement of the anterior leaflet toward the ventricular septum (1). Laceration of the Anterior Mitral leaflet to Prevent Outflow Obstruction (LAMPOON) is a catheter-based technique designed to alleviate the risk of obstruction by mimicking surgical anterior leaflet resection. The optimal result of the LAMPOON procedure is a complete midline laceration of the anterior leaflet which, following TMVR, exposes open cells of the transcatheter valve. These exposed cells are thought to permit additional blood flow through the LVOT and decrease the risk of obstruction (2). LAMPOON is considered for patients who have a predicted residual LVOT neo-left ventricular outflow tract (neo-LVOT) area <200 mm^2 and are therefore anticipated to have significant LVOT obstruction from TMVR (3).

Despite the growing clinical experience with this technique, a controlled clinical trial comparing the outcomes of patients undergoing TMVR with vs. without LAMPOON has never been designed nor conducted. It would be impossible to conduct such a trial in which the control intervention (i.e., TMVR without LAMPOON) would be anticipated to cause immediate LVOT obstruction following valve implantation. Thus, while the LAMPOON technique has been shown to be safe and feasible, its impact on left ventricular outflow hemodynamics has never been investigated.

For this purpose, we conducted a computational (*in silico*) controlled study of TMVR with LAMPOON vs. TMVR without LAMPOON. We used a validated *in silico* approach using post-procedure computed tomography (CT) scans from subjects at prohibitive risk of LVOT obstruction who successfully underwent TMVR with LAMPOON (4). 3-D anatomical and flow information were extracted from the CT datasets and used as inputs into personalized computational fluid dynamics (CFD) models. For each subject, hemodynamics of TMVR with and without LAMPOON were simulated and compared. We *hypothesized* that LAMPOON improves flow dynamics through the LVOT in patients with a small neo-LVOT.

Abbreviations: CFD, computational fluid dynamics; CT, computed tomography; LAMPOON, intentional laceration of the anterior mitral leaflet to prevent left ventricular outflow tract obstruction; LVOT, left ventricular outflow tract; TMVR, transcatheter mitral valve replacement.

MATERIALS AND METHODS

LAMPOON Trial Dataset

De-identified subject data from the LAMPOON investigational device exemption trial (NCT03015194) were retrospectively evaluated under an Institutional Review Board approved protocol (4). All subjects in that trial (N = 30) were considered at prohibitive risk for TMVR-related LVOT obstruction based on a predicted end-systolic neo-LVOT area of <200 mm^2. Subjects underwent a valve-in-ring or valve-in-mitral annular calcification procedure with the SAPIEN 3 valve (Edwards Lifesciences, Irvine, CA, United States) with retrograde LAMPOON prior to valve implantation. The LAMPOON technique and 30-day clinical outcomes have been previously reported (2, 4). Briefly, this technique involves three main steps: (1) anterior leaflet traversal with a guidewire, followed by (2) leaflet laceration by electrifying and pulling the guidewire from base to tip, immediately followed by (3) TMVR. Complete details on the utilized retrograde technique and newer LAMPOON technique iterations were recently described (5).

Selection of Study Cohort

Inclusion criteria for this study were: (1) the availability of a post-procedure, multi-phase CT scan with contrast-enhancement, and (2) a splayed anterior leaflet that was visible on post-procedure CT and exposed cells of the implanted transcatheter valve. Of the thirty subjects in the LAMPOON investigational device exemption trial, sixteen subjects did not have adequate visualization of the anterior mitral leaflet on the post-procedure CT scan due to image quality, and two subjects did not have an available post-procedure CT due to patient death. Of the remaining twelve subjects, four had CTs in which we could not visualize exposed cells of the transcatheter valve, despite a successful anterior leaflet laceration. Thus, eight subjects were selected for the present study who had a splayed anterior leaflet which exposed open cells of the implanted transcatheter valve, as verified on post-procedure CT. These eight subjects were at risk of a *fixed* LVOT obstruction from TMVR due to a small predicted neo-LVOT, and not a *dynamic* obstruction due to a long anterior leaflet.

Post-procedure Computed Tomography Datasets

Contrast-enhanced, multi-phase CT scans were acquired after the procedure, either pre-discharge or within 30-days of follow-up. CT images were reconstructed in 10% intervals over

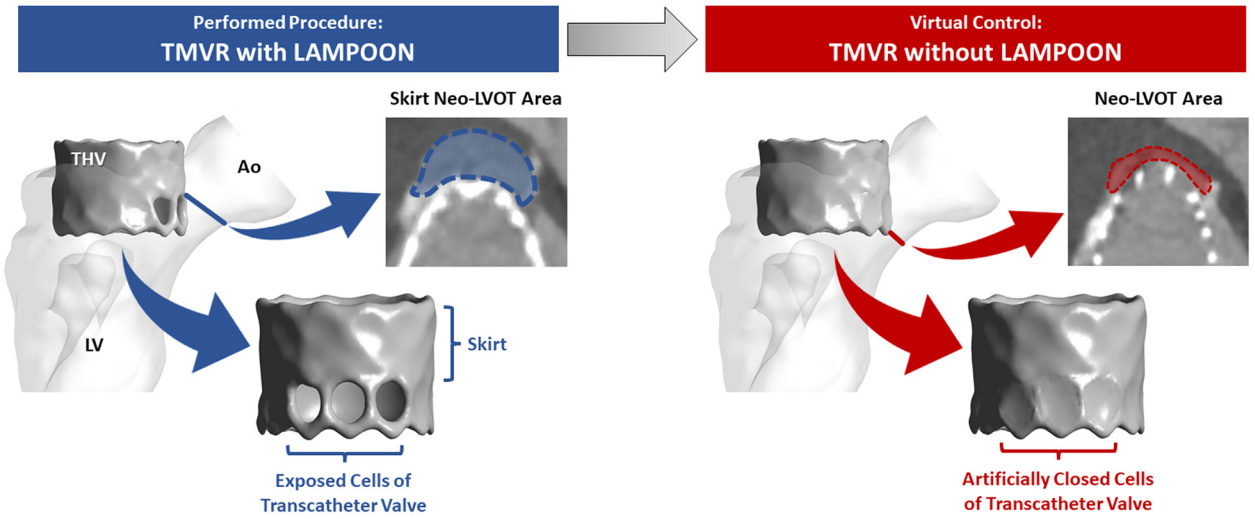

FIGURE 1 | 3D anatomical models created for each subject. The left model represents the actual performed procedure (TMVR with LAMPOON). In this model, the left ventricular anatomy and implanted transcatheter valve geometry were segmented directly from the post-procedure CT dataset. The number and location of transcatheter valve cells exposed by LAMPOON were modeled based on visualization of the anterior leaflet splay in the post-procedure CT dataset. To simulate a "virtual control" procedure in which LAMPOON was not performed (TMVR without LAMPOON), we *artificially* closed the exposed cells of the transcatheter valve as shown in the right model. Ao, aorta; LV, left ventricle; THV, transcatheter heart valve.

the cardiac cycle within <1.0-mm slice thickness. Mimics 20.0 (Materialize, Leuven, Belgium) image post-processing software was used to generate 3-D models of the left ventricle and aorta using previously described segmentation techniques (6). The left ventricular volume was segmented from the CT images for all phases across the cardiac cycle, and the time rate of change in volume was calculated to provide time-varying flow rate. This method for deriving flow rate from left ventricular volumes has been described previously (7).

3D Models Created for Each Subject

Two different 3D models were created for each subject using the post-procedure CT datasets. The first model represented "TMVR with LAMPOON." In this model, the *actual* implanted transcatheter valve and splayed anterior leaflet were reconstructed in 3D from the post-procedure CT (**Figure 1**, left). These reconstructions of the implanted valve therefore incorporated the *actual* valve deployment depth, angulation, and expansion characteristics. The positions of transcatheter valve cells exposed by LAMPOON were identified visually on the post-procedure CT, and these exposed cells were intentionally left patent in this model.

The second model represented "TMVR without LAMPOON." In this model, the exposed cells of the transcatheter valve were *artificially closed*, mimicking a completely intact anterior leaflet geometry (**Figure 1**, right). Since the model of "TMVR with LAMPOON" mimicked the performed interventional procedure, the model of "TMVR without LAMPOON" was considered to mimic a control "virtual procedure." Both models were designed to be anatomically identical other than the presence or absence of the splayed anterior leaflet.

Measurement of Neo-Left Ventricular Outflow Tract and Skirt Neo-Left Ventricular Outflow Tract Area

Computed tomography datasets were utilized to measure the neo-LVOT and skirt neo-LVOT area. The neo-LVOT area was measured in a plane perpendicular to the LVOT and located at the narrowest point along the residual LVOT after TMVR (**Figure 1**, right). Following LAMPOON, the transcatheter valve skirt still protrudes into the LVOT, creating a narrowing at the transcatheter valve skirt called the "skirt" neo-LVOT (8). **Figure 1** illustrates differences between the neo-LVOT and skirt neo-LVOT. The skirt neo-LVOT area was measured in a plane perpendicular to the LVOT and located at the level of the transcatheter valve skirt (**Figure 1**, left). Both neo-LVOT and skirt neo-LVOT area measurements were first predicted on baseline CT, and then measured on post-procedure CT.

Computational Fluid Dynamics Simulations

Computational fluid dynamics (CFD) is a method used to simulate fluid flow with computer modeling. In this study, we utilized a validated CFD workflow for simulating patient-specific LVOT hemodynamics based on cardiac CT data (7). Patient-specific CFD simulations were performed for both modeled conditions (TMVR with and without LAMPOON) for each subject. The output of these simulations provided spatially varying velocity and pressure data across the entire left ventricle and aorta. The workflow used for performing the CFD simulations has been previously described and validated against clinical measurements from Doppler echocardiography (7). The average difference between CFD-derived and

echocardiography-derived peak LVOT velocity measurements was <10%, indicating a good agreement between the CFD simulations and clinical measurements. This CFD workflow is briefly summarized below.

All CFD simulations were performed for the peak-systolic phase of the cardiac cycle. The cardiac phase of the post-procedure CT scan which most closely coincided with the peak systolic flow rate was selected for creating a 3D model of the left heart anatomy and implanted transcatheter valve. For each 3D model, an inlet was placed at the left ventricular apex, and an outlet was placed at the sino-tubular junction. 3-Matic 12.0 (Materialize, Leuven, Belgium) computer aided design software was used to place a virtual wall at the level of the bioprosthetic valve leaflets to prevent regurgitant flow. A volumetric mesh was then generated using ANSYS Fluent Meshing (Ansys, Inc. Canonsburg, PA, United States). This mesh included polyhedral elements with an edge length of 0.5 mm, and a prismatic boundary layer mesh (10 layers with geometric growth of 1.05) which was applied on the left ventricular wall. The total number of mesh elements per patient model was on average ∼1,800,000 elements. Transition-to-turbulence characteristics in the flow field were accounted for using the scale-adaptive simulation

TABLE 1 | Baseline, procedural, and post-procedural characteristics.

	Subject 1	Subject 2	Subject 3	Subject 4	Subject 5	Subject 6	Subject 7	Subject 8
Baseline characteristics								
Age, years	85	82	50	75	84	80	83	61
Gender	Female	Female	Female	Female	Female	Female	Female	Female
Ejection fraction, %	61	65	56	53	54	67	67	70
LVEDV, mL from echo	75	56	48	40	36	78	65	27
Body surface area, m^2	1.73	1.81	1.77	1.68	1.57	1.99	1.8	1.43
Mitral pathology	MR	MS	MS	MS	MS	MR	MR	MS
Aortic stenosis	None	Mild	None	None	None	None	None	Mild
Neo-LVOT area at end-systole (predicted), mm^2	111	57	143	81	108	168	59	55
Skirt neo-LVOT area at end-systole (predicted), mm^2	241	278	210	247	236	333	216	189
Procedural characteristics								
TMVR setting	Valve-in-Ring	Valve-in-MAC	Valve-in-Ring	Valve-in-MAC	Valve-in-MAC	Valve-in-MAC	Valve-in-MAC	Valve-in-MAC
Successful leaflet laceration	Yes	Yes	Yes	Yes	Yes	Yes	Yes	Yes
Successful TMVR	Yes	Yes	Yes	Yes	Yes	Yes	Yes	Yes
Implanted SAPIEN size, mm	26	29	23	29	29	29	29	29
No. of THV cells exposed by splayed leaflet	1.5	2	2	1	3	2	2.5	2
Combined area of THV cells exposed by splayed leaflet, mm^2	41	86	55	45	87	88	88	70
Deployment depth, % in LV	53	77	46	85	71	58	59	39
Para-valvular regurgitation	None	Mild	None	Trace	Mild	None	None	Trace
Post-procedural characteristics								
Time of post-procedure CT scan	30-day	30-day	Pre-discharge	Pre-discharge	30-day	30-day	Pre-discharge	30-day
Post-procedure peak flow rate, L/min	13.3	18.8	21.3	15.3	20.3	37.8	24.8	30.5
Neo-LVOT area at end-systole, mm^2	211	187	293	42	19	223	30	221
Neo-LVOT area at peak-systole, mm^2	266	256	379	153	129	250	49	337
Skirt neo-LVOT area at end-systole, mm^2	320	427	307	145	211	341	182	316
Skirt neo-LVOT area at peak-systole, mm^2	344	418	351	176	231	313	162	358

Echocardiography was used to derive ejection fraction, left ventricular end-diastolic volume, aortic stenosis severity, and para-valvular regurgitation severity. The peak flow rate was obtained from the time-varying CT-derived left ventricular volumes. CT, computed tomography; LV, left ventricle; LVEDV, left ventricular end-diastolic volume; MAC, mitral annular calcification; MR, mitral regurgitation; MS, mitral stenosis; THV, transcatheter heart valve; TMVR, transcatheter mitral valvereplacement.

turbulence model. Turbulence boundary conditions included (1) hydraulic diameter (which is the inlet diameter, D_H) and (2) turbulence intensity (approximated using $0.16 \times Re_D{}^{-0.125}$, where Re_D is the Reynolds number based on the patient-specific flow rate and the hydraulic diameter).

The time-varying left ventricular volume curve (obtained from the post-procedure CT scan) was used to calculate a peak systolic flow rate, which was then prescribed as the inlet boundary condition. The outlet boundary condition was set to a zero-reference pressure. All structures were assumed to be rigid and non-permeable, and a no-slip boundary condition was applied at the walls. Blood was modeled as a single-phase Newtonian fluid with a density of 1060 kg/m^3 and dynamic viscosity of 0.0034 poise. The 3-D Navier-Stokes equations were solved in ANSYS Fluent 19.0 using the SIMPLE scheme for pressure-velocity coupling. A bounded second-order implicit transient formulation was utilized with a time step of 0.001 s. The solution was considered converged when residuals in momentum and turbulence variables declined below 10^{-4}. Three-thousand time steps were simulated, with the last time step being used for data analysis.

Obtaining Simulated Hemodynamics

Hemodynamic metrics were extracted from each CFD simulation, including the peak LVOT velocity (V_{peak}), peak LVOT pressure gradient (ΔP_{peak}), and peak LVOT effective orifice area (EOA_{peak}). To calculate ΔP_{peak}, the ventricular

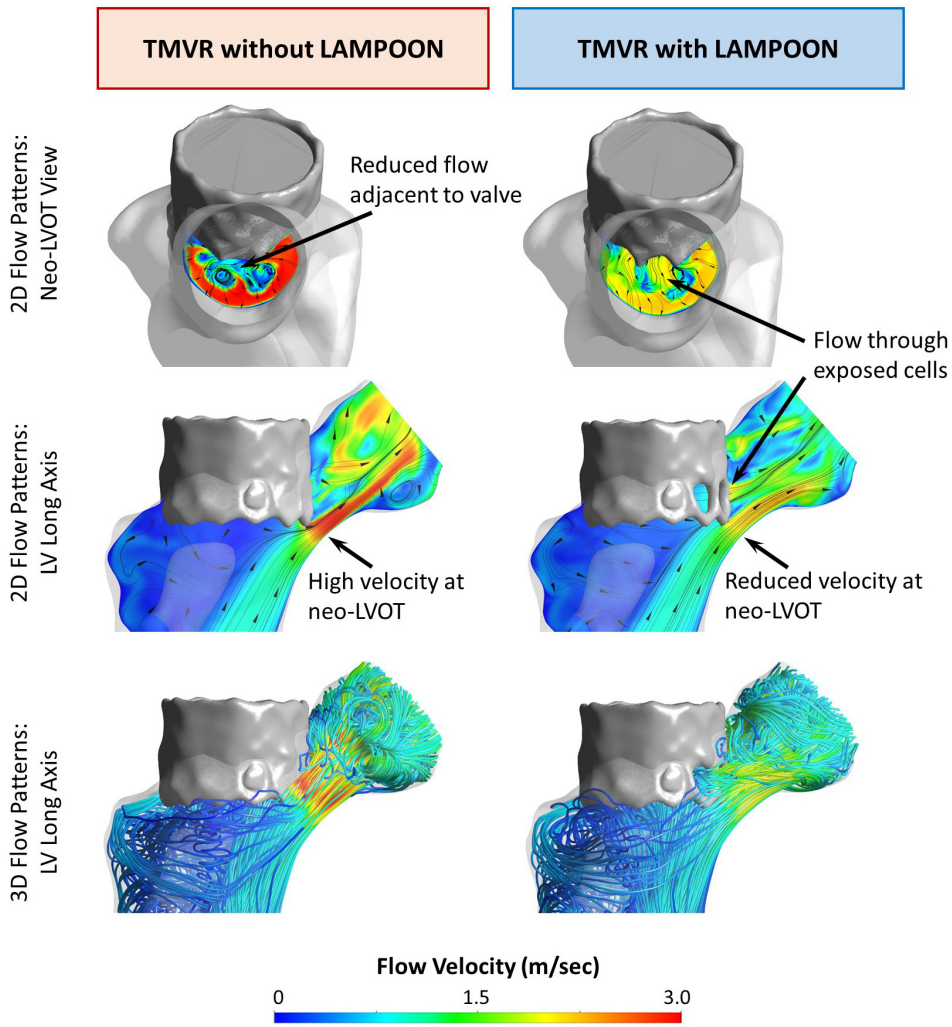

FIGURE 2 | Effect of LAMPOON on left ventricular flow patterns. Simulated flow patterns for a representative subject (Subject 5) are shown in color maps (red = highest velocity, blue = lowest velocity) with streamlines. The left column shows the flow simulation for the virtual control procedure (TMVR without LAMPOON). For this condition, all flow is directed through the narrowed residual LVOT (neo-LVOT), resulting in a narrowed and high-velocity outflow jet. Additionally, there is a region of reduced flow in the immediate vicinity of the valve (upper left image). The right column shows the flow simulation for the actual performed procedure (TMVR with LAMPOON). For this condition, additional flow occurs through exposed cells of the transcatheter valve due to LAMPOON. Following LAMPOON, the velocity of flow through the neo-LVOT is reduced, and there is improved flow in the immediate vicinity of the valve (upper right image). Ao, aorta; LV, left ventricle; neo-LVOT, neo-left ventricular outflow tract; THV, transcatheter heart valve.

pressure was derived from an average pressure across the model inlet (LV apical plane), and the aortic pressure was derived from an average pressure across the model outlet (sino-tubular junction plane). ΔP_{peak} was then calculated as the difference between the ventricular and aortic pressures. EOA_{peak} was calculated as the ratio of the peak volumetric flow rate (Q_{peak}) to the peak outflow velocity (V_{peak}) (9).

Data Analysis

All data analyses were performed with the MedCalc statistical software package (MedCalc, Ostend, Belgium). Simulated hemodynamics for each subject were compared between the two modeled conditions (TMVR with and without LAMPOON) using the paired samples *t*-test or Wilcoxon test for parametric and non-parametric data, respectively. Statistical significance was defined as $p < 0.05$.

RESULTS

Subject Characteristics

Baseline, procedural and post-procedural characteristics are shown in **Table 1**. All subjects were considered to be at prohibitive risk of LVOT obstruction based on small ventricular anatomy and small LVOT clearance (end-systolic neo-LVOT area <200 mm^2 as predicted on baseline CT), and therefore were considered candidates for the LAMPOON procedure. All subjects included were female, likely due to the selection of patients with small ventricular anatomy for LAMPOON. The indication for mitral valve replacement was mitral regurgitation in three subjects, and mitral stenosis in five subjects.

All subjects underwent successful midline anterior leaflet laceration (LAMPOON procedure) immediately followed by investigational use of the SAPIEN 3 transcatheter heart valve in

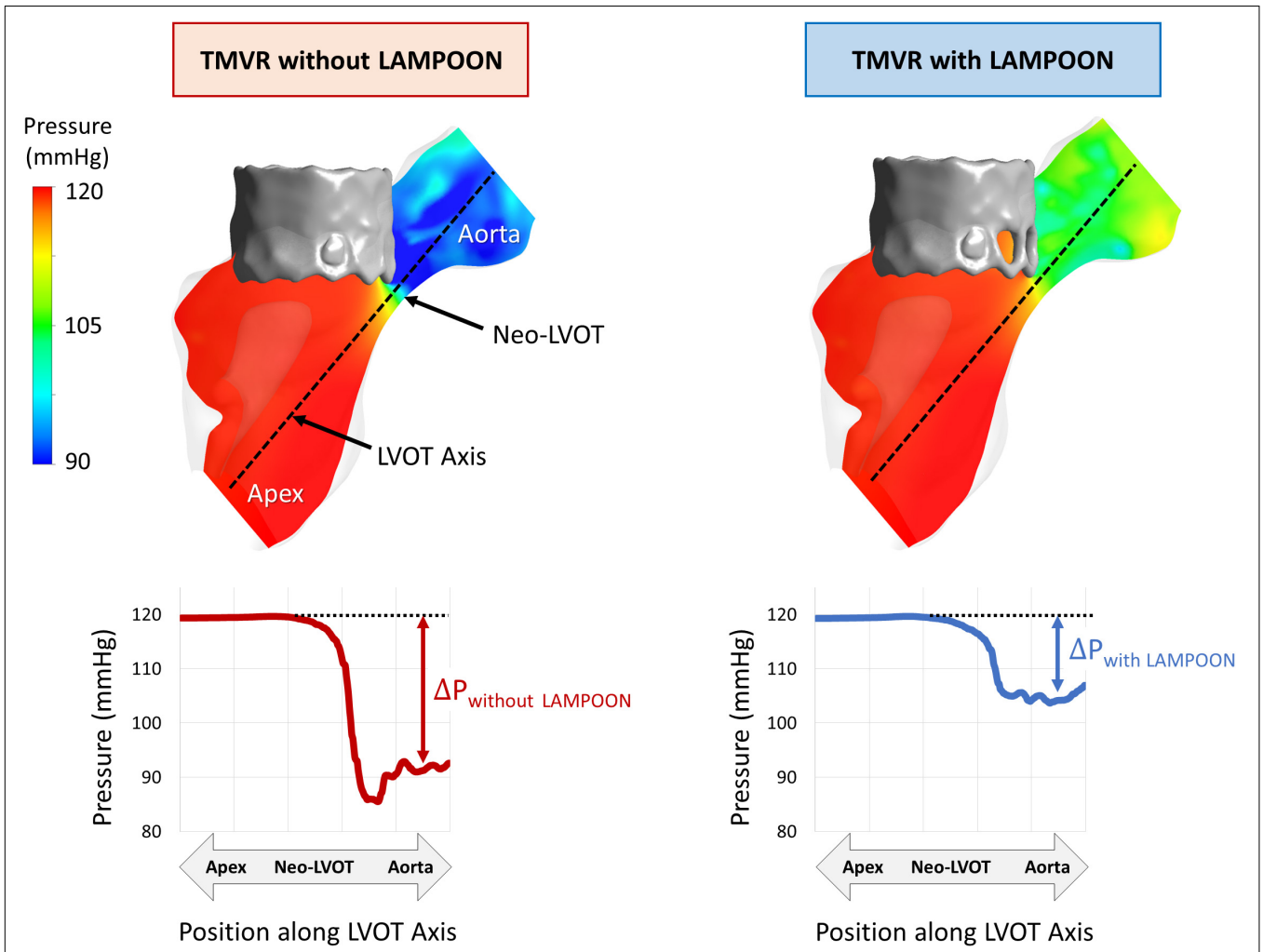

FIGURE 3 | Effect of LAMPOON on left ventricular pressure fields. Simulated pressure fields for a representative subject (Subject 5) are shown in color maps (red = highest pressure, blue = lowest pressure). The left column shows the simulated pressure drop at the LVOT for the virtual control procedure (TMVR without LAMPOON). The right column shows the simulated pressure drop at the LVOT for the actual performed procedure (TMVR with LAMPOON). The simulated LVOT gradient is substantially reduced following LAMPOON. In this subject, LAMPOON exposed three cells of the transcatheter valve, corresponding to a total increase in flow area of 87 mm^2.

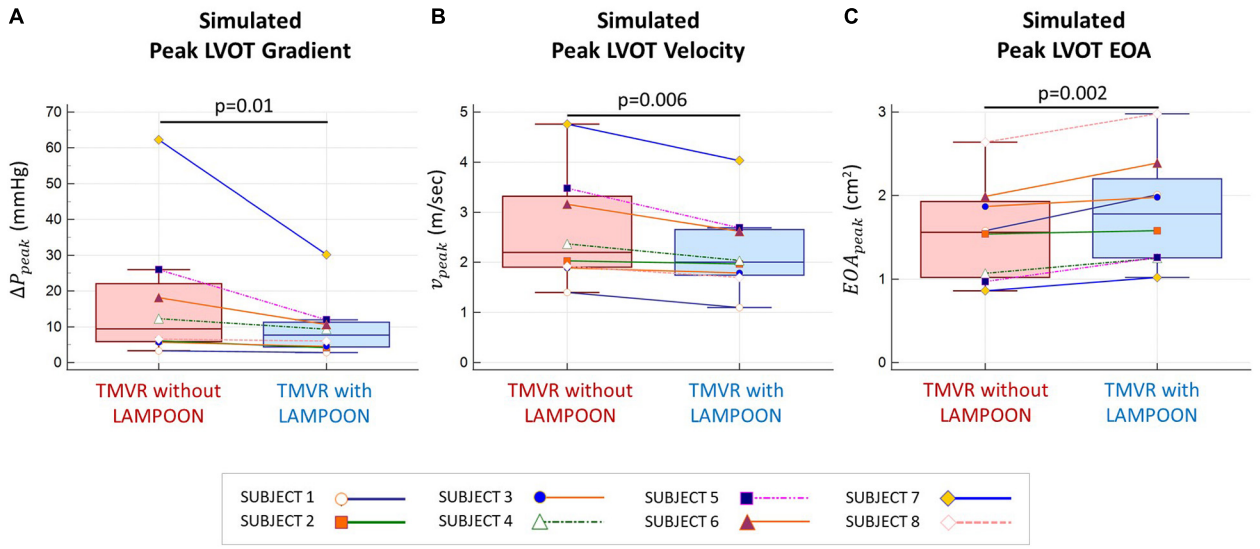

FIGURE 4 | Comparison of simulated hemodynamics following TMVR with and without LAMPOON. Simulated hemodynamics following TMVR with LAMPOON were superior to those following TMVR without LAMPOON for all subjects. Following LAMPOON, the simulated peak outflow gradient (ΔP_{peak}) and velocity (v_{peak}) decreased in all subjects ($p < 0.05$ for both comparisons) **(A,B)**. Additionally, the simulated peak effective orifice area (EOA_{peak}) increased following LAMPOON in all subjects ($p < 0.05$) **(C)**. LVOT, left ventricular outflow tract.

the mitral position. The setting of valve replacement was valve-in-ring for two subjects, and valve-in-mitral annular calcification for six subjects. Following valve implantation, all subjects had trace or no para-valvular regurgitation. The number of transcatheter valve cells exposed by the splayed anterior mitral leaflet ranged from 1 to 3 cells. The combined area of the exposed cells ranged from 41 to 88 mm^2, and the area of a single exposed cell was on average 36 ± 7 mm^2. Valve deployment depth (percent deployed in left ventricle) ranged from 39 to 85%. At follow up, the peak systolic flow rate (calculated from the post-procedure CT-derived LV volumes) ranged from 13 to 38 L/min.

Effect of LAMPOON on Simulated Left Ventricular Flow Patterns

Simulations of left ventricular flow patterns are depicted by color maps (red = highest velocity, blue = lowest velocity) with streamlines for a representative subject (Subject 5) (**Figure 2**). For the condition of the virtual control procedure (TMVR without LAMPOON), flow acceleration occurred at the level of the neo-LVOT, resulting in a narrowed outflow jet (**Figure 2**, left panel). In this condition, the neo-LVOT was shown to be the predominant geometric narrowing for systolic flow. All forward flow was directed through the neo-LVOT, causing an increase in velocity at this location due to the reduced flow area. Additionally, there was a region of reduced flow adjacent to the transcatheter valve due to the narrowed outflow jet, as noted in the neo-LVOT short-axis view (**Figure 2**, upper left image).

For the condition of the performed interventional procedure (TMVR with LAMPOON), flow occurred both through the neo-LVOT and through exposed cells of the transcatheter valve (**Figure 2**, right panel). LAMPOON provided an additional source of flow into the LVOT, leading to a reduction in outflow velocity due to the increased flow area. The region of reduced flow adjacent to the valve in the case of TMVR without LAMPOON was decreased in the case of TMVR with LAMPOON, thus reflecting flow closer to normal flow physiology (**Figure 2**, upper right image). Following TMVR with LAMPOON, the main impediment to forward flow was observed to be the transcatheter valve skirt which still projected into the native LVOT.

Effect of LAMPOON on Simulated Left Ventricular Pressure Fields

Simulations of left ventricular pressure fields are depicted by color maps (red = highest pressure, blue = lowest pressure) for a representative subject (Subject 5) (**Figure 3**). For the condition of the virtual control procedure (TMVR without LAMPOON), there was a substantial pressure drop which occurred at the location of the neo-LVOT, corresponding to the location of geometric narrowing. For the condition of the performed interventional procedure (TMVR with LAMPOON), the simulated pressure drop was reduced at the neo-LVOT due to the increase in flow area from the splayed anterior leaflet. In this subject, the splayed anterior leaflet from LAMPOON exposed three cells of the transcatheter valve, corresponding to a total increase in flow area of 87 mm^2.

Comparison of Simulated Hemodynamics

As compared to TMVR without LAMPOON, TMVR with LAMPOON resulted in lower V_{peak}, lower ΔP_{peak}, and higher EOA_{peak} by 14 ±7% ($p = 0.006$), 31 ±17% ($p = 0.01$), and 17 ±9% ($p = 0.002$), respectively (**Figure 4**). Following LAMPOON, V_{peak} decreased from 2.6 ±1.1 m/s to 2.2 ±0.9 m/s, ΔP_{peak}

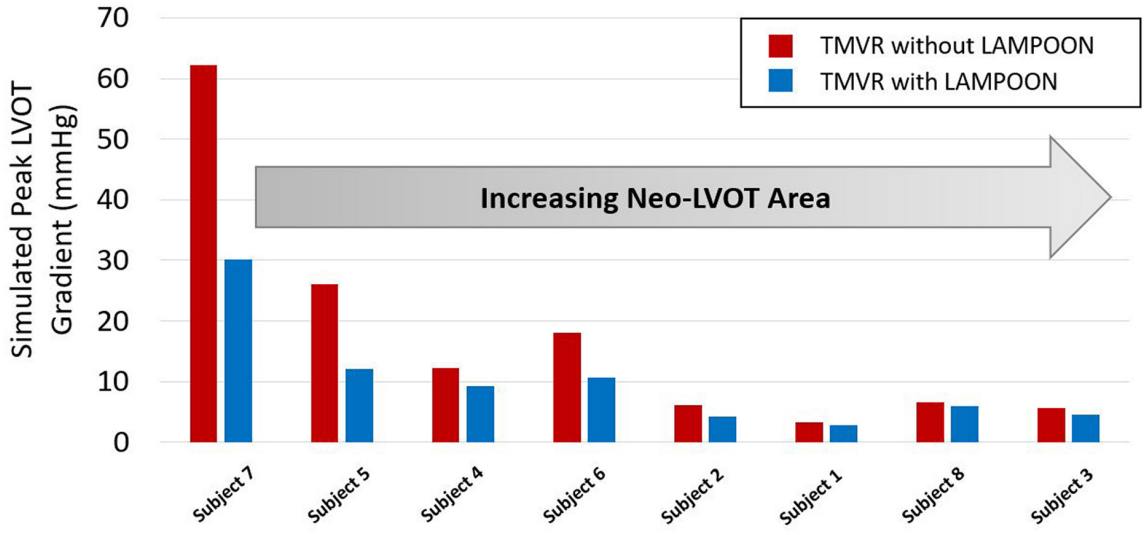

Neo-LVOT Area at Peak Flow (mm^2)	49	129	153	250	256	266	337	379
Skirt Neo-LVOT Area at Peak Flow (mm^2)	162	231	176	313	418	344	358	351
Peak Flow Rate (L/min)	24.8	20.3	15.3	37.8	18.8	13.3	30.5	21.3

FIGURE 5 | Relationship between post-procedure neo-LVOT area and hemodynamic improvement with LAMPOON. Subjects with a smaller post-procedure neo-LVOT area experienced a greater hemodynamic improvement with LAMPOON. The largest improvement in simulated LVOT gradient (32 mmHg reduction in gradient) was observed in the subject with the smallest post-procedure neo-LVOT area (49 mm^2). As neo-LVOT area increased beyond 250 mm^2, there was a smaller hemodynamic improvement with LAMPOON (<2 mmHg reduction in gradient). Neo-LVOT area = cross-sectional area at the narrowest point of the neo-left ventricular outflow tract. Skirt neo-LVOT area = cross-sectional area of the neo-left ventricular outflow tract measured at the level of the transcatheter valve skirt.

decreased from 17.5 ±19.6 mmHg to 10.0 ± 8.8 mmHg, and EOA_{peak} increased from 1.6 ±0.6 cm^2 to 1.8 ±0.7 cm^2 ($p < 0.05$ for all comparisons). Subject 7 had a substantially larger simulated LVOT gradient than the other subjects and could be considered an outlier (**Figure 4A**). However, when we excluded this subject from the analysis, we observed the same significant trend for the effect of LAMPOON on simulated LVOT gradient ($p = 0.02$).

Relationship Between Neo-Left Ventricular Outflow Tract Area and LAMPOON Efficacy

LAMPOON was most effective in subjects who had a small post-procedure neo-LVOT area, as measured on post-procedure CT (**Figure 5**). The largest hemodynamic improvement with LAMPOON was observed in Subject 7 who had the smallest post-procedure neo-LVOT area across all subjects (49 mm^2). This subject experienced a 32 mmHg reduction in the simulated LVOT gradient following LAMPOON. 3D flow patterns in this subject were also shown to substantially improve following LAMPOON, as evidenced by more centrally directed flow along the LVOT (**Supplementary Video 1**).

As the post-procedure neo-LVOT area increased beyond 250 mm^2, LAMPOON began to demonstrate a smaller hemodynamic effect. For all subjects with a post-procedure neo-LVOT area greater than 250 mm^2, the simulated LVOT gradient reduced by less than 2 mmHg following LAMPOON. This finding is also illustrated in **Figure 6** which shows simulations of flow patterns in two representative subjects with different neo-LVOT dimensions.

DISCUSSION

This study evaluated the hemodynamic impact of LAMPOON in TMVR using patient-specific *in silico* models. The main finding was that LAMPOON improved outflow hemodynamics in all subjects, with a larger hemodynamic effect in the setting of a smaller post-procedure neo-LVOT area. Because of the impossibility of performing a controlled clinical trial of TMVR with vs. without LAMPOON, the present *in silico* study is the first to provide quantitative insight into the hemodynamic effect of LAMPOON.

Left ventricular outflow tract obstruction is a significant problem for the broader adoption of TMVR as a therapy for

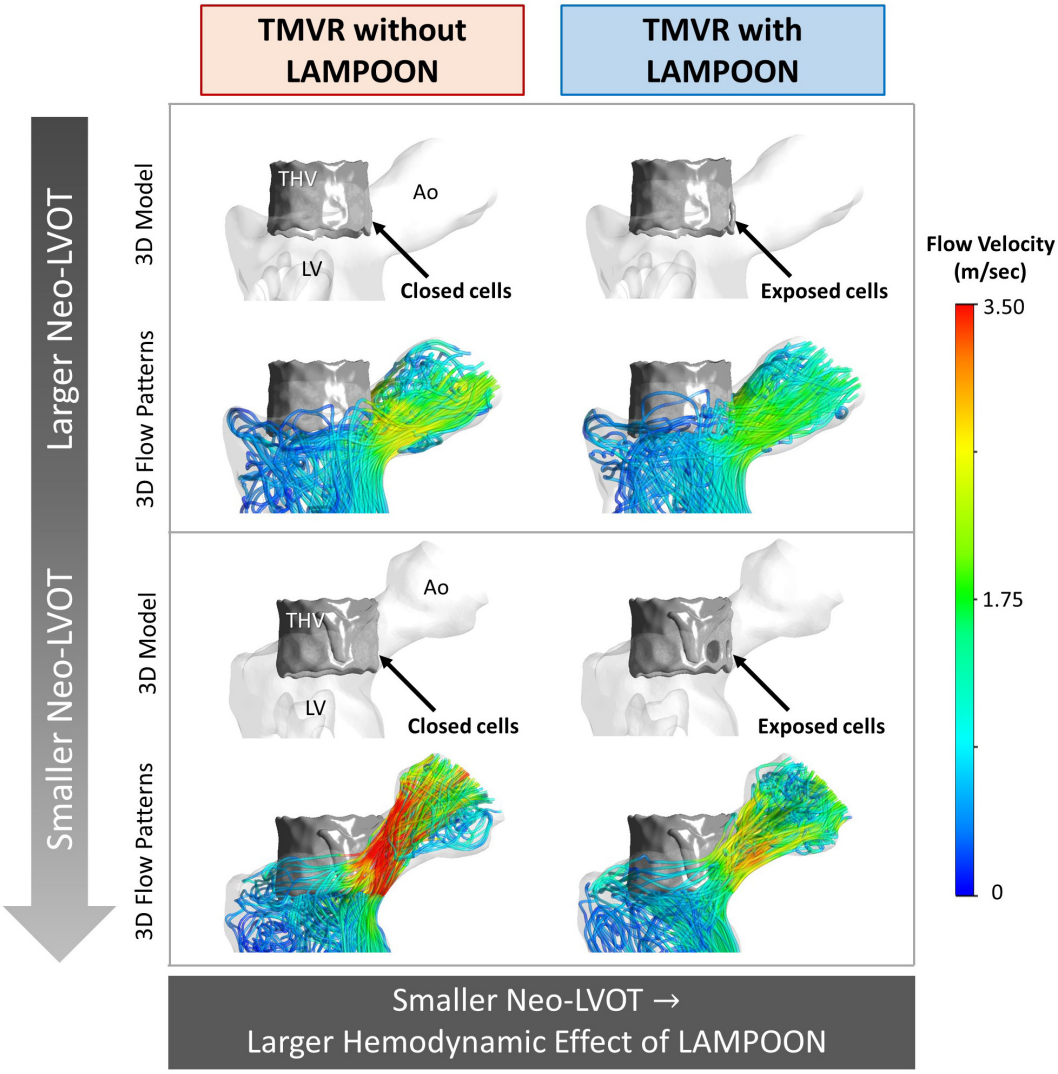

FIGURE 6 | Flow simulations demonstrating the relationship between neo-LVOT size and LAMPOON efficacy. Two representative subjects are shown, where the subject shown in the top panel (Subject 6) has a larger neo-LVOT area as compared to the subject shown in the bottom panel (Subject 7). 3D models and simulated flow patterns are shown for the conditions of TMVR with and without LAMPOON. As neo-LVOT area decreases, the hemodynamic effect of LAMPOON increases. The total area of the transcatheter valve cells exposed by the splayed anterior leaflet were identical in both subjects (88 mm^2). Ao, aorta; LV, left ventricle; neo-LVOT, neo-left ventricular outflow tract; THV, transcatheter heart valve.

patients with mitral valve disease who are not otherwise surgical candidates. The risk of LVOT obstruction is a primary reason for screen failure in TMVR device trials (10). For patients at prohibitive risk of obstruction, LAMPOON is a potential option to mitigate the risk of obstruction. To date, all clinical studies of LAMPOON to have been single-arm studies to assess clinical safety and feasibility of the technique (4, 11, 12).

The hemodynamic impact of LAMPOON in TMVR has not previously been investigated since patients who are considered for LAMPOON are anticipated to be at prohibitive risk of LVOT obstruction and therefore are not considered anatomical candidates for the control procedure (TMVR without LAMPOON) which would be needed to compare hemodynamic outcomes. The only way to quantitatively assess the hemodynamic impact of the LAMPOON procedure would be to perform a controlled *in vivo* (animal), *in vitro* (bench), or *in silico* (computational) study. *In vivo* studies are not always feasible due to procedural and anatomical limitations of the animal model. *In vitro* studies are more feasible but are also often very tedious to perform and can be costly. We chose to perform a controlled *in silico* study, which allowed us to use each subject as their own virtual comparator.

In silico modeling revealed that LAMPOON leads to a consistent improvement in hemodynamics following TMVR. Mechanistically, splaying the anterior mitral leaflet allows additional flow into the LVOT which decreases LVOT velocity and pressure gradient, while increasing the effective orifice area. The average number of transcatheter valve cells exposed by

LAMPOON was 2 ±0.6 cells which corresponded to a total increase in outflow area of 70 ±20 mm^2. On average, the area of a single exposed cell was 36 ±7 mm^2. This small increment in outflow area led to a critical improvement in simulated hemodynamics, particularly for subjects with a smaller post-procedure neo-LVOT area (**Figure 5**). In this study, TMVR without LAMPOON was modeled by artificially closing the exposed transcatheter valve cells to mimic an intact anterior leaflet. However, in the clinical setting, the anterior leaflet may not only drape the cells but also hang lower beyond the valve frame. Thus, the actual improvement in hemodynamics with LAMPOON may be even more dramatic than what was calculated in this study.

Flow simulations in this study also validated the importance of the skirt neo-LVOT concept when predicting the risk of LVOT obstruction following TMVR with LAMPOON. The skirt neo-LVOT area is measured at the level of the transcatheter valve skirt, and represents the main impediment to forward flow following TMVR with anterior leaflet resection or LAMPOON (8). In the subject with the smallest post-procedure neo-LVOT area (Subject 7), there was the largest hemodynamic improvement with LAMPOON (>30 mmHg decrease in simulated LVOT gradient). However, despite this improvement, this subject still had a 30 mmHg simulated LVOT gradient post-LAMPOON due to a small skirt neo-LVOT area (162 mm^2). While initial clinical data suggested a skirt neo-LVOT area of <150 mm^2 should be avoided to prevent significant LVOT obstruction (catheterization gradient >30 mmHg), a more recent study from our group has shown that a skirt neo-LVOT area >180 mm^2 is ideal to ensure survival with measurable clinical benefit (e.g., improvement in Kansas City Cardiomyopathy Questionnaire Score) (9). Thus, flow simulations in this study corroborate the clinical observation that LVOT obstruction may still occur following LAMPOON in the case of a small skirt neo-LVOT, and confirm that the skirt neo-LVOT should be routinely and carefully evaluated prior to performing TMVR with LAMPOON.

This study also highlighted that there can be differences between the *anticipated* risk of LVOT obstruction and the *actual* risk of LVOT obstruction in patients undergoing TMVR. All subjects in this study were initially thought to be at prohibitive risk for obstruction based on a predicted end-systolic neo-LVOT area of <200 mm^2 measured on baseline CT. However, the neo-LVOT area measured on post-procedure CT was found to be substantially larger (>100 mm^2) than the predicted neo-LVOT area at baseline in four subjects (Subjects 1, 2, 3, and 8) (**Table 1**), indicating that the actual risk of obstruction was substantially lower than the anticipated risk of obstruction. These four subjects experienced the least simulated hemodynamic benefit with LAMPOON. These data suggests that, in patients undergoing a valve-in-ring or valve-in-mitral annular calcification procedure, the anticipated risk of obstruction may in fact differ from the actual risk based on factors such as valve deployment depth (more atrial vs. more ventricular) or the valve deployment orientation (coaxial vs. canted with respect to the mitral valve). Personalized computational modeling may eventually help in better predicting the hemodynamic outcome of patients (13), and should account for a range of valve deployment scenarios. Recent interventional techniques have also enabled more predictable deployment of the transcatheter valve in the predicted landing zone, and may help improve future predictions of LVOT obstruction risk (14, 15).

In silico studies have the potential to provide key insights into the performance of novel interventional procedures such as LAMPOON which may be impossible to evaluate in a controlled clinical trial. The advantages of *in silico* studies are to (1) avoid the costs associated with conventional clinical trials, (2) avoid risk to patients, and (3) study unique metrics which may be difficult or impossible to attain in a clinical setting. Within the realm of structural heart disease interventions, prior *in silico* studies have evaluated para-valvular regurgitation in transcatheter aortic valve replacement (16, 17), device size selection for left atrial appendage occlusion (18), and LVOT hemodynamics in the setting of TMVR (7, 19, 20). In the future, *in silico* trials may also be used to supplement conventional clinical trial evidence and support the regulatory process of new devices and procedures (21). With appropriate validation, *in silico* data can represent a potentially valuable form of evidence which can be obtained at a reduced cost and without risk to patients (22).

Limitations

This was a retrospective study with a small sample size. As adoption of the LAMPOON technique expands, larger datasets will be needed to corroborate the findings of this study. The modeling of blood flow in this study using CFD may be limited given the assumptions of fixed left ventricular walls with zero wall velocity during peak systole, and steady flow boundary conditions. Since the pressure gradient across a normal aortic valve should be negligible relative to the gradient across an obstructed LVOT, we did not model an aortic valve in our simulations for simplicity. The anterior mitral leaflet was modeled depending on whether the leaflet could be reliably segmented on the post-procedure CT dataset. The posterior mitral leaflet was not modeled since this leaflet is not affected by the LAMPOON procedure and should not impact flow in the LVOT. The value of our CFD workflow is to provide a simplified, rapid approach to simulate LVOT hemodynamics. This method has been previously validated and has demonstrated good accuracy (<10% error) when compared to clinical hemodynamic measurements (7). Despite the discussed limitations, this study provides unique insight into the hemodynamic effect of LAMPOON which would have been impossible to study in a clinical setting.

CONCLUSION

A controlled *in silico* study was performed to investigate the hemodynamic impact of LAMPOON in TMVR. LAMPOON achieved a critical increment in outflow area which resulted in a consistent improvement in hemodynamic outcomes and 3D flow patterns following TMVR. Patients with a smaller post-procedure neo-LVOT area experienced a greater hemodynamic improvement with LAMPOON. This study demonstrates the

potential for *in silico* studies to evaluate procedures virtually which may improve cost-effectiveness and patient safety as compared to a conventional clinical trial.

DATA AVAILABILITY STATEMENT

Data can be made available upon reasonable request to NHLBI.

ETHICS STATEMENT

All subject data were acquired and analyzed under Institutional Review Board approvals at the National Institutes of Health (NCT03015194). The patients/participants provided their written informed consent to participate in this study.

AUTHOR CONTRIBUTIONS

KK, ZW, VS, RL, VB, AY, and JO: conception and design of the work. EP, AG, JK, RL, and VB: acquisition and compilation of clinical data. KK and ZW: development of methods for computer simulations. KK, ZW, AS, PB, and EP: initial drafting of manuscript. All authors analysis and interpretation of data, critical review of manuscript for important intellectual content, and final approval of manuscript.

FUNDING

This study was supported by American Heart Association Pre-doctoral Fellowship 20PRE35200392 (Kohli) and National Institutes of Health (NIH) grant R01EB027774 (Oshinski).

ACKNOWLEDGMENTS

We would like to acknowledge helpful technical discussions with the members of the Cardiovascular Fluid Mechanics (CFM) Laboratory at Georgia Tech. We gratefully acknowledge Daniel A. Herzka, Ph.D. for de-identifying and compiling the entire cohort of subject image data utilized in this study. We also acknowledge the use of ANSYS software which was provided through an Academic Partnership between ANSYS, Inc. and the CFM Lab. Finally, we acknowledge Vivian Truong for her assistance with cardiac image post-processing.

SUPPLEMENTARY MATERIAL

The Supplementary Material for this article can be found online at: https://www.frontiersin.org/articles/10.3389/fcvm.2022.869259/full#supplementary-material

REFERENCES

1. Yoon SH, Whisenant BK, Bleiziffer S, Delgado V, Dhoble A, Schofer N, et al. Outcomes of transcatheter mitral valve replacement for degenerated bioprostheses, failed annuloplasty rings, and mitral annular calcification. *Eur Heart J.* (2018). 40, 441–451. doi: 10.1093/eurheartj/ehy590 PMID: 30357365
2. Babaliaros VC, Greenbaum AB, Khan JM, Rogers T, Wang DD, Eng MH, et al. Intentional percutaneous laceration of the anterior mitral leaflet to prevent outflow obstruction during transcatheter mitral valve replacement: first-in-human experience. *JACC Cardiovasc Interv.* (2017) 10:798–809. doi: 10.1016/j.jcin.2017.01.035
3. Babaliaros VC, Lederman RJ, Gleason PT, Khan JM, Kohli K, Sahu A, et al. The art of SAPIEN 3 transcatheter mitral valve replacement in valve-in-ring and valve-in-mitral-annular-calcification procedures. *JACC Cardiovasc Interv.* (2021) 14:2195–214. doi: 10.1016/j.jcin.2021.08.044
4. Khan JM, Babaliaros VC, Greenbaum AB, Foerst JR, Yazdani S, McCabe JM, et al. Anterior leaflet laceration to prevent ventricular outflow tract obstruction during transcatheter mitral valve replacement. *J Am Coll Cardiol.* (2019) 73:2521–34. doi: 10.1016/j.jacc.2019.02.076
5. Case BC, Lisko JC, Babaliaros VC, Greenbaum AB, Satler L, Ben-Dor I, et al. Lampoon techniques to prevent or manage left ventricular outflow tract obstruction in transcatheter mitral valve replacement. *Ann Cardiothorac Surg.* (2021) 10:172–9. doi: 10.21037/ACS-2020-MV-25
6. Kohli K, Wei ZA, Yoganathan AP, Oshinski JN, Leipsic J, Blanke P. Transcatheter mitral valve planning and the Neo-LVOT: utilization of virtual simulation models and 3D printing. *Curr Treat Options Cardiovasc Med.* (2018) 20:99. doi: 10.1007/s11936-018-0694-z
7. Kohli K, Wei ZA, Sadri V, Netto T, Lisko JC, Greenbaum AB, et al. A simplified in silico model of left ventricular outflow in patients after transcatheter mitral valve replacement with anterior leaflet laceration. *Ann Biomed Eng.* (2021) 49:1449–61. doi: 10.1007/s10439-021-02740-z
8. Khan JM, Rogers T, Babaliaros VC, Fusari M, Greenbaum AB, Lederman RJ. Predicting left ventricular outflow tract obstruction despite anterior mitral leaflet resection: the "Skirt NeoLVOT.". *JACC Cardiovasc Imaging.* (2018) 11:1356–9. doi: 10.1016/j.jcmg.2018.04.005
9. Kohli K, Wei ZA, Sadri V, Khan JM, Lisko JC, Netto T, et al. Dynamic nature of the LVOT following transcatheter mitral valve replacement with LAMPOON: new insights from post-procedure imaging. *Eur Heart J Cardiovasc Imaging.* (2022) 23:650–62. doi: 10.1093/ehjci/jeab074
10. Coisne A, Pontana F, Tchétché D, Richardson M, Longère B, Vahdat O, et al. Transcatheter mitral valve replacement: factors associated with screening success and failure. *Eurointervention.* (2019) 15:e983–9. doi: 10.4244/eij-d-19-00444
11. Kasel AM, Rumpf M, Frangieh AH, Mayr P, Joner M, Xhepa E, et al. International LAMPOON: first european experience with laceration of the anterior mitral valve leaflet prior to transseptal transcatheter mitral valve implantation. *Eurointerv J.* (2018) 14:746–9. doi: 10.4244/eij-d-18-00201
12. Lisko JC, Greenbaum AB, Khan JM, Kamioka N, Gleason PT, Byku I, et al. Antegrade intentional laceration of the anterior mitral leaflet to prevent left ventricular outflow. *Circ Cardiovasc Interv.* (2020) 13:e008903. doi: 10.1161/CIRCINTERVENTIONS.119.008903
13. Kohli K, Wei A, Sadri V, Pierce E, Zhang Y, Wang D, et al. Framework for planning TMVR using 3-D imaging, in silico modeling, and virtual reality. *Struct Heart J Heart Team.* (2020) 4:336–41. doi: 10.1080/24748706.2020.1762268
14. Greenbaum AB, Lisko JC, Gleason PT, Kamioka N, Metcalf DP, Greenbaum MA, et al. Annular-to-apical "emory angle" to ensure coaxial mitral implantation of the SAPIEN 3 valve. *JACC Cardiovasc Interv.* (2020) 13:2447–50. doi: 10.1016/j.jcin.2020.07.024
15. Greenbaum AB, Perdoncin E, Paone G, Grubb KJ, Xie JX, Gleason PT, et al. Tableside skirt modification of the SAPIEN 3 valve to reduce paravalvular leak during transcatheter mitral valve replacement. *JACC Cardiovasc Interv.* (2021) 14:932–4. doi: 10.1016/j.jcin.2021.01.016
16. Mao W, Wang Q, Kodali S, Sun W. Numerical parametric study of paravalvular leak following a transcatheter aortic valve deployment into a patient-specific aortic root. *J Biomech Eng.* (2018) 140:1–11. doi: 10.1115/1.4040457

17. Halim J, Brouwer J, Lycke M, Swaans MJ, Van der Heyden J. Transcatheter aortic valve replacement: impact of pre-procedural FEops HEARTguide assessment on device size selection in borderline annulus size cases. *Neth Heart J.* (2021) 29:654–61. doi: 10.1007/s12471-021-01620-4
18. Buysschaert I, Viaene D. Clinical impact of preprocedural CT-based 3D computational simulation of left atrial appendage occlusion with amulet. *J Interv Cardiol.* (2021) 2021:9972228. doi: 10.1155/2021/9972228
19. de Vecchi A, Marlevi D, Nordsletten DA, Ntalas I, Leipsic J, Bapat V, et al. Left ventricular outflow obstruction predicts increase in systolic pressure gradients and blood residence time after transcatheter mitral valve replacement. *Sci Rep.* (2018) 8:15540. doi: 10.1038/s41598-018-33836-7
20. Alharbi Y, Otton J, Muller DWM, Geelan-Small P, Lovell NH, Al Abed A, et al. Predicting the outcome of transcatheter mitral valve implantation using image-based computational models. *J Cardiovasc Comput Tomogr.* (2019). 14, 335–342. doi: 10.1016/j.jcct.2019.11.016 PMID: 31862348
21. Pappalardo F, Russo G, Tshinanu FM, Viceconti M. In silico clinical trials: concepts and early adoptions. *Brief Bioinformatics.* (2019) 20:1699–708. doi: 10.1093/bib/bby043
22. Sarrami-Foroushani A, Lassila T, MacRaild M, Asquith J, Roes KCB, Byrne JV, et al. In-silico trial of intracranial flow diverters replicates and expands insights from conventional clinical trials. *Nat Commun.* (2021) 12:1–12. doi: 10.1038/s41467-021-23998-w

Conflict of Interest: KK has served as a consultant for Abbott Vascular. PB has served as a consultant for Edwards Lifesciences, Tendyne, Neovasc, and Circle Imaging. AG has served as a proctor for Edwards Lifesciences, Medtronic, and Abbott Vascular; and has served as a consultant for and is an equity holder in Transmural Systems. VB has served as a consultant for Edwards Lifesciences and Abbott Vascular; and has served as a consultant for and is an equity holder in Transmural Systems. JK and RL were co-inventors on patents, assigned to the NIH, on devices for leaflet laceration.

The remaining authors declare that the research was conducted in the absence of any commercial or financial relationships that could be construed as a potential conflict of interest.

Publisher's Note: All claims expressed in this article are solely those of the authors and do not necessarily represent those of their affiliated organizations, or those of the publisher, the editors and the reviewers. Any product that may be evaluated in this article, or claim that may be made by its manufacturer, is not guaranteed or endorsed by the publisher.

frontiers | Frontiers in Bioengineering and Biotechnology

TYPE Original Research
PUBLISHED 14 October 2022
DOI 10.3389/fbioe.2022.1032034

OPEN ACCESS

EDITED BY
Francesco Sturla,
IRCCS San Donato Polyclinic, Italy

REVIEWED BY
Hao Gao,
University of Glasgow, United Kingdom
Salvatore Pasta,
University of Palermo, Italy

*CORRESPONDENCE
Gil Marom,
maromgil@tau.ac.il

SPECIALTY SECTION
This article was submitted to Biomechanics, a section of the journal Frontiers in Bioengineering and Biotechnology

RECEIVED 30 August 2022
ACCEPTED 26 September 2022
PUBLISHED 14 October 2022

CITATION
Weissmann J, Charles CJ, Richards AM, Yap CH and Marom G (2022), Material property alterations for phenotypes of heart failure with preserved ejection fraction: A numerical study of subject-specific porcine models.
Front. Bioeng. Biotechnol. 10:1032034.
doi: 10.3389/fbioe.2022.1032034

Material property alterations for phenotypes of heart failure with preserved ejection fraction: A numerical study of subject-specific porcine models

Jonathan Weissmann[1], Christopher J. Charles[2,3,4], A. Mark Richards[3,4], Choon Hwai Yap[5] and Gil Marom[6]*

[1]Department of Biomedical Engineering, Tel Aviv University, Tel Aviv, Israel, [2]Department of Surgery, Yong Loo Lin School of Medicine, National University of Singapore, Singapore, Singapore, [3]Cardiovascular Research Institute, National University of Singapore, Singapore, Singapore, [4]Christchurch Heart Institute, Department of Medicine, University of Otago, Christchurch, New Zealand, [5]Department of Bioengineering, Imperial College London, London, United Kingdom, [6]School of Mechanical Engineering, Tel Aviv University, Tel Aviv, Israel

A substantial proportion of heart failure patients have a preserved left ventricular (LV) ejection fraction (HFpEF). This condition carries a high burden of morbidity and mortality and has limited therapeutic options. left ventricular pressure overload leads to an increase in myocardial collagen content, causing left ventricular stiffening that contributes to the development of heart failure patients have a preserved left ventricular ejection fraction. Although several heart failure patients have a preserved left ventricular ejection fraction models have been developed in recent years to aid the investigation of mechanical alterations, none has investigated different phenotypes of the disease and evaluated the alterations in material properties. In this study, two similar healthy swine were subjected to progressive and prolonged pressure overload to induce diastolic heart failure characteristics, providing a preclinical model of heart failure patients have a preserved left ventricular ejection fraction. Cardiac magnetic resonance imaging (cMRI) scans and intracardiac pressures were recorded before and after induction. In both healthy and disease states, a corresponding finite element (FE) cardiac model was developed *via* mesh morphing of the Living Heart Porcine model. The material properties were derived by calibrating to its passive and active behavior. The change in the passive behavior was predominantly isotropic when comparing the geometries before and after induction. Myocardial thickening allowed for a steady transition in the passive properties while maintaining tissue incompressibility. This study highlights the importance of hypertrophy as an initial compensatory response and might also pave the way for assessing disease severity.

KEYWORDS

heart failure with preserved ejection fraction, phenotypes, finite element analysis, computational modelling, material properties, animal modeling

Introduction

Heart failure (HF) is a leading cause of morbidity and mortality (Roger, 2021). HF with preserved ejection fraction (HFpEF) is characterized by an ejection fraction above 50% and increased left ventricular (LV) filling pressure (Heidenreich et al., 2022). It is estimated to affect a considerable proportion of HF patients (Clark and Velazquez, 2020). In the United States alone, the prevalence of HF is estimated to be 6 million, which is approximately 1.8% of the total United States population (Roger, 2021). HFpEF is associated with increased morbidity and mortality, including a 35% 2-year rate of HF hospitalization and a 14% 2-year mortality (Dunlay et al., 2017), even in asymptomatic patients (Kane et al., 2011). The prevalence rate continues to rise significantly owing to the aging of the population and the increasing prevalence of comorbidities such as hypertension, obesity, and diabetes (AlJaroudi et al., 2012; Shah and Solomon, 2012; Kitzman and Shah, 2016; Virani et al., 2020). Despite the large number of patients, few pharmacological or device-driven therapies have been shown to improve clinical outcomes or lower mortality rates (Bhuiyan and Maurer, 2011; Wintrich et al., 2020; Anker et al., 2021).

A key contributing etiology of HFpEF is LV stiffening due to myocardial remodeling. Progressive and prolonged LV pressure overload leads to an increase in myocardial collagen content, causing both regional and global LV stiffening as well as elevated LV filling pressures (Borbély et al., 2005; Zile et al., 2015). However, this stiffening mechanism is still not fully understood, and the variety of phenotypes makes an accurate assessment difficult (Shah and Solomon, 2012; Sengupta and Marwick, 2018; Shah et al., 2020; Roh et al., 2022).

Numerical analysis enables non-invasive mechanical assessment of the cardiovascular system (Chandran, 2010; Niederer et al., 2011; Votta et al., 2013; Sahli Costabal et al., 2018; Wisneski et al., 2020; Cutugno et al., 2021). In recent years, models have been developed to investigate the impact of HFpEF on heart function (Poh et al., 2012; Adeniran et al., 2015; Dabiri et al., 2018; Escher et al., 2020). Global tissue stiffness has been examined using finite element (FE) modeling by comparing the mechanical properties of an HFpEF cardiac ventricle to a healthy heart of a different subject (Sack et al., 2018). Torres et al. (2020) have recently investigated LV stiffening in response to progressive pressure overload. A predictor variable for LV stiffness was derived from computed stress magnitudes in the circumferential and longitudinal directions. It was based on clinical echocardiogram strain measurements in selective heart regions and the adaptation of an ellipsoidal model. Although tissue stiffening has been corroborated by these models, a more comprehensive description of the material properties is required to establish a better pathophysiological understanding.

In this study, we aim to compare material properties before and after the elevation of the LV filling pressure. Four FE models were developed for healthy and HFpEF scenarios based on an animal study, where swine were recorded before and after HFpEF induction. This study is the first to compare healthy and HFpEF conditions of the same subject by calibrating their material properties. The same technique can be applied to a larger study population, to quantify the changes in material properties in HFpEF and aid in the classification of disease variants.

Materials and methods

Animal experiment

Yorkshire Landrace pigs at the age of 3–4 months were subjected to progressive and prolonged pressure overload using an aortic inflatable cuff over a 5-week period to induce diastolic HF characteristics (Charles et al., 2020). Cardiac magnetic resonance imaging (cMRI) scans and LV pressures were recorded on days 1 and 42, pre- and post-cuff placement, representing healthy and disease conditions, respectively. A subset of two normal pigs with similar body weight (19.9 and 20.5 kg), surface area (0.74 and 0.77 m^2), and cardiac characteristics (Table 1) were chosen from the full cohort. During the experiment, the two pig models demonstrated good development of HFpEF characteristics, including LV hypertrophy and preserved ejection fraction. The study was conducted as part of the Asian neTwork for Translational Research and Cardiovascular Trials (ATTRaCT) program and was authorized by the Institutional Animal Care and Use Committee (IACUC) of the National University of Singapore (Protocol R15-0090).

Geometrical modeling

For each pig model, the geometries of normal and HFpEF anatomies were reconstructed based on recordings before and after HF induction. The recordings were segmented at end diastole and were followed by smoothing with volume preservation (Weissmann et al., 2021). The living heart porcine model (LHPM; Simulia, Dassault Systèmes, Providence, RI, United States) (Baillargeon et al., 2014, 2017; SIMULIA, 2016) was morphed based on the reconstructed geometries, using Abaqus solver (Simulia, Dassault Systèmes), to generate multiple FE models. A detailed description of the algorithm can be found in our published work (Weissmann et al., 2021).

For each pig, the LV wall thickness was measured before and after the induction of HFpEF to evaluate the muscular growth due to hypertrophy. Short-axis slices at end-diastole were analyzed and the LV mass (LVM) was calculated by subtracting endocardial from epicardial volume. The value

TABLE 1 Pressure and volume magnitudes of the healthy configuration before the HF induction.

	End-systole		End-diastole		Maximum pressure (mmHg)	Stroke volume (ml)	Ejection fraction (%)
	Volume (ml)	Pressure (mmHg)	Volume (ml)	Pressure (mmHg)			
Case 1	22	81	55	12	85	34	61
Case 2	20	80	56	13	84	36	64

was normalized to body surface area (LVMI), which was calculated using the Mosteller formula (Mosteller, 1987).

Material properties calibration

The material characteristics of the LV tissue include passive and active properties embedded in the LHPM (Simulia, 2016). The passive behavior was defined according to the Holzapfel and Ogden (2009) constitutive model. The strain energy function is comprised of isochoric (ψ_{iso}) and volumetric (ψ_{vol}) components as follows:

$$\psi_{iso} = \frac{a}{2b}e^{b(I_1-3)} + \sum_{i=f,s}\frac{a_i}{2b_i}\left\{e^{b_i(I_{4i}-1)^2}-1\right\} + \frac{a_{fs}}{2b_{fs}}\left\{e^{b_{fs}(I_{8fs})^2}-1\right\}$$

$$\psi_{vol} = \frac{1}{D}\left(\frac{J^2-1}{2} - \ln(J)\right)$$

where the tissue stiffness is determined in the isotropic direction (a, b), fiber direction (a_f, b_f), sheet direction (a_s, b_s), and the connection between the fibers and sheet (a_{fs}, b_{fs}). $I_1 := tr(C)$, $I_{4i} := C : (f_0 \otimes f_0)$, and $I_{8fs} := C : sym(f_0 \otimes s_0)$ are invariants, C is the right Cauchy-Green tensor, and f_0 and s_0 are vectors that define the fiber and sheet directions, respectively. Sym () operator represents symmetrical disposition with respect to the axes of deformation (Merodio and Ogden, 2006), J is the third deformation gradient invariant, and $D = 2/K$ where D is the incompressibility parameter and K is the bulk modulus.

The coefficients of the isochoric function were determined using the analytic pressure-volume curve suggested by Klotz et al. (2006). The curve was customized for each case with the end diastolic pressure (EDP) and end diastolic volume (EDV) obtained from clinical measurements. Further details of the configuration of the "Klotz" curve are provided in the Supplementary Material.

A genetic algorithm was implemented to obtain an optimal set of passive material parameters matching the Klotz curve while accounting for local and global minima. An initial generation was chosen randomly, and for each parameter, specified bounds were chosen to allow a wide range of physiological values (Göktepe et al., 2011; Wang et al., 2013; Nikou et al., 2015) (Table 2). The algorithm used default settings for selection, recombination, and mutation (Pohlheim and Marenbaeh, 1996). Each set of parameters was ranked by a fitness function, which computed an overall distance between the desired Klotz curve and an FEA-generated pressure-volume curve. The next generation was created by applying recombination and mutation attributes to the sets of parameters with the lowest scores. Iterative selection was performed for three generations until a score within 2.5% of the target value was found. This process was implemented using an in-house *Python* script, which generated an Abaqus input file for each set of parameters, executed the solver, and analyzed the FEA results.

TABLE 2 The passive parameter bounds.

Parameter	Lower bound	Upper bound
a (MPa)	1.0×10^{-5}	3.5×10^{-3}
b	1	25
a_f (MPa)	5.5×10^{-5}	5.0×10^{-3}
b_f	5	90
a_s (MPa)	1.0×10^{-5}	1.0×10^{-3}
b_s	5.5	50.5
a_{fs} (MPa)	4.5×10^{-5}	2.0×10^{-4}
b_{fs}	2.25	10

For each model, a second calibration of the HFpEF conditions was performed to quantify potential changes in the passive behavior by eliminating the influence of geometrical alterations. The healthy FE models, prior to the induction, were compared to the Klotz curves, using volume and pressure measurements taken after the induction of HFpEF. The algorithm ran under identical conditions and predefined boundaries as in the first calibration. To enable more degrees of freedom, as an alternative to hypertrophy, the incompressibility parameter D was also included in the calibration. The first calibration values were utilized as an initial guess in the second calibration to obtain minimal alterations relative to the healthy state.

To synchronize the pressure and volume magnitudes during heart contraction, an alteration in contractility was facilitated by the active sarcomere tension (Guccione and McCulloch, 1993;

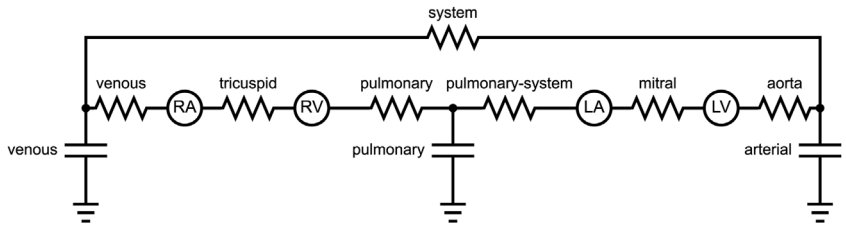

FIGURE 1
Electrical representation of the blood flow model.

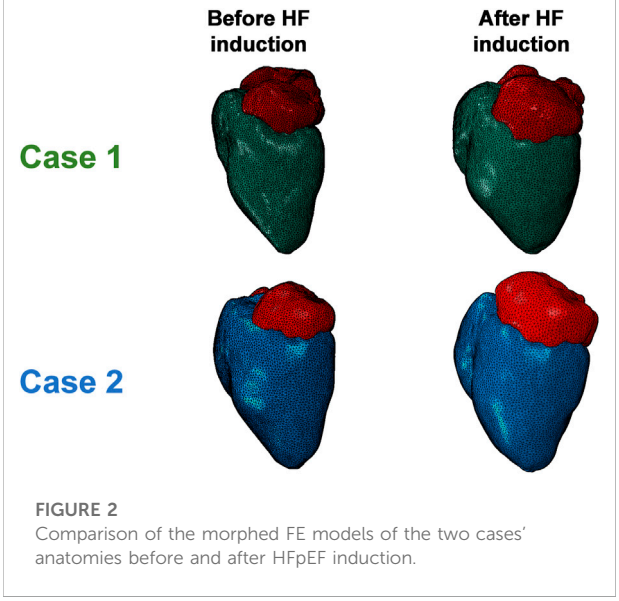

FIGURE 2
Comparison of the morphed FE models of the two cases' anatomies before and after HFpEF induction.

Genet et al., 2014; Sack et al., 2016). More information can be found in the supplementary material section.

Circulatory system

The embedded blood flow model in the LHPM uses a lumped parameter approach. Figure 1 shows a schematic illustration of the blood flow model, with resistors representing flow resistances and capacitors representing structural compliance. The blood flow was modeled by inducing fluid exchange between the various heart chambers. The capacitors are mechanically represented by reservoirs and their pressure-volume response is controlled by springs. For each model, the venous compliance and the aortic valve, systemic and venous resistances were adjusted to obtain pressure–volume loops similar to clinical measurements. The HFpEF lumped settings and the corresponding healthy ones differed only in their resistance, such that the aortic and systemic resistances were increased in our HFpEF models, representing the aortic cuffing that induced HFpEF in the animal. To maintain proper venous return in our models, the venous resistance was also slightly lowered. The lumped parameters are listed in Supplementary Table S1.

Results

Model geometry

A visualization of the FE models following cMRI segmentation and mesh morphing is shown in Figure 2. The LHPM was used as a baseline mesh, and was morphed to generate cardiac models matching those of our animal models, both before and after induction of HFpEF. A previously developed mesh-morphing algorithm was used for this, which can accurately match imaged wall and septal thicknesses, and has the advantage of preserving fine structural details captured in the baseline mesh (Crick et al., 1998; Weissmann et al., 2021). For each model, long- and short-axis cross sections in the initial healthy configuration and the post induction HF configuration are presented in Figure 3. The LV mass value was determined for each case and is shown in Table 3. Albeit similar physical properties at normal condition, the mass properties have changed after induction, as the hypertrophy in Case 1 was substantially larger, predominantly if normalized to the body surface area. (Figure 4; Table 3).

Material parameter estimation

The material parameters (a, b, a_f, b_f, a_s, b_s, a_{fs}, b_{fs}) were calibrated for the subject-specific anatomies and produced appropriate results for all models, as previously reported in the literature (Göktepe et al., 2011; Wang et al., 2013; Nikou et al., 2015; Genet et al., 2016; Dabiri et al., 2018; Peirlinck et al., 2019; Heidari et al., 2022). Table 4 lists the values of the eight calibrated passive material parameters for the two cases. The FE passive filling curves were plotted against the corresponding analytical Klotz curves to graphically highlight the optimization efficiency (Figure 5). R^2 scores were calculated for

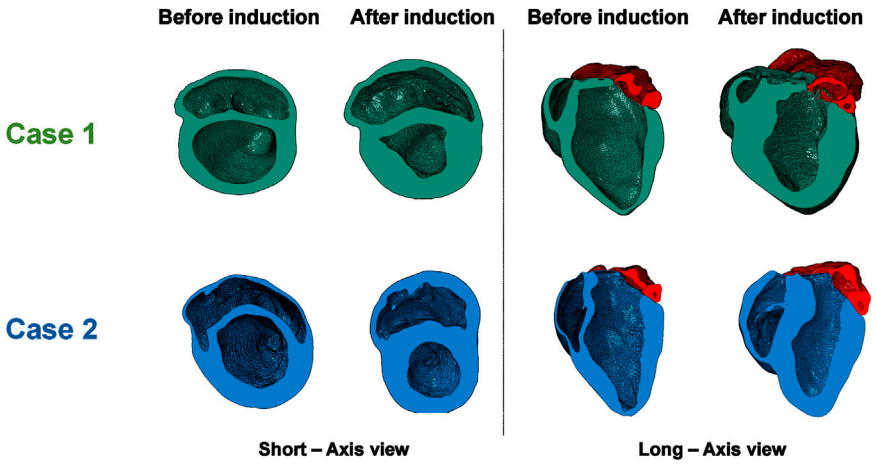

FIGURE 3
Long and short axis views of the two cases before and after HFpEF induction.

TABLE 3 Left ventricular mass properties before and after induction.

	Case 1			Case 2		
	Normal	HFpEF	Growth (%)	Normal	HFpEF	Growth (%)
LVM (*g*)	49	132	269	49	122	250
LVMI (g/m^2)	66	136	206	63	120	190

quantitative fitting evaluation, with R^2 of 0.999 and 0.997 for the healthy and unhealthy configurations, respectively, in both models.

For comparison, the material properties were also calibrated against the HFpEF condition using the healthy anatomy, i.e., without introducing geometric alteration related to hypertrophy. Figure 2 shows this calibration with an identical "Klotz" curve as in Figure 5. The R^2 scores for a HFpEF condition with normal geometry were 0.998 and 0.999 for Cases 1 and 2, respectively. The differences between the passive properties of normal and HFpEF without anatomical alterations are shown in Table 5. From the results, the major alteration was observed in a single parameter, while the change in the other parameters was minimal. When the calibration accounted for hypertrophic conditions (Table 4), change was observed in all parameters.

Cardiac cycle simulation

The sixth cardiac cycle analysis was analyzed to ensure fully converged results (Sack et al., 2018) and stable periodic solutions with closed pressure-volume loops (Figure 6). The computed pressure was within the clinical range for both models before and after the induction, with maximal pressures of 85 mmHg for normal configurations and 150 mmHg for HFpEF conditions.

The EDV and ESV compared adequately between the imaging studies and the computational results, with less than a 5% inaccuracy. Accordingly, *in silico* stroke volume (SV) matched *in vivo* measurements for all HF models in all configurations. The computed SVs in Case 1 were 32.2 ml and 31.2 ml for normal and HFpEF conditions, respectively, compared to 33.5 ml and 30.5 ml *in vivo* measurements. Similarly, in Case 2, the SVs were 35.4 ml and 34.0 ml, vs. 36.1 ml and 34.4 ml measured *in vivo*. The changes in EF in both HF conditions are illustrated in Figure 7.

Strain assessment and validation

Supplementary Video S1 shows the beating heart models during the cardiac cycle with varying maximal principal strains. The HFpEF models for Case 1, with an increased hypertrophy, have shown similar magnitudes relative to the

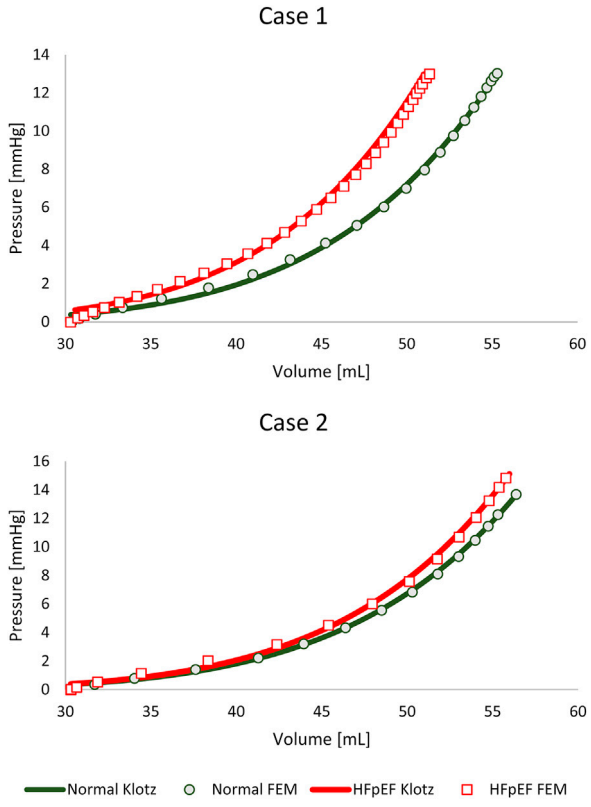

FIGURE 4
The passive filling FE results and the corresponding "Klotz" curves for the four models.

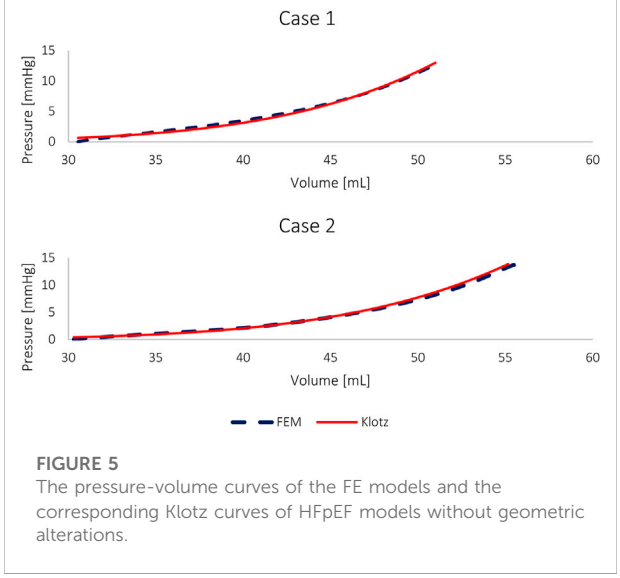

FIGURE 5
The pressure-volume curves of the FE models and the corresponding Klotz curves of HFpEF models without geometric alterations.

TABLE 4 The passive material properties for each cardiac model before and after the induction of HFpEF.

	Case 1		Case 2	
	Normal	**HFpEF**	**Normal**	**HFpEF**
a (MPa)	8.69×10^{-4}	2.12×10^{-4}	1.43×10^{-4}	1.48×10^{-3}
b	$1.51 \times 10^{+1}$	$1.96 \times 10^{+1}$	4.28	$1.23 \times 10^{+1}$
a_f (MPa)	2.26×10^{-3}	3.83×10^{-3}	4.86×10^{-3}	4.86×10^{-3}
b_f	$4.33 \times 10^{+1}$	$8.42 \times 10^{+1}$	$8.63 \times 10^{+1}$	$8.63 \times 10^{+1}$
a_s (MPa)	8.02×10^{-4}	8.89×10^{-4}	8.61×10^{-4}	8.61×10^{-4}
b_s	$1.20 \times 10^{+1}$	$4.42 \times 10^{+1}$	$3.39 \times 10^{+1}$	$3.39 \times 10^{+1}$
a_{fs} (MPa)	1.63×10^{-4}	1.22×10^{-4}	8.50×10^{-5}	1.72×10^{-4}
b_{fs}	9.39	8.50	9.43	5.51

corresponding normal heart, whereas the strains in the HFpEF model for Case 2 have shown a reduction. These strains were computed per element and may suggest the focused impact of hypertrophy on specific segments. To further assess the strain and to validate the results, global FE strain measurements in the longitudinal and circumferential directions were computed across the endocardium and compared to *in vivo* strain data. Although echo-derived strain data is considered reliable, it is most challenging given the time-dependent variation in position and particularly while analyzing cross-sectional images. The end-systolic phase was chosen as the target configuration, and the end-diastolic phase was defined as the reference configuration. To best fit the FE results to the *in vivo* strain measurements, curve lengths from long and short axis slices were measured manually rather than using the built-in strain results.

The results of the FE models have shown a reduction in myofiber longitudinal strain within the LV, with 18% vs. 15% for Case 1 and 17% vs. 14% for Case 2. A slight increase was observed in the endocardial circumferential strain: 21% vs. 23% and 25% vs. 26% for Cases 1 and 2, respectively. The global strains, which were calculated from the FE results, are commensurate with the clinical measurements listed in Table 6. The accuracy in predicting longitudinal strain was higher than the circumferential strain. The latter is more complicated to accurately measure given the image resolution and the high variability between slices. Furthermore, the overall measurements can also be affected by the myofiber orientation.

Discussion

In this study, we used cMRI scans from HFpEF induced pigs to determine changes in material properties and to assess different phenotypes of the disease. Subject-specific FE models were developed based on the living heart porcine model to represent anatomies before and after induction.

TABLE 5 The passive material properties for each cardiac model, for normal condition and HFpEF condition while the normal geometry was maintained.

	Case 1		Case 2	
	Normal	HFpEF-Normal Geometry	Normal	HFpEF - Normal Geometry
a (MPa)	8.69×10^{-4}	8.69×10^{-4}	1.43×10^{-4}	1.43×10^{-4}
b	$1.51 \times 10^{+1}$	$2.01 \times 10^{+1}$	4.28	8.28
a_f (MPa)	2.26×10^{-3}	2.26×10^{-3}	4.86×10^{-3}	4.86×10^{-3}
b_f	$4.33 \times 10^{+1}$	$4.33 \times 10^{+1}$	$8.63 \times 10^{+1}$	$8.63 \times 10^{+1}$
a_s (MPa)	8.02×10^{-4}	8.02×10^{-4}	8.61×10^{-4}	8.61×10^{-4}
b_s	$1.20 \times 10^{+1}$	$1.20 \times 10^{+1}$	$3.39 \times 10^{+1}$	$3.39 \times 10^{+1}$
a_{fs} (MPa)	1.63×10^{-4}	1.63×10^{-4}	8.50×10^{-5}	8.50×10^{-5}
b_{fs}	9.39	9.39	9.43	9.43

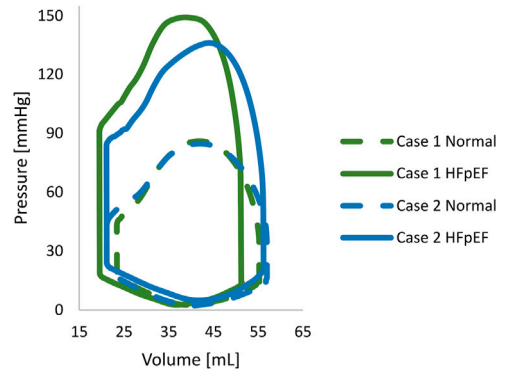

FIGURE 6
The pressure-volume loop of each porcine normal. The normal and HFpEF configurations are denoted by continuous and dashed lines, respectively.

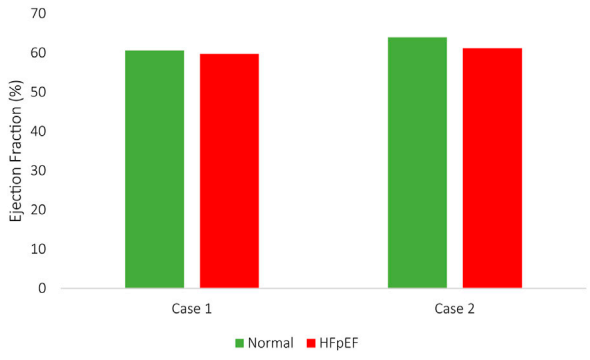

FIGURE 7
The ejection fraction of normal and HFpEF configurations.

Geometrical reconstruction

The geometries in this study were constructed to match the cMRI recordings by morphing the cardiac porcine model of the living heart. It is considered a highly demanding model, as it enables the investigation of the four heart chambers as well as the coupled electrophysiology. The use of animal subjects and a non-symmetrical geometry enables realistic modeling of the disease and allows exploring alterations in the material properties more precisely.

The phenotype classification was determined according to the degree of hypertrophy in response to the increased overload. This compensatory mechanism can result in heart failure when it occurs excessively (Kehat and Molkentin, 2010). The computed LVMI has shown a substantial twofold increase in myocardial mass in both pigs. In Case 1, myocardial thickening was greater, implying a more pathologic scenario.

Material properties

All FE models were calibrated from the same initial volume to normalize them and to reduce material discrepancies due to volume alterations (Figures 4, 5). Furthermore, selecting a reference point allowed to limit the number of solutions of the multivariate analysis, as there is often more than one possible solution. For each model, the best solution was chosen after running the stochastic algorithm three times for each scenario, using the same scoring method. The set of material properties with the optimal score was used for our comparison.

The pressure-volume curves of both cases before the induction of HFpEF are in close range, attesting to the resemblance between the two initial calibrated configurations. The volume was estimated from a small number of slices, resulting in a measurement error range of 10% (El-Rewaidy and Fahmy, 2016), which is more than the volumetric calibration error. Differences in pressure magnitudes

TABLE 6 Endocardial longitudinal and circumferential strains in percentages from manual echocardiogram length measurements.

	Case 1		Case 2	
	Longitudinal	**circumferential**	**Longitudinal**	**circumferential**
Normal	20%	28%	27%	30%
HFpEF	12%	28%	18%	32%

of less than 1 mmHg are also considered minor (Tolia et al., 2018), since the physiologic pressures were estimated from E/e' measurements according to Nagueh's formula (Nagueh et al., 1997).

It is important to underscore that the curves are ultimately determined by the patient-specific anatomy and the material properties, as demonstrated by the variability between the post induction configurations and their corresponding curves. To eliminate alterations in the cardiac anatomy due to remodeling, thus isolating the impact of the passive material parameters, the initial anatomy was modified to fit the HFpEF pressure volume curve (Figure 7). The change was primarily isotropic (*a*, *b*), with negligible impact on the remaining parameters. These results are not biased by initial parameter constraints (Nikou et al., 2015), nor by parameter significance ranking (Nair et al., 2007). Importantly, to keep the parameters in the physiological range, the stiffness of the heart had to rise, resulting in a drop in the incompressibility parameter *D*, which yielded an increase in the bulk modulus of three orders of magnitude greater than the increase in parameter *a* (Göktepe et al., 2011). The reduction in the incompressibility parameter *D* also leads to a shift of the Klotz curve toward lower volumes (to the left). The range of the *D* parameter (0.1–0.25 MPa) was chosen to ensure that the influence of incompressibility on the material properties is minimal (Sack et al., 2018). Interestingly, the change in the myocardial passive behavior is predominantly isotropic direction 2) when comparing the same geometry before and after induction (Table 5). Our calibration algorithm ran under identical conditions in all models, including initial volume setting as well as predefined boundaries for each parameter, to assure normalization and to reduce material discrepancies due to volume alteration. No additional constraints were added, allowing all the parameters to change randomly until an optimal solution was obtained. Importantly, this is the first article to compare HFpEF to normal heart of the exact subject, thus allowing for an accurate assessment of myocardial changes. Our findings suggest that cardiac hypertrophy may enable the preservation of the passive material properties in the physiological range while tissue incompressibility is maintained. It is consistent with the convention that hypertrophy serves as an initial compensatory response to sustain cardiac function (Hein et al., 2003). Finally, we compared two HFpEF phenotypes. High variability in material properties was observed following the realistic calibration of the two models (Table 4). The hypertrophy magnitude triggered dissimilar changes in different parameters, emphasizing the importance of addressing all material properties for accurate calibration.

Cardiac cycle simulation

Pressure-volume curves of the LV (PV-loops) were generated to represent normal and HFpEF conditions (Figure 6). The converged cardiac cycles accurately described clinical observations, with a difference of less than 5%. This error is minor, considering physiological variations in volume, pressure, and timing during cardiac function and over *in-vivo* sampling. While the PV-loops representing the normal configurations of the two cases are in close resemblance, this is not the case in the HFpEF configurations. The differences in the HFpEF curves are demonstrated both in the PV values and the shape of the curves. These changes can be explained by the degree and direction of the hypertrophy, which engenders alterations in the material properties.

A quantitative assessment of the models was performed by comparing the strains of the HFpEF and normal configurations. The strain measurement difference between the cardiac subjects before and after induction has shown an expected reduction in longitudinal strain at diastole. The FE estimations agreed with the clinical data, with only a negligible increase in the circumferential strain. The relative error between the FE results and the clinical data can be explained by the different imaging modalities, i.e., cMRI vs. echocardiography, respectively. Furthermore, the model geometries were reconstructed without adjusting the orientation of the muscle fibers. Nonetheless, the trends were largely the same, and the cardiac behavior was similar.

Study limitations and future directions

Several key factors contribute to diastolic HF formation and include both systolic and diastolic abnormalities (Sengupta and Marwick, 2018). The FE analysis in this study addressed the alteration in mechanical properties of the LV as well as geometrical changes such as hypertrophy (Aurigemma and Gaasch, 2004; Torres et al., 2020). Investigation of the LV systolic mechanics is beyond the scope of this paper. In our investigation, we assumed the

change in material properties to be homogeneous across the LV and uniform in all directions. The calibration process was based on echocardiographic estimation of intra-cardiac pressures normalized by weight rather than direct catheter readings. Moreover, the FE models relied on cMRI recordings that were only obtained before and after HF induction. Sequential MRI monitoring during the induction process could provide additional information on disease progression and tissue remodeling and is the goal of our subsequent study. Here, we sought to investigate changes in global passive material properties of similar baseline anatomies to induce different representations of HFpEF.

Conclusion

This study evaluates material property alteration in two different phenotypes of HFpEF using subject-specific cardiac models for porcine hearts before and after the application of progressive and prolonged pressure overload. The change in the myocardial passive behavior was isotropic and its magnitude was heavily reliant on the degree of hypertrophy. When hypertrophy was excluded, elevation in incompressibility was enforced, triggering alterations only in parameter b. This study is the first to quantify and compare alterations in material properties and incompressibility in different HFpEF phenotypes. The results underline the advantage of computational modeling in understanding complex cardiac representation *via* tissue behavior quantification.

Data availability statement

The original contributions presented in the study are included in the article/Supplementary Material, further inquiries can be directed to the corresponding author.

Ethics statement

The animal study was reviewed and approved by the Institutional Animal Care and Use Committee (IACUC) and by the National University of Singapore (Protocol R15-0090).

Author contributions

JW: Conceptualization, Data curation, Methodology, Software, Validation, Investigation, Writing-original draft. CJC: Writing-review, Editing, Resources, Investigation. AMR: Investigation, Resources, Writing-review, Editing. CHY: Writing-review, Editing, Validation, Methodology, Conceptualization. GM: Conceptualization, Funding acquisition, Methodology, Resources, Supervision, Validation, Writing-review, Editing.

Funding

This work was partially supported by the Carl Gans International Research Collaboration and Workshop on Mechanics Inspired by Biology and by the ATTRaCT SPF grant from the Biomedical Research Council of Singapore and the National Medical Research Council (NMRC) of Singapore.

Acknowledgments

This publication is part of a research work by JW towards a Ph.D. at Tel Aviv University. JW and GM disclose that they are members of Simulia's Living Heart Project who provided the software. This work was partially supported by the Carl Gans International Research Collaboration and Workshop on Mechanics Inspired by Biology and by the ATTRaCT SPF grant from the Biomedical Research Council of Singapore and the National Medical Research Council (NMRC) of Singapore.

Conflict of interest

The authors declare that the research was conducted in the absence of any commercial or financial relationships that could be construed as a potential conflict of interest.

Publisher's note

Supplementary material

The Supplementary Material for this article can be found online at: https://www.frontiersin.org/articles/10.3389/fbioe.2022.1032034/full#supplementary-material

References

Adeniran, I., MacIver, D. H., Hancox, J. C., and Zhang, H. (2015). Abnormal calcium homeostasis in heart failure with preserved ejection fraction is related to both reduced contractile function and incomplete relaxation: An electromechanically detailed biophysical modeling study. *Front. Physiol.* 6, 78. doi:10.3389/FPHYS.2015.00078

AlJaroudi, W., Alraies, M. C., Halley, C., Rodriguez, L., Grimm, R. A., Thomas, J. D., et al. (2012). Impact of progression of diastolic dysfunction on mortality in patients with normal ejection fraction. *Circulation* 125, 782–788. doi:10.1161/CIRCULATIONAHA.111.066423

Anker, S. D., Butler, J., Filippatos, G., Ferreira, J. P., Bocchi, E., Böhm, M., et al. (2021). Empagliflozin in heart failure with a preserved ejection fraction. *N. Engl. J. Med.* 385, 1451–1461. doi:10.1056/nejmoa2107038

Aurigemma, G. P., and Gaasch, W. H. (2004). Diastolic heart failure. *N. Engl. J. Med.* 351, 1097–1105. doi:10.1056/NEJMCP022709

Baillargeon, B. P., Sack, K. L., Acevedo-Bolton, G., Ennis, D. B., Kassab, G. S., Franz, T., et al. (2017). "Establishing creditability of the living heart porcine model," in *Proceedings of the summer Biomechanics, bioengineering and biotransport conference* (AZ, USA: Tuscon), 346–347. 978-0-692-89782-9.SB3C2017.

Baillargeon, B., Rebelo, N., Fox, D. D., Taylor, R. L., and Kuhl, E. (2014). The living heart Project: A robust and integrative simulator for human heart function. *Eur. J. Mech. - A/Solids* 48, 38–47. doi:10.1016/J.EUROMECHSOL.2014.04.001

Bhuiyan, T., and Maurer, M. S. (2011). Heart failure with preserved ejection fraction: Persistent diagnosis, therapeutic enigma. *Curr. Cardiovasc. Risk Rep.* 5, 440–449. doi:10.1007/S12170-011-0184-2

Borbély, A., Van Der Velden, J., Papp, Z., Bronzwaer, J. G. F., Edes, I., Stienen, G. J. M., et al. (2005). Cardiomyocyte stiffness in diastolic heart failure. *Circulation* 111, 774–781. doi:10.1161/01.CIR.0000155257.33485.6D

Chandran, K. B. (2010). Role of computational simulations in heart valve dynamics and design of valvular prostheses. *Cardiovasc. Eng. Technol.* 1, 18–38. doi:10.1007/S13239-010-0002-X

Charles, C. J., Lee, P., Li, R. R., Yeung, T., Ibraham Mazlan, S. M., Tay, Z. W., et al. (2020). A porcine model of heart failure with preserved ejection fraction: Magnetic resonance imaging and metabolic energetics. *Esc. Heart Fail.* 7, 93–103. doi:10.1002/EHF2.12536

Clark, K. A. A., and Velazquez, E. J. (2020). Heart failure with preserved ejection fraction: Time for a reset. *JAMA* 324, 1506–1508. doi:10.1001/JAMA.2020.15566

Crick, S. J., Sheppard, M. N., Ho, S. Y., Gebstein, L., and Anderson, R. H. (1998). Anatomy of the pig heart: Comparisons with normal human cardiac structure. *J. Anat.* 193 (1), 105–119. doi:10.1046/J.1469-7580.1998.19310105.X

Cutugno, S., Agnese, V., Gentile, G., Raffa, G. M., Wisneski, A. D., Guccione, J. M., et al. (2021). Patient-specific analysis of ascending thoracic aortic aneurysm with the living heart human model. *Bioengineering* 8, 175. doi:10.3390/BIOENGINEERING8110175

Dabiri, Y., Sack, K. L., Shaul, S., Sengupta, P. P., and Guccione, J. M. (2018). Relationship of transmural variations in myofiber contractility to left ventricular ejection fraction: Implications for modeling heart failure phenotype with preserved ejection fraction. *Front. Physiol.* 9, 1003. doi:10.3389/fphys.2018.01003

Dunlay, S. M., Roger, V. L., and Redfield, M. M. (2017). Epidemiology of heart failure with preserved ejection fraction. *Nat. Rev. Cardiol.* 1410 (14), 591–602. doi:10.1038/nrcardio.2017.65

El-Rewaidy, H., and Fahmy, A. S. (2016). Improved estimation of the cardiac global function using combined long and short axis MRI images of the heart. *Biomed. Eng. Online* 15, 45–14. doi:10.1186/s12938-016-0156-3

Escher, A., Choi, Y., Callaghan, F., Thamsen, B., Kertzscher, U., Schweiger, M., et al. (2020). A valveless pulsatile pump for heart failure with preserved ejection fraction: Hemo- and fluid dynamic feasibility. *Ann. Biomed. Eng.* 48, 1821–1836. doi:10.1007/S10439-020-02492-2

Genet, M., Lee, L. C., Baillargeon, B., Guccione, J. M., and Kuhl, E. (2016). Modeling pathologies of diastolic and systolic heart failure. *Ann. Biomed. Eng.* 44, 112–127. doi:10.1007/S10439-015-1351-2

Genet, M., Lee, L. C., Nguyen, R., Haraldsson, H., Acevedo-Bolton, G., Zhang, Z., et al. (2014). Distribution of normal human left ventricular myofiber stress at end diastole and end systole: A target for *in silico* design of heart failure treatments. *J. Appl. Physiology* 117, 142–152. doi:10.1152/JAPPLPHYSIOL.00255.2014

Göktepe, S., Acharya, S. N. S., Wong, J., and Kuhl, E. (2011). Computational modeling of passive myocardium. *Int. J. Numer. method. Biomed. Eng.* 27, 1–12. doi:10.1002/CNM.1402

Guccione, J. M., and McCulloch, A. D. (1993). Mechanics of active contraction in cardiac muscle: Part I--Constitutive relations for fiber stress that describe deactivation. *J. Biomech. Eng.* 115, 72–81. doi:10.1115/1.2895473

Guccione, J. M., Moonly, S. M., Moustakidis, P., Costa, K. D., Moulton, M. J., Ratcliffe, M. B., et al. (2001). Mechanism underlying mechanical dysfunction in the border zone of left ventricular aneurysm: A finite element model study. *Ann. Thorac. Surg.* 71, 654–662. doi:10.1016/S0003-4975(00)02338-9

Heidari, A., Elkhodary, K. I., Pop, C., Badran, M., Vali, H., Abdel-Raouf, Y. M. A., et al. (2022). Patient-specific finite element analysis of heart failure and the impact of surgical intervention in pulmonary hypertension secondary to mitral valve disease. *Med. Biol. Eng. Comput.* 60 (6), 1723–1744. doi:10.1007/S11517-022-02556-6

Heidenreich, P. A., Bozkurt, B., Aguilar, D., Allen, L. A., Byun, J. J., Colvin, M. M., et al. (2022). 2022 AHA/ACC/HFSA guideline for the management of heart failure: A report of the American college of cardiology/American heart association joint committee on clinical practice guidelines. *Circulation* 145 (18), e895–e1032. doi:10.1161/CIR.0000000000001063

Hein, S., Arnon, E., Kostin, S., Schönburg, M., Elsässer, A., Polyakova, V., et al. (2003). Progression from compensated hypertrophy to failure in the pressure-overloaded human heart. *Circulation* 107, 984–991. doi:10.1161/01.CIR.0000051865.66123.B7

Holzapfel, G. A., and Ogden, R. W. (2009). Constitutive modelling of passive myocardium: A structurally based framework for material characterization. *Phil. Trans. R. Soc. A* 367, 3445–3475. doi:10.1098/RSTA.2009.0091

Kane, G. C., Karon, B. L., Mahoney, D. W., Redfield, M. M., Roger, V. L., Burnett, J. C., et al. (2011). Progression of left ventricular diastolic dysfunction and risk of heart failure. *JAMA - J. Am. Med. Assoc.* 306, 856–863. doi:10.1001/jama.2011.1201

Kehat, I., and Molkentin, J. D. (2010). Molecular pathways underlying cardiac remodeling during pathophysiological stimulation. *Circulation* 122, 2727–2735. doi:10.1161/CIRCULATIONAHA.110.942268

Kitzman, D. W., and Shah, S. J. (2016). The HFpEF obesity phenotype: The elephant in the room. *J. Am. Coll. Cardiol.* 68, 200–203. doi:10.1016/J.JACC.2016.05.019

Klotz, S., Hay, I., Dickstein, M. L., Yi, G. H., Wang, J., Maurer, M. S., et al. (2006). Single-beat estimation of end-diastolic pressure-volume relationship: A novel method with potential for noninvasive application. *Am. J. Physiology-Heart Circulatory Physiology* 291, H403–H412. doi:10.1152/AJPHEART.01240.2005

Merodio, J., and Ogden, R. W. (2006). The influence of the invariant on the stress–deformation and ellipticity characteristics of doubly fiber-reinforced non-linearly elastic solids. *Int. J. Non. Linear. Mech.* 41, 556–563. doi:10.1016/J.IJNONLINMEC.2006.02.001

Mosteller, R. D. (1987). Simplified calculation of body-surface area. *N. Engl. J. Med.* 317, 1098. doi:10.1056/NEJM198710223171717

Nagueh, S. F., Middleton, K. J., Kopelen, H. A., Zoghbi, W. A., and Quiñones, M. A. (1997). Doppler tissue imaging: A noninvasive technique for evaluation of left ventricular relaxation and estimation of filling pressures. *J. Am. Coll. Cardiol.* 30, 1527–1533. doi:10.1016/S0735-1097(97)00344-6

Nair, A. U., Taggart, D. G., and Vetter, F. J. (2007). Optimizing cardiac material parameters with a genetic algorithm. *J. Biomech.* 40, 1646–1650. doi:10.1016/J.JBIOMECH.2006.07.018

Niederer, S. A., Kerfoot, E., Benson, A. P., Bernabeu, M. O., Bernus, O., Bradley, C., et al. (2011). Verification of cardiac tissue electrophysiology simulators using an N-version benchmark. *Phil. Trans. R. Soc. A* 369, 4331–4351. doi:10.1098/RSTA.2011.0139

Nikou, A., Dorsey, S. M., McGarvey, J. R., Gorman, J. H., Burdick, J. A., Pilla, J. J., et al. (2015). Computational modeling of healthy myocardium in diastole. *Ann. Biomed. Eng.* 444 44, 980–992. doi:10.1007/S10439-015-1403-7

Peirlinck, M., Sahli Costabal, F., Sack, K. L., Choy, J. S., Kassab, G. S., Guccione, J. M., et al. (2019). Using machine learning to characterize heart failure across the scales. *Biomech. Model. Mechanobiol.* 18, 1987–2001. doi:10.1007/S10237-019-01190-W

Poh, K. K., Lee, L. C., Shen, L., Chong, E., Tan, Y. L., Chai, P., et al. (2012). Left ventricular fluid dynamics in heart failure: Echocardiographic measurement and utilities of vortex formation time. *Eur. Heart J. - Cardiovasc. Imaging* 13, 385–393. doi:10.1093/EJECHOCARD/JER288

Pohlheim, H., and Marenbaeh, P. (1996). Generation of structured process models using Genetic Programming. *Lect. Notes Comput. Sci. Incl. Subser. Lect. Notes Artif. Intell. Lect. Notes Bioinforma.* 1143, 102–109. doi:10.1007/BFB0032776

Roger, V. L. (2021). Epidemiology of heart failure. *Circ. Res.* 128, 1421–1434. doi:10.1161/CIRCRESAHA.121.318172

Roh, J., Hill, J. A., Singh, A., Valero-Muñoz, M., and Sam, F. (2022). Heart failure with preserved ejection fraction: Heterogeneous syndrome, diverse preclinical models. *Circ. Res.* 130, 1906–1925. doi:10.1161/CIRCRESAHA.122.320257

Sack, K. L., Aliotta, E., Ennis, D. B., Choy, J. S., Kassab, G. S., Guccione, J. M., et al. (2018). Construction and validation of subject-specific biventricular finite-element models of healthy and failing swine hearts from high-resolution DT-MRI. *Front. Physiol.* 9, 539. doi:10.3389/fphys.2018.00539

Sack, K. L., Baillargeon, B., Acevedo-Bolton, G., Genet, M., Rebelo, N., Kuhl, E., et al. (2016). Partial LVAD restores ventricular outputs and normalizes LV but not RV stress distributions in the acutely failing heart *in silico*. *Int. J. Artif. Organs* 39, 421–430. doi:10.5301/IJAO.5000520

Sahli Costabal, F., Yao, J., and Kuhl, E. (2018). Predicting the cardiac toxicity of drugs using a novel multiscale exposure-response simulator. *Comput. Methods Biomech. Biomed. Engin.* 21, 232–246. doi:10.1080/10255842.2018.1439479

Sengupta, P. P., and Marwick, T. H. (2018). The many dimensions of diastolic function: A curse or a blessing? *JACC Cardiovasc. Imaging* 11, 409–410. doi:10.1016/J.JCMG.2017.05.015

Shah, A. M., and Solomon, S. D. (2012). Phenotypic and pathophysiological heterogeneity in heart failure with preserved ejection fraction. *Eur. Heart J.* 33, 1716–1717. doi:10.1093/EURHEARTJ/EHS124

Shah, S. J., Borlaug, B. A., Kitzman, D. W., McCulloch, A. D., Blaxall, B. C., Agarwal, R., et al. (2020). Research priorities for heart failure with preserved ejection fraction. *Circulation* 141, 1001–1026. doi:10.1161/CIRCULATIONAHA.119.041886

Simulia, D. S. (2016). *Simulia living heart porcine model R1b, model documentation*. France: Dassault Systèmes.

Tolia, S., Khan, Z., Gholkar, G., and Zughaib, M. (2018). Validating left ventricular filling pressure measurements in patients with congestive heart failure: CardioMEMS™ pulmonary arterial diastolic pressure versus left atrial pressure measurement by transthoracic echocardiography. *Cardiol. Res. Pract.* 2018, 8568356. doi:10.1155/2018/8568356

Torres, W. M., Barlow, S. C., Moore, A., Freeburg, L. A., Hoenes, A., Doviak, H., et al. (2020). Changes in myocardial microstructure and mechanics with progressive left ventricular pressure overload. *JACC Basic Transl. Sci.* 5, 463–480. doi:10.1016/J.JACBTS.2020.02.007

Virani, S. S., Alonso, A., Benjamin, E. J., Bittencourt, M. S., Callaway, C. W., Carson, A. P., et al. (2020). Heart disease and stroke statistics—2020 update: A report from the American heart association. *Circulation* 141 (9), e139–e596. doi:10.1161/cir.0000000000000757

Votta, E., Le, T. B., Stevanella, M., Fusini, L., Caiani, E. G., Redaelli, A., et al. (2013). Toward patient-specific simulations of cardiac valves: State-of-the-art and future directions. *J. Biomech.* 46, 217–228. doi:10.1016/J.JBIOMECH.2012.10.026

Wang, H. M., Gao, H., Luo, X. Y., Berry, C., Griffith, B. E., Ogden, R. W., et al. (2013). Structure-based finite strain modelling of the human left ventricle in diastole. *Int. J. Numer. method. Biomed. Eng.* 29, 83–103. doi:10.1002/CNM.2497

Weissmann, J., Charles, C. J., Richards, A. M., Yap, C. H., and Marom, G. (2021). Cardiac mesh morphing method for finite element modeling of heart failure with preserved ejection fraction. *J. Mech. Behav. Biomed. Mat.* 126, 104937. doi:10.1016/J.JMBBM.2021.104937

Wintrich, J., Kindermann, I., Ukena, C., Selejan, S., Werner, C., Maack, C., et al. (2020). Therapeutic approaches in heart failure with preserved ejection fraction: Past, present, and future. *Clin. Res. Cardiol.* 109, 1079–1098. doi:10.1007/s00392-020-01633-w

Wisneski, A. D., Wang, Y., Deuse, T., Hill, A. C., Pasta, S., Sack, K. L., et al. (2020). Impact of aortic stenosis on myofiber stress: Translational application of left ventricle-aortic coupling simulation. *Front. Physiol.* 11, 574211. doi:10.3389/fphys.2020.574211

Zile, M. R., Baicu, C. F., Ikonomidis, J. S., Stroud, R. E., Nietert, P. J., Bradshaw, A. D., et al. (2015). Myocardial stiffness in patients with heart failure and a preserved ejection fraction: Contributions of collagen and titin. *Circulation* 131, 1247–1259. doi:10.1161/CIRCULATIONAHA.114.013215

frontiers | Frontiers in Bioengineering and Biotechnology

TYPE Original Research
PUBLISHED 26 October 2022
DOI 10.3389/fbioe.2022.1033450

OPEN ACCESS

EDITED BY
Francesco Sturla,
IRCCS San Donato Polyclinic, Italy

REVIEWED BY
Dalin Tang,
Worcester Polytechnic Institute, United States
Paolo Di Achille,
Google, United States
Valentina Mazzi,
Politecnico di Torino, Italy

*CORRESPONDENCE
Alireza Jafarinia,
alireza.jafarinia@tugraz.at
Xiao Yun Xu,
yun.xu@imperial.ac.uk

†These authors have contributed equally to this work and share first authorship

SPECIALTY SECTION
This article was submitted to Biomechanics, a section of the journal Frontiers in Bioengineering and Biotechnology

RECEIVED 31 August 2022
ACCEPTED 13 October 2022
PUBLISHED 26 October 2022

CITATION
Jafarinia A, Armour CH, Gibbs RGJ, Xu XY and Hochrainer T (2022), Shear-driven modelling of thrombus formation in type B aortic dissection. *Front. Bioeng. Biotechnol.* 10:1033450. doi: 10.3389/fbioe.2022.1033450

Shear-driven modelling of thrombus formation in type B aortic dissection

Alireza Jafarinia[1*†], Chlöe H. Armour[2†], Richard G. J. Gibbs[3], Xiao Yun Xu[2*] and Thomas Hochrainer[1]

[1]Institute of Strength of Materials, Graz University of Technology, Graz, Austria, [2]Department of Chemical Engineering, Imperial College London, London, United Kingdom, [3]Regional Vascular Unit, St Mary's Hospital, Imperial College Healthcare National Health Service Trust, Imperial College London, London, United Kingdom

Background: Type B aortic dissection (TBAD) is a dangerous pathological condition with a high mortality rate. TBAD is initiated by an intimal tear that allows blood to flow between the aortic wall layers, causing them to separate. As a result, alongside the original aorta (true lumen), a false lumen (FL) develops. TBAD compromises the whole cardiovascular system, in the worst case resulting in complete aortic rupture. Clinical studies have shown that dilation and rupture of the FL are related to the failure of the FL to thrombose. Complete FL thrombosis has been found to improve the clinical outcomes of patients with chronic TBAD and is the desired outcome of any treatment. Partial FL thrombosis has been associated with late dissection-related deaths and the requirement for re-intervention, thus the level of FL thrombosis is dominant in classifying the risk of TBAD patients. Therefore, it is important to investigate and understand under which conditions complete thrombosis of the FL occurs.

Method: Local FL hemodynamics play an essential role in thrombus formation and growth. In this study, we developed a simplified phenomenological model to predict FL thrombosis in TBAD under physiological flow conditions. Based on an existing shear-driven thrombosis model, a comprehensive model reduction study was performed to improve computational efficiency. The reduced model has been implemented in Ansys CFX and applied to a TBAD case following thoracic endovascular aortic repair (TEVAR) to test the model. Predicted thrombus formation based on post-TEVAR geometry at 1-month was compared to actual thrombus formation observed on a 3-year follow-up CT scan.

Results: The predicted FL status is in excellent agreement with the 3-year follow-up scan, both in terms of thrombus location and total volume, thus validating the new model. The computational cost of the new model is significantly lower than the previous thrombus model, with an approximate 65% reduction in computational time. Such improvement means the new model is a significant step towards clinical applicability.

Conclusion: The thrombosis model developed in this study is accurate and efficient at predicting FL thrombosis based on patient-specific data, and may assist clinicians in choosing individualized treatments in the future.

KEYWORDS

type B aortic dissection, thoracic endovascular aortic repair, false lumen thrombosis, phenomenological modelling, computational fluid dynamics

1 Introduction

Aortic dissection (AD) is a dangerous pathological condition with a high mortality rate. AD is characterized by an intimal tear that allows blood to flow between the aortic wall layers, causing them to separate. As a result, alongside the original aorta known as the true lumen (TL), a new false lumen (FL) develops. The FL can rapidly extend along the aorta and serves as an alternative pathway for the blood flow. It is common for secondary re-entry tears to develop, creating additional communication channels between the TL and FL. This aortic disaster compromises the whole cardiovascular system, which in the worst case can lead to complete rupture of the aorta (Elefteriades et al., 1992). Based on the Stanford classification system of AD (Daily, 1970), if AD occurs in the ascending aorta, it is classified as a type A aortic dissection (TAAD), and if it originates in the descending aorta, it is classified as a type B aortic dissection (TBAD). In TAAD, urgent surgical intervention is necessary because more critical complications can occur due to blood flow to the brain being compromised (Salameh and Ratchford, 2016). In TBAD, depending on the patient's conditions, medical treatment (non-invasive management of the patient with anti-hypertensive drugs) or thoracic endovascular aortic repair (TEVAR) are typically adopted (Pape et al., 2015). TEVAR is a minimally-invasive procedure in which a stent-graft is inserted into the TL to cover the primary entry tear to stop blood flow into the FL and to provide structural support to the weakened vessel to promote TL remodeling.

The local hemodynamic conditions in the FL contribute to the formation and growth of thrombus (Menichini and Xu, 2016). Based on the level of FL thrombosis, the FL status is classified as patent FL, partially thrombosed FL, and completely thrombosed FL (Tsai et al., 2007). Partial thrombosis is the simultaneous presence of thrombus and flow in the FL. Similarly, the presence of only flow and only thrombus corresponds to patent FL and completely thrombosed FL, respectively (Tsai et al., 2007; Trimarchi et al., 2013). Clinical studies have shown that dilation and rupture of the FL are related to the failure of the FL to thrombose (Evangelista et al., 2012). A significant predictor for late dissection-related deaths and retreatment of the descending aorta is the FL thrombosis status, with studies showing that FL growth rate and mortality of AD patients are significantly higher in the case of a partially thrombosed FL (Bernard et al., 2001; Akutsu et al., 2004; Sueyoshi et al., 2004; Trimarchi et al., 2006; Tsai et al., 2007; Fattouch et al., 2009; Trimarchi et al., 2013).

Tsai et al. (2007) showed that the risk of death for patients with a partially thrombosed FL is 2.7 times higher than for patients with a patent FL. They hypothesized that a so-called "blind sac", which occludes the distal tear, results in aneurysmal dilation or rupture. The risk of rupture might also increase because of local hypoxia in the aortic wall adjacent to the formed thrombus. Similar to aortic aneurysms, hypoxia can increase local inflammations, neovascularization, and localized wall weakening (Satta et al., 1996; Vorp et al., 2001). Thus the aortic wall might be more prone to failure. However, not all clinical studies support that a partial thrombus leads to an increased risk of death (Sueyoshi et al., 2009).

Complete thrombosis of FL has been shown to improve the clinical outcomes of chronic TBAD patients (Bernard et al., 2001; Akutsu et al., 2004; Sueyoshi et al., 2004; Trimarchi et al., 2006; Tsai et al., 2007; Fattouch et al., 2009; Trimarchi et al., 2013; Tanaka et al., 2014; Naim et al., 2016). In particular, it decreases the death risk and is associated with the lowest FL growth rates. Hence, complete FL thrombosis is the desired outcome of any treatment, to slow down or potentially stop the dissection progression. Therefore, it is important to investigate and understand under which conditions complete FL thrombosis occurs.

Since thrombus formation can be inhibited due to hemodynamic conditions (well perfused regions with high velocities and shear rates), TEVAR can be used to promote favourable thrombosis conditions by limiting blood flow into the FL through occlusion of the primary entry tear. Nienaber et al. (2009) showed that up to 91.3% of patients who underwent TEVAR achieved complete FL thrombosis and the positive morphological remodeling over time.

Clinical decision-making is usually confined to identifying high-risk patients based on recommended guidelines. Given the clear evidence of the importance of FL thrombosis status in TBAD, modelling thrombosis and predicting how a patient's dissection will develop is highly desirable to aid clinicians in providing the appropriate treatment.

Menichini et al. (2016) presented the first study predicting FL thrombosis in patient-specific geometries of TBAD patients, using a hemodynamics-based model which was first developed and tested in idealised cases (Menichini and Xu, 2016). The model has been further developed and applied in clinically focused studies (Menichini et al., 2018; Armour et al., 2020b), with the most up-to-date form of the model being presented and utilised in a study on the influence of FL perfused side branches on thrombosis (Armour et al., 2022). In the model, thrombus formation depends on local hemodynamic conditions in the FL, which are influenced by the dissection morphology, such as the location, size, number

of intimal tears, and the dimensions of the FL. Among the quantities related to hemodynamic conditions, shear rate and shear stress play a significant role in driving FL thrombosis (Menichini et al., 2016; Menichini and Xu, 2016; Menichini et al., 2018; Jafarinia et al., 2020; Armour et al., 2022).

Five field variables (resting, activated, and bound platelets, coagulant, and residence time) which simplify and represent the coagulation cascade and hemostasis process are modelled through a series of convection-diffusion-reaction equations to predict thrombosis (Menichini and Xu, 2016). The model's kinetic parameters are not related to specific biochemical reactions in the homeostasis process; therefore, these parameters are artificially accelerated. Understanding the relation between computational and actual time would require analysis of the model using a substantial amount of follow-up patient scans. However, such suitable time-resolved data on thrombus formation is very sparse, which makes the modeling process challenging. As a result, there is no connection between simulation time and real time taken for thrombus to form.

To reduce the complexity of the model and make it more efficient, it is beneficial to reduce the number of equations and variables. Melito et al. (2020) performed a sensitivity analysis on Menichini and Xu's 2016 model and showed that not all the model parameters influence thrombus formation, meaning that the model can be reduced. Model reduction is of interest for several reasons. First, reducing the number of equations and input parameters allows for easier control of the thrombus formation process. Each input parameter is a potential source of uncertainty; therefore, reducing the number of input parameters makes the thrombus formation model less prone to output variation. Second, model reduction will significantly reduce the computational cost. Menichini and Xu's 2016 model requires five partial differential equations to be solved alongside the Navier-stokes equations, meaning simulations take on the order of 1–2 weeks to complete depending on patient-specific details such as cardiac cycle length. The computational cost increases even more when considering structural wall mechanics by performing fluid-structure-interaction (FSI) simulations - Chong et al. (2022) performed an integrated FSI-thrombus study in an idealised geometry with Menichini and Xu's 2016 model, with simulations taking 2–3 months to complete.

Given that the key aim of this field of work is clinical impact and being able to predict thrombus formation for making clinical decisions, reducing the computational time and improving applicability are imperative. Thus, this study aims at developing a new thrombosis model, starting from the work of Menichini and Xu (2016), guided by the sensitivity analysis by Melito et al. (2020). This paper presents a new and simplified thrombosis model, along with validation of the model in a patient-specific post-TEVAR TBAD case.

2 Materials and methods

2.1 Thrombus growth model

The newly developed model predicts thrombus formation through a single equation, known as the coagulant equation. The coagulant equation (Eq. 1) is interpreted as the lumped effect of all the biochemical reactions in the coagulation cascade. Coagulant is released into the domain from the wall based on the specific conditions at the wall. Furthermore, it can be formed in the domain *via* a source term that drives coagulant production in regions where coagulant is already present. Hence, the coagulant is modelled through a diffusion-reaction equation.

The degree of thrombosis is represented by the concentration of coagulant (Eq. 6) and thrombus growth begins in regions of low cycle-averaged wall shear stress and cycle-averaged bulk shear rate. However, the negative influence of high instantaneous shear rates on the hemostasis process and thrombus formation is highlighted in several studies (Goel and Diamond, 2002; Taylor et al., 2014, 2016). Thus, to avoid thrombus growth in high shear rate zones, the instantaneous shear rate on the surface of the thrombus plays an important role and is incorporated into the coagulant equation. This allows for instantaneous control over the thrombus growth, while also allowing for the growth rate to significantly increase without facing numerical inaccuracy or instability in recirculation and low shear rate zones.

The model is based on the following assumptions:

1) The thrombus formation can initiate from the wall only if cycle-averaged shear stress $\langle \tau_w \rangle$ falls below the threshold value of 0.15Pa. This value is taken from Armour et al. (2022), the most up to date version of Menichini & Xu's model (2016), which has tuned the TAWSS threshold based on application of the model to multiple patient-specific geometries over numerous studies. In the current study we refer to $\langle \tau_w \rangle$ as time-averaged wall shear stress (TAWSS). Where this condition is met, there will be a flux of coagulant c into the domain from the wall.
2) The growth of thrombus into the bulk of the domain is only controlled by the shear rate $\dot{\gamma}$. Thrombus forms and grows in regions of low cycle-averaged shear rate $\langle \dot{\gamma} \rangle$. Simultaneously, thrombus growth is inhibited at high shear rates by computing the instantaneous shear rate at the surface of the thrombus. This criterion is implemented in the source term of the coagulant equation (Eq. 1).
3) The thrombus model is coupled with the modified Navier-Stokes equations, where the effect of a growing thrombus on flow is modelled through a fictitious body force. Incorporating the fictitious body force into Navier-Stokes equations was proposed by (Fogelson, 1992) and employed by (Menichini and Xu, 2016). The thrombus forms where the concentration of coagulant is sufficiently higher than a threshold value.

TABLE 1 Thrombus formation model parameters.

Parameter	Symbol	Value	Unit
Coagulant diffusivity	D_c	1e-08	m^2/s
Coagulant kinetic constant	k_c	2×10^5	$mol/m^3/s$
Coagulant concentration threshold	c_t	2×10^4	mol/m^3
Coagulant kinetic constant at wall	k_{cw}	2×10^4	$mol/m^3/s$
Coagulant concentration threshold at wall	c_{wt}	2×10^5	mol/m^3
Shear rate threshold	$\dot{\gamma}_t$	1	s^{-1}
Cycle-averaged shear rate threshold	$\langle\dot{\gamma}\rangle_t$	1	s^{-1}

The coagulant equation is

$$\frac{\partial c}{\partial t} = \nabla\cdot\left(D_{c_{eff}}\nabla c\right) + S_c\ \phi_{\langle\dot{\gamma}\rangle}\ \phi_{\dot{\gamma}}, \tag{1}$$

where

$$S_c = \underbrace{k_c\frac{c^2}{c^2+c_t^2}}_{\text{Coagulant production}}, \tag{2}$$

$$\phi_{\langle\dot{\gamma}\rangle} = \underbrace{\left(\frac{\langle\dot{\gamma}\rangle_t^2}{\langle\dot{\gamma}\rangle^2+\langle\dot{\gamma}\rangle_t^2}\right)^2}_{\text{Growth enhancement in low}\langle\dot{\gamma}\rangle}, \tag{3}$$

$$\phi_{\dot{\gamma}} = \underbrace{\left(1-\left(1-\frac{\dot{\gamma}_t^2}{\dot{\gamma}^2+\dot{\gamma}_t^2}\right)\left(\frac{|\nabla\phi_{th}|^2}{|\nabla\phi_{th}|^2+1}\right)\right)}_{\text{Inhibition of growth due to high }\dot{\gamma}\text{ at the surface}}, \tag{4}$$

and

$$D_{c_{eff}} = D_c\ \phi_{\langle\dot{\gamma}\rangle}^2, \tag{5}$$

where c is coagulant, c_t denotes a threshold value above which it is assumed that thrombus begins to form, D_c is the constant coagulant diffusivity, $D_{c_{eff}}$ is the shear enhanced coagulant diffusivity, k_c is the coagulant kinetic constant, and $\langle\dot{\gamma}\rangle_t$ is the cycle-averaged shear rate threshold. Numerical values for constant parameters are reported in Table 1. The values for these parameters were chosen during model development to ensure the predicted thrombus patterns matched those of the original model (Menichini and Xu, 2016) in an idealised geometry. Since thrombus formation and growth occur over a much larger timescale (weeks/months) compared to the period of a cardiac cycle (second), our strategy was to artificially accelerate the kinetics of thrombosis as explained in the original paper by Menichini and Xu (2016). As a result, the simulated thrombus growth time has no correlation with real time growth observed in the patient.

The degree of thrombosis ϕ_{th} depends on the coagulant concentration, as

$$\phi_{th}(c, c_t) = \frac{c^2}{c^2+{c_t}^2}. \tag{6}$$

ϕ_{th} ranges between $0 \le \phi_{th} \le 1$. For visualising results, complete thrombosis was defined as $\phi_{th} \ge 0.8$.

The Neumann boundary condition on the wall is

$$D_{c_{eff}}\frac{\partial c}{\partial \boldsymbol{n}} = \begin{cases} k_{cw} & \langle\tau_w\rangle \le 0.15\text{Pa} \quad \text{and} \quad c_w \le c_{wt} \\ 0 & \text{Otherwise} \end{cases}, \tag{7}$$

where k_{cw} is the coagulant kinetic constant at the wall, c_w is the concentration of coagulant at the wall, and c_{wt} is the coagulant concentration threshold at the wall. The values of k_{cw} and c_{wt} are reported in Table 1.

2.2 Rheological model

The thrombus growth model is fully embedded in the CFD model in order to account for the effect of thrombus growth on flow and the haemodynamic conditions that drive the thrombosis process. Hemodynamics and thrombus formation are coupled through the modified Navier-Stokes equation. The blood is modeled as a non-Newtonian, incompressible fluid. Assuming a constant density ρ, the mass balance reduces to the velocity field's solenoidality, i.e., the continuity equation $\nabla\cdot\boldsymbol{u} = 0$. The modified Navier-Stokes equation which couples blood flow with thrombus growth reads

$$\rho\left[\frac{\partial \boldsymbol{u}}{\partial t} + (\boldsymbol{u}\cdot\nabla)\boldsymbol{u}\right] = -\nabla p + \nabla\cdot\boldsymbol{\tau} - k_{th}\phi_{th}\boldsymbol{u}, \tag{8}$$

with pressure p and the extra stress tensor $\boldsymbol{\tau}$. The Navier-Stokes equation is modified by a sink term $k_{th}\phi_{th}\boldsymbol{u}$, which accounts for the degree of local thrombosis through the variable ϕ_{th} and a coefficient k_{th} which is chosen to effectively stop the flow when ϕ_{th} approaches a value of 1 (Menichini et al., 2016). The coupling of the thrombosis model with the Navier-Stokes equations means that while the hemodynamic conditions are driving the thrombus growth, the thrombus growth also influences the flow field.

The extra stress tensor $\boldsymbol{\tau}$ is determined by a model equation taking into account the shear-rate dependent behavior of the dynamic viscosity η. The rheological model of blood as a shear-thinning liquid determines the extra stress tensor as a function of the rate-of-deformation tensor,

$$\boldsymbol{\tau} = 2\eta(\dot{\gamma})\boldsymbol{D}. \tag{9}$$

where the rate-of-deformation tensor $\boldsymbol{D}$ is defined as the symmetric part of the velocity gradient $\nabla\boldsymbol{u}$,

$$\boldsymbol{D} = \frac{1}{2}\left(\nabla\boldsymbol{u} + \nabla\boldsymbol{u}^T\right), \tag{10}$$

and viscous stress and rate of strain magnitudes are given by

$$|\boldsymbol{\tau}| = \sqrt{\text{tr}(\boldsymbol{\tau}^2)/2}, \tag{11}$$

$$\dot{\gamma} = \sqrt{2\text{tr}(\boldsymbol{D}^2)}. \tag{12}$$

TABLE 2 Values of model parameters of the rheological and thrombus models.

Parameter description	Symbol	Value	Unit
Viscosity at zero shear rate	η_0	1.581×10^{-2}	Pa s
Viscosity at infinite shear rate	η_∞	2.779×10^{-3}	Pa s
Time constant	λ	1.561	s
Power index	n_η	0.475	—
Blood density	ρ	1.060×10^3	kg/m^3

Carreau's model (Carreau, 1968) is then implemented for rheological modeling,

$$\eta(\dot{\gamma}) = \eta_\infty + (\eta_0 - \eta_\infty)\left[1 + (\lambda\dot{\gamma})^2\right]^{(n_\eta - 1)/2}. \quad (13)$$

Both parameters η_0 and η_∞ represent a limiting behavior of the model. For low shear rates the viscosity tends to η_0, the zero-shear viscosity (1st Newtonian plateau). In contrast, for high shear rates, the viscosity tends to η_∞ (2nd Newtonian plateau). The power-law region is defined by n_η, and λ determines the shape of the transition from the first Newtonian plateau to the power-law region.

The model parameters η_0, η_∞, λ, and n_η were determined from experimental data, as reported by Jafarinia et al. (2020). The values are listed in Table 2.

2.3 Patient-specific modelling

The simplified model was applied to a patient-specific case to demonstrate the model's capability of predicting thrombosis in a physiological dissection geometry. Computer tomography (CT) data from a TBAD patient treated with TEVAR using a Gore TAG device (Gore Medical, Flagstaff, AZ, United States) as part of the ADSORB trial (Brunkwall et al., 2014) is employed in this study to evaluate the simplified phenomenological thrombosis model in a patient-specific geometry. Formal ethical approval was not required for this study, as prior agreement was made to undertake computational modeling using anonymized images and data. CT scans were taken one-month and 3-year post-TEVAR using a Brilliance 40 (Philips Healthcare, Best, Netherlands) scanner with a kVp of 120 and voxel size of $0.47 \times 0.47 \times 0.8$ mm^3. From these CT scans, geometries were segmented using Mimics (Materialize HQ, Leuven) and are shown in Figures 1A,B. The thrombus model was implemented in the 1-month post-TEVAR geometry as a starting morphology and was run until thrombus growth

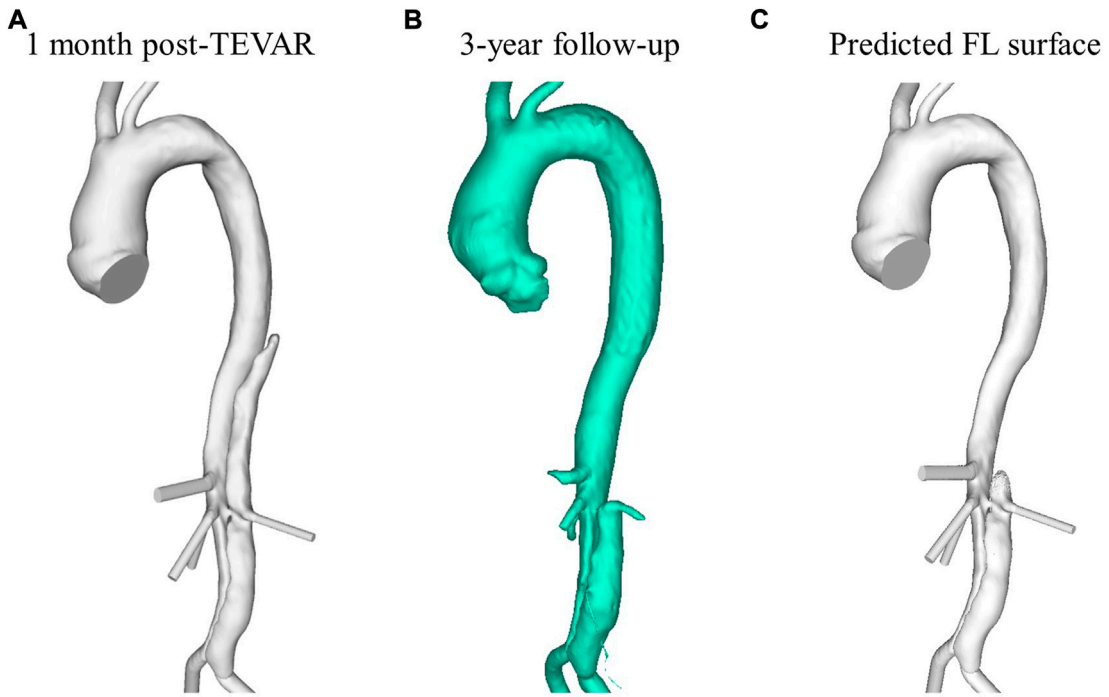

FIGURE 1
Reconstructed aorta from **(A)** 1-month post-TEVAR and **(B)** 3-year follow up CT scan. **(C)** Predicted FL surface after thrombus growth over 20 cardiac cycles using the model presented in this study.

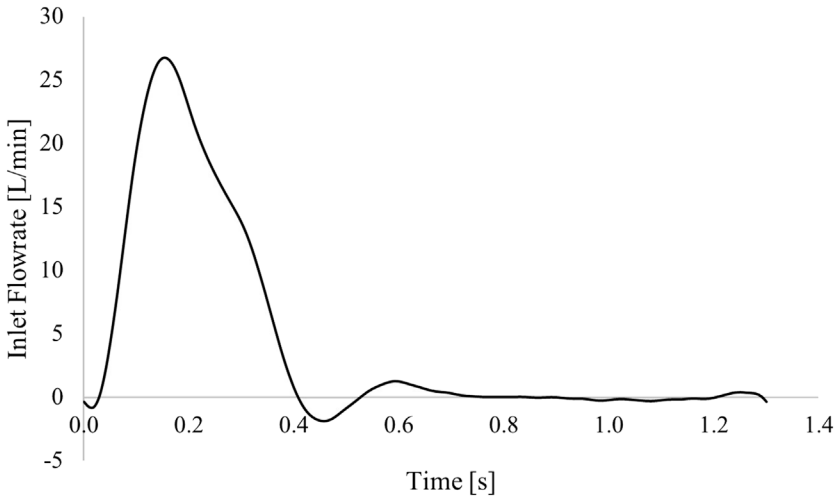

FIGURE 2
Inlet flow rate applied in the simulation.

plateaued. Given the accelerated kinetics, our model was designed to predict the final status of false lumen thrombosis rather than the actual growth rate. For this patient, the final simulated false lumen thrombosis was compared with the 3-year follow-up scan. However, there was no time resolved data so although the CT scan was taken after 3 years it is not necessarily the case that it took 3 years for the thrombus to form.

All major side branches were included when segmenting the geometry for simulation, those being the brachiocephalic artery, left common carotid artery, celiac trunk, superior mesenteric artery, right and left renal arteries, and right and left iliac arteries. The left subclavian artery was occluded by the stent graft. The model was meshed in ICEM (v15, Ansys Inc.) using tetrahedral core elements and ten prismatic layers at the wall. Mesh sensitivity tests were conducted to ensure a grid-independent solution. For each mesh created, mean and maximum wall shear stress and velocity were evaluated on multiple analysis planes in the dissection. The final mesh was chosen when the hemodynamic parameters varied by less than 5% between the selected mesh and a more refined mesh. The final mesh contained approximately 5.5 million elements.

As no patient-specific flow data was available for this case, boundary conditions were extracted from the literature. A flat inlet velocity profile of period 1.3 s was applied at the inlet (Dillon-Murphy et al., 2016) (Figure 2), and 3-element Windkessel (3-EWK) models were applied at all outlets. To tune the 3-EWK models, compliance and total resistance values for each branch were taken from the literature (Dillon-Murphy et al., 2016). Proximal and distal resistances were then calculated based on the total resistance and the branch diameter following the methodology presented by Pirola et al. (2019). Table 3 reports the 3-EWK parameters for each branch.

The simulation was run in Ansys CFX (Ansys, v.15), using a time step of 0.005 s. Two flow-only cycles were run to initialise the domain and calculate the necessary cycle-averaged parameters before the thrombosis model was switched on. The simulation ran for 20 cardiac cycles after which no significant further change in thrombus volume was observed - total predicted thrombus volume varied by ≤ 1% over the final 6 cardiac cycles.

3 Results

Figure 3 shows velocity fields throughout the second systolic phase and TAWSS contours at the end of the second cardiac cycle of the simulation. It can be seen that there are very low velocities throughout the thoracic FL. Compared to the TL, velocities are also low in the abdominal FL; however, a relatively high-velocity jet can be observed in the middle of the abdominal FL. This is where there is a small re-entry tear resulting in blood flow exchange between TL and FL. This can be seen clearly in Figure 4. Helical flow is present from peak systole through to diastole both in the abdominal region and lower thoracic region close to the renal artery. The low velocities in the thoracic FL mean that the TAWSS is close to zero, while higher TAWSS values are observed in the abdominal FL as the velocity jet disperses, with particularly high values opposite the re-entry tear where the velocity jet hits the FL wall (Figure 3D).

The low TAWSS throughout the thoracic FL results in the model predicting complete thrombosis in this region. Figure 1C shows the final FL surface after thrombus formation over 20 cardiac cycles. Due to the increased flow and high TAWSS in the abdominal region, very little thrombus is formed there.

TABLE 3 3-Element Windkessel parameters for all branches. Branches include brachiocephalic (BRAC) and left common carotid (LCCA) artery, celiac trunk (CEL), superior mesentric artery (SMA), right (RR) and left (LR) renal, and right (RI) and left (LI) iliac. Reported parameters are proximal resistance (R1), distal resistance (R2) and compliance (C).

	BRAC	LCCA	CEL	SMA	RR	LR	RI	LI
R1 [$\times 10^8$ *Pa s.m*$^{-3}$]	0.62	2.27	1.66	2.61	3.04	4.18	0.94	0.70
R2 [$\times 10^9$ *Pa s.m*$^{-3}$]	1.40	1.13	0.97	1.02	1.38	1.20	1.48	1.48
C [$\times 10^{-9} m^3.Pa^{-1}$]	13.74	6.14	4.37	3.87	3.56	3.34	0.70	0.64

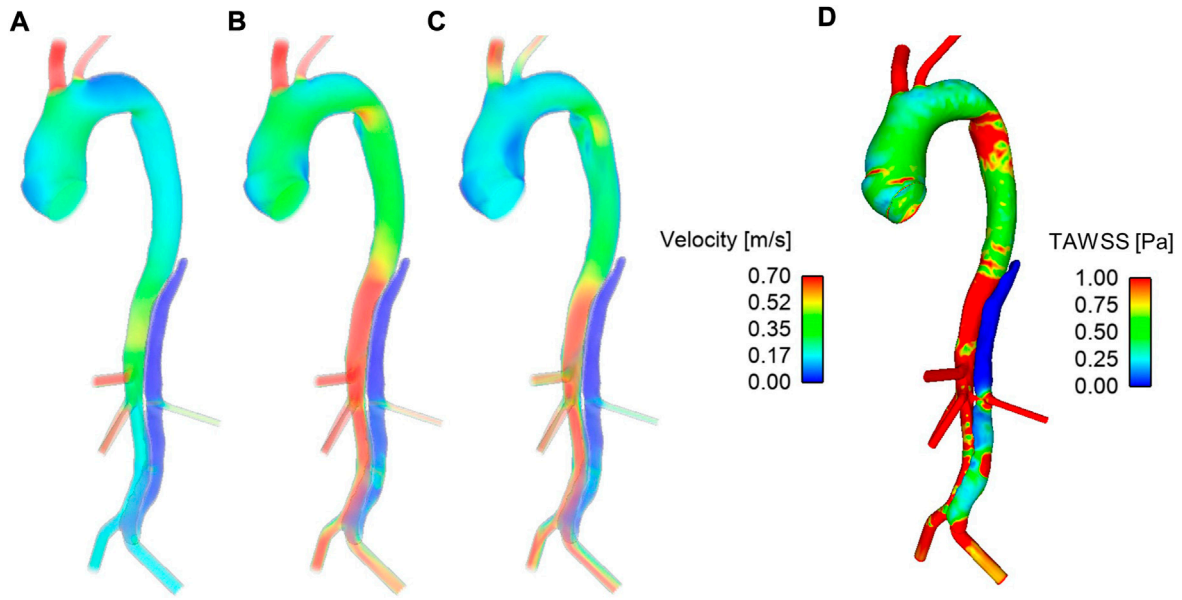

FIGURE 3
Velocity fields at **(A)** mid-systolic acceleration, **(B)** peak systole, and **(C)** mid-systolic deceleration during the second cardiac cycle of the simulation. **(D)** Time-averaged wall shear stress (TAWSS) contours after the second cardiac cycle of the simulation.

This is in line with what was clinically observed in this patient at the 3-year follow-up, as seen in Figure 1B.

4 Discussion

Understanding FL thrombosis is critical in monitoring and treating TBAD patients. With prognosis linked to the degree of thrombus formation (Tsai et al., 2007; Qin et al., 2012), being able to predict the extent and location of thrombus formation when a patient first presents would be very beneficial. The hemodynamics-based model developed by Menichini and Xu (2016) was a great step towards clinical application of thrombus modelling, with results showing the model's capability of predicting thrombus formation in patient-specific geometries (Menichini et al., 2016, 2018; Armour et al., 2020b). Sensitivity tests on the model performed by (Melito et al., 2020) demonstrated that there was potential for simplification to reduce computational cost and improve clinical applicability. This study did just that, removing four of the five variables modelled by Menichini and Xu (2016) (bound, resting and activated platelets, and residence time) and presented a simple one-species, phenomenological thrombus model.

Our results show that the current, simplified model can predict thrombus formation in a patient-specific geometry in accordance with patient-specific measurements. Hemodynamic analysis and thrombus predictions with the original model presented by Menichini et al. (2016) have previously been presented for this patient (Armour et al., 2020b). Figure 5 shows the evolution of the aorta surface, i.e., specifically the surface of the descending aorta FL, at multiple time points as the thrombus grows in the FL, for both the simplified, Figure 5A, and the original, Figure 5B, model. It can be seen that in the thoracic FL, growth patterns are similar for both models; however, complete thrombosis of the thoracic FL was predicted quicker with the simplified model.

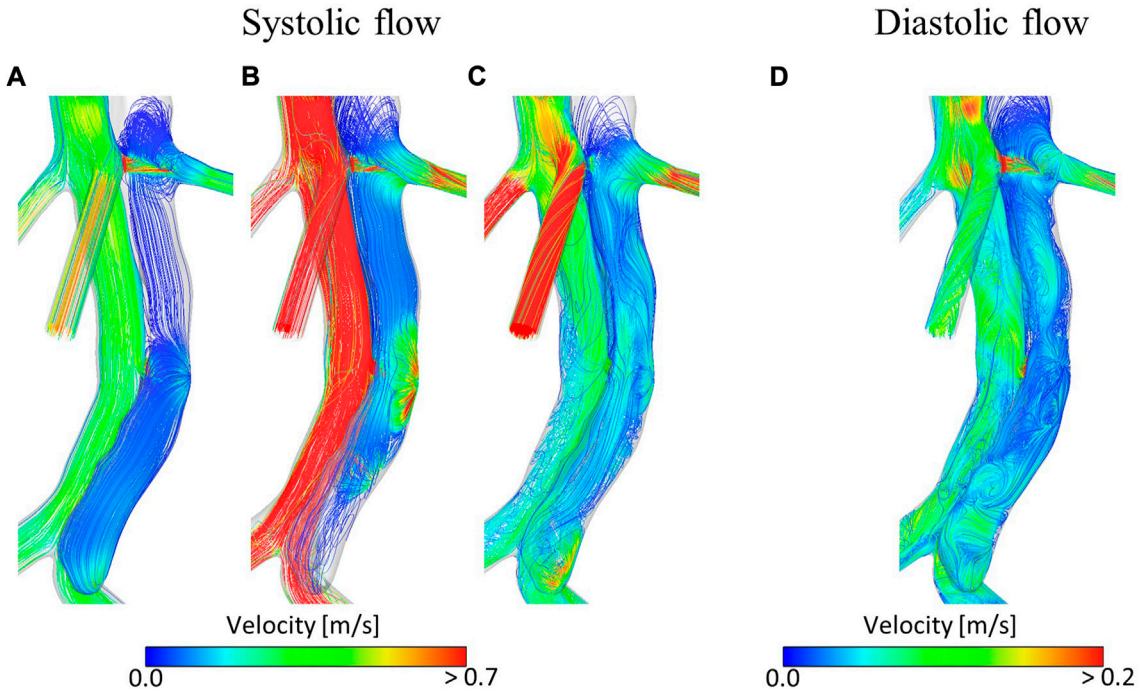

FIGURE 4
Velocity streamlines at **(A)** mid-systolic acceleration, **(B)** peak systole, **(C)** mid-systolic deceleration, **(D)** early diastole during the second cardiac cycle of the simulation.

The volume of thrombus in the thoracic FL was measured at the end of each cardiac cycle and is shown in Figure 6. These results show that the original model saw an initially quicker thrombus growth rate, with the growth rate then slowing down and the final thrombus volume being reached after approximately 16 cardiac cycles. In the simplified model the growth rate was mostly constant from the beginning, with the final thrombus volume being reached after approximately 12 cardiac cycles.

An unintended result of the simplified model was improved thrombosis prediction in the abdominal FL. Very little thrombus was predicted by the simplified model (levels not observable in the images) while significant thrombus formation was predicted in the original model. As explained in Section 2.1, the parameters listed in Table 1 were chosen to ensure predicted thrombus results of the simplified model matched the results of the original model in an idealised geometry. In both models, all equations and parameters interact to control the thrombosis process, and with four of the five species originally modelled being removed in the simplified model, it is understandable that the numerical values for the model parameters common to both models differ. However, given the simplified model is derived from the original based on the general concept of hemodynamic-based thrombus formation, hemodynamic parameters can be compared when discussing differences in predicted thrombus patterns. Specifically, the differences in predicted abdominal thrombus formation may be influenced, although not solely, by the differing bulk shear rate threshold values. The original model had a bulk shear rate threshold of 50 s^{-1}, while the simplified model has a bulk shear rate threshold of 1 s^{-1}. In this specific patient, the influence of this change was significant. There were areas in the abdominal FL where the TAWSS was below the threshold of 0.15 Pa, which resulted in coagulant beginning to form on the wall in both models. However, the shear rates in this region were above 1 s^{-1}, thus inhibiting thrombus formation in the simplified model, and below 50 s^{-1}, thus a substantial amount of thrombus grew in the original model. Figure 1B shows that at the 3-year follow-up very little thrombus was observed in the abdominal FL, in line with the results of the simplified model.

Computational time was significantly reduced with the simplified model. Running the simulation in parallel using 24 cores, the original model took just over 10 h per cycle, while the simplified model took approximately 3.5 h per cycle. This is an approximate 65% reduction in computational time. Reduced computational time due to the reduction in modelled species combined with the fewer number of cycles needed to reach the final thrombus volume means the simplified model is a significant step towards clinical applicability.

A key limitation of this study is that no patient-specific flow data was available, thus for the inlet and outlet boundary conditions data from the literature was utilised. Armour et al. (2020a) showed that TAWSS magnitudes are highly impacted

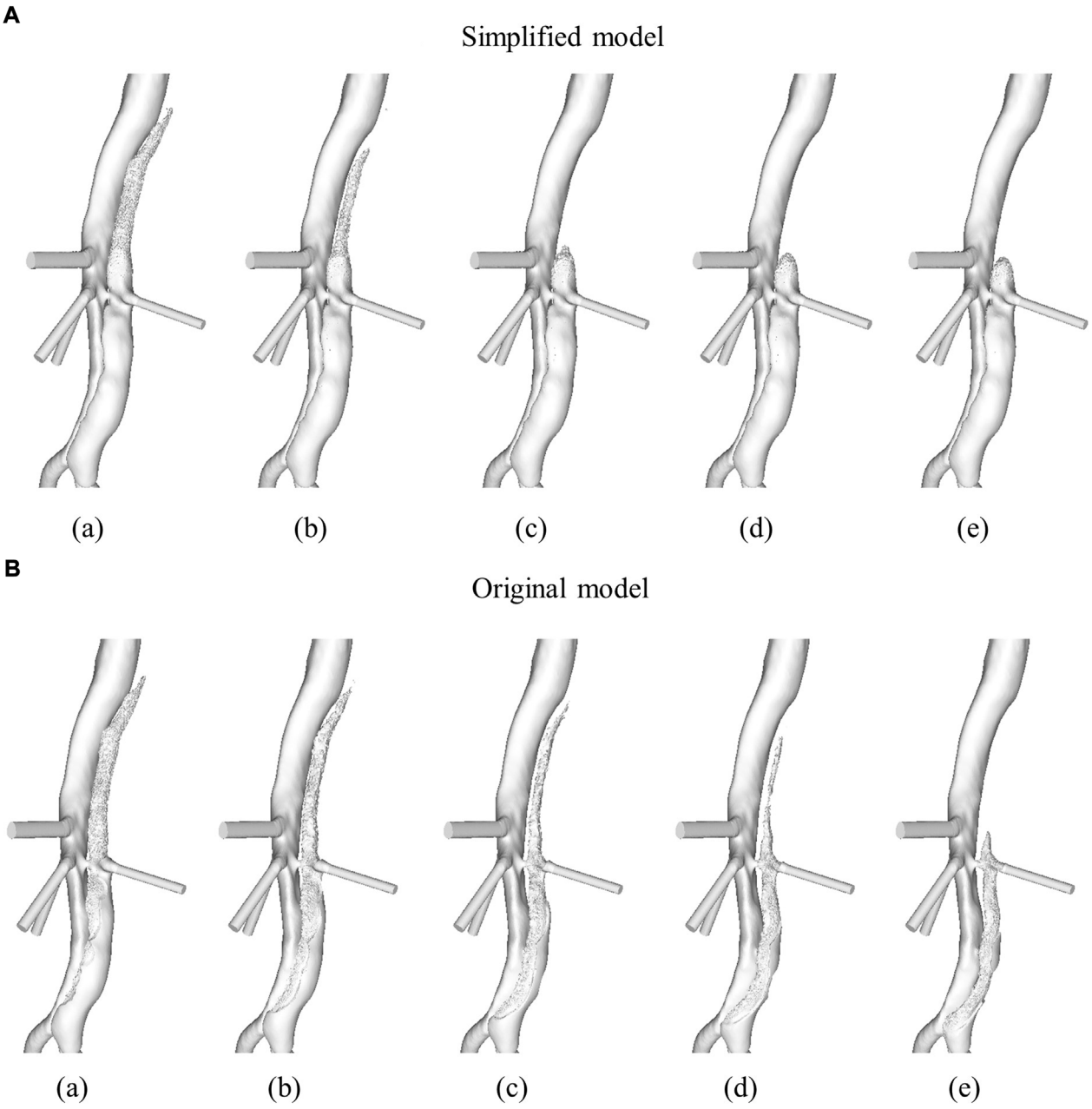

FIGURE 5
Evolution of the descending aorta false lumen surface due to thrombus formation in **(A)** simplified model and **(B)** original model. Time points presented are after **(a)** 6, **(b)** 9, **(c)** 12, **(d)** 15, and **(e)** 20 cardiac cycles. Figure adapted from Armour et al. (2020b).

when non-patient-specific stroke volumes are used. While it appears that the generic inlet boundary condition did not significantly impact thrombus results in this case, likely due to the fact that there was very little flow in the thoracic FL where the thrombus formed, and therefore any error in TAWSS values would be insignificant, this may not hold in all cases. In patients where the thrombus is forming in a more perfused section of the FL, the TAWSS patterns will be more influential. Application of the model to a larger patient cohort would allow for the model to be tested across a range of morphologies and flow fields to ensure accuracy and applicability in all TBAD cases, building upon the single patient study presented here. In this way, the role of current values for shear rate threshold and other parameters can be further investigated. Additionally, performing a global sensitivity analysis, similar to the study of Melito et al. (2020), would be beneficial for revealing the sensitivity of the results to

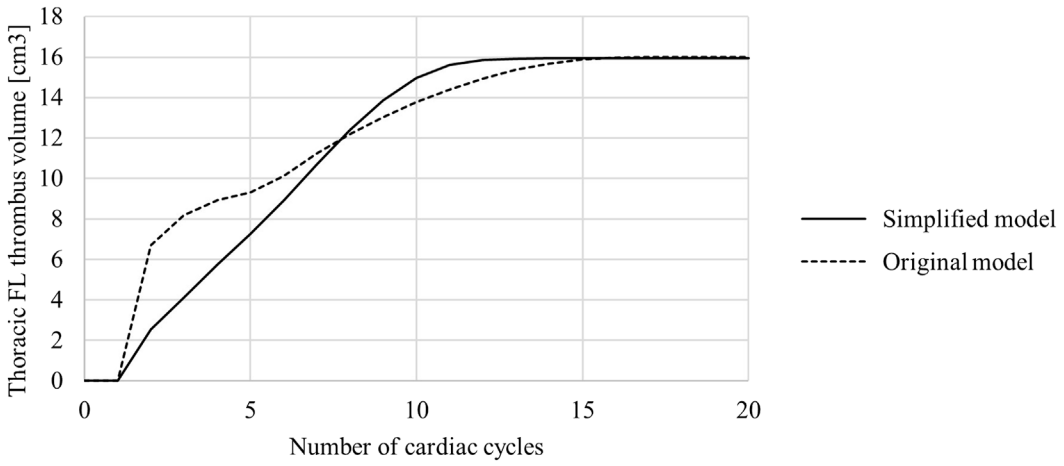

FIGURE 6
Thoracic false lumen (FL) thrombus volume in the original and simplified model. Volume was measured at the end of each cardiac cycle.

each parameter. Future work can also explore the use of mesh deformation, such as the work presented by Di Achille et al. (2016), to capture the finer details at the evolving thrombus surface as our mesh sensitivity tests were conducted on the thrombus-free hemodynamics only. Furthermore, our simulation assumed a rigid wall. In a study using an idealised geometry, Chong et al. (2022) demonstrated that accounting for wall compliance and flap motion can results in a 25% increase in the volume of thrombus formed. Flap stiffness varies from patient to patient, and tends to increase with the age of dissection (Peterss et al., 2016), thus the flap may have been less mobile in this post-TEVAR case making the rigid wall assumption less impactful. Again, this limitation can be assessed in future work, however our initial results show that the rigid wall assumption may be feasible for quick model predictions. Finally, the time taken for thrombus growth in the simulation has no correlation to the real time taken for the thrombus to grow in the patient. A carefully planned study with an extensive set of follow-up scans showing progressive thrombus growth in a patient would allow for the relationship between these two time scales to be elucidated.

Data availability statement

The raw data supporting the conclusion of this article will be made available by the authors, without undue reservation.

Ethics statement

Ethical review and approval was not required for the study on human participants in accordance with the local legislation and institutional requirements. Written informed consent for participation was not required for this study in accordance with the national legislation and the institutional requirements.

Author contributions

Methodology, AJ and CA; Formal analysis, AJ and CA; Writing—original draft preparation, AJ and CA; Writing—review and editing, AJ, CA, XX, and TH; Data curation, RG; Funding acquisition and project administration, XX and TH; Supervision, XX and TH.

Funding

CA was supported through a PhD scholarship awarded through United Kingdom Engineering and Physical Sciences Research Council Doctoral Training Partnership grant to Imperial College London [EP/R512540/1]. This work was funded by Graz University of Technology, Austria, through the LEAD Project on “Mechanics, Modeling, and Simulation of Aortic Dissection”. This work is supported by TU Graz University of Technology open access publishing fund.

Conflict of interest

The authors declare that the research was conducted in the absence of any commercial or financial relationships that could be construed as a potential conflict of interest.

Publisher's note

References

Akutsu, K., Nejima, J., Kiuchi, K., Sasaki, K., Ochi, M., Tanaka, K., et al. (2004). Effects of the patent false lumen on the long-term outcome of type B acute aortic dissection. *Eur. J. Cardio-Thorac. Surg.* 26, 359–366. doi:10.1016/j.ejcts.2004.03.026

Armour, C. H., Guo, B., Pirola, S., Saitta, S., Liu, Y., Dong, Z., et al. (2020a). The influence of inlet velocity profile on predicted flow in type B aortic dissection. *Biomech. Model. Mechanobiol.* 20, 481–490. doi:10.1007/s10237-020-01395-4

Armour, C. H., Menichini, C., Hanna, L., Gibbs, R. G. J., and Xu, X. Y. (2022). "Computational modeling of flow and thrombus formation in type B aortic dissection: The influence of false lumen perfused side branches," in *Solid (Bio) mechanics: Challenges of the next decade. Studies in mechanobiology, tissue engineering and biomaterials* (Cham: Springer), 53–72. chap. 2.

Armour, C. H., Menichini, C., Milinis, K., Gibbs, R. G., and Xu, X. Y. (2020b). Location of reentry tears affects false lumen thrombosis in aortic dissection following TEVAR. *J. Endovasc. Ther.* 27, 396–404. doi:10.1177/1526602820917962

Bernard, Y., Zimmermann, H., Chocron, S., Litzler, J.-F., Kastler, B., Etievent, J.-P., et al. (2001). False lumen patency as a predictor of late outcome in aortic dissection. *Am. J. Cardiol.* 87, 1378–1382. doi:10.1016/s0002-9149(01)01556-9

Brunkwall, J., Kasprzak, P., Verhoeven, E., Heijmen, R., Taylor, P., Alric, P., et al. (2014). Endovascular repair of acute uncomplicated aortic type b dissection promotes aortic remodelling: 1 year results of the ADSORB trial. *Eur. J. Vasc. Endovasc. Surg.* 48, 285–291. doi:10.1016/j.ejvs.2014.05.012

Carreau, P. J. (1968). *Rheological equations from molecular network theories*. Madison: University of Wisconsin. Ph.D. thesis. doi:10.1122/1.549276

Chong, M. Y., Gu, B., Armour, C. H., Dokos, S., Oong, Z. C., Xu, X. Y., et al. (2022). An integrated fluid-structure interaction and thrombosis model for type b aortic dissection. *Biomech. Model. Mechanobiol.* 21, 261–275. doi:10.1007/s10237-021-01534-5

Daily, P. O., Trueblood, H. W., Stinson, E. B., Wuerflein, R. D., and Shumway, N. E. (1970). Management of acute aortic dissections. *Ann. Thorac. Surg.* 10, 237–247. doi:10.1016/s0003-4975(10)65594-4

Di Achille, P., Tellides, G., and Humphrey, J. D. (2016). Hemodynamics-driven deposition of intraluminal thrombus in abdominal aortic aneurysms. *Int. J. Numer. Method. Biomed. Eng.* 33, e2828. doi:10.1002/cnm.2828

Dillon-Murphy, D., Noorani, A., Nordsletten, D., and Figueroa, C. A. (2016). Multi-modality image-based computational analysis of haemodynamics in aortic dissection. *Biomech. Model. Mechanobiol.* 15, 857–876. doi:10.1007/s10237-015-0729-2

Elefteriades, J. A., Hartleroad, J., Gusberg, R., Salazar, A., Black, H., Kopf, G., et al. (1992). Long-term experience with descending aortic dissection: the complication-specific approach. *Ann. Thorac. Surg.* 53, 11–21. doi:10.1016/0003-4975(92)90752-p

Evangelista, A., Salas, A., Ribera, A., Ferreira-González, I., Cuellar, H., Pineda, V., et al. (2012). Long-term outcome of aortic dissection with patent false lumen. *Circulation* 125, 3133–3141. doi:10.1161/circulationaha.111.090266

Fattouch, K., Sampognaro, R., Navarra, E., Caruso, M., Pisano, C., Coppola, G., et al. (2009). Long-term results after repair of type A acute aortic dissection according to false lumen patency. *Ann. Thorac. Surg.* 88, 1244–1250. doi:10.1016/j.athoracsur.2009.06.055

Fogelson, A. L. (1992). Continuum models of platelet aggregation: formulation and mechanical properties. *SIAM J. Appl. Math.* 52, 1089–1110. doi:10.1137/0152064

Goel, M. S., and Diamond, S. L. (2002). Adhesion of normal erythrocytes at depressed venous shear rates to activated neutrophils, activated platelets, and fibrin polymerized from plasma. *Blood* 100, 3797–3803. doi:10.1182/blood-2002-03-0712

Jafarinia, A., Müller, T. S., Windberger, U., Brenn, G., and Hochrainer, T. (2020). Blood rheology influence on false lumen thrombosis in type B aortic dissection. *J. Biosci. Bioeng.* 7, 13–24.

Melito, G. M., Jafarinia, A., Hochrainer, T., and Ellermann, K. (2020). Sensitivity analysis of a phenomenological thrombosis model and growth rate characterisation. *J. Biosci. Bioeng.* 7, 31–40.

Menichini, C., Cheng, Z., Gibbs, R. G. J., and Xu, X. Y. (2016). Predicting false lumen thrombosis in patient-specific models of aortic dissection. *J. R. Soc. Interface* 13, 20160759. doi:10.1098/rsif.2016.0759

Menichini, C., Cheng, Z., Gibbs, R. G., and Xu, X. Y. (2018). A computational model for false lumen thrombosis in type B aortic dissection following thoracic endovascular repair. *J. Biomech.* 66, 36–43. doi:10.1016/j.jbiomech.2017.10.029

Menichini, C., and Xu, X. Y. (2016). Mathematical modeling of thrombus formation in idealized models of aortic dissection: initial findings and potential applications. *J. Math. Biol.* 73, 1205–1226. doi:10.1007/s00285-016-0986-4

Naim, W. N. W. A., Ganesan, P. B., Sun, Z., Liew, Y. M., Qian, Y., Lee, C. J., et al. (2016). Prediction of thrombus formation using vortical structures presentation in Stanford type B aortic dissection: a preliminary study using CFD approach. *Appl. Math. Model.* 40, 3115–3127. doi:10.1016/j.apm.2015.09.096

Nienaber, C. A., Rousseau, H., Eggebrecht, H., Kische, S., Fattori, R., Rehders, T. C., et al. (2009). Randomized comparison of strategies for type B aortic dissection: the investigation of stent grafts in aortic dissection (instead) trial. *Circulation* 120, 2519–2528. doi:10.1161/circulationaha.109.886408

Pape, L. A., Awais, M., Woznicki, E. M., Suzuki, T., Trimarchi, S., Evangelista, A., et al. (2015). Presentation, diagnosis, and outcomes of acute aortic dissection: 17-year trends from the international registry of acute aortic dissection. *J. Am. Coll. Cardiol.* 66, 350–358. doi:10.1016/j.jacc.2015.05.029

Peterss, S., Mansour, A. M., Ross, J. A., Vaitkeviciute, I., Charilaou, P., Dumfarth, J., et al. (2016). Changing pathology of the thoracic aorta from acute to chronic dissection: Literature review and insights. *J. Am. Coll. Cardiol.* 68, 1054–1065. doi:10.1016/j.jacc.2016.05.091

Pirola, S., Guo, B., Menichini, C., Saitta, S., Fu, W., Dong, Z., et al. (2019). 4-D Flow mri-based computational analysis of blood flow in patient-specific aortic dissection. *IEEE Trans. Biomed. Eng.* 66, 3411–3419. doi:10.1109/TBME.2019.2904885

Qin, Y. L., Deng, G., Li, T. X., Jing, R. W., and Teng, G. J. (2012). Risk factors of incomplete thrombosis in the false lumen after endovascular treatment of extensive acute type B aortic dissection. *J. Vasc. Surg.* 56, 1232–1238. doi:10.1016/j.jvs.2012.04.019

Salameh, M. J., and Ratchford, E. V. (2016). Aortic dissection. *Vasc. Med.* 21, 276–280. doi:10.1177/1358863X16632898

Satta, J., Läärä, E., and Juvonen, T. (1996). Intraluminal thrombus predicts rupture of an abdominal aortic aneurysm. *J. Vasc. Surg.* 23, 737–739. doi:10.1016/s0741-5214(96)80062-0

Sueyoshi, E., Sakamoto, I., Hayashi, K., Yamaguchi, T., and Imada, T. (2004). Growth rate of aortic diameter in patients with type B aortic dissection during the chronic phase. *Circulation* 110, II256–61. doi:10.1161/01.cir.0000138386.48852.b6

Sueyoshi, E., Sakamoto, I., and Uetani, M. (2009). Growth rate of affected aorta in patients with type B partially closed aortic dissection. *Ann. Thorac. Surg.* 88, 1251–1257. doi:10.1016/j.athoracsur.2009.06.023

Tanaka, A., Sakakibara, M., Ishii, H., Hayashida, R., Jinno, Y., Okumura, S., et al. (2014). Influence of the false lumen status on clinical outcomes in patients with acute type B aortic dissection. *J. Vasc. Surg.* 59, 321–326. doi:10.1016/j.jvs.2013.08.031

Taylor, J. O., Meyer, R. S., Deutsch, S., and Manning, K. B. (2016). Development of a computational model for macroscopic predictions of device-induced thrombosis. *Biomech. Model. Mechanobiol.* 15, 1713–1731. doi:10.1007/s10237-016-0793-2

Taylor, J., Witmer, K., Neuberger, T., Craven, B., Meyer, R. S., Deutsch, S., et al. (2014). *In vitro* quantification of time dependent thrombus size using magnetic resonance imaging and computational simulations of thrombus surface shear stresses. *J. Biomech. Eng.* 136, 071012. doi:10.1115/1.4027613

Trimarchi, S., Nienaber, C. A., Rampoldi, V., Myrmel, T., Suzuki, T., Bossone, E., et al. (2006). Role and results of surgery in acute type B aortic dissection: insights from the international registry of acute aortic dissection (IRAD). *Circulation* 114, I357–I364. doi:10.1161/circulationaha.105.000620

Trimarchi, S., Tolenaar, J. L., Jonker, F. H. W., Murray, B., Tsai, T. T., Eagle, K. A., et al. (2013). Importance of false lumen thrombosis in type B aortic dissection prognosis. *J. Thorac. Cardiovasc. Surg.* 145, S208–S212. doi:10.1016/j.jtcvs.2012.11.048

Tsai, T. T., Evangelista, A., Nienaber, C. A., Myrmel, T., Meinhardt, G., Cooper, J. V., et al. (2007). Partial thrombosis of the false lumen in patients with acute type B aortic dissection. *N. Engl. J. Med. Overseas. Ed.* 357, 349–359. doi:10.1056/nejmoa063232

Vorp, D. A., Lee, P. C., Wang, D. H. J., Makaroun, M. S., Nemoto, E. M., Ogawa, S., et al. (2001). Association of intraluminal thrombus in abdominal aortic aneurysm with local hypoxia and wall weakening. *J. Vasc. Surg.* 34, 291–299. doi:10.1067/mva.2001.114813

frontiers | Frontiers in Bioengineering and Biotechnology

TYPE Original Research
PUBLISHED 25 November 2022
DOI 10.3389/fbioe.2022.1031600

OPEN ACCESS

EDITED BY
Claudio Chiastra,
Politecnico di Torino, Italy

REVIEWED BY
Fredrik Fossan,
Norwegian University of Science and Technology, Norway
Miquel Aguirre,
Ecole des Mines de Saint-Étienne, France

*CORRESPONDENCE
Maarten Uyttenboogaart,
m.uyttenboogaart@umcg.nl

SPECIALTY SECTION
This article was submitted to Biomechanics, a section of the journal Frontiers in Bioengineering and Biotechnology

RECEIVED 30 August 2022
ACCEPTED 08 November 2022
PUBLISHED 25 November 2022

CITATION
Shen Y, van der Harst JJ, Wei Y, Bokkers RPH, van Dijk JMC and Uyttenboogaart M (2022), Validation of a cerebral hemodynamic model with personalized calibration in patients with aneurysmal subarachnoid hemorrhage. *Front. Bioeng. Biotechnol.* 10:1031600. doi: 10.3389/fbioe.2022.1031600

Validation of a cerebral hemodynamic model with personalized calibration in patients with aneurysmal subarachnoid hemorrhage

Yuanyuan Shen[1], J. Joep van der Harst[2], Yanji Wei[3], Reinoud P. H. Bokkers[4], J. Marc C. van Dijk[1] and Maarten Uyttenboogaart[2,4]*

[1]Department of Neurosurgery, University Medical Center Groningen, University of Groningen, Groningen, Netherlands, [2]Department of Neurology, University Medical Center Groningen, University of Groningen, Groningen, Netherlands, [3]Eastern Institute for Advanced Study, Yongriver Institute of Technology, Ningbo, China, [4]Department of Radiology, Medical Imaging Center, University Medical Center Groningen, University of Groningen, Groningen, Netherlands

This study aims to validate a numerical model developed for assessing personalized circle of Willis (CoW) hemodynamics under pathological conditions. Based on 66 computed tomography angiography images, investigations were obtained from 43 acute aneurysmal subarachnoid hemorrhage (aSAH) patients from a local neurovascular center. The mean flow velocity of each artery in the CoW measured using transcranial Doppler (TCD) and simulated by the numerical model was obtained for comparison. The intraclass correlation coefficient (ICC) over all cerebral arteries for TCD and the numerical model was 0.88 (N = 561; 95% CI 0.84–0.90). In a subgroup of patients who had developed delayed cerebral ischemia (DCI), the ICC had decreased to 0.72 but remained constant with respect to changes in blood pressure, Fisher grade, and location of ruptured aneurysm. Our numerical model showed good agreement with TCD in assessing the flow velocity in the CoW of patients with aSAH. In conclusion, the proposed model can satisfactorily reproduce the cerebral hemodynamics under aSAH conditions by personalizing the numerical model with TCD measurements.

Clinical trial registration: [http://www.trialregister.nl/], identifier [NL8114].

KEYWORDS

cerebral hemodynamic, circle of Willis (CoW), numerical modeling, subarachnoid hemorrhage, transcranial Doppler (TCD)

Introduction

The circle of Willis (CoW) plays a pivotal role in the distribution of blood throughout the brain and in the development of cerebrovascular disease (CVD). Knowledge of the blood flow through the CoW is frequently used in clinical practice, for instance to evaluate hemodynamic impairment in patients with an internal carotid artery occlusion. Furthermore, mechanical forces such as wall shear stress in individual vascular segments of the CoW has been found to correlate with intracranial aneurysm development (Tanweer et al., 2014). Thus, studying the hemodynamics of the CoW helps us understand the pathology of CVD.

Computed tomographic and magnetic resonance angiography (CTA/MRA) and transcranial Doppler (TCD) are the most commonly used techniques in clinical practice to collect information regarding blood flow through the CoW. Both CTA and MRA can accurately depict blood flow through the CoW but offer only morphological information. MR technics may provide additional information on the flow velocity and direction of blood flow in the CoW, but these methods are time-consuming and expensive (Van Laar et al., 2006; Amin-Hanjani et al., 2015; Hartkamp et al., 2018). TCD is an alternative noninvasive bedside tool that can be used to assess the proximal cerebral blood flow (CBF) but is highly operator dependent and limited by patients' bone window conditions (Lui et al., 2005; Lorenz et al., 2009).

Numerical models have been proposed as an alternative method for determining blood flow through the CoW. Previous studies have shown that these models can assess multiple hemodynamic parameters, such as flow velocity and pressure throughout the CoW. Multiple studies have already revealed that various hemodynamic parameters are associated with the development of intracranial aneurysm and carotid artery stenosis. However, their conclusions are all conceptual, and no specific threshold of abnormal hemodynamics has been drawn yet. Numerical models are not used in clinical practice due to their complexity and unproved accuracy. The existing validated models have been attested at a group average level (Reymond et al., 2009) or with a very small number of participants (Reymond et al., 2011; Groen et al., 2018), failing to meet the required sample size of an accuracy test study [50 cases for an expected ICC of 0.8 (de Vet et al., 2011)]. Therefore, with unknown prediction error, it is hard to draw a threshold of abnormal hemodynamics on the basis of a numerical model for any CVD development, e.g., the rupture of aneurysm and tendency of plaque formation in the carotid artery. The prediction error of a numerical model is essential before its personalized application in clinical research.

Moreover, many of the validation studies have been performed in healthy volunteers (Helthuis et al., 2020) or in a physiological state (Alastruey et al., 2007; Liu et al., 2015), while the cerebrovascular environment significantly changes under pathological conditions, especially after the onset of aneurysmal subarachnoid hemorrhage (aSAH), when cerebral vasospasm is prone to occur, the arterial diameter does not vary equally throughout the CoW and the spastic artery might show a beaded pattern. Changes of vascular compliance is another important issue. Elevated blood pressure after subarachnoid hemorrhage (SAH) may lead to an increase in vascular smooth muscle cell tone, which contributes to increased cerebrovascular resistance not only at the level of the CoW (Warnert et al., 2016) (relating to the setting of stiffness constant) but also at the level of smaller arterioles (relating to the setting of boundary conditions). Whether a numerical model can assess CBF under such complicated situations is worth investigating.

In this study, we aimed to validate the accuracy of an in-house–developed numerical model (Shen, et al., 2022) that simulates CBF in the CoW in the subacute phase after aSAH, in which vasospasm reaches a peak at day 6–8 after the rupture of intracranial aneurysm (Weir et al., 1978). Prospectively collected CTA and TCD data of aSAH patients were used in this study, covering the spasm peak period to the greatest extent, thus guaranteeing that the study sample is representative of extensive pathological CBF conditions.

Methods

This study was approved by the institutional ethical review board of the University Medical Center Groningen. The objection register was verified before data collection, and patient consent was therefore not required. The protocol of this study has been previously published (Shen et al., 2020); the Netherlands Trial Register Identifier: NL8114.

Subjects

Clinical and imaging data were collected from a previously completed prospective cohort study (the transcranial Doppler and CT angiography for investigating cerebral vasospasm in subarachnoid hemorrhage—TACTICS—study), which involved adult aSAH patients who had paired TCD and CTA performed at day 5 and day 10 after the onset of aSAH (van der Harst et al., 2019); TCD and CTA were performed within 24 h of each other.

Clinical features

Demographics, blood pressure, Fisher scale, and clinical outcome information were obtained from the TACTICS database. High arterial blood pressure was defined as a systolic blood pressure (sBp) over 140 mmHg. The Fisher

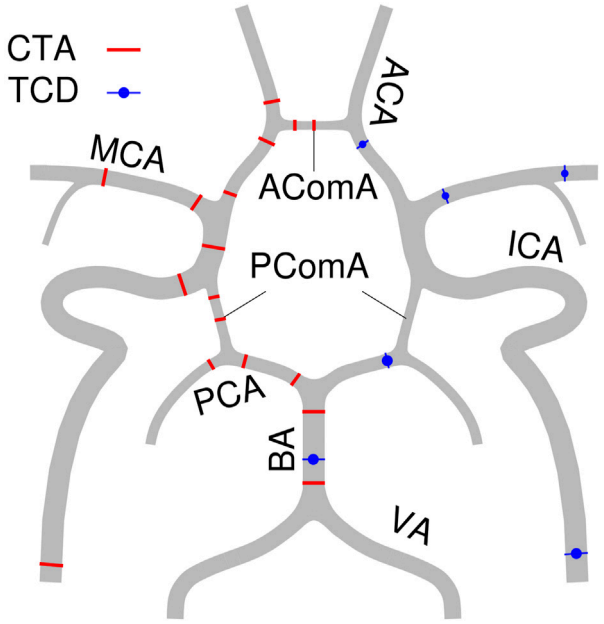

FIGURE 1
Locations of CTA and TCD measurements.

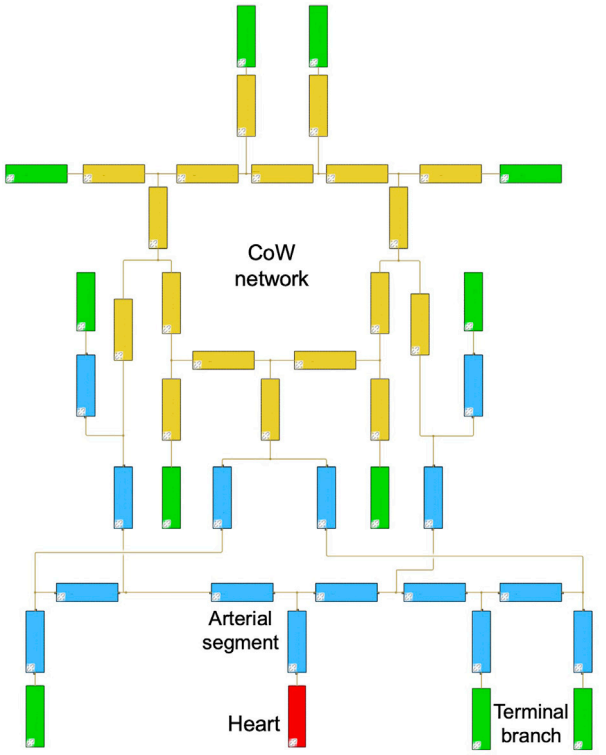

FIGURE 2
Block diagrams of the common arterial network.

Grading Scale based on patients' CT examination at admission was used to rate the severity of SAH (Fisher et al., 1980). Delayed cerebral ischemia (DCI) was defined as neurological deterioration and/or new ischemic lesions on follow-up imaging, not explained otherwise (van der Harst et al., 2019). The parent artery was defined as the artery with aneurysm, and the nonparent artery was the artery that was free from aneurysm.

Transcranial Doppler

Flow velocity measurements with TCD were obtained by trained neurophysiology technicians, according to a standardized protocol (van der Harst et al., 2019). The mean flow velocity of nine cerebral arteries were collected: bilateral distal cervical part of the internal carotid artery (ICA) [C1 segment according to Bouthillier classification of ICA segments (Bouthillier et al., 1996)], bilateral proximal middle cerebral artery (MCA), bilateral anterior cerebral artery (ACA), basilar artery (BA), and bilateral posterior cerebral artery (PCA).

CT angiography

CTA images were acquired on Siemens CT scanners (Siemens AG, München, Germany) in accordance with a standardized imaging protocol, and the CTA images were reconstructed to 0.60–0.75 mm slices (van der Harst et al., 2019). Two physicians (Y.S. and M.U.), blinded to the TCD results and clinical information, evaluated the images for scan quality and measured the diameter of the distal and proximal points of each artery from the brain CTA using the TeraRecon AquariusNET iNtuition Viewer [V.4.4.13 (P4)]. The CTA was excluded if the images were determined as uninterpretable due to movement, insufficient contrast in the arteries, or severe artifacts due to clip/coils.

Three points of each ACA, MCA, PCA, and ICA, as well as two points of BA and three communicating arteries were measured for simulation. The details of these locations have previously been described in the study protocol (Shen et al., 2020) and is sketched in Figure 1.

In the numerical model, each artery segment is depicted as a uniform thin and homogeneous deformable tube, the diameter of which is the volume-equivalent diameter by multiple measure points from CTA.

Numerical model

The hemodynamic model used in this study is based on a block-diagram hydraulics toolbox, Simulink Simscape Fluids library. One of the distinguishing features of the present

model is that it provides an intuitive and a simple way to construct patient-specific models by interconnecting a series of hydraulic components that represent artery segments. The applied common artery network consisted of 18 intracranial artery segments to capture flow feature in the CoW and 15 artery segments from the main body to offer a background blood flow. For personalized simulation, the input diameters were updated with the measured diameters per case. The diameters were assigned 0 if the artery segment was absent in CTA. By this way, the personalized CoW simulation was carried out with the common network as shown in Figure 2.

In the numerical model, the prescribed flow rate was applied at the root of the ascending aorta, and the three-element Windkessel model (WK3) was employed at each terminal branch to avoid unexpected reflection. The conventional approach (Alastruey et al., 2007) assumed that the flow rate was proportional to the cross-section area, as the peripheral resistance of each terminal branch was determined by the given flow distribution. This assumption may be invalid for patients with aSAH. A recent study (Helthuis et al., 2020) employed a structured tree and a simple autoregulatory model at the distal boundary conditions based on the measurement from healthy volunteers. It is unclear what the impact of aSAH is on edema and autoregulation, particularly during severe vascular spasms. The present numerical model proposed a three-step procedure, with the patient's TCD and blood pressure measurements as input, to calibrate the personalized resistance and compliance of WK3. This procedure tailored the boundary of the Simulink model per patient per case under different aSAH conditions. The implementation of the three-step procedure is as follows:

1) Determining the peripheral resistance at each terminal branch with a linear electric circuit model, using the mean blood pressure and mean flow rate as input;
2) Correcting the Young's modulus and peripheral compliance of the main body artery segments by using systolic and diastolic blood pressure as input;
3) Correcting the compliance of the cerebral arterial segments by adjusting the Young's modulus of the cerebral segments based on the results of the tentative simulation in (2), using the systolic and diastolic flow rates as input.

This calibration procedure is important because peripheral resistance plays a dominant role in the flow distribution in terminal branches and segments in the CoW, and we found that the optimal peripheral resistance was highly scattered for patients with aSAH, as showed in Figure 5 in (Shen et al., 2020; Shen, et al., 2022).

The simulation ran for 10 cardiac cycles to achieve the steady periodic state that commonly takes 1 minute of computational time per case. Furthermore, the details of this numerical model have been described in previous studies (Shen et al., 2020; Shen, et al., 2022).

TABLE 1 Baseline patient characteristics.

	Patients	Investigations
Total	43	66
Age (years)[a]	58.35 (10.35)	59.55 (10.21)
Sex[b]		
Female	31 (72.1)	48 (72.7)
Male	12 (27.9)	18 (27.3)
Fisher scale[b]		
1	1 (2.3)	2 (3)
2	3 (7.0)	4 (6.1)
3	19 (44.2)	30 (45.5)
4	20 (46.5)	30 (45.5)
Delayed cerebral ischemia[b]		
Present	7 (16.3)	7 (10.6)
Absent	36 (83.7)	59 (89.4)
Aneurysm location[b,c]		
Anterior circulation	31 (70.5)	49 (72.1)
AComA	17	26
M1	8	13
M2	3	6
A1	1	1
A2–3	2	3
Posterior circulation	13 (29.5)	19 (27.9)
P1	5	8
PComA	5	7
BA	3	4

AComA: anterior communicating artery; A1: pre communicating segment of anterior cerebral artery (ACA); A2: ACA, post communicating segment; A3: ACA, precallosal segment; M1: horizontal segment of middle cerebral artery (MCA); M2: MCA, insular segment; P1 pre communicating segment of posterior cerebral artery; PComA: posterior communicating artery; BA: basilar artery.
[a]Mean (standard deviation);
[b]Case number (%).
[c]One patient had ruptured aneurysm on RM1 and unruptured one on LM1.

Statistical analysis

The agreement on the mean flow velocity through the CoW from TCD and the numerical model was calculated by the intraclass correlation coefficient (ICC), based on a single rater type, consistency, and a two-way random model (Koo and Li, 2016). The Bland–Altman plot was generated to describe the correlation between the difference and mean of flow velocity measurements. Base 10 logarithmic transformations were performed to study the limits of agreement by percentile. High blood pressure, a high Fisher score (scale 3 or 4), close to ruptured aneurysm, and DCI were taken as potential negative factors associated with the accuracy of the numerical model. The ICC of each subgroup (dichotomized by blood pressure, Fisher score, location of ruptured aneurysm, and DCI) was considered to assess whether the prementioned factors were application restrictions of the numerical model. Statistical analyses were

TABLE 2 Agreement analysis per cerebral artery.

	Flow velocity	Paired difference[a]	Limits-of-agreement (%)	ICC (95%CI)	N
Overall	-	-	-	0.88 (0.86 0.90)	568
ICA	30.0 (27.0,35.0)	0.4 (−0.2, 1.0)	0.75, 1.36	0.75 (0.66, 0.82)	131
MCA	69.5 (55.0,96.0)	1.4 (0.9, 3.1)	0.80, 1.39	0.85 (0.79, 0.89)	130
ACA	67.0 (46.0, 85.0)	1.5 (0.8, 4.3)	0.73, 1.67	0.78 (0.70, 0.84)	127
PCA	39.0 (30.0, 50.5)	0.8 (−0.3, 1.3)	0.89, 1.15	0.98 (0.97, 0.98)	125
BA	38.0 (32.0, 53.0)	7.2 (2.1, 16.4)	0.81, 2.09	0.87 (0.78, 0.92)	55

The mean flow velocity of each artery measured by TCD and paired difference from simulated flow velocity (V_{TCD}, Vsimulated) were non-parametrically distributed. They are reported by median (interquartile range) in the unit cm/s.
Limits of agreement: in 95% cases, the simulated flow velocity may differ from TCD measurement by (1 − x) below to (x − 1) above.
ICC: intraclass correlation coefficient, single rater type, consistency, two-way random model.
[a]The paired differences were not equal to 0 by Wilcoxon signed-rank test.

performed using SPSS version 25.0 (SPSS Inc.) and R version 4.0.2.

Patient and public involvement

Data were collected from a completed prospective study. The objection register was checked before data collection. Informed consent was not required. The patients and public were not involved in the study design.

Results

Patient characteristics

Fifty-nine consecutive patients (37 women, 22 men, 57 ± 11 years) were included from the TACTICS database. Fifty-two investigations were excluded based on poor CTA image quality or long interval time between TCD and CTA. As such, 66 CTA data sets from 43 patients were available with sufficient image quality (Table 1). The study flow chart is presented in the supplementary 1.

Correlation between transcranial Doppler and numerical model

TCD-measured mean flow velocities, paired difference between TCD and the numerical model, limits of agreement of the two methods, and ICC consistency are presented in Table 2. The ICC over all 568 arteries was 0.88 (95% CI, 0.86–0.90). The ICA had the lowest ICC of 0.75 (95% CI, 0.66–0.82), followed by ACA with 0.78 (95% CI, 0.70–0.84); the ICC of MCA, BA, and PCA was 0.85, 0.87, and 0.98, respectively. The scatter plots of the two logarithmic measurements grouped by DCI are presented in Figure 3.

The magnitudes of differences remained the same over the whole range of mean measurements in the Bland–Altman plots, except for the ACA and BA. Therefore, base 10 logarithmic transformations of the flow velocity were performed to yield logarithmic Bland–Altman plots, and the percentile differences are shown in Figure 4 (Martin Bland and Altman, 1986). The plots show a slight systematic underestimation of the numerical model when compared to TCD. The percentile differences are equally spread along the x-axis. The smallest antilogarithmic limits of agreements were in the PCA between 0.89 and 1.15, followed by the MCA (0.80 and 1.39), ICA (0.75 and 1.36), and ACA (0.73 and 1.67), while the widest were in the BA between 0.81 and 2.09.

In the subgroup analysis, the ICC of the DCI group decreased by 0.2 when compared to the non-DCI group (ICC 0.93) without a 95% CI overlap of their ICCs. The ICC difference within the blood pressure, Fisher scale, and ruptured intracerebral aneurysm location groups was 0.04, 0.06, and 0.07, respectively; all overlapped within each pair's 95% CI of the ICC (Table 3). The scatter plots of the paired subgroups are displayed in Figure 5.

The ICC in the nonparent artery group was 0.87 (95% CI, 0.83–0.89), similar to the group with the parent artery (supplementary 2). The ICC in a sub–data set that excluded the second scan from 23 patients who offered two investigations is 0.87 (95% CI 0.83–0.90), similar to that of the full data set (supplementary 3).

Discussion

This study validates our in-house–developed numerical model for simulating CBF in the CoW in patients with aSAH. With an ICC of 0.88 (N = 568; 95% CI 0.86–0.90), the model accurately simulated flow velocities, according to the ICC reporting guideline (poor if <0.5, moderate if between 0.5 and

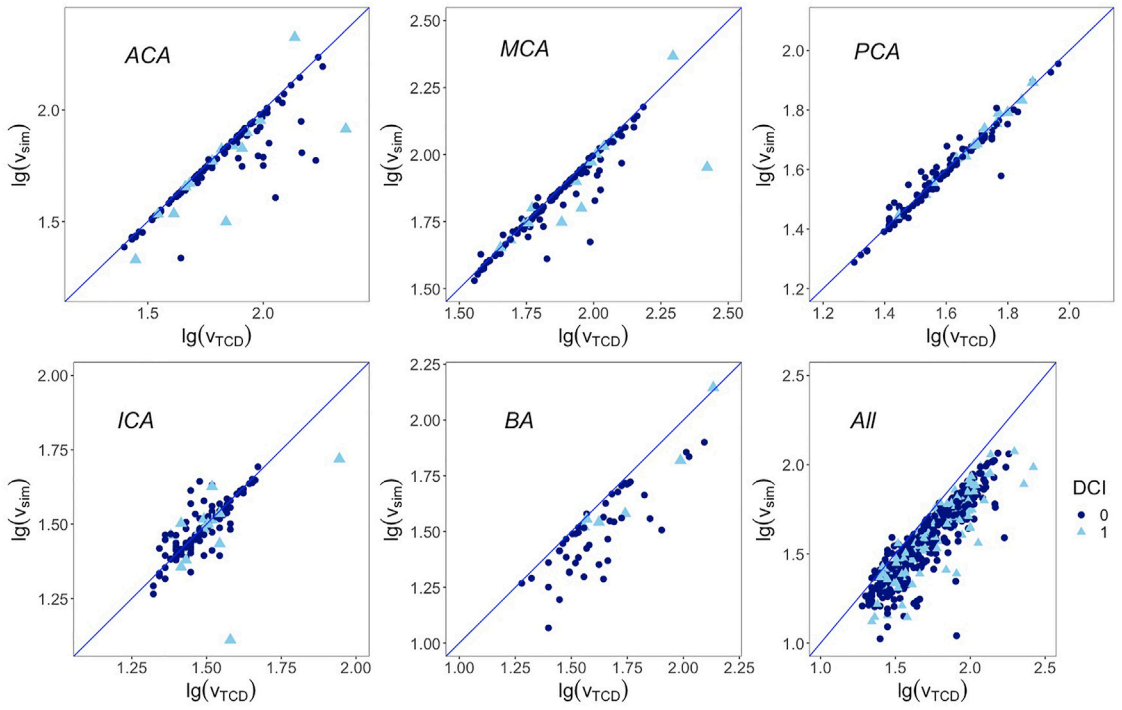

FIGURE 3
Correlation between base 10 logarithmic mean flow velocity from TCD on the x-axis and from simulation on the y-axis. Blue line represents the regression line y = x. First row from left to right: anterior cerebral artery, middle cerebral artery, and posterior cerebral artery; second row from left to right: internal carotid artery, basilar artery, and overall arteries. DCI: delayed cerebral ischemia. 1 represents cases that developed DCI afterward, 0 represents cases that are free from DCI.

0.75, good if between 0.75 and 0.9, and excellent if >0.9) (Koo and Li, 2016).

MRI is another noninvasive technique to measure the CBF. Previous studies have shown that the correlation between the MR technique and TCD is between 0.49 and 0.80 (Sorond et al., 2010; Meckel et al., 2013). Helthuis et al. (2020) validated a linear model with NOVA-MRI on simulating CBF among 20 healthy people and reported an ICC of 0.86 with the exclusion of 8 outliers out of 279 cerebral artery segments.

TCD is the most widely used application in clinical practice to determine CBF. However, it is not a perfect gold standard for cerebral flow velocity measurement. It is a highly operator-dependent instrument. The reliability of TCD in measuring CBF at the MCA has been reported to be between 0.76 and 0.82 depending on the patient's bone window condition (Lorenz et al., 2009; Muñoz Venturelli et al., 2017). The reliability of the TCD measurements in the ACA and PCA may even be lower than those in the MCA. The expected validity of the numerical model, using TCD as a comparison test, cannot be more than the square root of the product of its reliability and the reliability of TCD. Therefore, the accuracy of the presented numerical model on simulating flow velocity has a maximum of 0.91 (Birnbaum et al., 1968). As such, the presented numerical model showed a good accuracy under various aSAH conditions over all cerebral artery segments measured in the CoW.

Scrutinizing the agreement at each cerebral artery, the presented numerical model showed a good agreement in the PCA, MCA, and ICA, with relatively bigger limits of agreement at the BA and ACA. In 95% of the cases, the simulated PCA flow velocity may differ from the TCD measurement by 11% below to 15% above; for the MCA, it is 20% below to 39% above, and 25% below to 36% above for the ICA.

The base 10 logarithmic Bland–Altman plot of the ACA reported a relatively wide range of limits of agreement with TCD from 27% below to 67% above. Its ICC also led to a relatively lower accuracy. When checking these outliers in Figure 3, it has been revealed that they belonged to patients who had developed DCI afterward. Whether the fast flow velocity or DCI caused a less accurate simulation in the ACA cannot be determined using the current data set. The other reason from the wide range of limits of agreement is that the ACA is divided into the A1 segment as the pre communicating part and A2 segment as the post communicating part in our numerical model, while in the TCD report only the flow velocity of the ACA was recorded, without a clear distinction between the A1 and A2 segments.

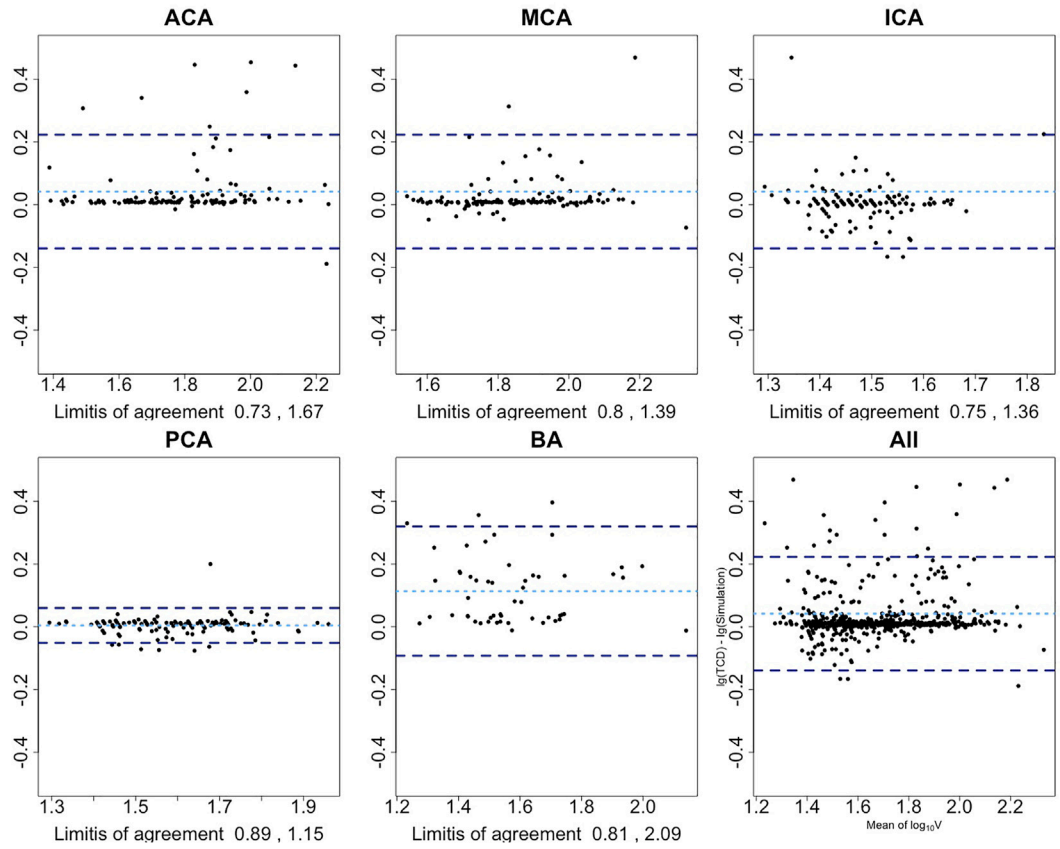

FIGURE 4
Bland–Altman plots show the agreement among the presented numerical model and TCD after base 10 logarithmic transformation. x-axis is the average mean of base 10 logarithmic flow velocity measured by TCD and simulation; y-axis is the difference between two logarithmic measures. Light blue dotted line represents the mean difference of two logarithmic velocities; two dark blue dotted lines represent 1.96 SD above or below the mean difference. Limits-of-agreement are listed at the bottom of each artery plot. First row from left to right: anterior cerebral artery, middle cerebral artery, and internal carotid artery; second row from left to right: posterior cerebral artery, basilar artery, and overall arteries.

TABLE 3 Subgroup analysis.

—	N	ICC (95%CI)	Limits-of-agreement (%)
Systolic blood pressure			
>140 mmHg	350	0.87 (0.85–0.90)	0.74, 1.53
≤140 mmHg	218	0.91 (0.88–0.93)	0.78, 1.46
Fisher scale			
3,4	515	0.88 (0.86–0.90)	0.75, 1.52
1,2	53	0.94 (0.90–0.97)	0.77, 1.41
Ruptured aneurysm location			
Anterior circulation	398	0.86 (0.83–0.89)	0.74, 1.53
Posterior circulation	170	0.93 (0.88–0.95)	0.77, 1.47
Delayed cerebral ischemia			
Yes	62	0.73 (0.59–0.83)	0.64, 1.92
No	506	0.93 (0.92–0.94)	0.77, 1.45

ICC: intraclass correlation coefficient, single rater type, consistency, two-way random model.

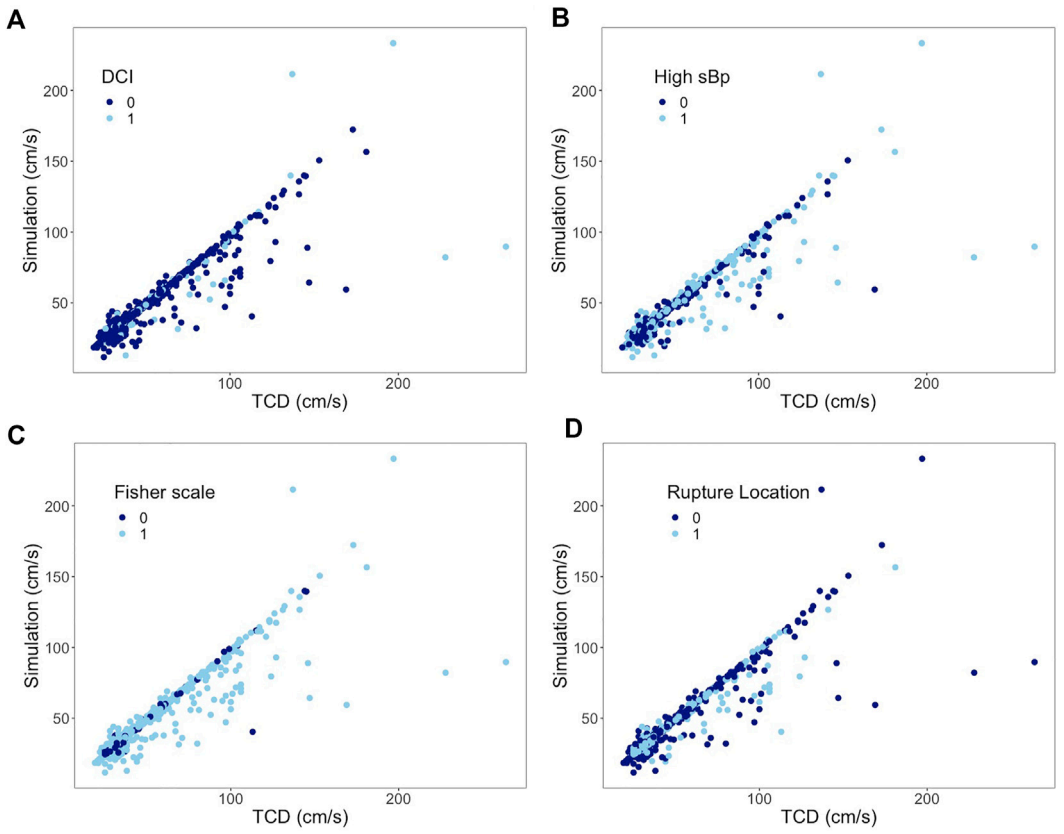

FIGURE 5
Subgroup analysis of all arteries. Correlation between mean flow velocities from TCD measurement on the x-axis and from simulation on the y-axis. **(A)** 0 represents non-DCI; 1 represents DCI. **(B)** 0 represents sBp ≤ 140 mmHg; 1 represents sBp higher than 140 mmHg. **(C)** 0 represents Fisher scale grade 1 or 2; 1 represents Fisher scale grade 3 or 4. **(D)** 0 represents ruptured aneurysm located at anterior CoW; 1 represents ruptured aneurysm at posterior CoW.

In 95% cases, the simulated BA flow velocity differed from the TCD measurement by 19% below to 109% above. The board range of limits of agreement is consistent with the range of its 95% CIs of ICC. This might be due to the setting of the BA in our numerical model. Though there are many paired arteries along the way from the beginning to the end of the BA (e.g., superior cerebellar artery), they are neglected in this lumped model. Such simplification shall lead to differences from reality. The other reason for this wide measurement error is insufficient data power for the BA analysis as we have reported in the study protocol (Shen et al., 2020). Therefore, the inherent measurement error of the BA segment in this numerical model might be overestimated with the current data set.

To understand the restrictions of the numerical model under various acute pathologic conditions, we stratified the data set by blood pressure, Fisher scale, location of ruptured aneurysm, and DCI. One may hypothesize that vasospasm might influence the accuracy of the numerical model under aSAH conditions. Vasospasm at the level of the CoW is correlated with the change of vascular smooth muscle cell tone, which would influence arterial wall stiffness in the numerical model. With vasospasm, arteries not only have reduced diameter but occasionally also exhibit a beaded pattern in their geometry. The influence of such a pattern is not accounted for in the presented model. The degree of local vasospasm is closely related to the amount of SAH and location of the ruptured aneurysm. Global and local edema after aSAH theoretically have sophisticated impacts on the setting of the numerical model as well.

The 95% CIs of ICC reported in Table 3 overlap between the paired subgroups stratified by the Fisher score or location of ruptured aneurysm, which means that the difference of paired ICC is random rather than a true difference. It implies that the model could simulate the flow velocity accurately regardless of the amount of SAH and bleeding location. High blood pressure was, furthermore, not found to affect the ICC between both techniques.

In the DCI group, the ICC was found to be lower without an overlap of their 95% CIs. Most of the outliners presented in

Figure 3 are from patients who had developed DCI afterward. DCI as a complication might present during the course of aSAH, in which insufficient blood flow plays a conspicuous role (van Gijn et al., 2007). The boundary condition of the presented model, i.e., resistance, was calculated based on the Hagen–Poiseuille flow, which likely predominated the CBF of each terminal branch. The obtained resistance might have difficulties to properly derive the perfusion of each terminal branch under extreme pathological conditions which would lead to discrepancy. Whether a poor simulation by this model could identify DCI at the early course of aSAH is worth investigating in the future.

Strength and limitation

This study is the first to validate a numerical model with sufficient population sampling and under the pathological condition of aSAH between day 5 and 10 after the onset. In order to present the model's validity under all circumstances of aSAH and to explore the limitation of this numerical model, we included every sample after checking the outlier was not due to typing error (none was found). The simulation accuracy of each artery in the CoW is particularly reported by the measurement error, in favor of the presented numerical model's personalized application for further clinical research. Its application limitations were further explored by multiple clinical parameters.

One limitation of the study design is the time interval between the artery morphology exam and flow velocity measurement. The aSAH patient is prone to suffer cerebral vasospasm which subsides by day 12 (Weir et al., 1978). Cerebral vasospasm after the onset is progressive and varies among individuals. Morphological information and flow velocity collected synchronously are thus important conditions for this validation purpose. MR technic can collect angiographic images and flow velocities simultaneously. However, due to the relatively long exam duration, severe patients (e.g., with delirium) are unable to endure the MR exam, which would lead to selection bias. An ideal study plan is thus impossible in practice for this research purpose. We excluded investigations where paired CTA and TCD performed longer than 24 h to avoid morphological changes, thus the diameter presented in the CTA image could represent the one while TCD was performed to the most extent.

Fifty-two investigations out of 118 were excluded due to the long time interval or poor CTA image quality. Besides the abovementioned reason, most investigations those were excluded were owing to severe image artifacts. All CTA images used in this study were captured after the repair of aneurysms. Thus, it is inevitable to have severe artifacts in some images that interfered with the segmental diameter measurement in the CoW. However, this exclusion rate might lead to selection bias.

Another limitation in this validation study has been the diameter measurements. As previously stated, the validity of the presented numerical model in this study setting highly depended on both the reliability of TCD and the numerical model. Since this numerical model took artery diameters as the input, its reliability was highly determined by the reliability of the measurements. To avoid bias, we used the semiautomatic central lumen calculation. The diameter measurement bias underestimated the ICC of the presented numerical model. Researchers using an automatic diameter-measuring tool can expect a more accurate CBF with this model. For others without a special image processing tool, the precision of the diameters measured from the daily image viewer can still accurately simulate the presented numerical model. Thus, the measurement bias could be the point of strength for external validation of this study.

The abovementioned limitations lead to another strength of this numerical model: it is applicable even for ordinary clinical practice without special equipment settings, while CTA and TCD are both common in a neurovascular center. Besides, based on arterial imaging stored in the medical files, the presented numerical model can even be applied in retrospective studies.

In addition, this study is an internal validation study, which tends to overestimate. An external validation should be carried out in the future.

Clinical implications

When compared to the correlations of MRI techniques with TCD, mathematic models, and MR techniques for detecting CBF, the presented numerical model shows a good agreement even in the subacute phase of patients with aSAH. TCD, MR techniques, and the numerical model can detect patients' CBF specifically and noninvasively. However, none of the three methods can measure the real *in vivo* blood flow. This study has shown that personalized hemodynamics of CBF simulation by our numerical model can act as a supplement to TCD and MR techniques by providing global hemodynamics of the CoW.

The present numerical framework integrated patients' commonly available morphology information and flow measurements to provide a comprehensive cerebral flow information. Time consumption of this numerical model from diameter measurement to personalized simulation on a PC was done within 20 min. The present study sheds light on the potential application of the hemodynamic model for clinical practices.

With personalized WK3 parameters, the model can assess the blood flow in the three communicating arteries, which are hardly detected by either TCD or MR exam, and the limited data measured can provide a global cerebral hemodynamic map that could serve as the boundary condition for higher level simulations, such as the 3D CFD model; it may be potentially used to investigate the hemodynamics of the CoW and CVD—e.g., a recent systematic review has demonstrated that

despite the well-known association between the configuration of the CoW and the presence or rupture of intracranial aneurysm, a qualified hemodynamic assessment tool to identify such factors in clinical practices is still lacking (Shen, et al., 2022). The model may also be used to predict cerebral hemodynamic improvement if patients' CoW configuration get altered (e.g., during intracranial bypass operation and carotid endarterectomy).

Conclusion

The presented numerical model can be a useful and generalizable tool for reconstructing personalized CoW hemodynamics by integrating limited clinical measurements. With this model, hemodynamic studies focused on CVD can be performed without special equipment setting.

Data availability statement

The raw data supporting the conclusions of this article will be made available by the authors, without undue reservation.

Ethics statement

The studies involving human participants were reviewed and approved by the institutional ethical review board of the University Medical Center Groningen. Written informed consent for participation was not required for this study in accordance with the national legislation and the institutional requirements.

Author contributions

YS designed the study, collected and analyzed the data, and drafted the manuscript. JH provided the patients' data and critically revised the manuscript. YW developed the numerical model and performed the simulation, and partially drafted the manuscript. RB assisted the data analysis and critically revised the manuscript. JD supervised the study and critically revised the manuscript. MU as the corresponding researcher is responsible for the quality of the data and technically assisted with the collection of the data and critically revised the manuscript.

Funding

YS receives financial support from China Scholarship Council (CSC, File No. 201706320024).

Conflict of interest

The authors declare that the research was conducted in the absence of any commercial or financial relationships that could be construed as a potential conflict of interest.

Publisher's note

All claims expressed in this article are solely those of the authors and do not necessarily represent those of their affiliated organizations, or those of the publisher, editors, and reviewers. Any product that may be evaluated in this article, or claim that may be made by its manufacturer, is not guaranteed or endorsed by the publisher.

Supplementary material

The Supplementary Material for this article can be found online at: https://www.frontiersin.org/articles/10.3389/fbioe.2022.1031600/full#supplementary-material

References

Alastruey, J., Parker, K., Peiro, J., Byrd, S., and Sherwin, S. (2007). Modelling the circle of Willis to assess the effects of anatomical variations and occlusions on cerebral flows. *J. Biomechanics* 40 (8), 1794–1805. doi:10.1016/j.jbiomech.2006.07.008

Amin-Hanjani, S., Xinjian, D., Dilip, K. P., and Keith, R. (2015) 'Effect of age and vascular anatomy on blood flow in major cerebral vessels'. *J. Cereb. Blood Flow Metabolism*. Nature Publishing Group 35(2). pp, 312–318.doi:10.1038/jcbfm.2014.203

Birnbaum, A., Lord, F. M., and Novick, M. R. (1968). "Statistical theories of mental test scores', Some latent trait models and their use in inferring an examinee's ability," in *Statistical theories of mental test scores*. Editors F. M. Lord and M. R. Novick (Reading, MA: Addison-Wesley), 379–479.

Bouthillier, A., Van Loveren, H. R., and Keller, J. T. (1996). Segments of the internal carotid artery: A new classification. *Neurosurgery* 38 (3), 425–433. doi:10.1097/00006123-199603000-00001

de Vet, H. C. W. (2011). *Measurement in medicine*. Cambridge: Cambridge University Press. doi:10.1017/CBO9780511996214

Fisher, C. M., Kistler, J. P., and Davis, J. M. (1980) Relation of cerebral vasospasm to subarachnoid hemorrhage visualized by computerized tomographic scanning. Neurosurgery 1. 6, 1–9. doi:10.1097/00006123-198001000-00001

Groen, D., Richardson, R. A., Coy, R., Schiller, U. D., Chandrashekar, H., Robertson, F., et al. (2018). Validation of patient-specific cerebral blood flow simulation using transcranial Doppler measurements. *Front. Physiol.* 9, 721–813. doi:10.3389/fphys.2018.00721

Hartkamp, N. S., Petersen, E. T., Chappell, M. A., Okell, T. W., Uyttenboogaart, M., Zeebregts, C. J., et al. (2018). Relationship between haemodynamic impairment and collateral blood flow in carotid artery disease. *J. Cereb. Blood Flow. Metab.* 38 (11), 2021–2032. doi:10.1177/0271678x17724027

Helthuis, J. H. G., van Doormaal, T. P., Amin-Hanjani, S., Du, X., Charbel, F. T., Hillen, B., et al. (2020). A patient-specific cerebral blood flow model. *J. Biomechanics* 98, 109445. doi:10.1016/j.jbiomech.2019.109445

Koo, T. K., and Li, M. Y. (2016). A guideline of selecting and reporting intraclass correlation coefficients for reliability research. *J. Chiropr. Med.* 15 (2), 155–163. doi:10.1016/j.jcm.2016.02.012

Liu, B., Li, Q., Wang, J., Xiang, H., Ge, H., Wang, H., et al. (2015). A highly similar mathematical model for cerebral blood flow velocity in geriatric patients with suspected cerebrovascular disease. *Sci. Rep.* 5, 15771–15777. doi:10.1038/srep15771

Lorenz, M. W. (2009) 'Effects of poor bone window on the assessment of cerebral autoregulation with transcranial Doppler sonography - a source of systematic bias and strategies to avoid it'. *J. Neurological Sci.* Elsevier B.V 283(1–2). pp, 49–56. doi:10.1016/j.jns.2009.02.329

Lui, E. Y. L., Steinman, A. H., Cobbold, R. S., and Johnston, K. W. (2005). Human factors as a source of error in peak Doppler velocity measurement. *J. Vasc. Surg.* 42 (5), 972.e1–972.e10. doi:10.1016/j.jvs.2005.07.014

Martin Bland, J., and Altman, D. G. (1986). Statistical methods for assessing agreement between two methods of clinical measurement. *Lancet* 327 (8476), 307–310. doi:10.1016/S0140-6736(86)90837-8

Meckel, S., Leitner, L., Bonati, L. H., Santini, F., Schubert, T., Stalder, A. F., et al. (2013). Intracranial artery velocity measurement using 4D PC MRI at 3 T: Comparison with transcranial ultrasound techniques and 2D PC MRI. *Neuroradiology* 55 (4), 389–398. doi:10.1007/s00234-012-1103-z

Muñoz Venturelli, P., Brunser, A. M., Gaete, J., Illanes, S., Lopez, J., Olavarria, V. V., et al. (2017). Reliability of hand-held transcranial Doppler with M-mode ultrasound in middle cerebral artery measurement. *J. Med. Ultrasound* 25 (2), 76–81. doi:10.1016/j.jmu.2016.12.001

Reymond, P., Bohraus, Y., Perren, F., Lazeyras, F., and Stergiopulos, N. (2011). Validation of a patient-specific one-dimensional model of the systemic arterial tree. *Am. J. Physiology-Heart Circulatory Physiology* 301 (3), 1173–H1182. doi:10.1152/ajpheart.00821.2010

Reymond, P., Merenda, F., Perren, F., Rufenacht, D., and Stergiopulos, N. (2009). Validation of a one-dimensional model of the systemic arterial tree. *Am. J. Physiology-Heart Circulatory Physiology* 297 (1), 208–222. doi:10.1152/ajpheart.00037.2009

Shen, Y., Molenberg, R., Bokkers, R. P. H., Wei, Y., Uyttenboogaart, M., and van Dijk, J. M. C. (2022). The role of hemodynamics through the circle of Willis in the development of intracranial aneurysm: A systematic review of numerical models. *J. Personalized Med.* 12 (6), 1008. doi:10.3390/jpm12061008

Shen, Y., Wei, Y., Bokkers, R. P. H., Uyttenboogaart, M., and Van Dijk, J. M. C. (2022). Patient-specific cerebral blood flow simulation based on commonly available clinical datasets. *Front. Bioeng. Biotechnol.* 10, 835347. doi:10.3389/fbioe.2022.835347

Shen, Y., Wei, Y., Bokkers, R. P. H., Uyttenboogaart, M., and van Dijk, J. M. C. (2020). Study protocol of validating a numerical model to assess the blood flow in the circle of Willis. *BMJ Open* 10 (6), e036404–e036406. doi:10.1136/bmjopen-2019-036404

Sorond, F. A., Hollenberg, N. K., Panych, L. P., and Fisher, N. D. L. (2010). Brain blood flow and velocity correlations between magnetic resonance imaging and transcranial Doppler sonography. *J. Ultrasound Med.* 29 (7), 1017–1022. doi:10.7863/jum.2010.29.7.1017

Tanweer, O., Wilson, T. A., Metaxa, E., Riina, H. A., and Meng, H. (2014). A comparative review of the hemodynamics and pathogenesis of cerebral and abdominal aortic aneurysms: Lessons to learn from each other. *J. Cerebrovasc. Endovasc. Neurosurg.* 16 (4), 335–349. doi:10.7461/jcen.2014.16.4.335

van der Harst, J. J., Luijckx, G. J. R., Elting, J. W. J., Bokkers, R. P., van den Bergh, W. M., Eshghi, O. S., et al. (2019). Transcranial Doppler versus CT-angiography for detection of cerebral vasospasm in relation to delayed cerebral ischemia after aneurysmal subarachnoid hemorrhage: A prospective single-center cohort study. *Crit. Care Explor.* 1 (1), e0001. doi:10.1097/cce.0000000000000001

van Gijn, J., Kerr, R. S., and Rinkel, G. J. (2007). Subarachnoid haemorrhage. *Lancet* 369 (9558), 306–318. doi:10.1016/S0140-6736(07)60153-6

Van Laar, P. J., Hendrikse, J., Golay, X., Lu, H., van Osch, M. J., and van der Grond, J. (2006). *In vivo* flow territory mapping of major brain feeding arteries. *NeuroImage* 29 (1), 136–144. doi:10.1016/j.neuroimage.2005.07.011

Warnert, E. A. H., Hart, E. C., Hall, J. E., Murphy, K., and Wise, R. G. (2016). The major cerebral arteries proximal to the Circle of Willis contribute to cerebrovascular resistance in humans. *J. Cereb. Blood Flow. Metab.* 36 (8), 1384–1395. doi:10.1177/0271678X15617952

Weir, B., Grace, M., Hansen, J., and Rothberg, C. (1978). Time course of vasospasm in man. *J. Neurosurg.* 48 (2), 173–178. doi:10.3171/jns.1978.48.2.0173

frontiers | Frontiers in Medical Technology

TYPE Original Research
PUBLISHED 29 November 2022
DOI 10.3389/fmedt.2022.1008540

OPEN ACCESS

EDITED BY
Claudio Chiastra,
Politecnico di Torino, Italy

REVIEWED BY
Ankush Aggarwal,
University of Glasgow, United Kingdom
Robert Gaul,
Trinity College Dublin, Ireland
Farhad R. Nezami,
Harvard Medical School, United States

*CORRESPONDENCE
Heather N. Hayenga
heather.hayenga@utdallas.edu

†These authors have contributed equally to this work

SPECIALTY SECTION
This article was submitted to Cardiovascular Medtech, a section of the journal Frontiers in Medical Technology

RECEIVED 31 July 2022
ACCEPTED 07 November 2022
PUBLISHED 29 November 2022

CITATION
Warren JL, Yoo JE, Meyer CA, Molony DS, Samady H and Hayenga HN (2022) Automated finite element approach to generate anatomical patient-specific biomechanical models of atherosclerotic arteries from virtual histology-intravascular ultrasound.
Front. Med. Technol. 4:1008540.
doi: 10.3389/fmedt.2022.1008540

Automated finite element approach to generate anatomical patient-specific biomechanical models of atherosclerotic arteries from virtual histology-intravascular ultrasound

Jeremy L. Warren[1†], John E. Yoo[1†], Clark A. Meyer[1], David S. Molony[2], Habib Samady[2] and Heather N. Hayenga[1*]

[1]Department of Bioengineering, University of Texas at Dallas, Richardson, TX, United States, [2]Northeast Georgia Health System, Georgia Heart Institute, Gainesville, GA, United States

Despite advancements in early detection and treatment, atherosclerosis remains the leading cause of death across all cardiovascular diseases (CVD). Biomechanical analysis of atherosclerotic lesions has the potential to reveal biomechanically instable or rupture-prone regions. Treatment decisions rarely consider the biomechanics of the stenosed lesion due in-part to difficulties in obtaining this information in a clinical setting. Previous 3D FEA approaches have incompletely incorporated the complex curvature of arterial geometry, material heterogeneity, and use of patient-specific data. To address these limitations and clinical need, herein we present a user-friendly fully automated program to reconstruct and simulate the wall mechanics of patient-specific atherosclerotic coronary arteries. The program enables 3D reconstruction from patient-specific data with heterogenous tissue assignment and complex arterial curvature. Eleven arteries with coronary artery disease (CAD) underwent baseline and 6-month follow-up angiographic and virtual histology-intravascular ultrasound (VH-IVUS) imaging. VH-IVUS images were processed to remove background noise, extract VH plaque material data, and luminal and outer contours. Angiography data was used to orient the artery profiles along the 3D centerlines. The resulting surface mesh is then resampled for uniformity and tetrahedralized to generate the volumetric mesh using TetGen. A mesh convergence study revealed edge lengths between 0.04 mm and 0.2 mm produced constituent volumes that were largely unchanged, hence, to save computational resources, a value of 0.2 mm was used throughout. Materials are assigned and finite element analysis (FEA) is then performed to determine stresses and strains across the artery wall. In a representative artery, the highest average effective stress was in calcium elements with 235 kPa while necrotic elements had the lowest average stress, reaching as low as 0.79 kPa. After applying nodal smoothening, the maximum effective stress across 11 arteries remained below 288 kPa, implying biomechanically stable plaques. Indeed, all atherosclerotic plaques remained unruptured at the 6-month longitudinal

follow up diagnosis. These results suggest our automated analysis may facilitate assessment of atherosclerotic plaque stability.

KEYWORDS

coronary artery disease (CAD), computational modeling, cardiovascular, finite element analysis (FEA), FEBio, biomechanics

Introduction

Understanding the adverse sequelae of atherosclerotic plaques is critical, as plaques are at the root of many cardiovascular illnesses (1). Plaque size, composition, blood flow, and calcium accumulation can all be detected using current imaging techniques. Current methods for assessing the risk of a major adverse cardiac event (MACE) include the Framingham Risk Score (FRS), Coronary Artery Calcium (CAC) score, Carotid Intima-Medial Thickness (CIMT), and Fractional Flow Reserve (FFR). However, these methods do not account for the structural mechanics of the artery wall, which influences acute instability risk as well as growth and remodeling of atherosclerotic plaque. Our novel method aims to address this deficit by modelling the biomechanics of a patient-specific artery.

In the last few decades, characteristics contributing to the instability of plaques have been established (2–4). Structurally, rupture-prone characteristics include thin-fibrous caps (<65 μm in thickness), large lipid core, and calcified nodules near the lumen. Characteristics defining erosion-prone areas include intimal thickening and fibrous atheroma with little/no lipid core (3, 5). Spatial correlation between plaque instability and areas of high mechanical stress that exceeds the strength of the artery were previously found (6). Maximum stress values >300 kPa in the plaque cap have been linked to follow-up rupture locations in several investigations (6–8). Ultimately, quantifying the structural mechanics of patient-specific plaques and stresses experienced by plaque constituents is a better indicator of rupture potential than size alone.

Image-based computational approaches allow for personalized risk assessment and enhanced treatment planning. Herein we present an automated method to go from 3D reconstruction of coronary artery meshes to execution and FE mechanical analysis. High-resolution imaging data can now be used to construct and evaluate comprehensive 3-D patient-specific models of arterial vasculature. Previously, research in this area was done using 2-D cross-sectional VH-IVUS images of arterial tissue or linear modeling (9, 10). Advances in medical imaging and computational approaches have paved the way for researchers to further investigate structural loading occurring in a 3-D patient-specific model. Recent approaches modelling arterial biomechanics using volumetric geometry have been successful in utilizing various imaging modalities and material models yet were limited in scope. That is they either use a limited set of materials or a single homogenized material to represent plaque constituents (11, 12), require additional manual segmentation (13, 14), and neglect arterial curvature, branching or bifurcations (12–14). In short, previous approaches do not fully address the inherent heterogeneous nature of atherosclerotic artery tissue or the complex curvature presented by coronary artery geometry (11). The publicly available automated method presented herein embraces heterogenous tissue variability and leverages patient-specific data to build an accurate 3D representation of the patient's atherosclerotic artery. The outcomes from this model seek to provide a diagnostic risk-assessment tool to assess the mechanical integrity of a patient-specific atherosclerotic artery.

Materials and methods

The methods presented in the following subsections outline our approach for automatically generating volumetric meshes using VH-IVUS images and coronary angiography data (**Figure 1**). The algorithm was developed using the MATLAB (R2022a) scripting language and a 11-artery dataset, from 11 patients, consisting of coronary VH-IVUS images and angiography data. The script and user interface allows the user to modify meshing parameters of the arterial geometry as well as simulation parameters for FEBio.

Data acquisition

A dataset of twenty-seven patients between 2007 and 2009 with moderate coronary artery disease (CAD) enrolled in an Atorvastatin clinical trial at Emory University (ClinicalTrials.gov; Identifier: NCT00576576) (15, 16). All patients received optimal medical therapy for cardiovascular risk factors, including 80 mg atorvastatin daily. According to standard of care, all patients underwent baseline and 6-month follow-up biplane coronary angiography as well as EKG-gated (R-wave peak) radiofrequency backscatter virtual histology-IVUS (VH-IVUS) image acquisition of the proximal left anterior descending (LAD) and left main (LM) coronary arteries (20 MHz Eagle Eye® Gold Catheter, Volcano Corp., Rancho Cordova, CA). Clinically, angiography provides 3D geometry and indicates areas of stenosis of the artery, while

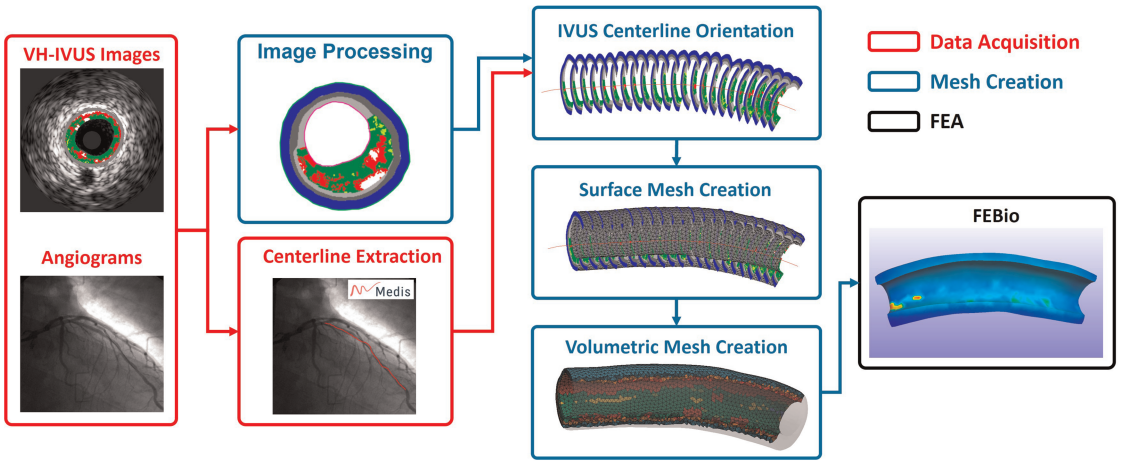

FIGURE 1
Simplified workflow highlighting the steps in creating a patient-specific artery model with material properties. Artery centerline is extracted from angiogram data (Red). VH-IVUS images are processed to extract individual plaque constituent data, oriented along the 3D centerline, and meshed to create the volumetric finite elements (Blue). FE analysis is solved in FEBio (Black).

IVUS imaging enables visualization of the properties of the artery wall. Virtual Histology (VH, Volcano Corp.) converts the IVUS radiofrequency spectrum to construct a color-coded tissue map overlay on the IVUS images. The tissue map consists of four materials: fibrous tissue (densely packed collagen fibers), fibrofatty tissue (loosely packed collagen fibers with minimal lipid deposition), dense calcium (calcium deposits), and necrotic core (high lipid content and areas of necrosis) (**Figure 2**) (17–19). VH-IVUS images were acquired at an automated motorized pullback (0.5 mm/s) from approximately 60 mm down the LAD up to the guide catheter in the aorta. Lastly, Doppler derived pressure data was acquired in the LM and distal LAD coronary arteries using a 0.355 mm monitoring guidewire (ComboWire, Volcano Corp.). Of note, none of the patients in the trial experienced a plaque rupture or MACE after 6-months.

After approval by Emory University and UT Dallas Institutional Review Boards, data collected in the clinical trial was used for FEA analysis. Of this dataset, for the development of our methods, we used arteries from eleven different patients who exhibited varying degrees of tortuosity, plaque heterogeneity, and number of branches to best represent the range of inputs that may be seen in the clinic. Hence, we will refer to these arteries as numbered from one to eleven for the remainder of this manuscript. Analyzed arteries excluding arteries 8, 9, and 11 have bifurcations present. Patient specific diastolic and systolic pressure values are recorded in **Supplementary Table S1**. The mean systolic pressure across the dataset of 17 kPa (131 ± 24.8 mmHg) was used for each arterial model (**Supplementary Table S1**). Lastly, 3D centerline coordinates were extracted from the angiogram videos using QAngio (20) and exported for use in the mesh creation process (**Figure 2**).

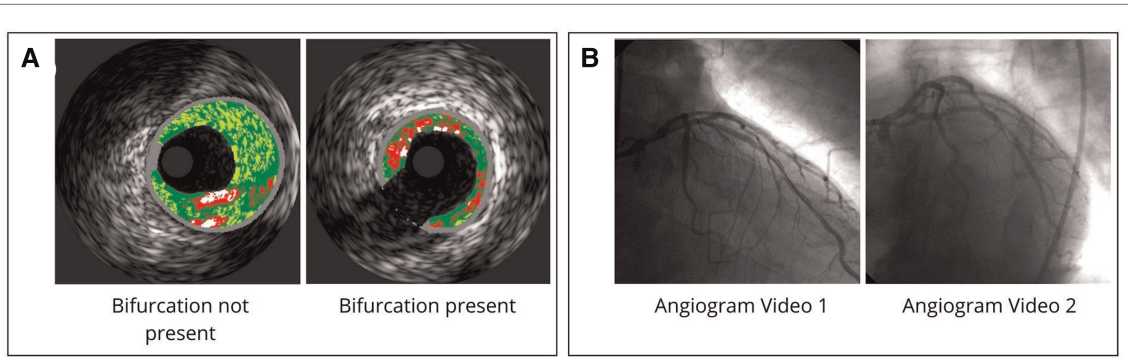

FIGURE 2
VH-IVUS and angiogram data. (**A**) Example of VH-IVUS images comparing bifurcated and non-bifurcated areas. (**B**) Angiogram data acquired from coronary angiography videos from two perspectives.

Mesh creation

VH-IVUS image processing and centerline orientation

Generic IVUS imaging produces grayscale images (Figures 3A,F) which are then processed using virtual histology (Figures 3B,G) and exported. These VH-IVUS images are filtered to remove background noise and separated into material groups depending on pixel RGB values (calcium, necrotic core, arterial wall, fibrofatty, and fibrous) (Figures 3C,H). These filtered images are then masked, and islands are removed using an area-opening algorithm (21).

To create a support layer of tissues for protecting thin arterial walls, a perivascular "sleeve" layer with a predefined thickness (0.2 mm radially) is added (Figures 3D,I) and the lumen and outer surface profiles are extracted (Figures 3E,J). The sleeve layer acts as a buffer and was implemented for two reasons. First, it allows the creation of volumetric elements where the artery is too thin. Second, it provides an external buffer for the artery wall to push against during pressurization, ensuring model stability during the simulation. Pixel coordinates and profiles are then scaled to millimeters (1 pixel = 0.02 mm) and oriented in 3-D along the centerline. In the case of bifurcated arterial segments, an additional step is used to obtain the branched geometry. Here, the code performs a radial sweep to find discontinuous IVUS pixels and identify where a branch occurs within the inner and outer profiles. These images are flagged and the inner/outer profile coordinates corresponding to the branched gap are stored for use in the surface mesh creation step.

Surface mesh

The luminal and outer surface profiles extracted from the VH-IVUS images are used to create a first pass approximation of the arterial mesh *via* procedural lofting. The ends of the arterial mesh are closed by lofting from the outer edges to the luminal edges. In the case of bifurcated arteries, IVUS images containing a branch are flagged and the luminal/outer profile coordinates within the branch are stored (Figure 4A). These profiles are still used to create the first-pass approximation of the mesh and hence, the nodes correlating to the branched regions are easily identified. The faces in the mesh connected to the branch nodes are removed and the resulting holes are used to identify edge sequences for branch creation. The coordinates along these edges are averaged for the luminal and outer surfaces separately and subtracted to create a normal vector between them, defining the branch angle (Figure 4B). This branch angle is then used to project the two edge sequences (luminal and outer) onto an orthogonal plane at a predefined distance offset from the outer surface of the mesh. Here, the two edge

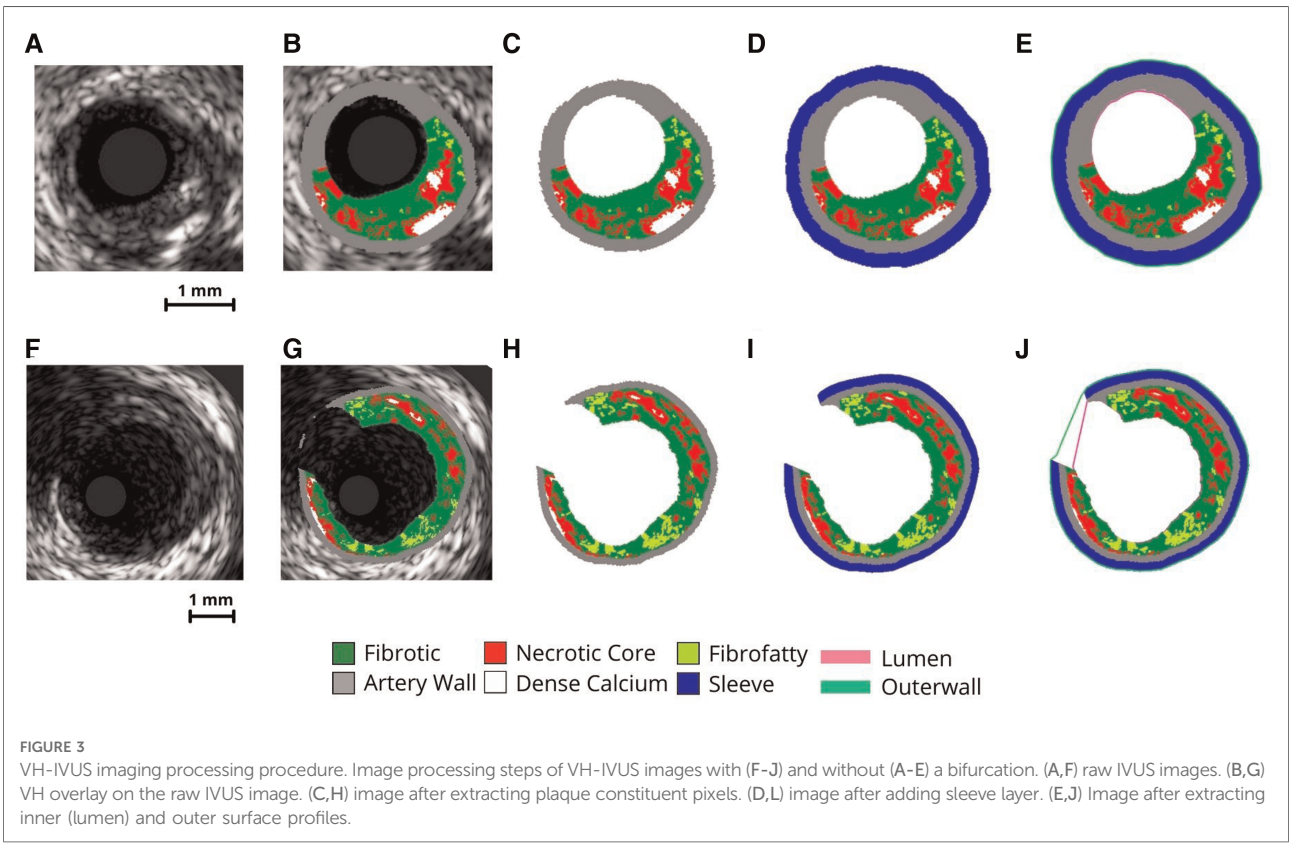

FIGURE 3
VH-IVUS imaging processing procedure. Image processing steps of VH-IVUS images with (F–J) and without (A–E) a bifurcation. (A,F) raw IVUS images. (B,G) VH overlay on the raw IVUS image. (C,H) image after extracting plaque constituent pixels. (D,L) image after adding sleeve layer. (E,J) Image after extracting inner (lumen) and outer surface profiles.

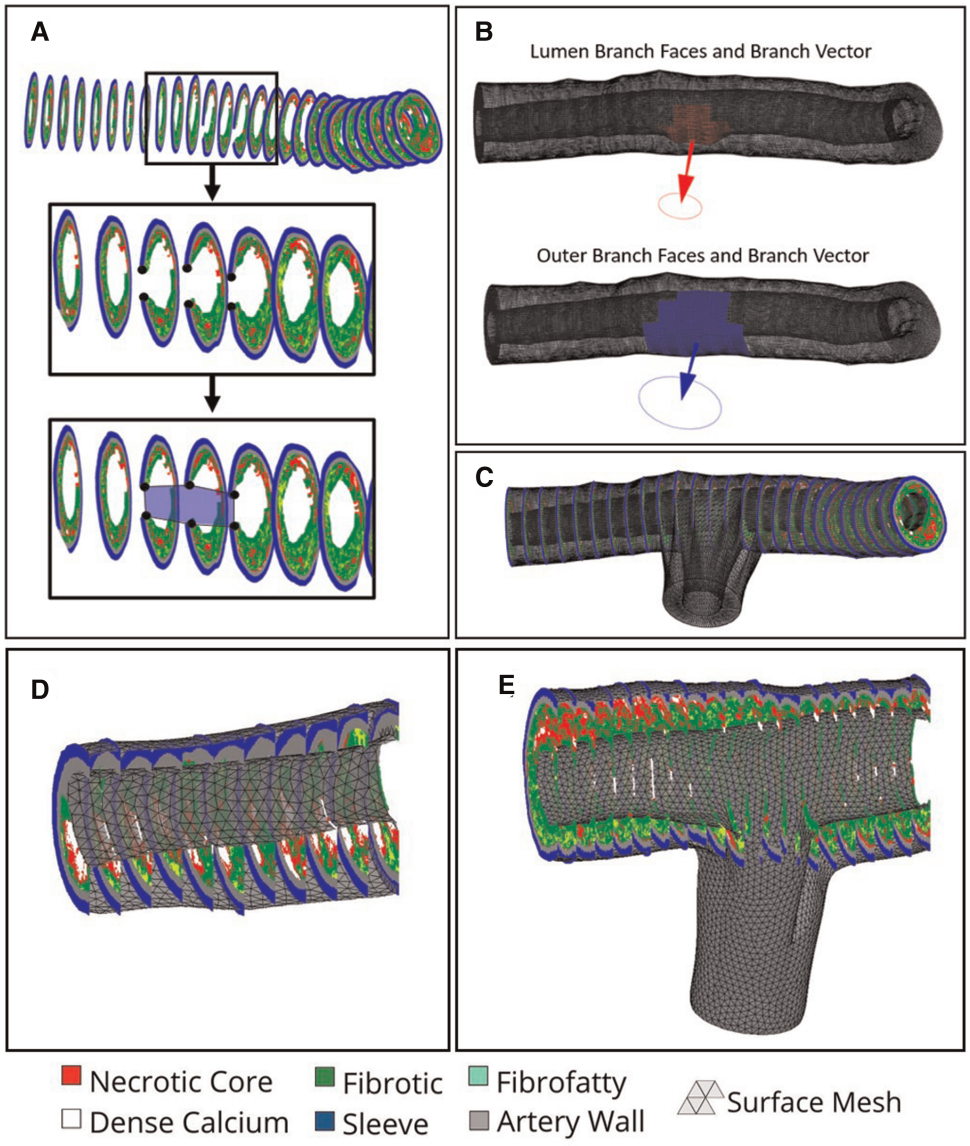

FIGURE 4
Branch creation procedure. (**A**) Black dots overlayed on VH-IVUS image represent the inner and outer coordinates proximal to the branch region in blue. (**B**) Computed Normal vectors to plan the branch lofting procedure. (**C**) Branched mesh post lofting procedure merged with main arterial mesh. (**D**) non-bifurcated and (**E**) bifurcated arterial meshes, respectively, after smoothing and resampling is applied.

sequences will typically overlap, causing problems when lofting to the projected edges. Hence, the edges along the luminal branch edge sequence are dilated and projected back onto the mesh wherein the faces on the outer surface that lie inside the projected space are removed. Such an assumption is blind to the true thickness of the branched artery wall; however, it is necessary since the thickness of the branched artery wall cannot be determined from the axial VH-IVUS images. Next, we loft the branch edge sequence to the projected nodes *via* a spline loft. The spline loft requires additional computation of start and end vectors parallel to the mesh faces and orthogonal to the projection plane, respectively. Once complete, the branch is closed by lofting the outer edges on the projected plane to the luminal edges on the projected plane (**Figure 4C**). This procedure is completed for each branch and results in a closed-volume first-pass approximation of the arterial mesh. Though this first-pass approximation resembles the real arterial structure, it comprises of non-uniform triangles and significantly varying edge lengths. Hence, we apply Humphrey class smoothing (22) and a resampling algorithm to create the uniform triangular mesh (**Figures 4D,E**).

Volumetric mesh

The final step in the mesh creation procedure is to generate the volumetric mesh *via* tetrahedralization in preparation for FEA. Currently, our method uses linear tetrahedral-4 (tet4) element shapes, although the user interface allows for nonlinear tet10 element shapes to be used instead. The decision to use tetrahedral element shapes was informed by (23) which pointed toward tetrahedral elements as the most applicable shape for biomechanical loading and use with nonlinear material models. Although other element shapes exist, tetrahedral elements allow for automated utilization of the open source tetrahedralization code TetGen (24), implemented within the GIBBON library (25), to automate the creation of the finite elements. Additionally, TetGen allows the use of command line flags to control the various optimization parameters used when tetrahedralizing the mesh. Here we use a maximum volume constraint paired with an edge length constraint to maximize element quality and produce elements with uniform volumes and edge lengths. The values of each constraint are automatically calculated in our code using the mean edge length of the surface mesh as well as a user-defined mesh resampling resolution.

Material assignment

As shown in **Table 1**, each artery is composed of 5 types of materials: arterial wall, fibrotic, calcium, necrotic core, and sleeve. Materials were assigned based on their specific VH-IVUS color (i.e., RGB value). The material properties were assumed to be linear elastic as suggested by previous studies (26).

Up until this point, VH-IVUS images have been processed and the surface mesh and volumetric meshes have been generated. However, the finite elements have not yet been associated with a particular material type. We use the arterial centerline and VH-IVUS pixel coordinates to associate each finite element with a tissue type (**Figure 8A**) and the associated material properties (**Table 1**). To do so, the centroid of each element in the volumetric mesh is first calculated. We then loop through each element centroid, find the nearest VH-IVUS pixel coordinate, and assign the material type associated with that coordinate to the element (**Supplementary Figure S3**). Naturally, one can see how the computational cost of comparing millions of VH-IVUS pixel coordinates with each element centroid increases exponentially with the number of elements. Therefore, to decrease computational cost, VH-IVUS pixel coordinates and element centroids are first pre-indexed into overlapping sections along the centerline. Materials are then assigned to each element by only searching the VH-IVUS pixel coordinates within the element's section rather than searching the entire mesh domain. This approach significantly reduces the number of calculations needed, thereby decreasing the time and computational resources needed to assign materials. Preliminary analysis of this process has shown that the time taken to assign materials with this optimization technique takes ~15 min or on average between 20–40x less time; significant reductions in memory use and computational resources allow for faster material assignment with higher resolution meshes. Once materials are assigned, the volumetric mesh can be prepared for analysis in FEBio.

TABLE 1 Material properties used for FEA. VH-IVUS color, associated Young's modulus (MPa), and Poisson's ratio for each material type used in the FEA simulations (26).

Material	Color	Young's modulus (MPa)	Poisson's ratio
Arterial Wall	Grey	0.3	0.48
Fibrotic	Dark Green	0.6	0.48
Fibrofatty	Light Green	0.5	0.48
Calcium	White	10	0.48
Necrotic Core	Red	0.02	0.48
Sleeve	User Defined	0.4	0.48

FEBio setup - loads, boundary conditions, and solver parameters

Here we outline the loads, boundary conditions and assumptions within the FE model. Since the aim of our method is to model the general structural mechanics within the artery wall, the loads, BCs, and assumptions presented herein are not geared toward a specific model, but rather to provide a base framework for future modification and improvement. An overview of only the necessary conditions for general modelling of arterial mechanics is provided.

Luminal loading

Loading conditions replicate in-vivo conditions with physiologically relevant pressure loads defined at the faces of the lumen surface (**Figure 5**, left). In the current version of the model, a static pressure load representing systolic blood pressure is used. However, this value is user-defined, allowing the use of patient-specific pressure values or, with slight modification, the incorporation of a time-dependent load curve to be used. Pressure loads are defined at the mesh faces but FEBio distributes these values to the associated nodes internally. The pressure is applied over the course of one second with a small time-step to capture the small deformations and ensure model convergence. Here it must be noted that although the goal of our method is a simplified general model, care must be taken when choosing the time step and pressure loads. Larger pressure loads will inherently result in larger deformations and hence, a smaller time step

10.3389/fmedt.2022.1008540

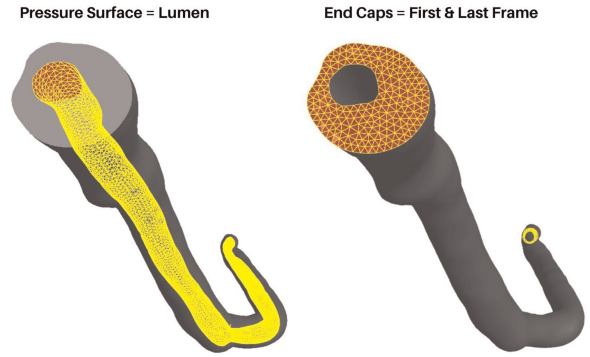

FIGURE 5
Boundary conditions and loading. The luminal surface (Left) is used to apply pressure loads and the end caps (Right) are fixed in x, y, and z axes.

must be chosen. Additionally, it is worth noting that a static load does not represent the dynamic pulsatile loading exhibited in-vivo. However, as previously mentioned, we aimed to create a basic framework to model general arterial biomechanics without introducing any unnecessary complexity in the current iteration.

Boundary conditions and assumptions

As is the case with all finite element models, boundary conditions (BCs) must be carefully chosen by considering relevant observations and assumptions. In the case of coronary artery segments, they are not simply floating in free space nor isolated from surrounding tissues. They are surrounded by various perivascular tissues, in direct contact with the myocardium, and in-line with arterial tissue outside the scope of the VH-IVUS imaging domain. However, one can still gain useful insight into the general arterial biomechanics by using simplified boundary and loading conditions. Therefore, BCs were chosen to ensure model convergence while replicating pseudo-physiological conditions. Nodes connected to the surfaces at the ends of the main artery line as well as the ends of the branches are fixed in all axes (**Figure 5**, right). Rotational, compressive, or tensile forces generated by heart contraction were not considered. Another factor not considered are residual stresses present in the artery in-vivo. The advent of bi-axial artery tissue testing and the opening-angle theory present in arterial continuum mechanics models made it clear that residual stresses are always present in the vasculature. For uniquely heterogenous tissues, these factors, although widely studied and published since the 1990s (27–29), require additional experiments and procedures that are difficult to conduct without destroying the tissue itself. Therefore, we do not consider residual stresses in our model and focused solely on the biomechanics at play during pressurization.

Results

Our algorithm is capable of automatically generating a biomechanical model from patient-specific VH-IVUS images and angiograms. The algorithm was developed using MATLAB scripting language and open-source programs such as TetGen and FEBio. Depending on the number of IVUS slices, meshing resolution, curvature complexity, type of computer, etc., the time taken to reconstruct a mesh will vary broadly. For example, a mesh reconstruction with 200 frames and 0.2 resolution took around 15 min on a generic consumer laptop. User-friendly step-by-step instructions as well as the source code are available on GitHub: https://github.com/VMBL-UTD/Automated-Artery-Reconstruction.

Mesh convergence study

A mesh convergence study was conducted to determine the resolution that best captured the volumes of each plaque constituent. Although the speed and power of computer processors only increases with time according to Moore's law, it is still worth considering such a mesh convergence study to minimize computational resource consumption and problem complexity. The mesh resampling value is a user-defined parameter and refers to the triangular and tetrahedral edge lengths (in millimeters) of the surface and volumetric meshes, respectively. Hence, within this section the terms "resampling value", "edge length", and "resolution" are used interchangeably.

For this study, a representative full artery mesh was reconstructed using resampling values ranging from 0.04 mm to 0.4 mm in steps of 0.005 mm. Additionally, the total volumes of each plaque constituent (medial, adventitial, necrotic, calcium, fibrotic, and fibrofatty) were calculated at each resampling value (**Figure 6**). It is also worth noting that although the sleeve element volumes were also considered in this study, mesh convergence was primarily determined by the actual plaque constituents taken from VH-IVUS data. Coarser mesh resolutions (larger resample values) resulted in inconsistent variations in constituent volumes, whereas finer meshes (smaller resample values) saw the convergence of constituent volumes. Edge lengths above 0.2 mm resulted in varying constituent volumes with increasingly inconsistent volumes; going from a resampling value of 0.3 to 0.35, for example, resulted in large differences in fibrotic element volumes. Edge lengths between 0.2 mm and 0.04 mm produced constituent volumes that were largely unchanged, hence, for the purpose of the following subsections and to save computational resources, a value of 0.2 mm was used. The mesh convergence results verify that the model behaved as expected (i.e., finer resolutions between 0.04 mm to 0.2 mm, resulted in more precise constituent volume).

Once the meshing resolutions that best captured plaque constituent volumes were identified, we conducted a stress-based convergence study to quantify the impact of mesh

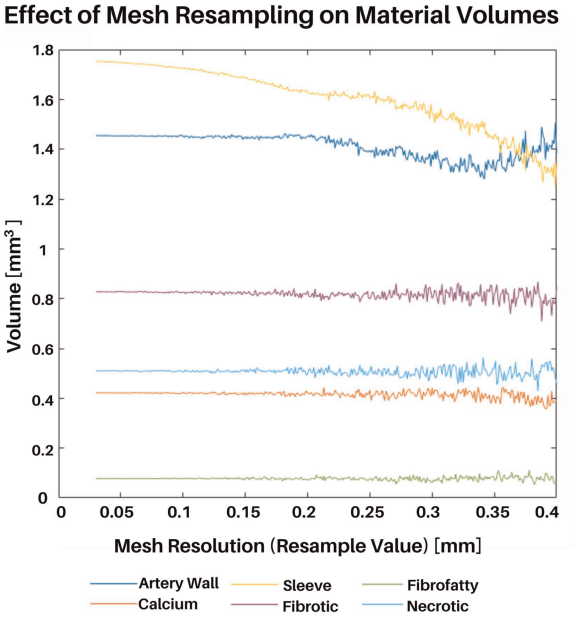

FIGURE 6
Mesh convergence study. An entire representative artery was reconstructed at various mesh resolutions. Meshing resolutions ranging from 0.04 mm to 0.4 mm in steps of 0.005 were used (x-axis). The total volume of each plaque constituent was calculated at each resolution (y-axis).

resolution on stress distribution (**Figure 7**, **Supplementary Table S2**). This study was designed to show how the distribution of effective stress, displacement, and element size change with different mesh resolutions as compared to the original VH-IVUS images. A representative section of the artery was reconstructed using 5 IVUS images at resolutions of 0.2, 0.15, 0.10, and 0.05 mm and the same simulation parameters, as outlined in "FEBio setup - loads, boundary conditions, and solver parameters", were utilized. Owing to the fixed boundary conditions (in x, y, and z) applied to the nodes at the end caps, peak stresses were in the elements nearest the end caps. Hence, we chose to use a cross sectional view from the middle of the segment where the fixed boundary conditions would have less of an effect on the stress distribution. Regarding deformation, the thinnest region of the cross-section consistently had the largest displacement magnitude as expected. Maximum displacement values gradually increase with finer resolution (i.e., maximum displacement increases from 0.11 to 0.14 mm at resolutions 0.2 to 0.05 mm, respectively). Volumetrically, the size of the elements decreased linearly with smaller edge-length values which aligned with the outcomes of the volumetric mesh independence study. Mechanically, effective stress in the artery also decreased as the resolution neared a 1:1 ratio with the VH-IVUS pixel size. This pattern can be attributed to a shear locking phenomenon typically experienced by linear element shapes wherein they are unable to accurately capture deformation in nonlinear materials. The trend of stress increasing with finer resolutions could also be attributed to our material assignment method. Though the material assignment method does apply similar materials globally, larger meshes resulted in less consistent local material assignment. This discrepancy arises because our current approach uses element centroids to find the nearest VH-IVUS pixel for material assignment. Due to the image pixel edge-length value being significantly smaller than the mesh, a neighboring pixel could be nearer to an element's centroid when a slightly different resolution is applied. An example of this limitation is seen in **Figure 7B** where the volume of the red necrotic core pixels is over approximated in larger meshes and more precisely represented with finer resolutions. Moreover, the stress distribution in **Figure 7B** are clearly impacted by coarser resolutions. This result paired with the plaque heterogeneity seen in the VH-IVUS image suggests that finer resolutions are better suited for a more precise representation of the VH-IVUS pixels. Furthermore, we found that using nonlinear tet10 element shapes results in more consistent stress calculations compared to linear tet4 elements at the same meshing resolutions (**Supplementary Figure S4**). **Supplementary Table S3** quantifies the percent difference in stress values as a function of element shape and mesh resolution for each material type. The user interface (GitHub repository: https://github.com/VMBL-UTD/Automated-Artery-Reconstruction) allows the user to modify the resolution and element type. Yet, one must also be aware that finer meshes can significantly increase computational time and required resources when reconstructing the mesh and running the FEA simulation.

Volumetric differences between straight and curved geometry

We sought to determine if the volume of the plaque constituents and/or wall mechanics differed between straight and curved arterial geometry. Original works utilized straight meshes reconstructed from IVUS (32). Yet, angiogram data allows the realization of a curved centerline and hence a more anatomically accurate arterial reconstruction. One of the inputs to the mesh creation script allows the user to define whether the geometry uses the curved centerline or not. Plaque constituent volumes can then be computed from the volumetric mesh and wall mechanics from the FE simulation.

In a representative mesh, the relative volumes of the plaque constituents were 52.48% sleeve material, 17.78% fibrotic/fibrous cap, 18.34% arterial wall, 6.47% fibrofatty, 3.21% necrotic core, and 1.71% dense calcium in the straight reconstruction. The curved centerline artery reconstruction was composed of 52.02% buffer material, 17.95% fibrotic/

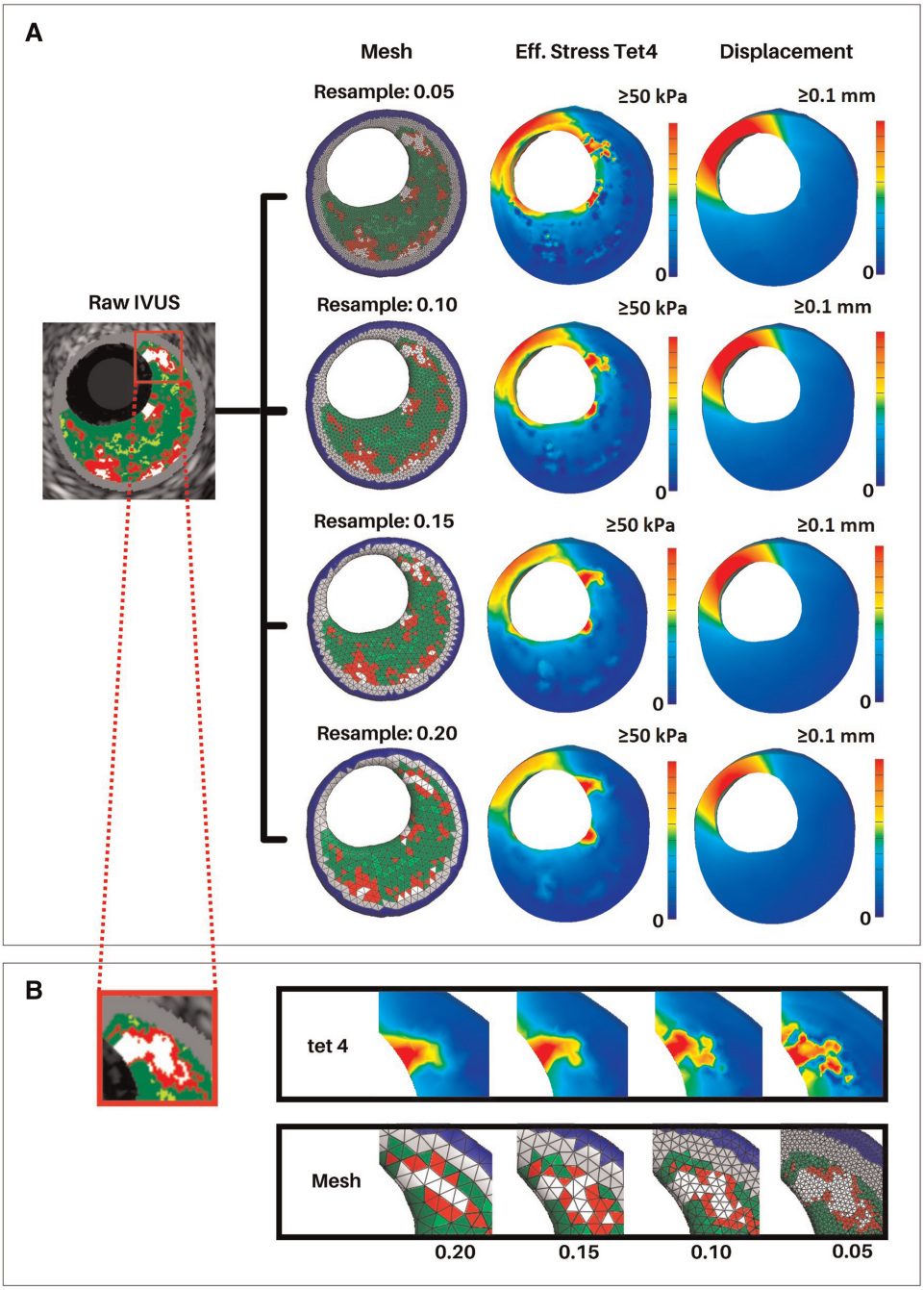

FIGURE 7
Effective stress and displacement with varying mesh resolutions. Arterial meshes of a short 5 VH-IVUS slice artery segment were reconstructed at resolutions of 0.05, 0.1, 0.15, and 0.2 mm. Similar simulation parameters were used in all meshes to calculate effective stress and displacement in FEBio. (A) First column shows the middle slice of the reconstructed meshes. Second and third columns show cross-sectional views of the effective stress and displacement, respectively. (B) Close-up view of a calcified region of the middle VH-IVUS image and corresponding regions of the arterial mesh. The top row shows effective stress, and the bottom row shows the mesh at each resolution.

fibrous cap, 18.49% arterial wall, 6.57% fibrofatty, 3.24% necrotic core, and 1.73% dense calcium. Statistical analysis between the plaque constituent volumes was conducted in R (version 4.1.3). Simple correlation test ($p < 0.05$, $R = 0.99$) shows there is a high correlation between the constituent volumes. Thus, using curved geometry instead of straight geometry does not create statistically significant differences in plaque constituent volumes.

Effective stress

A representative arterial mesh (Artery 4) was chosen to illustrate the FEA results. Note that these results are not intended to suggest any sort of global interpretation but rather display our method's FEA capabilities. Materials were assigned according to "Material assignment" and a sleeve thickness of 0.2 mm was used (Figure 8A). Boundary conditions, assumptions, and loading parameters outlined in "Luminal loading" and "Boundary conditions and assumptions" were also used for this analysis and Von Mises elemental stresses were calculated for each plaque constituent

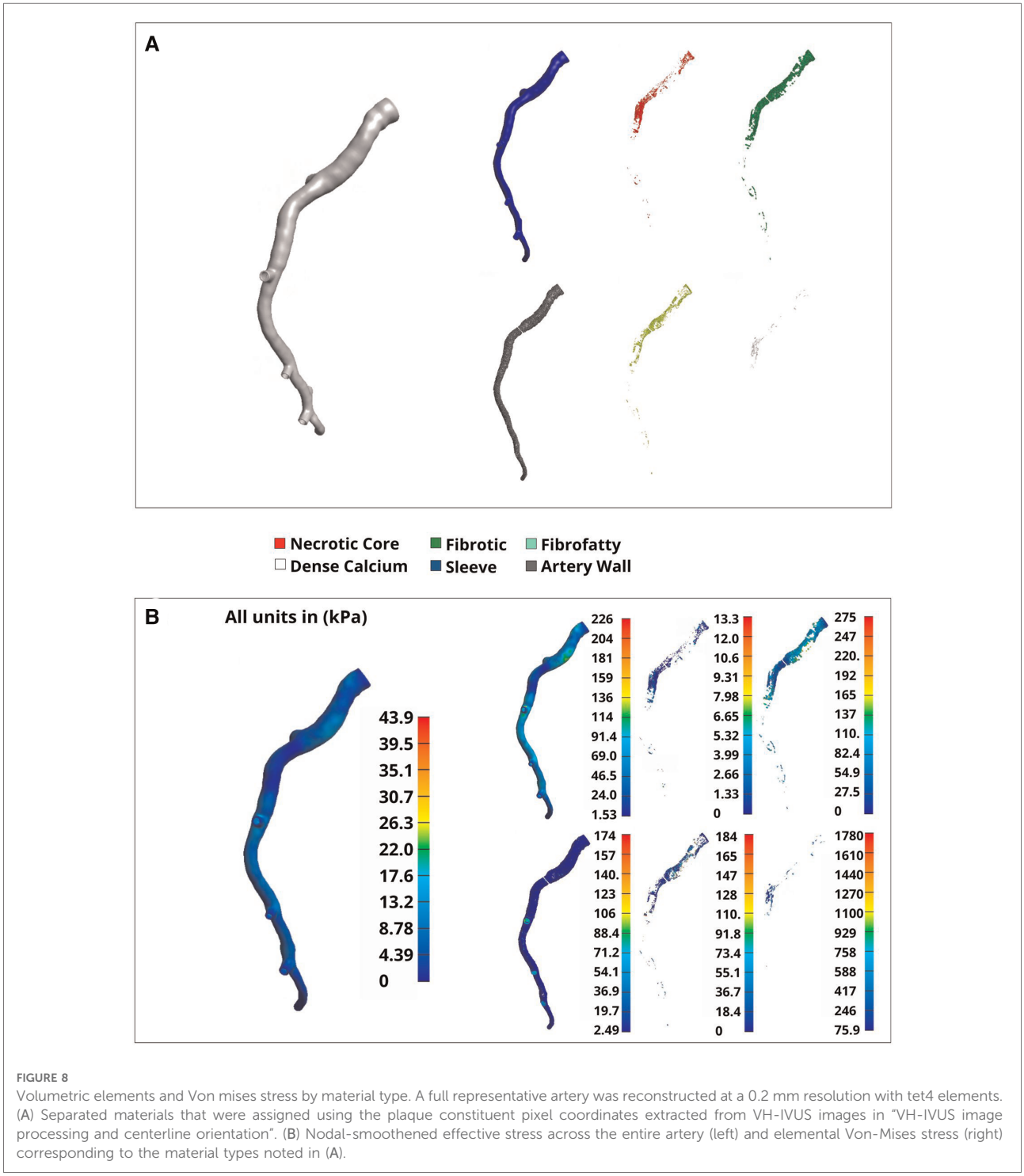

FIGURE 8
Volumetric elements and Von mises stress by material type. A full representative artery was reconstructed at a 0.2 mm resolution with tet4 elements. (A) Separated materials that were assigned using the plaque constituent pixel coordinates extracted from VH-IVUS images in "VH-IVUS image processing and centerline orientation". (B) Nodal-smoothened effective stress across the entire artery (left) and elemental Von-Mises stress (right) corresponding to the material types noted in (A).

(Figure 8B). Elemental stress was highest in calcified elements with an average of 288.17 kPa and lowest in necrotic elements with an average of 2.2 kPa. After applying nodal smoothening, the average effective stresses across the entire artery segment remained below 60 kPa. Of note, the thickness of the sleeve layer can impact simulation results and stress values. In the same representative artery, a discrete range of sleeve thicknesses from 0 (no sleeve) to 0.4 mm corresponded to a change in mean stress from 28 kPa to 19 kPa, respectively. Figures and tables displaying various mesh characteristics and results for all 11 arteries used for development of our method are included in the supplementary material (Supplementary Figures S1, S2, and Supplementary Table S1).

Discussion

Understanding the state of stress inside atherosclerotic coronary arteries is paramount for improved patient care and treatment planning. The automated method presented herein uses patient-specific VH-IVUS images and angiogram data to produce volumetric arterial meshes. FEA is then applied to the volumetric mesh to calculate the stresses and strains that develop in the artery. A simple way to determine the biomechanics of a patient's artery will give insight into the state of a patient's disease. Previous studies have utilized VH-IVUS or OCT imaging to generate 2D planar FEA simulations of atherosclerotic plaque (26, 31, 32). Moreover, 3D FEA models of coronary arteries have also been developed, utilizing a single generalized homogeneous material for the entire artery or a limited set of heterogenous materials (33, 34). These methods provide useful insight into both planar and 3D stresses that develop within a plaque buildup during the cardiac cycle. However, the full 3D complexity of the plaque structure is impossible to be accurately depicted in planar simulations and the use of homogenous or limited materials in previous 3D simulations fail to address the complex heterogenous nature of plaque. Another factor to note is the amount of manual intervention required to generate the FE meshes in each approach. Images had to be manually cleaned and processed to extract the inner and outer arterial profiles and plaque constituents. Our method addresses each of these shortcomings, opting to combine the use of 2D images for reconstructing the mesh, 3D spatial locations of materials extracted from VH-IVUS to address material heterogeneity, and automation to limit any manual intervention. Additionally, the complex curvature of coronary arteries, captured *via* coronary angiography, is also incorporated; resulting in a method capable of automatically generating anatomically accurate arterial meshes in 3D at the press of a button.

As with all modern computational methods, the results from FEA are not definitive and results must be interpreted with care. The complex, heterogeneous nature of arterial tissue and nonlinearity of soft tissues allow only an approximate solution to be realized (35). Additionally, special care must be taken when choosing boundary conditions and loads capable of replicating physiological conditions while also minimizing computational resources and complexity. For example, fixing nodes along the end caps can result in higher stresses in adjacent elements, hence skewing the distribution of stress in nearby regions. Boundary conditions and assumptions are absolutely necessary in any computational model; however, one must also be weary of oversimplifications and misinterpreting the results. Another area requiring close attention are material properties. We currently use the widely accepted linear neo-Hookean material model presented by Paritala et. al (26), while works from Hoffman et. al (36) and Holzapfel et al. (37), have proposed Mooney-Rivlin or modified versions for atherosclerotic constituents. The nonlinear Mooney-Rivlin material model is a third-order model, which is postulated to be better suited for describing shear deformation in elastic materials (38) as compared to the second-order Neo-Hookean model currently used. However, we did not aim to quantify the difference or implications of either model but rather, offer a robust method capable of easily interchanging between material models if desired.

The stresses presented herein are within ranges seen in the literature. Work by Paritala et al. found stresses in a stenosed artery to range between 0.002 to 286.1 kPa, with a large percentage of the higher stresses focused on the plaque shoulder (26). Wang et al. reported wall stresses between 0.3634 and 450.4 kPa in planar 2D FEA simulations (39). Some variation is expected, owing to differences in materials properties or mesh reconstruction methods employed, but the stress results of our FEA lie within both ranges. Additionally, none of the atherosclerotic plaques presented herein ruptured at follow-up (16). This stability is also consistent with our results as the nodal-smoothened values from our FEA were below the suggested 300 kPa rupture threshold (40). In summary, our values are within previously published literature values.

The method presented herein aims to display the current capabilities for automated arterial mesh reconstruction, yet, as with all computational methods, this approach does come with its limitations. One shortcoming is the material assignment method. Currently, our material assignment method ("Material assignment") simply assigns one of five materials to each element using the nearest spatial location of the VH-IVUS pixels extracted in "VH-IVUS image processing and centerline orientation". This generic approach does not refine the transition in material stiffness at the boundary of stiff and soft materials, which may result in larger stresses in these areas (e.g., adjacent calcium and necrotic elements) as seen in Figure 7 and Supplementary Table S2. This limitation is an important and common issue in heterogeneous FE models and gives rise to the need to

address material heterogeneity while minimizing additional computational resources. Of note, if desired, the user can modify the mesh resample value to address this limitation. However, to save computational resources one may consider alternative meshing approaches such as finer resolution around material boundaries or adaptive remeshing to potentially minimize numerical errors and ensure a refined transition between stiff and soft materials. Additionally, the user interface allows for manipulation of the element shape used during analysis. The code defaults to linear tet4 element shapes but nonlinear tet10 element shapes can be applied for the analysis instead; this choice will increase the amount of computational power needed for simulation and influence the biomechanical analysis (**Supplementary Figure S4**). A second limitation is seen in the default material model. Currently, the code defaults to using a Neo-Hookean material model which is less accurate for predicting the nonlinear response exhibited by biological tissues. This material model was chosen as a mere surrogate for the development of the algorithm but can easily be modified to use a different material model if desired. This versatility gives users the ability to define custom material models or choose from another one of the multitude of models currently implemented in the FEBio software. Although not explicitly implemented in the user interface, a custom plug-in can also be implemented with FEBio allowing for fully customized material models to be used which may be better suited for other applications. A third limitation of our method is its inability to predict plaque rupture or fully characterize plaque stability. This limitation has been a topic of interest in cardiovascular research for many years (41, 42) and a variety of predictive measures have been suggested namely, necrotic core thickness (3), fibrous cap thickness (43), and microcalcifications (5). Due to the difficulties involved with obtaining such geometrical features from VH-IVUS imaging, these aspects were not analyzed in the manuscript. However, the incorporation of different imaging modalities that are capable of identifying such structures would expand the capability of our method and enhance outcomes. In fact, the objective of this manuscript is to detail our novel, automated meshing algorithm and its potential for biomechanical analysis. We hope widespread adaptation of our method will result in valuable and insightful innovation regarding the limitations mentioned above and advancement in the realm of vascular biomechanical analysis and patient-specific precision healthcare.

In addition to acute analysis, continued development of our methods will yield novel insights into the state of cardiovascular disease. It is beyond the scope of this manuscript, but future studies can use this model to analyze the biomechanics between baseline and follow-up data to allow for more insight into the state of growth and remodeling occurring in the artery. Co-registration efforts by Timmins et al. (44) have already been used to identify how hemodynamics effects atherosclerotic progression. Such works would also allow for more insight into structural mechanical analysis as it relates to rupture mechanisms and prediction capabilities, opening the door for translational medicine and enhanced treatment options. The groundwork presented herein details an automated, user-friendly, 3D, and robust biomechanical modeling approach that has the potential to broaden research insights and utility for clinical applications.

Data availability statement

The datasets presented in this study can be found in online repositories. The names of the repository/repositories and accession number(s) can be found below: https://github.com/VMBL-UTD/Automated-Artery-Reconstruction.

Ethics statement

The studies involving human participants were reviewed and approved by Emory University and UT Dallas Institutional Review Board. The patients/participants provided their written informed consent to participate in this study.

Author contributions

HH conceived and designed the study; JY and JW collected the data; JY and JW performed the simulation and data analysis. JY and JW drafted the manuscript, and all authors edited and approved the manuscript prior to submission.

Funding

The authors gratefully acknowledge funding for this work provided by the National Heart, Lung, And Blood Institute of the National Institutes of Health (1R01HL136776-01A1) and the National Science Foundation Louis Stokes Alliance for Minority Participation (LSAMP) Fellowship. The content is solely the responsibility of the authors and does not necessarily represent the official views of the National Institutes of Health.

Acknowledgments

Members of the Vascular Mechanobiology Lab, namely Brian J. Torres for his help analyzing the initial VHIVUS dataset.

Conflict of interest

The authors declare that the research was conducted in the absence of any commercial or financial relationships that could be construed as a potential conflict of interest.

Publisher's note

All claims expressed in this article are solely those of the authors and do not necessarily represent those of their affiliated organizations, or those of the publisher, the editors, and the reviewers. Any product that may be evaluated in this article, or claim that may be made by its manufacturer, is not guaranteed, or endorsed by the publisher.

Supplementary material

The Supplementary Material for this article can be found online at https://www.frontiersin.org/articles/10.3389/fmedt.2022.1008540/full#supplementary-material..

References

1. Kelly-Arnold A, Maldonado N, Laudier D, Aikawa E, Cardoso L, Weinbaum S. Revised microcalcification hypothesis for fibrous cap rupture in human coronary arteries. *Proc Natl Acad Sci U S A*. (2013) 110(26):10741–6. doi: 10.1073/pnas.1308814110

2. Gurfinkel E, Vigliano C, Janavel J, Fornoni D, Caponi G, Meckert P, et al. Presence of vulnerable coronary plaques in middle-aged individuals who suffered a brain death. *Eur Heart J*. (2009) 30(23):2845–53. doi: 10.1093/eurheartj/ehp303

3. Ohayon J, Finet G, Gharib A, Herzka D, Tracqui P, Heroux J, et al. Necrotic core thickness and positive arterial remodeling index: emergent biomechanical factors for evaluating the risk of plaque rupture. *Am J Physiol Heart Circ Physiol*. (2008) 295(2):H717–27. doi: 10.1152/ajpheart.00005.2008

4. Maehara A, Cristea E, Mintz G, Lansky A, Dressler O, Biro S, et al. Definitions and methodology for the grayscale and radiofrequency intravascular ultrasound and coronary angiographic analyses. *JACC Cardiovasc Imaging*. (2012) 5(3):S1–9. doi: 10.1016/j.jcmg.2011.11.019

5. Vengrenyuk Y, Carlier S, Xanthos S, Cardoso L, Ganatos P, Virmani R, et al. A hypothesis for vulnerable plaque rupture due to stress-induced debonding around cellular microcalcifications in thin fibrous caps. *Proc Natl Acad Sci U S A*. (2006) 103(40):14678–83. doi: 10.1073/pnas.0606310103

6. Kwak B, Bäck M, Bochaton-Piallat M, Caligiuri G, Daemen M, Davies P, et al. Biomechanical factors in atherosclerosis: mechanisms and clinical implications. *Eur Heart J*. (2014) 35(43):3013–20, 3020a–3020d, doi: 10.1093/eurheartj/ehu353

7. Li Z, Howarth S, Tang T, Gillard J. How critical is fibrous cap thickness to carotid plaque stability? A flow-plaque interaction model. *Stroke*. (2006) 37(5):1195–9. doi: 10.1161/01.STR.0000217331.61083.3b

8. Corban M, Eshtehardi P, Suo J, McDaniel M, Timmins L, Rassoul-Arzrumly E, et al. Combination of plaque burden, wall shear stress, and plaque phenotype has incremental value for prediction of coronary atherosclerotic plaque progression and vulnerability. *Atherosclerosis*. (2014) 232(2):271–6. doi: 10.1016/j.atherosclerosis.2013.11.049

9. Timmins L, Molony D, Eshtehardi P, Rasoul-Arzrumly E, Lam A, Hung O, et al. Quantification of the focal progression of coronary atherosclerosis through automated co-registration of virtual histology-intravascular ultrasound imaging data. *Int J Cardiovasc Imaging*. (2017) 33(1):13–24. doi: 10.1007/s10554-016-0969-y

10. Teng Z, Brown A, Calvert P, Parker R, Obaid D, Huang Y, et al. Coronary plaque structural stress is associated with plaque composition and subtype and higher in acute coronary syndrome: the BEACON I (biomechanical evaluation of atheromatous coronary arteries) study. *Circ Cardiovasc Imaging*. (2014) 7(3):461–70. doi: 10.1161/CIRCIMAGING.113.001526

11. Noble C, Carlson K, Neumann E, Dragomir-Daescu D, Erdemir A, Lerman A, et al. Patient specific characterization of artery and plaque material properties in peripheral artery disease. *J Mech Behav Biomed Mater*. (2020) 101:103453. doi: 10.1016/j.jmbbm.2019.103453

12. Kadry K, Olender M, Marlevi D, Edelman E, Nezami F. A platform for high-fidelity patient-specific structural modelling of atherosclerotic arteries: from intravascular imaging to three-dimensional stress distributions. *J R Soc Interface*. (2021) 18:20210436. doi: 10.1098/rsif.2021.0436

13. Wang J, Paritala P, Mendieta J, Komori Y, Raffel O, Gu Y, et al. Optical coherence tomography-based patient-specific coronary artery reconstruction and fluid–structure interaction simulation. *Biomech Model Mechanobiol*. (2020) 19(1):7–20. doi: 10.1007/s10237-019-01191-9

14. Guo X, Giddens D, Molony D, Yang C, Samady H, Zheng J, et al. A multi-modality image-based FSI modeling approach for prediction of coronary plaque progression using IVUS and OCT data with follow-up. *J Biomech Eng*. (2019) 141(9):091003. doi: 10.1115/1.4043866

15. Samady H, Eshtehardi P, McDaniel M, Suo J, Dhawan S, Maynard C, et al. Coronary artery wall shear stress is associated with progression and transformation of atherosclerotic plaque and arterial remodeling in patients with coronary artery disease. *Circulation*. (2011) 124(7):779–88. doi: 10.1161/CIRCULATIONAHA.111.021824

16. Eshtehardi P, McDaniel M, Dhawan S, Binongo J, Krishnan S, Golub L, et al. Effect of intensive atorvastatin therapy on coronary atherosclerosis progression, composition, arterial remodeling, and microvascular function. *J Invasive Cardiol*. (2012) 24(10):522–9. https://www.hmpgloballearningnetwork.com/site/jic/articles/effect-intensive-atorvastatin-therapy-coronary-atherosclerosis-progression-composition-arte

17. Nair A, Margolis MP, Kuban BD, Vince DG. Automated coronary plaque characterisation with intravascular ultrasound backscatter: ex vivo validation. *J EuroAPCI*. (2007) 3(1):113–20. PMID: 19737694

18. Villiger M, Otsuka K, Karanasos A, Doradla P, Ren J, Lippok N, et al. Coronary plaque microstructure and composition modify optical polarization: a new endogenous contrast mechanism for optical frequency domain imaging. *JACC Cardiovasc Imaging*. (2018) 11(11):1666–76. doi: 10.1016/j.jcmg.2017.09.023

19. Gubarkova E, Dudenkova V, Feldchtein F, Timofeeva L, Kiseleva E, Kuznetsov S, et al. Multi-modal optical imaging characterization of atherosclerotic plaques. *J Biophotonics*. (2016) 9(10):1009–20. doi: 10.1002/jbio.201500223

20. "QAngio.". Medis Medical Imaging, The Netherlands, 2014.

21. Vincent L. Grayscale area opening and closing, their efficient implementation and applications. Proc. EURASIP Workshop on Mathematical Morphology and its Applications to Signal Processing, Barcelona, Spain (1993). pp. 22–7

22. Vollmer J, Mencl R, Muller H. Improved laplacian smoothing of noisy surface meshes. *Comput Graph Forum*. (1999) 18(3):131–8. doi: 10.1111/1467-8659.00334

23. Maas S, Ellis B, Ateshian G, Weiss J. FEBio: finite elements for biomechanics. *J Biomech Eng*. (2012) 134(1):011005. doi: 10.1115/1.4005694

24. Si H. Tetgen, a delaunay-based quality tetrahedral mesh generator. *ACM Trans Math Softw*. (2015) 41(2):1–36. doi: 10.1145/2629697

25. Moerman K. GIBBON: the geometry and image-based bioengineering add-on. *J Open Source Softw*. (2018) 3(22):506. doi: 10.21105/joss.00506

26. Paritala P, Yarlagadda P, Wang J, Gu Y, Li Z. Numerical investigation of atherosclerotic plaque rupture using optical coherence tomography imaging and XFEM. *Eng Fract Mech*. (2018) 204:531–41. doi: 10.1016/j.engfracmech.2018.11.002

27. Chuong C, Fung Y. On residual stresses in arteries. *J Biomech Eng*. (1986) 108(2):189–92. doi: 10.1115/1.3138600

28. Sigaeva T, Sommer G, Holzapfel G, di Martino E-S. Anisotropic residual stresses in arteries. *J R Soc Interface*. (2019) 16(151):20190029. doi: 10.1098/rsif.2019.0029

29. Fung Y. What are the residual stresses doing in our blood vessels? *Ann Biomed Eng*. (1991) 19(3):237–49. doi: 10.1007/BF02584301

30. Klingensmith J, Schoenhagen P, Tajaddini A, Halliburton S, Tuzcu E, Nissen S, et al. Automated three-dimensional assessment of coronary artery anatomy with intravascular ultrasound scanning. *Am Heart J*. (2003) 145(5):795–805. doi: 10.1016/S0002-8703(03)00089-9

31. Gómez A, Tacheau A, Le Floc'h S, Pettigrew R, Cloutier G, Finet G, et al. Intravascular ultrasound imaging of human coronary atherosclerotic plaque: novel morpho-elastic biomarkers of instability. In: Ohayon J, Finet G, Pettigrew RV, editors., *Biomechanics of coronary atherosclerotic plaque*. Elsevier (2021). p. 465–89. doi: 10.1016/B978-0-12-817195-0.00020-2.

32. Wang H, Wang L, Zheng J, Zhu J, Maehara A, Yang C, et al. Using 2D in vivo ivus-based models for human coronary plaque progression analysis and comparison with 3d fsi models. *Procedia Eng*. (2015) 126:451–5. doi: 10.1016/j.proeng.2015.11.269

33. Huang Y, Teng Z, Sadat U, Graves M, Bennett M, Gillard J. The influence of computational strategy on prediction of mechanical stress in carotid atherosclerotic plaques: comparison of 2D structure-only, 3D structure-only, one-way and fully coupled fluid-structure interaction analyses. *J Biomech*. (2014) 47(6):1465–71. doi: 10.1016/j.jbiomech.2014.01.030

34. Nieuwstadt H, Akyildiz A, Speelman L, Virmani R, van der Lugt A, van der Steen A, et al. The influence of axial image resolution on atherosclerotic plaque stress computations. *J Biomech*. (2013) 46(4):689–95. doi: 10.1016/j.jbiomech.2012.11.042

35. Gholipour A, Ghayesh M, Zander A. Nonlinear biomechanics of bifurcated atherosclerotic coronary arteries. *Int J Eng Sci*. (2018) 133:60–83. doi: 10.1016/j.ijengsci.2018.08.003

36. Hoffman A, Teng Z, Zheng J, Wu Z, Woodard P, Billiar K, et al. Stiffness properties of Adventitia, Media, and full thickness human atherosclerotic carotid arteries in the axial and circumferential directions. *J Biomech Eng*. (2017) 139(12):1245011–6. doi: 10.1115/1.4037794

37. Holzapfel G, Sommer G, Gasser C, Regitnig P. Determination of layer-specific mechanical properties of human coronary arteries with nonatherosclerotic intimal thickening and related constitutive modeling determination of layer-specific mechanical prop-erties of human coronary arteries with nonatherosclerotic intimal thickening and related constitutive modeling. *Am J Physiol Heart Circ Physiol*. (2005) 289:2048–58. doi: 10.1152/ajpheart.00934.2004.-At

38. Zahnd G, Schrauwen J, Karanasos A, Regar E, Niessen W, van Walsum T, et al. Fusion of fibrous cap thickness and wall shear stress to assess plaque vulnerability in coronary arteries: a pilot study. *Int J Comput Assist Radiol Surg*. (2016) 11(10):1779–90. doi: 10.1007/s11548-016-1422-3

39. Wang L, Zhu J, Maehara A, Lv R, Qu Y, Zhang X, et al. Quantifying patient-specific in vivo coronary plaque material properties for accurate stress/strain calculations: an IVUS-based multi-patient study. *Front Physiol*. (2021) 12. doi: 10.3389/fphys.2021.721195

40. Cheng G, Loree H, Kamm R, Fishbein M, Lee R. Distribution of circumferential stress in ruptured and stable atherosclerotic lesions. A structural analysis with histopathological correlation. *Circulation*. (1993) 87(4):1179–87. doi: 10.1161/01.CIR.87.4.1179

41. Gasser T, Miller C, Polzer S, Roy J. A quarter of a century biomechanical rupture risk assessment of abdominal aortic aneurysms. Achievements, clinical relevance, and ongoing developments. *Int J Numer Method Biomed Eng*. (2022) :e3587. doi: 10.1002/cnm.3587

42. Obaid D, Calvert P, McNab D, West N, Bennett M. Identification of coronary plaque sub-types using virtual histology intravascular ultrasound is affected by inter-observer variability and differences in plaque definitions. *Circ Cardiovasc Imaging*. (2012) 5(1):86–93. doi: 10.1161/CIRCIMAGING.111.965442

43. Gao H, Long Q. Effects of varied lipid core volume and fibrous cap thickness on stress distribution in carotid arterial plaques. *J Biomech*. (2008) 41(14):3053–9. doi: 10.1016/j.jbiomech.2008.07.011

44. Timmins L, Suever J, Eshtehardi P, McDaniel M, Oshinski J, Samady H, et al. Framework to co-register longitudinal virtual histology-intravascular ultrasound data in the circumferential direction. *IEEE Trans Med Imaging*. (2013) 32(11):1989–96. doi: 10.1109/TMI.2013.2269275

frontiers | Frontiers in Medical Technology

TYPE Original Research
PUBLISHED 06 December 2022
DOI 10.3389/fmedt.2022.1034801

OPEN ACCESS

EDITED BY
Selene Pirola,
Delft University of Technology, Netherlands

REVIEWED BY
Jennifer Frattolin,
Imperial College London, United Kingdom,
Ryo Torii,
University College London, United Kingdom,
Claudio Chiastra,
Politecnico di Torino, Italy

*CORRESPONDENCE
Amanda Randles
amanda.randles@duke.edu

SPECIALTY SECTION
This article was submitted to Cardiovascular Medtech, a section of the journal Frontiers in Medical Technology

RECEIVED 02 September 2022
ACCEPTED 10 November 2022
PUBLISHED 06 December 2022

CITATION
Tanade C, Chen SJ, Leopold JA and Randles A (2022) Analysis identifying minimal governing parameters for clinically accurate *in silico* fractional flow reserve.
Front. Med. Technol. 4:1034801.
doi: 10.3389/fmedt.2022.1034801

Analysis identifying minimal governing parameters for clinically accurate *in silico* fractional flow reserve

Cyrus Tanade[1], S. James Chen[2], Jane A. Leopold[3] and Amanda Randles[1]*

[1]Department of Biomedical Engineering, Duke University, Durham, NC, United States, [2]Department of Medicine, University of Colorado, Aurora, CO, United States, [3]Division of Cardiovascular Medicine, Brigham and Women's Hospital, Boston, MA, United States

Background: Personalized hemodynamic models can accurately compute fractional flow reserve (FFR) from coronary angiograms and clinical measurements ($FFR_{baseline}$), but obtaining patient-specific data could be challenging and sometimes not feasible. Understanding which measurements need to be patient-tuned vs. patient-generalized would inform models with minimal inputs that could expedite data collection and simulation pipelines.
Aims: To determine the minimum set of patient-specific inputs to compute FFR using invasive measurement of FFR ($FFR_{invasive}$) as gold standard.
Materials and Methods: Personalized coronary geometries ($N = 50$) were derived from patient coronary angiograms. A computational fluid dynamics framework, $FFR_{baseline}$, was parameterized with patient-specific inputs: coronary geometry, stenosis geometry, mean arterial pressure, cardiac output, heart rate, hematocrit, and distal pressure location. $FFR_{baseline}$ was validated against $FFR_{invasive}$ and used as the baseline to elucidate the impact of uncertainty on personalized inputs through global uncertainty analysis. $FFR_{streamlined}$ was created by only incorporating the most sensitive inputs and $FFR_{semi-streamlined}$ additionally included patient-specific distal location.
Results: $FFR_{baseline}$ was validated against $FFR_{invasive}$ via correlation ($r = 0.714$, $p < 0.001$), agreement (mean difference: 0.01 ± 0.09), and diagnostic performance (sensitivity: 89.5%, specificity: 93.6%, PPV: 89.5%, NPV: 93.6%, AUC: 0.95). $FFR_{semi-streamlined}$ provided identical diagnostic performance with $FFR_{baseline}$. Compared to $FFR_{baseline}$ vs. $FFR_{invasive}$, $FFR_{streamlined}$ vs. $FFR_{invasive}$ had decreased correlation ($r = 0.64$, $p < 0.001$), improved agreement (mean difference: 0.01 ± 0.08), and comparable diagnostic performance (sensitivity: 79.0%, specificity: 90.3%, PPV: 83.3%, NPV: 87.5%, AUC: 0.90).
Conclusion: Streamlined models could match the diagnostic performance of the baseline with a full gamut of patient-specific measurements. Capturing coronary hemodynamics depended most on accurate geometry reconstruction and cardiac output measurement.

KEYWORDS

fractional flow reserve, computational fluid dynamics, patient-specific modeling, sensitivity analysis, uncertainty quantication, Sobol analysis

1. Introduction

Computational blood flow models that minimize the number of patient-tuned parameters required to extract diagnostic phenomarkers accurately may circumvent clinical data acquisition challenges and help enable interventional planning. One particular application is coronary artery disease—a leading cause of death and disability worldwide, with 7 million deaths and 129 million disability-adjusted life years lost annually (1). Invasively-measured fractional flow reserve ($FFR_{invasive}$) is the gold standard for identifying atherosclerotic lesions requiring intervention (2, 3). In recent years, computational fluid dynamics (CFD) models that predict FFR have emerged. These models are either based on coronary angiography (4, 5) or computed tomography (6, 7). Some of these models have been used extensively for research, such as VIRTUHeart (8–12), or have been made available to market, namely FFR_{CT} (HeartFlow, Mountain View, CA, USA) (13, 14), FFR_{angio} (CathWorks, Kfar-saba, Israel) (15–17), CAAS-vFFR (Pie Medical, Maastricht, The Netherlands) (18, 19), and QFR (Medis Medical Imaging, Leiden, The Netherlands and Pulse Medical Technology Inc., Shanghai, China) (20–22). However, these models require many clinically-measured inputs to accurately capture the effect of stenoses. In theory, a CFD model incorporating a maximum number of patient-tuned inputs would calculate the most accurate FFR. Requiring large numbers of invasively-measured parameters is challenging, costly, and sometimes not feasible. CFD models incorporating extensive patient-specific measurements have limited use when patients lack the complete set of necessary parameters for flow simulation. The pervasiveness of missing data in electronic health records increases the prevalence of such cases (23–25). Contrary to intuition, requiring full patient-specificity, which includes personalizing the computational domain, physical properties of blood vessels, and boundary conditions that dictate flow, may not even be required to recover diagnostic phenomarkers accurately. A low-cost CFD model based on only a few patient-derived measurements could streamline costly clinical data acquisition pipelines without compromising the diagnostic performance of fully personalized models. Prior sensitivity analysis and uncertainty quantification studies have attempted to identify the key anatomic and physiologic parameters contributing to FFR, but these studies often rely on models that have not been validated against $FFR_{invasive}$ measurements and are limited by small cohort sizes (11, 26–29).

Prior studies have demonstrated that accurately capturing stenosis geometry (in terms of minimal luminal radius and stenosis length) through imaging and prescribing flow distribution down the coronary tree (27) are the most sensitive inputs. Controlling flow distribution throughout the coronary tree is a function of terminal branch geometry as determined by Murray's Law, which may indicate that coronary anatomy is the overriding input (30). Ensuring accurate coronary anatomy could allow some leeway for the variance of other parameters. When patient-tuned values do not drastically deviate from patient averages, patient-generalized inputs could result in the same FFR calculation. As the focus has been on identifying sensitive inputs, it is unknown which parameters are insensitive to FFR and could be relegated to patient averages, or patient-generalized parameters, without sacrificing diagnostic performance (31). We hypothesized that on top of accurately segmenting the overall coronary tree, an accurate model with minimized inputs would require prescribing flow distribution parameters and capturing the geometric severity of stenoses on a per-patient level. In this work, we present a patient-specific CFD FFR model ($FFR_{baseline}$) and validated the model in a cohort of 50 patients. Sobol decomposition techniques were used to derive optimized, low-cost models ($FFR_{semi-streamlined}$ and $FFR_{streamlined}$) with minimal patient-specific clinical inputs without sacrificing diagnostic performance and agreement compared to $FFR_{invasive}$.

2. Materials and methods

2.1. Patient data

This study did not involve human tissue samples, direct patient experimentation, or interaction. The protocol was approved by the Massachusetts General Brigham Institutional Review Board (IRB Protocol #2015P001084). The IRB did not require individual patients to sign informed consent since the study was not prospective and there was no patient interaction or intervention performed. Patient data, consisting of coronary angiograms and clinical measurements, were acquired from 50 patients who underwent a clinically indicated coronary angiogram and were found to have angiographically-documented coronary artery disease at Brigham and Women's Hospital, Boston, MA, USA. Exclusion criteria were prior coronary artery bypass graft surgery, ST-elevation myocardial infarction, chronic total occlusion, and ostial lesions. The 50 patients were randomly selected. Angiograms included at least 4 standard orthogonal views of the left coronary circulation and 2 standard orthogonal views of the right coronary circulation (**Figure 1A**). Clinical measurements were collected during coronary angiography to inform personalized blood flow simulations, including aortic blood pressure, cardiac output, heart rate, and hematocrit. Routine FFR measurements were performed by administering intravenous adenosine ($140\,mcg/kg/min \times 120\,s$) to induce hyperemic conditions. A coronary guidewire pressure sensor (Volcano Corporation, San Diego, CA) was placed distal to the coronary stenosis for *in vivo* FFR computation. An

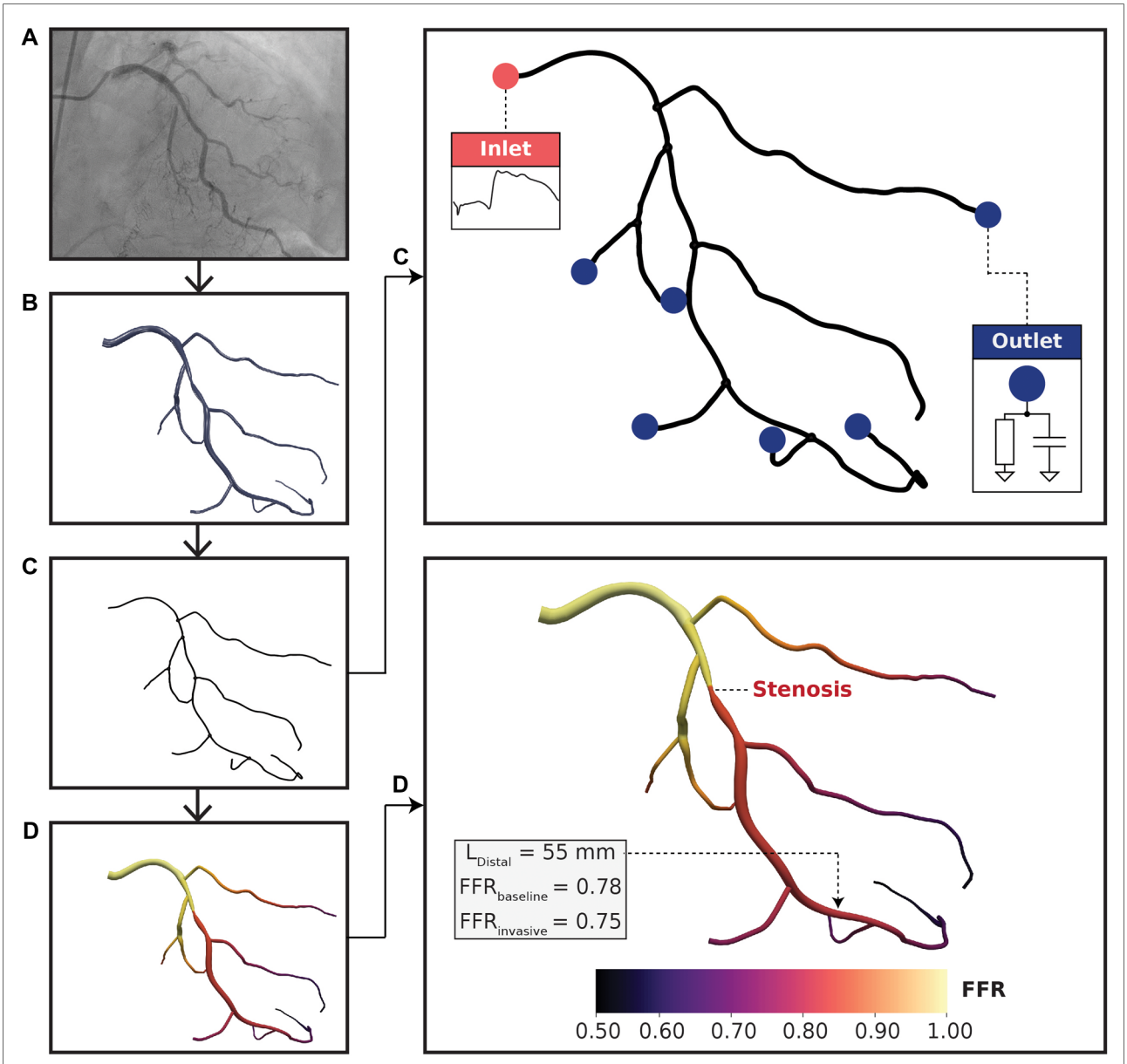

FIGURE 1
Computational fluid dynamics modeling pipeline. (**A**) Coronary angiograms were acquired for each patient. At least 4 or 2 standard orthogonal views were collected for left and right coronary trees, respectively. (**B**) A three-dimensional (3D) arterial tree model was semi-automatically reconstructed using a pair of coronary angiograms. (**C**) Vessel centerlines were extracted from the 3D reconstructed geometry for one-dimensional (1D) simulation. Pulsatile flow rate was used at the inlet boundary condition and 2-element Windkessel models were used at the outlet boundary conditions. The lumped parameter models consisted of resistance-compliance components, where resistances were related to terminal vessel anatomy. (**D**) FFR results mapped on a left coronary vessel. The distal location (L_{Distal}) was labeled by an expert physician and was situated 55 mm downstream to the distal-end of the stenosis. $FFR_{baseline}$ and $FFR_{invasive}$ resulted in the same FFR classification with minimal discrepancy.

experienced interventional cardiologist selected the location of distal pressure measurement, ranging 5–65 mm with respect to the distal-end of the stenosis. FFR $\leq$ 0.80 was considered ischemic and FFR $>$ 0.80 was considered non-ischemic. The researchers performing the coronary reconstructions and CFD simulations were blinded to clinically measured FFR values until CFD validations were completed.

2.2. Coronary geometry reconstruction

Three-dimensional (3D) full coronary tree models (Figure 1B) were reconstructed from pairs of coronary angiograms using a semi-automated algorithm described in (32, 33). The algorithm first computed two-dimensional vessel centerlines with corresponding cross-sectional

diameters semi-automatically on the pair of images. Afterward, a fully automated computation was used to generate the 3D coronary tree models in stereolithography (STL). Reconstructions were validated topologically and anatomically by an expert interventional cardiologist using ImageJ v1.52k (NIH, Bethesda, MD, USA) via comparing the minimal luminal diameter of the stenotic lesion segment in 3D models with the minimal diameter of the same diseased arterial segment in angiograms, which were additional cine runs acquired different from the pair of images (or the 3rd view) as used for 3D reconstruction. All identifiable (>1 mm) main and side branch vessels were reconstructed from 2D coronary angiography data. To create one-dimensional (1D) geometries (**Figure 1C**), vessel centerlines with corresponding hydraulic diameters were extracted from the reconstructed STL models using Mimics (Materialise, Leuven, BE). Vessel lengths were computed from centerline outputs at a resolution of 100 micrometers. The centerline data was validated by comparing the minimal luminal diameter between the 1D model with physician-measured ground truths on angiograms. These 1D full coronary tree models were used as inputs to personalized CFD simulations. Coronary anatomy was used to define the computational domain and was required to be reconstructed accurately on a per-patient level.

2.3. 1D computational model

2.3.1. Model assumptions

Blood was modeled as an incompressible Newtonian fluid with $\rho = 1,060\,\mathrm{kg/m^3}$. Dynamic viscosity was computed per-patient using an empirical relationship between viscosity and hematocrit from (34):

$$\mu = \frac{\mu_0}{1-\phi} \tag{1}$$

where μ is the dynamic viscosity of blood, μ_0 is the dynamic viscosity of plasma, and ϕ is hematocrit. We assumed a constant plasma hematocrit of 1.2 cP (4, 5, 34). The 1D blood flow simulator inherently uses elastic walls, but we enforced quasi-rigid walls. We noted area deformations of 0.78% when averaged across all cases, all vessels, and over all time points. The area deformations here were comparable to other 1D models (35) that enforced quasi-rigid walls.

2.3.2. Mathematical formulation

We used a 1D blood flow model described in (36, 37). The 1D blood flow simulator was based on the following governing equations:

$$\frac{\partial A}{\partial t} + \frac{\partial Q}{\partial x} = 0 \tag{2}$$

$$\frac{\partial Q}{\partial t} + \frac{\partial}{\partial x}\left(\alpha\frac{Q^2}{A}\right) + \frac{A}{\rho}\frac{\partial P}{\partial x} = -C_f\frac{Q}{A} \tag{3}$$

where A is vessel cross-sectional area, Q is flow rate, P is pressure, ρ is density of blood, α describes the velocity profile, and $C_f = 22\pi\mu$ is a frictional term. α and C_f were estimated from experimental data that have been used in 1D models (36–39). P and A are related by the following constitutive equation:

$$P = P_{\mathrm{ext}} + \beta(\sqrt{A} - \sqrt{A_0}),\ \ \beta = \frac{\sqrt{\pi}hE}{(1-\nu^2)A_0} \tag{4}$$

where P_{ext} is external pressure exerted on vessels and A_0 is the undeformed cross-sectional area when $P = P_{\mathrm{ext}}$. β describes arterial stiffness and is a function of A_0, wall thickness ($h = 0.945$ mm) (40), elastic modulus ($E = 1.41$ MPa) (41), and Poisson's ratio ($\nu = 0.5$) (42). The conservation of mass (Equation 2), conservation of momentum (Equation 3), and pressure-area constitutive relationship (Equation 4) were solved using a MacCormack finite difference scheme.

To model pressure drop across stenoses, we coupled the 1D model with an explicit pressure loss term:

$$\Delta P_s = \frac{\mu K_v}{2\pi r_u^3}Q + \frac{\rho K_t}{2A_u^2}\left(\frac{A_u}{A_s} - 1\right)^2|Q|Q + \frac{\rho K_u L_s}{A_u}\frac{\partial Q}{\partial t} \tag{5}$$

where ΔP_s is pressure drop across a focal stenosis, r_u is radius of an unstenosed artery, A_u is cross-sectional area of an unstenosed artery, A_s is cross-sectional area of a stenosed artery, and L_s is stenosis length. The stenosis model (**Equation 5**) was coupled to the 1D governing equations via the continuity of total pressure. The anatomical position of stenoses were labelled by expert interventional cardiologists. r_u was estimated from physician labeled stenosis degree and minimal luminal radius (r_s), using the following expression:

$$\text{Stenosis degree} = \left(1 - \frac{\mathrm{r_s}}{\mathrm{r_u}}\right) \times 100\% \tag{6}$$

A_s was parameterized using the minimal luminal diameter. K_v, K_t, and K_u are viscous, "turbulent," and inertial coefficients, respectively. The "turbulent" term reflects non-linear effects of converging or diverging flow patterns, for example swirling or chaotic flow downstream of the distal end of a stenosis. These coefficients were parameterized as

$K_v = 32(0.83L_s + 1.64D_s) \times (A_u/A_s)^2/D_u$, $K_t = 1.52$, and $K_u = 1.2$ based on (36). D_u and D_s are unstenosed and stenosed arterial diameters, respectively.

2.3.3. Personalized boundary conditions

To tune the boundary conditions to each patient, a pulsatile flow rate waveform was incorporated at the inlet and 2-element Windkessel models at the outlets (**Figure 1C**). Left and right coronary waveforms were derived from (43) and scaled to a patient-specific level using clinically measured cardiac output, heart rate, and flow dominance at resting state. Hyperemia was simulated by scaling up the flow rate based on empirical observations, where the left and right circulations were scaled up by 4*x* and 3*x*, respectively (44).

A 2-element Windkessel model, consisting of peripheral resistance (R_p) and compliance (C), was applied to the ends of each terminal vessel to account for the effect of microvascular hemodynamics (45):

$$Q = \frac{P}{R_p} + C\frac{dP}{dt} \tag{7}$$

C was assumed to be constant at $9\,\mathrm{cm^4\,s^2\,g^{-1}}$ based on patient averages from (36). R_p was distributed among the terminal branches using resistance-radius relationships commonly used for coronary simulations (4, 5, 14, 46):

$$R_i = P_{\mathrm{mean}} \cdot \frac{\sum_{j=1}^{N_{\mathrm{terminal}}} r_j^3}{Q_{\mathrm{ostial}} r_i^3} \tag{8}$$

where R_i is the peripheral resistance at each terminal branch, P_{mean} is mean arterial pressure, Q_{ostial} is flow rate at the ostium, r is the average terminal branch radius, and N_{terminal} is the number of terminal branches. Resting state mean arterial pressure and inlet flow rate were both obtained from clinical measurements and terminal branch radii were computed via 1D vessel centerlines. Specifically, the ostial flow rate was determined as a fraction of cardiac output via flow dominance (4, 5). Terminal resistances were scaled down by a factor of 0.22*x* (4, 5, 14, 44) from the resting state to estimate hyperemia.

2.3.4. Model convergence

Blood flow was simulated for 20 cardiac cycles based on temporal convergence tests, and the last cardiac cycle was used for analysis (**Figure 1D**). The grid spacing, or Euclidean distance between fluid points, was set to 500 micrometers based on grid invariance tests. The time step was 10^{-5} s to satisfy the Courant-Friedrichs-Lewy condition. The convergence criterion was L_2 error $<10^{-3}$ based on similar CFD studies (4, 5, 47–50). The metric of interest was time-averaged pressure at the distal location. Pressure at the distal location was selected because this was used to compute FFR. Temporal and spatial convergence data could be found in **Supplementary Figure S1 and Table S1**, respectively.

2.4. Defining the streamlined model for calculating fractional flow reserve

Understanding which clinical inputs could be relegated to patient averages was the first step to developing a streamlined computational FFR framework. We used global uncertainty analysis to elucidate which raw clinical measurements were critical to computing FFR accurately, as defined by a validated baseline model with all parameters derived from patient data, $\mathrm{FFR_{baseline}}$.

2.4.1. Mathematical basis of global uncertainty quantification

We employed variance-based global uncertainty quantification techniques as explained by Eck et al. (51). Global was selected over local uncertainty quantification to most uniformly sample the multi-dimensional parameter space and capture non-additive, non-monotonic, and non-linear effects and interactions between inputs (51). Global uncertainty quantification enabled assessment of the individual contribution of input parameters to the overall variance in FFR as well as the interaction between input parameters. Sobol indices were used to quantify the impact of clinical inputs on FFR:

$$S_i = \frac{\mathbb{V}[\mathbb{E}[\mathbb{Y}|\mathbb{Z}_i]]}{\mathbb{V}[\mathbb{Y}]} \tag{9}$$

$$S_{ij} = \frac{\mathbb{V}[\mathbb{E}[\mathbb{Y}|\mathbb{Z}_i, \mathbb{Z}_j]]}{\mathbb{V}[\mathbb{Y}]} \tag{10}$$

$$S_{Ti} = 1 - \frac{\mathbb{V}[\mathbb{E}[\mathbb{Y}|\mathbb{Z}_{-i}]]}{\mathbb{V}[\mathbb{Y}]} \tag{11}$$

where S_i captures the main effect of input parameter Z_i (neglecting interaction between inputs) to the total variance $\mathbb{V}[\mathbb{Y}]$, S_{ij} quantifies the effect of interaction between inputs Z_i and Z_j, and S_{Ti} quantifies the sum total of main and interaction effects. The $\mathbb{V}[\mathbb{E}[\mathbb{Y}|\mathbb{Z}_i]]$ term is the variance of the expected value of output Y given a fixed value of input parameter Z_i. Z_{-i} is a set of all input parameters excluding Z_i. When $S_i \approx S_{Ti}$, interaction effects are negligible, suggesting that main effects drove the variance in Y.

2.4.2. Parameterizing clinical inputs

Incorporating a complete set of inputs could be injudicious if many parameters do not significantly contribute to FFR, which would in effect only enlarge the sample space needlessly. The

raw inputs to define personalized blood flow simulations included mean arterial pressure, cardiac output, coronary geometry, heart rate, stenosis anatomy, hematocrit, and distal location. We considered stenosis anatomy separately from coronary geometry. Explicit pressure drop terms were required to accurately evaluate ischemic burden, and these terms were parameterized via stenosis geometry: stenosis length and stenosis radius at the minimum luminal diameter (30, 31). Cardiac output was used to parameterize the inlet flow rate waveform and peripheral resistance at the outlets. To prevent diluting the parameter space with insignificant parameters, the raw inputs were narrowed to mean arterial pressure, cardiac output, stenosis degree, and distal location based on what has been shown to be significant from prior works (27, 31). As inlet flow rate was found to be insignificant in the literature (27, 31, 52), we only evaluated cardiac output as it pertained to peripheral resistance and relegated cardiac output as it pertained to inlet flow rate as patient-generalized. The importance of distal location has been discussed in (53) and was also considered potentially significant. From this point forward, we define distal location as the anatomic location of pressure sampling distal to the stenosis. **Supplementary Figure S2** summarizes the raw inputs we investigated within the context of the CFD framework.

The uncertainty bounds, or range of allowed uncertainty, for each clinical input was either derived from literature or estimated from the patient population (**Table 1**). All uncertainty bounds in clinical inputs were modeled as normal distributions (51). Patient-specific cardiac output and mean arterial pressure were varied by multiplying with scaling factors, modeled as normal distributions with means of unity and standard deviations from literature-derived coefficients of variations (27, 54). The error bound in stenosis degree was modeled to reflect the worst-case inter-observer variability. The difference in stenosis degrees measured by an interventional cardiologist and a researcher, with measurements blinded to each other, was used to parameterize a normal distribution of uncertainty. The mean was fixed to zero to reflect the case when both observers agreed perfectly. The standard deviation directly quantified the error bound and was added to the baseline stenosis degree to probe uncertainty. For distal location, we estimated a coefficient of variation (CV = 0.117; see **Supplementary Figure S3**) and mean (30 mm) based on the patient population and clinical recommendations (55). The values sampled from the resulting normal distribution were used as the distal location to compute FFR in the global uncertainty analysis.

TABLE 1 Input parameter bounds to study the impact of patient-specificity on FFR.

Clinical input	Type	Distribution
Distal location (mm)	Value	$N(30.0, 3.5)$
Cardiac output (%)	Factor	$N(1, 0.153)$
Stenosis degree (%)	Addition	$N(0, 16.9)$
Mean arterial pressure (%)	Factor	$N(1, 0.056)$

Normal distributions denoted as $N(\mu, \sigma)$.

2.4.3. Evaluating the relative contribution of clinical inputs to fractional flow reserve

After defining the parameters and range of uncertainties to explore, we needed to perturb $FFR_{baseline}$ models to compute Sobol indices and evaluate the relative contribution to FFR. The normal distributions in **Table 1** were sampled according to a second order Saltelli sequence. This sampling technique has been shown to minimize error rates in estimating the Sobol indices (56, 57). Sobol indices were considered as converged when the bootstrapped 95% confidence interval width of the main and total effects were smaller than 10% of the maximum Sobol index for each parameter (58). FFR was computed for every combination of the four clinical inputs from the Saltelli sequence. Sobol indices were computed on the aggregate of all FFR values to relate the impact of uncertainty in clinical inputs to the resulting FFR value. Based on tests, over 1 million simulations were required to achieve converged Sobol indices. A high number of simulations were also noted by Eck et al. (51) to obtain convergence. We used an embarassingly parallel scheme to run multiple simulations simultaneously. The simulations were completed with wall clock duration of two weeks on 32 compute nodes. Sobol indices exceeding a threshold of 0.05 were considered significant (51).

2.4.4. Establishing and evaluating $FFR_{streamlined}$

The Sobol indices were used to identify which clinical inputs were most important and inform on streamlining the CFD framework. Patient-generalized values were used for parameters that had relatively little contribution to FFR. These values were computed by taking the average over the entire cohort of patients to be used as inputs in the streamlined model. One parameter that could be patient-generalized from the get-go was inlet flow rate waveform. As prior studies (27, 31, 52) demonstrated that the inlet flow rate waveform contributed minimally to FFR, two canonical hyperemic waveforms were created (**Figure 2**), one for the left coronary artery (LCA) and one for the right coronary artery (RCA).

After identifying all the patient-generalized parameters via global uncertainty quantification, the streamlined model was compared to the baseline framework and clinical ground-truths. Correlation between streamlined models ($FFR_{semi-streamlined}$ and $FFR_{streamlined}$) with $FFR_{baseline}$ and $FFR_{invasive}$ was determined using a least-squares linear regression. Bland-Altman analysis was used to evaluate the mean differences between streamlined models with $FFR_{baseline}$ and $FFR_{invasive}$. We also evaluated ability of streamlined models to classify ischemic vs. non-ischemic stenoses

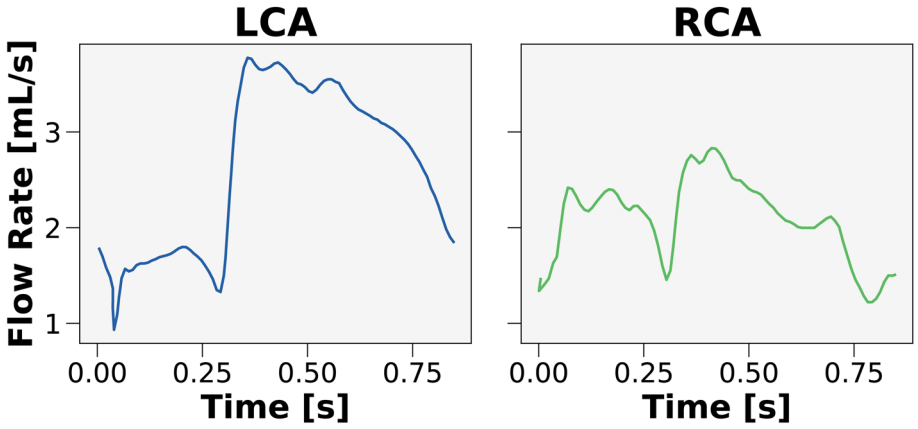

FIGURE 2
Canonical waveforms for the left and right coronary circulation. Hyperemic pulsatile flow rate waveforms were used as inputs to the streamlined model for the left (LCA) and right (RCA) coronary arteries. The waveforms were generalized over the 50 patients in the cohort.

identified by $FFR_{invasive}$, using metrics such as sensitivity, specificity, positive predictive value, negative predictive value, and overall accuracy. Finally, receiver-operating characteristics (ROC) curves were used to compute an area under the curve (AUC) and to recover the 0.80 ischemic threshold to evaluate bias. An unbiased model would recover the 0.80 threshold and trade-off the true positive and false positive rate. The optimum threshold from an ROC curve was taken as the point that maximizes sensitivity (or true positive rate) and minimizes 1-specificity (or false positive rate).

2.4.5. Determining if relative contribution is generalizable across patients

As a secondary endpoint to this work, we evaluated whether Sobol indices varied across patients. Previous works have conventionally aggregated the Sobol indices over all patients in the cohort, but the relative importance of each input parameter to FFR may not generalize across differing patient anatomy and physiology (11, 27, 31). To this end, we performed a global repeated measures analysis of variance (ANOVA), where anatomic and hemodynamic variations subdivided the Sobol indices. Specifically, anatomy was subdivided by LCA and RCA. We considered two hemodynamic variations. Ischemia-inducing disease was considered at the clinical threshold of 0.80. Patients were stratified using this classification to probe how the impact of patient-specificity could differ between functionally significant and insignificant stenoses. As a positive control, we also incorporated the grey-zone FFR—a range of FFR values, between 0.75–0.85, traditionally known to be of uncertain ischemic burden (59). Subdividing by grey-zone provided a baseline variance to compare with coronary vessel and ischemia classification subgroups. Successive factorial ANOVAs were performed to reveal the most important subdivisions in the parameter space using variance.

2.5. Statistical analysis

The Kolmogorov-Smirnov test was used to ensure that the data followed the central limit theorem. Predicted FFR was evaluated against the clinical ground-truth via least-squares correlation and Bland-Altman analysis. ANOVA and post hoc tests were performed on JMP Pro 16 (JMP Statistical Discovery LLC, Cary, NC, USA). Diagnostic performance metrics between models were compared using paired t-test or Wilcoxon signed-rank test. A value of $p < 0.05$ was considered significant.

3. Results

3.1. Patient and clinical characteristics

A retrospective cohort of 50 patients was created from adults with angiographically documented coronary artery disease, involving at least one vessel with $FFR_{invasive}$ measurement between January 1, 2016 and August 1, 2018. Patient characteristics are highlighted in **Table 2**. A total of 69.4% of patients were male. The mean age was 66.5 years. 2.0% had hypertension, 8.2% had hypercholesterolemia, and 32.7% had diabetes mellitus. The mean left ventricular ejection fraction was 58.2%. The most common medications at the time of cardiac catheterization were lipid lowering agents (93.9%), aspirin (87.8%), and ACEi/ARB (59.2%). Stenosis characteristics are presented in **Table 3**. 79.6% of stenoses were right dominant, 12.2% were left dominant, and

TABLE 2 Aggregated characteristics of patients ($N = 50$).

Age (years)	66.5 ± 9.5
Female (%)	30.6
Hypertension (%)	2.0
Hypercholesterolemia (%)	8.2
Diabetes mellitus (%)	
Type I	8.2
Type II	24.5
Tobacco use (%)	
Current	4.1
Former	36.7
Never	59.2
Prior MI (%)	44.9
Prior PCI (%)	46.9
Prior CABG (%)	0.0
Congestive heart failure (%)	34.7
Peripheral arterial disease (%)	26.5
Chronic kidney disease (%)	28.6
Weight (kg)	87.8 ± 20.6
Systolic blood pressure* (mmHg)	125.8 ± 25.8
Diastolic blood pressure* (mmHg)	67.1 ± 12.7
Heart rate* (bpm)	70.8 ± 13.7
Cardiac output* (L/min)	4.5 ± 1.5
Left ventricular ejection fraction (%)	58.2 ± 10.8
Medications (%)	
Aspirin	87.8
P2Y12 inhibitors	38.8
Anticoagulants	26.5
Lipid lowering agents	93.9
ACEi/ARB	59.2
Nitrates	20.4

Values are mean ± SD or *n* (%). *Values are in resting state conditions. MI, myocardial infarction; PCI, percutaneous coronary intervention; CABG, coronary artery bypass graft.

TABLE 3 Aggregated characteristics of vessels ($N = 50$).

Vessel dominance (%)	
Right	79.6
Left	12.2
Co-dominant	8.2
SYNTAX score (%)	
Low	2.0
Medium	12.2
High	85.7
Invasive FFR vessel (%)	
LAD	53.1
LCx	20.4
RCA	26.5
Minimal luminal diameter (mm)	1.4 ± 0.4
Minimal luminal area (mm^2)	1.7 ± 0.9
Stenosis degree (%)	55.6 ± 17.2
Plaque Eccentricity (%)	
Concentric	65.3
Eccentric	34.7
Calcified (%)	44.9
Tortuous (%)	10.2
Thrombus (%)	8.2
Aneurysm (%)	2.0

Values are mean ± SD or *n* (%). Invasive FFR, fractional flow reserve; LAD, left anterior descending artery; LCx, left circumflex artery; RCA, right coronary artery.

8.2% were co-dominant circulations. The mean stenosis degree was 55.6%. Stenosis that underwent intervention were found in the left anterior descending artery (53.1%), left circumflex artery (20.4%), and right coronary artery (26.5%). The majority of stenoses were concentric (65.3%).

3.2. Patient-specific 1D coronary models agree with clinical measurements

The first step in developing a streamlined framework was to validate a baseline CFD framework with full patient-tuned inputs—representing the best-case scenario. The baseline framework, $FFR_{baseline}$, was validated in 50 patients who had angiographically documented coronary artery disease. We validated $FFR_{baseline}$ against $FFR_{invasive}$. The correlation coefficient was 0.71 ($p < 0.0001$) and the mean difference was 0.01 ± 0.09 (Figure 3). Diagnostic performance of $FFR_{baseline}$ to discern ischemic stenoses are summarized in Table 5. The sensitivity was 89.5% (95% CI: 66.9–98.7%), specificity was 93.6% (95% CI: 78.6–99.2%), and overall accuracy was 92.0% (95% CI: 80.8–97.8%). Furthermore, the positive predictive value was 89.5% (95% CI: 68.8–97.0%) and the negative predictive value was 93.6% (95% CI: 79.6–98.2%).

3.3. Cardiac output and stenosis degree contributed most to fractional flow reserve

When aggregating all 50 patients, the uncertainty analysis (Figure 4) indicated that cardiac output and stenosis degree contributed most to the variance in FFR. Distal location and mean arterial pressure also exceeded the threshold for sensitivity, but contributed less to the variance in FFR than cardiac output and stenosis degree. While distal location exceeded the threshold for significance, Sobol indices are relative metrics and the effect sizes of cardiac output and stenosis degree exceeded distal location. To minimize the number of parameters, we created two streamlined models. $FFR_{semi-streamlined}$ incorporated patient-generalized mean

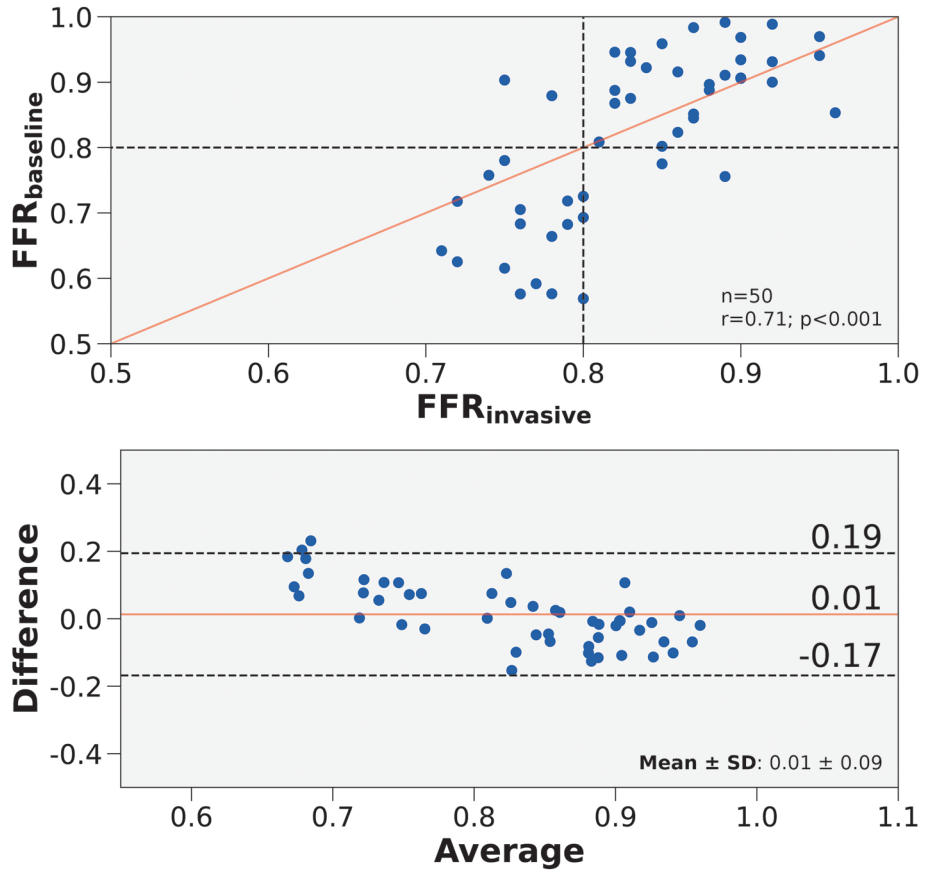

FIGURE 3
Correlation and agreement of $FFR_{baseline}$ compared to $FFR_{invasive}$. (Top) Scatter plot of $FFR_{baseline}$ and $FFR_{invasive}$ for 50 vessels. The number of stenoses and Pearson's *r* are presented in the lower right hand corner. Interrupted lines represent the 0.80 ischemic threshold and the solid red line represents ideal correlation. (Bottom) Bland-Altman plot displaying the mean difference between $FFR_{baseline}$ and $FFR_{invasive}$ for 50 vessels. The mean difference and standard deviation are presented in the lower right corner. Black interrupted lines indicate the upper and lower limits of agreement (σ: ± 1.96) and the solid red line indicates mean difference.

arterial pressure, and patient-specific cardiac output, stenosis degree, and distal location. $FFR_{streamlined}$ used patient-generalized distal location and mean arterial pressure, and patient-specific cardiac output and stenosis degree. The total and main effects were not statistically different, which meant that interaction effects between input parameters were insignificant.

3.4. Streamlined models maintain diagnostic performance

To test our findings from the aggregated Sobol indices, we parameterized the streamlined models with patient-generalized mean arterial pressure (87.3 mmHg), heart rate (70.8 bpm), hematocrit (39.2%), and ostial diameter (3.9 mm) (Table 4). With an average hematocrit of 39.2%, the average dynamic viscosity was 1.97 cP, which was comparable to viscosities used in other works at hyperemic state (4, 5). Patient-generalized cardiac output (4.5 L/min) was used to derive inlet flow waveforms, but patient-specific cardiac output was used to compute peripheral resistance. A patient-generalized distal location of 30 mm was used for $FFR_{semi-streamlined}$.

$FFR_{semi-streamlined}$ compared well against $FFR_{baseline}$ in terms of correlation ($r = 0.96$, $p < 0.001$) and agreement (mean difference $= 0.00 \pm 0.04$) (Figure 5A). Compared to $FFR_{baseline}$ vs. $FFR_{invasive}$, $FFR_{semi-streamlined}$ vs. $FFR_{invasive}$ had slightly improved correlation ($r = 0.75$, $p < 0.001$) and agreement (mean difference $= 0.01 \pm 0.08$) (Figure 5B). $FFR_{streamlined}$ compared well against $FFR_{baseline}$ in terms of correlation ($r = 0.84$, $p < 0.001$) and agreement (mean difference $= 0.01 \pm 0.07$) (Figure 5C). Compared to $FFR_{baseline}$ vs. $FFR_{invasive}$, $FFR_{streamlined}$ vs. $FFR_{invasive}$ had a decrease in correlation ($r = 0.64$, $p < 0.001$) but a slight improvement in agreement (mean difference $= 0.01 \pm 0.08$)

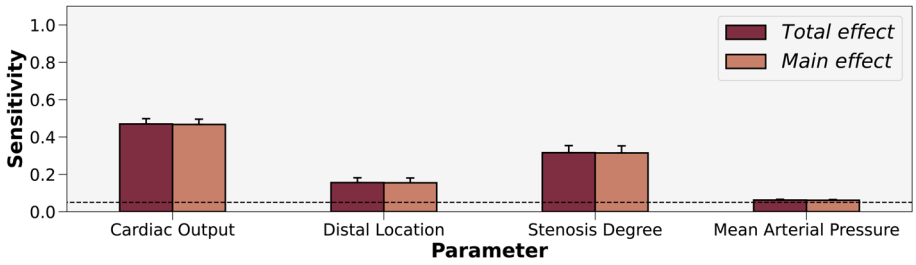

FIGURE 4
Sobol sensitivity indices of patient-tuned parameters on FFR. Total and main effects are displayed for cardiac output, distal location, stenosis degree, and mean arterial pressure. Cardiac output and stenosis degree contribute most to the variance in FFR. The horizontal interrupted line at 0.05 shows the threshold for sensitivity.

TABLE 4 Patient-generalized clinical inputs.

Mean arterial pressure (mmHg)	87.3
Heart rate (bpm)	70.8
Cardiac output (L/min)	4.5
Hematocrit (%)	39.2
Ostial diameter (mm)	3.9

Clinical inputs were averaged over 50 patients and used to parameterize the streamlined model. Mean arterial pressure, heart rate, and cardiac output are in resting state conditions. Cardiac output was patient-generalized only as it pertained to inlet flow rate. Ostial diameter was obtained through coronary geometry reconstruction.

TABLE 5 Diagnostic performance of $FFR_{streamlined}$, $FFR_{semi-streamlined}$, and $FFR_{baseline}$ to detect ischemic stenoses at the clinical threshold of 0.80.

Metric	$FFR_{streamlined}$	$FFR_{semi-streamlined}$	$FFR_{baseline}$
Sensitivity	79.0 (54.4–94.0)	89.5 (66.9–98.7)	89.5 (66.9–98.7)
Specificity	90.3 (74.3–98.0)	93.6 (78.6–99.2)	93.6 (78.6–99.2)
PPV	83.3 (62.5–93.8)	89.5 (68.8–97.0)	89.5 (68.8–97.0)
NPV	87.5 (74.4–94.4)	93.6 (79.6–98.2)	93.6 (79.6–98.2)
Overall accuracy	86.0 (73.3–94.2)	92.0 (80.8–97.8)	92.0 (80.8–97.8)

(Figure 5D). The average percentage discrepancy compared to $FFR_{baseline}$ was 3.3% for $FFR_{semi-streamlined}$ and 5.7% for $FFR_{streamlined}$.

In terms of diagnostic performance to identify ischemic stenoses, the sensitivity was 89.5% (95% CI: 66.9–98.7%), specificity was 93.6% (95% CI: 78.6–99.2%), and overall accuracy was 92.0% (95% CI: 80.8–97.8%) for $FFR_{semi-streamlined}$, which was identical to $FFR_{baseline}$. As for $FFR_{streamlined}$, the sensitivity was 79.0% (95% CI: 54.4–94.0%), specificity was 90.3% (95% CI: 74.3–98.0%), and overall accuracy was 86.0% (95% CI: 73.3–94.2%). To compare between the models (Table 5), we applied paired Wilcoxon signed-ranked tests with Holm-Bonferroni correction. The diagnostic metrics were not statistically significant for $FFR_{streamlined}$ vs. $FFR_{baseline}$ ($p = 0.125$) and the diagnostic metrics were identical between $FFR_{semi-streamlined}$ vs. $FFR_{baseline}$. We further validated the streamlined models by evaluating AUC and recovering the ischemic threshold (Figure 6). The idealized case, $FFR_{baseline}$, had an AUC of 0.95, and the ischemic threshold was recovered to be 0.79–0.80. $FFR_{semi-streamlined}$ had an AUC of 0.96 and the ischemic threshold ranged between 0.79–0.81. $FFR_{streamlined}$ had an AUC of 0.90 and the ischemic threshold ranged between 0.78–0.80.

3.5. Relative contribution of clinical inputs influenced by anatomy

As a secondary endpoint, we also evaluated whether Sobol indices could be generalized across patients. Using global ANOVA, grey-zone ($p = 0.0356$), anatomy ($p = 0.0357$), and the repeated measures of the Sobol indices ($p < 0.0001$) were statistically significant main effects (Supplementary Table S2). The interaction effect of the repeated measures with anatomy ($p = 0.0293$) was significant. Since the repeated measures captured most of the effect size and contributed to the significant interaction effect, we subdivided the clinical inputs and performed a factorial ANOVA. Distal location was found to have no significant effects (Supplementary Table S3). Anatomy had a significant main effect for cardiac output ($p = 0.0279$) (Supplementary Table S4), stenosis degree ($p = 0.0025$) (Supplementary Table S5), and mean arterial pressure ($p = 0.0266$) (Supplementary Table S6). Since the contribution of mean arterial pressure to FFR was the least in the aggregated global uncertainty quantification results (Figure 4), we focused on elucidating how cardiac output and stenosis degree varied by anatomy via post hoc analysis.

Through two-tailed t-tests (Figure 7A), the impact of patient-specificity differed between LCA and RCA for cardiac output and stenosis degree. Specifically, uncertainty in cardiac output had a larger effect on the LCA than RCA ($p < 0.05$), and uncertainty in stenosis degree had a larger effect on the

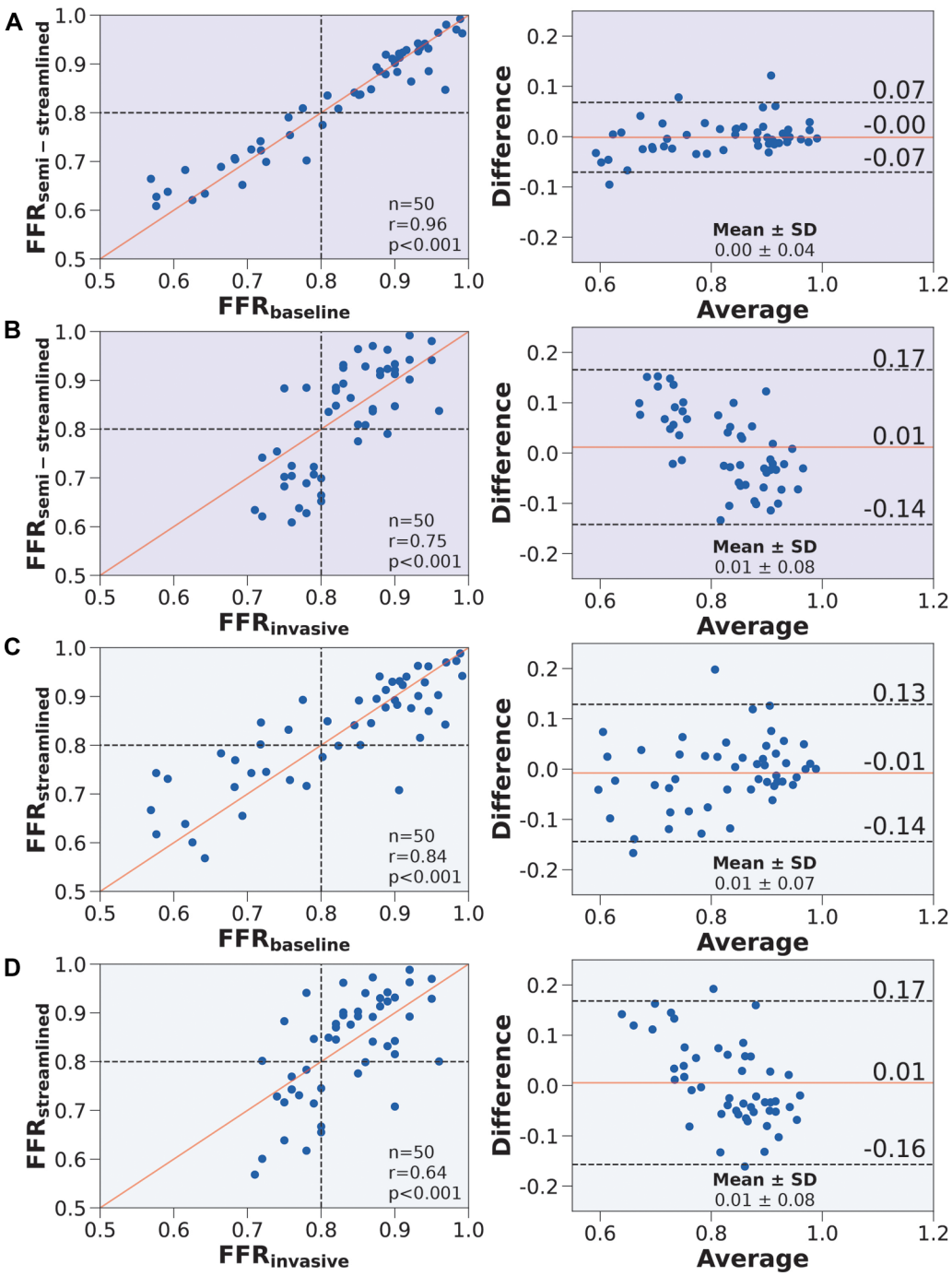

FIGURE 5
Correlation and agreement comparing $FFR_{semi-streamlined}$, $FFR_{streamlined}$, $FFR_{baseline}$, and $FFR_{invasive}$. (Left) Scatter plots. The number of stenoses and Pearson's *r* are presented in the lower right hand corner. Interrupted lines represent the 0.80 ischemic threshold and the solid red line represents ideal correlation. (Right) Bland-Altman plots. The mean difference and standard deviation are presented in the lower right corner. Black interrupted lines indicate the upper and lower limits of agreement (σ: ± 1.96) and the solid red line indicates mean difference. We compared (A) $FFR_{semi-streamlined}$ to $FFR_{baseline}$, (B) $FFR_{semi-streamlined}$ to $FFR_{invasive}$, (C) $FFR_{streamlined}$ to $FFR_{baseline}$, and (D) $FFR_{streamlined}$ to $FFR_{invasive}$.

RCA than LCA ($p < 0.001$). However, examining variances are relative metrics, and demonstrating statistically significant differences in total effects may not translate to crossing the ischemic threshold or motivating a different treatment strategy. To test if the impact of patient-specificity in cardiac output and stenosis degree could change treatment strategy,

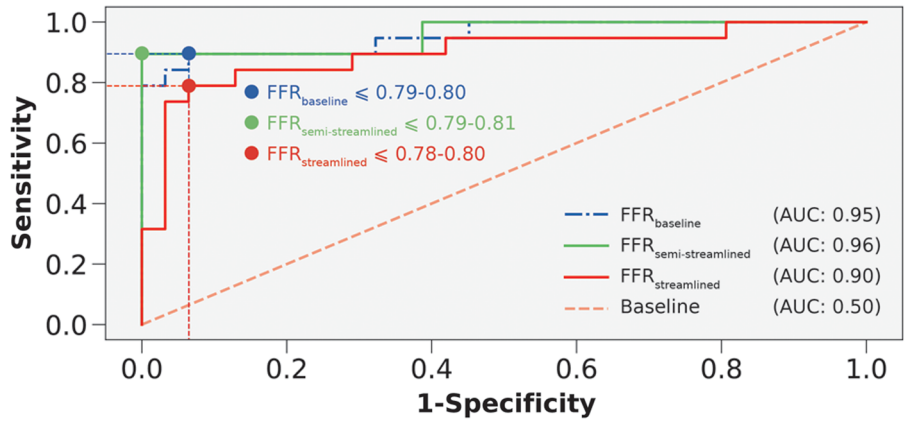

FIGURE 6
Receiver-operating characteristics curves to compare $FFR_{semi-streamlined}$, $FFR_{streamlined}$, and $FFR_{baseline}$. AUC is area under the curve. Interrupted vertical and horizontal lines indicate the sensitivity and 1-specificity values that correspond to the optimum threshold. Blue, green, and red colored circles represent the threshold overlaid on the receiver-operating characteristics curves.

we re-sampled the normal distributions of cardiac output and stenosis degree simultaneously while restricting distal location and mean arterial pressure to their patient-specific baselines. To quantify variability in FFR, we computed an average within-patient range of FFR values across the population as a function of increasing error. Since uncertainty was modeled using normal distribution, we re-sampled the normal distributions with increasing standard deviations. The results indicated that the average range of FFR values was slightly higher in the RCA than LCA across all standard deviations (Figure 7B). We examined the proportion of the cohort that was reclassified due to uncertainty. The reclassification proportion (RP) also increased with increasing standard deviation, but demonstrated that the RCA was more sensitive to reclassification than the LCA at all standard deviation levels (Figure 7B). Both FFR range and RP curves plateaued after one standard deviation. At one standard deviation, 50% of cases were reclassified in the RCA and 25% of cases were reclassified in the LCA (Figure 7C). The patients that were reclassified were more sensitive to uncertainty and the patients that were never reclassified were less sensitive to uncertainty. In short, cardiac output and stenosis degree needed to be patient-tuned, and the impact of uncertainty could have differing effects between anatomies and patients.

4. Discussion

This study demonstrates the potential for CFD frameworks with minimal patient-tuned inputs to match the accuracy and diagnostic performance of frameworks with a full gamut of patient-tuned parameters, which is important because obtaining patient-specific parameters for CFD simulations is difficult and not always possible. Through global uncertainty analyses, we not only identified that stenosis degree and cardiac output (when used to parameterize peripheral resistance) were required on a per-patient level, in addition to accurately reconstructing coronary trees, but also demonstrated the validity of the findings by creating streamlined models to compare with baseline and clinical ground-truths. $FFR_{semi-streamlined}$ had nearly-identical results with the $FFR_{baseline}$ and $FFR_{streamlined}$ was comparable in accuracy and diagnostic performance to the $FFR_{baseline}$. Furthermore, the impact of uncertainty on stenosis degree and cardiac output was shown to cause reclassification in some patients, and the impact of uncertainty had a larger effect on the RCA than LCA for stenosis degree and on the LCA than RCA for cardiac output. These results could help increase the reach and translatability of CFD frameworks for cases with missing data and scenarios when clinical data collection could be challenging.

4.1. $FFR_{baseline}$ compares well to categorical and continuous $FFR_{invasive}$

To create a low cost CFD framework, it was important to first demonstrate an accurate baseline high cost model compared to clinical measurements. This work used a cohort of 50 patients with a representative disease prevalence of 38% that is comparable to other studies (16, 17), and the baseline 1D FFR framework was validated against clinical ground-truths. $FFR_{baseline}$ had generally superior diagnostic performance and comparable correlation and agreement compared to computed tomography-based models (13, 60), albeit on a much smaller sample of patients. On a per-study

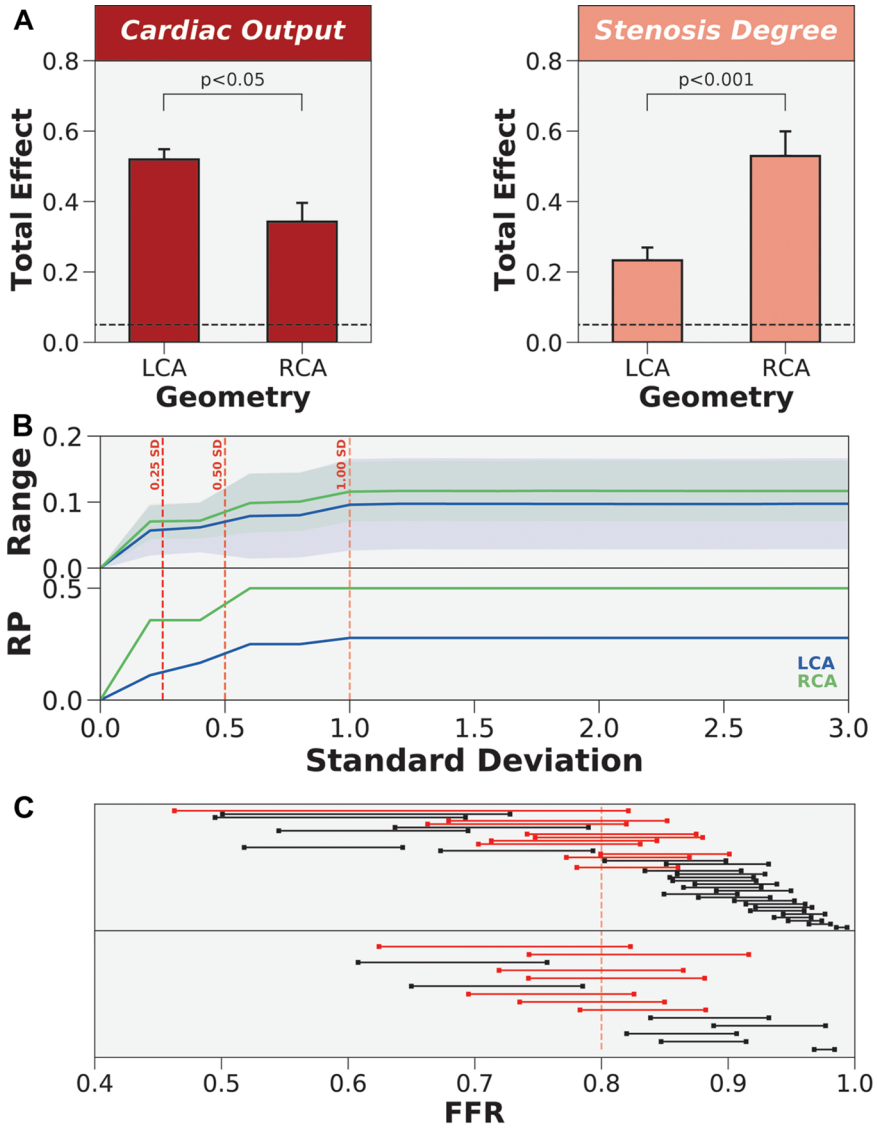

FIGURE 7
The differing impact of patient-specificity in cardiac output and stenosis degree between anatomies. (A) Coronary anatomy had differing effects on cardiac output and stenosis degree. LCA is left coronary artery and RCA is right coronary artery. (B) Re-sampling the global parameter space to estimate FFR range and reclassification proportion (RP) when only varying cardiac output and stenosis degree. Normal distributions of uncertainty were re-sampled at increasing levels of standard deviation (SD). (C) Dumbbell plot showing the range of FFR values when re-sampling to include 1 standard deviation of the variability in cardiac output and stenosis degree. Red dumbbells indicate re-classified cases and black dumbbells indicate cases without re-classification.

basis, $FFR_{baseline}$ had comparable mean differences and diagnostic performance compared to other 3D or 0D coronary angiography-based models (8, 19, 20, 61–68). The studies that validate angiography-based 1D FFR is generally less than 0D or 3D models. Of note, Mohee et al. (69) validated a coronary angiography-based 1D model against invasive FFR. $FFR_{baseline}$ had better correlation and diagnostic performance. Other global uncertainty analysis studies have generally validated their models with smaller patient cohorts and use 3D models as ground-truth. Fossan et al. (27) validated their 1D model of FFR in 13 patients with 24 stenoses, but used 3D FFR models as ground-truth. Morris et al. (11) validated a pseudotransient model in 20 patients against full transient 3D CFD models. There were also studies focusing on idealized or few patient-specific geometries (26, 28, 51). In contrast, the high cost, patient-tuned, 1D model had high diagnostic performance (sensitivity = 89.5%, specificity = 93.6%) compared to clinical measurements of FFR and provided a robust baseline of models to investigate patient-specificity.

4.2. Streamlining clinical inputs maintain comparatively high diagnostic performance

To develop streamlined models, we explored how the variance contribution of clinical inputs impacted FFR. We found that cardiac output, stenosis degree, and distal location crossed the 0.05 threshold for sensitivity, and mean arterial pressure narrowly crossed the threshold. The effect size for cardiac output and stenosis degree far exceeded that of distal location. Based on the global uncertainty quantification results, we created streamlined models using only personalized values for coronary anatomy (including stenosis anatomy) and cardiac output for $FFR_{streamlined}$ and additionally with patient-specific distal location for $FFR_{semi-streamlined}$.

The semi-streamlined model had identical diagnostic performance with the baseline and slightly better accuracy and mean difference. The streamlined model maintained high diagnostic performance (sensitivity = 79.0%, specificity = 90.3%) while introducing minimal bias as compared to the baseline model (mean difference = 0.01 ± 0.07) and clinical measurements (mean difference = 0.01 ± 0.08). We also successfully recovered the ischemic threshold using ROC curves and demonstrated minimal bias for all three models. The semi-streamlined model had nearly identical AUC with the baseline model. This finding indicated that it was possible to use a streamlined set of inputs, and nearly identical performance could be maintained if there was a patient-specific distal location. The streamlined model had slightly lower AUC and represents a worst-case scenario, where a relatively high diagnostic performance could still be maintained without a clinically-indicated distal location.

In the streamlined framework, only two waveforms were used for the entire population, one for the LCA and one for the RCA. This indicated that patient-derived waveforms may not be needed. A common ostial diameter was used to convert coronary flow velocity to flow rates, which suggested that coronary anatomy did not matter at the inlet but mattered in terminal branches when controlling flow distribution around the coronary tree. As $FFR_{semi-streamlined}$ almost perfectly matched $FFR_{baseline}$, mean arterial pressure, heart rate, and hematocrit did not tangibly influence FFR. The discrepancy in performance between $FFR_{semi-streamlined}$ and $FFR_{streamlined}$ could be solely attributed to distal location. While a relatively high diagnostic performance was maintained with $FFR_{streamlined}$, the non-negligible influence of distal location on FFR was observed here and was also consistent with the global uncertainty analysis results.

We demonstrated that peripheral resistance and stenosis anatomy contributed most to the variance in FFR, and that peripheral resistance had the largest variance contribution. These results are consistent with current literature (11, 27–29) that also investigated the contribution of input parameters to FFR using global uncertainty quantification. In this study, we further identified cardiac output as the input that contributed most to peripheral resistance. We used a patient-generalized mean arterial pressure to determine peripheral resistances, which demonstrated that cardiac output was more important than mean arterial pressure in distributing flow down the coronary tree. Ultimately, the framework has the flexibility to accept a full set of patient-tuned inputs, representing the best-case scenario, but could also simulate cases with missing data using the streamlined models without compromising much diagnostic performance.

4.3. Impact of geometry reconstruction and cardiac output differ by coronary vessel

Coronary arteries can widely vary in anatomy and physiology (70–72), especially in diseased cases where there could be disturbed blood flow dynamics. Existing sensitivity analysis and uncertainty quantification studies assume generalizability (11, 27). We further investigated the impact of uncertainty across anatomy (LCA vs. RCA) and physiology (ischemic vs. non-ischemic identified by $FFR_{invasive}$, grey-zone vs. non-grey-zone). The grey-zone is a known cluster of FFR values where there is uncertainty on how to treat patients (59, 73). Global repeated measures ANOVA identified that the main effect of anatomy was significant and had the same effect size as grey-zone. From a variance perspective, the results indicated that the difference between grey-zone and non-grey-zone cases was comparable to the difference between LCA and RCA. Therefore, the impact of uncertainty was not generalizable across coronary geometry. There was also a significant interaction effect between anatomy and the repeated measure of total effects in clinical inputs. We first subdivided the repeated measures and found that cardiac output and stenosis degree had significant main effects, which highlighted that the impact of uncertainty was not generalizable in these clinical inputs. Conversely, distal location had no statistically significant main or interaction effects. To characterize how the impact of uncertainty varied in the LCA and RCA, we performed post hoc analyses and discovered that uncertainty in cardiac output had a larger effect on the LCA than RCA and uncertainty in stenosis degree had a larger effect on the RCA than LCA. The impact of error on FFR was not only different across anatomy, but how the effect differed also varied between clinical inputs. As total effects are relative, we also re-sampled the global parameter space to examine whether the uncertainty could cause reclassification and warrant a different treatment strategy. The parameter space was re-sampled incrementally, from the baseline inputs to 3 standard deviations of the error parameter space. These results demonstrated that the

magnitude of error in cardiac output and stenosis degree was sufficient to reclassify a considerable proportion of the population. Measuring accurate clinical inputs should be prioritized on a coronary anatomy-specific level. Hence, accurate anatomic reconstruction and measurement of cardiac output were important in accurately computing FFR.

4.4. Clinical translatability of streamlined 1D models

It is important to consider whether the pathway to clinical translation is feasible. While models such as FFR_{angio} (CathWorks, Kfar-saba, Israel) (15–17) have already paved the way for clinical translation, these state-of-the-art frameworks rely on a full gamut of patient-specific inputs for accurate FFR assessment. This work indicated that a few clinical parameters were needed, namely cardiac output and stenosis degree at the minimum, to maintain diagnostic performance as compared to the invasive gold-standard. Clinical measurements such as mean arterial pressure, heart rate, and hematocrit could be omitted. This finding could be useful in the event of missing data, which is a pervasive issue seen intra- and inter-clinic (23–25). Streamlining the clinical measurement process expands the utility of currently available techniques and may reduce the barrier for clinical translation. Further, the streamlined models have several advantages over other 1D models currently undergoing the process for clinical translation. The average computation time for the 1D framework was 10.1 ± 4.7 min. Our calculation time was more than twice as fast as other 1D models, such as 23.9 ± 11.2 min with Siemens cFFR (74) and 27.1 ± 7.5 min with Toshiba CT-FFR (75). Both streamlined models also had superior diagnostic performance, correlation, and mean differences compared to the Siemens and Toshiba 1D models (75, 76). Accurate geometry segmentation was shown to be an important factor, and is typically a bottleneck even for 1D simulations (77). Applying our semi-automated algorithm, accurate coronary reconstructions were completed within 10 min (32, 78). The streamlined framework contributes to clinical translatability by identifying the measurements that could be patient-generalized and those that need to be patient-specific for accurate FFR computation.

4.5. Limitations

Regarding limitations, the patient population was retrospective and from a single center. A prospective study from multiple centers would provide a more robust validation, but the point of this work was to develop an optimized model from a fully patient-specific model, and validating with clinically measured FFR demonstrated that both models were accurate. Second, the correlation between $FFR_{baseline}$ and $FFR_{invasive}$ was moderate. There are multiple ways to validate $FFR_{baseline}$ against the clinical ground-truth. FFR is fundamentally a dichotomous metric used to refer patients to percutaneous coronary intervention ($FFR \leq 0.80$) or optimal medical therapy ($FFR > 0.80$). In this work, we validated both continuous and categorical FFR. While the Bland-Altman mean differences indicated negligible bias, the correlation was moderate. $FFR_{baseline}$ was comparable to other studies in the literature. The vast majority of 1D FFR models validate against 3D models (27, 29, 52, 79–81). Compared to studies that also validated with invasive FFR (75, 76, 82), $FFR_{baseline}$ had generally higher correlation. Categorical FFR was validated using diagnostic performance metrics (i.e., sensitivity, specificity, positive predictive value, negative predictive value, accuracy, AUC) and exceeded 90% for nearly all metrics. Third, the effect of adenosine was considered generalizable across the cohort. Lo et al. (83) recently compared patient-specific outflow conditions based on myocardial perfusion from positron emission tomography data to the conventional scaling method. They found that the effect of adenosine could be overestimated and result in overestimating FFR severity. The $FFR_{baseline}$ vs. $FFR_{invasive}$ slope exceeded unity, which could indicate that our model overestimated hyperemia because of using scaling laws. This could be rectified in future works by acquiring myocardial perfusion data and tuning hyperemia on a per-patient level (83, 84). Fourth, the factorial study subdividing patient-specificity by anatomic and hemodynamic classes was limited. Although we explored coronary anatomy, ischemic vs. non-ischemic stenoses, and grey-zone cases, the study could have also explored differing effects of patient-specificity on factors such as age, sex, and the presence of co-morbidities. A larger cohort would be required to expand on the number of factors investigated. We also primarily focused on focal lesions. Including complex coronary disease, such as ostial and bifurcation stenoses, would require separate sensitivity studies as we expect hemodynamics to differ from focal stenoses. For example, ostial stenoses may have an impact on inlet coronary waveforms and bifurcation stenoses may increase the importance of segmenting accurate stenoses.

4.6. Conclusion

In this study, we developed two streamlined models with minimal clinical inputs that could compute FFR accurately. This work demonstrated that patient-generalized parameters could be used to accurately recover diagnostic phenomarkers and that the impact of error was not generalizable across varying anatomy and physiology. We presented a flexible framework that could enable cases with missing data to be simulated accurately. Additionally, the proposed framework

could help improve the translatability and use of CFD models to guide interventional planning.

Data availability statement

The raw data supporting the conclusions of this article will be made available by the authors, without undue reservation.

Ethics statement

The studies involving human participants were reviewed and approved by Massachusetts General Brigham Institutional Review Board. Written informed consent for participation was not required for this study in accordance with the national legislation and the institutional requirements.

Author contributions

CT and AR: conception and design of the study. SJC and JL: acquisition and compilation of clinical data. SJC: 3D coronary arterial tree reconstruction. CT: computer simulations and statistical analyses. CT and AR: initial drafting of the manuscript. All authors contributed to the article and approved the submitted version.

Funding

This work was supported by the Coulter Foundation (SJC, JL, AR); NSF GRFP under Grant No. DGE 164486 (CT); American Heart Association AIM 19AIML34980000, NHLBI U01 HL125215 (JL); and NSF 1943036 and NIH U01CA253511 (AR). The content does not necessarily represent the official views of the NIH or NSF. The content is solely the responsibility of the authors and does not necessarily represent the official views of the AHA, NIH, or the NSF.

Acknowledgments

We thank Simbarashe Chidyagwai, Christopher W. Jensen, and Sayan Roychowdhury for fruitful discussions. In addition, we acknowledge Dr. Madhurima Vardhan and Dr. Bradley Feiger for helpful technical discussions. Lastly, we appreciate Duke OIT for computing support.

Conflict of interest

The authors declare that the research was conducted in the absence of any commercial or financial relationships that could be construed as a potential conflict of interest.

Publisher's note

All claims expressed in this article are solely those of the authors and do not necessarily represent those of their affiliated organizations, or those of the publisher, the editors and the reviewers. Any product that may be evaluated in this article, or claim that may be made by its manufacturer, is not guaranteed or endorsed by the publisher.

Supplementary material

The Supplementary Material for this article can be found online at: https://www.frontiersin.org/articles/10.3389/fmedt.2022.1034801/full#supplementary-material.

References

1. Ralapanawa U, Sivakanesan R. Epidemiology, the magnitude of coronary artery disease, acute coronary syndrome: a narrative review. *J Epidemiol Glob Health*. (2021) 11:169–77. doi: 10.2991/jegh.k.201217.001

2. Tonino PA, De Bruyne B, Pijls NH, Siebert U, Ikeno F, vant Veer M, et al. Fractional flow reserve versus angiography for guiding percutaneous coronary intervention. *N Engl J Med*. (2009) 360:213–24. doi: 10.1056/NEJMoa0807611

3. De Bruyne B, Pijls NH, Kalesan B, Barbato E, Tonino PA, Piroth Z, et al. Fractional flow reserve–guided PCI versus medical therapy in stable coronary disease. *N Engl J Med*. (2012) 367:991–1001. doi: 10.1056/NEJMoa1205361

4. Vardhan M, Gounley J, Chen SJ, Kahn AM, Leopold JA, Randles A. The importance of side branches in modeling 3D hemodynamics from angiograms for patients with coronary artery disease. *Sci Rep*. (2019) 9:1–10. doi: 10.1038/s41598-019-45342-5

5. Vardhan M, Gounley J, Chen SJ, Chi EC, Kahn AM, Leopold JA, et al. Non-invasive characterization of complex coronary lesions. *Sci Rep*. (2021) 11:1–15. doi: 10.1038/s41598-021-86360-6

6. Giannopoulos AA, Tang A, Ge Y, Cheezum MK, Steigner ML, Fujimoto S, et al. Diagnostic performance of a lattice Boltzmann-based method for ct-based fractional flow reserve. *EuroIntervention*. (2018) 13:1696–704. doi: 10.4244/EIJ-D-17-00019

7. Chandola G, Zhang JM, Tan RS, Chai P, Teo L, Allen JC, et al. Computed tomography coronary angiography and computational fluid dynamics based fractional flow reserve before and after percutaneous coronary intervention. *Front Bioeng Biotechnol*. (2021) 9:739667. doi: 10.3389/fbioe.2021.739667

8. Morris PD, Ryan D, Morton AC, Lycett R, Lawford PV, Hose DR, et al. Virtual fractional flow reserve from coronary angiography: modeling the significance of coronary lesions. *JACC: Cardiovasc Interv*. (2013) 6:149–57. doi: 10.1016/j.jcin.2012.08.024

9. Morris PD, Vosse FNvd, Lawford PV, Hose DR, Gunn JP. "Virtual" (computed) fractional flow reserve: current challenges and limitations. *JACC: Cardiovasc Interv*. (2015) 8:1009–17. doi: 10.1016/j.jcin.2015.04.006

10. Morris PD, Narracott A, Tengg-Kobligk Hv, Soto DAS, Hsiao S, Lungu A, et al. Computational fluid dynamics modelling in cardiovascular medicine. *Heart*. (2016) 102:18–28. doi: 10.1136/heartjnl-2015-308044

11. Morris PD, Soto DAS, Feher JFA, Rafiroiu D, Lungu A, Varma S, et al. Fast virtual fractional flow reserve based upon steady-state computational fluid dynamics analysis: results from the VIRTU-fast study. *JACC: Basic Transl Sci*. (2017) 2:434–46. doi: 10.1016/j.jacbts.2017.04.003

12. Morris PD, Curzen N, Gunn JP. Angiography-derived fractional flow reserve: more or less physiology? *J Am Heart Assoc*. (2020) 9:e015586. doi: 10.1161/JAHA.119.015586

13. Nørgaard BL, Leipsic J, Gaur S, Seneviratne S, Ko BS, Ito H, et al. Diagnostic performance of noninvasive fractional flow reserve derived from coronary computed tomography angiography in suspected coronary artery disease: the NXT trial (analysis of coronary blood flow using CT angiography: next steps). *J Am Coll Cardiol*. (2014) 63:1145–55. doi: 10.1016/j.jacc.2013.11.043

14. Taylor CA, Fonte TA, Min JK. Computational fluid dynamics applied to cardiac computed tomography for noninvasive quantification of fractional flow reserve: scientific basis. *J Am Coll Cardiol*. (2013) 61:2233–41. doi: 10.1016/j.jacc.2012.11.083

15. Pellicano M, Lavi I, De Bruyne B, Vaknin-Assa H, Assali A, Valtzer O, et al. Validation study of image-based fractional flow reserve during coronary angiography. *Circulation: Cardiovasc Interv*. (2017) 10:e005259. doi: 10.1161/CIRCINTERVENTIONS.116.005259

16. Fearon WF, Achenbach S, Engstrom T, Assali A, Shlofmitz R, Jeremias A, et al. Accuracy of fractional flow reserve derived from coronary angiography. *Circulation*. (2019) 139:477–84. doi: 10.1161/CIRCULATIONAHA.118.037350

17. Witberg G, De BB, Fearon WF, Achenbach S, Engstrom T, Matsuo H, et al. Diagnostic performance of angiogram-derived fractional flow reserve. *JACC: Cardiovasc Interv*. (2020) 13:488–97. doi: 10.1016/j.jcin.2019.10.045

18. Masdjedi K, Zandvoort LV, Balbi M, Gijsen F, Ligthart J, Rutten M, et al. Validation of a three-dimensional quantitative coronary angiography-based software to calculate fractional flow reserve: the FAST study. *EuroIntervention*. (2020) 16:591–9. doi: 10.4244/EIJ-D-19-00466

19. Masdjedi K, Tanaka N, Van Belle E, Porouchani S, Linke A, Woitek FJ, et al. Vessel fractional flow reserve (vFFR) for the assessment of stenosis severity: the FAST II study. *EuroIntervention*. (2022) 17:1498–505. doi: 10.4244/EIJ-D-21-00471

20. Westra J, Andersen BK, Campo G, Matsuo H, Koltowski L, Eftekhari A, et al. Diagnostic performance of in-procedure angiography-derived quantitative flow reserve compared to pressure-derived fractional flow reserve: the FAVOR II Europe-Japan study. *J Am Heart Assoc*. (2018) 7:e009603. doi: 10.1161/JAHA.118.009603

21. Westra J, Tu S, Winther S, Nissen L, Vestergaard MB, Andersen BK, et al. Evaluation of coronary artery stenosis by quantitative flow ratio during invasive coronary angiography. *Circulation: Cardiovasc Imaging*. (2018) 11:e007107. doi: 10.1161/CIRCIMAGING.117.007107

22. Andersen BK, Vestergaard MB, Andreasen LN, Tu S, Krusell L, Maeng M, et al. CRT-400.12 feasibility, diagnostic precision of in-procedure computed fractional flow reserve: the wire-free invasive functional imaging (WIFI) study. *JACC: Cardiovasc Interv*. (2017) 10:S51. doi: 10.1016/j.jcin.2016.12.177

23. Wells BJ, Chagin KM, Nowacki AS, Kattan MW. Strategies for handling missing data in electronic health record derived data. *eGEMs*. (2013) 1:1035. doi: 10.13063/2327-9214.1035

24. Krantz MJ, Kaul S. The ATLAS ACS 2-TIMI 51 trial, the burden of missing data. *J Am Coll Cardiol*. (2013) 62:777–81. doi: 10.1016/j.jacc.2013.05.024

25. Yang DX, Khera R, Miccio JA, Jairam V, Chang E, Yu JB, et al. Prevalence of missing data in the national cancer database and association with overall survival. *JAMA Netw Open*. (2021) 4:e211793. doi: 10.1001/jamanetworkopen.2021.1793

26. Sturdy J, Kjernlie JK, Nydal HM, Eck VG, Hellevik LR. Uncertainty quantification of computational coronary stenosis assessment and model based mitigation of image resolution limitations. *J Comput Sci*. (2019) 31:137–50. doi: 10.1016/J.JOCS.2019.01.004

27. Fossan FE, Sturdy J, Müller LO, Strand A, Bråten AT, Jørgensen A, et al. Uncertainty quantification and sensitivity analysis for computational FFR estimation in stable coronary artery disease. *Cardiovasc Eng Technol*. (2018) 9:597–622. doi: 10.1007/s13239-018-00388-w

28. Sankaran S, Kim HJ, Choi G, Taylor CA. Uncertainty quantification in coronary blood flow simulations: impact of geometry, boundary conditions and blood viscosity. *J Biomech*. (2016) 49:2540–7. doi: 10.1016/j.jbiomech.2016.01.002

29. Yin M, Yazdani A, Karniadakis GE. One-dimensional modeling of fractional flow reserve in coronary artery disease: uncertainty quantification and Bayesian optimization. *Comput Methods Appl Mech Eng*. (2019) 353:66–85. doi: 10.1016/j.cma.2019.05.005

30. Itu L, Rapaka S, Passerini T, Georgescu B, Schwemmer C, Schoebinger M, et al. A machine-learning approach for computation of fractional flow reserve from coronary computed tomography. *J Appl Physiol Respir Environ Exerc Physiol*. (2016) 121:42–52. doi: 10.1152/japplphysiol.00752.2015

31. Tanade C, Feiger B, Vardhan M, Chen SJ, Leopold JA, Randles A. Global sensitivity analysis for clinically validated 1d models of fractional flow reserve. IEEE, Mexico: *2021 43rd Annual International Conference of the IEEE Engineering in Medicine & Biology Society (EMBC)* (2021). p. 4395–4398. Available at http://dx.doi.org10.1109/EMBC46164.2021.9629890

32. Chen SJ, Carroll JD. 3-d reconstruction of coronary arterial tree to optimize angiographic visualization. *IEEE Trans Med Imaging*. (2000) 19:318–36. doi: 10.1109/42.848183

33. Green NE, Chen SYJ, Hansgen AR, Messenger JC, Groves BM, Carroll JD. Angiographic views used for percutaneous coronary interventions: a three-dimensional analysis of physician-determined vs. computer-generated views. *Catheter Cardiovasc Interv*. (2005) 64:451–9. doi: 10.1002/ccd.20331

34. Pirofsky B. The determination of blood viscosity in man by a method based on Poiseuille's law. *J Clin Invest*. (1953) 32:292–8. doi: 10.1172/JCI102738

35. Blanco PJ, Bulant CA, Müller LO, Talou GDM, Bezerra CG, Lemos PA, et al. Comparison of 1D and 3D models for the estimation of fractional flow reserve. *Sci Rep*. (2018) 8:17275. doi: 10.1038/s41598-018-35344-0

36. Feiger B, Kochar A, Gounley J, Bonadonna D, Daneshmand M, Randles A. Determining the impacts of venoarterial extracorporeal membrane oxygenation on cerebral oxygenation using a one-dimensional blood flow simulator. *J Biomech*. (2020) 104:109707. doi: 10.1016/j.jbiomech.2020.109707

37. Feiger B, Adebiyi A, Randles A. Multiscale modeling of blood flow to assess neurological complications in patients supported by venoarterial extracorporeal membrane oxygenation. *Comput Biol Med*. (2021) 129:104155. doi: 10.1016/j.compbiomed.2020.104155

38. Smith NP, Pullan AJ, Hunter PJ. An anatomically based model of transient coronary blood flow in the heart. *SIAM J Appl Math*. (2001) 62:990–1018. doi: 10.1137/S0036139999355199

39. Alastruey J, Khir AW, Matthys KS, Segers P, Sherwin SJ, Verdonck PR, et al. Pulse wave propagation in a model human arterial network: assessment of 1-D visco-elastic simulations against in vitro measurements. *J Biomech*. (2011) 44:2250–8. doi: 10.1016/j.jbiomech.2011.05.041

40. Gradus-Pizlo I, Sawada SG, Wright D, Segar DS, Feigenbaum H. Detection of subclinical coronary atherosclerosis using two-dimensional, high-resolution transthoracic echocardiography. *J Am Coll Cardiol*. (2001) 37:1422–9. doi: 10.1016/S0735-1097(01)01160-3

41. Karimi A, Navidbakhsh M, Shojaei A, Faghihi S. Measurement of the uniaxial mechanical properties of healthy and atherosclerotic human coronary arteries. *Mater Sci Eng C*. (2013) 33:2550–4. doi: 10.1016/j.msec.2013.02.016

42. Baldewsing RA, de Korte CL, Schaar JA, Mastik F, van Der Steen AFW. A finite element model for performing intravascular ultrasound elastography of human atherosclerotic coronary arteries. *Ultrasound Med Biol*. (2004) 30:803–13. doi: 10.1016/j.ultrasmedbio.2004.04.005

43. Hadjiloizou N, Davies JE, Malik IS, Aguado-Sierra J, Willson K, Foale RA, et al. Differences in cardiac microcirculatory wave patterns between the proximal left mainstem and proximal right coronary artery. *Am J Physiol Heart Circ Physiol*. (2008) 295:H1198–205. doi: 10.1152/ajpheart.00510.2008

44. Wilson RF, Wyche K, Christensen BV, Zimmer S, Laxson DD. Effects of adenosine on human coronary arterial circulation. *Circulation*. (1990) 82:1595–606. doi: 10.1161/01.CIR.82.5.1595

45. Westerhof N, Lankhaar JW, Westerhof BE. The arterial Windkessel. *Med Biol Eng Comput*. (2009) 47:131–41. doi: 10.1007/s11517-008-0359-2

46. Sharma P, Itu L, Zheng X, Kamen A, Bernhardt D, Suciu C, et al. A framework for personalization of coronary flow computations during rest and hyperemia. IEEE, San Diego, CA, USA: *2012 Annual International Conference of the IEEE Engineering in Medicine and Biology Society* (2012). p. 6665–6668. Available at http://dx.doi.org/10.1109/EMBC.2012.6347523

47. Mirramezani M, Diamond SL, Litt HI, Shadden SC. Reduced order models for transstenotic pressure drop in the coronary arteries. *J Biomech Eng*. (2019) 141:0310051. doi: 10.1115/1.4042184

48. Madhavan S, Kemmerling EMC. The effect of inlet and outlet boundary conditions in image-based CFD modeling of aortic flow. *Biomed Eng Online*. (2018) 17:66. doi: 10.1186/s12938-018-0497-1

49. Les AS, Shadden SC, Figueroa CA, Park JM, Tedesco MM, Herfkens RJ, et al. Quantification of hemodynamics in abdominal aortic aneurysms during rest and exercise using magnetic resonance imaging and computational fluid dynamics. *Ann Biomed Eng*. (2010) 38:1288–313. doi: 10.1007/s10439-010-9949-x

50. Gamilov T, Kopylov P, Simakov S. Computational simulations of fractional flow reserve variability. In: Karasözen B, Manguoğlu M, Tezer-Sezgin M, Göktepe S, Uğur O, editors. *Numerical Mathematics and Advanced Applications ENUMATH 2015*. Lecture Notes in Computational Science and Engineering. Cham: Springer International Publishing (2016). p. 499–507. Available at http://dx.doi.org/10.1007/978-3-319-39929-4˙48

51. Eck VG, Donders WP, Sturdy J, Feinberg J, Delhaas T, Hellevik LR, et al. A guide to uncertainty quantification and sensitivity analysis for cardiovascular applications. *Int J Numer Method Biomed Eng*. (2016) 32:e02755. doi: 10.1002/cnm.2755

52. Müller LO, Fossan FE, Bråten AT, Jørgensen A, Wiseth R, Hellevik LR. Impact of baseline coronary flow and its distribution on fractional flow reserve prediction. *Int J Numer Method Biomed Eng*. (2019) 37:e3246. doi: 10.1002/cnm.3246

53. Nørgaard BL, Fairbairn TA, Safian RD, Rabbat MG, Ko B, Jensen JM, et al. Coronary CT angiography-derived fractional flow reserve testing in patients with stable coronary artery disease: recommendations on interpretation and reporting. *Radiology: Cardiothoracic Imaging*. (2019) 1:e190050. doi: 10.1148/ryct.2019190050

54. Dubin J, Wallerson DC, Cody RJ, Devereux RB. Comparative accuracy of Doppler echocardiographic methods for clinical stroke volume determination. *Am Heart J*. (1990) 120:116–23. doi: 10.1016/0002-8703(90)90168-w

55. Toth GG, Johnson NP, Jeremias A, Pellicano M, Vranckx P, Fearon WF, et al. Standardization of fractional flow reserve measurements. *J Am Coll Cardiol*. (2016) 68:742–53. doi: 10.1016/j.jacc.2016.05.067

56. Saltelli A. Making best use of model evaluations to compute sensitivity indices. *Comput Phys Commun*. (2002) 145:280–97. doi: 10.1016/S0010-4655(02)00280-1

57. Saltelli A, Annoni P, Azzini I, Campolongo F, Ratto M, Tarantola S. Variance based sensitivity analysis of model output. Design and estimator for the total sensitivity index. *Comput Phys Commun*. (2010) 181:259–70. doi: 10.1016/j.cpc.2009.09.018

58. Hsieh NH, Reisfeld B, Bois FY, Chiu WA. Applying a global sensitivity analysis workflow to improve the computational efficiencies in physiologically-based pharmacokinetic modeling. *Front Pharmacol*. (2018) 9:588. doi: 10.3389/fphar.2018.00588

59. Petraco R, Sen S, Nijjer S, Echavarria-Pinto M, Escaned J, Francis DP, et al. Fractional flow reserve-guided revascularization: practical implications of a diagnostic gray zone and measurement variability on clinical decisions. *JACC: Cardiovasc Interv*. (2013) 6:222–5. doi: 10.1016/j.jcin.2012.10.014

60. Driessen RS, Danad I, Stuijfzand WJ, Raijmakers PG, Schumacher SP, van Diemen PA, et al. Comparison of coronary computed tomography angiography, fractional flow reserve, and perfusion imaging for ischemia diagnosis. *J Am Coll Cardiol*. (2019) 73:161–73. doi: 10.1016/j.jacc.2018.10.056

61. Tu S, Barbato E, Köszegi Z, Yang J, Sun Z, Holm NR, et al. Fractional flow reserve calculation from 3-dimensional quantitative coronary angiography and TIMI frame count. *JACC: Cardiovasc Interv*. (2014) 7:768–77. doi: 10.1016/j.jcin.2014.03.004

62. Tröbs M, Achenbach S, Röther J, Redel T, Scheuering M, Winneberger D, et al. Comparison of fractional flow reserve based on computational fluid dynamics modeling using coronary angiographic vessel morphology versus invasively measured fractional flow reserve. *Am J Cardiol*. (2016) 117:29–35. doi: 10.1016/j.amjcard.2015.10.008

63. Kornowski R, Lavi I, Pellicano M, Xaplanteris P, Vaknin-Assa H, Assali A, et al. Fractional flow reserve derived from routine coronary angiograms. *J Am Coll Cardiol*. (2016) 68:2235–7. doi: 10.1016/j.jacc.2016.08.051

64. Tu S, Westra J, Yang J, Birgelen Cv, Ferrara A, Pellicano M, et al. Diagnostic accuracy of fast computational approaches to derive fractional flow reserve from diagnostic coronary angiography: the international multicenter favor pilot study. *JACC: Cardiovasc Interv*. (2016) 9:2024–35. doi: 10.1016/j.jcin.2016.07.013

65. Xu B, Tu S, Qiao S, Qu X, Chen Y, Yang J, et al. Diagnostic accuracy of angiography-based quantitative flow ratio measurements for online assessment of coronary stenosis. *J Am Coll Cardiol*. (2017) 70:3077–87. doi: 10.1016/j.jacc.2017.10.035

66. Legutko J, Kleczynski P, Dziewierz A, Rzeszutko L, Bartus S, Bagienski M, et al. P2378Correlation between quantitative flow ratio (QFR) and fractional flow reserve (FFR). *Eur Heart J*. (2017) 38:ehx502.P2378. doi: 10.1093/eurheartj/ehx502.P2378

67. van Rosendael AR, Koning G, Dimitriu-Leen AC, Smit JM, Montero-Cabezas JM, van der Kley F, et al. Accuracy and reproducibility of fast fractional flow reserve computation from invasive coronary angiography. *Int J Cardiovasc Imaging*. (2017) 33:1305–12. doi: 10.1007/s10554-017-1190-3

68. Pellicano M, Lavi I, De Bruyne B, Vaknin-Assa H, Assali A, Valtzer O, et al. Validation study of image-based fractional flow reserve during coronary angiography. *Circulation: Cardiovasc Interv*. (2017) 10:e005259. doi: 10.1161/CIRCINTERVENTIONS.116.005259

69. Mohee K, Mynard JP, Dhunnoo G, Davies R, Nithiarasu P, Halcox JP, et al. Diagnostic performance of virtual fractional flow reserve derived from routine coronary angiography using segmentation free reduced order (1-dimensional) flow modelling. *JRSM Cardiovasc Dis*. (2020) 9:2048004020967578. doi: 10.1177/2048004020967578

70. Chiu IS, Anderson RH. Can we better understand the known variations in coronary arterial anatomy? *Ann Thorac Surg*. (2012) 94:1751–60. doi: 10.1016/j.athoracsur.2012.05.133

71. Brown BG, Bolson E, Frimer M, Dodge HT. Quantitative coronary arteriography: estimation of dimensions, hemodynamic resistance, and atheroma mass of coronary artery lesions using the arteriogram and digital computation. *Circulation*. (1977) 55:329–37. doi: 10.1161/01.CIR.55.2.329

72. Brinkman AM, Baker PB, Newman WP, Vigorito R, Friedman MH. Variability of human coronary artery geometry: an angiographic study of the left anterior descending arteries of 30 autopsy hearts. *Ann Biomed Eng*. (1994) 22:34–44. doi: 10.1007/BF02368220

73. Kang DY, Ahn JM, Lee CH, Lee PH, Park DW, Kang SJ, et al. Deferred vs. performed revascularization for coronary stenosis with grey-zone fractional flow reserve values: data from the IRIS-FFR registry. *Eur Heart J*. (2018) 39:1610–9. doi: 10.1093/eurheartj/ehy079

74. Lossnitzer D, Chandra L, Rutsch M, Becher T, Overhoff D, Janssen S, et al. Additional value of machine-learning computed tomographic angiography-based fractional flow reserve compared to standard computed tomographic angiography. *J Clin Med*. (2020) 9:676. doi: 10.3390/jcm9030676

75. Ko BS, Cameron JD, Munnur RK, Wong DTL, Fujisawa Y, Sakaguchi T, et al. Noninvasive CT-derived FFR based on structural and fluid analysis. *JACC: Cardiovasc Imaging*. (2017) 10:663–73. doi: 10.1016/j.jcmg.2016.07.005

76. Kruk M, Wardziak Ł, Demkow M, Pleban W, Pre˛gowski J, Dzielińska Z, et al. Workstation-based calculation of CTA-based FFR for intermediate stenosis. *JACC: Cardiovasc Imaging*. (2016) 9:690–9. doi: 10.1016/j.jcmg.2015.09.019

77. Torii R, Yacoub MH. CT-based fractional flow reserve: development and expanded application. *Glob Cardiol Sci Pract*. (2021) 2021:e202120. doi: 10.21542/gcsp.2021.20

78. Chen SJ, Carroll JD. 3-D reconstruction of coronary arterial tree to optimize angiographic visualization. *IEEE Trans Med Imaging*. (2000) 19:318–36. doi: 10.1109/42.848183

79. Blanco PJ, Bulant CA, Müller LO, Talou GM, Bezerra CG, Lemos P, et al. Comparison of 1D and 3D models for the estimation of fractional flow reserve. *Sci Rep*. (2018) 8:1–12. doi: 10.1038/s41598-018-35344-0

80. Boileau E, Pant S, Roobottom C, Sazonov I, Deng J, Xie X, et al. Estimating the accuracy of a reduced-order model for the calculation of fractional flow reserve (FFR). *Int J Numer Method Biomed Eng*. (2018) 34:e2908. doi: 10.1002/cnm.2908

81. Saha S, Purushotham T, Prakash KA. Comparison of fractional flow reserve value of patient-specific left anterior descending artery using 1D and 3D CFD analysis. *Int J Adv Eng Sci Appl Math*. (2019) 11:244–53. doi: 10.1007/s12572-020-00257-7

82. Carson JM, Pant S, Roobottom C, Alcock R, Blanco PJ, Bulant CA, et al. Non-invasive coronary CT angiography-derived fractional flow reserve: a benchmark study comparing the diagnostic performance of four different computational methodologies. *Int J Numer Method Biomed Eng*. (2019) 35:e3235. doi: 10.1002/cnm.3235

83. Lo EW, Menezes LJ, Torii R. On outflow boundary conditions for CT-based computation of FFR: examination using PET images. *Med Eng Phys*. (2020) 76:79–87. doi: 10.1016/j.medengphy.2019.10.007

84. Papamanolis L, Kim HJ, Jaquet C, Sinclair M, Schaap M, Danad I, et al. Myocardial perfusion simulation for coronary artery disease: a coupled patient-specific multiscale model. *Ann Biomed Eng*. (2021) 49:1432–47. doi: 10.1007/s10439-020-02681-z

frontiers | Frontiers in Medical Technology

TYPE Original Research
PUBLISHED 22 December 2022
DOI 10.3389/fmedt.2022.1018058

OPEN ACCESS

EDITED BY
Claudio Chiastra,
Politecnico di Torino, Italy

REVIEWED BY
Francesco Capuano,
Universitat Politecnica de Catalunya, Spain
Amirhossein Arzani,
The University of Utah, United States

*CORRESPONDENCE
Federico Canè
federico.cane1990@gmail.com

SPECIALTY SECTION
This article was submitted to Cardiovascular Medtech, a section of the journal Frontiers in Medical Technology

RECEIVED 12 August 2022
ACCEPTED 15 November 2022
PUBLISHED 22 December 2022

CITATION
Canè F, Delcour L, Luigi Redaelli AC, Segers P and Degroote J (2022) A CFD study on the interplay of torsion and vortex guidance by the mitral valve on the left ventricular wash-out making use of overset meshes (Chimera technique).
Front. Med. Technol. 4:1018058.
doi: 10.3389/fmedt.2022.1018058

A CFD study on the interplay of torsion and vortex guidance by the mitral valve on the left ventricular wash-out making use of overset meshes (Chimera technique)

Federico Canè[1]*, Lucas Delcour[2], Alberto Cesare Luigi Redaelli[3], Patrick Segers[1] and Joris Degroote[2]

[1]IBiTech – bioMMeda, Department of Electronics and Information Systems, Ghent University, Ghent, Belgium, [2]Department of Electromechanical, Systems and Metal Engineering, Ghent University, Ghent, Belgium, [3]Department of Electronics, Information and Bioengineering, Politecnico di Milano, Milano, Italy

Cardiovascular disease often occurs with silent and gradual alterations of cardiac blood flow that can lead to the onset of chronic pathological conditions. Image-based patient-specific Computational Fluid Dynamics (CFD) models allow for an extensive quantification of the flow field beyond the direct capabilities of medical imaging techniques that could support the clinicians in the early diagnosis, follow-up, and treatment planning of patients. Nonetheless, the large and impulsive kinematics of the left ventricle (LV) and the mitral valve (MV) pose relevant modeling challenges. Arbitrary Lagrangian-Eulerian (ALE) based computational fluid dynamics (CFD) methods struggle with the complex 3D mesh handling of rapidly moving valve leaflets within the left ventricle (LV). We, therefore, developed a Chimera-based (overset meshing) method to build a patient-specific 3D CFD model of the beating LV which includes a patient-inspired kinematic model of the mitral valve (LVMV). Simulations were performed with and without torsion. In addition, to evaluate how the intracardiac LV flow is impacted by the MV leaflet kinematics, a third version of the model without the MV was generated (LV with torsion). For all model versions, six cardiac cycles were simulated. All simulations demonstrated cycle-to-cycle variations that persisted after six cycles but were albeit marginal in terms of the magnitude of standard deviation of velocity and vorticity which may be related to the dissipative nature of the numerical scheme used. The MV was found to have a crucial role in the development of the intraventricular flow by enhancing the direct flow, the apical washout, and the propagation of the inlet jet towards the apical region. Consequently, the MV is an essential feature in the patient-specific CFD modeling of the LV. The impact of torsion was marginal on velocity, vorticity, wall shear stress, and energy loss, whereas it resulted to be significant in the evaluation of particle residence times. Therefore, including torsion could be considered in patient-specific CFD models of the LV, particularly when aiming to study stasis and residence time. We conclude that, despite some technical limitations encountered, the Chimera technique

is a promising alternative for ALE methods for 3D CFD models of the heart that include the motion of valve leaflets.

KEYWORDS

left ventricle, ventricular torsion, mitral valve, Chimera technique, overset meshes, residence time

Introduction

Cardiovascular disease is the main cause of death worldwide, accounting for 17.8 million deaths expected to increase up to 23.6 million by 2030 (1). Most often, this entails a chronic process whereby pathophysiological changes in cardiac function progress slowly (e.g., development of cardiac hypertrophy, cardiac dilatation, valvular dysfunction) and unnoticed, until reaching a point of no return with the development of symptoms, or occurrence of a fatality as myocardial infarction or stroke. In many cardiovascular pathologies, unphysiological intraventricular hemodynamics is a consequence and/or direct cause of the pathology (e.g., valve dysfunction), leading to flow disturbing and energy dissipating jets, altered intraventricular swirling patterns with less energy-efficient filling and emptying of the ventricular chamber, and effects on blood residence times within the cardiac cavity. Furthermore, therapeutic interventions - especially those related to resting valve function - may drastically alter flow patterns within the heart cavities. A fundamental understanding of intraventricular hemodynamics should lead to an improved assessment of deviations from normal physiological flow, earlier detection of chronic abnormalities, better assessment of therapeutic efficacy, and further refinements in surgical techniques or cardiovascular medical device design.

Among the techniques used to investigate the intraventricular flow field, Computational Fluid Dynamics (CFD) modelling offers the advantage to compute flow metrics with finer spatial and temporal resolution than possible with any available *in vivo* imaging technique. Compared to in-vitro benchmarks, it is much more flexible in performing parametric and comparative studies thanks to the ease of tuning and isolating the parameter under investigation. Therefore, with the relentless improvement of computational power and the growth of computational models, it would be paramount if patient-specific CFD simulations could finally be used as a clinical support tool in cardiovascular surgical planning and diagnostics (2).

The investigation of the intraventricular flow features in relation to the LV pathophysiological condition has been evaluated with several flow-based biomarkers. The diastolic vortex formation interplays both with the pumping efficiency (such as flow washout, ventricular energetics) and the biological nature of the blood flow (blood clots). This dual-side efficiency has been thoroughly investigated focusing on sustaining the blood motility up to the apex and, preventing thrombus formation, and has become a key feature in terms of wash-out of the ventricular chamber and ventricular energetics (3). The clinical contribution of CFD modelling is potentially multidisciplinary and groundbreaking, ranging from the early detection of cardiovascular diseases (heart failure conditions, pulmonary hypertension, aortic and cerebral aneurysms, aortic dissection, cardiac valve pathologies), to the assessment of cardiovascular devices and therapies (prosthetic valves, stent, and ventricular assist device placement, cardiac resynchronization therapy) (4). The MV leaflets motion can be computationally replicated *via* a kinematic model, preferably based on measurements from 4D medical images, or a Fluid-Structure Interaction (FSI) model (5).

The first MV models were highly simplified, implementing the valve as a planar orifice that was either open or closed [on-off approach (6–8)] or with a time-varying cross-sectional area (6, 9, 10), therefore neglecting the MV leaflets' configuration, their kinematics and interaction with the flow field. Next generation models considered both the morphology and the motion of the leaflets. These valve models can be classified into the patient-inspired (often based on parametric models) or patient-specific MV models, segmented from medical images. Among the patient-inspired MV models: (i) Chnafa et al. (11–13) segmented the moving MV annulus from 4D CT scans and modeled the MV leaflets as a continuous elliptical shape with a given thickness, which instantaneously switches between the open and the closed configuration, thus neglecting the opening and closing phases; (ii) Seo et al. (14) defined the MV morphology based on the anatomical measurements by Ranganathan et al. (15) with the Anterior (AL) and Posterior (PL) leaflets following rigid rotations with different angular profiles. Contributions among patient-specific MV models are: (i) Mihalef et al. (16) modeled the whole heart using machine-learning algorithms to robustly estimate the patient's morphological and functional parameters from multiple 4D CT datasets with claimed precision of 90%; (ii) Bavo et al. (17) segmented the LV and MV kinematics from 4D transesophageal echocardiographic images.

Even though patient-specific MV models based on 4D medical images can account for the fluctuations and curvature changes, the limited thickness of the leaflets (around 2 mm), compared to their other dimensions, in combination with their fast opening and closing dynamics, makes it challenging for the currently used imaging modalities to visualize the

valve with a sufficiently high spatial and temporal resolution, especially during the opening and closing phases. A whole branch of research is dedicated to combining the different imaging techniques to enhance their advantages. In addition to the 4D medical images used to derive geometrical and kinematical patient-specific models (ultrasound, CT or MRI), the 4D flow MRI is a promising cardiac imaging technique, which allows to quantify the intracardiac flow without the need of performing CFD modelling. Nonetheless, at the current stage, it still suffers from a coarser spatial and temporal resolution in comparison with CFD and FSI simulations (18). In this case, the motion of the ventricular walls is entirely prescribed by medical images, with 1 temporal configuration the mitral valve segmented by medical images, and thus not computed from the resulting pressures. Hence, the model is Computational Fluid Dynamics (CFD) with moving boundary but not Fluid-Structure Interaction (FSI)'.

On the other hand, FSI modeling requires: (i) the definition of the constitutive and structural properties, which is more straightforward for materials composing prosthetic mechanical valves rather than the natural leaflets; (ii) a finer description of the MV anatomy including the details, such as the chordae tendinae and papillary muscles, not essential in kinematic models. For these reasons, patient-specific FSI models coupling the LV and MV rarely succeeded to combine simultaneously multiple features: the patient-specific LV model with both mitral and aortic valves by Su et al. (19) is limited to a 2D geometry, otherwise the 3D MV is placed within a fixed tube (18) or limited to the filling phase (20). Recently, there have been a few breakthroughs in coupling patient-specific MV and LV models with FSI and they have been used to study the effects of impaired myocardial active relaxation (21) or the transapical neo-chordae implantation (22, 23).

Regardless of whether the MV kinematics is prescribed in CFD simulations or calculated in FSI simulations, the computational approaches typically used to solve the flow (and structural) equations of problems involving moving meshes can be boundary-conforming, such as the Arbitrary Lagrangian-Eulerian (ALE) approach, or non-boundary conforming, such as the Immersed Boundary Method (IBM). In the former, the boundary mesh deforms accordingly to the motion of valves in providing an accurate WSS computation on their surface. In the latter, the effect of the moving immersed body on the fluid is taken into account by adding a source term in the Navier–Stokes equations resulting in a more suitable approach for complex geometries. In addition to these most common techniques, one has to mention: the smoothed particles hydrodynamics, which is a meshless approach used successfully to overcome the lack of complete valve coaptation during systole (24, 25); the Chimera (or overset) technique, which is particularly suitable in handling problems with different components in motion, used to investigate the hemodynamics within a pulsatile left ventricular assist device (26). The Chimera technique has the advantage over ALE that it allows tackling the separation of the fluid domain that occurs during the valve coaptation without a local fictitious increase of viscosity or added source term in the Navier-Stokes equations, whereas, over the IBM approach, complex geometries can be represented with boundary layer meshes resulting in a more accurate computation of interface wall shear stress.

In previous work, we built a patient-specific CFD model of the LV chamber based on the Chimera technique. Firstly, we generated a semi-automatic algorithm to generate 4D meshes of the LV with 1-to-1 vertex correspondence to replicate the patient-specific cardiac motion (27). Secondly, we investigated the impact of the LV torsion on the fluid dynamics using the Chimera technique (28). A major limitation of that study, however, was the absence of the mitral valve in the model, known to highly impact the intraventricular flow field and a key structural element in the formation of the ventricle-filling vortex ring in diastole. Therefore, we propose a workflow to build patient-specific CFD models of the LV with a kinematic model of the MV based on the Chimera technique, which is promising to tackle the several challenges involved in cardiac modeling. Bearing in mind that many cardiac pathologies (cardiomyopathies, hypertrophy, diabetes, hypertension, ischemia, normal aging) influence ventricular torsion, simulations are performed in a model with and without physiological torsion.

Materials and methods

Medical imaging dataset segmentation

The heart of a 27 years old healthy male volunteer was scanned using a cine-MRI short-axis dataset and a cine-MRI radial dataset at the Policlinico San Donato using a Gradient Recalled Echo (GRE) sequence within 30 time-instants spanning 1 cardiac cycle. The study was performed with the ethical approval of the hospital and the informed consent of the subject. The short axis dataset had an in-plane resolution of 1.17 mm and a through-plane resolution of 8 mm, whereas the radial dataset shared the same in-plane resolution and was acquired every 10° along the rotation axis passing through the LV apex and MV centroid. The 4D geometries of the LV were manually segmented using Materialise Mimics 18.0® from the cine-MRI short-axis dataset, while the 4D annulus and one configuration of the leaflets at the A-wave peak, due to high uncertainty linked with the highly impulsive leaflets and the low spatial and temporal resolution, were segmented from the cine-MRI radial dataset within an in-house Matlab-code developed by the Biomechs groups of Politecnico di Milano.

Mesh generation

The Chimera (or overset) technique defines the shape of the fluid domain with one or multiple component Boundary Layer (BL) grids attached to the moving walls that are overlapping a 3D Cartesian grid which is stationary. Interpolation schemes transfer the flow field solution (pressure and velocities) from the component to the background mesh, and vice versa. The Chimera technique is particularly helpful when dealing with complex deforming geometries, and avoids complex remeshing of an ALE technique. A detailed description of the Chimera technique can be found in the Methods section of Canè et al. (29).

In this section, we describe the steps taken to generate three component grids: (i) one anterior MV mesh connected conformally to the anterior part of the LV mesh; (ii) one posterior MV mesh connected conformally to the posterior part of the LV mesh (posterior LVMV mesh, shown in green) and (iii) an inlet plug mesh overlapping with both LVMV meshes to close the fluid domain (**Figure 1C**: conformal fused LVMV).

The surface mesh of the MV leaflets is generated by connecting the MV annulus, modeled in a static configuration defined from the averaging of its 4D configurations over a cardiac cycle, with the profile of the MV free edge of the valve at the A-wave peak (**Figure 1A**). The anterior and posterior BL MV meshes were created around the MV surface, bearing in mind that they represent the fluid region in contact with the MV surface mesh, following these steps:

(1) Two copies of the segmented MV surface mesh (represented in cyan) were generated and translated, sliding along the LV endocardial mesh, so that the space encompassed between the two copies (shown with the dotted red line in **Figure 1**.B.1) represents the MV with a thickness of 2 mm. Subsequently, the lower edges of the copies are connected (shown with the yellow line, Figure 1B.1);
(2) A collar mesh (shown with a black line in Figure 1B.2) overlapping with the LV endocardial surface mesh at the upper and lower part of the leaflets is created and fused with the surface leaflet meshes, generated in the previous step;
(3) The resulting mesh is divided into the anterior and posterior leaflets (shown in red and green, respectively, in **Figure 1B.3**), sharing six overlapping layers, with the following steps performed both for the anterior and posterior leaflets;
(4) As preparation to build the three-blocks BL mesh for each leaflet, the surface mesh of this region is divided into three surfaces: the upper mesh, which is composed of the upper collar and upper leaflet grids (shown in orange, **Figures 1B.4A,B**), the free edge (shown in blue, **Figures 1B.4A,B**), the lower mesh (composed of the lower collar and lower leaflet, shown in magenta, **Figures 1B.4A,B**). Separately for the anterior and posterior leaflet (**Figures 1B.4A,B**), the upper and lower surface meshes are extruded with a thickness of 4 mm to build the first two blocks of each leaflet (shown in red and green, in **Figures 1B.4A,B**);
(5) The third block is generated by extruding the surface shown in yellow (**Figures 1B.5A,B**), resulting from the fusion between the free edge surface and the contiguous surfaces created at step 5, towards the inner direction with a thickness of 4 mm (**Figures 1B.6A,B**).

The mesh separation between the anterior and posterior leaflet (step 3) is fundamental during valve closure because the Chimera technique allows the intersection between different component grids, but not self-intersection, which may become problematic during valve closure.

We enabled manual cut-control and ensured that the overset interface occurred along a vertical direction between the anterior and posterior LVMV meshes wall and along a horizontal direction between the inlet plug and the anterior and posterior LVMV meshes. The overlapping between the component grids was conformal on the external surface of the three boundary layer meshes. The final three component grids are displayed in **Figure 1C** (anterior LVMV mesh in red; posterior LVMV mesh in green and an inlet plug mesh overlapping with both LVMV meshes to close the fluid domain in blue).

The opening angles were not assigned homogeneously to the leaflets, but *via* a shaping function that divided the MV into four zones (anterior and posterior leaflet, front and posterior commissure) (**Figure 2**). The finer control was essential to leave more space during early diastole between the MV leaflets and the LV wall in correspondence with the commissures, which otherwise would have been too narrow to fit the valve, resulting in negative volume errors. The quality criteria used for the 4D generated meshes are a maximum skewness of 0.9 and a minimum scaled Jacobian of 0.02. The number of mesh elements is 737 k, 496 k, 346 k, 2.5 M for the anterior LVMV grid, the posterior LVMV grid, the inlet plug, and the background grid, respectively.

The mesh sensitivity analysis was performed in our previous study without the mitral valve (28), evaluating the combinations of a background grid with an edge length of 0.5 mm and 0.7 mm and a component grid with 100 k and 300 k elements. The comparison of the different meshes was based on the investigation of the WSS, the endocardial pressure, pressure, and velocity along predefined trajectories. A finer mesh resolution of the component boundary layer grid allows for a finer evaluation of the flow velocity profile and hence the wall shear stress without significant impact on the computed variables or the computational time. Therefore, the

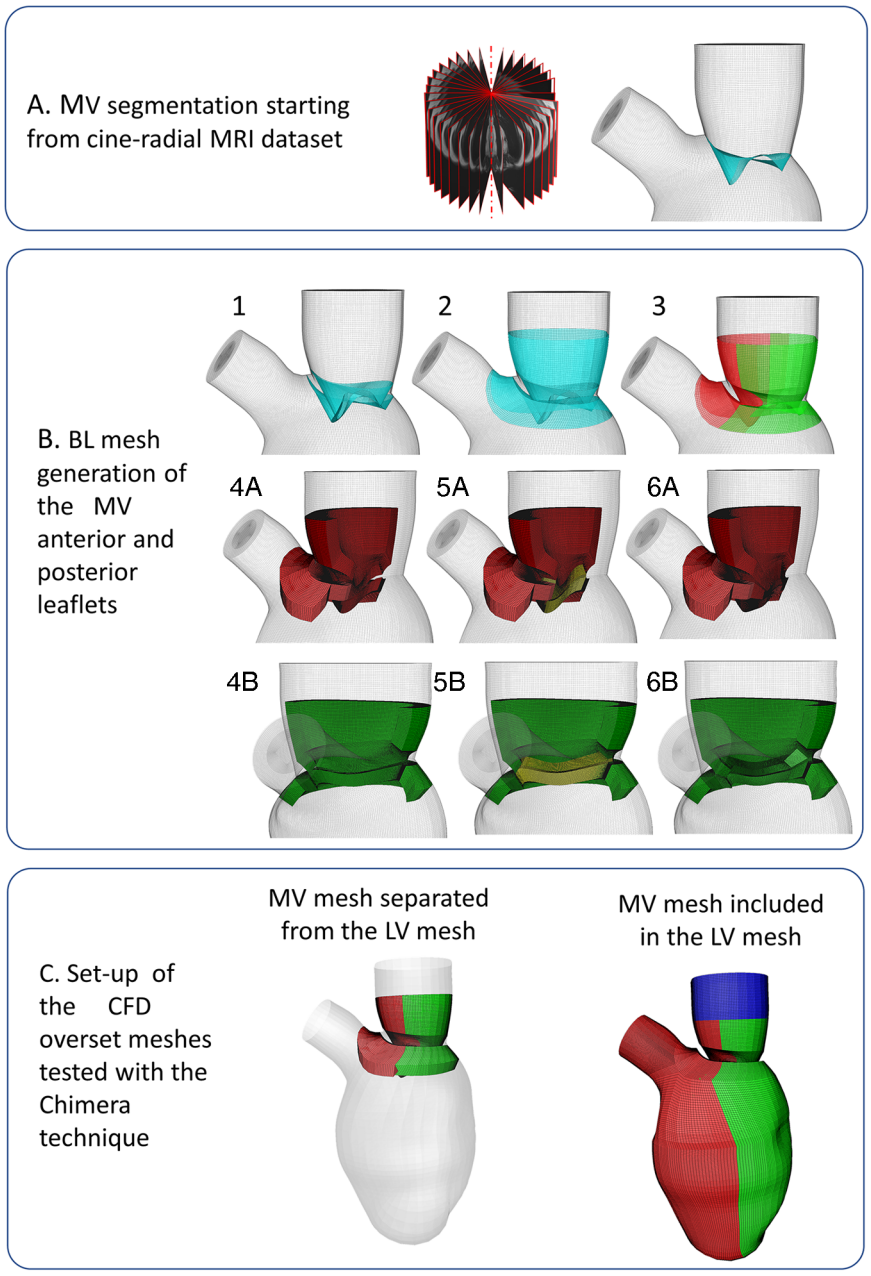

FIGURE 1
(panel A) Mitral valve segmentation from cine-radial MRI images; (panel B) Creation of the mitral valve mesh; (panel C) Tested meshes configurations: not-working separated LV-MV configuration on the left, working conformally connected fused LV-MV on the right.

component grid with 300 k elements was chosen, in combination with the background grid with an edge length of 0.5 mm. In the case with the MV, the near-wall mesh resolution was refined to increase the overlapping between the component grids, resulting in 737 k, 496 k, and 346 k for the anterior LVMV grid, the posterior LVMV grid, the inlet plug, respectively. A background grid with an edge length of 0.7 mm (2.5 M elements) was chosen to solve an unexpected vanishing error of the fluid zone corresponding to the posterior LVMV grid when using a background grid with an edge length of 0.5 mm.

Torsional implementation

Torsion has been applied as a rotation of the LV sac with respect to the vertical axis passing through the MV centroid and the apex. The intensity of the rotation varies linearly

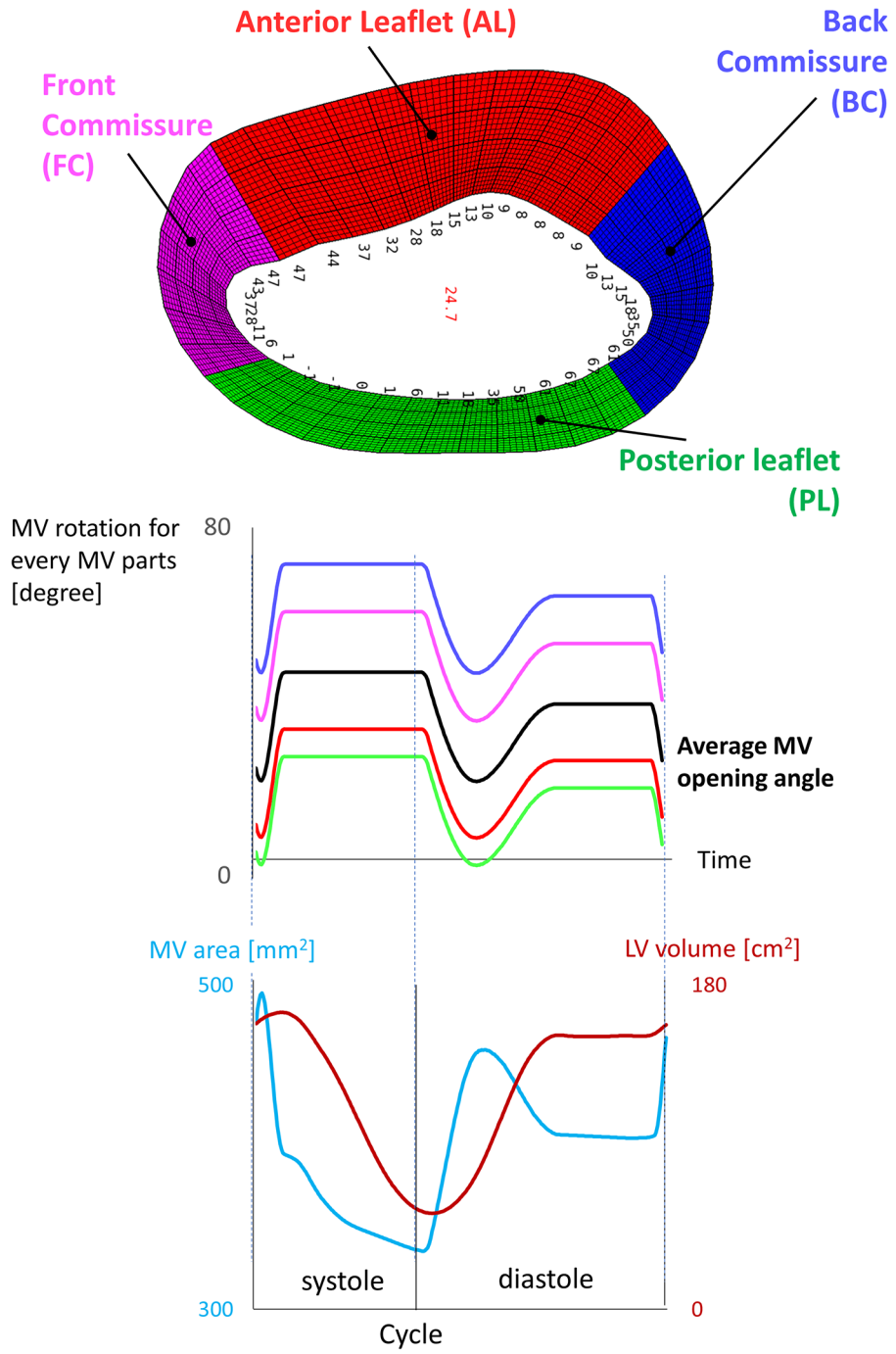

FIGURE 2
Kinematic model of the mitral valve reporting the average angle for each zone of the valve.

during the cardiac cycle and is defined with a piecewise ramp-like function: the twist and the uncoil occur during systole and diastole, respectively. The maximum rotational angle occurs at end-systole and, in the physiological torsion (referred to as Torsion) case, it was based on the measurement of the angle encompassed by the centroid of the papillary muscles between end-diastole and end-systole ($\gamma = 13°$). In a second simulation, torsion was omitted (referred to as No Torsion).

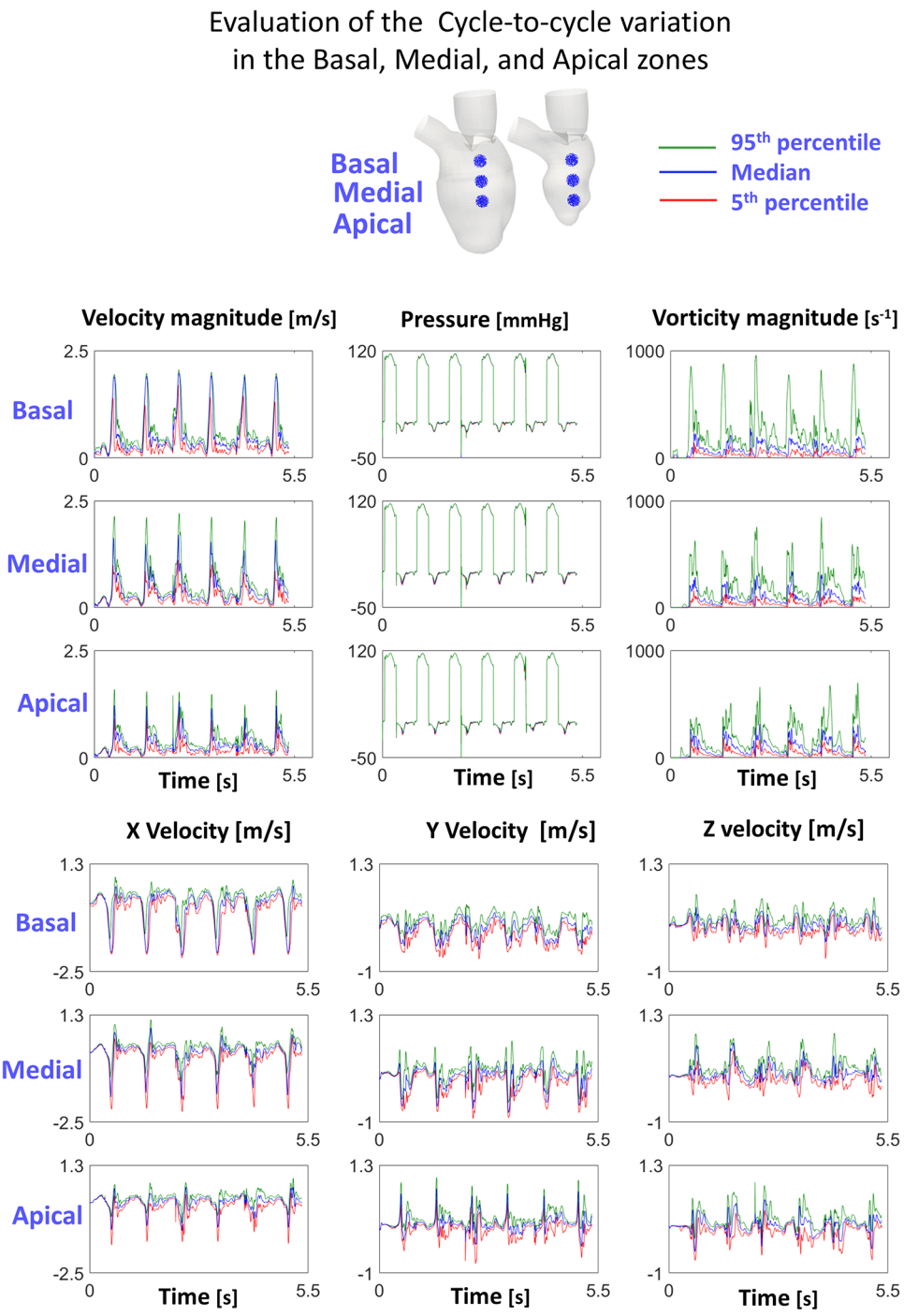

FIGURE 3
Cycle-to-cycle variation in the investigated cloud points shows that the transitional effects are still relevant.

Temporal interpolation

The anterior and posterior LVMV meshes were generated on the existing and already interpolated 4D BL meshes of the LV using a Natural Cubic spline, resulting in 290 temporal configurations spanning one cardiac cycle and a time step of 3 ms. For more details on the temporal interpolation method, the reader is referred to (28).

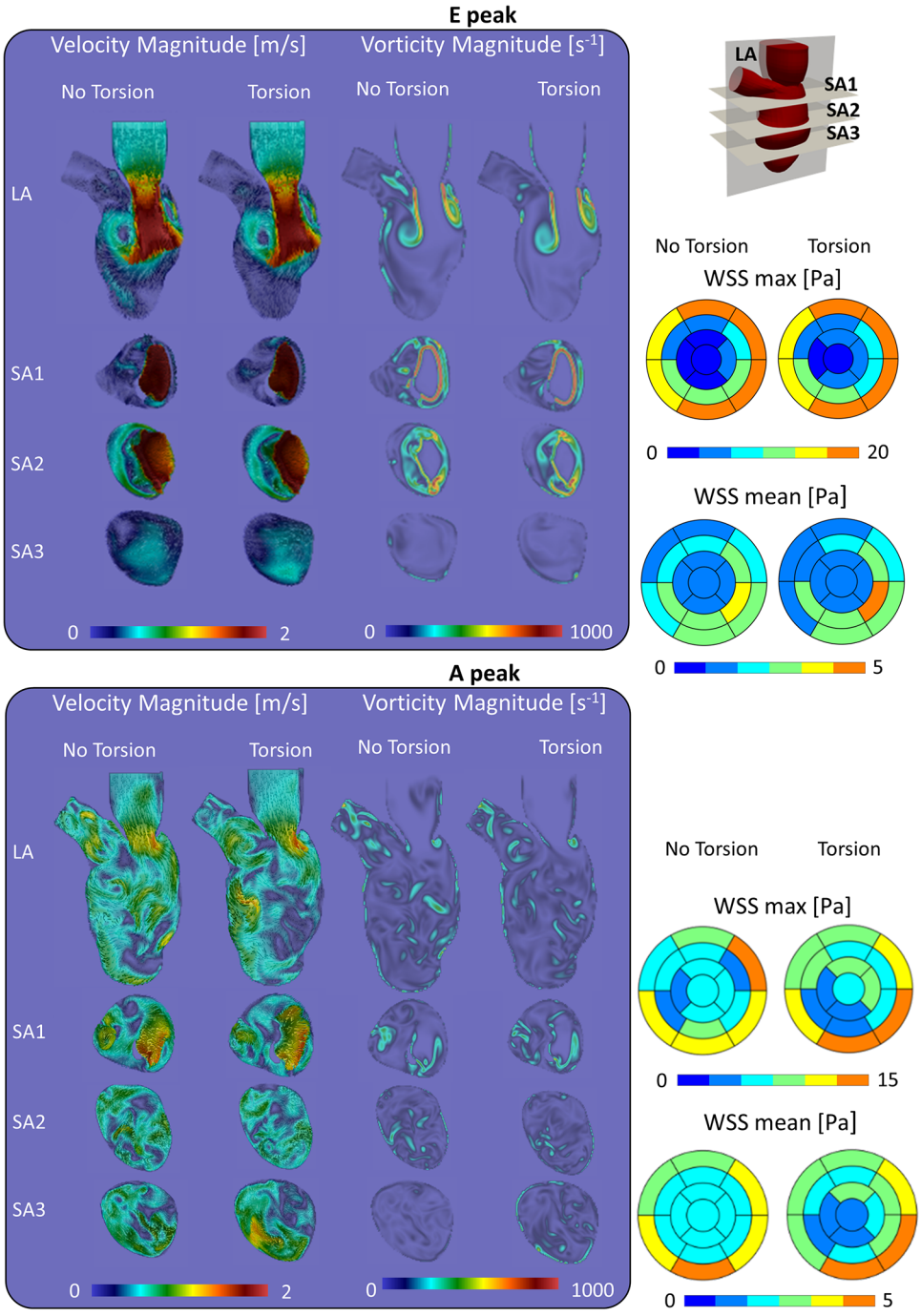

FIGURE 4
Velocity, vorticity and wall shear stress during the diastolic peaks show a marginal impact of torsion on the investigated variables.

CFD set-up

Our Chimera-based CFD model was defined in Fluent 2019 R3®, with the fluid domain represented by three BL component grids (anterior LVMV, posterior LVMV, inlet plug) embedded in a 3D Cartesian grid. The initialization of the overset interface subdivided the cells of the meshes into four categories (dead, solve, receptor, donor) and established the connectivity between the participating zones to exchange variables during the computation of the Navier-Stokes equations. The cut-control feature was required for finer control on the cells to disable (dead cells), allowing to specify

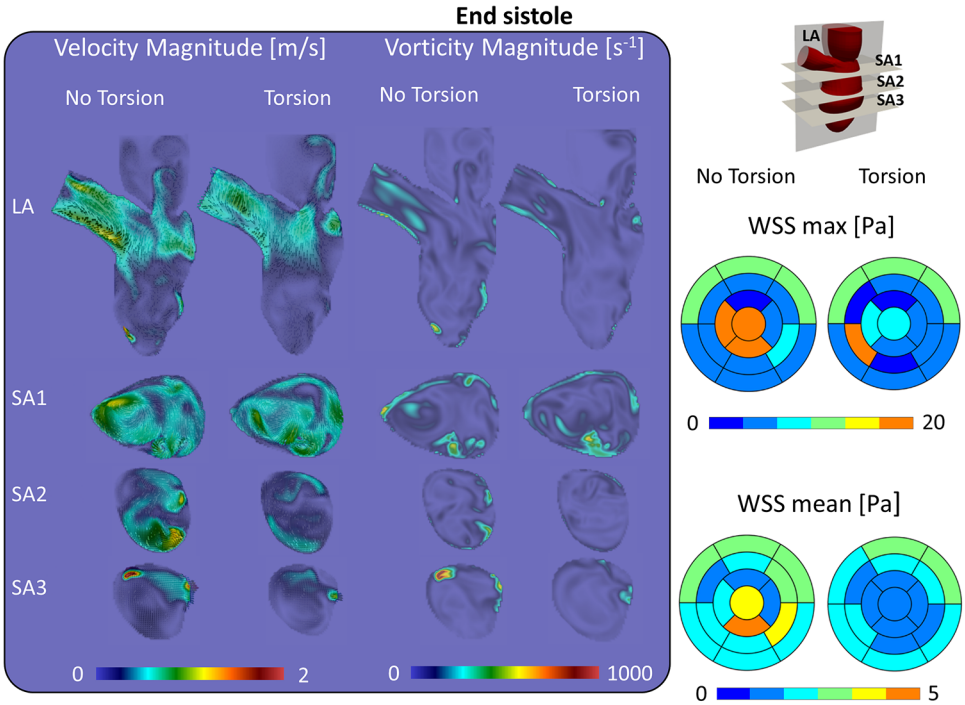

Residence Time of particles released from inlet

Particles percentage [%]	LVMV no Torsion	LVMV Torsion
Ejected 1° beat	67.1	76.9
Ejected 2° beat	24.5	17.3
Residing in the LV	8.4	5.9

Velocity distribution of particles residing in the LV after 2 beats

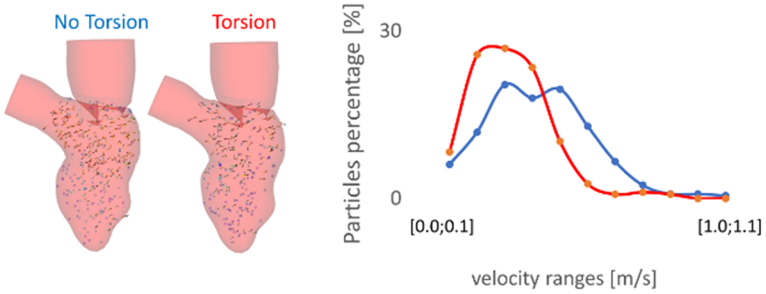

FIGURE 5
(Top) Velocity, vorticity, wall shear stress contours during end systole show a slight increase of these variables in the case disregarding torsion; (middle) the percentage of particles ejected is higher in the torsion case (+9.8%), nonetheless after two beats the difference decreases below 3%; (Bottom) the case without torsion induces a better motility of the particles residing in the left ventricle.

the wall zones not to be cut by the fluid zones. In our case, the wall zones of the anterior and posterior LVMV meshes were excluded from the cutting of the posterior and anterior fluid zones, respectively.

As in (28), a coupled solver scheme was used for the pressure-velocity coupling, together with a 2nd order upwind scheme for the convective terms and a 1st order implicit scheme for the time discretization. Blood was modeled as a homogeneous and Newtonian fluid [$\rho = 1{,}060$ kg/m^3, $\mu = 0.003$ kg/(m·s)]. Alternating on-off boundary conditions were imposed as follows: inlet pressure set at 7 mmHg and outlet as a wall during diastole; outlet pressure set at 120 mmHg and

inlet as a wall during systole. Our model is without turbulence model. The flow regime inside the LV is debatable due to the highly transient dynamicity involved and, in agreement with Chnafa et al. (11–13), we believe that the main large-scale hemodynamic features (such as jets, main vortices, and ejection) can be characterized even with the laminar flow assumption. Six cardiac cycles were simulated on a Dell PowerEdge R620 server (2 × Intel Xeon E5-2680v2 CPUs at 2.8 GHz) and the HPC-UGent cluster system. In the former, one cardiac cycle was computed in about 24 h using eight cores. In the latter, the computation time depended on the number of nodes and the architecture of the available cluster unit.

Post-processing

The comparison of the fluid dynamics in the simulated cases is based on the computation of the velocity and vorticity magnitude, the energy loss (EL), the wall shear stress (WSS) distribution, and the Residence Time (RT). The velocity and vorticity are separated into classes (reported in **Supplementary Material Tables S1–S6** in the Supplementary Material) in ascending order according to the magnitude to quantitively assess the differences of the contours and are evaluated in three short-axis planes (SA1, SA2, SA3, from top to bottom) and one long axis plane (LA).

The EL is computed from the viscous term of the incompressible Navier-Stokes, as follows:

$$\Phi_V = \frac{1}{2}\mu \sum_{i=1}^{3}\sum_{j=1}^{3}\left[\left(\frac{\partial \boldsymbol{u}_i}{\partial \boldsymbol{x}_j}+\frac{\partial \boldsymbol{u}_j}{\partial \boldsymbol{x}_i}\right)\right]^2$$

$$E_L = \int_{t0}^{t1}\sum_{i=1}^{\text{num voxels}} \phi_V V_i \, \mathrm{d}t$$

where $\frac{1}{2}\left[\left(\frac{\partial \boldsymbol{u}_i}{\partial \boldsymbol{x}_j}+\frac{\partial \boldsymbol{u}_j}{\partial \boldsymbol{x}_i}\right)\right]$ is the strain rate tensor, V_i the volume of the cell (0.343 mm^3), μ the blood viscosity [0.003 kg/(m·s)], and dt the time step of the integration.

Regarding the RT, 4,500 massless particles were seeded at the nodes of the inlet surface mesh at the beginning of the 5th diastole and moved along the velocity field during the last two cardiac cycles, using the particle paths computation in Tecplot 360 EX 2,019 R1. For the RT computation, the particles were classified into three categories: (i) ejected within the 1st beat (direct flow); (ii) ejected within the 2nd beat; (iii) residing in the LV after 2 beats.

Both the EL and the RT were evaluated during the 5th and 6th cardiac cycles, whereas the remaining variables during characteristic time-points of the 6th cardiac cycle. The chosen characteristic time-points were the diastolic E-peak and A-peak and end-systole.

The cycle-to-cycle variation was estimated by computing the median, 5th and 95th percentile of velocity and vorticity magnitude, pressure, and velocity components, within three spherical cloud points (N_{points} = 1,000 points, radius = 5 mm) distributed along the axis passing through the MV centroid and the LV apex. In addition to studying the impact of torsion, we also compared results to a case without the presence of the MV. We also assessed the impact of the cycle-to-cycle variation by computing the standard deviation of the velocity and vorticity magnitude in the LA plane at the diastolic E-peak, being the time step with the largest velocity gradient. The reported quantities were computed using data from the 3rd–6th cycle and evaluated for the three simulated cases (LV Torsion, LVMV No Torsion, LVMV Torsion).

In the bulls' eye representation, which divides the LV endocardium into 17 sectors, we reported the mean and maximum WSS as the difference in every sector between the investigated cases (Torsion - No Torsion, LVMV - LV) to highlight visually the zones impacted by Torsion and the MV. Visually, the first case (Torsion, LVMV) dominates in the red zones, whereas the second case (Torsion, LV) in the blue zones.

Results

Influence of torsion on intraventricular hemodynamics

Figure 3 displays 5th percentile, median, and 95th percentile values of velocity (magnitude and components), pressure, and vorticity as a function of time within the three control volumes for the reference case with physiological torsion and the presence of the mitral valve. Cycle-to-cycle variation is still prominent after six cardiac cycles, especially for vorticity and y and z components of velocity. The evaluation of the standard deviation of the velocity and vorticity magnitude allowed us to quantify the impact of the cycle-to-cycle variation. Even though the cycle-to-cycle variation is still visible after six cycles, the maximum value of the standard deviation at the E-peak is 3.8 10^{-8} m/s and 3.5 10^{-5} s^{-1} in the LA plane at the diastolic E-peak for the velocity and vorticity magnitude, respectively (**Figure 6**). The higher values of the standard deviation are reached within the tract between the atrium and ventricle, and their magnitude is amplified by the presence of the MV.

At the E-peak of diastole (**Figure 4**, upper panel), the inlet jet reaches the peak velocity magnitude of 2.0 m/s with the formation of two vortical structures that impinge the posterior endocardial wall in every simulated case. Both the velocity and vorticity distributions are highly comparable between the Torsion and No torsion cases (**Supplementary Material Tables S1,S2**). Omitting torsion leads to a slight increase in

10.3389/fmedt.2022.1018058

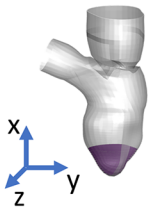

Residence Time of particles released from apex

Particles percentage [%]	LV case	LVMV case
Ejected 1° beat	44.4%	67.9%
Ejected 2° beat	27.2%	21%
Residing in the LV	28.4%	11.1%

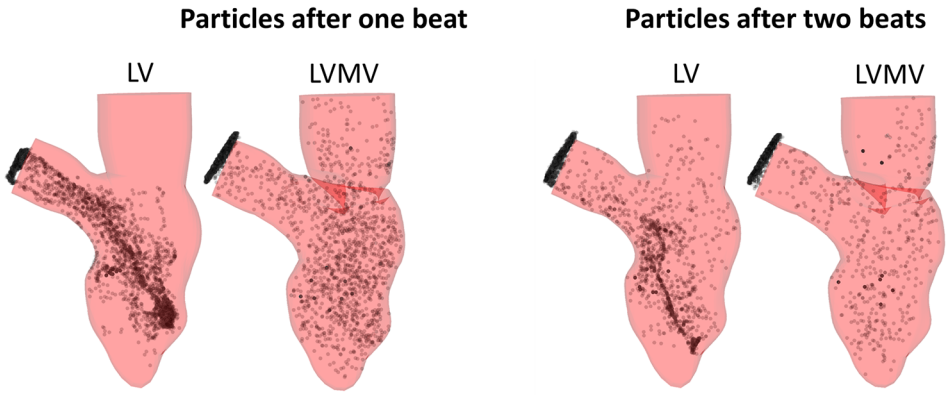

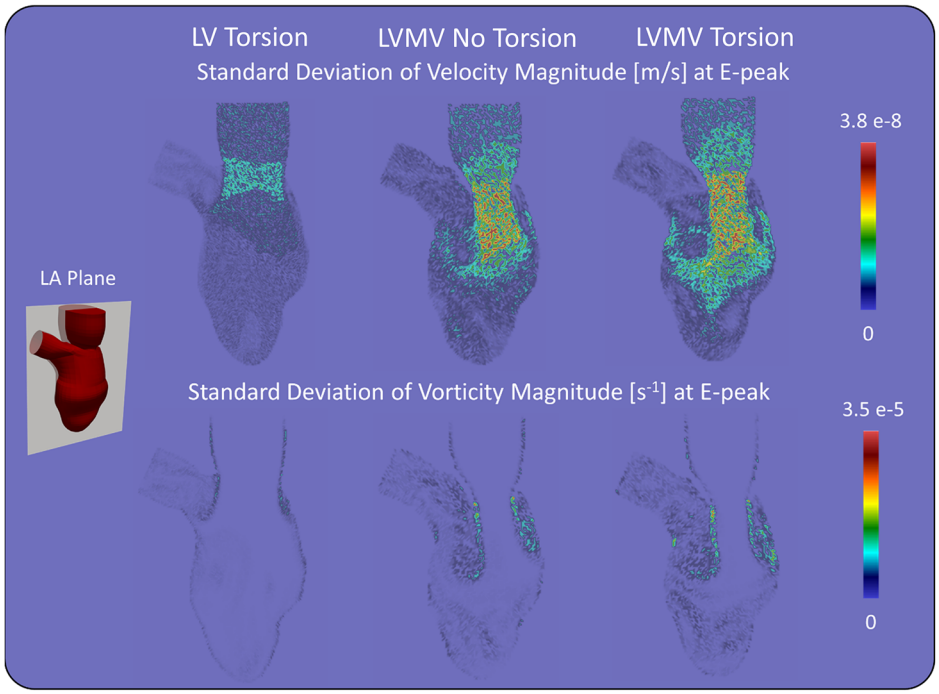

FIGURE 6
(Top) Residence time of the particles released from the apex show how the mitral valve enhances the apical wash-out. (Bottom) Standard deviation of velocity and vorticity magnitude in the LA plane between the 3rd, 4th, 5th, 6th cycle at the E-peak computed for the case with torsion and without MV (LV Torsion), the case without torsion and with MV (LVMV No Torsion), and the case with torsion and MV (LVMV Torsion).

velocity magnitude in the long axis (LA) and SA1 planes and a mild decrease in the SA3 plane; a slight increase in vorticity is found in the SA1 plane.

At the diastolic A-peak (Figure 4, bottom panel), two main features can be noted regardless of the torsional degree: (i) both the peak of velocity (0.7 m/s) and vorticity (800 s^{-1}) lost intensity; (ii) the two main E-peak vortex structures dissipated into smaller vortices more uniformly distributed in the LV domain. Disregarding torsion induces a mild increase in velocity magnitude in the LA, SA1 and a moderate increase in the SA3 plane (Supplementary Material Tables S3,S4).

At the end-systolic configuration (Figure 5, upper panel), the maximum velocity magnitude is around 0.65 m/s and 0.43 m/s, whereas the vorticity magnitude reaches 680 s^{-1} and 520 s^{-1} in the No Torsion and Torsion case, respectively. Omitting torsion leads to a mild increase in velocity and vorticity magnitude in all the investigated planes, but confined to small areas (Supplementary Material Tables S5,S6).

In a model that incorporates the mitral valve, torsion has a mixed impact on the maximum and mean WSS with a moderate change (increase/decrease) during diastole (changes in the order of 13% and 6%, respectively) and somewhat stronger changes (increase/decrease) at end systole (64% and 25%, respectively). Whether values decreased or increased was dependent on the region considered, as clear from Supplementary Material Tables S7–S10 in the Supplementary Material, where a detailed analysis of maximal and mean WSS in the different ventricular segments for the models with and without the mitral valve and with/without torsion is found.

Energy dissipation (EL) is about 14% higher for physiological torsion (9.7 mJ) over cycle 5 (4.8 mJ) and 6 (4.8 mJ) than when torsion is omitted (8.4 mJ, with 4.1 mJ in cycle 5 and 4.3 mJ in cycle 6).

Figure 5 encompasses the results that were obtained on particle residence times. When particles are released from the inlet, discarding torsion leads to a reduction of the particles ejected within the 1st beat of −9.8% (=76.9%–67.1%) with a consequent increase of both the particles ejected during the 2nd beat (+7.2%) and residing in the LV after two beats (+2.5%) (Supplementary Material Table S1). Within two beats, 91.6% of the particles left the LV without torsion, while this becomes 94.1% when torsion is present. Looking at the velocity of the particles residing after 2 beats, 287 (out of 378) have a velocity lower than 0.5 m/s without torsion; with torsion, this applies to 250 (out of 264) particles.

Influence of the mitral valve on intraventricular hemodynamics

At the E-peak (Figure 7), the MV increases the maximum velocity magnitude from 1.0 m/s to 2.0 m/s and extends the areas with velocity beyond 1 m/s by 14%, 3.5%, 23.8%, and 71.5% in the LA, SA1, SA2, SA3 planes, respectively. With the MV, the vortices originate at the tip of the MV leaflets instead of the annulus, resulting in enlarged vortices in the SA1 (the vorticity within 0–250 s^{-1} and beyond 750 s^{-1} increased by 5.3% and by 0.6%, respectively) and in the SA2 plane (the vorticity over 250 s^{-1} increased by 20.8%).

At the A-peak (Figure 7), the MV increases the maximum velocity magnitude from 0.5 m/s to 0.8 m/s, and the areas with velocity beyond 0.25 m/s enlarge by 37.9%, 29.3%, 45.5%, 52% in the LA, SA1, SA2, SA3 planes, respectively. The MV slightly enhances the vorticity above 250 s^{-1} by 1.1%, 4.8%, and 0.9%, in the LA, SA1, and SA3 planes, respectively.

As can be expected from the impact on the velocity field, the presence of the mitral valve increases maximal and mean WSS at all levels in the left ventricle (Supplementary Material Tables S9,S10) with the largest impact for the medial (4–8-fold increase in mean and maximal WSS) and apical segments (2–3-fold increase in mean and maximal WSS).

Focusing on the influence induced by the presence of the mitral valve leaflets in washing out of the LV (Figure 6), we studied clearance of particles released from the apex for a simulation with and without valve (and with torsion applied to both cases). With the valve present, 76.9% and 21% of the particles released from the apical region are ejected during the 1st and 2nd beat, respectively, with the remaining 11.1% of the particles residing in the LV after two beats. In absence of the valve, 44% and 27.2% of the particles were ejected during the 1st and 2nd beat, respectively, with 28.4% residing in the LV.

Discussion

In this manuscript, we developed a Chimera-based patient-specific model of the LV coupled with a patient-inspired moving MV and showcased the model to assess the impact of torsion and the presence of the mitral leaflets on intraventricular hemodynamics. The open MV was segmented from cine-radial MRI images and leaflet motion was defined using a kinematic model. We tested the Chimera technique because it is particularly suited to combine the large motion of the LV endocardium with the impulsive kinematics of the MV leaflets. The Chimera technique allowed us to overcome the main limitations faced in previous work based on the ALE approach where CFD simulations in a deforming LV with mitral valve limited to one cardiac cycle (17), due to excessively distorted mesh resulting in negative volumes errors, or even to the diastolic phase (30).

Despite the obvious advantages of the Chimera technique over ALE for the given study case, we did experience unexpected technical difficulties while setting up the problem. Initially, the BL meshes of the MV leaflets were separated from the BL mesh of the LV (Figure 1C: separated LVMV):

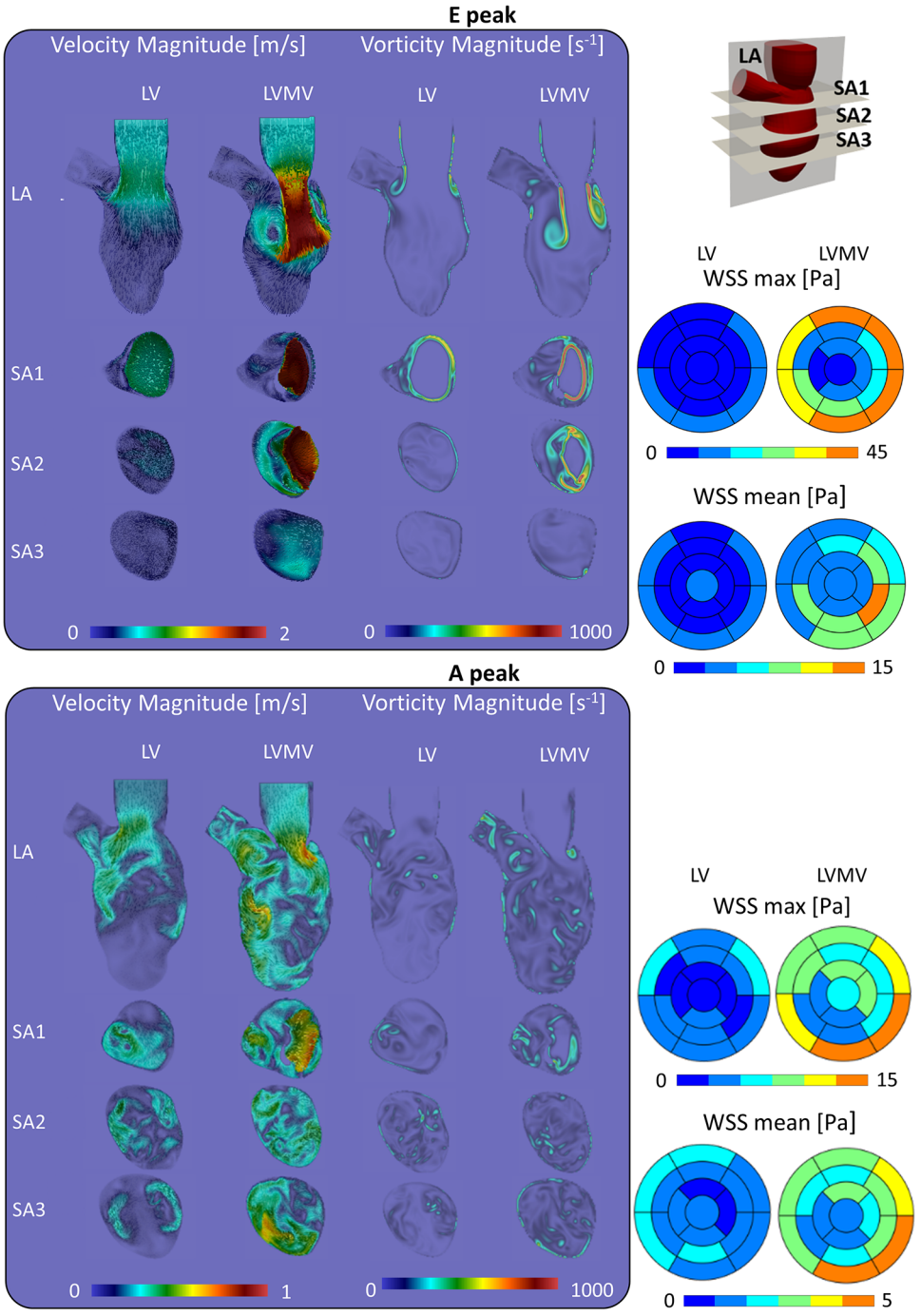

FIGURE 7
Impact of the mitral valve in the torsion case on the velocity, vorticity and wall shear stress during the diastolic.

one anterior MV mesh; one posterior MV mesh; one LV mesh, whose generation is described in in (27, 28). With this mesh configuration, however, we experienced sudden vanishing of some component zones during the CFD calculation, regardless of several attempts involving the definition of customized cut-control, the BL thickness, the mesh densities, the temporal interpolation, and smooth connecting angles.

This unforeseen dead zone error forced us to include the MV leaflets directly into the moving LV mesh resulting in limitations for the MV opening angles to preserve the mesh

quality. Therefore, despite the claimed advantages of the Chimera technique in terms of handling mesh motion, the software version used in this study should be further optimized. We are aware that the proposed model (with a 2nd order upwind scheme for the convective terms and a 1st order implicit scheme for the temporal discretization) is based on a dissipative numerical scheme that is not ideal to capture the transitional nature of the intraventricular flow field. This numerical scheme was actually imposed by the implementation of the Chimera technique (with further limitations due to the presence of moving boundary conditions) in Fluent software 2019 R3®. The reported limitation is not intrinsic to the Chimera technique as such, but rather dependent on the implementation within software packages, which isn't surprising considering that it is relatively recent (i.e., introduced in Fluent 2018). We tried to minimize the numerical viscosity effect by using reasonably small time steps of 3 ms and a fine grid.

Cycle-to-cycle variation after six cardiac cycles indicates that, even with perfectly repeatable moving (and alternating on-off pressure-wall) boundary conditions, the transitional-to-turbulent flow regime induces differences in the flow field from cycle to cycle. The analysis of the simulated cases highlights that the cycle-to-cycle variation affects more the shape and (marginally) the contours distribution rather than the magnitude of the computed variables. Nonetheless, the effects of the cycle-to-cycle variations might be underestimated in the simulated cases due to the dissipative nature of the numerical schemes. For this reason, cycle-to-cycle variation might be more prominent when using numerical schemes with higher order discretization [as in (12)] and further investigations are required.

Simulating multiple cardiac cycles is a good practice to get rid of the transitional effects, as confirmed by several studies: Long et al. (7), Vasudevan et al. (29), Seo et al. (4), Mangual et al. (31), Chnafa et al. (12) simulated 4, 4, 5, 10, 35 cycles, respectively. Among these, it is worth noticing that only Chnafa et al. (12) reported the cycle-to-cycle variations in the wall shear stress of the diastasis during the 20th and 21st cycles. In the referred case, five cycles were simulated to washout the initial conditions, and the results were reported based on phase-averaging over 30 additional cycles. In the other reported studies, even if multiple cycles were simulated, the analysis is often limited to the last cycle without reporting additional checks about the vanishing of the transient effects (4, 7, 29, 31). More precise recommendations to objectively assess when a CFD calculation has reached a regime state may be helpful to the community. In this context, it is worth remembering that the multi-laboratory study promoted by the FDA to support the use of CFD simulations from a regulatory perspective is at a standstill (32), with CFD-use limited to the design stage and considered appropriate for evaluating relative design changes rather than assessing absolute quantities (33) (ISO 14,708-5). In our case, the RT computation became of interest only after performing the CFD simulations, making it impossible to compute the advection-diffusion-reaction equation using Overset Meshes technique in Fluent 2019 R3. Therefore, the RT computation was based on particle tracking methods. A comparison of the different methodologies to compute residence time (e.g., Eulerian residence time or ERT) in the LV cavity could be of interest as further development.

Overall, we noticed only minor differences in velocity, wall shear stress, and vorticity contours in the simulations with and without torsion (**Figures 4** and **5** and **Supplementary Material Tables S1–S6**). Interestingly, energy dissipation was found about 14% higher in the physiological torsion case compared to the simulation discarding torsion. Nonetheless, given that energy losses are of an order of one thousand of the total cardiac energy (order of a few J) in both simulated cases, the impact of torsion on the energy loss is considered marginal and unlikely of physiological relevance. Moreover, the impact on the energy loss becomes even more marginal considering that the use of low-order dissipative schemes leads to an overestimation of the energy loss. Vasudevan et al. (29) recently investigated the effects of torsional motion on the LV in the fluid dynamics of five healthy human fetal and two healthy adult porcine hearts. The MV geometry was based on detailed anatomical measurements from a database of 10 adult porcine specimens (34) and the opening angles of the leaflets were derived from the three-chamber view of MRI data. Flow and energy dynamics were evaluated varying the torsional degree (0°, 5°, 15°), with and without the mitral valve and the papillary muscles, and under a diseased condition. They found that the impact of ventricular torsion was minor and irrelevant on flow patterns, energy losses, ejection work, and wall shear stress, and the impact on the residence time was not evaluated. In our case, the effects of torsion on velocity and vorticity magnitude were negligible, whereas energy loss increased by 14% when considering torsion. It is hard to assess the physiological significance of this finding; as discussed further, torsion has a meaningful impact on the residence time and particle clearing from the left ventricle, of which the beneficial effects on reducing the risk of blood stasis and thrombus formation may outweigh the energy cost. Indeed, physiological torsion was found to have a favorable effect on removing particles from the LV at the first beat (+9.8%) that reduces up to 2% after two beats. On the other hand, the motility of the particles residing in the LV chamber was reduced by torsion.

To the best of our knowledge, there are no other studies that evaluated the particle residence time in function of the LV torsion, other than our previous study without the MV (28). In that study, however, the mitral valve leaflets were not considered, and given the huge impact of the leaflets on intraventricular hemodynamics (see further), results should not be compared. Mangual et al. (14) injected a virtual tracer

inside the LV, of which about 80% is ejected within two beats in the healthy cases (mean ejection fraction and stroke volume equal to 55% and 74 ml, respectively), while this dropped to 20% in the cases with dilated cardiomyopathy (mean ejection fraction and stroke volume equal to 17.8% and 41 ml, respectively). Therefore, the flow after two beats is higher in our case (94.2%). A likely factor leading to this higher value is the high ejection fraction of 67% and stroke volume of 109 ml for this case. Also, the implementation of the MV into the LV mesh limited the opening angle of the valve (to preserve the mesh quality), which may have led to a more energetic incoming jet, generating more swirling flow, and enhancing particle evacuation.

Beyond the study on the torsional effects, we also performed simulations (including torsion) without the MV, well known to have a dramatic impact on intraventricular hemodynamics. Starting from the contours of velocity, vorticity, and WSS, the presence of the mitral valve induced several effects, among which: (i) the formation of the vortical structures at the free edge of the valve instead of the annulus, resulting in a more central position of the vortices with respect to the long axis of the ventricle; (ii) an increased velocity peak of the inlet jet induced by the narrowing of the mitral orifice area; (iii) as a result of the combination of (i) and (ii), the jet and the vortical patterns better penetrate towards the apex, with enhanced local washout, as can be seen by the vorticity and wall shear stress (**Figure 7**). Our findings about the influence of the valve in the flow field agree with the ones of Bavo et al. (17) and Seo et al. (14). In our case, the apical washout was also assessed by releasing the particles in the apical region and computing their residence time with and without the mitral valve (**Figure 6**). In this regard, we found out that the valve enhances the direct flow (67.9% vs. 44.4%) and the particles ejected in two beats (88.9% vs. 71.6%). The presence of the valve also has an impact on the faith of particles released from the inlet. In previous work that did not include the mitral valve, physiological torsion decreased the direct flow and the particles ejected within two beats. Conversely, in the current study, torsion enhances the direct flow and the particles ejected within two beats increase. From a clinical perspective, we strongly believe that the residence time and the velocity distribution of the residing particles provide more significant insights to assess the predisposition to stasis rather than velocity, vorticity, or wall shear stress. Torsion does seem to have an impact on these parameters. It may therefore be safe to consider torsion in patient-specific CFD models, especially when these studies target stasis and residence time. In that context, future studies should also evaluate the impact of the Trabeculae Carneae. This will, however, require more advanced mesh handling methods that can cope with small cavities that compress and expand as the ventricle contracts and relaxes.

Our study has some important limitations. The patient-specific LV model has a limited opening angle of the MV, because of the unforeseen dead zone error of the Chimera technique which forced us to include the MV mesh into the LV mesh. This results in a flow field (peak velocity = 2 m/s) more intense than a typical physiological case, which induces instabilities at the tip of the MV at the E-peak. We also believe that the 8 mm slice thickness of our cine-MRI short-axis imaging dataset considerably limited the accuracy of the segmentation of our patient-specific LV model. Therefore, the proposed workflow should be tested on imaging datasets with higher resolution.

The validation of the proposed model could not be performed at the current stage due to limitations of the medical imaging dataset and the Chimera technique (as implemented in Fluent 2019 R3). The low spatial and temporal resolution of the cine-radial MRI imaging dataset prevented the comparison between the patient-inspired kinematic model of the MV and the cine-radial MRI images. Furthermore, the E-peak velocity of 2 m/s imposed by the limitations of the Chimera technique invalidates a direct comparison between the CFD simulations and 4D flow MRI data.

The mitral valve is not sealed during systole resulting in a gap between the MV leaflets during systole. The on-off (pressure-wall) boundary approach was mainly used because in our simulations the flow is driven by the contraction and dilation of the LV chamber, but also because (theoretically) this would have allowed us to avoid regurgitation across the mitral valve during systole given that the volume of our modeled left atrium is fixed. Nonetheless, the minimal motion of the MV leaflets during systole, as indicated by the decrease of the MV orifice area (visible in **Figure 2**), induces a backflow towards the left ventricle with a peak velocity of 0.4 m/s. Our boundary conditions should be investigated with a new medical imaging dataset that results in a more physiological SV. Furthermore, we could not overcome some important technical difficulties related to the Chimera technique, among which problems with cut-control and insufficient compatibility with the flow solver (e.g., a 2nd order temporal discretization, particles tracking already in Fluent).

The presented model, without turbulence model, can be assumed as a DNS approach able to solve the main large-scale hemodynamic features (such as jets, main vortices, and ejection) scales of the flow field, but it lacks the resolution needed to resolve the smaller flow details. Therefore, much more refined background grids and/or higher order schemes should be further pursued to capture the smaller-scale flow feature of the flow field, transitional flows, and the dissipation of the small scale of the vortices more accurately. Lastly, ventricular torsion was superimposed to the 4D meshes of the LV sac as a global uniform rotation due to the inability to derive this motion component from MRI and CT medical images. A more advanced model that could account for the local variations of the torsional motion might have a relevant impact on our findings.

Finally, only one patient-specific CFD model of the LV has been established. Therefore, caution is warranted to interpret these findings and assess their physiological and clinical relevance. More simulations of physiological and pathological cases are needed to confirm these findings in a sufficient number of cases that is statistically significant. The presented workflow should have the necessary versatility to be applied to both physiological and pathological cases.

Conclusion

In this study, we presented a Chimera-based patient-specific model of the LV coupled with a patient-inspired kinematic model of the MV. We assessed the impact of torsion in the LV fluid dynamics by simulating multiple cardiac cycles with and without physiological torsion. Our results indicate that torsion has a minimal effect on velocity, vorticity, wall shear stress, and energy loss. With the implementation of the mitral valve, torsion enhanced both the direct flow and (minorly) the particles ejected within two beats, while it reduced the motility of the particles. The MV enhanced the propagation of the inlet jet and promoted both the general and apical washout.

Data availability statement

The original contributions presented in the study are included in the article/**Supplementary Material**, further inquiries can be directed to the corresponding author/s.

Ethics statement

The studies involving human participants were reviewed and approved by San Donato Hospital. The patients/participants provided their written informed consent to participate in this study. Written informed consent was obtained from the individual(s) for the publication of any potentially identifiable images or data included in this article.

Author contributions

PS: conceived of the presented idea and outlined the research goal. FC: developed the computational framework and performed the numerical simulations. LD and JD: supported FC in the technical development of the CFD model. AR organized the MRI scans acquisition of the LV and the MV. All authors contributed to the article and approved the submitted version.

Acknowledgments

This work was supported by the European Commission within the Horizon 2020 Framework through the MSCA-ITN-ETN European Training Networks (project number 642458).

Conflict of interest

The authors declare that the research was conducted in the absence of any commercial or financial relationships that could be construed as a potential conflict of interest.

Publisher's note

Supplementary material

The Supplementary Material for this article can be found online at: https://www.frontiersin.org/articles/10.3389/fmedt.2022.1018058/full#supplementary-material.

References

1. World Health Organization. World health organization cardiovascular disease risk charts: revised models to estimate risk in 21 global regions. *Lancet Glob.* (2019) 7(10):e1332–45. doi: 10.1016/S2214-109X(19)30318-3

2. Morris PD, Narracott A, Von Tengg-Kobligk H, Soto DAS, Hsiao S, Lungu A, et al. Computational fluid dynamics modelling in cardiovascular medicine. *Heart.* (2016) 102(1):18–28. doi: 10.1136/heartjnl-2015-308044

3. Domenichini F, Pedrizzetti G. Asymptotic model of fluid–tissue interaction for mitral valve dynamics. *Cardiovasc Eng Technol.* (2015) 6(2):95–104. doi: 10.1007/s13239-014-0201-y

4. Seo JH, Mittal R. Effect of diastolic flow patterns on the function of the left ventricle. *Phys Fluids.* (2013) 25(11):110801. doi: 10.1063/1.4819067

5. Mittal R, Hee J, Vedula V, Choi YJ, Liu H, Huang HH, et al. Computational modeling of cardiac hemodynamics: current status and future outlook. *J Comput Phys.* (2016) 305:1065–82. doi: 10.1016/j.jcp.2015.11.022

6. Doenst T, Spiegel K, Reik M, Markl M, Hennig J, Nitzsche S, et al. Fluid-dynamic modeling of the human left ventricle: methodology and application to surgical ventricular reconstruction. *Ann Thorac Surg.* (2009) 87(4):1187–95. doi: 10.1016/j.athoracsur.2009.01.036

7. Long Q, Merrifield R, Xu XY, Kilner P, Firmin DN, Yang GZ. Subject-specific computational simulation of left ventricular flow based on magnetic resonance imaging. Proceedings of the institution of mechanical engineers. *H J Med Eng*. (2008) 222(4):475–85. doi: 10.1243/09544119JEIM310

8. Watanabe H, Sugiura S, Kafuku H, Hisada T. Multiphysics simulation of left ventricular filling dynamics using fluid-structure interaction finite element method. *Biophys J*. (2004) 87(3):2074–85. doi: 10.1529/biophysj.103.035840

9. Krittian S, Janoske U, Oertel H, Böhlke T. Partitioned fluid–solid coupling for cardiovascular blood flow. *Ann Biomed Eng*. (2010) 38(4):1426–41. doi: 10.1007/s10439-009-9895-7

10. Schenkel T, Malve M, Reik M, Markl M, Jung B, Oertel H. MRI-based CFD analysis of flow in a human left ventricle: methodology and application to a healthy heart. *Ann Biomed Eng*. (2009) 37(3):503–15. doi: 10.1007/s10439-008-9627-4

11. Chnafa C, Mendez S, Nicoud F. Image-based large-eddy simulation in a realistic left heart. *Comput Fluids*. (2014) 94:173–87. doi: 10.1016/j.compfluid.2014.01.030

12. Chnafa C, Mendez S, Nicoud F. Image-based simulations show important flow fluctuations in a normal left ventricle: what could be the implications? *Ann Biomed Eng*. (2016) 44(11):3346–58. doi: 10.1007/s10439-016-1614-6

13. Chnafa C, Mendez S, Moreno R, Nicoud F. Using image-based CFD to investigate the intracardiac turbulence. *Modeling Simul Appl*. (2015) 14 (November):113–7. doi: 10.1007/978-3-319-05230-4_4

14. Seo JH, Vedula V, Abraham T, Lardo AC, Dawoud F, Luo H, et al. Effect of the mitral valve on diastolic flow patterns. *Phys Fluids*. (2014) 26(12) 1.4904094. doi: 10.1063/1.4904094

15. Ranganathan N, Lam JH, Wigle ED, Silver MD. Morphology of the human mitral valve. II. the Value Leaflets. *Circ*. (1970) 41(3):459–67. doi: 10.1161/01.CIR.41.3.459

16. Mihalef V, Ionasec RI, Sharma P, Georgescu B, Voigt I, Suehling M, et al. Patient-specific modelling of whole heart anatomy, dynamics and haemodynamics from four-dimensional cardiac CT images. *Interface Focus*. (2011) 1(3):286–96. doi: 10.1098/rsfs.2010.0036

17. Bavo AM, Pouch AM, Degroote J, Vierendeels J, Gorman JH, Gorman RC, et al. Patient-specific CFD simulation of intraventricular haemodynamics based on 3D ultrasound imaging. *Biomed Eng Online*. (2016) 15(1):107. doi: 10.1186/s12938-016-0231-9

18. Ma X, Gao H, Griffith BE, Berry C, Luo X. Image-based fluid-structure interaction model of the human mitral valve. *Comput Fluids*. (2013) 71:417–25. doi: 10.1016/j.compfluid.2012.10.025

19. Su B, Zhong L, Wang XK, Zhang JM, Tan RS, Allen JC, et al. Numerical simulation of patient-specific left ventricular model with both mitral and aortic valves by FSI approach. *Comput Methods Prog Bio*. (2014) 113(2):474–82. doi: 10.1016/j.cmpb.2013.11.009

20. Govindarajan V, Mousel J, Udaykumar HS, Vigmostad SC, McPherson DD, Kim H, et al. Synergy between diastolic mitral valve function and left ventricular flow AIDS in valve closure and blood transport during systole. *Sci Rep*. (2018) 8 (1):1–14. doi: 10.1038/s41598-018-24469-x

21. Gao H, Feng L, Qi N, Berry C, Griffith BE, Luo X. A coupled mitral valve — left ventricle model with fluid – structure interaction. *Med. Eng. Phys*. (2017) 47:128–36. doi: 10.1016/j.medengphy.2017.06.042

22. Caballero A, Mao W, McKay R, Sun W. Transapical mitral valve repair with neochordae implantation: fSI analysis of neochordae number and complexity of leaflet prolapse. *Int J Numer Method Biomed Eng*. (2020) 36(3):1–16. doi: 10.1002/cnm.3297

23. Caballero A, McKay R, Sun W. Computer simulations of transapical mitral valve repair with neochordae implantation: clinical implications. *JTCVS Open*. (2020) 3(C):27–44. doi: 10.1016/j.xjon.2020.05.010

24. Biffi B, Gritti M, Grasso A, Milano EG, Fontana M, Alkareef H, et al. A workflow for patient-specific fluid – structure interaction analysis of the mitral valve: A proof of concept on a mitral regurgitation case. 2019;(xxxx).

25. Mao W, Caballero A, McKay R, Primiano C, Sun W. Fully-coupled fluid-structure interaction simulation of the aortic and mitral valves in a realistic 3D left ventricle model. *PLoS One*. (2017) 12(9):e0184729. doi: 10.1371/journal.pone.0184729

26. Al-azawy MG, Turan A, Revell A. *An overset mesh approach for valve closure: an LVAD application. Proceedings of the 9th international joint conference on biomedical engineering systems and technologies (BIOSTEC 2016)* (2016).1(Biostec):145–51.

27. Canè F, Verhegghe B, De Beule M, Bertrand PB, Van Der Geest RJ, Segers P, et al. *From 4D medical images (CT, MRI, and ultrasound) to 4D structured mesh models of the left ventricular endocardium for patient-specific simulations. Biomed research international* (2018).

28. Canè F, Selmi M, De Santis G, Redaelli A, Segers P, Degroote J. Mixed impact of torsion on LV hemodynamics: a CFD study based on the chimera technique. *Comput Biol Med*. (2019) 112(July):103363. doi: 10.1016/j.compbiomed.2019.103363

29. Vasudevan V, Wiputra H, Yap CH. Torsional motion of the left ventricle does not affect ventricular fluid dynamics of both foetal and adult hearts. *J Biomech*. (2019) 96:109357. doi: 10.1016/j.jbiomech.2019.109357

30. Bavo AM, Pouch AM, Degroote J, Vierendeels J, Gorman JH, Gorman RC, et al. Patient-specific CFD models for intraventricular flow analysis from 3D ultrasound imaging: comparison of three clinical cases. *J Biomech*. (2017) 50:144–50. doi: 10.1016/j.jbiomech.2016.11.039

31. Mangual JO, Kraigher-krainer E, De LA, Toncelli L, Shah A, Solomon S, et al. Comparative numerical study on left ventricular fluid dynamics after dilated cardiomyopathy. *J Biomech*. (2013) 46(10):1611–7. doi: 10.1016/j.jbiomech.2013.04.012

32. Stewart SFC, Hariharan P, Paterson EG, Burgreen GW, Reddy V, Day SW, et al. Results of FDA's first interlaboratory computational study of a nozzle with a sudden contraction and conical diffuser. *Cardiovasc Eng Technol*. (2013) 4 (4):374–91. doi: 10.1007/s13239-013-0166-2

33. Malinauskas RA, Hariharan P, Day SW, Herbertson LH, Buesen M, Steinseifer U, et al. FDA benchmark medical device flow models for CFD validation. *ASAIO Journal*. (2017) 63:150–60. doi: 10.1097/MAT.0000000000000499

34. Kunzelman KS, Cochran RP, Verrier ED, Eberhart RC. Anatomic basis for mitral valve modelling. *J. Heart Valve Dis*. (1994) 3(5):491–6

frontiers | Frontiers in Cardiovascular Medicine

TYPE Original Research
PUBLISHED 05 January 2023
DOI 10.3389/fcvm.2022.1040053

OPEN ACCESS

EDITED BY
Selene Pirola,
Delft University of Technology,
Netherlands

REVIEWED BY
Simone Saitta,
Politecnico di Milano, Italy
Stephane Avril,
Institut Mines-Télécom, France

*CORRESPONDENCE
Atefeh Abdolmanafi
✉ atefehabdolmanafi@vitaamedical.com

SPECIALTY SECTION
This article was submitted to Cardiovascular Imaging, a section of the journal Frontiers in Cardiovascular Medicine

RECEIVED 08 September 2022
ACCEPTED 28 November 2022
PUBLISHED 05 January 2023

CITATION
Abdolmanafi A, Forneris A, Moore RD and Di Martino ES (2023) Deep-learning method for fully automatic segmentation of the abdominal aortic aneurysm from computed tomography imaging. *Front. Cardiovasc. Med.* 9:1040053. doi: 10.3389/fcvm.2022.1040053

Deep-learning method for fully automatic segmentation of the abdominal aortic aneurysm from computed tomography imaging

Atefeh Abdolmanafi[1]*, Arianna Forneris[1,2], Randy D. Moore[1,3] and Elena S. Di Martino[1,2]

[1]R&D Department, ViTAA Medical Solutions, Montreal, QC, Canada, [2]Department of Biomedical Engineering, Schulich School of Engineering, University of Calgary, Calgary, AB, Canada, [3]Division of Vascular Surgery, University of Calgary, Calgary, AB, Canada

Abdominal aortic aneurysm (AAA) is one of the leading causes of death worldwide. AAAs often remain asymptomatic until they are either close to rupturing or they cause pressure to the spine and/or other organs. Fast progression has been linked to future clinical outcomes. Therefore, a reliable and efficient system to quantify geometric properties and growth will enable better clinical prognoses for aneurysms. Different imaging systems can be used to locate and characterize an aneurysm; computed tomography (CT) is the modality of choice in many clinical centers to monitor later stages of the disease and plan surgical treatment. The lack of accurate and automated techniques to segment the outer wall and lumen of the aneurysm results in either simplified measurements that focus on few salient features or time-consuming segmentation affected by high inter- and intra-operator variability. To overcome these limitations, we propose a model for segmenting AAA tissues automatically by using a trained deep learning-based approach. The model is composed of three different steps starting with the extraction of the aorta and iliac arteries followed by the detection of the lumen and other AAA tissues. The results of the automated segmentation demonstrate very good agreement when compared to manual segmentation performed by an expert.

KEYWORDS

abdominal aortic aneurysm, computed tomography imaging, deep learning, medical image analysis, tissue characterization

1. Introduction

Abdominal aortic aneurysm (AAA) is defined as a focal dilation of the aorta where the maximum diameter exceeds the normal diameter by at least 1.5 times (1). When not diagnosed and treated, an aneurysm may continue to enlarge until it ruptures, resulting in significant mortality and morbidity (2). AAA is accompanied by the alteration of the major structural proteins (elastin and collagen) in the aortic wall, which results in irreversible enlargement and loss of structural integrity. The majority of aneurysms are characterized by the presence of intraluminal thrombus (ILT), which is associated

with hypoxia and is a locus of inflammatory processes that contribute to arterial wall weakening and growth (1–3). Calcification is often present in AAAs and is recognized as one of the factors contributing to the progression of aneurysmal disease through local stiffening and stress concentration (4, 5).

The presence of an aneurysm and its progression are normally assessed using CT imaging. Figure 1 shows an axial image from a CT scan of the abdomen of a patient. The aorta, a small fraction of the whole image, is located anteriorly to the spinal column and is composed of the wall, lumen, ILT, and calcification. The adoption of a three-dimensional assessment of the aorta is limited by the lack of standardized automated segmentation tools for the aorta, in particular for the aortic wall (6).

Several traditional machine-learning methods have been proposed to segment the different surfaces and volumes comprising the aneurysm, including the wall-to-lumen/thrombus interface and the lumen volume. Applications have included graph cut theory (7, 8), intensity- and gradient-based segmentation approaches (9), and variable neighborhood search (10). Many studies have focused on identifying the ILT as the wall-to-ILT surface is difficult to segment due to similarities in the image intensity with neighboring structures. The ILT was segmented using a trained deep convolutional neural network (CNN) on post-operative CT images by López-Linares et al. (11). A level set method was applied to detect the ILT and the outer wall boundary by Zohios et al. (12). A segmentation of the lumen and ILT was also achieved using an active contour approach by Lareyre et al. (13). A semi-automatic interactive image segmentation method was proposed by Maiora et al. (14) to detect the aorta. In this approach, the gray level co-occurrence matrix (GLCM) and the local binary patterns were used as features to train a random forest classifier. An intensity-based approach followed by neural networks was used to detect the lumen and wall contours by Shum et al. (15). Another contour-based segmentation approach to extract the aorta was proposed by Drapikowski and Domagala (16). An interactive segmentation model based on active shape was developed to extract the AAA tissues after manual segmentation of the first slice of the CT stack by de Bruijne et al. (17). A semi-automatic, interactive image segmentation model was also proposed by Maiora et al. (18) to detect lumen and ILT.

One recurring feature of published methods to segment the aortic wall is the need for some user intervention (semi-automated methods). Another commonality is the use of pre-processing steps, often used to define thresholds. These methods lack generality due to the possible inconsistencies between operators and the considerable geometrical and structural variability among different patients' aneurysms.

More recently, convolutional neural networks have been proposed for AAA segmentation from CT images (19–23). CNNs are very good feature extractors and good classifiers to discriminate between various extracted tissues, but they are not recommended for detecting and segmenting different tissues.

Finally, there are a few published examples of deep convolutional neural networks to segment the aorta, for example, the work by López-Linares et al. (24). In another recent study, thrombus segmentation using a region-based convolutional neural network was performed by Hwang et al. (25). A thrombus segmentation model followed by lumen segmentation using a U-net was proposed by Brutti et al. (26). Most of these recent studies approach the segmentation by directly segmenting the thrombus first. The ILT has a very irregular morphology and inconsistent tissue properties that vary considerably from patient to patient and even within one patient. Therefore, starting the segmentation directly by detecting the thrombus, results in training the model on very inconsistent features.

This study proposes a fully automatic segmentation model to segment the whole AAA. The model first detects the "aorta" as a whole, including the aortic wall, ILT, lumen, and calcification, and masks the original image to remove all surrounding similar organs and structures for more precise wall segmentation. This allows the subsequent networks to concentrate on identifying the wall, ILT, lumen, and calcification within an image that comprises only the aorta.

2. Materials and methods

For the purpose of this article, the ROI was defined as the abdominal aorta including wall, lumen, ILT, and calcification from the celiac artery to the common iliac arteries, and the external and internal iliac arteries. The proposed model is composed of four trained networks. The first network receives the original CT image to detect and extract the ROI including the abdominal aorta and iliac arteries. Histogram equalization was performed on the input images to ensure that the trained model will be generalized to CT images from different CT scanners. The output of the first network is received by the second network to detect and extract the lumen. By extracting the lumen from the ROI, the remaining tissue is a combination of wall and ILT (ILT/wall). The third network receives the extracted ILT/wall and categorizes it slice-by-slice as calcified if any calcification is detected. Otherwise, the ILT/wall is categorized as non-calcified (Figure 2). A final fourth network was trained separately for landmark detection. This network receives the original CT image to detect and extract the ROI including the abdominal aorta, iliac, celiac, and renal arteries. The celiac and renal arteries are considered landmarks. The model architecture and segmentation steps are shown in Figure 2.

Experiments were performed according to the following steps: 1. Designing the model. 2. Fine-tuning and transfer

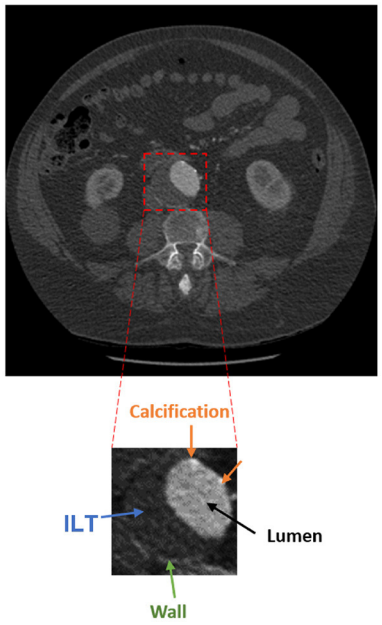

FIGURE 1
Axial acquisition of an abdominal CT scan showing an AAA. The aorta is a small fraction of the whole image and is composed of the lumen (black), ILT (blue), wall (green), and calcification (orange).

learning to adapt a pre-trained network to our segmentation problem. 3. Training and validation of the networks at each step of the model. 4. Evaluating the performance of the final trained model on a set of 19 new patients that were not involved in any of the training, validation, and test sets. 5. Selecting two challenging cases and evaluating the performance of the final model on challenging cases. 6. Evaluating the performance of the proposed segmentation model on an external cohort of patients from a different institution. All the experiments were performed in MATLAB R2021b.

2.1. Data collection

The experiments were performed on 6030 CT slices from abdominal CT scans obtained from 56 different patients with AAA. Image acquisition was performed at the Peter Lougheed Centre in Calgary, Alberta, Canada.

The studies involving human participants were reviewed and approved by the Conjoint Health Research Ethics Board (CHREB), University of Calgary. Written informed consent to participate in this study was provided by the patient/participants.

The imaging protocol consisted of retrospectively gated multi-phase CT angiography (64-row helical GE Medical System CT scanner) with variable radiation dose to capture the R-R interval, with spatial resolution of approximately $0.7 \times 0.7 \times 2.0$ mm. Notably, some scans had lower or higher image resolution varying from $0.6 \times 0.6 \times 2$ mm to $0.9 \times 0.9 \times 2$ mm. Gantry rotation time was equal to 0.35 s. Inclusion criteria were patients with diagnosed AAA from 2016 to 2020, aged 18+, and no prior aortic surgery.

We evaluated the generalizability of the algorithm performance on CT images obtained from 19 different patients that were not included in any of the training, validation, and test sets. This dataset had the same inclusion criteria.

As an external validation, we evaluated the performance of our proposed segmentation model on CT images obtained from six AAA patients with imaging performed at a different center. The images were collected from Centre hospitalier de l'Université de Montréal (CHUM) using TOSHIBA CT scanner with a spatial resolution of 0.8 x 0.8 x 0.8 mm.

Due to the retrospective nature of the study, we have demographic information only on a subset of 47 patients. The mean age±standard deviation is 77.4 ± 8.0. Also, five out of 47 patients are female.

All data were annotated by an expert operator using the commercial segmentation software Simpleware (Simpleware ScanIP, R-2020.09). On a subset of 10 patients, the manual annotations were validated pixel-by-pixel by an experienced vascular radiologist. The segmentation accuracy was deemed acceptable by the radiologist to be used as ground truth. To further verify the quality of the expert operator segmentation, an additional operator was trained, and inter-operator variability was quantified by comparing the masks obtained by the two on 19 patients.

2.2. Detection and extraction of the ROI

Inspired by the study of Chen et al. (27), we employed a Resnet-based fully convolutional network (FCN) with dilated convolutions. This network, an encoder–decoder with dilated convolution based on ResNet-18 architecture, was used as a pre-trained network. The model was developed in two steps: design of the model and transfer learning. First, we trained the model in different steps by detecting the ROI, which is the whole aortic structure including a combination of the aortic wall, ILT, lumen, and calcification. This way, the model searches for a combination of the aortic wall, lumen, ILT, and calcification as an extra feature, which helps remove all surrounding structures and organs with almost the same gray-scale level as the aortic wall. As a consequence, in the next steps, all other tissues including ILT, wall, and lumen can be segmented more accurately. Transfer learning and fine-tuning were performed by initializing the weights of the networks at each step by the weights of the pre-trained network and finding the optimal learning parameters. Each network is composed of stacked complex building blocks, each consisting of a combination of

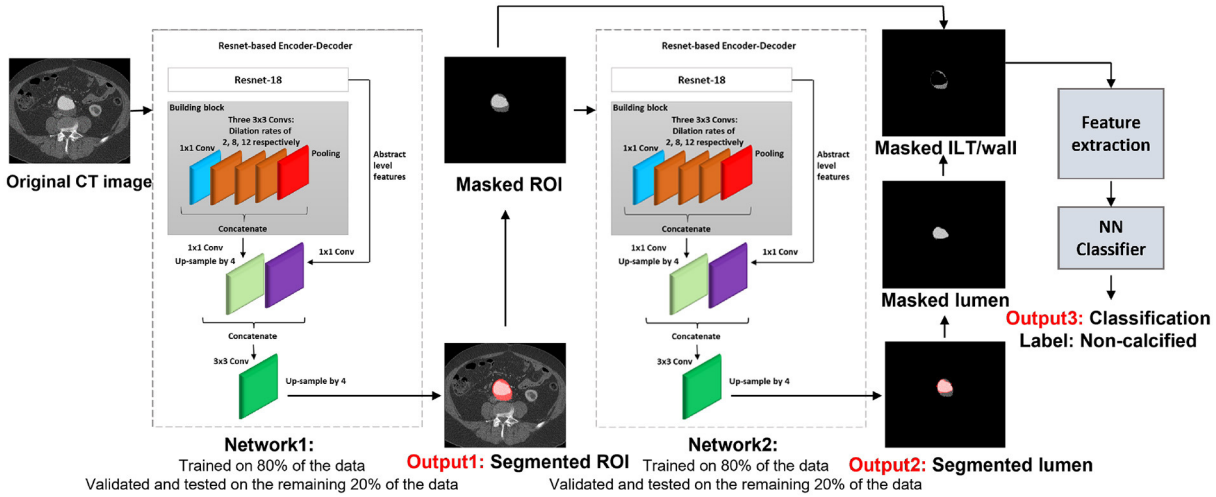

FIGURE 2
Visual representation of the network architecture and output for AAA tissue segmentation.

convolutional layers with kernel sizes of 1×1 and 3×3. The output features from each building block are concatenated into a single vector, which is the input of the next block. 1×1 convolutions were used for dimensionality reduction. The factorization of convolutions into small convolutions reduced the number of parameters as well as the computational cost while maintaining high efficiency. Dilated convolutions were used instead of standard convolutions for a larger field of view with the same computational cost, stride, and number of parameters as the standard convolution. This resulted in denser output features and higher segmentation performance. Dilated convolution was applied as follows:

$$y[i] = \Sigma_k x[i + r.k]w(k) \quad (1)$$

where x is the input feature map and y is the output feature map. Dilated convolution was applied with a convolutional filter w over the input feature map x at each location i of the output feature map y for dimensionality reduction and providing a larger field of view.

We started fine-tuning from deeper network layers using grid searching for an extensive interval of values. Upper layers in the network architecture are responsible to extract more generic features of the images such as edges, borders, and shapes, which are common attributes in various applications. Caution was taken to allay over-fitting concerns in consideration of our small patient data set. The weights of all other layers remained constant by forcing the learning rates to zero for those layers. The learning process was performed using Adam as the model optimization algorithm. The optimization algorithm is used to minimize the loss function. The most important learning parameter that controls the adjustment of the model according to the updated weights at each iteration is the learning rate. The scheduling rate controls the learning rate at the end of each epoch according to the behavior of the learning curves and model convergence. In fast model convergence, the scheduling rate can be decreased after a few epochs but in slow convergence, a larger scheduling rate is required. Momentum is another parameter to be considered. Momentum is responsible to control the step sizes, while the optimization algorithm is searching for the global minimum. Small values of momentum may result in sub-optimal results since the algorithm can reach a local minimum by taking a small searching step and incorrectly consider it as the global minimum. The optimal learning parameters were obtained by evaluating the model performance on the validation set for each assigned value. The optimal learning parameter was determined to be 0.02. The momentum and scheduling rate were assigned as 0.8 and 0.9 at each step of the fine-tuning. The dilation rate was assigned as 2 and 4 for the last two blocks. An up-sampling factor of 4 was assigned to the decoder to up-sample the encoder output. The output of the decoder was combined with the low-level features after applying 1 x 1 convolution. The ROI was labeled as the first class and all the other surrounding tissues and the image background were labeled as the second class. Since the ROI is a small fraction of the whole image, we considered weighted loss functions. The performance of the network was evaluated by using both weighted cross-entropy and weighted generalized dice as loss functions. Weighted cross-entropy demonstrated better performance with the weight defined as follows:

$$w = (N - \Sigma_n p_n)/\Sigma_n p_n \quad (2)$$

where N is the number of images annotated as foreground with predicted probabilistic map elements p_n. Adam network

optimizer was applied with L2 regularization of 0.0005, mini-batch size of 8, and validation patience of 6. The dataset was split into training, validation, and test sets. A total of 80% of the data was randomly selected for training, and the remaining 20% was split into two for validation and test sets. To avoid any bias, we ensured that there was no overlap between the three datasets. To validate the performance of the model on new patients' data, leave-one-out cross-validation was performed by leaving one patient data as the validation set and training the model on the data of all the other patients. This process was repeated 32 times for a subset of 32 different patients used in this study. To evaluate the results, at each step of the work, we measured the per-class accuracy, sensitivity, specificity, BF-score, and intersection-over-union (IoU) score based on the obtained confusion matrix as follows:

$$Accuracy = \frac{TP + TN}{TP + TN + FP + FN} \tag{3}$$

$$Sensitivity = \frac{TP}{TP + FN} \tag{4}$$

$$Specificity = \frac{TN}{TN + FP} \tag{5}$$

$$Precision = \frac{TP}{TP + FP} \tag{6}$$

$$BFscore = \frac{2 \times Precision \times Sensitivity}{Precision + Sensitivity} \tag{7}$$

$$IoUscore = \frac{TP}{TP + FP + FN} \tag{8}$$

where TP, FP, FN, and TN are true positive, false positive, false negative, and true negative, respectively, for each patient.

2.3. Lumen, wall, and calcification detection

In this step, we segmented and extracted the lumen from the ROI. By extracting the lumen from the ROI, the remaining tissues are a combination of ILT and wall (ILT/wall). The same configuration of Resnet-based FCN was adapted in this step for lumen segmentation. The output of the previous step (extracted ROI including the whole aortic structure) was fed into the network for further processing to detect and extract the lumen. The lumen and the image background were labeled as the foreground and background, respectively, to train the model. A total of 80% of the data was used as the training set, and the remaining 20% was split into the validation and test sets. The results were validated by measuring the per-class accuracy, sensitivity, specificity, BF-score, and IoU-score using the obtained confusion matrix. Leave-one-out cross-validation was performed, and the process was repeated 32 times for a sub-set of 32 different patients used in this study.

In the next step, we evaluated the extracted ILT/wall to discriminate between calcified and non-calcified regions. Since calcification may not occur in all images, it is not efficient to train an FCN with a small number of images to detect calcification. With the existing dataset, we chose to discriminate between calcified and non-calcified ILT/walls by extracting deep features from all the extracted ILT/walls and training a classifier to consider the similarity between deep features and classify the calcified vs. non-calcified slices. Deep features are apt to describe various tissues and are strong discriminators. In CNN, the defined filter at each convolutional layer is responsible to move along the whole image with a defined stride and create a feature map. The upper layers of the network are responsible to extract abstract-level image information such as borders, shapes, and corners, while deeper layers are responsible to extract detailed image information such as complex texture features. A combination of a CNN as a feature extractor and a feed forward neural network as the classifier was applied. All the extracted ILT/walls were labeled manually as calcified or non-calcified. To be consistent in using the networks, we used features from the ILT/walls that were detected and extracted in the previous step. The extracted deep features were fed to a feed-forward neural network with 479 hidden layer neurons, which acts as the classifier. To find the optimal hidden size for the network, we evaluated the performance of the network for an extensive interval of hidden size values from 100 to 500. The training process was based on the scaled conjugate gradient method, while the parameter Sigma estimates the weight change for the second derivative approximation. To obtain the optimal value of Sigma, the performance of the classifier was evaluated by assigning various values from 0.0001 to 0.01. The highest performance of the network was obtained for the value of 0.085. The training was performed for 1,153 epochs, with a maximum validation failure of 191. For the number of epochs and validation failures, the performance of the network was evaluated for values ranging from 1 to 2,500 and 0 to 500, respectively.

2.4. Landmark detection

For added generality, we decided to perform the landmark detection separately from the rest of the structures in the aorta. The location of celiac and iliac arteries were considered as landmarks. Automated segmentation lends itself to be used successfully in accurately determining changes from baseline to follow-ups if appropriate landmarks are identified and labeled to ensure that the same segments of the aorta are evaluated for both baseline and follow-up. In addition, the renal artery was also included as a landmark because it is used by clinicians

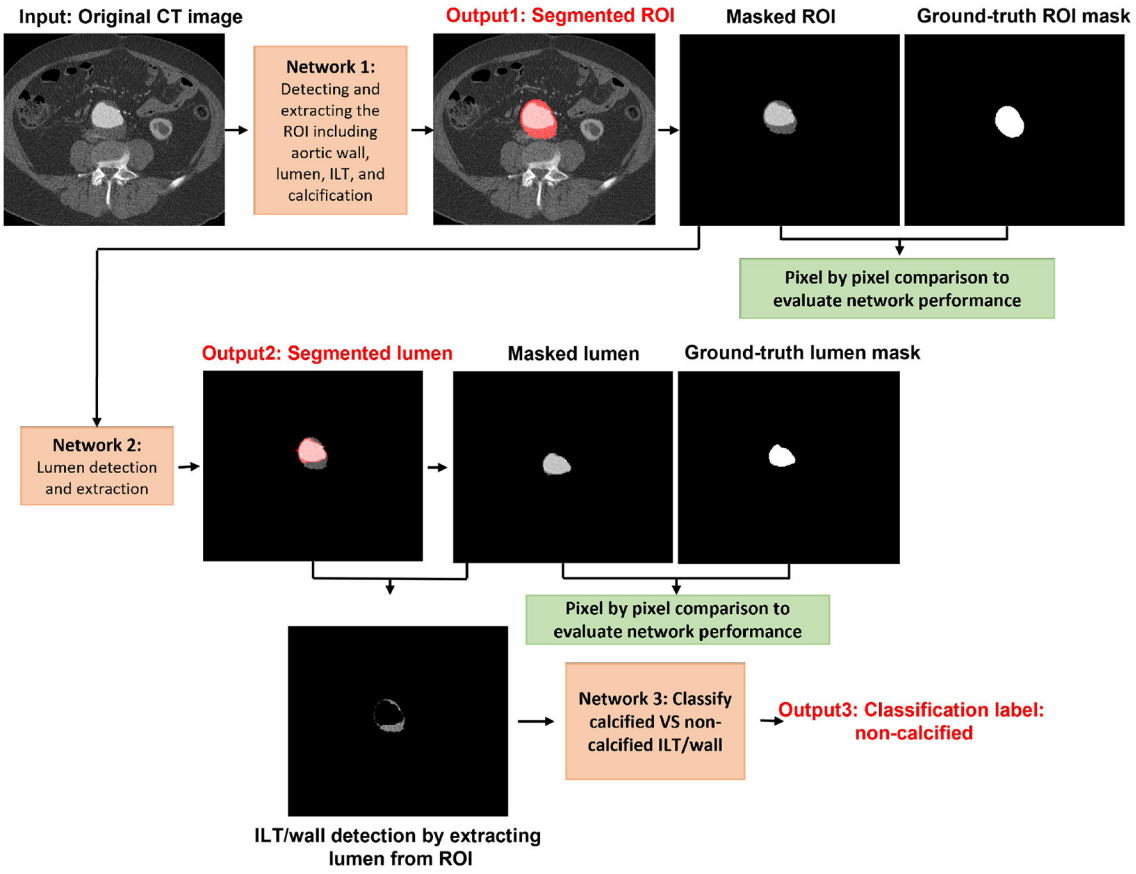

FIGURE 3
Visual representation of each network output for segmenting the ROI including the abdominal aorta, lumen, ILT, and wall. Calcification accumulation in ILT and wall was determined in the final step.

when planning surgical repair. To detect landmarks, the same configuration of the first network was trained to segment the aorta, iliac, celiac, and renal arteries as the ROI. Eighty percent of the data was selected randomly as a training set, and the remaining 20% of data was split equally into validation and test sets. We ensured that there was no overlap between any of the training, validation, and test sets. To evaluate the landmark network performance, the output of the network was compared against the ground truth by measuring accuracy, sensitivity, specificity, BF-score, and IoU-score on the test set.

3. Results

In the first step of the model, we segmented and extracted the ROI including the abdominal aorta and iliac arteries using a Resnet-based FCN (Figure 3). The measured per-class accuracy, sensitivity, specificity, BF-score, and IoU-score for the extraction of the ROI are shown in Table 1. Leave-one-out cross-validation was performed by leaving one patient data as the validation set and training the model on the data of all the other patients. The measured accuracy over all 32 patients was obtained as 0.94 $\pm$ 0.04. A network with the same configuration was trained in the second step to detect the lumen from the extracted ROIs (Figure 3). The measured accuracy, sensitivity, specificity, BF-score, and IoU-score for lumen extraction are shown in Table 1. At this step, leave-one-out cross-validation was performed, for a sub-set of 32 different patients used in this study. The measured accuracy over all 32 patients was obtained as 0.95 $\pm$ 0.03. Finally, a neural network was trained to classify the ILT/walls as calcified or non-calcified (Figure 3). The results are shown in Table 2.

The results of landmark detection are shown in Table 1 and Figure 4. The final 3D reconstruction was performed in Simpleware (Synopsis) following the extracted ROIs for four different patients using our proposed automatic segmentation algorithm (Figure 5) only to visualize the results of our proposed segmentation model in 3D.

After preparing the network architecture and finding the optimal parameters and training options, the performance

TABLE 1 Measured accuracy, sensitivity, specificity, BF-score, and IoU-score to evaluate the performance of the segmentation model.

Tissues under review	Accuracy	Sensitivity	Specificity	BF-Score	IoU-Score
Aorta	0.99 ± 0.01	0.98 ± 0.02	0.99 ± 0.01	0.97 ± 0.03	0.98 ± 0.02
Lumen	0.98 ± 0.01	0.97 ± 0.03	0.99 ± 0.01	0.99 ± 0.01	0.97 ± 0.03
Landmark	0.99 ± 0.01	0.97 ± 0.03	0.99 ± 0.01	0.98 ± 0.02	0.97 ± 0.03

TABLE 2 Measured accuracy, sensitivity, and specificity for the classification of calcified vs. non-calcified ILT/wall.

Tissues under review	Accuracy	Sensitivity	Specificity
Calcified ILT/wall	0.91	0.91	0.90
Non-calcified ILT/wall	0.85	0.81	0.90

of the final trained networks was evaluated on 19 different patients with AAA. These patients were never introduced to the trained networks. They were not included in any of the training, test, or validation sets and were used solely to evaluate the generalizability of the proposed model. Measured accuracy, sensitivity, specificity, BF-score, and IoU-score of all 19 patients are shown in Table 3. In these 19 patients, we selected two challenging cases to report the model performance. Patients 1 and 2 were considered challenging cases. Patient 1 presented a very tortuous aorta. This tortuosity created a visual artifact in the axial CT acquisition and resulted in a select number of images presenting two lumens in the middle portion of the aorta. The iliac bifurcation for patient 2 also presented some tortuosity, with the two iliac arteries developing mostly in a horizontal direction with respect to the acquisition plane instead of the longitudinal direction. Therefore, the iliac arteries of this patient did not appear as circular but as structures elongated in the acquisition plane. The CT images of these two challenging cases were used as the input of each trained network. The mean and standard deviation of the accuracy, sensitivity, specificity, BF-score, and IoU-score were measured for each patient separately. The results are shown in Tables 4–6.

We also evaluated the performance of the segmentation model on an external cohort. The images were collected from a different center and CT scanner that were never introduced to the network and were not included in any of the training, test, or validation sets. The results are shown in Table 7.

Results of inter-operator variability are shown in Table 8. This comparison was performed by comparing the masks created by two expert operators.

4. Discussion

In this study, we proposed a fully automatic model to segment the whole AAA. The following considerations were taken into account in designing the model to improve the existing limitations of recent studies. Most of the recent articles started by training a deep learning model to segment and extract the ILT/wall as a first step (24–26). The ILT is a complex tissue with highly inconsistent properties. It is highly variable among patients not only as a result of patient variability but also as a result of the stage of disease progression and thrombus formation. Furthermore, within the same patient we may have ILT exhibiting different features (more or less porous, more or less calcified) depending on how the ILT is responding and adapting to the regional environment and also depending on the deposition and formation stage of the thrombus. In addition, the aorta is a small subset of an abdominal CT scan image and many of the structures in view have similar intensities. For this reason, the direct segmentation of the ILT/wall is challenging and increases the need to include pre-processing steps. We overcame this limitation by proposing a model which segments and extracts the aorta including ILT/wall and lumen in two main steps: 1. Segmenting and extracting the whole aortic structure as the ROI in the first step. To achieve this, in addition to the extracted deep features from the ROI, we introduced an extra feature to the network to look for the whole aortic structure as a combination of the aortic wall, ILT, lumen, and calcification. The early detection and extraction of the ROI removes all the surrounding organs and structures resulting in precise and accurate detection of the ILT/wall and lumen in the next step. 2. Training the second network to receive the extracted ROI as the input and recognize the lumen in the ROI. Once the lumen is segmented and extracted from the ROI, the remaining tissue is the ILT/wall.

The use of pre-processing steps for AAA images can lead to problems due to the variations in the background at different levels along the abdomen. Most pre-processing methods are based on filtering and defining specific thresholds, which cannot be generalized to a variety of CT acquisitions (8–11, 13, 19, 20, 22–24, 28, 29). Our only pre-processing step is histogram equalization to ensure that the proposed segmentation model can be applicable to different CT scanners.

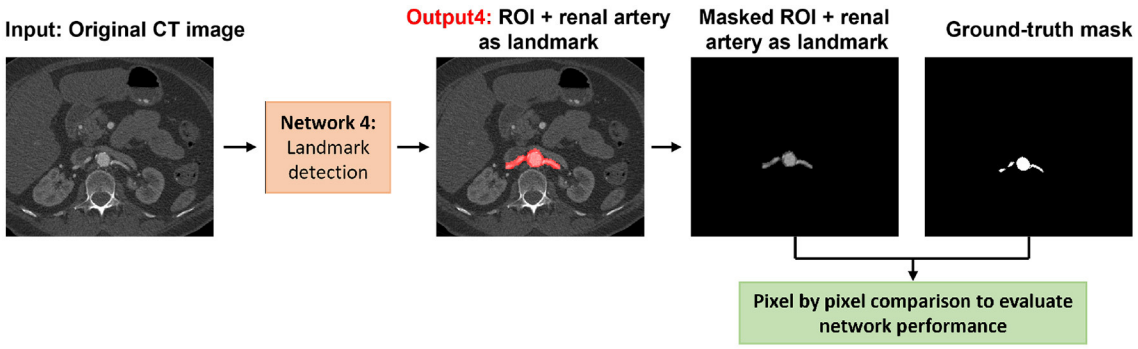

FIGURE 4
Visual representation of the landmark detection including the detection of the aorta, iliac, celiac, and renal arteries.

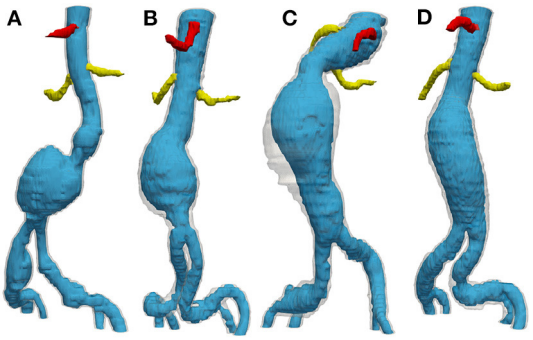

FIGURE 5
3D reconstruction obtained from the results of the automatic segmentation model for four different patients **(A–D)**. For each patient, the lumen is visualized in blue, the aortic ILT/wall is transparent, while the celiac and renal arteries are shown in red and yellow, respectively.

One of the improvements of our approach with respect to many prior studies is that it does not employ patch-based segmentation using CNNs (19–24). In a CNN-patch-based segmentation, the patches will overlap in order to analyze all the pixels, resulting in a redundant feature extraction which is computationally expensive and time-consuming. Moreover, since the input size is fixed in CNNS, the patch size needs to be adapted to it.

Fully convolutional networks can overcome the limitations of patch-based segmentation using CNNs. FCNs can be trained on a smaller number of images with higher pixel-wise segmentation precision. In FCNs, the pooling operators are replaced by up-sampling operators to enhance the output resolution. An arbitrary image size can be fed to the network since there is no fully connected layer involved in the network architecture and the network is trained end-to-end, pixel-to-pixel to optimize the process for accurate segmentation. One of the clearest advantages is that extensive pre-processing is not necessary when using FCNs. Another advantage of our method with respect to existing FCN studies (24–26) is the automatic extraction of the ROI using semantic segmentation, which greatly simplified the subsequent steps of segmenting the structures inside the aorta.

One of the main limitations of this study is the use of 2D segmentation, which may cause inconsistencies between two adjacent slices. To address the limitations of our proposed model, we plan on implementing a 3D version of the networks, once a sufficient number of patients is available. Future improvements can also be achieved by training on more data from different CT scanners and different institutions.

A possible future advantage of using a fully automatic segmentation model is to eliminate the need for a contrast agent during CT angiography imaging since the detection of the AAA tissues is not done visually. The automatic model can detect various tissues by recognizing their features including shape, borders, and detailed texture instead of relying mainly on differences in pixel intensities.

5. Conclusion

This study was focused on developing an automatic deep learning-based segmentation model for the segmentation of the whole AAA, including the wall, lumen, ILT, and calcification in the aorta and iliac arteries. The proposed model overcomes many existing limitations of automated segmentation models by introducing a first step of detecting and extracting the full aortic structure from the image. Future studies will focus on extending the fully automatic segmentation model to cover other aortic diseases including thoracic AA and dissections.

TABLE 3 Measured accuracy, sensitivity, specificity, BF-score, and IoU-score to evaluate the model performance on 19 different patients, which were not included in any of the training, test, and validation sets and were only used for algorithm verification.

Tissues under review	Accuracy	Sensitivity	Specificity	BF-Score	IoU-Score
Aorta	0.94 ± 0.06	0.88 ± 0.09	0.99 ± 0.01	0.92 ± 0.08	0.88 ± 0.09
Lumen	0.96 ± 0.04	0.92 ± 0.08	0.99 ± 0.01	0.93 ± 0.07	0.92 ± 0.08
Landmark	0.92 ± 0.06	0.84 ± 0.10	0.99 ± 0.01	0.86 ± 0.09	0.84 ± 0.09

We reported mean (±) std of measured accuracies, sensitivities, specificities, BF-scores, and IoU-scores in all 19 patients.

TABLE 4 Measured accuracy, sensitivity, specificity, BF-score, and IoU-score for the detection of the aorta in CT images of the two challenging cases.

Patients	Aorta accuracy	Aorta sensitivity	Aorta specificity	Aorta BF-score	Aorta IoU-score
Patient1	0.98 ± 0.02	0.95 ± 0.05	0.99 ± 0.01	0.92 ± 0.08	0.95 ± 0.05
Patient2	0.96 ± 0.04	0.91 ± 0.09	0.99 ± 0.01	0.89 ± 0.09	0.91 ± 0.09

TABLE 5 Measured accuracy, sensitivity, specificity, BF-score, and IoU-score for lumen detection in CT images of the two challenging cases.

Patients	Lumen accuracy	Lumen sensitivity	Lumen specificity	Lumen BF-score	Lumen IoU-score
Patient1	0.99 ± 0.01	0.98 ± 0.02	0.99 ± 0.01	0.92 ± 0.08	0.98 ± 0.02
Patient2	0.96 ± 0.04	0.93 ± 0.07	0.99 ± 0.01	0.92 ± 0.08	0.93 ± 0.07

TABLE 6 Measured accuracy, sensitivity, specificity, BF-score, and IoU-score for the landmark detection including the aorta, iliac, celiac, and renal arteries on CT images of the two challenging cases.

Patients	Landmark accuracy	Landmark sensitivity	Landmark specificity	Landmark BF-score	Landmark IoU-score
Patient1	0.97 ± 0.03	0.95 ± 0.05	0.99 ± 0.01	0.93 ± 0.07	0.95 ± 0.05
Patient2	0.96 ± 0.04	0.91 ± 0.09	0.99 ± 0.01	0.93 ± 0.07	0.91 ± 0.09

TABLE 7 Measured accuracy, sensitivity, specificity, BF-score, and IoU-score to evaluate the model performance on an external cohort of six different patients that were not included in any of the training, test, and validation sets and were only used for algorithm verification.

Tissues under review	Accuracy	Sensitivity	Specificity	BF-Score	IoU-Score
Aorta	0.94 ± 0.06	0.88 ± 0.09	0.99 ± 0.01	0.88 ± 0.10	0.88 ± 0.09
Lumen	0.98 ± 0.02	0.96 ± 0.03	0.99 ± 0.01	0.91 ± 0.09	0.96 ± 0.04
Landmark	0.94 ± 0.05	0.88 ± 0.10	0.99 ± 0.01	0.90 ± 0.09	0.88 ± 0.10

We reported the mean (±) std of measured accuracies, sensitivities, specificities, BF-scores, and IoU-scores in all six patients.

TABLE 8 Inter-operator variability by comparison the segmentation masks created by two expert operators.

Operators	Tissues under review	Accuracy	Sensitivity	Specificity	BF-Score	IoU-Score
Operator1 VS Operator2	Aorta	0.98 ± 0.02	0.95 ± 0.05	0.99 ± 0.01	0.98 ± 0.02	0.95 ± 0.05
	Lumen	0.94 ± 0.05	0.88 ± 0.10	0.99 ± 0.01	0.98 ± 0.02	0.88 ± 0.11
	Landmark	0.97 ± 0.03	0.94 ± 0.06	0.99 ± 0.01	0.97 ± 0.02	0.94 ± 0.04

The results are reported as mean (±) std of all the measured accuracy, sensitivity, specificity, BF-score, and IoU-score for the CT images of all 19 patients.

6. Patent

A PCT entitled "METHOD AND SYSTEM FOR SEGMENTING AND CHARACTERIZING AORTIC TISSUES" was filed with the international application number PCT/IB2022/051558.

Data availability statement

The datasets presented in this article are not readily available because this dataset is confidential. Requests to access the datasets should be directed to elenadimartino@vitaamedical.com.

Ethics statement

The studies involving human participants were reviewed and approved by Conjoint Health Research Ethics Board (CHREB), University of Calgary. The patients/participants provided their written informed consent to participate in this study. Written informed consent was obtained from the individual(s) for the publication of any potentially identifiable images or data included in this article.

Author contributions

AA: conceptualization, investigation, methodology, software, validation, writing—original draft, and visualization. AF: data curation, ground-truth creation, conceptualization, and writing—review and editing. RM: investigation, patient recruitment, and writing—review and editing. ED: conceptualization, supervision, and writing—review and editing. All authors contributed to the article and approved the submitted version.

Funding

This work was supported by ViTAA Medical Solutions and Mitacs through the Mitacs Accelerate Program.

Acknowledgments

We thank Dr. Gilles Soulez (Department of Radiology, Radiation-Oncology, and Nuclear Medicine, University of Montreal) for reviewing and validating the manual annotations and for the images from CHUM Montreal.

Conflict of interest

All authors have equity interest in ViTAA Medical Solutions.

Publisher's note

All claims expressed in this article are solely those of the authors and do not necessarily represent those of their affiliated organizations, or those of the publisher, the editors and the reviewers. Any product that may be evaluated in this article, or claim that may be made by its manufacturer, is not guaranteed or endorsed by the publisher.

References

1. Zhu C, Leach JR, Wang Y, Gasper W, Saloner D, Hope MD. Intraluminal thrombus predicts rapid growth of abdominal aortic aneurysms. *Radiology*. (2020) 294:707–13. doi: 10.1148/radiol.2020191723

2. Wilson JS, Virag L, Di Achille P, Karšaj I, Humphrey JD. Biochemomechanics of intraluminal thrombus in abdominal aortic aneurysms. *J Biomech Eng*. (2013) 135:021011. doi: 10.1115/1.4023437

3. Stenbaek J, Kalin B, Swedenborg J. Growth of thrombus may be a better predictor of rupture than diameter in patients with abdominal aortic aneurysms. *Eur J Vascular Endovasc Surgery*. (2000) 20:466–9. doi: 10.1053/ejvs.2000.1217

4. Buijs RV, Willems TP, Tio RA, Boersma HH, Tielliu IF, Slart RH, et al. Calcification as a risk factor for rupture of abdominal aortic aneurysm. *Eur J Vascular Endovasc Surgery*. (2013) 46:542–8. doi: 10.1016/j.ejvs.2013.09.006

5. Li ZY, Jean U, Tang TY, Soh E, See TC, Gillard JH, et al. Impact of calcification and intraluminal thrombus on the computed wall stresses of abdominal aortic aneurysm. *J Vasc Surg*. (2008) 47:928–35. doi: 10.1016/j.jvs.2008.01.006

6. Chaikof EL, Dalman RL, Eskandari MK, Jackson BM, Lee WA, Mansour MA, et al. The society for vascular surgery practice guidelines on the care of patients with an abdominal aortic aneurysm. *J Vasc Surg*. (2018) 67:2–77. doi: 10.1016/j.jvs.2017.10.044

7. Duquette AA, Jodoin PM, Bouchot O, Lalande A. 3D segmentation of abdominal aorta from CT-scan and MR images. *Comput Med Imaging Graphics*. (2012) 36:294–303. doi: 10.1016/j.compmedimag.2011.12.001

8. Deng X, Zheng Y, Xu Y, Xi X, Li N, Yin Y. Graph cut based automatic aorta segmentation with an adaptive smoothness constraint in 3D abdominal CT images. *Neurocomputing*. (2018) 310:46–58. doi: 10.1016/j.neucom.2018.05.019

9. Siriapisith T, Kusakunniran W, Haddawy P. Outer wall segmentation of abdominal aortic aneurysm by variable neighborhood search through intensity and gradient spaces. *J Digit Imaging*. (2018) 31:490–504. doi: 10.1007/s10278-018-0049-z

10. Siriapisith T, Kusakunniran W, Haddawy P. 3D segmentation of exterior wall surface of abdominal aortic aneurysm from CT images using variable neighborhood search. *Comput Biol Med*. (2019) 107:73–85. doi: 10.1016/j.compbiomed.2019.01.027

11. López-Linares K, Aranjuelo N, Kabongo L, Maclair G, Lete N, Ceresa M, et al. Fully automatic detection and segmentation of abdominal aortic thrombus in post-operative CTA images using deep convolutional neural networks. *Med Image Anal*. (2018) 46:202–14. doi: 10.1016/j.media.2018.03.010

12. Zohios C, Kossioris G, Papaharilaou Y. Geometrical methods for level set based abdominal aortic aneurysm thrombus and outer wall 2D image segmentation. *Comput Methods Programs Biomed*. (2012) 107:202–17. doi: 10.1016/j.cmpb.2011.06.009

13. Lareyre F, Adam C, Carrier M, Dommerc C, Mialhe C, Raffort J. A fully automated pipeline for mining abdominal aortic aneurysm using image segmentation. *Sci Rep*. (2019) 9:1–14. doi: 10.1038/s41598-019-50251-8

14. Maiora J, Papakostas G, Kaburlasos V, Grana M. A proposal of texture features for interactive CTA Segmentation by active learning. *Stud Health Technol Inform*. (2014) 207:311–20. doi: 10.3233/978-1-61499-474-9-311

15. Shum J, DiMartino ES, Goldhammer A, Goldman DH, Acker LC, Patel G, et al. Semiautomatic vessel wall detection and quantification of wall thickness in computed tomography images of human abdominal aortic aneurysms. *Med Phys*. (2010) 37:638–48. doi: 10.1118/1.3284976

16. Drapikowski P, Domagala Z. Semi-automatic segmentation of CT/MRI images based on active contour method for 3d reconstruction of abdominal aortic aneurysms. *Image Process Commun*. (2014) 19:13. doi: 10.1515/ipc-2015-0002

17. de Bruijne M, van Ginneken B, Viergever MA, Niessen WJ. Interactive segmentation of abdominal aortic aneurysms in CTA images. *Med Image Anal*. (2004) 8:127–8. doi: 10.1016/j.media.2004.01.001

18. Maiora J, Ayerdi B, Gra na M. Random forest active learning for AAA thrombus segmentation in computed tomography angiography images. *Neurocomputing*. (2014) 126:71–7. doi: 10.1016/j.neucom.2013.01.051

19. Caradu C, Spampinato B, Vrancianu AM, Bérard X, Ducasse E. Fully automatic volume segmentation of infra-renal abdominal aortic aneurysm CT images with deep learning approaches versus physician controlled manual segmentation. *J Vasc Surg*. (2020) 74:246–256.e6. doi: 10.1016/j.jvs.2020.11.036

20. Fantazzini A, Esposito M, Finotello A, Auricchio F, Pane B, Basso C, et al. 3D automatic segmentation of aortic computed tomography angiography combining multi-view 2D convolutional neural networks. *Cardiovasc Eng Technol*. (2020) 11:576–86. doi: 10.1007/s13239-020-00481-z

21. Lareyre F, Adam C, Carrier M, Raffort J. Automated segmentation of the human abdominal vascular system using a hybrid approach combining expert system and supervised deep learning. *J Clin Med*. (2021) 10:3347. doi: 10.3390/jcm10153347

22. Wang D, Zhang R, Zhu J, Teng Z, Huang Y, Spiga F, et al. Neural network fusion: a novel CT-MR aortic aneurysm image segmentation method. In: *Medical Imaging 2018: Image Processing, Vol. 10574*. SPIE (2018). p. 542–9.

23. Mohammadi S, Mohammadi M, Dehlaghi V, Ahmadi A. Automatic segmentation, detection, and diagnosis of abdominal aortic aneurysm (AAA) using convolutional neural networks and hough circles algorithm. *Cardiovasc Eng Technol*. (2019) 10:490–9. doi: 10.1007/s13239-019-00421-6

24. López-Linares K, García I, García-Familiar A, Macía I, Ballester MAG. 3D convolutional neural network for abdominal aortic aneurysm segmentation. *arXiv preprint arXiv:190300879*. (2019). doi: 10.48550/arXiv.1903.00879

25. Hwang B, Kim J, Lee S, Kim E, Kim J, Jung Y, et al. Automatic detection and segmentation of thrombi in abdominal aortic aneurysms using a mask region-based convolutional neural network with optimized loss functions. *Sensors*. (2022) 22:3643. doi: 10.3390/s22103643

26. Brutti F, Fantazzini A, Finotello A, Müller LO, Auricchio F, Pane B, et al. Deep learning to automatically segment and analyze abdominal aortic aneurysm from computed tomography angiography. *Cardiovasc Eng Technol*. (2022) 13:535–47. doi: 10.1007/s13239-021-00594-z

27. Chen LC, Zhu Y, Papandreou G, Schroff F, Adam H. Encoder-decoder with atrous separable convolution for semantic image segmentation. In: *Proceedings of the European Conference on Computer Vision (ECCV)*. (2018). p. 801–18.

28. Lalys F, Yan V, Kaladji A, Lucas A, Esneault S. Generic thrombus segmentation from pre-and post-operative CTA. *Int J Comput Assist Radiol Surg*. (2017) 12:1501–10. doi: 10.1007/s11548-017-1591-8

29. Habib S, Dehmeshki J. Automatic segmentation of abdominal aortic aneurysm. In: *2018 IEEE 13th International Scientific and Technical Conference on Computer Sciences and Information Technologies (CSIT)*, *Vol. 1*. Lviv: IEEE (2018). p. 412–5.

frontiers | Frontiers in Medical Technology

TYPE Original Research
PUBLISHED 06 January 2023
DOI 10.3389/fmedt.2022.1052213

OPEN ACCESS

EDITED BY
Francesco Sturla,
IRCCS San Donato Polyclinic, Italy

REVIEWED BY
Doran Mix,
University of Rochester, United States
Francesco Maffessanti,
Maria Cecilia Hospital, Italy
Elena S. Di Martino,
University of Calgary, Canada

*CORRESPONDENCE
Larissa C. Jansen
l.c.jansen@tue.nl

SPECIALTY SECTION
This article was submitted to Cardiovascular Medtech, a section of the journal Frontiers in Medical Technology

RECEIVED 23 September 2022
ACCEPTED 28 November 2022
PUBLISHED 06 January 2023

CITATION
Jansen LC, Schwab H-M, van de Vosse FN, van Sambeek MRHM and Lopata RGP (2023) Local and global distensibility assessment of abdominal aortic aneurysms *in vivo* from probe tracked 2D ultrasound images. Front. Med. Technol. 4:1052213. doi: 10.3389/fmedt.2022.1052213

Local and global distensibility assessment of abdominal aortic aneurysms *in vivo* from probe tracked 2D ultrasound images

Larissa C. Jansen[1,2]*, Hans-Martin Schwab[1], Frans N. van de Vosse[3], Marc R. H. M. van Sambeek[1,2] and Richard G. P. Lopata[1]

[1]Photoacoustics and Ultrasound Laboratory Eindhoven (PULS/e), Department of Biomedical Engineering, Eindhoven University of Technology, Eindhoven, Netherlands, [2]Department of Vascular Surgery, Catharina Hospital Eindhoven, Eindhoven, Netherlands, [3]Cardiovascular Biomechanics, Department of Biomedical Engineering, Eindhoven University of Technology, Eindhoven, Netherlands

Rupture risk estimation of abdominal aortic aneurysm (AAA) patients is currently based on the maximum diameter of the AAA. Mechanical properties that characterize the mechanical state of the vessel may serve as a better rupture risk predictor. Non-electrocardiogram-gated (non-ECG-gated) freehand 2D ultrasound imaging is a fast approach from which a reconstructed volumetric image of the aorta can be obtained. From this 3D image, the geometry, volume, and maximum diameter can be obtained. The distortion caused by the pulsatility of the vessel during the acquisition is usually neglected, while it could provide additional quantitative parameters of the vessel wall. In this study, a framework was established to semi-automatically segment probe tracked images of healthy aortas ($N = 10$) and AAAs ($N = 16$), after which patient-specific geometries of the vessel at end diastole (ED), end systole (ES), and at the mean arterial pressure (MAP) state were automatically assessed using heart frequency detection and envelope detection. After registration AAA geometries were compared to the gold standard computed tomography (CT). Local mechanical properties, i.e., compliance, distensibility and circumferential strain, were computed from the assessed ED and ES geometries for healthy aortas and AAAs, and by using measured brachial pulse pressure values. Globally, volume, compliance, and distensibility were computed. Geometries were in good agreement with CT geometries, with a median similarity index and interquartile range of 0.91 [0.90–0.92] and mean Hausdorff distance and interquartile range of 4.7 [3.9–5.6] mm. As expected, distensibility (Healthy aortas: $80 \pm 15{\cdot}10^{-3}$ kPa^{-1}; AAAs: $29 \pm 9.6{\cdot}10^{-3}$ kPa^{-1}) and circumferential strain (Healthy aortas: 0.25 ± 0.03; AAAs: 0.15 ± 0.03) were larger in healthy vessels compared to AAAs. Circumferential strain values were in accordance with literature. Global healthy aorta distensibility was significantly different from AAAs, as was demonstrated with a Wilcoxon test (p-value $= 2{\cdot}10^{-5}$). Improved image contrast and lateral resolution could help to further improve segmentation to improve mechanical characterization. The presented work has demonstrated how besides accurate geometrical assessment freehand 2D ultrasound imaging is a promising tool for additional mechanical property characterization of AAAs.

KEYWORDS

distensibility, cardiovascular, patient specific geometries, ultrasound imaging, abdominal aortic aneurysm (AAA)

Introduction

Patients with an abdominal aortic aneurysm (AAA), a local dilatation of the abdominal aorta, are at risk for aneurysm rupture. Currently, this risk is considered high when the diameter reaches a threshold of 5.0 cm for females or 5.5 cm for males, or when the diameter growth exceeds a threshold of 1.0 cm per year (1, 2). However, previous studies have shown that AAAs can rupture before reaching the diameter threshold or can remain stable after exceeding the threshold (3–5). From a mechanical perspective, the vessel wall will rupture once the stress on the wall exceeds the wall strength. Therefore, there is a need for a more patient specific approach that includes mechanical characterization.

Finite element models are tools that can be used to estimate the mechanical state of the vessel during patient follow-up, and to model growth and remodeling of the vascular tissue. Different mechanical properties such as vessel wall stress, strain, and shear modulus can be assessed indirectly (6, 7). However, modeling AAAs adequately requires patient specific information on the shape and material properties of the vessel. Computed tomography (CT) is considered the gold standard to extract the patient specific geometry. This imaging technique, however, involves the use of ionizing radiation and nephrotoxic contrast agent. Furthermore, it typically lacks temporal information. Alternatively, Magnetic Resonance Imaging (MRI) could be used to extract both the geometry and dynamic information. However, MRI has high costs and long scanning times. Ultrasound (US) imaging is an imaging technique which is considered safe, has low costs, and can easily be used at the patient's bedside. An additional advantage of time resolved US imaging is the availability of temporal information, from which mechanical properties can be assessed. These properties can be used to personalize mechanical models, rather than using properties from literature (6, 7). Examples of these properties are wall strain, compliance, and distensibility. Compliance measures the ability of the vessel to increase and decrease in volume resulting from a change in intravascular pressure (8). Distensibility captures this volume change and takes the initial size of the vessel into account (9).

One way to assess distensibility was by evaluating the diameter change at the maximal diameter location (10). However, this approach lacks characterization of the complete vessel. Alternatively, maximum mean segmental dilatation has been assessed using 2D tissue doppler imaging in a single longitudinal imaging plane, from which segmental compliance and distensibility were computed (11, 12). Although a vessel segment, rather than a single location of the vessel is evaluated with this approach, compliance and distensibility computed from diameter change along a single line assumes the vessel to be a circle. Specifically in aneurysms, this is not a valid assumption. Hence, an area or volume-based computation would be more accurate.

With the development of matrix arrays for 3D US imaging, the aneurysm volume can now be assessed (13). Moreover, with time-resolved 3D US, vessel dimension changes during the cardiac cycle can be captured (6). However, the main disadvantages of this imaging approach are the limited temporal resolution, field of view, and image quality. Another 3D approach is freehand 2D US with 3D image reconstruction, where an operator moves a 2D US transducer, that is connected to a probe tracker, after which a single 3D volume is reconstructed offline. Compared to imaging with a matrix array, this approach has lower costs, higher volume quality and an improved field of view (14–17). So far, with electrocardiogram-gated (ECG-gated) or non-ECG-gated freehand 2D US of AAAs, the patient specific geometry and volume have been assessed, from which the vessel diameter and area at the maximal aneurysm diameter location have been computed (14, 15, 17–19). It was previously demonstrated that reproducible AAA volume measurements can be obtained from 3D reconstructions obtained with freehand 2D US (17). Furthermore, it has been shown that AAA volumes measured from volumetric images that were reconstructed from freehand 2D US are comparable to those obtained with computed tomography angiography (CTA) (14). However, registration with CT geometries and quantification of similarity and overlap between the geometries has not been demonstrated yet.

What is often neglected with non-ECG-gated freehand 2D US of AAAs is the pulsatile motion of the vessel, even though it distorts volumetric image reconstruction and volume computation. ECG gating has been used to obtain a volume in the same phase of the cardiac cycle (18, 19). However, the acquisition time is then extended from seconds to minutes and the measurement becomes more susceptible to patient motion. In a freehand 2D US study on carotids, it was demonstrated how heart frequency detection and filtering can correct for the pulsatile motion by considering the individual frames, rather than the reconstructed volumetric image (20). In this way, mean arterial pressure (MAP) state geometries of carotid arteries could be obtained. Since the pulsatility, that is captured during the acquisition, can be filtered out, it could also be exploited for estimation of local vessel properties, such as circumferential strain and in combination with a pulse pressure measurement, distensibility or pressure modulus.

In this study, distensibility of healthy abdominal aortas and AAAs was locally and globally assessed from fast, non-EGC-gated, freehand 2D US acquisitions and non-invasive blood-pressure measurements. A semi-automatic segmentation and automatic spatiotemporal signal processing framework were developed to obtain the vessel geometry at end diastole (ED), end systole (ES) and MAP. Distensibility and mean circumferential strain were estimated locally by evaluating area changes, and distensibility was assessed globally from volume changes. Feasibility of this approach was evaluated by registration and comparison of aneurysm geometries with geometries obtained from the gold standard CT. To evaluate if our approach is sensitive to different levels of distension, mechanical properties of healthy aortas and AAAs were assessed, and compared to previous studies.

Materials and methods

Study population

This study was approved by the local medical ethics committee of the Catharina Hospital, Eindhoven (NL). Young healthy volunteers ($N = 12$) and AAA patients ($N = 26$) participated in this study after giving their written, informed consent. After initial review of the US data, 2 healthy volunteer and 7 AAA datasets were excluded due to poor image quality, and 3 AAA datasets were excluded due to excessive motion as a result of breathing during the US measurement. The remaining AAA patients ($n = 16$, age range: 58–90 years) were grouped into two categories. The patients of the first group ($n = 9$) had undergone a CTA scan as part of regular clinical practice, whereas the second group ($n = 9$) consisted of patients that underwent a brachial blood pressure (BP) measurement prior to the US acquisition. Two patients were included in both groups, since both brachial BP and a CTA scan were available. The healthy volunteers ($N = 10$, age range: of 24–29 years) underwent a brachial BP measurement besides the US acquisitions. The age, brachial BP values and AAA maximal diameter are summarized in Table 1.

Data collection

Brachial blood pressure measurement

Prior to the US measurement, the diastolic and systolic BP were measured with an arm-cuff while the subject was in supine position. van 't Veer et al. showed that brachial cuff pressure measurements overestimate the diastolic BP (P_{dia}) by 12% and underestimate the systolic BP (P_{sys}) by 5% compared with direct intra-aortic pressures (9). Hence the measured brachial cuff measurements were corrected accordingly.

Freehand 2D ultrasound imaging

A series of 2D US images of the abdominal aorta were acquired while moving a CA431 2D curved array probe (center frequency: 2.6 MHz) connected to a commercial Esaote Mylab70.2 US system (Esaote Europe, Maastricht, the Netherlands) manually on the abdomen (Figure 1A). The entire acquisition was performed during breath-hold, while the subject was in supine position. As the measurement was performed freehand, the length of the acquisition and distance covered by the probe varied from measurement to measurement. The probe was connected to an electromagnetic probe tracking device (Curefab, Munich, Germany), which recorded the 3D probe orientation and a time stamp for every acquired image during the acquisition. The probe tracker was calibrated prior to usage. A study by Feurer et al. demonstrated that this probe tracker has a satisfactory reliability and accuracy (21). Their study showed a mean point accuracy of 1.52 mm and mean total error of distance measurements of 0.9%. Data was stored at a 25 Hz sampling rate. As the measurement was performed freehand, the length of the acquisition and distance covered by the probe varied from measurement to measurement. Consequently, the distance between samples varied per subject, depending on the speed of the probe.

Post-processing computed tomography datasets

CTA scans were acquired within 1 month (Table 2) from the US acquisition as part of regular clinical practice using a 256 slice CT scanner (Philips Healthcare, Best, the Netherlands), with a slice

TABLE 1 Summary of the age, gender (female/male), brachial diastolic BP (p_{dia}) and systolic BP (p_{sys}) for all 10 healthy volunteers (V1–V10) and 16 patients.

	Age (years)	F/M	BP (mmHg)			Age (years)	F/M	D_{max} (mm)	BP (mmHg)			Age (years)	F/M	D_{max} (mm)	BP (mmHg)	
			P_{dia}	P_{sys}					P_{dia}	P_{sys}					P_{dia}	P_{sys}
V1	25	M	68	115	A1	75	F	52	-	-	B1	90	F	52	152	96
V2	27	M	79	126	A2*	80	M	55	163	93	B2	78	F	39	102	71
V3	25	F	78	110	A3	84	M	57	-	-	B3	72	M	52	112	68
V4	28	M	81	118	A4	73	M	56	-	-	B4	58	M	41	135	78
V5	29	F	81	107	A5	73	M	54	-	-	B5	74	M	40	136	91
V6	26	M	60	110	A6	79	M	56	-	-	B6	74	M	45	141	87
V7	25	M	69	118	A7	72	M	86	-	-	B7*	80	M	55	163	93
V8	24	F	64	110	A8	76	M	60	-	-	B8	83	M	48	165	87
V9	26	F	57	102	A9**	69	M	51	180	94	B9**	69	M	51	180	94
V10	25	F	55	108												
μV	26	-	69	112	μA	76	-	59	-	-	μB	75	-	47	143	85

The patients were divided into two groups, based on the types of measurements available. Patients of group A (A1–A9) underwent a CTA scan. Patients of group B (B1–B9) underwent a brachial BP measurement. Patient A2 and A9 belong to both categories indicated by one or two asterisks. Per group, the mean (μ) values are shown.

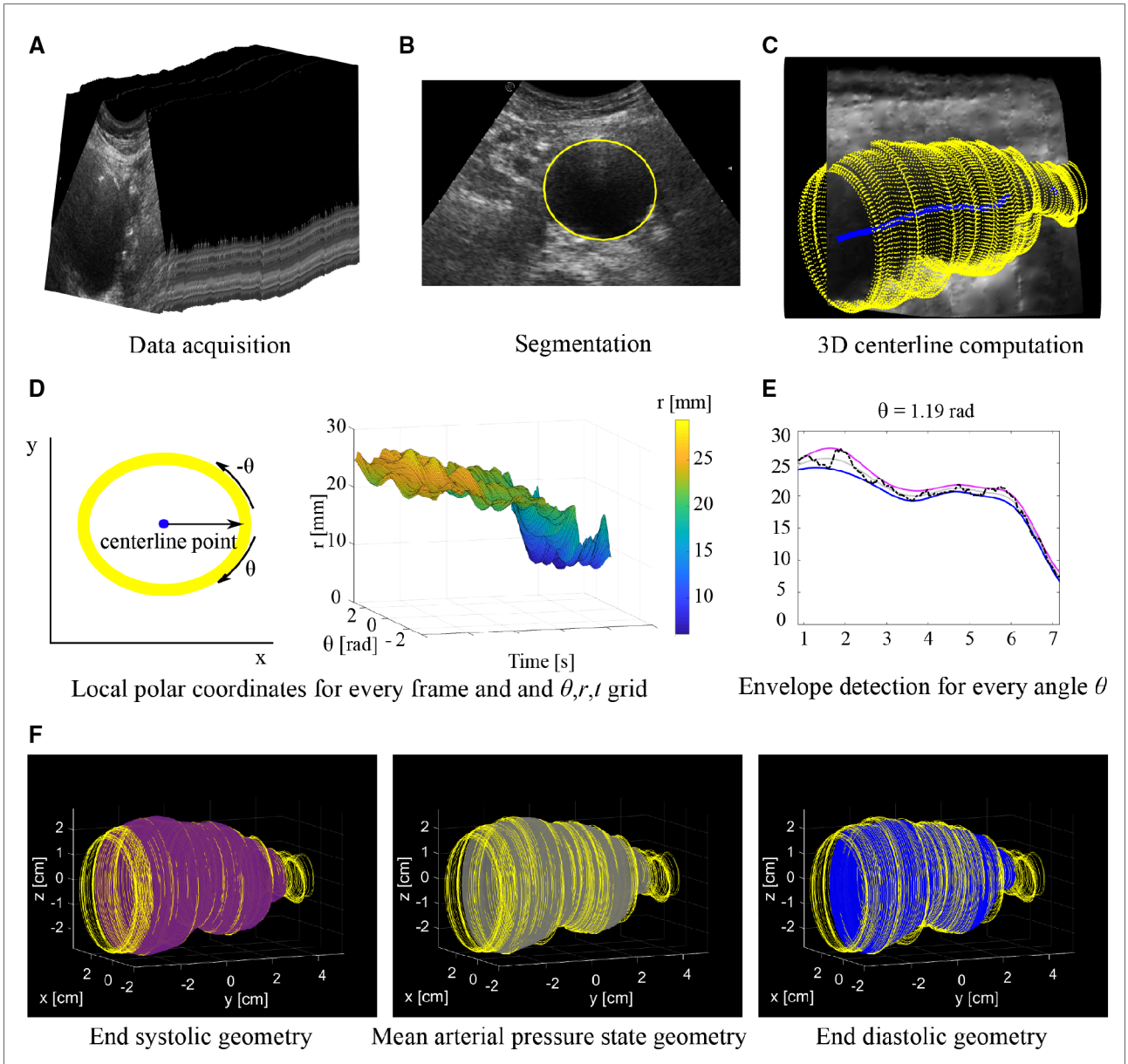

FIGURE 1
Overview of workflow. (**A**) Series of 2D US frames acquired with freehand 2D US imaging. (**B**) Segmentation is performed on the individual 2D US frames. (**C**) Contours segmented from each frame (yellow) are mapped into 3D space together with the 3D centerline (blue). (**D**) Conversion of coordinates of each frame to a local polar coordinate system centered around the center line and generating a *θ, r, t* grid. (**E**) Envelope detection on a radius time signal (black line) for a single angle *θ*. The radii at end diastole (blue line) and end systole (purple line) are estimated from which the radii at the mean arterial pressure state (grey line) are derived. (**F**) Final 3D geometries with from left to right: End systole (purple), mean arterial pressure state (grey) and end diastole (blue). Geometries are shown together with the original contours (yellow).

thickness of 3 mm. Hemodyn post-processing software (Philips Medical System and Eindhoven University of technology, the Netherlands) was used to semi-automatically obtain the 3D geometries of the aneurysm (7). With this software, the lumen-wall interface was segmented using a 3D active contour. In case intraluminal thrombus was present, the thrombus-wall interface and lumen-wall interface were segmented. Small manual adaptations were made after the segmentation process.

Geometry assessment

Segmentation of transverse 2D US images

Segmentation was performed to extract the lumen-wall interface of the aorta in the transverse images of the freehand acquisition. In the case intraluminal thrombus was present in AAAs, the thrombus-wall interface was segmented. Prior to segmentation, a Euclidean shortening flow filter, a well-known

TABLE 2 Similarity indices and median hausdorff distances with interquartile range (IQR) of AAA geometries assessed from freehand 2D US data that were registered and compared to CT geometries.

Subject	Similarity index (−)	HD (mm), median (IQR)	Time between US and CT (days)
A1	0.88	6.6 [5.7–8.4]	20
A2	0.93	3.2 [2.8–3.8]	1
A3	0.91	4.5 [4.5–4.8]	11
A4	0.91	4.1 [3.6–4.8]	6
A5	0.93	3.0 [2.2–4.0]	2
A6	0.91	5.2 [4.4–6.8]	6
A7	0.90	7.3 [6.7–8.2]	2
A8	0.91	5.1 [4.5–6.0]	31
A9	0.90	4.7 [3.8–5.6]	27
median + IQ range	0.91 [0.90–0.92]	4.7 [3.9–5.6]	

edge preserving de-speckling filter (22), was applied followed by a Gaussian filter with a 3 by 3 kernel size. These filters were applied to enhance the contrast between the wall and lumen region by reducing noise. Next, lumen-wall or thrombus-wall interface contours were segmented semi-automatically using an in-house toolbox, based on a star-Kalman approach by Guerrero et al. (23) that was adapted by de Ruijter et al. (20) and implemented in MATLAB (R2019b, Mathworks Inc., Natick, MA, USA). In this algorithm the lumen-wall or thrombus-wall interface is approximated by an ellipse-shape. The segmentation algorithm was initialized by manually defining an ellipse at the aorta location in the first frame. Next, the star algorithm was used to find the interface in the next frame. For this algorithm, a search region was defined around the ellipse of the previous frame. Within this search region the best edge positions, representing the lumen-wall or thrombus-wall interface positions, in the next frame were detected using step edge detection (24). The search region was extruded both inwards and outwards with respect to the ellipse, resulting in a radial thickness of 2.5 and 7 mm for healthy aortas and AAAs respectively. A larger search region was used for AAAs compared to healthy aortas, as besides geometry change due to pulsation, morphological vessel shape changes can occur from one frame to the next. Next, an ellipse was fitted through the high probability edge positions found in this search region, which was the final segmentation for this frame as well as the starting contour for a new search of the vessel wall in the next frame (Figure 1B). Using a Kalman filter, adapted from Guerrero et al., the frame-to-frame ellipse estimates were stabilized (20, 23).

3D centerline detection

A 3D centerline was computed based on the centers of mass of the contours of the ED frames, which were automatically detected using heart frequency analysis. A heart frequency range was automatically detected from the artery area-time signal in the Fourier domain. The area of the lumen was obtained by converting the segmented contours into a binary mask, from which the lumen area was extracted using the pixel dimensions. Next, the area per frame signal was resampled to have equidistant time steps. The heart frequency range was then detected from the power-density spectrum of this signal, where it was defined as the highest peak in the physiological range of the power-density spectrum ± 0.2 Hz, allowing for a ± 12 beats per minute change throughout the acquisition. Next, the smallest radii in the signal separated by a period range corresponding to the detected heart frequency range were detected. Then, the signal was converted back to the original sampling in time and the frames closest to the timepoints of the smallest radii were defined as the ED frames. Next, the segmented contours of each ED frame were mapped from the local image coordinate system to the 3D Cartesian coordinate system according to the probe tracker orientation data. Finally, the 3D centerline (Figure 1C) was generated using 3D spline interpolation between the ellipse center points of the ED frame contours. A moving average filter with a kernel size of 15 samples was applied to the centerline, to smooth the centerline. Centerline coordinates were obtained for the remaining frames by computing the intersection of the centerline with the image planes of each frame.

End diastolic, end systolic and mean arterial pressure state geometry assessment

To obtain estimates of the ED, ES and MAP geometries, the contours were locally converted into the polar coordinate system (r, θ) with the local centerline location as the origin (Figure 1D). Then for each contour, the r, θ contour points were resampled to have equidistant angle intervals θ. Next, the r, θ coordinates of all contours were combined in a 3D grid with time t as the third dimension (r, θ, t). This was followed by envelope detection on the r-t signal for each angle θ individually to obtain radii at ES, r_{es}. Next, the r-t signal was reversed by multiplying it with −1. Envelope detection on this signal provided the radii at ED, r_{ed} (Figure 1E). The envelope detection was constrained such that only peaks separated by at least the minimal period of the heart frequency range were detected. The radii at MAP, r_{map}, were assessed for each angle θ from the previously assessed r_{ed} and r_{es} according to:

$$r_{map} = 0.5\,(r_{es} - r_{ed}) + r_{ed} \quad (1)$$

As the interpolation of the r-t signals were performed for each angle θ individually, local irregularities may occur. Hence, ellipses were fitted to the θ-r coordinates for every contour, after which the coordinates were transferred back to image

coordinate system followed by mapping the newly obtained contours to 3D space (Figure 1F).

Comparison with computed tomography

Registration

To register an US geometry with a CT geometry, the optimal translation and rotation that maximizes the overall similarity between the point clouds was found using an iterative closest point (ICP) algorithm (25, 26). An ICP algorithm minimizes the distances between two 3D point clouds according to the minimal distance difference principle. This is followed by computation of the global rotation and translation that aligns the two point clouds. An optimum is provided in result of an iterative process that runs until the root mean square error is under a set threshold, or when a set number of iterations is completed. In this study a publicly available ICP algorithm (compatible with MATLAB) was used for the registration process (27). Upon visual inspection of the results, the number of iterations was set to 30. Next the contours of the US data are transformed to the new registered position by rigid transformation of the coordinates using the global rotation and translation that was previously computed.

Comparison metrics

To compare US and CT geometries, the similarity between the registered freehand US and CT geometries was measured. First, the US and CT point clouds were resampled to series of equidistant contours in the vessel length direction, i.e., the y-direction, with a spacing of circa 0.2 mm depending on the initial sparsity of the US contours. Next, for every y-location, the similarity was quantified using the similarity index (SI), also known as Dice coefficient. This is a measure for spatial overlap, defined as

$$SI = \frac{2 \cdot (P_{US} \cap P_{CT})}{P_{US} + P_{CT}} \tag{2}$$

with P_{US} and P_{CT} being the set of pixels present in binary masks generated from US contours and CT contours at each y-location. The Hausdorff distance (HD) was used to calculate the maximum of the minimum distances between the registered US contour points $A = \{a_1, a_2, \ldots. a_n\}$ and CT contour points $B = \{b_1, b_2, \ldots. b_n\}$ of each y-location and is defined as

$$d(A, B) = \max\left\{ \max_{a \in A} \min_{b \in B} |b - a|, \max_{b \in B} \min_{a \in A} |a - b| \right\} \tag{3}$$

with $|a–b|$ and $|b–a|$ being the Euclidean distance between a and b (28). For each geometry, the SI and the median HD and interquartile range were computed. Furthermore, an overall median SI and HD and interquartile range were computed.

Mechanical property assessment

Distensibility was computed locally and globally by evaluating area change and volume change respectively and by using the measured pulse pressure data. First the compliance was computed locally, C_{local}, and globally, C_{global}, according to Equations 4, 5:

$$C_{local} = \frac{\Delta A}{\Delta P} \tag{4}$$

$$C_{global} = \frac{\Delta V}{\Delta P} \tag{5}$$

where ΔA and ΔV represent the area and volume change between ES and ED, respectively, and ΔP is the pulse pressure. Area change was obtained by converting the ED and ES contours in binary masks, from which the area of the lumen pixels was computed. To extract the volume change, the ED and ES contours were first converted into surface meshes. Next, they were converted into closed solid structures from which the volumes were computed using SpaceClaim software (SpaceClaim, Ansys, 2019 R3). Next, the distensibility was determined locally, D_{local}, and globally, D_{global}, according to Equations 6, 7:

$$D_{local} = \frac{1}{A_{ED}} C_{local} \tag{6}$$

$$D_{global} = \frac{1}{V_{ED}} C_{global} \tag{7}$$

where A_{ED} and V_{ED} represent the area and volume at ED respectively. Besides these properties, strain, ε_{circ}, was computed locally from the circumference of the aorta at ED and ES according to:

$$\varepsilon_{circ} = \frac{l_{ES} - l_{ED}}{l_{ED}} \tag{8}$$

where l_{ES} and l_{ED} represent the circumference of the aorta at ES and ED respectively. The circumferences were extracted from the binary masks of the ES and ED contours. For this computation, the aortic tissue was assumed to be incompressible and isotropic, and to have small strains. A Wilcoxon test was performed to test whether distensibility was significant between AAA and healthy aortas (p-value <0.05).

Results

Geometries

Figure 2 shows examples of ED and ES geometries assessed from a freehand 2D US dataset of AAA patients B1 and B3 and volunteers V5 and V8 together with a reconstructed cross-

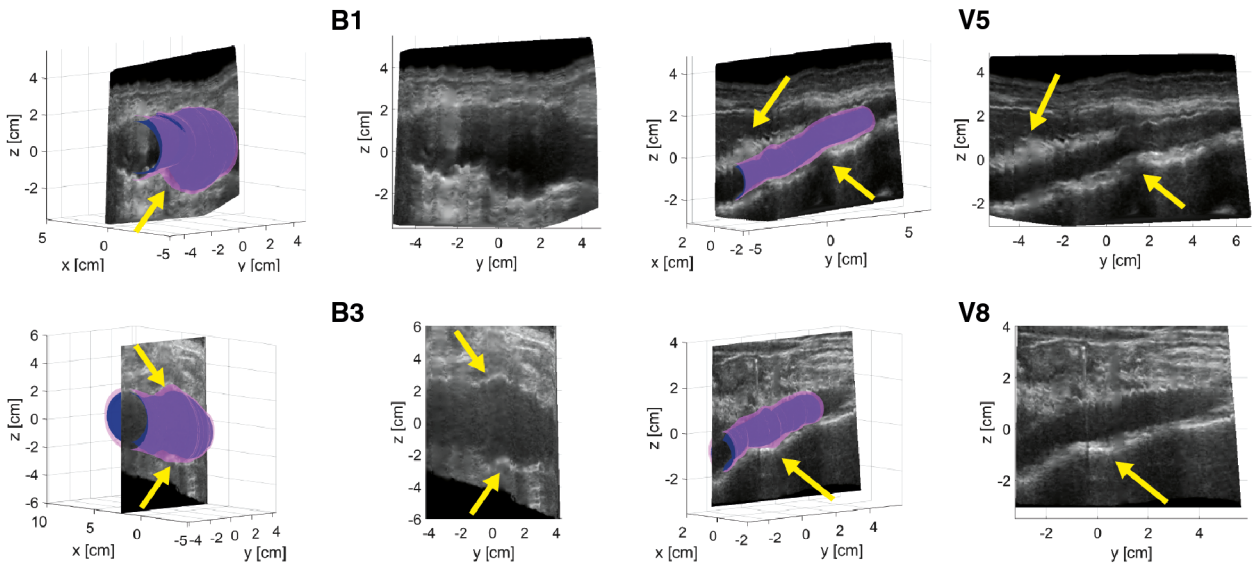

FIGURE 2
Examples of ED (blue) and ES (purple) geometries of AAAs of patients B1 and B3 and healthy aortas of volunteers V5 and V8. A longitudinal cross-section reconstruction extracted by interpolation of the individual series of US frames is shown separately and together with the geometries. Yellow arrows point at regions of large geometry changes in AAAs and poor image quality regions of healthy aortas.

section of the US image data showing the vessel throughout the sweep in the longitudinal direction. The distension, present during the acquisition is clearly visible in the US cross-sections. Furthermore, it shows that the vessel dimensions change over the length of the vessel. It can be appreciated that the geometries overall match with the vessel shape. For the AAAs there are regions where a large change in vessel dimension occurs, as indicated with the yellow arrows in Figure 2. Here the ES geometry is more enlarged compared to the ED geometry than in other regions. For the healthy vessels, there are some regions where the wall is less visible due to reduced image quality, indicated by the arrows in Figure 2. In these regions the difference between ES and ED is either strongly increased or strongly decreased compared to the rest of the vessel. The average length of the region that was segmented frame by frame is 60 mm ± 21 ($N = 10$) for volunteers and 65 mm ± 15 for AAA patients ($N = 16$).

Figure 3A shows the registered CT geometry and US geometry of patient A2 with a similarity index of 0.93. The figure shows that the US geometry generally follows the shape and size of the CT geometry. Furthermore, this example demonstrates that a large field of view can be achieved with freehand 2D US. However, the full aorta including the aneurysm shoulders is not included. In Figure 3B an example is shown of the CT image data together with the AAA wall outline of the CT geometry and US geometry at y-location

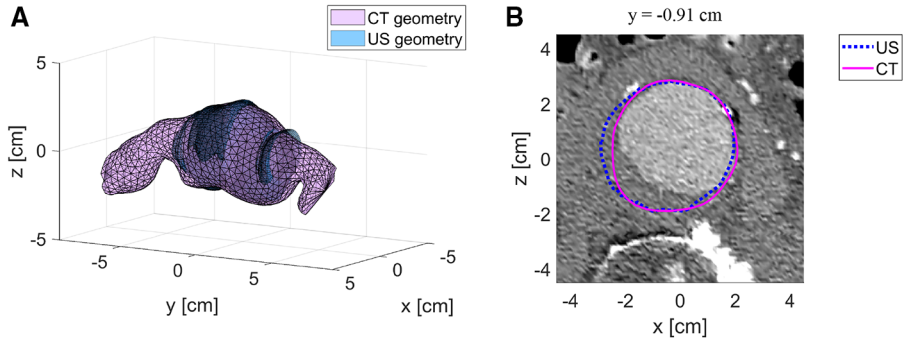

FIGURE 3
Example of registered US geometry with CT geometry. (A) US geometry of patient A2 (blue) with the corresponding CT geometry (purple) after registration. (B) Example of a CT image with the US contour (blue) and CT contour (purple) at location $y = -0.91$ cm.

−0.91 cm of Figure 3A. This image shows that deviations are visible at the location where thrombus is present and at the side wall regions. As shown in Table 2, SIs of the nine patients range between 0.88 and 0.93 and the overall median SI and interquartile range is 0.91 [0.90–0.92]. The median HD of the patients are in the range of 3.0 and 7.3 mm, where the overall median HD and interquartile range is 4.7 [3.9–5.6] mm.

Mechanical properties

Figures 4, 5 show the local distensibility and circumferential strain mapped onto the MAP geometry for healthy volunteers and AAA patients respectively. These are shown together with an interpolated longitudinal cross-section obtained from the acquired US frames. The mean and standard deviation of the local distensibility and strain values are shown in Table 3. The mean distensibility ranges between 60 and $105{\cdot}10^{-3}$ kPa^{-1} and 21 and $60{\cdot}10^{-3}$ kPa^{-1} for healthy aortas and AAAs respectively. For both healthy aortas and AAAs, variation in distensibility is visible along the length of the vessel. In some volunteers the variation is more gradual (V1, V3, V4, V6, V7, V9, V10), whereas for others the patterns are more scattered (V2, V5, V8). For 7 out of 10 healthy aortas, a decline in distensibility is visible from the proximal to the distal side of the aorta. For volunteers V2 and V5 there are regions where the wall is less visible, as indicated with blue arrows. As shown in Figure 2, the distension is increased in this region for V5. Hence an increase in distensibility is visible in Figure 4. For volunteers V8 and V9, a change of vessel direction is visible, as indicated with the purple arrows. For AAAs, besides the dilated aneurysm region, less dilated regions were also analyzed. In these regions, for patients B4, B5, B6, B7 and B9, the distensibility and strain are larger compared to the dilated region. On the contrary, for patients B1, B3 and B8, an increased distensibility is observed in the dilated region, compared to the less dilated regions (Figure 5). These regions correspond to regions where a large change in vessel shape occurs, as is visible in Figure 2.

Global mechanical properties are shown in Table 4. Distensibility of the healthy aortas with a mean and standard deviation of $80 \pm 15{\cdot}10^{-3}$ kPa^{-1} is larger compared to the AAAs, where the mean and standard deviation is $29 \pm 9.6{\cdot}10^{-3}$ kPa^{-1}. Figure 6 shows that there is a clear distinction between the global distensibility of AAAs compared to healthy aortas. Distensibility of the AAA wall is significantly different from the healthy aorta distensibility (Wilcoxon test: p-value $= 2{\cdot}10^{-5}$).

Discussion

In this study, healthy abdominal aorta and AAA geometries were assessed from fast probe-tracked freehand 2D US acquisitions, using semi-automatic segmentation and fully automated signal processing. The presence of pulsatility in the acquired data, which typically distorts volumetric image reconstruction, allows for retrieving distensibility both locally by evaluating area change, and globally by evaluating volume change. Furthermore, geometries of AAA patients were compared to CT geometries obtained within 1 month of the US acquisition, showing good similarity. Distensibility was estimated in healthy aortas and AAAs to evaluate whether the approach is sensitive to different and expected levels of distensibility, in both cylindrical and more complex geometries. Moreover, a comparison of the material properties with those found in previous studies was performed.

Using the star-Kalman algorithm, ellipse-shaped contours were detected in each consecutive frame. Although ellipses can closely resemble the aorta shape, they do not fully match with the vessel shape. To achieve this, an additional 2D active contour can be used. These are energy minimizing functions that attract to the lumen-wall or thrombus-wall interface image features and are constrained by internal forces. As with AAAs the diameter changes significantly over the length and AAAs have various shapes and sizes, tuning such an active contour for each frame and for every aorta remains challenging. Furthermore, in the side wall regions, i.e., regions where the radial wall direction is parallel to the lateral axis of the US image, these active contours may fail if not tuned properly. The ellipse approach that was used in our study was robust in images where the image quality at the sides of the aorta was reduced, but the flexibility of the approach is limited, which may lead to errors in some geometries. Therefore, in this study only the ellipse estimate was used. Alternatively, minor manual adaptions could be incorporated to improve the final geometry as was shown in a study by Rouet et al. (29).

Heart frequency detection was used, such that the ED frames could automatically be detected from the area over time signal obtained from the segmented contours. The centers of these frames were then mapped to 3D space and used to generate a centerline. Compared to the study by de Ruijter et al., the centerline was interpolated in 3D space (Figure 1), rather than in the image coordinate system, such that correction for the probe position was considered (20). A single heart frequency was often not distinguishable from the power-density spectrum. Therefore, a frequency range was detected, allowing for small frequency changes when searching for the minima that represent the end diastolic frames. The frequency change throughout the acquisition is likely due to heart frequency changes that commonly occur during breath-hold (30). The acquisitions were performed during breath-hold to limit motion of the aorta within the body due to breathing, which cannot be detected with the probe tracker. When breathing is constant, breathing motion could be filtered out. This would limit the chance to get heart

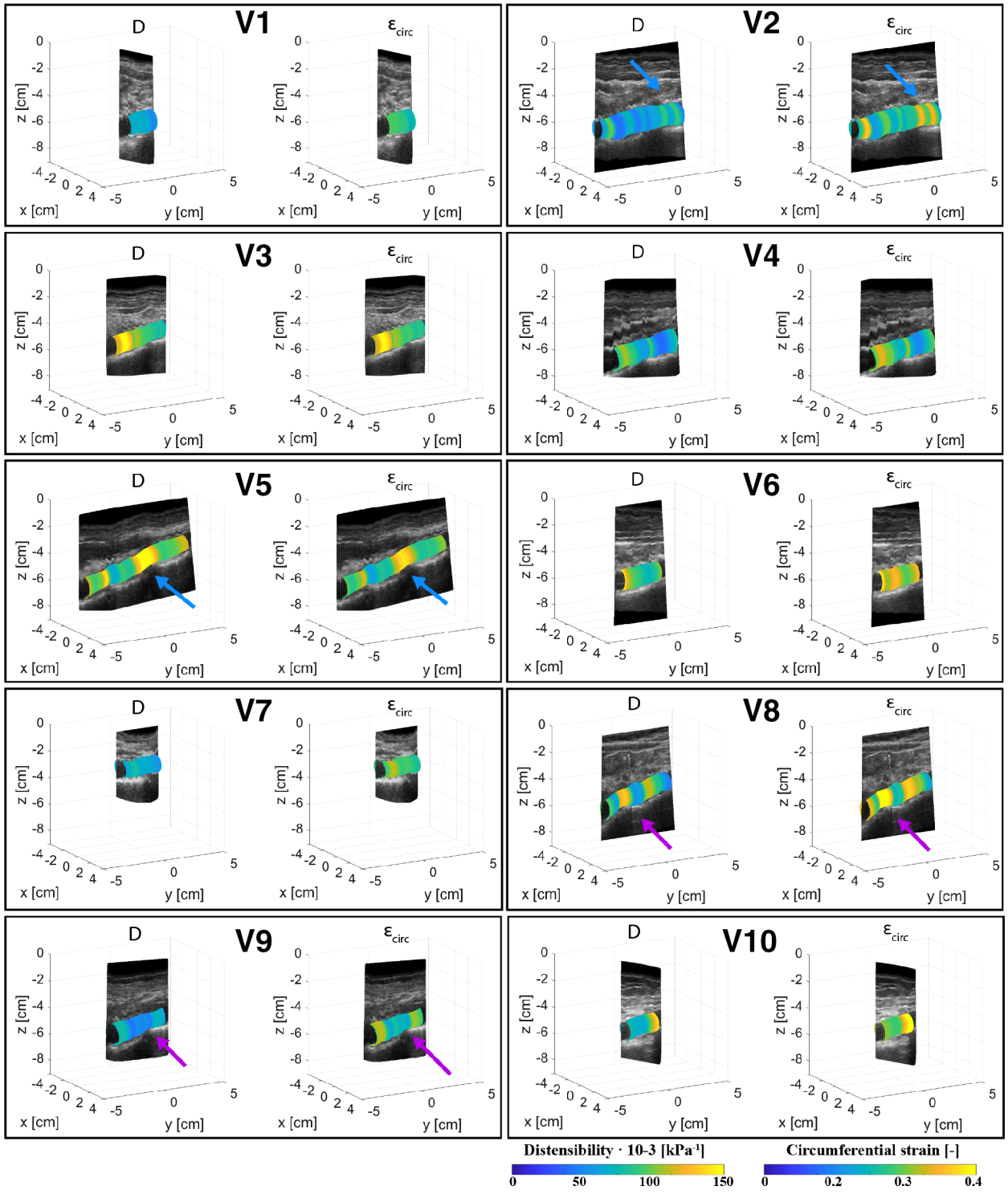

FIGURE 4
Overview of the assessed mechanical properties distensibility, D·10^{-3} (kPa^{-1}), and circumferential strain, ε_{circ} (–), of volunteers V1–V10 mapped onto the mean arterial pressure state geometry and visualized with an interpolated cross-section of the acquired US images. Blue arrows point at locations of poor echogenicity and purple arrows point at regions where the vessel direction changes.

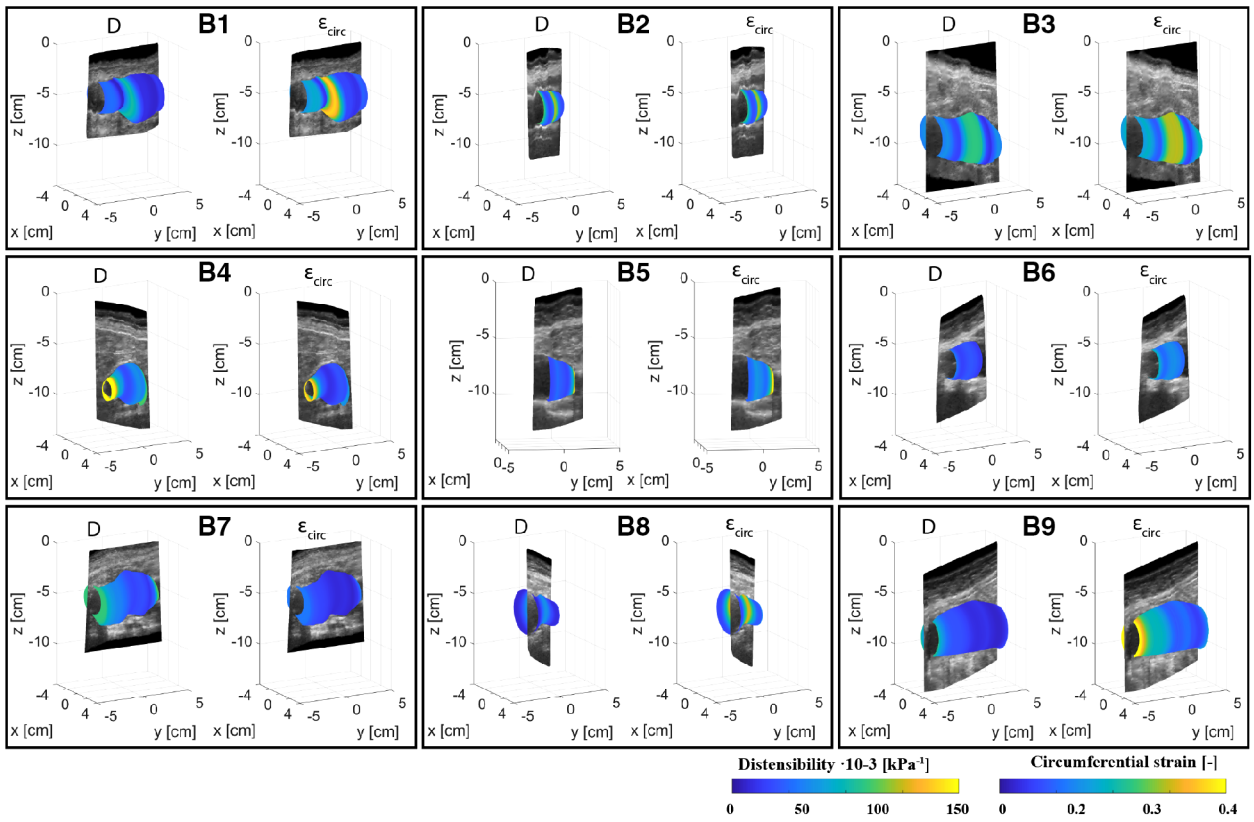

FIGURE 5
Overview of the assessed mechanical properties distensibility, D·10^{-3} (kPa^{-1}), and circumferential strain, ε_{circ} (–), of AAA patients B1–B9 mapped onto the mean arterial pressure state geometry and visualized with an interpolated cross-section of the acquired US images.

frequency changes throughout the acquisition and it would allow for extended acquisition time.

To obtain estimates of ED and ES geometries, envelope detection was applied on radius-time signals originating from the segmented contours of each frame. The approach relies strongly on the segmentation quality and erroneous radii can lead to inaccuracies in the final geometry. By performing the detection in the *r-t* domain with equidistant timesteps and by constraining peak detection with a minimal peak distance corresponding to the found heart frequency range, erroneous detection of peaks is limited. Figure 2 shows that overall, the geometries correspond well to the US data. However, in regions with large geometry change, which occurs in some AAAs, the ES geometry seems to overestimate the expansion of the vessel, which likely leads to the high distensibility values found in these regions (Figure 5). This could be circumvented by reducing the speed of the probe during the acquisition, such that more heartbeats occur over the length of the vessel. In this way changes due to geometry and changes due to vessel expansion are likely better distinguished such that envelope detection can improve locally. Probe speeds were manually increased for the AAAs, as the time of the breath-hold was commonly shorter for patients, opposed to healthy volunteers. In some datasets, regions with reduced image quality were present. In these regions the difference between the ES geometry and ED geometry was either larger or smaller compared to regions of good image quality, as observed in Figure 2. Furthermore, from Figure 4 it was observed that in these regions the distensibility either strongly increased or decreased compared to other regions.

The MAP AAA geometries obtained were compared to CT geometries by evaluating the similarity and overlap after registration. As shown in Table 2, the median SI and IQ range is 0.91 [0.90–0.92] and the overall median HD and IQ range is 4.7 [3.9–5.6] mm. These values are in the same range as those reported in conventional 3D US studies (7, 29, 31). This demonstrates that the approach proposed for geometry assessment has a high accuracy and is not inferior to 3D US-based approaches, while with this imaging approach additional mechanical properties can locally be assessed using

TABLE 3 Overview of mean local distensibility, D_{local}, and mean local circumferential strain, ε_{circ}, of healthy volunteers (V1–V10) and AAA patients (B1–B9).

	Volunteers			AAA patients	
	$D_{local}\cdot10^{-3}$ (kPa)	ε_{circ} (−)		$D_{local}\cdot10^{-3}$ (kPa)	ε_{circ} (−)
V1	63 ± 7.9	0.23 ± 0.03	B1	27 ± 20	0.13 ± 0.09
V2	65 ± 15	0.24 ± 0.05	B2	59 ± 31	0.16 ± 0.08
V3	105 ± 23	0.28 ± 0.05	B3	45 ± 19	0.16 ± 0.08
V4	77 ± 20	0.24 ± 0.05	B4	42 ± 28	0.18 ± 0.10
V5	104 ± 24	0.25 ± 0.05	B5	60 ± 60	0.22 ± 0.18
V6	90 ± 16	0.30 ± 0.04	B6	27 ± 5.7	0.12 ± 0.02
V7	67 ± 6.5	0.25 ± 0.02	B7	23 ± 12	0.13 ± 0.07
V8	83 ± 20	0.29 ± 0.06	B8	24 ± 15	0.14 ± 0.08
V9	60 ± 13	0.23 ± 0.05	B9	21 ± 13	0.14 ± 0.07
V10	89 ± 27	0.31 ± 0.08			

For each subject, the mean and standard deviation are reported.

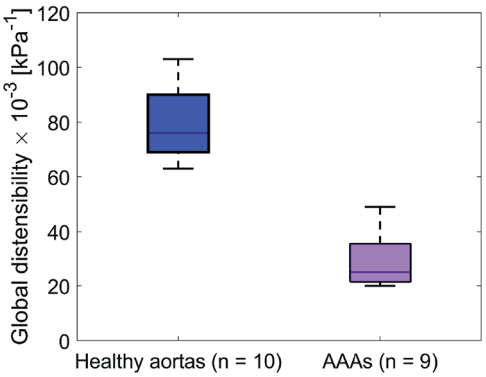

FIGURE 6
Boxplot of the global distensibility·10^{-3} (kPa^{-1}) of healthy aortas (blue) and AAAs (purple).

a 2D US system. Visual inspection of the resulting geometries reveals reduced performance in regions where thrombus is present (Figure 3) and where the angle between the US beam direction and the radial direction of the wall is large, i.e., the side wall regions. Hence, as expected, structures in these regions are less clearly visible in US images. Multi-perspective US imaging can help improve the lateral resolution, which can help improve segmentation quality in these regions (32). Registration was performed by iteratively minimizing the distances between the 3D point clouds of the CT and US geometries. Registration of the two datasets is challenging as the AAA is not rigid. Therefore, we limited the time between the US scan and CT scan as much as possible (Table 2). Furthermore, we used the mean arterial pressure state geometry for registration with the CT geometry. In the future, registration can be refined by matching image features.

Distensibility and strain were computed from the assessed ED and ES geometries and the brachial pressure measurements. Local assessments were performed by evaluating area change between ED and ES and global assessment of distensibility was performed by evaluating volume change. As illustrated in Figure 6 and Table 4, global distensibility values were larger for healthy aortas ($80 \pm 15 \cdot 10^{-3}$ kPa^{-1}) in comparison with AAAs ($29 \pm 9.6 \cdot 10^{-3}$ kPa^{-1}). Compared to previous studies (Table 5), distensibility values of healthy aortas are larger, but are in the same order of magnitude (11, 33). In our study, larger values than in previous literature are likely found, because the healthy volunteers are younger compared to those from previous studies. There is a biological variability in vessel

TABLE 4 Overview of global mechanical properties of healthy volunteers (V1–V10) and AAA patients (B1–B9).

	Volunteers				AAA patients			
	V_{ED} (ml)	V_{ES} (ml)	C_{global} (ml/kPa)	$D_{global}\cdot10^{-3}$ (kPa^{-3})		V_{ED} (ml)	V_{ES} (ml)	C_{global} (ml/kPa)	$D_{global}\cdot10^{-3}$ (kPa^{-1})
V1	3.65	5.51	0.23	63	B1	76	95	1.9	25
V2	12.2	18.7	0.78	64	B2	40	50	1.0	25
V3	5.16	8.47	0.53	103	B3	101	139	5.0	49
V4	10.3	15.3	0.71	69	B4	33	45	1.2	37
V5	10.4	16.2	1.06	102	B5	24	31	0.8	35
V6	3.75	6.56	0.34	90	B6	30	38	0.8	28
V7	4.12	6.64	0.30	73	B7	92	112	1.8	20
V8	6.37	10.5	0.52	82	B8	18	23	0.4	22
V9	6.67	10.2	0.47	70	B9	95	122	1.9	20
V10	3.09	5.20	0.24	79					
μV	-	-	-	80 ± 15	μB	-	-	-	29 ± 9.6

Global properties V_{ED} (ml), V_{ES} (ml), C_{global} (ml/kPa) and $D_{global}\cdot10^{-3}$ (kPa^{-1}) are reported.

TABLE 5 Comparison of our distensibility findings with other studies.

Study	System	Distension assessment	Distensibility·10^{-3} (kPa^{-1})	AAA diameter (mm)	Age mean (±SD)
Our study	Freehand 2D US	Volume; healthy	80 ± 15	-	26 ± 2
		Volume; AAAs	29 ± 9.6	47 ± 6	75 ± 9
		Area; healthy; local	60–105 (range)	-	26 ± 2
		Area; AAA; local	21–60 (range)	47 ± 6	75 ± 9
Long et al. (2004a)	Tissue Doppler	Mean segmental diameter; healthy	37 ± 13	-	34 ± 10
Long et al. (2004b)	Tissue Doppler	Mean segmental diameter; AAAs	6.1 ± 3.6	39 ± 9	70 ± 7.6
Rose et al. (2010)	Cine MR	Area; healthy	50 ± 17	-	29 ± 4
Zha et al. (2017)	CT	Area; below renal artery; AAAs	10.5 ± 2.2	>3.0 cm	67.2 ± 6.8
		Area; at max diameter; AAAs	4.9 ± 1.8		
Van 't Veer et al. (2008)	MRI	Volume, AAAs	2 ± 0.5	58 ± 6.0	73.6 ± 6.4
Molacek et al. (2011)	CT	Area; AAA region	3.7–56 (range)	60 ± 16	65
		Area; AAA Non-dilated region	12–42 (range)		

properties over the length of the vessel. A decline in distensibility from the proximal to the distal side of the aorta was visible for 7 out of 10 healthy aortas (**Figure 4**). Analysis of the local distensibility maps (**Figure 4**) and visual inspection of the US data and geometries (**Figure 2**) showed that regions of poor image quality apparently lead to overestimation or underestimation of distensibility. Circumferential strain values of the young healthy adults in our study (0.25 ± 0.03) were comparable to findings by a previous study on young adults (34, 35). Circumferential strains were assessed under the assumptions that the vessels exhibit small strains and that the aortic tissue is incompressible and isotropic, which are simplifications that are often used to model aortas and AAAs (36). Furthermore, the local circumference change is estimated from the spatiotemporal data that was available in the close neighborhood. In the future, higher frame rates and improved image quality can potentially lead to a more local approach where the local heterogeneity in the circumference of the wall could be studied, by using methods such as speckle tracking (34, 35).

As illustrated in **Figure 5**, distensibility was for most AAA cases smaller in dilated vessel regions compared to the non-dilated, or less dilated regions, which is in accordance with previous studies (37–39). As shown in **Table 5** distensibility values of the AAA patients fell within the range of a study by Molacek et al. but were larger than those obtained in other studies (9, 12, 38, 39). Although the geometries match well with the gold standard, segmentation errors may lead to over or underestimation of distensibility. Commonly, diameter-based distension values are computed from US data for distensibility computation. The compliance of the vessel is then often computed with the assumption that an increase in diameter leads to an area change that is twice as big (11, 12). This has been derived for circular shapes (40). However, AAAs are typically non-circular and healthy abdominal aortas are not necessarily a circle (41). Hence this assumption is not fully reliable. Evaluation of area change, or volume change would allow for accurate compliance assessment. US imaging is considered safer than MRI or CT. However, with US imaging the image is generally reduced in the side wall regions compared to the upper and lower wall regions, due to the physics of US. This can lead to inaccuracies in area or volume measurements. Multiperspective US imaging or artificial intelligence techniques that can optimize the image quality could further improve the reliability of compliance assessment from lumen area change as opposed to a diameter-based approach.

Freehand 2D US acquisition is fast and save and can easily be performed in the clinical workflow. In addition to this, the offline segmentation of the vessel wall is semi-automatic, and the remainder of the workflow is fully automatic, allowing for quick analysis. With the approach we propose, we can obtain both patient-specific geometries and mechanical properties such as distensibility and circumferential strain. Locally we could estimate the distension of the vessel based on automatically detected sample points in the end diastolic and end systolic phase of the cardiac cycle. The spatial resolution, temporal resolution and the field-of-view that can be achieved with freehand 2D US clearly outperform those provided by conventional 3D US imaging. Hence, this approach can provide more complete data (i.e., full geometry, local material properties) for making a personalized finite element model of the aneurysm, as was previously performed with conventional 3D US imaging (6), but with a simpler 2D US device. Furthermore, application may now be considered for AAA follow-up studies. These

studies can help to determine how these biomechanical parameters relate to AAA growth and AAA rupture risk. Distensibility assessment from freehand 2D US is not limited to wall distension only and could be extended for studying distension of the lumen-thrombus interface as well.

A limitation of the imaging approach in this study is the fixed sampling rate of 25 Hz of the acquisition system combined with the probe tracker. As the probe is moved freehand, the distance between frames may vary within one acquisition and between acquisitions of different subjects. It is expected that local estimations of distensibility are more accurate in regions where the samples are closer together, i.e., with slower probe speeds. Specifically in regions where besides changes due to pulsatility, the vessel dimension changes significantly within one heartbeat, unexpected values of distensibility were observed. There is a tradeoff between field-of-view and sample density. A too slow probe speed will reduce patient comfort. Moreover, the image quality may be hampered by patient body motion and motions due to breathing. In the future, instructing and training sonographers to perform the acquisition with reasonable speeds can help to reduce the geometrical spacing between frames as much as possible, while maintaining a large field-of-view.

What remains challenging with freehand 2D US is assessment of the full geometry. The average length of the captured region that was segmented was 60 mm ± 21 for volunteers and 65 mm ± 15 for AAA patients. Due to bowel gas and obesity, the image quality can locally be reduced, leading to incomplete measurements, as has previously been reported in studies with freehand 2D US (14, 15, 17). However, similar challenges occur with conventional 2D US imaging or 3D US imaging with a matrix array. The focus of this study was to evaluate quality of geometry assessment compared to CT and to demonstrate assessment of distensibility based on area change and volume change. Therefore, datasets that included a part of the region of interest were still included and only datasets with poor image quality throughout the entire acquisition were discarded. Acquisitions are performed during breath-hold, which limits acquisition time and thereby the field of view. To increase the field of view, multiple acquisitions could be performed, where the best data of each acquisition could be included and registered. Alternatively, acquisitions could be performed without breath-hold. Besides this, additional training for freehand 2D US imaging could help to improve image quality and field of view.

Freehand 2D US acquisition is fast and save and can easily be performed in the clinical workflow. In addition to this, the offline segmentation of the lumen-wall or thrombus-wall interface is semi-automatic, and the remainder of the workflow is fully automatic, allowing for quick analysis. Distensibility assessment from freehand 2D US is not limited to wall distension only and could be extended for studying distension of the lumen-thrombus interface, which could help to further model and characterize AAAs.

Conclusion

To conclude, in this study we propose a novel approach that uses the pulsatility that is captured with freehand 2D US imaging for distensibility assessment of AAAs. Where pulsatility typically hampers reconstruction of volumetric images and is therefore neglected, it can be utilized to retrieve additional information from the dataset besides geometries. Registration and comparison with CT showed good overall overlap between geometries. Furthermore, results are comparable to studies that assessed geometries from 3D US data obtained with a matrix probe, while the higher frame rate of freehand 2D US combined with signal processing allows for local distensibility assessment. The method performs as expected in regions with sufficient image quality but needs improvements for regions with large geometry changes and poor image quality. This could be mitigated by reducing the probe speed, advanced motion filtering of motions due to breathing, and by performing multi-perspective ultrasound imaging. In the future, the approach can be further expanded with quantification of distension of the lumen-thrombus interface.

Data availability statement

The raw data supporting the conclusions of this article will be made available by the authors, without undue reservation.

Ethics statement

The studies involving human participants were reviewed and approved by Medical research Ethics Committees United (MEC-U). The patients/participants provided their written informed consent to participate in this study.

Author contributions

All authors: conception and design of the work. LJ, MS: Acquisition and compilation of the clinical data. LJ: Development of methods for computer-based image analysis and data processing. LJ: Initial drafting of manuscript. All authors: Analysis and interpretation of data, critical review of

manuscript, and final approval of manuscript. All authors contributed to the article and approved the submitted version.

Funding

This research was funded by the NWO perspective program ultra-X-treme (P32-17), Project ElastiX.

Acknowledgments

The acquisitions in this study were carried out with a probe tracker system. We want to thank S. Wittmeier of Curefab and J. de Ruijter of PULS/e group for their valuable technical support.

Conflict of interest

The authors declare that the research was conducted in the absence of any commercial or financial relationships that could be construed as a potential conflict of interest.

Publisher's note

References

1. Chaikof EL, Dalman RL, Eskandari MK, Jackson BM, Lee WA, Mansour MA, et al. The society for vascular surgery practice guidelines on the care of patients with an abdominal aortic aneurysm. *J Vasc Surg.* (2018) 67(1):2–77.e2. doi: 10.1016/j.jvs.2017.10.044

2. Moll FL, Powell JT, Fraedrich G, Verzini F, Haulon S, Waltham M, et al. Management of abdominal aortic aneurysms clinical practice guidelines of the European society for vascular surgery. *Eur J Vasc Endovasc Surg.* (2011) 41 (Suppl 1):S1–S58. doi: 10.1016/j.ejvs.2010.09.011

3. Scott RAP, Wilson NM, Ashton HA, Kay DN. Influence of screening on the incidence of ruptured abdominal aortic aneurysm: 5-year results of a randomized controlled study. *Br J Surg.* (2005) 82(8):1066–70. doi: 10.1002/bjs.1800820821

4. Nicholls SC, Gardner JB, Meissner MH, Johansen KH. Rupture in small abdominal aortic aneurysms. *J Vasc Surg.* (1998) 28(5):884–8. doi: 10.1016/S0741-5214(98)70065-5

5. Reed WW, Hallett JW, Damiano MA, Ballard DJ. Learning from the last ultrasound: a population-based study of patients with abdominal aortic aneurysm. *Arch Intern Med.* (1997) 157(18):2064–8. doi: 10.1001/archinte.1997.00440390050007

6. van Disseldorp EMJ, Petterson NJ, Rutten MCM, van de Vosse FN, van Sambeek MRHM, Lopata RGP. Patient specific wall stress analysis and mechanical characterization of abdominal aortic aneurysms using 4D ultrasound. *Eur J Vasc Endovasc Surg.* (2016) 52(5):635–42. doi: 10.1016/j.ejvs.2016.07.088

7. van Disseldorp EMJ, van Dronkelaar JJ, Pluim JPW, van de Vosse FN, van Sambeek MRHM, Lopata RGP. Ultrasound based wall stress analysis of abdominal aortic aneurysms using multiperspective imaging. *Eur J Vasc Endovasc Surg.* (2020) 59(1):81–91. doi: 10.1016/j.ejvs.2019.01.026

8. Spencer MP, Denison AB. Pulsatile blood flow in the vascular system. In: Hamilton, WF, Dow, P, editors. *Handbook of physiology*. Washington, DC: American Physiology Society (1963). p. 842.

9. van 't Veer M, Buth J, Merkx M, Tonino P, van den Bosch H, Pijls N, et al. Biomechanical properties of abdominal aortic aneurysms assessed by simultaneously measured pressure and volume changes in humans. *J Vasc Surg.* (2008) 48(6):1401–7. doi: 10.1016/j.jvs.2008.06.060

10. Hoegh A, Lindholt JS. Basic science review: vascular distensibility as a predictive tool in the management of small asymptomatic abdominal aortic aneurysms. *Vasc Endovascular Surg.* (2009) 43(4):333–8. doi: 10.1177/1538574409336019

11. Long A, Rouet L, Bissery A, Goeau-Brissonniere O, Sapoval M. Aortic compliance in healthy subjects: evaluation of tissue Doppler imaging. *Ultrasound Med Biol.* (2004a) 30(6):753–9. doi: 10.1016/j.ultrasmedbio.2004.03.007

12. Long A, Rouet L, Bissery A, Rossignol P, Mouradian D, Sapoval M. Compliance of abdominal aortic aneurysms: evaluation of tissue Doppler imaging. *Ultrasound Med Biol.* (2004b) 30(9):1099–108. doi: 10.1016/j.ultrasmedbio.2004.08.007

13. Long A, Rouet L, Debreuve A, Ardon R, Barbe C, Becquemin JP, et al. Abdominal aortic aneurysm imaging with 3-D ultrasound: 3-D-based maximum diameter measurement and volume quantification. *Ultrasound Med Biol.* (2013) 39(8):1325–36. doi: 10.1016/j.ultrasmedbio.2013.03.008

14. Zielinski AH, Bredahl KK, Ghulam QM, Rouet L, Dufour C, Sillesen HH, et al. Full-volume assessment of abdominal aortic aneurysm by improved-field-of-view 3-D ultrasound performs comparably to computed tomographic angiography. *Ultrasound Med Biol.* (2022) 48(2):283–92. doi: 10.1016/j.ultrasmedbio.2021.10.018

15. Zielinski AH, Bredahl KK, Ghulam Q, Rouet L, Dufour C, Sillesen HH, et al. Full-volume assessment of abdominal aortic aneurysms by 3-D ultrasound and magnetic tracking. *Ultrasound Med Biol.* (2020) 46(12):3440–7. doi: 10.1016/j.ultrasmedbio.2020.09.002

16. Mozaffari MH, Lee WS. Freehand 3-D ultrasound imaging: a systematic review. *Ultrasound Med Biol.* (2017) 43(10):2099–124. doi: 10.1016/j.ultrasmedbio.2017.06.009

17. Khan M, Rogers S, Carreira J, Ghosh J, McCollum C. Aneurysm geometry analyzed by the novel three-dimensional tomographic ultrasound relates to abdominal aortic aneurysm growth. *Ann Vasc Surg.* (2022) 87:469–77. doi: 10.1016/j.avsg.2022.05.017

18. Leotta DF, Paun M, Beach KW, Kohler TR, Zierler RE, Strandness DE. Measurement of abdominal aortic aneurysms with three-dimensional ultrasound imaging: preliminary report. *J Vasc Surg.* (2001) 33(4):700–7. doi: 10.1067/mva.2001.112812

19. Causey MW, Jayaraj A, Leotta DF, Paun M, Beach KW, Kohler TR, et al. Three-dimensional ultrasonography measurements after endovascular aneurysm repair. *Ann Vasc Surg.* (2013) 27(2):146–53. doi: 10.1016/j.avsg.2012.01.018

20. de Ruijter J, van Sambeek M, van de Vosse F, Lopata R. Automated 3D geometry segmentation of the healthy and diseased carotid artery in free-hand, probe tracked ultrasound images. *Med Phys.* (2020) 47(3):1034–47. doi: 10.1002/mp.13960

21. Feurer R, Hennersperger C, Runyan JB, Seifert CL, Pongratz J, Wilhelm M, et al. Reliability of a freehand three-dimensional ultrasonic device allowing anatomical orientation "at a glance": study protocol for 3D measurements with curefab CS®. *J Biomed Graph Comput.* (2012) 2(2):1–10. doi: 10.5430/jbgc.v2n2p1

22. Alvarez L, Guichard F, Lions PL, Morel JM. Axioms and fundamental equations of image processing. *Arch Ration Mech Anal.* (1993) 123(3):199–257. doi: 10.1007/BF00375127

23. Guerrero J, Salcudean SE, McEwen JA, Masri BA, Nicolaou S. Real-time vessel segmentation and tracking for ultrasound imaging applications. *IEEE Trans Med Imaging.* (2007) 26(8):1079–90. doi: 10.1109/TMI.2007.899180

24. Friedland N, Adam D. Automatic ventricular cavity boundary detection from sequential ultrasound images using simulated annealing. *IEEE Trans Med Imaging.* (1989) 8(4):344–53. doi: 10.1109/42.41487

25. Chen Y, Medioni G. Object modeling by registration of multiple range images. *Proc IEEE Int Conf Robot Autom*. (1991) 3:2724–9. doi: 10.1109/ROBOT.1991.132043

26. Besl PJ, McKay ND. A method for registration of 3-D shapes. *IEEE Trans Pattern Anal Mach Intell*. (1992) 14(2):239–56. doi: 10.1109/34.121791

27. Kjer H, Wilm J. *Evaluation of surface registration algorithms for PET motion correction [BSc thesis]*. Technical University of Denmark (2010).

28. Rote G. Computing the minimum hausdorff distance between two point sets on a line under translation. *Inf Process Lett*. (1991) 38(3):123–7. doi: 10.1016/0020-0190(91)90233-8

29. Rouet L, Mory B, Attia E, Bredahl K, Long A, Ardon R. A minimally interactive and reproducible method for abdominal aortic aneurysm quantification in 3D ultrasound and computed tomography with implicit template deformations. *Comput Med Imaging Graph*. (2017) 58:75–85. doi: 10.1016/j.compmedimag.2016.11.002

30. Grunovas A, Trinkunas E, Buliuolis A, Venskaityte E, Poderys J, Poderiene K. Cardiovascular response to breath-holding explained by changes of the indices and their dynamic interactions. *Biol Syst Open Access*. (2016) 5(1). doi: 10.4172/2329-6577.1000152

31. Kok AM, Nguyen VL, Speelman L, Brands PJ, Schurink GWH, van de Vosse FN, et al. Feasibility of wall stress analysis of abdominal aortic aneurysms using three-dimensional ultrasound. *J Vasc Surg*. (2015) 61(5):1175–84. doi: 10.1016/j.jvs.2014.12.043

32. Petterson NJ, van Sambeek MRHM, van de Vosse FN, Lopata RGP. Enhancing lateral contrast using multi-perspective ultrasound imaging of abdominal aortas. *Ultrasound Med Biol*. (2021) 47(3):535–45. doi: 10.1016/j.ultrasmedbio.2020.09.023

33. Rose JL, Lalande A, Bouchot O, Bourennane EB, Walker PM, Ugolini P, et al. Influence of age and sex on aortic distensibility assessed by MRI in healthy subjects. *Magn Reson Imaging*. (2010) 28(2):255–63. doi: 10.1016/j.mri.2009.07.001

34. Derwich W, Wittek A, Pfister K, Nelson K, Bereiter-Hahn J, Fritzen CP, et al. High resolution strain analysis comparing aorta and abdominal aortic aneurysm with real time three dimensional speckle tracking ultrasound. *Eur J Vasc Endovasc Surg*. (2016) 51(2):187–93. doi: 10.1016/j.ejvs.2015.07.042

35. Karatolios K, Wittek A, Nwe TH, Bihari P, Shelke A, Josef D, et al. Method for aortic wall strain measurement with three-dimensional ultrasound speckle tracking and fitted finite element analysis. *Ann Thorac Surg*. (2013) 96(5):1664–71. doi: 10.1016/j.athoracsur.2013.06.037

36. Humphrey JD, Holzapfel GA. Mechanics, mechanobiology, and modeling of human abdominal aorta and aneurysms. *J Biomech*. (2012) 45(5):805–14. doi: 10.1016/j.jbiomech.2011.11.021

37. Ganten MK, Krautter U, von Tengg-Kobligk H, Böckler D, Schumacher H, Stiller W, et al. Quantification of aortic distensibility in abdominal aortic aneurysm using ECG-gated multi-detector computed tomography. *Eur Radiol*. (2008) 18(5):966–73. doi: 10.1007/s00330-007-0833-5

38. Molacek J, Baxa J, Houdek K, Treska V, Ferda J. Assessment of abdominal aortic aneurysm wall distensibility with electrocardiography-gated computed tomography. *Ann Vasc Surg*. (2011) 25(8):1036–42. doi: 10.1016/j.avsg.2011.05.034

39. Zha Y, Peng G, Li L, Yang C, Lu X, Peng Z. Quantitative aortic distensibility measurement using CT in patients with abdominal aortic aneurysm: reproducibility and clinical relevance. *Biomed Res Int*. (2017) 2017. doi: 10.1155/2017/5436927

40. Reneman RS, van Merode T, Hick P, Muytjens AMM, Hoeks APG. Age-related changes in carotid artery wall properties in men. *Ultrasound Med Biol*. (1986) 12(6):465–71. doi: 10.1016/0301-5629(86)90218-8

41. Voges I, Jerosch-Herold M, Hedderich J, Pardun E, Hart C, Gabbert DD, et al. Normal values of aortic dimensions, distensibility, and pulse wave velocity in children and young adults: a cross-sectional study. *J Cardiovasc Magn Reson*. (2012) 14(1):1–13. doi: 10.1186/1532-429X-14-77

frontiers | Frontiers in Bioengineering and Biotechnology

TYPE Original Research
PUBLISHED 30 January 2023
DOI 10.3389/fbioe.2023.1096196

OPEN ACCESS

EDITED BY
Amirhossein Arzani,
The University of Utah, United States

REVIEWED BY
Seungik Baek,
Michigan State University, United States
Rana Zakerzadeh,
Duquesne University, United States
Estefania Peña,
University of Zaragoza, Spain

*CORRESPONDENCE
Simona Celi,
s.celi@ftgm.it

SPECIALTY SECTION
This article was submitted to Biomechanics, a section of the journal Frontiers in Bioengineering and Biotechnology

RECEIVED 11 November 2022
ACCEPTED 19 January 2023
PUBLISHED 30 January 2023

CITATION
Celi S, Gasparotti E, Capellini K, Bardi F, Scarpolini MA, Cavaliere C, Cademartiri F and Vignali E (2023), An image-based approach for the estimation of arterial local stiffness *in vivo*. *Front. Bioeng. Biotechnol.* 11:1096196. doi: 10.3389/fbioe.2023.1096196

An image-based approach for the estimation of arterial local stiffness *in vivo*

Simona Celi[1]*, Emanuele Gasparotti[1], Katia Capellini[1], Francesco Bardi[1,2], Martino Andrea Scarpolini[1,3], Carlo Cavaliere[4], Filippo Cademartiri[5] and Emanuele Vignali[1]

[1]BioCardioLab, UOC Bioingegneria, Fondazione Toscana G Monasterio, Massa, Italy, [2]Mines Saint-Etienne, Universit'e de Lyon, INSERM, SaInBioSE U1059, Lyon, France, [3]Dipartimento di Ingegneria Industriale, Università "Tor Vergata", Roma, Italy, [4]Dipartimento di Radiologia, IRCCS SynLab SDN, Napoli, Italy, [5]Dipartimento Immagini, Fondazione Toscana G. Monasterio, Pisa, Italy

The analysis of mechanobiology of arterial tissues remains an important topic of research for cardiovascular pathologies evaluation. In the current state of the art, the gold standard to characterize the tissue mechanical behavior is represented by experimental tests, requiring the harvesting of *ex-vivo* specimens. In recent years though, image-based techniques for the *in vivo* estimation of arterial tissue stiffness were presented. The aim of this study is to define a new approach to provide local distribution of arterial stiffness, estimated as the linearized Young's Modulus, based on the knowledge of *in vivo* patient-specific imaging data. In particular, the strain and stress are estimated with sectional contour length ratios and a Laplace hypothesis/inverse engineering approach, respectively, and then used to calculate the Young's Modulus. After describing the method, this was validated by using a set of Finite Element simulations as input. In particular, idealized cylinder and elbow shapes plus a single patient-specific geometry were simulated. Different stiffness distributions were tested for the simulated patient-specific case. After the validation from Finite Element data, the method was then applied to patient-specific ECG-gated Computed Tomography data by also introducing a mesh morphing approach to map the aortic surface along the cardiac phases. The validation process revealed satisfactory results. In the simulated patient-specific case, root mean square percentage errors below 10% for the homogeneous distribution and below 20% for proximal/distal distribution of stiffness. The method was then successfully used on the three ECG-gated patient-specific cases. The resulting distributions of stiffness exhibited significant heterogeneity, nevertheless the resulting Young's moduli were always contained within the 1–3 MPa range, which is in line with literature.

KEYWORDS

***in vivo* arterial stiffness, tissue mechanics, ECG-gated CT images, mesh-morphing, inverse engineering**

1 Introduction

The analysis of arterial tissue remains a pivotal topic of research in the field of cardiovascular pathologies. It was well established that a plethora of cardiovascular diseases find their origin within the mechanics and the biology of the vessel tissues (Humphrey and Schwartz. (2021)). Attention was focused on both large and small vessels including different types of pathologies like dissections, stenosis/atherosclerotic arteries and aneurysms (Celi et al. (2013); Gültekin et al. (2019); Vignali et al. (2020)). An aneurysm is defined as a local dilatation in the aortic wall, that is usually asymptomatic up to the sudden rupture which may be linked

with patient's death (Ramanath et al. (2009)). The current clinical practice is to define a critical aortic size criterion to determine the necessity of surgical implantation. The aneurysm pathology remains an open clinical challenge and it still requires a deep insight in terms of formation and progression mechanisms. Different studies reported that the critical state of an aneurysm case arises from the status of the tissue biomechanics and its degradation (Vignali et al. (2020); Vignali et al. (2021c)). The usage of the mechanical analysis principle could ideally provide an improved understanding of the aneurysm nature and, in general, of the arterial behavior under given pathological conditions.

Following this analysis principle, different groups have provided mechanical insights concerning the arterial tissues. In the current state of the art, various experimental testing procedures have been proposed, like uniaxial/biaxial traction tests (Vignali et al. (2021a); Peña et al. (2015)) and bulge inflation approaches (Duprey et al. (2016)). It is also worth noting that several studies were focused on the investigation of correlation of biological and mechanical features of the arterial tissue (Vignali et al. (2020; 2021c)), given their important link. This literature field presents a shared flaw, which is the necessity of *ex-vivo* tissue samples to be tested. Given this, the mechanical analysis is necessarily limited to post-operative cases, in which the surgical procedure has already been performed. Consequently, it is impossible to have a direct mechanical characterization of the arterial tissue without an invasive procedure.

Obtaining mechanical features of the arterial tissue non-invasively still represents an open research topic. Nevertheless, research efforts towards this direction have been made recently. Several image-based approaches have already been explored to estimate mechanical properties of soft tissues in general (Fanni et al. (2020); Di Lascio et al. (2014)). These *in vivo* estimation methods are made possible thanks to the recent advances in terms of clinical imaging (Celi et al. (2017)), which allow high-resolution reconstruction of cardiovascular structures at different cardiac phases. The dynamic nature of imaging techniques like ECG-gated Computed Tomography (CT), echography and 4D Magnetic Resonance Imaging (4D-MRI) opens the possibility to reconstruct the displacement fields of cardiovascular structures.

The main focus of non-invasive mechanical analysis resides mainly in strain estimation on vessels like the ascending aorta section. The reported *in vivo* strain evaluation techniques are usually based on mapping algorithms aimed at reconstructing the aortic kinematics along the cardiac cycle. Among the different mapping techniques, iterative registration approaches (Liu et al. (2019b); Narayanan et al. (2021)), projections along the normal of the aortic surface (Pasta et al. (2017)) and centerline-based decompositions with parametric templates (Farzaneh et al. (2019b; Farzaneh et al. (2019a)) were proposed. Beyond the knowledge of aortic strain, stress is still required for a stiffness estimation. Nevertheless, the *in vivo* evaluation of stress remains a difficult task. For this reason, different studies were limited to strain-only analyses (Pasta et al. (2017)), or presented assumptions on the load to infer simplified stress distributions (Duprey et al. (2016); Martin et al. (2013)). Some groups proposed iterative Finite Element (FE) approaches for the direct estimation of aortic stiffness (Krishnan et al. (2015)), but the requirement for multiple numerical simulations can be computationally onerous. Other groups also proposed aortic volumetric distensibility as a surrogate for stiffness estimation (Trabelsi et al. (2018)), but the global nature of the parameter did not allow for a local estimation of the material properties.

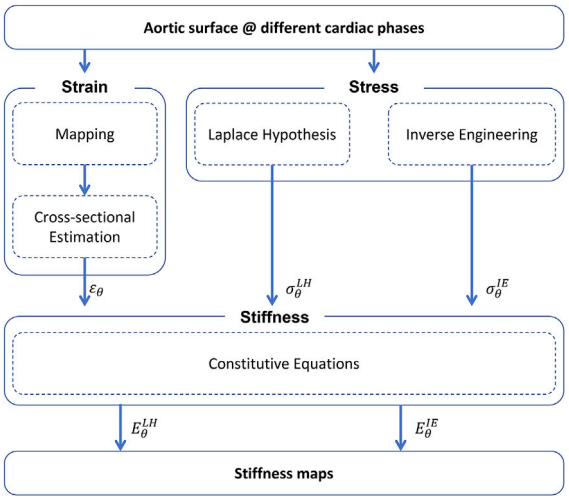

FIGURE 1
Summary of the workflow for the non-invasive stiffness estimation (ε_θ—circumferential strain, $\sigma_\theta^{LH,IE}$—circumferential stress estimated with Laplace Hypothesis (LH) or with inverse engineering (IE) approach, $E_\theta^{LH,IE}$—circumferential stiffness estimated with Laplace Hypothesis (LH) or with inverse engineering (IE) approach.

With the current study, a new method for the strain and stiffness estimation of the aortic vessel is proposed. The method aims at providing local information, in opposition with volumetric/global approaches (Trabelsi et al. (2018); Danpinid et al. (2009)) by relying on CT data, centerline calculation and mesh-morphing based mapping. Other previous studies relied on centerline-based information (Zeinali-Davarani et al. (2011)), nevertheless their focus was more centered on the abdominal aorta district and they used the centerline to map wall thickness interpolations along the vessel. To our knowledge, this is the first approach proposing a mesh-morphing sequence to allow for the mapping of the aortic surface along the different cardiac cycle phases. The morphing of the baseline mesh on the different deformed surfaces can allow for a fast method for mapping and, consequently, it gives a great potential for local strain evaluation. Concerning the stress, a further step to go beyond the literature relying on the Laplace hypothesis (Liu et al. (2019a); Martin et al. (2013)) could be imposed by relying on inverse FE simulations.

The aim of the current work is to propose a new approach to provide local distribution of arterial stiffness, based on the knowledge of *in vivo* patient-specific imaging data. The method is based on the calculation of aortic strain on the basis of contour length ratios for each section. For the estimation of stress, two approaches were tested: an approach based on Laplace hypothesis, and an approach based on an inverse engineering FE simulation to estimate the distribution of wall tension on the aortic geometry. The entire procedure was first validated on a set of FE simulations. The two estimation methods were first compared for the validation phase. Finally, the approach was applied on three patient-specific ECG-gated CT data to estimate the local stiffness distribution *in vivo*. The results are then presented and discussed to assess the new method performances and future applications.

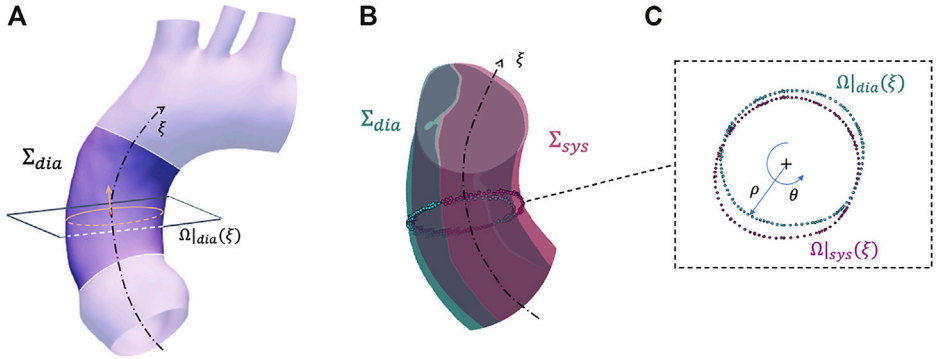

FIGURE 2
Summary of the strain estimation algorithm: example of a plane and closed contour definition on configuration Σ_{dia} **(A)**, corresponding closed contour definition on configuration Σ_{sys} **(B)** with closeup on plane with polar coordinates **(C)**.

2 Materials and methods

In this section the three main steps of the entire pipeline are presented: method description (Subsection 2.1), validation (Subsection 2.2) and application (Subsection 2.3).

2.1 Method for non-invasive stiffness estimation

The methods for the stiffness estimation are described in the workflow depicted in Figure 1. The workflow is divided in three main parts: strain i), stress ii) and stiffness iii) estimation.

Strain estimation—A mapping procedure is required first. The mapping purpose is to define a nodal mesh which can be tracked across each reconstructed aortic geometry. Each node must be mapped to represent the position of the same material point at each phase of the cardiac cycle. For this reason, it is fundamental to define a mesh for all phases with the same number of nodes and connectivity. To achieve this, a mesh morphing approach based on radial-basis functions interpolation is adopted (Capellini et al. (2018); Capellini et al. (2021)). Briefly, the surfaces at each of the different cardiac phases are calculated by taking the 0% phase as the reference mesh, that is the baseline surface configuration (Σ_{dia}). The baseline surface mesh is then morphed onto the deformed surfaces, according to radial basis functions interpolation. The source points to morph the initial mesh onto the other phases were selected on the basis of a sphere grid within the ascending aorta section. At each phase, specific sets of target points were chosen. After the procedure, the result is given by a set of deformed meshes, including the peak systolic phase (Σ_{sys}).

After the mapping procedure, a specific algorithm is developed to estimate the strain from the mapped aortic surfaces in the Σ_{dia} and Σ_{sys} configurations. The algorithm is based on sectional contour length ratios and it is summarized in Figure 2. The choice of defining sectional contours to estimate the strain is motivated by the fact that the imposed mapping does not account for physiological deformations of the vessel but it is based on surface fitting optimizations (Sieger et al. (2014)). In brief, the centerline (ξ) of the Σ_{dia} configuration is evaluated first. Then, for each centerline coordinate ξ, a set of nodes was extracted representing a given cross section of the vessel. The cross sectional points were selected according to a distance threshold from the surface Σ_{dia} and a given plane defined from the centerline tangent. It is important to highlight that it is sufficient to evaluate the centerline on the baseline configuration only, as the movement of the centerline itself is already taken into account by considering the corresponding cross sectional points, thanks to nodal mapping. It is reasonable to consider that during the cardiac cycle the aorta experiences longitudinal displacement as well. In fact, the mapping provided by the morphing of the baseline surface onto the deformed surface also accounts for axial displacement.

At the ξ centerline coordinate, a closed contour $\Omega|_{dia}(\xi)$ is defined by sorting the cross sectional points according to a polar coordinate conversion (Figure 2A). At this point, the $\Omega|_{dia}(\xi)$ radial contour length is defined as:

$$L|_{dia}(\xi) = \int_{\Omega|_{dia}(\xi)} \rho(\theta) d\theta \tag{1}$$

where $\rho(\theta)$ and θ are the polar coordinates (radial and circumferential, respectively) defined for the cross sectional plane at the ξ centerline coordinate point. Thanks to the mapping procedure, it was possible to identify the corresponding cross sectional nodes for each centerline node at the Σ_{sys} configuration. This permitted the definition of a closed contour at the ξ centerline coordinate within the Σ_{sys} configuration ($\Omega|_{sys}(\xi)$) and, by applying Eq. 1 again, the definition of the corresponding length ($L|_{sys}(\xi)$) (Figures 2B, C). As circumferential strain represents the change in the length along the aorta cross section, it is possible to define the sectional contour length ratio as:

$$\varepsilon_\theta(\xi) = \frac{L|_{sys}(\xi) - L|_{dia}(\xi)}{L|_{dia}(\xi)} \tag{2}$$

where $\varepsilon_\theta(\xi)$ is the circumferential strain at the aortic cross section identified by the centerline coordinate ξ. By assuming this, the obtained strain distribution results to be a function of the centerline coordinate ξ.

Stress estimation—For the evaluation of local stress distribution, two main approaches were adopted: a Laplace-hypothesis-based (LH) and an inverse-engineering-based (IE) method.

For the first method, the assumption of a thin walled surface is made for the aortic structure, with negligible curvature at the ascending section (Liu et al. (2019a)). The negligibility of curvature is checked according to the following condition (Zhang et al. (2013)):

$$m = \frac{R_0 - r}{R_0 - r/2} \approx 1 \tag{3}$$

where m is the curvature effect factor, R_0 is the centerline radius of curvature and r is the section radius. On the basis of this, it is safe to evaluate the circumferential stress as the wall hoop stress. By considering each cross section of the aortic centerline, the corresponding nodal circumferential stress according to the Laplace method is evaluated as:

$$\sigma_\theta^{LH}(\xi) = \frac{\Delta P \bar{\rho}}{\delta} \tag{4}$$

where $\sigma_\theta^{LH}(\xi)$ and δ are the circumferential stress and the thickness of the aortic vessel, while ΔP is the pressure difference between the systolic and diastolic condition and $\bar{\rho}$ is the mean radius at the centerline coordinate ξ. The mean radius was calculated by considering the mean radial coordinate, according to the polar coordinate system already defined for the sectional contour calculation (see Eq. 1).

For the second alternative method, an inverse engineering (IE) approach is chosen (Lu et al. (2008); Zhou et al. (2010)). It is well known that the wall tension in a pressurized membrane is equilibrium-determinate and it depends exclusively on the morphology. Briefly, a structural FE simulation is setup to evaluate the circumferential stress distribution at each node of the mapped mesh. To obtain a stress distribution, depending on the aortic morphology only, the deformed geometry in systolic configuration was loaded with an internal pressure of ΔP. The aorta was modeled as a membrane with a practically undeformable isotropic material (Young's modulus (E) > 10 GPa). By considering each cross section of the aortic centerline, the mean circumferential stress from the inverse method at a given point for the centerline can be evaluated as:

$$\sigma_\theta^{IE}(\xi) = \frac{1}{N} \sum_{i \in \Omega|_{sys}(\xi)}^{N} \sigma_\theta^{i}(\xi, \theta_i) \tag{5}$$

where $\sigma_\theta^{IE}(\xi)$ is the nodal maximum principal stress resulting from the simulation and N is the number of nodes in a sector of section $\Omega|_{sys}(\xi)$. By assuming this model, it is possible to account for curvature effect on stress within the aortic domain.

Stiffness estimation—The definition of stiffness from the evaluation of strain and stress is, at last, performed. To evaluate the stiffness, the model was assumed as linearized, given the possibility to assume small deformations occurring between diastolic and systolic phase (Vignali et al. (2021b); Roccabianca et al. (2014)). The assumption allowed for the adoption of the Hooke law as a constitutive equation to relate stress and strain. By assuming a negligible radial and longitudinal stress and by considering Eqs 2, 4, and 5, the following can be imposed to estimate the circumferential stiffness:

$$E_\theta^{LH}(\xi) = \frac{\sigma_\theta^{LH}(\xi)}{\varepsilon_\theta(\xi)}; \quad E_\theta^{IE}(\xi) = \frac{\sigma_\theta^{IE}(\xi)}{\varepsilon_\theta(\xi)} \tag{6}$$

where E_θ^{LH} and E_θ^{IE} represent the circumferential Young's moduli evaluated according to the two different stress estimation techniques already described.

2.2 Numerical validation

After defining the stiffness estimation methods, the technique was validated according to a FE approach. Firstly, idealized synthetic geometries were defined. In particular, a cylinder, a 45° and a 90° elbow geometries were defined, to assess the influence of curvature (Figure 3). All the idealized geometries were designed with a diameter of 32 mm and a length of 100 mm. In addition, a patient-specific test case was selected from a segmented aortic geometry. For all the cases, a thickness of 2 mm was assumed. The numerical workflow for the validation on the patient-specific simulated case is summarized in Figure 4. The geometry of the ascending aorta was taken from a

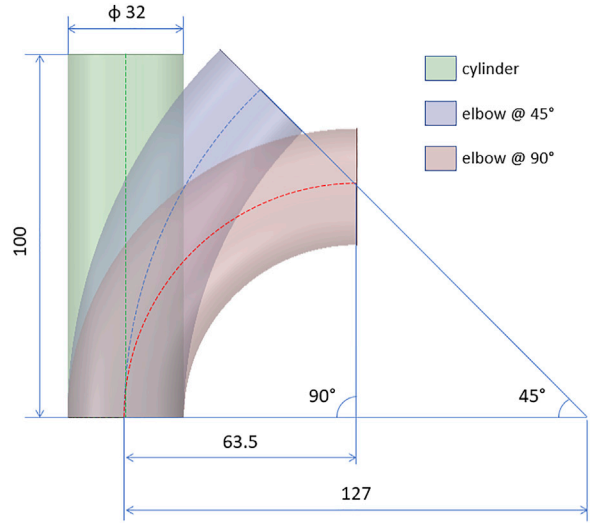

FIGURE 3
Design of the idealized geometries for the validation cases: cylinder and elbows at 45° and 90°. All quotations are given in mm.

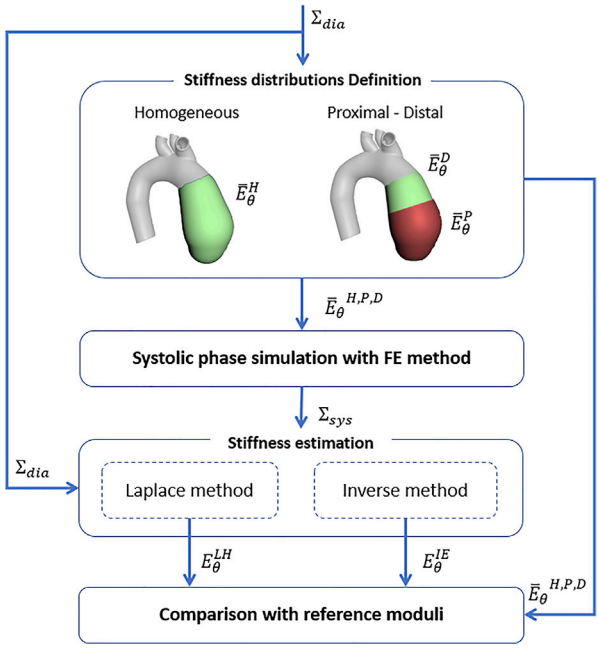

FIGURE 4
Numerical validation workflow for the stiffness estimation algorithm on the basis of FE simulations.

contrast-enhanced CT dataset with ECG-gating, obtained with a 320-detector scanner (Toshiba Aquilon One, Toshiba, Japan). Thanks to the ECG-gating, the diastolic phase was selected for the segmentation. The segmentation procedure was carried out through a semi-automatic region-growing algorithm following the approach previously described in Celi et al. (2021). The validation procedure can be summarized in three main phases: material properties distribution i), systolic phase definition ii), stiffness estimation application and comparison iii). All the simulation activities were carried out within the ANSYS environment.

Material properties distribution definition—For the idealized geometries, a linear elastic isotropic homogeneous distribution of stiffness was assumed. A single value of Young's modulus ($\bar{E}_\theta^H$ = 0.5 MPa) was imposed. Concerning instead the simulated patient-specific case, four main cases of Young's modulus distribution were simulated and used as validation: three linear elastic isotropic homogeneous (H) distribution with a single Young's Modulus ($\bar{E}_\theta^H$ = 0.5 MPa, 1.75 MPa, 3.0 MPa) i) and a single proximal/distal (PD) distribution with a proximal ($\bar{E}_\theta^P$ = 2.0 MPa) and distal ($\bar{E}_\theta^D$ = 0.5 MPa) Young's Modulus ii) (Figure 4). In the PD distribution case, the variation from $\bar{E}_\theta^P$ to $\bar{E}_\theta^D$ was implemented with a step transition. The values were chosen in order to be contained within the physiological range of stiffness of the ascending aorta (Lin et al. (2022)). In this way, it was possible to estimate the potential of the proposed method to evaluate the possibility to recover a local distribution of stiffness. The imposed values were taken as reference for the validation of the stiffness estimation method.

Systolic phase definition—For the idealized and patient-specific geometries with all the considered stiffness distributions, the surface configuration in the systolic phase was simulated. In particular, static structural simulations were imposed to obtain the systolic configuration starting from the diastolic configuration, designed for the idealized cases and segmented for the patient-specific case. In particular, an internal pressure of 40 mmHg, according to the physiological pressure difference between systole and diastole, was imposed for all cases. The aortic valve plane was constrained with a fixed displacement condition, while the radial displacement was left free for the aortic arch plane. It is worth noting that for all the FE validation cases it is not necessary to consider the mapping for strain estimation (see Figure 1), as the nodes are already mapped by the structured mesh.

Stiffness estimation application and comparison—The diastolic and systolic surfaces resulting from the FE simulations, for both the idealized and patient-specific models with all the stiffness distributions, were set as input for the estimation method described in Subsection 2.1. Both methods based on Laplace hypothesis and inverse engineering were used to calculate E_θ^{LH} and E_θ^{IE} as summarized in Eq. 6. The resulting stiffness maps and the Relative error (*RErr*) in percentage for both LH and IE method were considered. Additionally, the stiffness distributions resulting from the simulated patient-specific validation cases were evaluated along the normalized centerline coordinate ξ of both E_θ^{LH} and E_θ^{IE}. The average root mean square percentage error (RMSPE) along the centerline, relative to the reference values of Young's moduli imposed at simulation level, was considered for all validation cases.

2.3 Patient-specific cases

After evaluating the performances of the methods on FE validation cases, the estimation technique was imposed by using patient-specific data as input. The analysis procedure can be summarized in three main phases: image acquisition and processing i), systolic phase definition ii), stiffness estimation application iii).

Image acquisition and processing—Three patient-specific aortic morphology were reconstructed from *in vivo* data. In particular, three datasets of 5-phase ECG-gated CT images were acquired. The following percentages of cardiac cycle phases are considered for the analysis: 0%, 20%, 40%, 60% and 80%. The cases selected were three males (25, 89 and 64 y.o.) with tricuspid aortic valve conformation. The CT images were obtained with a 320-detector scanner (Toshiba Aquilon One, Toshiba, Japan) by adopting a iodinated contrast medium. For each phase of the three cases, the ascending aorta morphology was reconstructed according to a semi-automated segmentation algorithm. For each of the three patient-specific cases, the Signal-to-Noise-Ratio (SNR) was calculated by considering a ROI within the ascending aorta section and by calculating the ratio between the pixel mean and standard deviation.

Together with the morphologies, the systemic pressure range was acquired, according to the corresponding clinical record, for each analyzed case. In particular pressure ranges of 82–120 mmHg (Case 1), 78–122 mmHg (Case 2) and 80–124 mmHg (Case 3) were reported. It is important to notice that the pressure ranges (ΔP_1 = 38 mmHg, ΔP_2 = 44 mmHg, ΔP_3 = 44 mmHg) for the chosen cases can be considered as physiological. This aspect confirms the possibility to assume small deformations occurring between diastole and systole and to linearize the material response (Gundiah et al. (2008); Vignali et al. (2021b)).

Systolic peak phase definition—The resulting aortic surfaces from the image segmentation phase are adopted and used as input for the procedure described in Subsection 2.1. In brief, the segmented surfaces from clinical data were mapped according to the already described morphing technique and the baseline centerline was calculated. Then, the corresponding circumferential strain maps at each phase recorded by the ECG-gating process were calculated. Each strain map was calculated considering the 0% phase as the Σ_{dia} baseline reference. The Σ_{sys} phase was then individuated. To choose the Σ_{sys} phase among the different cardiac cycle phases form the ECG-gating, the different strain maps were analysed first. By assuming that the configuration revealing the maximum strain was the one associated with the most pressure difference, Σ_{sys} was chosen by selecting the phase revealing the highest circumferential strain for each case.

Stiffness estimation application—After the selection of the Σ_{sys}, the procedure for stiffness estimation was carried out, according to the methods already described in Subsection 2.1. The stiffness maps were evaluated on the ascending aorta section of the patient-specific cases by considering the baseline surface and the systolic phase only, as selected in the previous step. Additionally, the resulting stiffness maps and distributions along the centerline coordinate ξ were evaluated for each case.

3 Results

The results from the FE validation procedure are presented first. Concerning the simplified geometries, the curvature effect factor is reported first. According to Eq. 3, values of m = 1, m = 0.93 and m = 0.86 were calculated for the cylinder and the elbows at 45° and 90°, respectively. The results in terms of Young's modulus maps for cylinder and elbows geometries are presented in Figures 5A–F. The relative error maps, calculated according to the reference value imposed at simulation level, are reported as well (Figures 5G–L).

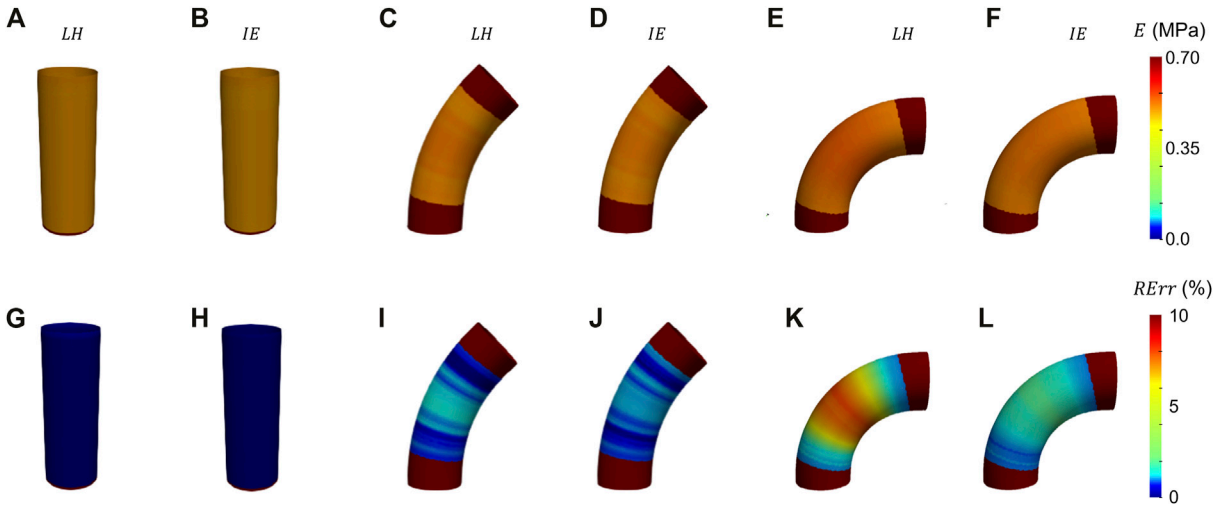

FIGURE 5
Young's modulus maps of FE validation for idealized geometries **(A–F)** with corresponding relative errors **(G–I)**. The maps are presented for both LH **(A, G, C, I, E, K)** and IE (**B, H, D, J, F, L**) methods.

TABLE 1 Table summarizing the Young's modulus RMSPE, relative to the reference values for all validation cases, including idealized and patient-specific.

Validation case		RMSPE for LH (%)	RMSPE for IE (%)
Idealized	Cylinder	1.4	0.6
	Elbow at 45°	2.2	1.7
	Elbow at 90°	6.0	4.4
Patient-specific	$\bar{E}_\theta^H$ = 0.50 MPa	10.1	9.6
	$\bar{E}_\theta^H$ = 1.75 MPa	9.9	9.7
	$\bar{E}_\theta^H$ = 3.00 MPa	9.4	8.5
	Proximal/Distal	16.3	16.1

The corresponding RMSPE values for all the idealized geometries are reported in Table 1.

Before presenting the patient-specific validation cases, the negligibility of the curvature was checked by evaluating the curvature effect factor. The geometry revealed an m factor suitable for the condition of Eq. 3 (m = 0.89). In Figures 6A, B, Figures 7A, B and Figures 8A, B the Young's modulus maps of the patient-specific validation cases with homogeneous material properties distributions are reported for the imposed values of $\bar{E}_\theta^H$ = 0.5 MPa, 1.75 MPa, 3.0 MPa. The *RErr* maps for are reported as well in Figures 6C, D, 7C, D, 8C, D. The results are presented for both LH and IE method. The distributions along the centerline coordinate for the patient-specific validation cases with homogeneous distributions case are reported in Figure 9. Highlights concerning the location of the centerline coordinate, including aortic root, ascending aorta and aortic arch, are represented in figure as well. The distributions according to both LH and IE methods exhibited approximately a constant trend for all the simulated cases of stiffness. The three reference values of $\bar{E}_\theta^H$ = 0.5 MPa, 1.75 MPa, 3.0 MPa are also reported in the graph with dashed lines. The corresponding RMSPE values are all reported in Table 1, with values ranging from 8.5% and to 10.1%.

In Figure 10 the Young's modulus maps of the second validation case with proximal/distal material properties distribution are reported. The different maps of E_θ^{LH} and E_θ^{IE} can be evaluated to determine the performances of both the Laplace-hypothesis-based (Figure 10A) and inverse-engineering-based (Figure 10B) estimation methods in the proximal/distal validation case. The *RErr* maps for are reported as well in Figures 6C, D for both LH and IE methods. The distributions along the centerline coordinate for the proximal/distal validation case are reported in Figure 11. The distributions according to both LH and IE methods exhibited a step-like behavior, with a higher stiffness in the proximal section, as expected. Similarly to the first validation case, the reference values and the highlights concerning the location of the centerline coordinate are reported in the plot. The corresponding RMSPE value are reported in Table 1, with values of 16.3% and 16.1% for the LH and IE methods, respectively.

The results from the patient-specific cases analyses are then presented. Given the equivalent performances of the estimation methods from the first FE validations, the IE method was chosen for the patient-specific analysis. The values of SNR for each of the patient-specific CT datasets were the following: 35.5 for case 1, 36.1 for case 2 and 37.0 for case 3. The circumferential strain maps at the

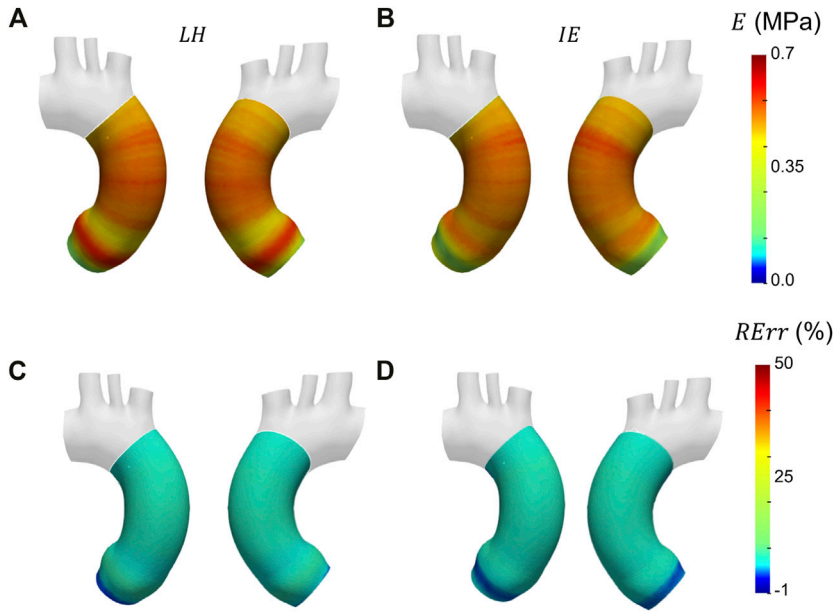

FIGURE 6
Young's modulus maps of FE validation for patient-specific geometry with homogeneous distribution with $\bar{E}_{\theta}^{H}$ = 0.5 MPa **(A, B)** with corresponding relative errors **(C, D)**. Both Laplace-hypothesis-based (E_{θ}^{LH}) **(A, C)** and inverse-engineering-based (E_{θ}^{IE}) **(B, D)** results are presented.

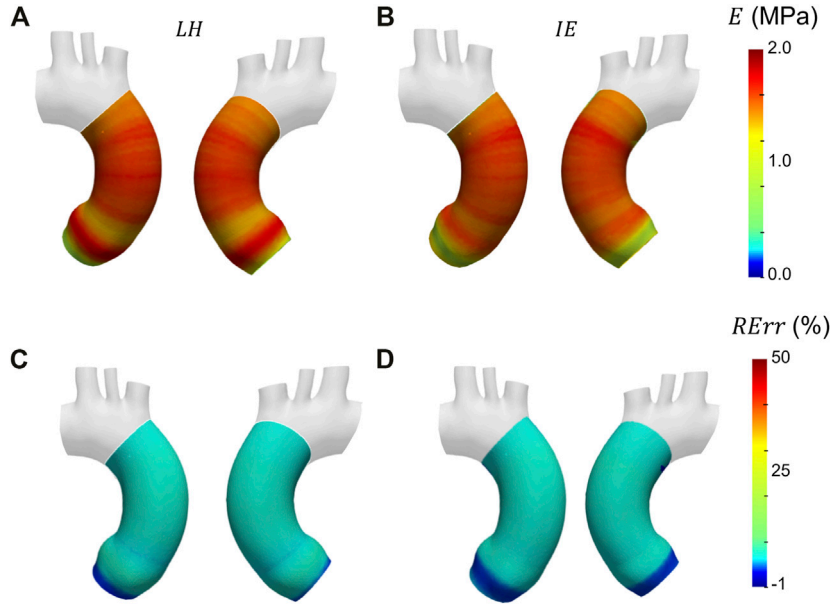

FIGURE 7
Young's modulus maps of FE validation for patient-specific geometry with homogeneous distribution with $\bar{E}_{\theta}^{H}$ = 1.75 MPa **(A, B)** with corresponding relative errors **(C, D)**. Both Laplace-hypothesis-based (E_{θ}^{LH}) **(A, C)** and inverse-engineering-based (E_{θ}^{IE}) **(B, D)** results are presented.

different cardiac phases from clinical data cases are presented in Figure 12 for all three cases. By inspecting the maximum strain value for each case, it was possible to select the systolic peak phase for each dataset: phase 20% for Case 1, phase 40% for Case 2 and Case 3. The only phase chosen as systolic peak was adopted for the stiffness calculation.

After selecting the systolic peak phase for each case on the basis of the strain, the results in terms of Young's modulus were calculated. The maps for the different patient-specific cases are reported in Figure 13. The Young's modulus trends as a function of centerline coordinate are also presented for all the patient-specific cases, as showed in Figure 14. For Case 1 and Case 2, a more homogeneous

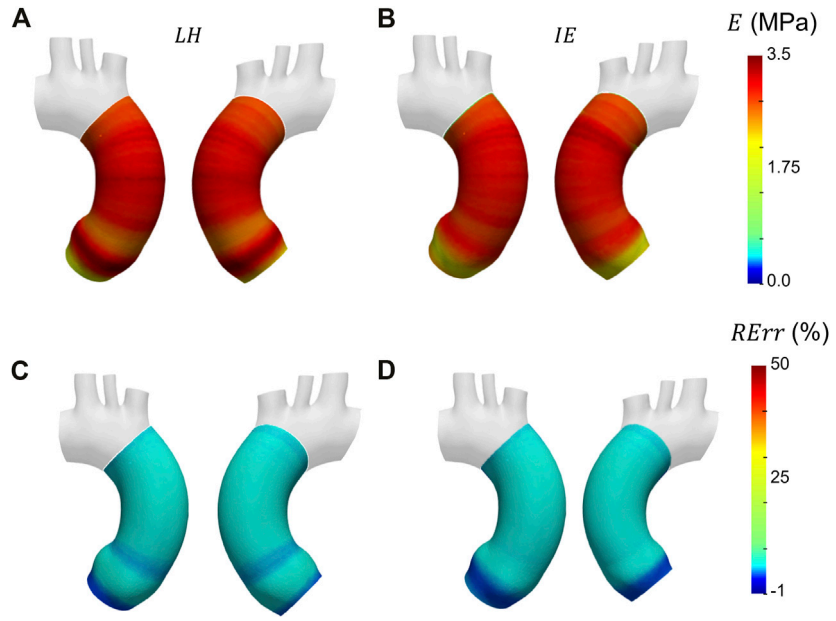

FIGURE 8
Young's modulus maps of FE validation for patient-specific geometry with homogeneous distribution with $\bar{E}_{\theta}^{H}$ = 3.0 MPa **(A, B)** with corresponding relative errors **(C, D)**. Both Laplace-hypothesis-based (E_{θ}^{LH}) **(A, C)** and inverse-engineering-based (E_{θ}^{IE}) **(B, D)** results are presented.

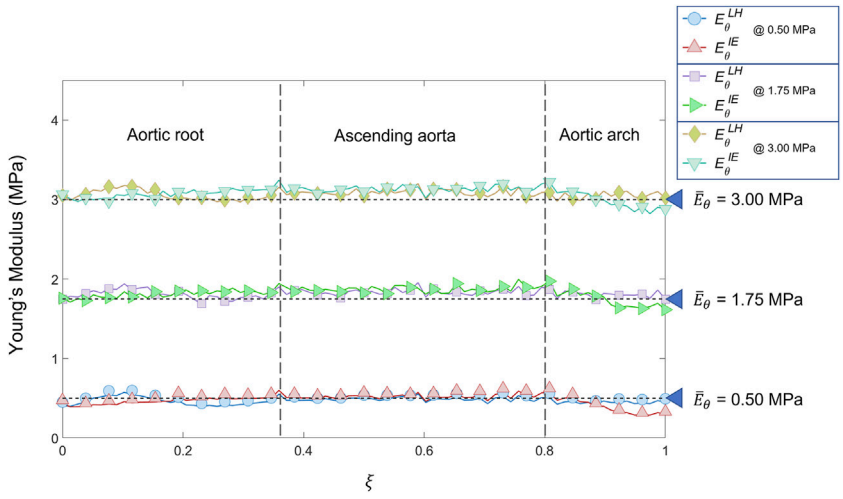

FIGURE 9
Young's modulus variation along the centerline coordinate according to both LH and IE methods for the patient-specific homogeneous distributions cases ($\bar{E}_{\theta}^{H}$ = 0.5 MPa, 1.75 MPa, 3.0 MPa) compared with the reference values.

trend was reported. On the contrary, the behavior of Case 3 appeared to be less homogeneous, as stiffer values were encountered in the ascending aorta in proximity of the aortic arch section.

4 Discussion

The results presented in the previous section demonstrate the effectiveness of the proposed technique for the stiffness estimation in the ascending aorta from *in vivo* data. The performances of both Laplace-hypothesis based and Inverse-engineering based approaches have been presented. In particular, the methods were first tested on FE-based validation cases in which homogeneous and heterogeneous Young's modulus distribution were imposed on both idealized and patient-specific geometries. The proposed approach was successfully implemented also with patient-specific data thanks to shape morphing techniques, revealing the strain and stiffness distribution of three real cases of ascending aortic sections.

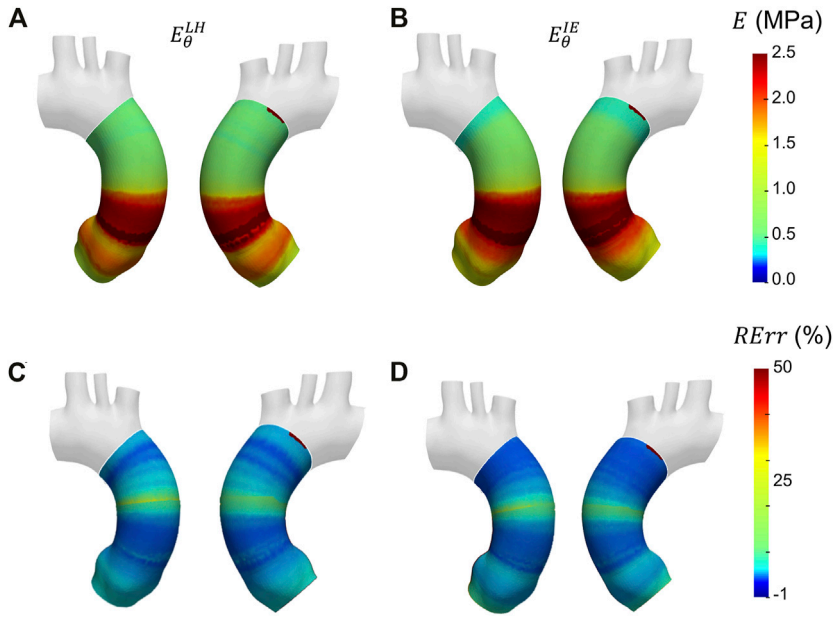

FIGURE 10
Young's modulus maps of FE validation for patient-specific geometry with proximal/distal distribution **(A, B)** with corresponding relative errors **(C, D)**. Both Laplace-hypothesis-based (E_θ^{LH}) **(A, C)** and inverse-engineering-based (E_θ^{IE}) **(B, D)** results are presented.

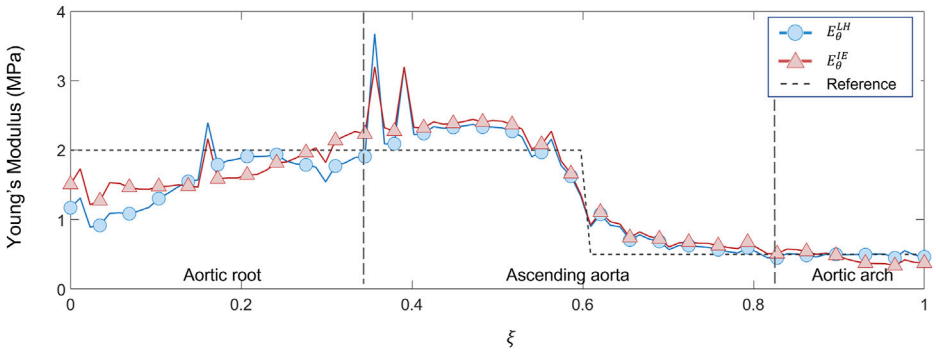

FIGURE 11
Young's modulus variation along the centerline coordinate according to both LH and IE methods for proximal/distal distribution case compared with the reference values.

The results from the validation on the idealized geometries are presented in Figure 5. From the resulting maps it is possible to assess that the produced errors are always below 10% for all the chosen cases. In particular, it is interesting to notice that for the ideal cylinder there is no substantial difference between the LH and IE estimation methods, as in both cases the results presented correspond to the Laplace theory. In both cases, the cylinder produces negligible errors, below 2% (see also Table 1). By introducing a curvature, the differences between the two methods emerge. In fact, by inspecting the results from the elbow cases, it is evident that the effect of curvature influences the performances of the LH method. This effect is particularly evident for the elbow at 90°, where the curvature factor equals to 0.86, in which the *RErr* values reach a maximum of 7% for the LH method, while the IE method produces maximum errors of 3%. These results demonstrate that the curvature effects the method performances, nevertheless both approaches produced satisfactory estimations of stiffness distribution with errors always remaining below the 10% threshold.

The results obtained in the patient-specific validation cases in which stiffness distribution was imposed as homogeneous are presented in the maps of Figure 6, Figure 7 and Figure 8. From the maps, it is possible to observe that according to both the estimation techniques that the homogeneity of the stiffness was correctly coped for all the imposed values of Young's modulus. This behavior is confirmed also by the Young's modulus trend as a function of centerline coordinate from Figure 9. For all the imposed values of Young's modulus, the same trends have been encountered. In particular, for the LH cases, a wider variation of stiffness values is

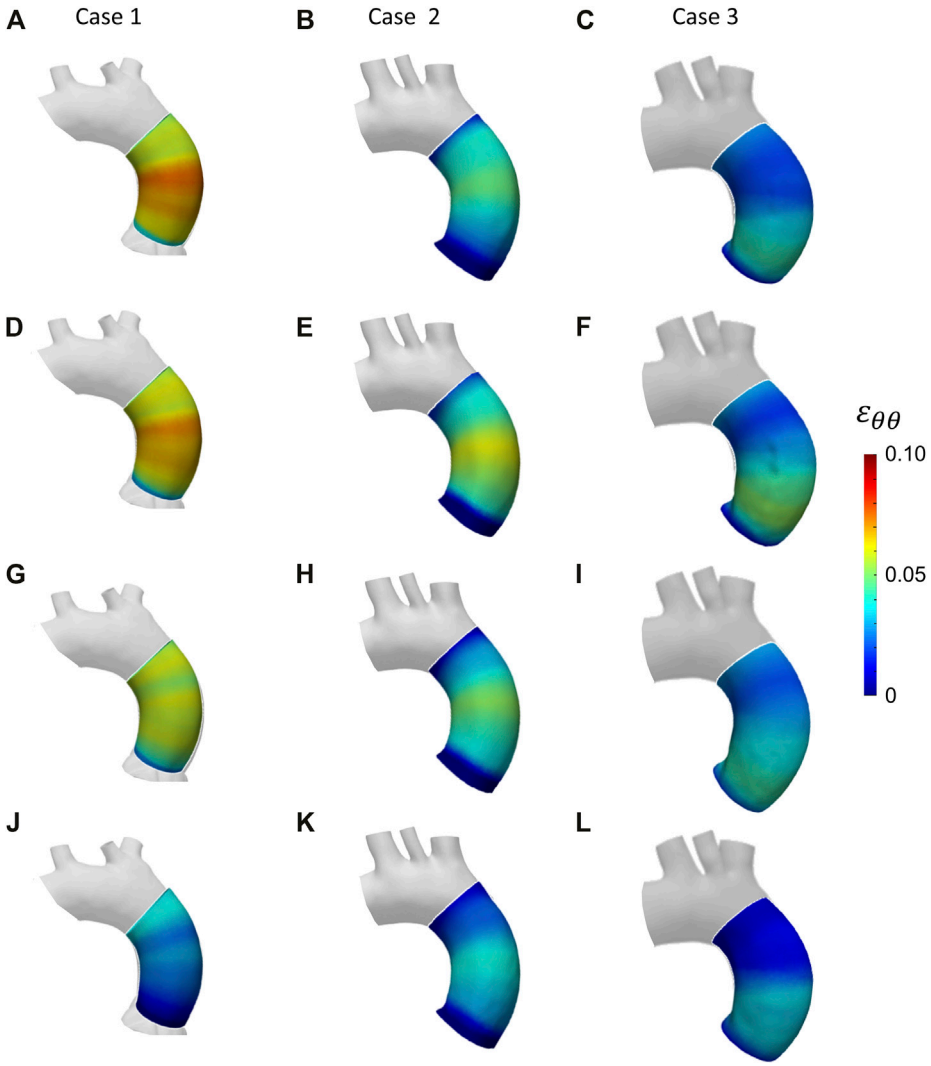

FIGURE 12
Circumferential strain maps at the four cardiac phases: 20% **(A–C)**; 40% **(D–F)**; 60% **(G–I)**; 80% (**J–L**) from patient-specific Case 1 **(A, D, G, J)**, Case 2 **(B, E, H, K)** and Case 3 (**C, F, I, L**).

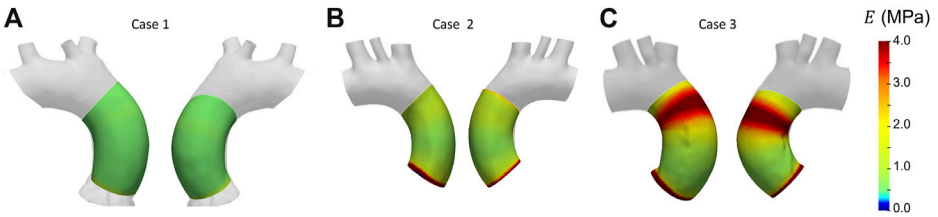

FIGURE 13
Young's modulus maps from patient-specific cases: Case 1 **(A)**, Case 2 **(B)** and Case 3 **(C)**.

encountered only within the aortic root section. This behavior can be assumed as a consequence of stress direct dependence on the section radius. This oscillation in the aortic root section is absent instead according to the IE method for all the three values of imposed Young's modulus. Underestimations are instead encountered within the aortic arch section for the E_{θ}^{IE} calculation. It is reasonable to assume these underestimations linked with E_{θ}^{IE} can be caused by imposed boundary conditions at FE simulation level. Nevertheless, it is interesting to highlight that both methods reveal a similar and constant trend within the ascending aorta section, as reported by both the maps of Figure 6,

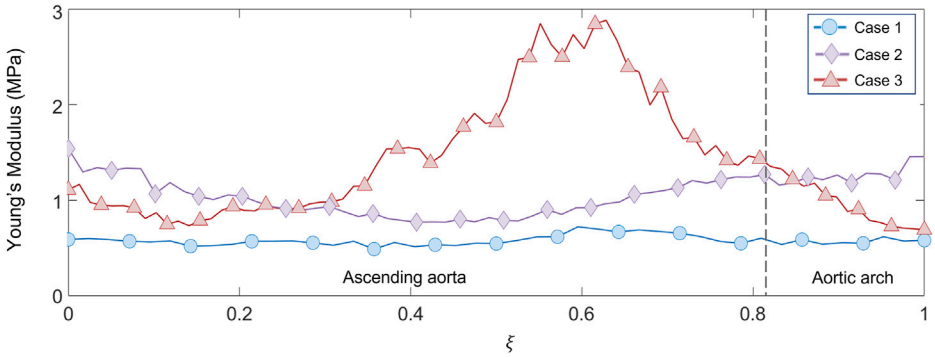

FIGURE 14
Young's modulus variation along the centerline coordinate for the three patient-specific cases.

Figure 7 and Figure 8 and also the plots of Figure 9. The similarity of LH and IE performances is also confirmed by the RMSPE values reported in Table 1. In all patient-specific validation cases, the RMSPE percentages were similar, with values around 10%. In particular, a maximum of 10.1% for the LH method with $\bar{E}_\theta^H$ = 0.5 MPa and a minimum of 8.5% for IE method with $\bar{E}_\theta^H$ = 3.0 MPa were experienced. Concerning homogeneous stiffness distributions for the patient-specific validation, these error values make plausible to assume that both LH and IE methods are comparable in terms of performances.

Similar trends were encountered also for the second validation case with heterogeneous distribution. From the maps of Figure 10, the underestimation area in the aortic root zone of the LH method map remains evident, as observed also in the previous validation case. Concerning the IE method, the same underestimation area in the aortic arch area, already observed in the homogeneous validation case, can be highlighted on the heterogeneous validation case. Nevertheless, both LH and IE methods correctly cope the zone distribution of the Young's moduli in the proximal and distal sections of the ascending aorta. In fact, the transition from the high stiffness ($\bar{E}_\theta^P$ = 2.0 MPa) area in the proximal section to the low stiffness ($\bar{E}_\theta^D$ = 0.5 MPa) area in the distal region is correctly marked in both E_θ^{LH} and E_θ^{IE} maps, as showed in Figures 10A, B. The same transitions can also be detected in the graphs of Figure 11, where the Young's modulus trend according to centerline coordinate is reported. The E_θ^{LH} is oscillating in the aortic root zone, as already observed in the first validation case. Additionally, the E_θ^{IE} underestimation in the aortic arch section remains even in this validation case. It is safe to assume that the underestimation of E_θ^{IE} in the aortic arch section remains linked with the boundary conditions imposed in the FE simulation, as already observed in the first validation case. It is interesting to observe that the estimations remain approximately equivalent, regardless of the method used, within the ascending aorta section. This aspect is confirmed by the presence of the same outliers, encountered in both E_θ^{LH} and E_θ^{IE} trends. Additionally, for both LH and IE case, it was possible to observe the transition along the centerline. The RMSPE are reported in Table 1. The errors are, in fact, equivalent for both LH (16.3%) and IE (16.1%) method. Higher percentage of errors are encountered for the heterogeneous case in comparison with the homogeneous case. This behavior can be motivated by considering that the sudden change in Young's modulus cannot be completely coped by the strain estimation approach, which necessarily introduces a smoothing action by considering cross sectional planes.

With these validation results, it was possible to assess the performances of the workflow. It was safe to assume that both LH and IE method revealed in general satisfactory performances, with similar errors for both validation cases. The IE method was chosen to proceed with the patient-specific cases. The strain maps at the given cardiac phases were calculated first (Figure 12). The evaluation of strain maps at the different phases allowed for the individuation of the systolic peak for each case, by evaluating the strain maximum. In all cases, a strain below 10% was encountered. The range reported was in accordance with previously observed data calculated on *in vivo* aortic cases (Bell et al. (2014); Satriano et al. (2018); Wilson et al. (2019)). It is also possible to observe heterogeneity from case to case. In particular, Case 1 exhibited the highest values of circumferential strain in comparison with the two other patient-specific cases. In addition, Case 3 revealed an area with high strains at the proximal section of the ascending aorta. The individuation of the systolic peak phase made possible the estimation of the Young's modulus (Figures 13, 14). The calculated stiffness distributions are in line with the reported strain maps. In fact, while Cases 1 and 2 revealed mainly an homogeneous distribution of Young's modulus, with average values of 0.6 MPa and 1.0 MPa respectively, Case 3 exhibited a marked heterogeneity, with a stiffer section close to the aortic arch and ranging from 0.7 MPa to 2.9 MPa. It is evident from both the maps of Figure 13 and the trends of Figure 14 that Case 3 revealed an increased stiffness in comparison with the other two cases, with peaks below 3.0 MPa. This phenomenon is in line with the already established connection between arterial stiffness and age, as Case 3 data are associated with the older patient case (Qiu and Onuh (2020)). It was plausible to expect this behavior, also considering the lower strain values encountered from the analysis of the different cardiac phases. Considering all three cases, the estimated values of Young's modulus were always contained within the 0.5–3.0 MPa range, which is in line with already reported physiological values from the state of the art (Lin et al. (2022); Vignali et al. (2021b)).

Further points of development and limitations of the current workflow can be highlighted. Both the proposed LH and IE do not take into account of inertial loading, as in both cases the assumption of quasi-static solicitations was made. A limitation is given by the reduced number of patient-specific cases tested after validation. To

better define the approach outcomes, a wider number of cases will be analyzed and presented in the future. The current method is limited on the estimation of circumferential strain only and it assigns a single value for each centerline-based slice of the aorta. Thus, a limitation of the estimation method in its current state is the impossibility to calculate the inner/outer curvature strain difference on the aorta surface by considering the whole contour length. Moreover, even if the mapping of the surface accounts for the axial displacement of sections, the approach based on the contour length cannot estimate the longitudinal strain. Further developments of the algorithm will allow in the future to estimate the axial deformation of the aorta and they will open up the path for the adoption of more complex constitutive models including anisotropy. Concerning hyperelasticity, it is well established that the aortic tissue has a non-linear mechanical response, given the presence of collagen fibers and the presented method does not account for these phenomena. Nevertheless, it was also established that deformations occurring between diastolic and systolic phase can be assumed as small (Gundiah et al. (2008); Vignali et al. (2021b)). This aspect confirms the hypothesis of linear material behavior assumed in the presented method. To further assess the effectiveness of the proposed method, it would be interesting to test the approach even on a complete aortic geometry, including epiaortic vessels and descending aorta. As an additional point of development, the method can be tested also with CT with ECG-gating with finer time sampling. Concerning the CT image quality, to assess the influence of noise on the presented procedure's outcomes a full uncertainty quantification process would be required. Nevertheless, the SNR assessment for the processed images of the three patient-specific cases confirmed that the image quality was satisfactory and in line with diagnostic standards (Shen et al. (2015)). In this way the method could have the potential to obtain a more accurate estimation of the systolic peak cardiac phase.

5 Conclusion

In summary, the current study presents a new method for local strain and stiffness estimation from *in vivo* ECG-gated CT aortic images, on the basis of mesh-morphing mapping and inverse engineering methods. The method was first validated on two test cases, obtained from FE simulations of aortic structures with different material properties local distributions. After a successful validation, the method was applied on three patient-specific aorta cases. The results demonstrated the successful obtainment of a regional *in vivo* characterization of patient-specific aortas in terms of deformations and stiffness.

Data availability statement

The raw data supporting the conclusions of this article will be made available by the authors, on request from the corresponding author, without undue reservation.

Author contributions

Conceptualization, SC, EG, and EV; implementation, EG, KC, FB, MS, and EV; method and code refinement, EG and EV; validation, EG and EV; data resources, CC and FC; writing–original draft preparation, SC, EG and EV; writing–review and editing, SC, EG, and EV; supervision, SC.

Funding

This study has received funding from the Marie Sklodowska-Curie grant agreement MeDiTATe project No 859836.

Conflict of interest

The authors declare that the research was conducted in the absence of any commercial or financial relationships that could be construed as a potential conflict of interest.

Publisher's note

References

Bell, V., Mitchell, W. A., Sigurðsson, S., Westenberg, J. J., Gotal, J. D., Torjesen, A. A., et al. (2014). Longitudinal and circumferential strain of the proximal aorta. *J. Am. Heart Assoc.* 3, e001536. doi:10.1161/JAHA.114.001536

Capellini, K., Gasparotti, E., Cella, U., Costa, E., Fanni, B. M., Groth, C., et al. (2021). A novel formulation for the study of the ascending aortic fluid dynamics with *in vivo* data. *Med. Eng. Phys.* 91, 68–78. doi:10.1016/j.medengphy.2020.09.005

Capellini, K., Vignali, E., Costa, E., Gasparotti, E., Biancolini, M. E., Landini, L., et al. (2018). Computational fluid dynamic study for aTAA hemodynamics: An integrated image-based and RBF mesh morphing approach. *J. Biomech. Eng.* 140, 40940. doi:10.1115/1.4040940

Celi, S., Martini, N., Pastormerlo, L., Positano, V., and Berti, S. (2017). Multimodality imaging for interventional cardiology. *Curr. Pharm. Des.* 23, 3285–3300. doi:10.2174/1381612823666170704171702

Celi, S., Vaghetti, M., Palmieri, C., and Berti, S. (2013). Superficial coronary calcium analysis by oct: Looking forward an imaging algorithm for an automatic 3d quantification. *Int. J. Cardiol.* 168, 2958–2960. doi:10.1016/j.ijcard.2013.03.115

Celi, S., Vignali, E., Capellini, K., and Gasparotti, E. (2021). On the role and effects of uncertainties in cardiovascular *in silico* analyses. *Front. Med. Technol.* 3, 748908. doi:10.3389/fmedt.2021.748908

Danpinid, A., Jianwen Luo, J., Vappou, J., Terdtoon, P., and Konofagou, E. E. (2009). Characterization of the stress-strain relationship of the abdominal aortic wall *in vivo*. *Annu. Int. Conf. IEEE Eng. Med. Biol. Soc.* 2009, 1960–1963. doi:10.1109/IEMBS.2009.5333466

Di Lascio, N., Stea, F., Kusmic, C., Sicari, R., and Faita, F. (2014). Non-invasive assessment of pulse wave velocity in mice by means of ultrasound images. *Atherosclerosis* 237, 31–37. doi:10.1016/j.atherosclerosis.2014.08.033

Duprey, A., Trabelsi, O., Vola, M., Favre, J. P., and Avril, S. (2016). Biaxial rupture properties of ascending thoracic aortic aneurysms. *Acta biomater.* 42, 273–285. doi:10.1016/j.actbio.2016.06.028

Fanni, B., Sauvage, E., Celi, S., Norman, W., Vignali, E., Landini, L., et al. (2020). A proof of concept of a non-invasive image-based material characterization method for enhanced patient-specific computational modeling. *Cardiovasc Eng. Tech.* 11, 532–543. doi:10.1007/s13239-020-00479-7

Farzaneh, S., Trabelsi, O., and Avril, S. (2019a). Inverse identification of local stiffness across ascending thoracic aortic aneurysms. *Biomech. Model. Mechanobiol.* 18, 137–153. doi:10.1007/s10237-018-1073-0

Farzaneh, S., Trabelsi, O., Chavent, B., and Avril, S. (2019b). Identifying local arterial stiffness to assess the risk of rupture of ascending thoracic aortic aneurysms. *Ann. Biomed. Eng.* 47, 1038–1050. doi:10.1007/s10439-019-02204-5

Gültekin, O., Hager, S. P., Dal, H., and Holzapfel, G. A. (2019). Computational modeling of progressive damage and rupture in fibrous biological tissues: Application to aortic dissection. *Biomech. Model. Mechanobiol.* 18, 1607–1628. doi:10.1007/s10237-019-01164-y

Gundiah, N., Matthews, P. B., Karimi, R., Azadani, A., Guccione, J., Guy, T. S., et al. (2008). Significant material property differences between the porcine ascending aorta and aortic sinuses. *J. Heart Valve Dis.* 17, 606–613.

Humphrey, J. D., and Schwartz, M. A. (2021). Vascular mechanobiology: Homeostasis, adaptation, and disease. *Annu. Rev. Biomed. Eng.* 23, 1–27. doi:10.1146/annurev-bioeng-092419-060810

Krishnan, K., Ge, L., Haraldsson, H., Hope, M. D., Saloner, D. A., Guccione, J. M., et al. (2015). Ascending thoracic aortic aneurysm wall stress analysis using patient-specific finite element modeling ofin vivomagnetic resonance imaging. *Interact. CardioVasc Thorac. Surg.* 21, 471–480. doi:10.1093/icvts/ivv186

Lin, S., Morgant, M. C., Marín-Castrillón, D. M., Walker, P. M., Aho Glélé, L. S. A., Boucher, A., et al. (2022). Aortic local biomechanical properties in ascending aortic aneurysms. *Acta Biomater.* 149, 40–50. doi:10.1016/j.actbio.2022.06.019

Liu, M., Liang, L., Liu, H., Zhang, M., Martin, C., and Sun, W. (2019a). On the computation of *in vivo* transmural mean stress of patient-specific aortic wall. *Biomech. Model. Mechanobiol.* 18, 387–398. doi:10.1007/s10237-018-1089-5

Liu, M., Liang, L., Sulejmani, F., Lou, X., Iannucci, G., Chen, E., et al. (2019b). Identification of *in vivo* nonlinear anisotropic mechanical properties of ascending thoracic aortic aneurysm from patient-specific ct scans. *Sci. Rep.* 9, 12983–13013. doi:10.1038/s41598-019-49438-w

Lu, J., Zhou, X., and Raghavan, M. L. (2008). Inverse method of stress analysis for cerebral aneurysms. *Biomech. Model. Mechanobiol.* 7, 477–486. doi:10.1007/s10237-007-0110-1

Martin, C., Sun, W., Pham, T., and Elefteriades, J. (2013). Predictive biomechanical analysis of ascending aortic aneurysm rupture potential. *Acta biomater.* 9, 9392–9400. doi:10.1016/j.actbio.2013.07.044

Narayanan, B., Olender, M. L., Marlevi, D., Edelman, E. R., and Nezami, F. R. (2021). An inverse method for mechanical characterization of heterogeneous diseased arteries using intravascular imaging. *Sci. Rep.* 11, 22540–22612. doi:10.1038/s41598-021-01874-3

Onuh, H., and Qiu, J. (2020). New progress on the study of aortic stiffness in age-related hypertension. *J. Hypertens.* 38, 1871–1877. doi:10.1097/HJH.0000000000002452

Pasta, S., Agnese, V., Di Giuseppe, M., Gentile, G., Raffa, G. M., Bellavia, D., et al. (2017). *In vivo* strain analysis of dilated ascending thoracic aorta by ecg-gated ct angiographic imaging. *Ann. Biomed. Eng.* 45, 2911–2920. doi:10.1007/s10439-017-1915-4

Peña, J. A., Martínez, M. A., and Peña, E. (2015). Layer-specific residual deformations and uniaxial and biaxial mechanical properties of thoracic porcine aorta. *J. Mech. Behav. Biomed. Mater.* 50, 55–69. doi:10.1016/j.jmbbm.2015.05.024

Ramanath, V. S., Oh, J. K., Sundt, T. M., III, and Eagle, K. A. (2009). Acute aortic syndromes and thoracic aortic aneurysm. *Mayo Clin. Proc.* 84, 465–481. doi:10.4065/84.5.465

Roccabianca, S., Figueroa, C., Tellides, G., and Humphrey, J. D. (2014). Quantification of regional differences in aortic stiffness in the aging human. *J. Mech. Behav. Biomed. Mater.* 29, 618–634. doi:10.1016/j.jmbbm.2013.01.026

Satriano, A., Guenther, Z., White, J. A., Merchant, N., Di Martino, E. S., Al-Qoofi, F., et al. (2018). Three-dimensional thoracic aorta principal strain analysis from routine ecg-gated computerized tomography: Feasibility in patients undergoing transcatheter aortic valve replacement. *BMC Cardiovasc Disord.* 18, 76–11. doi:10.1186/s12872-018-0818-0

Shen, Y., Sun, Z., Xu, L., Li, Y., Zhang, N., Yan, Z., et al. (2015). High-pitch, low-voltage and low-iodine-concentration ct angiography of aorta: Assessment of image quality and radiation dose with iterative reconstruction. *PloS one* 10, e0117469. doi:10.1371/journal.pone.0117469

Sieger, D., Menzel, S., and Botsch, M. (2014). Rbf morphing techniques for simulation-based design optimization. *Eng. Comput.* 30, 161–174. doi:10.1007/s00366-013-0330-1

Trabelsi, O., Gutierrez, M., Farzaneh, S., Duprey, A., and Avril, S. (2018). A non-invasive methodology for ataa rupture risk estimation. *J. Biomech.* 66, 119–126. doi:10.1016/j.jbiomech.2017.11.012

Vignali, E., di Bartolo, F., Gasparotti, E., Malacarne, A., Concistré, G., Chiaramonti, F., et al. (2020). Correlation between micro and macrostructural biaxial behavior of ascending thoracic aneurysm: A novel experimental technique. *Med. Eng. Phys.* 86, 78–85. doi:10.1016/j.medengphy.2020.10.012

Vignali, E., Gasparotti, E., Capellini, K., Fanni, B. M., Landini, L., Positano, V., et al. (2021a). Modeling biomechanical interaction between soft tissue and soft robotic instruments: Importance of constitutive anisotropic hyperelastic formulations. *Int. J. Robotics Res.* 40, 224–235. doi:10.1177/0278364920927476

Vignali, E., Gasparotti, E., Celi, S., and Avril, S. (2021b). Fully-coupled fsi computational analyses in the ascending thoracic aorta using patient-specific conditions and anisotropic material properties. *Front. Physiol.* 12, 732561. doi:10.3389/fphys.2021.732561

Vignali, E., Gasparotti, E., Landini, L., and Celi, S. (2021c). Development and realization of an experimental bench test for synchronized small angle light scattering and biaxial traction analysis of tissues. *Electronics* 10, 386. doi:10.3390/electronics10040386

Wilson, J. S., Taylor, W. R., and Oshinski, J. (2019). Assessment of the regional distribution of normalized circumferential strain in the thoracic and abdominal aorta using dense cardiovascular magnetic resonance. *J. Cardiovasc Magn. Reson* 21, 59–14. doi:10.1186/s12968-019-0565-0

Zeinali-Davarani, S., Raguin, L. G., Vorp, D. A., and Baek, S. (2011). Identification of *in vivo* material and geometric parameters of a human aorta: Toward patient-specific modeling of abdominal aortic aneurysm. *Biomech. Model. Mechanobiol.* 10, 689–699. doi:10.1007/s10237-010-0266-y

Zhang, S. H., Gao, C. R., Zhao, D. W., and Wang, G. D. (2013). Limit analysis of defect-free pipe elbow under internal pressure with mean yield criterion. *J. Iron Steel Res. Int.* 20, 11–15. doi:10.1016/s1006-706x(13)60075-8

Zhou, X., Raghavan, M. L., Harbaugh, R. E., and Lu, J. (2010). Patient-specific wall stress analysis in cerebral aneurysms using inverse shell model. *Ann. Biomed. Eng.* 38, 478–489. doi:10.1007/s10439-009-9839-2

frontiers | Frontiers in Cardiovascular Medicine

TYPE Original Research
PUBLISHED 02 February 2023
DOI 10.3389/fcvm.2023.1087568

OPEN ACCESS

EDITED BY
Selene Pirola,
Delft University of Technology, Netherlands

REVIEWED BY
Jaume Coll-Font,
Harvard Medical School, United States
Stefan Michael Sattler,
University of Copenhagen, Denmark

*CORRESPONDENCE
Patricia Zerlang Fruelund
✉ p.fruelund@rn.dk

SPECIALTY SECTION
This article was submitted to Cardiovascular Imaging, a section of the journal Frontiers in Cardiovascular Medicine

RECEIVED 02 November 2022
ACCEPTED 18 January 2023
PUBLISHED 02 February 2023

CITATION
Fruelund PZ, Van Dam PM, Melgaard J, Sommer A, Lundbye-Christensen S, Søgaard P, Zaremba T, Graff C and Riahi S (2023) Novel non-invasive ECG imaging method based on the 12-lead ECG for reconstruction of ventricular activation: A proof-of-concept study.
Front. Cardiovasc. Med. 10:1087568.
doi: 10.3389/fcvm.2023.1087568

Novel non-invasive ECG imaging method based on the 12-lead ECG for reconstruction of ventricular activation: A proof-of-concept study

Patricia Zerlang Fruelund[1,2]*, Peter M. Van Dam[3], Jacob Melgaard[4], Anders Sommer[1], Søren Lundbye-Christensen[5], Peter Søgaard[1,2], Tomas Zaremba[1], Claus Graff[4] and Sam Riahi[1,2]

[1]Department of Cardiology, Aalborg University Hospital, Aalborg, Denmark, [2]Department of Clinical Medicine, Aalborg University, Aalborg, Denmark, [3]Department of Cardiology, University Medical Center Utrecht, Utrecht, Netherlands, [4]Department of Health Science and Technology, Faculty of Medicine, Aalborg University, Aalborg, Denmark, [5]Unit of Clinical Biostatistics, Aalborg University Hospital, Aalborg, Denmark

Aim: Current non-invasive electrocardiographic imaging (ECGi) methods are often based on complex body surface potential mapping, limiting the clinical applicability. The aim of this pilot study was to evaluate the ability of a novel non-invasive ECGi method, based on the standard 12-lead ECG, to localize initial site of ventricular activation in right ventricular (RV) paced patients. Validation of the method was performed by comparing the ECGi reconstructed earliest site of activation against the true RV pacing site determined from cardiac computed tomography (CT).

Methods: This was a retrospective study using data from 34 patients, previously implanted with a dual chamber pacemaker due to advanced atrioventricular block. True RV lead position was determined from analysis of a post-implant cardiac CT scan. The ECGi method was based on an inverse-ECG algorithm applying electrophysiological rules. The algorithm integrated information from an RV paced 12-lead ECG together with a CT-derived patient-specific heart-thorax geometric model to reconstruct a 3D electrical ventricular activation map.

Results: The mean geodesic localization error (LE) between the ECGi reconstructed initial site of activation and the RV lead insertion site determined from CT was 13.9 ± 5.6 mm. The mean RV endocardial surface area was 146.0 ± 30.0 cm^2 and the mean circular LE area was 7.0 ± 5.2 cm^2 resulting in a relative LE of 5.0 ± 4.0%.

Conclusion: We demonstrated a novel non-invasive ECGi method, based on the 12-lead ECG, that accurately localized the RV pacing site in relation to the ventricular anatomy.

KEYWORDS

electrocardiography, non-invasive imaging, cardiac pacing, ventricular activation, patient-specific modeling, 12-lead electrocardiogram

1. Introduction

Along with QRS morphology from the 12-lead electrocardiogram (ECG), fluoroscopy is the main guiding tool for right ventricular (RV) pacemaker lead implantation. However, several studies have demonstrated the inaccuracy of both fluoroscopy and QRS morphology to determine RV lead implantation site (1–4). Interindividual variations in cardiac and thoracic anatomy, underlying myocardial pathology and variability in ECG electrode positioning influence the recorded ECG waveforms (5). Additionally, the activation patterns resulting from RV pacing at different lead positions may result only in subtle morphological QRS differences making interpretation difficult and thus reducing the usefulness of the 12-lead ECG to guide pacemaker implantation (3, 4). The inaccuracy of current implantation methods result in a high risk of unintended RV free wall implantations (2, 6). Therefore, new methods are needed to ensure optimal RV lead implantation.

Non-invasive electrocardiographic imaging (ECGi) provides 3D reconstruction of the cardiac electrical activity overcoming some of the limitations from the standard 12-lead ECG, potentially increasing the diagnostic value (7). However, ECGi methods require specialized technical equipment to obtain detailed mapping of body surface potentials using a dense array of electrodes placed on the patients thorax (8). Thus, the usefulness of current ECGi methods is limited and not easily implemented in everyday clinical practice (9, 10).

The aim of this pilot study was to evaluate the ability of a novel non-invasive ECGi method, based on the standard 12-lead ECG, to localize initial site of ventricular activation in RV paced patients. Validation of the method was performed by comparing the earliest site of activation estimated from the reconstructed ventricular activation model against the true RV pacing site determined from cardiac computed tomography (CT).

2. Materials and methods

2.1. Study population

Thirty-four patients who underwent *de novo* implantation of a dual chamber pacemaker due to advanced atrioventricular block at Aalborg University Hospital between December 2014 and December 2017 were retrospectively included. Patients with suspected fusion pacing or patients who had been upgraded to cardiac resynchronization therapy after primary pacemaker implantation were not considered eligible. Following data were acquired at time of study inclusion: clinical characteristics from electronic medical records, a contrast-enhanced cardiac CT scan, an RV paced 12-lead ECG including a 3D photography showing the ECG electrode positions and a transthoracic echocardiography.

2.2. Cardiac CT acquisition

If no contrast-enhanced cardiac CT, showing the RV lead position, was available (n = 30), a study specific cardiac CT was acquired using a second-generation dual source scanner (Siemens Somatom Definition Flash, Siemens Healthcarem Erlangen, Germany). During breath hold, the contrast-enhanced retrospective ECG gated scan was timed with contrast filling of both ventricular cavities. Reconstruction was done in diastole with a mean slice thickness of 0.95 ± 0.1 mm for the narrow field of view focused on the heart. The mean total dose length product (DLP) for the study-acquired CT scans was 114.9 ± 65.3 mGy cm and mean contrast dose (Iopromide 370 mg/ml) was 67.4 ± 9.6 ml.

A segmental approach was used to retrospectively categorize RV lead position (2). The RV long axis was divided into equal thirds and subsequently the RV lead position was analyzed in a short axis view. Lead position was categorized to be apical if located on the lower third of the RV septum. Lead position was categorized as septal if located on the upper two thirds of the RV septum. Leads positioned at the anteroseptal or posteroseptal junction were considered septal. Leads were categorized as free wall if positioned on the RV free wall regardless of long axis position.

2.3. Echocardiography

All patients had a transthoracic echocardiography performed at time of study inclusion using a 2.5-MHz transducer on a commercially available ultrasound system (VIVID E95, GE Healthcare, Milwaukee, WI, USA). The echocardiograms were analyzed using EchoPAC software (GE Healthcare, Milwaukee, WI, USA). Analyses included estimation of left ventricular ejection fraction (LVEF) and left ventricular (LV) volumes (11).

2.4. The 12-lead ECG based ECGi method

The ECGi method was based on an inverse-ECG algorithm that reconstructs the electrical activity of the ventricles by integrating information from an RV-paced 12-lead ECG, location of surface ECG electrode positions together with a CT-derived patient-specific heart-thorax geometric model (12). The electrical activation was reconstructed in a stepwise approach including collection of input data, processing input data and finally applying the inverse ECG algorithm (**Figure 1**).

For each patient, a standard 12-lead ECG during RV pacing was digitally recorded at time of study inclusion using the Cardiovit AT-102 plus resting ECG machine (Schiller, Baar, Switzerland). All ECG recordings were imported to the MUSE Cardiology Information System (GE Healthcare, Wauwatosa, WI, USA). In MUSE, QRS onset and thus duration was manually adjusted on median beats formed by version 23 of the Marquette 12SL algorithm to exclude the pacing spike. A single QRS onset was defined across the 12 leads as the earliest positive or negative deflection after a pacing spike. Furthermore, a 3D photography of the patient thorax was recorded documenting the position of the ECG electrodes at time of the ECG recording.

The patient specific heart-thorax geometric models were created from the cardiac CT scan using specialized research software (GeomPeacs, Peacs BV, Netherlands) (13). The model creation process was semi-automated, morphing a standard model to match the contours of the patient-specific cardiac and thoracic anatomy. The geometry was constructed as a triangular surface mesh with discrete nodes contouring the four heart valves, the endocardial and epicardial borders of the left and right ventricles and the thoracic walls. The 3D thorax photography of the ECG electrodes was merged with the thorax model, to correctly position the

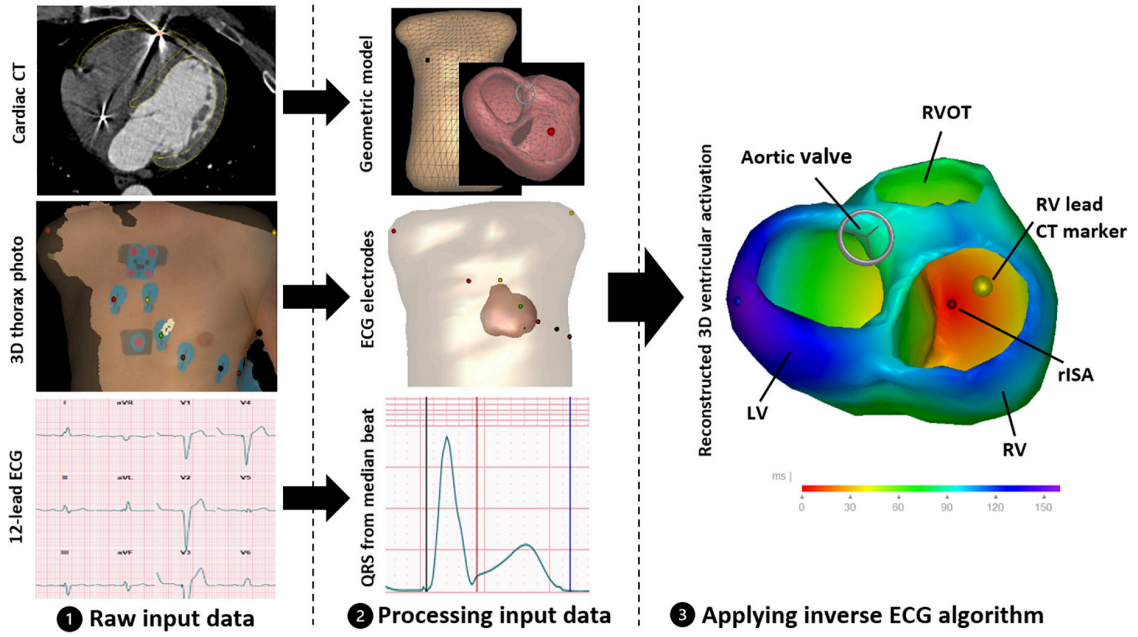

FIGURE 1
Summary of the stepwise process used for reconstructing 3D ventricular activation. (1) Collecting the raw input data including contrast-enhanced cardiac CT, 3D thorax photograph documenting the ECG electrode positions and 12-lead ECG with right ventricular pacing. (2) Processing the input data including creation of a patient-specific geometric model with ECG electrodes correctly positioned on the thorax model and defining QRS onset and duration using the 12-lead ECG median beat. (3) Integration of processed input data using the inverse ECG algorithm creating the 3D ventricular activation model. LV, left ventricle; RV, right ventricle; RVOT, right ventricular outflow tract; rISA, reconstructed initial site of activation (rISA).

ECG electrodes on the thorax model. Furthermore, also using the specialized DICOM software, the CT images were used to localize the RV lead implantation site and a marker was placed at the endocardial border of the heart geometry where the RV lead touched the RV endocardium.

Application of the algorithm was automated using specialized software (**Supplementary material**). The algorithm workflow, in short, was as follows:

a) The first step was to determine the QRS axis. The heart-thorax model was used to derive the vectorcardiogram (VCG) from the recorded 12-lead ECG, using the method described by Boonstra et al. (14). The mean QRS-axis was localized to the center of ventricular mass. Entry and exit points were then defined as the QRS axis crossing points of the right ventricular cavity in the heart model (**Figure 2**).
b) The Fastest Route Algorithm, together with a realistic myocardial propagation velocity (0.7–0.85 m/s), was used to compute depolarization times between the discrete nodes on the closed triangulated modeled myocardial surface mesh (15). In this algorithm, the anisotropic nature of the myocardial tissue was captured by a 2.5 times slower transmural velocity than the velocity over the ventricular surface (16). The current problem at hand required the localization of the RV stimulation site, thus limiting the search space for initial site of activation to just the RV endocardium. In the current approach the initial search for the RV lead stimulation site was restricted to the two QRS axis RV crossing points. Using the Fastest Route Algorithm, QRS durations were simulated initiating from discrete nodes around the two QRS axis crossing points and the discrete node resulting in the simulated QRS duration that best matched the recorded QRS duration was selected to be the initial estimate for RV stimulation site.
c) The cardiac depolarization sequence was used to compute ECGs applying the equivalent dipole layer model as a source model, where local transmembrane potentials simulated the local currents generated by the heart (17, 18). The effect of the constructed volume conductor model was computed using the boundary element method previously described (19, 20). Assigned conductivity values were 0.2 S/m for the thorax and ventricular muscles, and 0.6 S/m for the blood cavities.
d) Subsequently, the improvement procedure was started in which additional extra late break through points (foci) were added in the left cavity, mimicking (late) breakthroughs from the His-Purkinje system. The location and timing of the initial RV stimulation site and the added His-Purkinje nodes was optimized in an iterative procedure, matching the recorded ECG and simulated ECGs. The simulated ECGs were the result of the depolarization sequence generated from the location and timing of the combination of different foci.
e) Finally, the depolarization sequence resulting in a simulated ECG best matching the recorded ECG was chosen for final analysis.

2.5. Validation

Performance of the reconstructed electrical activation was assessed by calculating the localization error (LE) defined by the geodesic distance (shortest distances between two points on a curved surface) between the RV CT-marker and the reconstructed initial site of activation (rISA) (**Figure 3**). Furthermore, a circular area

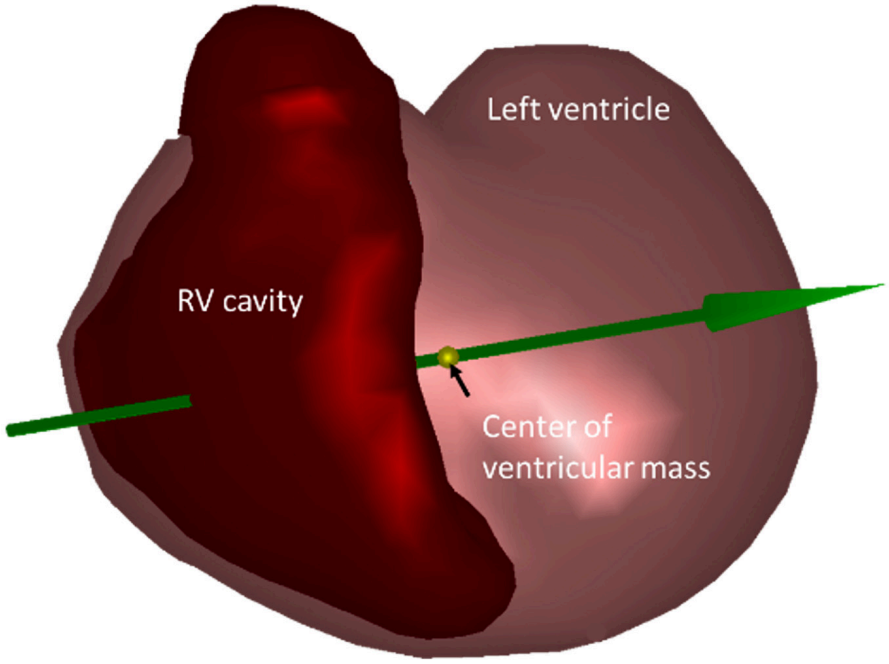

FIGURE 2
Geometric model of the heart showing the mean QRS axis (green arrow) located at the center of ventricular mass (yellow marker). The QRS axis crossing points are where the green arrow enters and exits the right ventricular (RV) cavity.

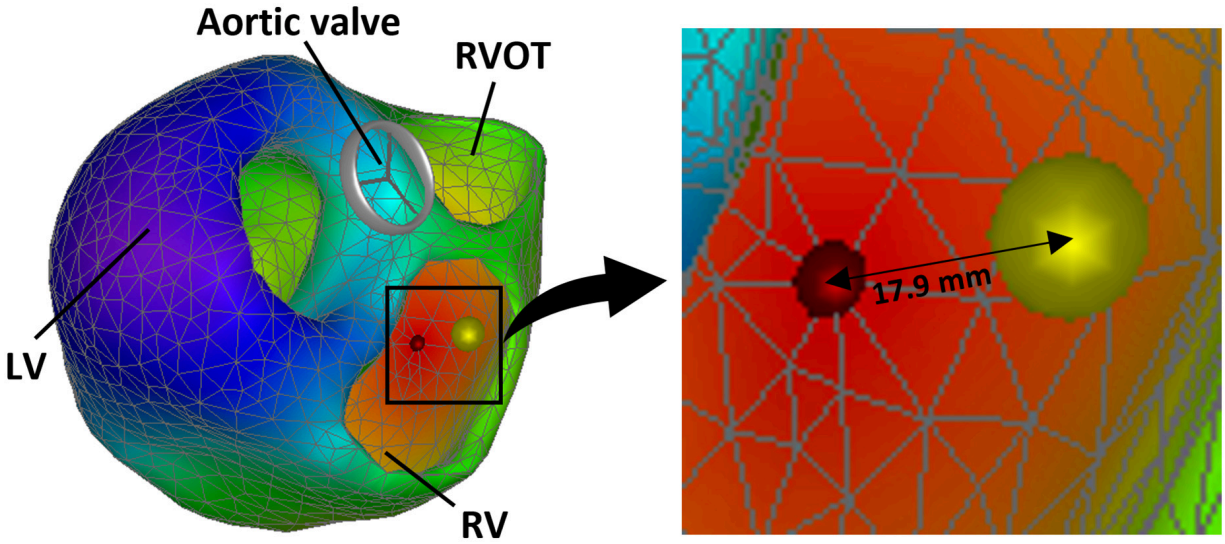

FIGURE 3
Reconstructed 3D ventricular electrical activation sequence showing the reconstructed initial site of activation (rISA) (red marker) and the right ventricular (RV) lead position assessed from computed tomography (CT) (yellow marker). The localization error (LE) is the geodesic distance between the center of the CT marker and the estimated initial site of activation. LV, left ventricle; RVOT, right ventricular outflow tract.

calculated using the LE as the radius was compared to the RV endocardial surface area to demonstrate the LE relative to the RV endocardial size.

The rISA was constrained to the discrete nodes of the ventricular geometric model whereas the marker for RV lead position was localized on the CT scan and imported into the heart model without this constraint. This created a potential default distance between the RV marker and the rISA. This was adjusted for by calculating a corrected localization error (cLE) defined as the distance from the rISA to the discrete node closest to the RV marker on the path between the rISA and the RV marker. A cLE of 0 mm meant that rISA was located in the triangle to where the RV lead marker was projected on to the endocardial model surface.

Performance of the reconstructed activation sequence was assessed comparing it with an activation sequence forced to initiate from the known RV lead insertion site. This was done to assess how sensitive the overall activation sequence was to change in initial site

of activation. Lastly, the correlation between the recorded ECG and the ECG fitting the reconstructed model was assessed.

2.6. Statistical analyses

Continuous variables are reported as mean ± standard deviation (range) unless severely skewed. Categorical values are reported as absolute numbers and percentages. For analyzing associations, unpaired *t*-test was used for binary independent variables and fractional polynomial regression was used for continuous independent variables. To compare different activation maps within one patient the Pearson correlation coefficient was used. $p < 0.05$ was considered statistically significant. STATA version 17 was used to perform the statistical analyses.

3. Results

3.1. Study cohort and characteristics

Patient characteristics (**Table 1**) showed that 20 (58.8%) were male with a mean age of 69.1 ± 11.9 years (range 24.9–84.7 years) at time of study inclusion and a mean duration of pacemaker treatment of 3.4 ± 0.8 years (range 2.6–5.5 years). All patients had a long RV paced QRS duration with a mean duration of 151.2 ± 12.9 ms (range 128–182 ms).

3.2. Localization error of reconstructed initial site of activation

The mean LE was 13.9 ± 5.6 mm (range 4.3–28.6 mm) (**Table 2** and **Figures 4**, **5**). For 17 (50.0%) of the 34 patients, the LE was < 15.0 mm and for 30 (88.2%) of the patients the LE was < 20.0 mm. There were four patients with an LE above 20.0 mm including one outlier with an LE of 28.6 mm. The mean distance from the RV CT marker to the nearest discrete node on the path to rISA was 4.3 ± 2.2 mm (range 1.0–8.7 mm). Correcting for this, the mean cLE was 9.6 ± 6.2 mm (range 0.0–24.6 mm). The mean RV endocardial surface area was 146.0 ± 30.0 cm^2 and the mean circular LE area was 7.0 ± 5.2 cm^2 resulting in a LE error of 5.0 ± 4.0% relative to the RV endocardial area.

Several variables possibly affecting local cardiac conduction properties, myocardial propagation velocity and quality of the input data were investigated for their potential to affect the accuracy of the localization algorithm. Following variables were tested for an association with LE: body mass index, gender, age, use of beta-blocker, ischemic heart disease, LVEF, LV end-diastolic volume, RV lead segmental position, noise in the recorded ECG, heart rate and QRS duration. Only the segmental RV lead position was significantly associated with the LE. The mean uncorrected LE among those with a non-septal lead position was 15.2 mm (95% CI 13.1–17.4) compared to 10.3 mm (95% CI 6.2–14.4, $p = 0.02$) among those with a septal lead position. This association remained significant for the cLE and in a sensitivity-analysis excluding the outlier.

TABLE 1 Patient characteristics.

	All (n = 34)
Age (years)	69.1 ± 11.9 (24.9–85.0)
Male	20 (58.8)
Duration of pacemaker treatment (years)	3.4 ± 0.8 (2.6–5.5)
Ischemic heart disease	4 (11.8)
Beta-blockers	17 (50.0)
Body mass index (kg/m^2)	29.5 ± 5.9 (19.6–48.2)
Echocardiographic parameters	
Left ventricular ejection fraction (%)	55.4 ± 7.6 (41.7–71.4)
Left ventricular end-diastolic volume (ml)	101.9 ± 28.3 (64.0–187.0)
Right ventricular paced ECG parameters	
QRS duration (ms)	151.2 ± 12.9 (128.0–182.0)
Heart rate (beats per minute)	66.5 ± 8.5 (50.0–86.0)

Values are expressed as mean ± standard deviation (range) or *n* (%).

3.3. Assessment of the activation sequence

The correlation between the initial reconstructed activation sequence and the activation sequence initiating from the RV CT marker position was 0.92 ± 0.06 (range 0.73–0.99) (**Table 2**). The correlation between activation maps was associated with the uncorrected and cLE, with increasing LE resulting in decreasing correlation between activation maps, $p = 0.01$. The correlation dropped significantly for LE > 18 mm (**Figure 6**). Mean correlation for LE < 18 mm was 0.94 ± 0.04 and for LE > 18 mm mean correlation was 0.82 ± 0.06.

3.4. Accuracy of the fitted ECG

Overall, the fitted ECG was highly correlated with the recorded ECG [median $r = 0.88$ (range 0.62–0.99)]. Correlation was > 0.8 in 28 (82%) patients. The correlation between the fitted ECG and the recorded ECG was not associated with the LE ($p = 0.22$).

3.5. Computation time

Having loaded the patient-specific model and 12-lead ECG into the specialized software system, the mean algorithm computation time used for reconstructing the ventricular activation was 1.1 ± 0.4 s per ECG using a standard laptop (Intel CORE i7 CPU).

4. Discussion

In this pilot study, we developed and validated a novel non-invasive ECGi method based on the 12-lead ECG for reconstructing ventricular activation during RV pacing and showed: (1) The rISA was accurately and effectively localized in relation to ventricular anatomy. (2) The reconstructed ventricular activation sequence was robust to small changes in initial site of activation.

Current ECGi methods are often based on more complex body surface potential mapping (BSM) derived from up to 256 leads (10).

10.3389/fcvm.2023.1087568

TABLE 2 Results.

Patient	RV lead location	QRS duration (ms)	LE (mm)	cLE (mm)	RV area (cm^2)	Relative LE (%)	Correlation (*r*)
1	Septal	156	8.7	0.0	178.3	1.3	0.98
2	Free wall	156	17.3	15.2	154.3	6.1	0.98
3	Apical	158	20.6	15.1	165.0	8.1	0.87
4	Apical	142	15.6	13.7	167.9	4.6	0.88
5	Apical	158	6.6	4.3	158.0	0.9	0.84
6	Free wall	170	13.4	11.7	173.2	3.2	0.92
7	Free wall	148	11.3	10.3	129.2	3.1	0.96
8	Septal	134	7.1	0.0	146.6	1.1	0.97
9	Free wall	160	12.0	8.2	122.6	3.7	0.94
10	Septal	132	9.5	6.6	125.6	6.0	0.97
11	Free wall	182	7.2	0.0	179.8	2.7	0.98
12	Apical	140	10.4	6.9	126.7	2.9	0.90
13	Septal	168	16.5	10.4	147.0	5.8	0.88
14	Septal	148	4.5	0.0	135.1	0.5	0.97
15	Apical	152	4.4	0.0	169.1	0.4	0.91
16	Apical	142	21.2	15.8	123.1	11.5	0.80
17	Free wall	172	17.9	10.9	158.6	7.1	0.73
18	Septal	130	7.2	0.0	168.2	1.0	0.92
19	Apical	164	18.0	14.3	246.0	4.1	0.94
20	Apical	156	14.6	8.3	172.4	3.9	0.98
21	Apical	156	12.4	5.4	173.7	4.9	0.96
22	Apical	128	7.5	4.5	104.3	1.9	0.98
23	Apical	166	15.2	13.7	118.6	6.1	0.90
24	Apical	138	16.7	12.9	97.5	9.0	0.99
25	Free wall	142	16.3	14.5	159.5	5.2	0.94
26	Apical	152	19.1	16.5	155.1	5.7	0.91
27	Apical	152	21.5	15.5	149.6	9.7	0.89
28	Septal	146	4.3	0.0	96.0	0.6	0.96
29	Septal	146	10.1	6.2	111.6	2.9	0.94
30	Septal	150	18.7	17.5	139.5	7.9	0.80
31	Apical	156	28.6	24.6	124.8	20.6	0.84
32	Apical	146	12.7	4.5	149.4	3.4	0.93
33	Apical	162	19.6	18.2	123.0	7.7	0.91
34	Apical	132	14.5	9.4	114.8	5.7	0.95
Mean ± SD		151.2 ± 12.9	13.9 ± 5.6	9.6 ± 6.2	146.0 ± 30.0	5.0 ± 4.0	0.92 ± 0.1

LE, localization error; cLE, corrected localization error; RV, right ventricular; SD, standard deviation.

Only few studies have investigated 12-lead ECG based methods similar to the method used in this study (21). This is, to our knowledge, the first 12-lead ECG based method tested using clinical data from RV paced patients. Previous studies have validated BSM-based ECGi-methods by assessing the LE between known pacing sites and rISA. Oosterhoff et al. found an average LE of 18 mm using pig hearts and 64-lead BSM (22). Using the smaller rabbit hearts, Han et al. found an LE of approximately 5 mm using 64-lead BSM (23). A study from 2015 used data from 29 pacemaker patients and found a mean LE of 8.6 mm using 224-lead BSM (24). In our study, using only the 10 standard ECG electrodes, we found a LE of 13.9 mm, which is comparable to the studies using multiple lead BSM.

It was not possible to evaluate the accuracy of the ECGi method using invasive electrocardiographic mapping as ground truth data, as it was not available for comparison (9). However, the RV lead position determined from CT provided a reliable fix point for comparison. The robustness of the activation sequence was tested comparing the initial reconstructed activation sequence and the activation sequence initiated from the RV CT marker position. As would be expected, we found an overall strong correlation (r = 0.92, range 0.73–0.99)

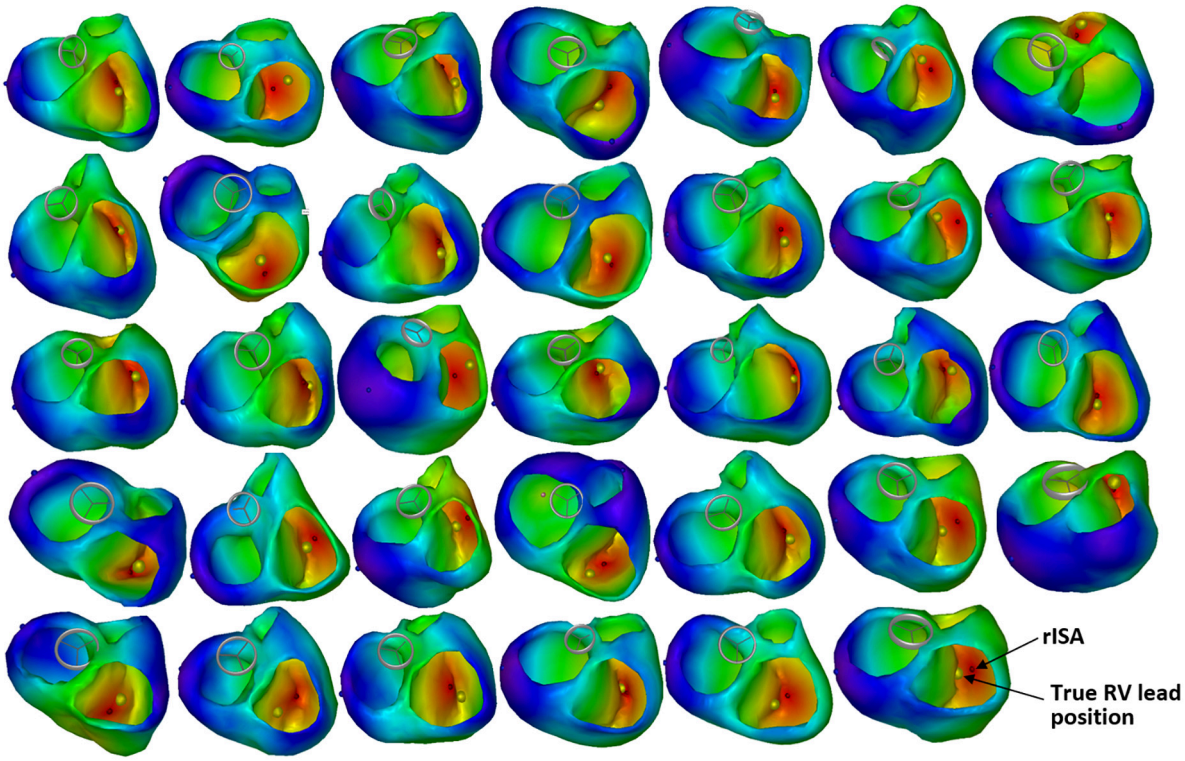

FIGURE 4
Reconstructed 3D ventricular activation models for all 34 patients. The red marker indicates the reconstructed initial site of activation (rISA), and the yellow marker indicates the true right ventricular (RV) lead position determined by computed tomography (CT).

indicating that despite varying degrees of LE, the reconstructed activation pattern is robust to smaller changes in initial site of activation. The used regularization method in the final optimization, minimizing the L2 error norm of the ECG signals, maximizes the correlation between measured and simulated ECG signals. Due to the smoothness of the initial estimate based on a physiological based activation pattern, no large variations are expected in the error function. Consequently, the found initial correlations are equivalent to the resulting fitting errors in the modeled activation pattern. However, it was not possible to compare the reconstructed activation sequence with invasive electrophysiological mapping and the accuracy of the reconstructed activation sequence needs to be confirmed in future studies using invasive electrocardiographic mapping for comparison.

ECGi is not a direct measurement of electrical activity of the heart, it is a reconstruction estimated by an algorithm using different input data. Regardless of the ECGi method used, there is some inherent sources of error depending on the algorithm used and the quality of the input data (9, 25, 26). In this study, ECG-gated CT scans were reconstructed in diastole. Cardiac motion and changes in size and myocardial thickness during the cardiac cycle results in small inaccuracies in the heart-thorax model when assessing ventricular activation during systole. Furthermore, several patients had incomplete thoracic borders on the CT scan, making the thorax model and positioning of the ECG electrodes less accurate. However, we investigated a wide range of variables with potential to affect the accuracy of the localization algorithm and only RV lead position seemed to significantly affect the LE. The mean LE for non-septal leads was higher than for the septal leads (**Table 2** and **Figure 5**). Leads located in the RV free wall or apex are closer to the body surface, and thus become more sensitive to the exact position of the ECG electrodes and local inhomogeneities like for instance the ribcage and lungs. The latter structures were not part of the reconstructed used volume conductor model. The spatial distribution of the 12-lead ECG may be too coarse to localize the exact position of RV leads on the free wall. Moreover, the volume conductor model is inaccurate, both in assigned general homogeneous conductivity values as well as the fact that the heart moves during contraction and the breathing cycle, which potentially influences the RV free wall more than the septum which is located in the middle of the heart. However, though the LE was larger for the non-septal RV leads, the LE was still small, and the method in general seems robust despite imperfections in the algorithm and the input data. Importantly, the method seems to be sensitive enough to distinguish between RV free wall and septal position (**Figure 4**).

Our ECGi method assumed a uniform conduction velocity throughout the myocardium. However, we do not know how well the method works when the assumptions in the algorithm are violated. Elderly pacemaker patients often suffer from ischemia, diabetes or hypertension with hypertrophic myocardium and fibrosis resulting in areas of slower conduction velocities (27, 28). This is accounted for indirectly, as the estimated QRS duration must be matched with the recorded QRS duration. However, detailed assessment of the activation sequence localizing ischemic or fibrotic areas with slow conduction is not possible with the current method. Despite this, the method showed to accurately localize the initial site of activation in a heterogenous cohort including both males and females with a wide range of QRS durations, body sizes, ages,

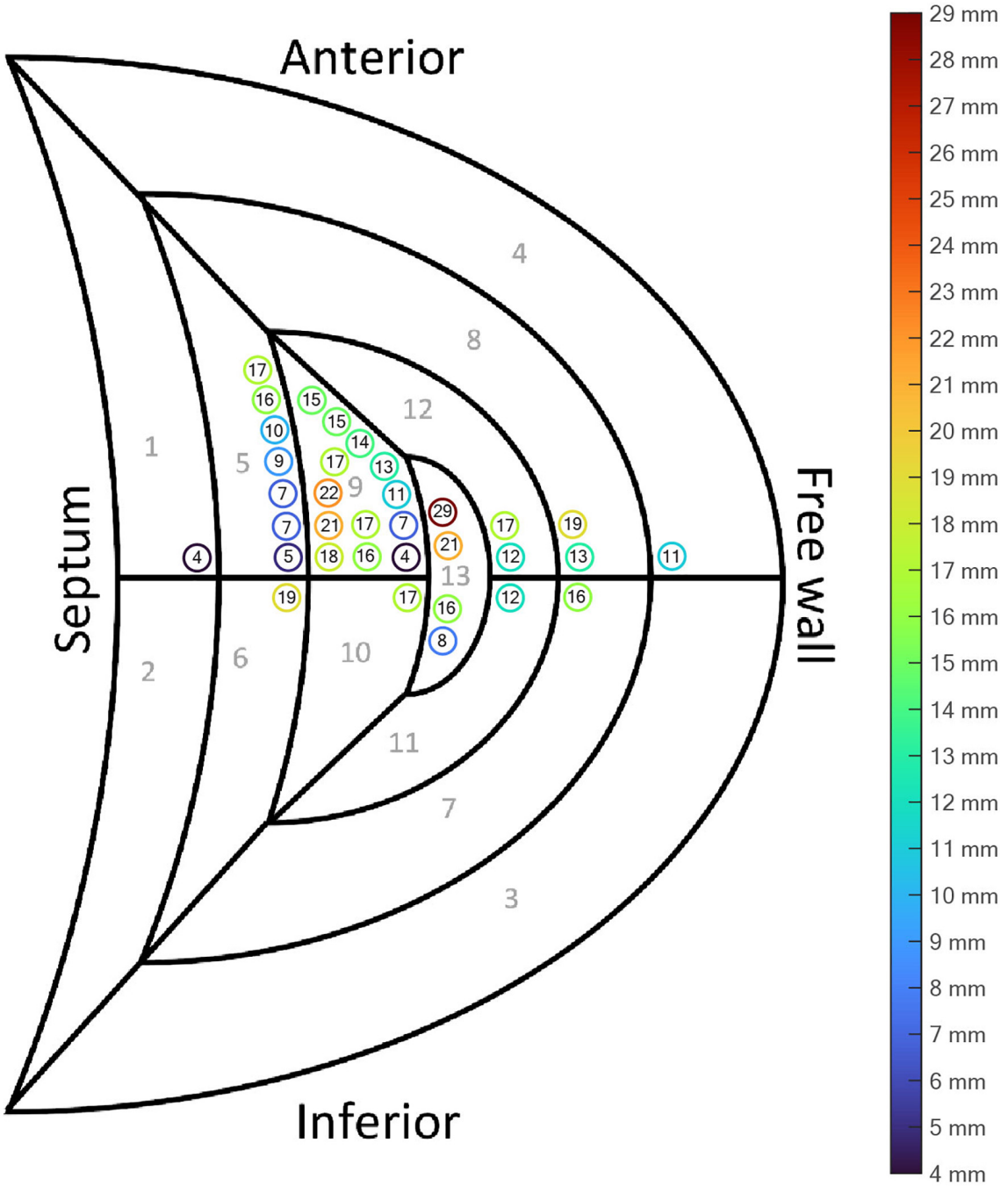

FIGURE 5
Segmental plot of the localization error (LE) according to the right ventricular (RV) lead position. The encircled numbers show the LE (mm) for each patient. The color of the circle is a visual representation of the distance.

LV functions and sizes as well as RV leads positioned throughout the RV endocardium.

Based on these promising results, further work to improve the accuracy of the method seems encouraging. The reconstructions are calculated almost real-time. Thus, potentially enabling intraprocedural model-assisted evaluation of ventricular activation and lead position in relation to ventricular anatomy ensuring optimal pacemaker lead implantation for the individual patient. Furthermore, providing a detailed electrical activation pattern, ECGi is highly relevant as a tool to guide and optimize cardiac resynchronyzation therapy (CRT) implantation (9, 29–31).

4.1. Limitations

As described in detail above, comparison with ground truth data from invasive electrocardiographic mapping was not available and the quality of the input data was varying possibly limiting the accuracy. The current method includes creating a patient-specific heart-thorax model, which is a cumbersome process requiring a cardiac CT scan. Future studies should investigate the feasibility of using a generic model to reduce the workload and avoid the need for a CT scan, making the method more manageable in a clinical setting.

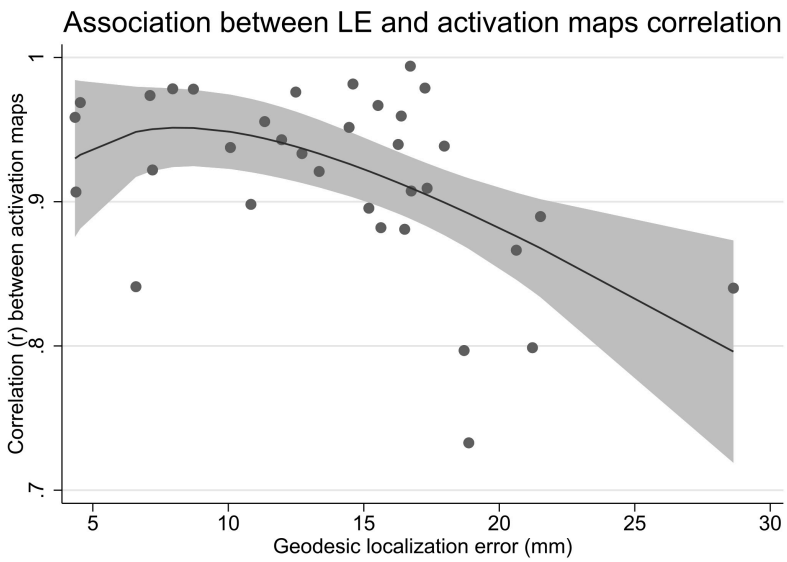

FIGURE 6
Association between the localization error and the correlation between initially reconstructed activation sequence and the activation sequence initiating from the true right ventricular lead position. LE, localization error.

5. Conclusion

In this pilot study, we demonstrated a novel non-invasive ECGi method, based on the readily available 12-lead ECG, which accurately and effectively localized initial site of activation in relation to ventricular anatomy and provided an estimate for the ventricular activation sequence during RV pacing.

Data availability statement

The raw data supporting the conclusions of this article will be made available by the authors, without undue reservation.

Ethics statement

Ethical review and approval was not required for the study on human participants in accordance with the local legislation and institutional requirements. The patients/participants provided their written informed consent to participate in this study.

Author contributions

PF: conceptualization, investigation, methodology, formal analysis, data curation, writing—original draft, and visualization. PV: conceptualization, methodology, software, visualization, and writing—review and editing. AS, JM, and TZ: conceptualization and writing—review and editing. SL-C: conceptualization, formal analysis, and writing—review and editing. PS: investigation and writing—review and editing. CG: conceptualization, methodology, data curation, and writing—review and editing. SR: conceptualization, methodology, writing—review and editing, and supervision. All authors contributed to the article and approved the submitted version.

Funding

This work was supported by the Svend Andersen's Foundation, Karl G. Andersen's Foundation, and Helsefonden (grant number 20-B-0193).

Conflict of interest

PV was owner of Peacs-BV and ECG-Excellence-BV. All specialized software used for the method has been developed by ECG-Excellence-BV.

The remaining authors declare that the research was conducted in the absence of any commercial or financial relationships that could be construed as a potential conflict of interest.

Publisher's note

All claims expressed in this article are solely those of the authors and do not necessarily represent those of their affiliated organizations, or those of the publisher, the editors and the reviewers. Any product that may be evaluated in this article, or claim that may be made by its manufacturer, is not guaranteed or endorsed by the publisher.

Supplementary material

The Supplementary Material for this article can be found online at: https://www.frontiersin.org/articles/10.3389/fcvm.2023.1087568/full#supplementary-material

References

1. Moore P, Coucher J, Ngai S, Stanton T, Wahi S, Gould P, et al. Imaging and right ventricular pacing lead position: a comparison of CT, MRI, and echocardiography. *Pacing Clin Electrophysiol.* (2016) 39:382–92. doi: 10.1111/pace.12817

2. Sommer A, Kronborg MB, Nørgaard BL, Gerdes C, Mortensen PT, Nielsen JC, et al. Left and right ventricular lead positions are imprecisely determined by fluoroscopy in cardiac resynchronization therapy: a comparison with cardiac computed tomography. *Europace.* (2014) 16:1334–41. doi: 10.1093/europace/euu056

3. Rowe MK, Moore P, Pratap J, Coucher J, Gould PA, Kaye GC. Surface ECG and fluoroscopy are not predictive of right ventricular septal lead position compared to cardiac CT. *Pacing Clin Electrophysiol.* (2017) 40:537–44. doi: 10.1111/pace.13066

4. Sommer A, Kronborg MB, Witt CT, Nørgaard BL, Nielsen JC, Norgaard BL, et al. The paced electrocardiogram cannot be used to identify left and right ventricular pacing sites in cardiac resynchronization therapy: validation by cardiac computed tomography. *Europace.* (2015) 17:432–8. doi: 10.1093/europace/euu323

5. Hoekema R, Uijen GJH, Van Erning L, Van Oosterom A. Interindividual variability of multilead electrocardiographic recordings: influence of heart position. *J Electrocardiol.* (1999) 32:137–48. doi: 10.1016/S0022-0736(99)90092-4

6. Hattori M, Naruse Y, Oginosawa Y, Matsue Y, Hanaki Y, Kowase S, et al. Prognostic impact of lead tip position confirmed via computed tomography in patients with right ventricular septal pacing. *Hear Rhythm.* (2019) 16:921–7. doi: 10.1016/j.hrthm.2019.01.008

7. Varma N, Ploux S, Ritter P, Wilkoff B, Eschalier R, Bordachar P. Noninvasive mapping of electrical dyssynchrony in heart failure and cardiac resynchronization therapy. *Card Electrophysiol Clin.* (2015) 7:125–34. doi: 10.1016/j.ccep.2014.11.012

8. Pereira H, Niederer S, Rinaldi CA. Electrocardiographic imaging for cardiac arrhythmias and resynchronization therapy. *Europace.* (2020) 22:1447–62. doi: 10.1093/europace/euaa165

9. Cluitmans M, Brooks DH, MacLeod R, Dössel O, Guillem MS, Van Dam PM, et al. Validation and opportunities of electrocardiographic imaging: from technical achievements to clinical applications. *Front Physiol.* (2018) 9:1305. doi: 10.3389/fphys.2018.01305

10. Bear L, Cuculich PS, Bernus O, Efimov I, Dubois R. Introduction to noninvasive cardiac mapping. *Card Electrophysiol Clin.* (2015) 7:1–16. doi: 10.1016/j.ccep.2014.11.015

11. Lang RM, Badano LP, Mor-Avi V, Afilalo J, Armstrong A, Ernande L, et al. Recommendations for cardiac chamber quantification by echocardiography in adults: an update from the American Society of Echocardiography and the European Association of Cardiovascular Imaging. *Eur Heart J Cardiovasc Imaging.* (2015) 16:233–70. doi: 10.1093/ehjci/jev014

12. Misra S, van Dam P, Chrispin J, Assis F, Keramati A, Kolandaivelu A, et al. Initial validation of a novel ECGI system for localization of premature ventricular contractions and ventricular tachycardia in structurally normal and abnormal hearts. *J Electrocardiol.* (2018) 51:801–8. doi: 10.1016/j.jelectrocard.2018.05.018

13. Van Dam PM, Gordon JP, Laks MM, Boyle NG. Development of new anatomy reconstruction software to localize cardiac isochrones to the cardiac surface from the 12 lead ECG. *J Electrocardiol.* (2015) 48:959–65. doi: 10.1016/j.jelectrocard.2015.08.036

14. Boonstra MJ, Hilderink BN, Locati ET, Asselbergs FW, Loh P, Van Dam PM. Novel CineECG enables anatomical 3D localization and classification of bundle branch blocks. *Europace.* (2021) 23:I80–7. doi: 10.1093/europace/euaa396

15. van Dam PM, Oostendorp TF, van Oosterom A. Application of the fastest route algorithm in the interactive simulation of the effect of local ischemia on the ECG. *Med Biol Eng Comput.* (2009) 47:11–20. doi: 10.1007/s11517-008-0391-2

16. Van Dam PM, Oostendorp TF, Linnenbank AC, Van Oosterom A. Non-invasive imaging of cardiac activation and recovery. *Ann Biomed Eng.* (2009) 37:1739–56. doi: 10.1007/s10439-009-9747-5

17. Van Oosterom A. The dominant T wave. *J Electrocardiol.* (2004) 37:193–7. doi: 10.1016/j.jelectrocard.2004.08.056

18. Van Oosterom A. Genesis of the T wave as based on an equivalent surface source model. *J Electrocardiol.* (2001) 34:217–27. doi: 10.1054/jelc.2001.28896

19. Meijs JW, Weier OW, Peters MJ, van Oosterom A, Oosterom AVAN. On the numerical accuracy of the boundary element method. *IEEE Trans Biomed Eng.* (1989) 36:1038–49. doi: 10.1109/10.40805

20. Geselowitz DB. Description of cardiac sources in anisotropic cardiac muscle. Application of bidomain model. *J Electrocardiol.* (1992) 25(Suppl.):65–7. doi: 10.1016/0022-0736(92)90063-6

21. Pezzuto S, Prinzen FW, Potse M, Maffessanti F, Regoli F, Caputo ML, et al. Reconstruction of three-dimensional biventricular activation based on the 12-lead electrocardiogram via patient-specific modelling. *Europace.* (2021) 23:640–7. doi: 10.1093/europace/euaa330

22. Oosterhoff P, Meijborg VMF, Van Dam PM, Van Dessel PFHM, Belterman CNW, Streekstra GJ, et al. Experimental validation of noninvasive epicardial and endocardial activation imaging. *Circ Arrhythmia Electrophysiol.* (2016) 9:e004104. doi: 10.1161/CIRCEP.116.004104

23. Han C, Pogwizd SM, Killingsworth CR, He B. Noninvasive imaging of three-dimensional cardiac activation sequence during pacing and ventricular tachycardia. *Hear Rhythm.* (2011) 8:1266–72. doi: 10.1016/j.hrthm.2011.03.014

24. Revishvili AS, Wissner E, Lebedev DS, Lemes C, Deiss S, Metzner A, et al. Validation of the mapping accuracy of a novel non-invasive epicardial and endocardial electrophysiology system. *Europace.* (2015) 17:1282–8. doi: 10.1093/europace/euu339

25. Tate JD, Good W, Zemzemi N, Boonstra M, van Dam P, Brooks DH, et al. Uncertainty quantification of the effects of segmentation variability in ECGI. *Funct Imaging Model Heart Int Work FIMH Proc FIMH.* (2021) 12738:515–22. doi: 10.1007/978-3-030-78710-3_49

26. Bear LR, Dogrusoz YS, Good W, Svehlikova J, Coll-Font J, Van Dam E, et al. The impact of torso signal processing on noninvasive electrocardiographic imaging reconstructions. *IEEE Trans Biomed Eng.* (2021) 68:436–47. doi: 10.1109/TBME.2020.3003465

27. King JH, Huang CLH, Fraser JA. Determinants of myocardial conduction velocity: implications for arrhythmogenesis. *Front Physiol.* (2013) 4:154. doi: 10.3389/fphys.2013.00154

28. Akar FG, Nass RD, Hahn S, Cingolani E, Shah M, Hesketh GG, et al. Dynamic changes in conduction velocity and gap junction properties during development of pacing-induced heart failure. *Am J Physiol Hear Circ Physiol.* (2007) 293:1223–30. doi: 10.1152/ajpheart.00079.2007

29. Melgaard J, van Dam PM, Sommer A, Fruelund P, Nielsen JC, Riahi S, et al. Non-invasive estimation of QLV from the standard 12-lead ECG in patients with left bundle branch block. *Front Physiol.* (2022) 13:939240. doi: 10.3389/fphys.2022.939240

30. Sedova K, Repin K, Donin G, Van Dam P, Kautzner J. Clinical utility of body surface potential mapping in CRT patients. *Arrhythmia Electrophysiol Rev.* (2021) 10:113–9. doi: 10.15420/aer.2021.14

31. Ploux S, Lumens J, Whinnett Z, Montaudon M, Strom M, Ramanathan C, et al. Noninvasive electrocardiographic mapping to improve patient selection for cardiac resynchronization therapy: beyond QRS duration and left bundle branch block morphology. *J Am Coll Cardiol.* (2013) 61:2435–43. doi: 10.1016/j.jacc.2013.01.093

frontiers | Frontiers in Medical Technology

TYPE Original Research
PUBLISHED 23 February 2023
DOI 10.3389/fmedt.2023.1130201

OPEN ACCESS

EDITED BY
Claudio Chiastra,
Polytechnic University of Turin, Italy

REVIEWED BY
Gabor Janiga,
Otto von Guericke University Magdeburg, Germany
Marc Horner,
Ansys, United States

*CORRESPONDENCE
Brent A. Craven
brent.craven@fda.hhs.gov
Keefe B. Manning
kbm10@psu.edu

SPECIALTY SECTION
This article was submitted to Cardiovascular Medtech, a section of the journal Frontiers in Medical Technology

RECEIVED 22 December 2022
ACCEPTED 09 February 2023
PUBLISHED 23 February 2023

CITATION
Bhardwaj S, Craven BA, Sever JE, Costanzo F, Simon SD and Manning KB (2023) Modeling flow in an *in vitro* anatomical cerebrovascular model with experimental validation.
Front. Med. Technol. 5:1130201.
doi: 10.3389/fmedt.2023.1130201

Modeling flow in an *in vitro* anatomical cerebrovascular model with experimental validation

Saurabh Bhardwaj[1], Brent A. Craven[2]*, Jacob E. Sever[1], Francesco Costanzo[1,3], Scott D. Simon[4] and Keefe B. Manning[1,5]*

[1]Department of Biomedical Engineering, Pennsylvania State University, University Park, PA, United States, [2]Office of Science and Engineering Laboratories, Center for Devices and Radiological Health, U.S. Food and Drug Administration, Silver Spring, MD, United States, [3]Department of Engineering Science and Mechanics, Pennsylvania State University, University Park, PA, United States, [4]Department of Neurosurgery, Penn State Hershey Medical Center, Hershey, PA, United States, [5]Department of Surgery, Penn State Hershey Medical Center, Hershey, PA, United States

Acute ischemic stroke (AIS) is a leading cause of mortality that occurs when an embolus becomes lodged in the cerebral vasculature and obstructs blood flow in the brain. The severity of AIS is determined by the location and how extensively emboli become lodged, which are dictated in large part by the cerebral flow and the dynamics of embolus migration which are difficult to measure *in vivo* in AIS patients. Computational fluid dynamics (CFD) can be used to predict the patient-specific hemodynamics and embolus migration and lodging in the cerebral vasculature to better understand the underlying mechanics of AIS. To be relied upon, however, the computational simulations must be verified and validated. In this study, a realistic *in vitro* experimental model and a corresponding computational model of the cerebral vasculature are established that can be used to investigate flow and embolus migration and lodging in the brain. First, the *in vitro* anatomical model is described, including how the flow distribution in the model is tuned to match physiological measurements from the literature. Measurements of pressure and flow rate for both normal and stroke conditions were acquired and corresponding CFD simulations were performed and compared with the experiments to validate the flow predictions. Overall, the CFD simulations were in relatively close agreement with the experiments, to within ±7% of the mean experimental data with many of the CFD predictions within the uncertainty of the experimental measurement. This work provides an *in vitro* benchmark data set for flow in a realistic cerebrovascular model and is a first step towards validating a computational model of AIS.

KEYWORDS

cerebrovascular model, cerebral blood flow, image based modeling, acute ischemic stroke, fluid dynamics

1. Introduction

Stroke is one of the leading causes of mortality worldwide (over 6.5 million deaths/year) (1), with acute ischemic stroke (AIS) accounting for 87% of the total stroke mortalities (2). AIS is a life-threatening medical condition that occurs when an embolus becomes lodged in the cerebral vasculature and obstructs blood flow in the brain. The available literature contains substantial

Abbreviations
CCA, common carotid artery; ICA, internal carotid artery; ECA, external carotid artery; LECA, left external carotid artery; RECA, right external carotid artery; MCA, middle cerebral artery; LMCA, left middle cerebral artery; RMCA, right middle cerebral artery; ACA, anterior cerebral artery; LAA, left anterior artery; RAA, right anterior artery; LSA left subclavian artery; RSA right subclavian artery.

research that has been performed to investigate cerebral blood flow (e.g., see (3–9)). A main focus of prior research has been to study regional cerebral blood flow, which forms the basis for identifying the causes of several diseases. Generally, the severity of AIS is determined by the location and how extensively emboli become lodged in the cerebral vasculature. It is extremely challenging, however, to measure the flow rate, pressure, and embolus migration in AIS patients. This level of information, though, is needed to explore the underlying causes and treatment of AIS.

The size and location of blood emboli in the cerebral vasculature have been the subject of several studies (10–16). The middle cerebral artery (MCA) is the location where emboli most frequently lodge (13). Measurements of the distribution of cerebral emboli within various arterial branches have been reported. A recent investigation using rats (14) showed that emboli shape and composition have a significant role in determining the severity of brain damage after they reach the cerebral vasculature. Using idealized Y-bifurcation geometries, Pollanen (15) and, more recently, Bushi et al. (16) conducted experiments on embolic particle migration. Beyond what volumetric flow patterns may imply, their research revealed a bias in the distribution of larger particles into the larger branching arteries like the common carotid artery (CCA), internal carotid artery (ICA), and the MCA. In their studies on embolus transport in the cerebral arteries, Chung et al. (10) used a more accurate anatomical model of the Circle of Willis and proposed a similar tendency of larger particles migrating toward the larger branching vessels. The distribution fraction of emboli across major arterial branches has been quantified in these experimental investigations corresponding to the associated volumetric flow patterns. But, they generally neglect the smaller branches along with the aortic arch in the anatomical model that can significantly influence the flow and embolus transport.

Computational fluid dynamics (CFD) can be used to predict patient-specific hemodynamics and embolus migration and lodging in the cerebral vasculature to better understand the underlying mechanics of AIS and to improve recanalization methods. Patient-specific CFD has become widely used for simulating blood flow in the cardiovascular system (17); examples include evaluating the hemodynamics of healthy and diseased blood vessels (18, 19), assisting in the design and assessment of vascular medical devices (20, 21), planning vascular surgeries, and predicting the results of interventions (22, 23). To be relied upon, however, the computational simulations must be verified and validated, which is difficult to achieve *in vivo*, particularly for embolus migration. Realistic *in vitro* models can be used to provide a rich data set for CFD validation. For example, researchers at the United States. Food and Drug Administration (FDA) and collaborators have developed benchmark models of a simplified nozzle, a centrifugal blood pump, and a vascular model of the inferior vena cava and have acquired flow measurements that are widely used for CFD validation (24–29).

The objective of this study is to establish an *in vitro* experimental model and a corresponding computational model of the cerebral vasculature that can be used to investigate flow and embolus migration and lodging in the brain. Levaraging a representative anatomical cerebrovascular model, computational simulations are performed with particular focus on comparing with experimental pressure and flow rate measurements. In addition to normal physiological flow conditions, the effect of arterial embolus occlusion in the MCA is considered to emulate a stroke to investigate its influence on cerebral blood flow.

2. Methods

2.1. Cerebrovascular model

A representative anatomical model of the aorta and cerebral vasculature was used in this study (**Figure 1**). The model was designed and fabricated by United Biologics (Irvine, CA, United States) based on patient medical image data from several sources (e.g., the NIH Visible Human Project, patient-specific CT data). The *in vitro* model (**Figure 1**) is made of silicone with an elastic modulus of 3.1–3.4 N/mm^2, which is representative of human arteries. The entire model includes the aorta, common carotid arteries, internal and external carotid arteries, axillary arteries, middle cerebral arteries, and anterior cerebral arteries. In addition, a corresponding computational model of the *in vitro* model was reconstructed from high-resolution 3D micro computed tomography (μ-CT) scans (**Figure 2A**).

2.2. *In vitro* experiments

A closed-loop circulatory flow system was designed that included a centrifugal pump (Cole-Parmer, IL, United States), reservoir, flow meter and ultrasonic flow probes, and pressure transducers as shown in **Figures 1A,B**. The flow loop was connected to the cerebrovascular model, which was placed in the supine orientation. The inlet and outlet flow rates and pressures were monitored using ultrasonic flow probes (Transonic Systems, Inc., Millis, MA) and pressure transducers (Merit Medical, South Jordan, UT), respectively. The pressure transducers were connected to an analog data acquisition module (DAQ, National Instruments, Texas, United States) and recorded using LabVIEW software (National Instruments, Texas, United States).

Similar to Riley et al. (26), the working fluid consisted of a mixture of water (60% by weight) and glycerol (40% by weight) to obtain a density and dynamic viscosity that is representative of blood (1.09 ± 0.03 g/ml and 3.98 ± 0.14 cP, respectively) at an operating temperature of 22.2°C. Experiments were performed using a steady inlet flow rate of 5.17 ± 0.078 L/min, corresponding to a Reynolds number (*Re*) in the inlet tube of approximately 3890. This inlet flow rate was chosen to correspond to a representative mean physiological cardiac output of an adult. An extended tube of 900 mm in length was attached to the model inlet such that the flow entering the model inlet was fully developed. To study the effect of a stroke condition on the mean arterial pressure and flow rate in the cerebral arteries, nylon spherical clots of three different sizes (3.15 mm, 4.75 mm, and 6.38 mm in diameter) were manually inserted into the right MCA (RMCA) to completely block the vessel and the corresponding flow through outlet 4, as depicted in **Figure 1C**.

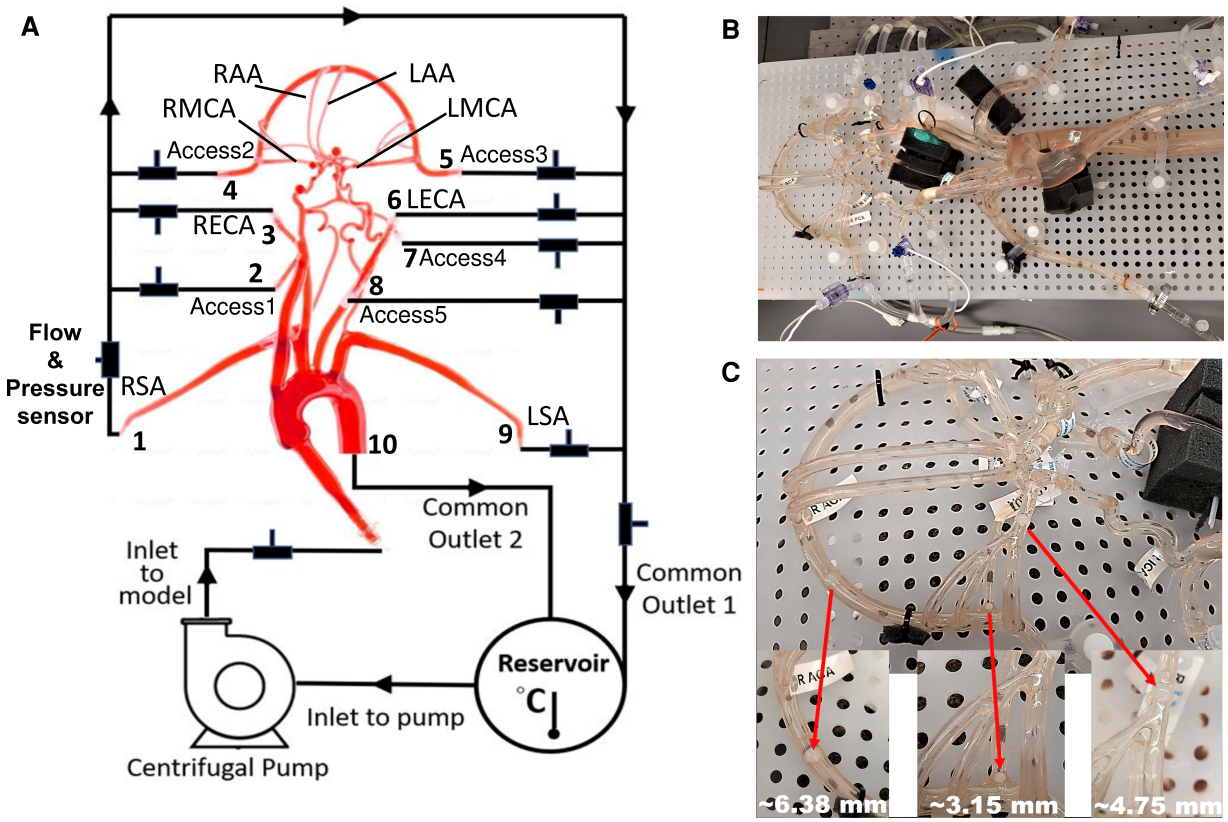

FIGURE 1
schematic and photographs of the *in vitro* circulatory flow loop illustrating the (**A**) experimental setup, (**B**) the flow loop setup with the instrumentation that was used to measure flow rate and pressure at various cerebrovascular outlets, and (**C**) location of nylon spherical clots used to mimic a stroke condition. Here, LSA and RSA are the left and right subclavian arteries, LECA and RECA are the left and right external carotid arteries, LMCA and RMCA are the left and right middle cerebral arteries, and LAA and RAA are the left and right anterior arteries, respectively.

Three separate experiments were performed for both conditions (normal and stroke) to measure the flow rate and pressure at the inlet and various outlets in order to provide boundary conditions for the CFD simulations and for validation. Because the fluid heats up as it is continuously pumped through the flow loop, we waited for 30 min to allow for the fluid temperature to reach a steady state (22.2°C) before measuring the flow rate and pressure. Importantly, the viscosity of the fluid was tuned to account for the effect of this temperature rise, so as to obtain the desired value of 3.98 cP at the steady-state operating temperature. The regional distribution of the flow rate was tuned to match available literature data (30, 31) by adjusting clamps downstream of the pressure and flow rate measurement sites. This yielded a regional flow distribution such that 73.2% of the flow passed through the descending aorta and 26.8% of the flow was distributed to the remaining arteries stemming from the aortic arch. The flow rates to individual arteries were also tuned to match that reported in the literature (30, 31), which are summarized in **Table 1**.

2.3. CFD mesh

The computational geometry was discretized in CF-Mesh+ (version 3.5.1; Creative Fields, Croatia) using an unstructured hexahedral mesh with 5 wall-normal inflation layers at the walls to resolve large velocity gradients. Three different resolutions of meshes were generated yielding coarse, medium, and fine meshes having 3 million, 6.5 million, and 9 million computational cells, respectively (**Figures 2B-D**). These generated meshes were used to perform a mesh refinement study to evaluate the sensitivity of the results to the mesh resolution. Using the *topoSet* utility in OpenFOAM, the mesh for the stroke condition was generated by removing the cells covering the section of the arteries that were blocked in the experiments by clots. After eliminating the cells at the clot insertion sites, the newly created surfaces were converted to walls.

2.4. Governing equations & boundary conditions

Using the 3D reconstructed model, CFD simulations of the flow were performed by solving the Reynolds-averaged Navier-Stokes (RANS) equations using the open-source computational continuum mechanics library, OpenFOAM (version 2106). The gravitational force is not considered in the present simulations. The effects of turbulence were modeled using the two-equation eddy-viscosity $k-\omega$ shear stress transport (SST) turbulence

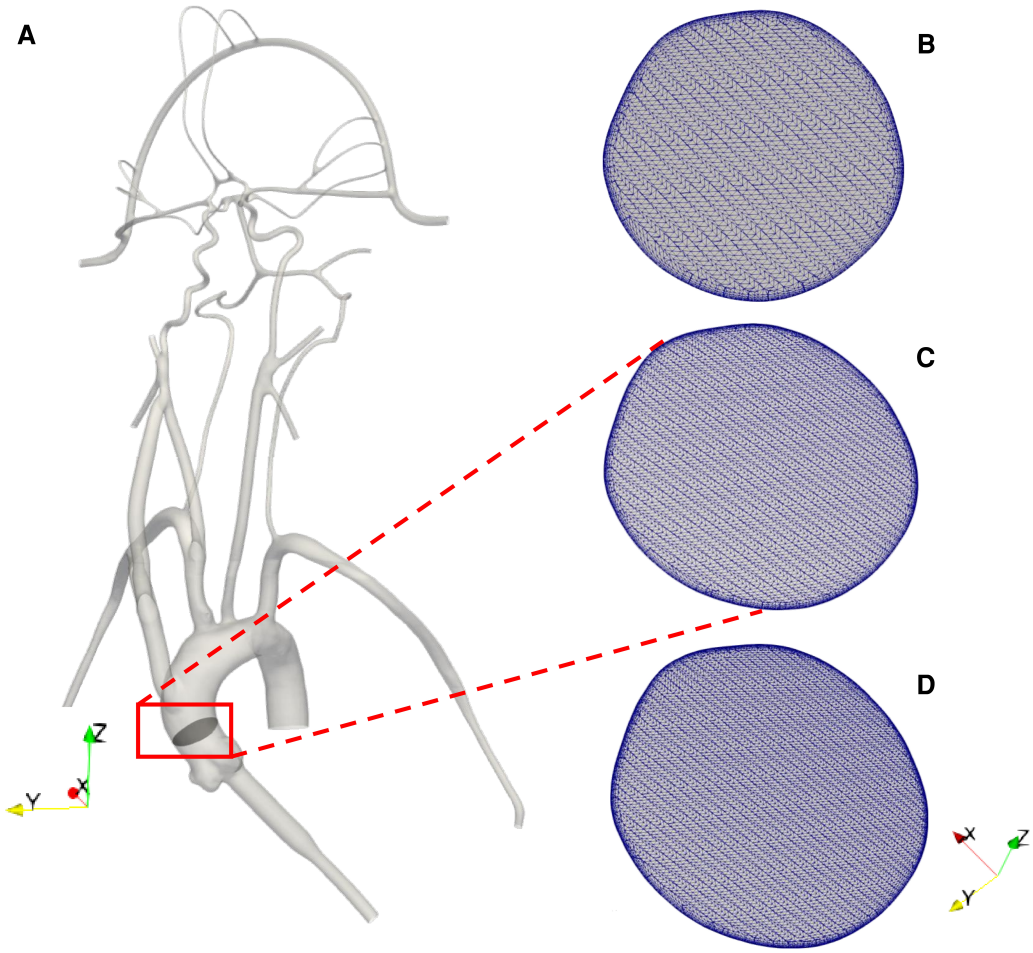

FIGURE 2
(A) 3D reconstructed computational model of the corresponding *in vitro* cerebrovascular model with a cut plane view in the aortic arch to show the mesh for the (B) 3 M, (C) 6.5 M and (D) 9 M cell meshes.

model (32, 33). The $k-\omega$ SST model was chosen because of its reported good behavior in adverse pressure gradients and separated flows (34), and because it has been shown to be capable of handling multi-regime (laminar, transitional, turbulent) flows (35).

The CFD boundary conditions were specified to match the corresponding *in vitro* experiments. A constant, uniform inlet velocity was applied to the extended inlet to obtain fully developed flow entering the inlet to the ascending aorta at a flow rate of 5.17 L/min. A no-slip velocity boundary condition was applied on the walls, which were assumed to be rigid. The *pressureInletOutletVelocity* condition in OpenFOAM was applied for the velocity on all outlet boundaries, which uses a zero-gradient Neumann condition on boundary faces with outflow and an extrapolated Dirichlet condition on faces with reversed inflow. A zero-gradient pressure condition was applied at the inlet and fixed static pressure boundary conditions were prescribed on all outlets. The values of outlet pressure were specified by iteratively performing simulations to match the measured flow rate through each outlet in the experiments to within ±10%.

TABLE 1 Distribution of cerebral volumetric flow rates from the literature. The flow rate values are reported as mean ± standard deviation (SD).

Vessel	Flow rate (L/min)	References
Common carotid	8.5 ± 0.9	(30)
	8.9	(31)
Internal carotid	5.3 ± 1.0	(30)
Subclavian	8.1 ± 0.8	(30)
Vertebral*	1.9 ± 0.5	(30)
Axillary	6.2 ± 0.9	(30)

*calculated difference between subclavian and axillary flow rates.

2.5. Numerical methods

Simulations were performed in OpenFOAM using second-order accurate discretization schemes, including second-order upwind for the advective terms. Preliminary steady simulations were performed by solving the steady RANS equations of motion using the semi-implicit method for pressure-linked equations (SIMPLE) solver, *simpleFoam*. The steady simulations did not

converge owing to regions of significant unsteady flow in the ascending aorta and the aortic arch. Fully transient flow simulations were performed using the hybrid pressure-implicit with splitting of operators (PISO)-SIMPLE solver, *pimpleFoam*. An initial unsteady simulation was performed for 4 s of physical time, which was determined to be the time that was needed for the flow to overcome the initial startup transient conditions and to obtain a stationary, quasi-steady flow state. Simulations were

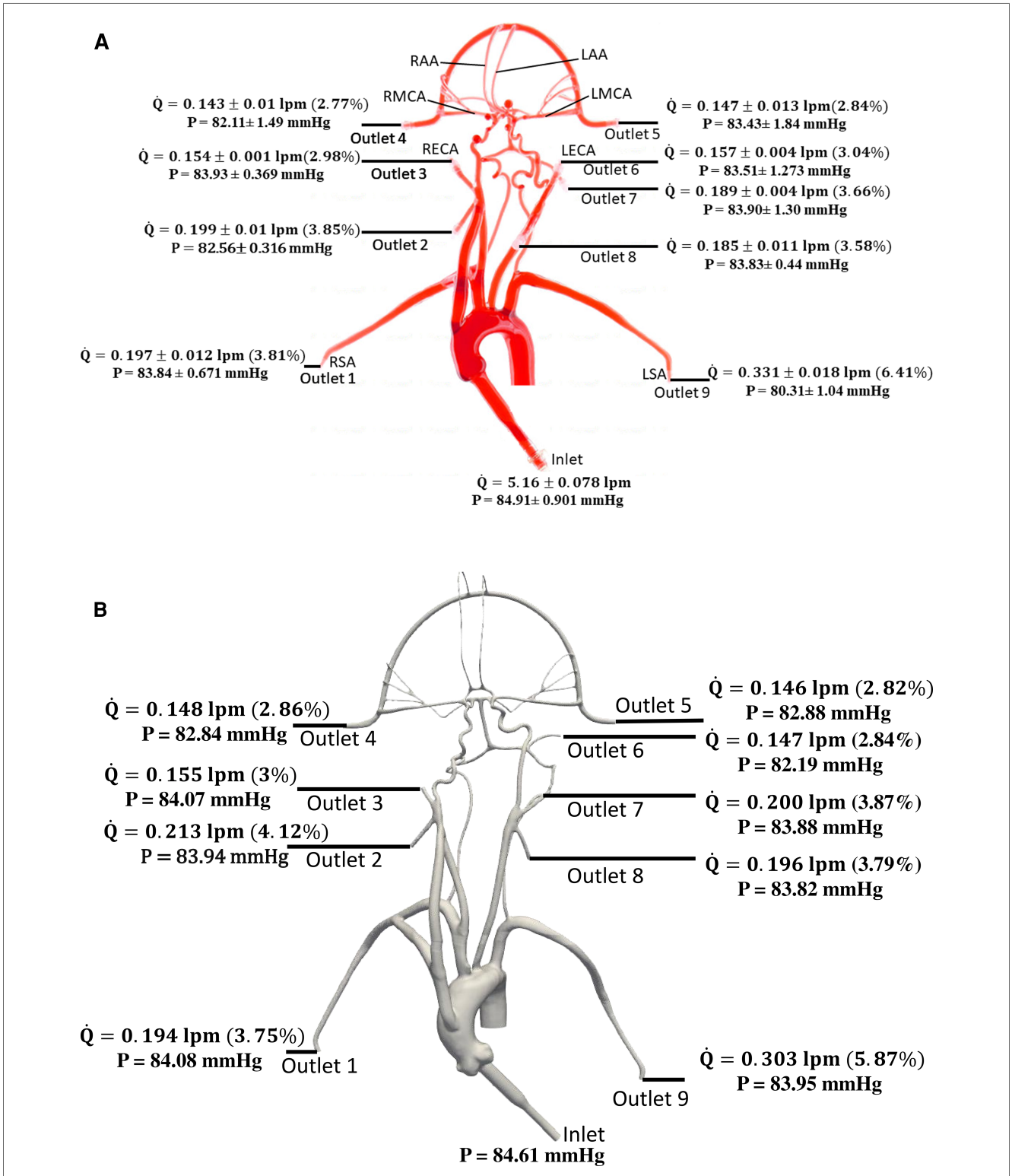

FIGURE 3
Mean volumetric flow rate and pressure values along with standard deviation at the inlet and all arterial outlets from (A) *in vitro* experiments and (B) CFD simulation for the normal condition. The percentage values shown in parentheses indicate the fraction of total inlet flow through each arterial outlet.

then run for another 4 s at these quasi-steady conditions while time-averaging the flow solution. The simulations were performed on 40 compute cores of a high-performance computing (HPC) system at the Institute for Computational and Data Sciences at the Pennsylvania State University. Post-processing and visualization of the simulation results were performed in ParaView (Kitware, Inc., Clifton Park, NY).

3. Results

3.1. *In vitro* experiments

The values of volumetric flow rate (L/min) and pressure (mmHg) measured at various arterial outlets are shown in Figure 3A. As mentioned in Section 2.2, the arteries stemming from the aortic arch, which includes the axillary, external, middle, anterior, and other arteries, receive 26.8% of the total flow rate entering the model and 73.2% of the fluid flows through the descending aorta. Out of the total flow rate, 10.23% travels through both axillary arteries, 6.02% through both external carotid arteries (ECA), and 5.62% through the middle and anterior cerebral arteries. This measured flow distribution matches physiological values from the available literature (30, 31). However, it is important to note that these distributions are based on the steady flow measurements, whereas the values reported in the literature are based on total volumetric flow rate values over a pulsatile cardiac cycle.

Changes in mean arterial pressure and volumetric flow rate were also measured for the stroke condition when there is no flow from outlet 4. The measurements showed that the mean pressure at all outlets decreased for the stroke condition. As illustrated in Figures 3, 4, the flow rate through the right arterial outlets as well as outlets 5 and 6 increased to compensate for the flow that was obstructed due to the emulated stroke.

3.2. CFD flow simulation

To verify that the $k-\omega$ SST turbulence model is behaving as expected and producing turbulent flow in regions of expected turbulence and laminar flow in the downstream cerebral arteries, we calculated the regional distribution of the turbulent viscosity ratio (ν_t/ν) that is defined as the ratio of turbulent viscosity (ν_t) to the molecular viscosity (ν). In regions where the $k-\omega$ SST model predicts turbulence, ν_t/ν is much larger than unity and in regions of laminar flow ν_t/ν is much less than 1. As illustrated

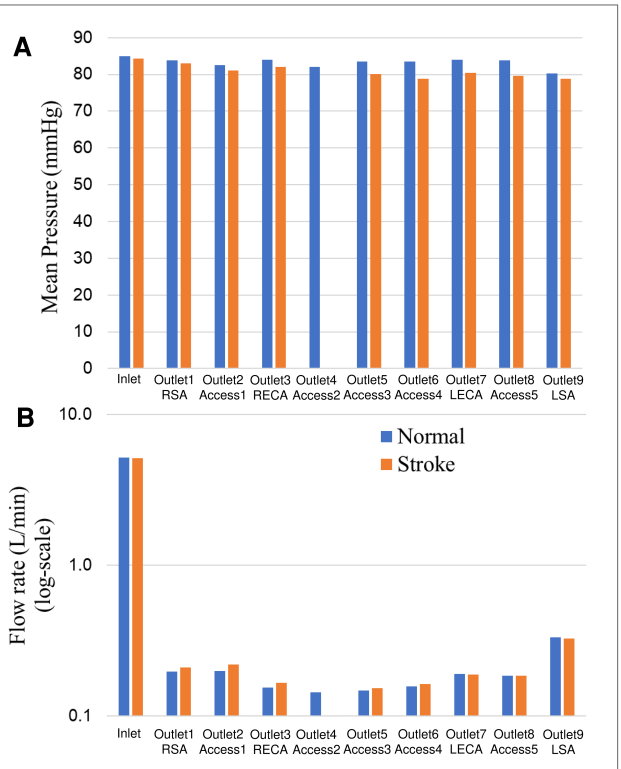

FIGURE 4
Comparison of (A) mean pressure and (B) flow rate (log scale) at the inlet and various aterial outlets for the normal and stroke conditions from *in vitro* experiments. The values of pressure and flow rate at outlet 4 for the stroke condition are zero because there is no flow due to the blockage.

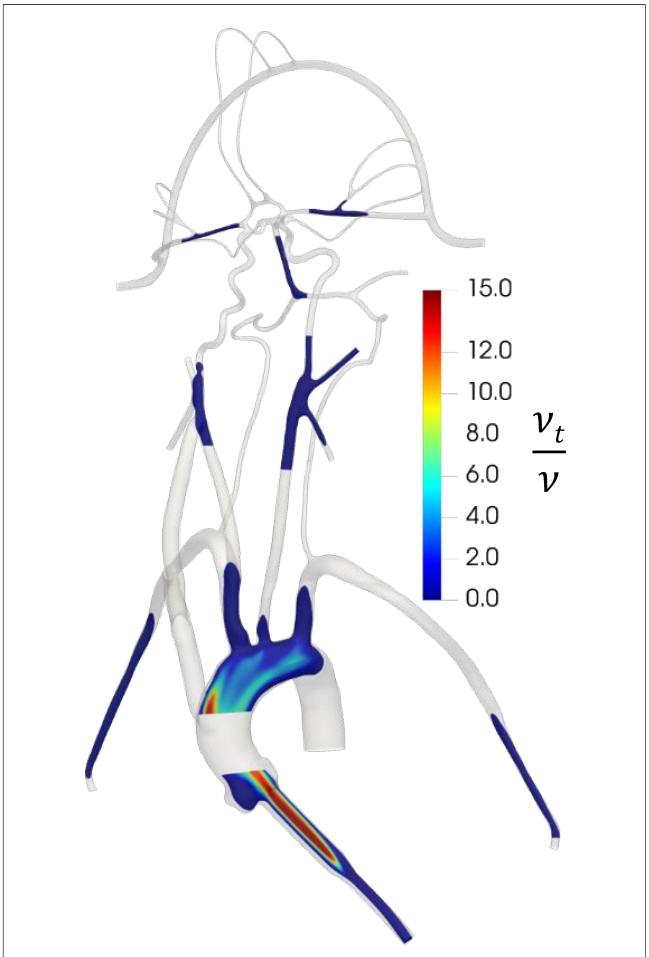

FIGURE 5
Contours of the distribution of the ratio of turbulent viscosity (ν_t) to molecular viscosity (ν) in the CFD model, illustrating regions of predicted turbulent flow where ν_t/ν is large and regions of laminar flow where ν_t/ν is small.

in Figure 5, the $k-\omega$ SST model predicts turbulent flow in the inlet and in the aorta where the flow is expected to be turbulent. In the downstream cerebral arteries, we observe that the predicted flow laminarizes, as evidenced by the negligible turbulent viscosity ratio, indicating that the turbulence model is inactive in this region, yielding laminar flow as expected.

To evaluate the sensitivity of the CFD results to the mesh resolution, we performed a mesh refinement study to compare the results from the coarse, medium, and fine meshes that contain 3 million, 6.5 million, and 9 million computational cells, respectively. For the same inlet flow rate and with the same outlet pressures applied to each model, we compared the predicted volumetric flow rate through each outlet for the normal physiological condition. The percent differences in the volumetric flow rate at outlet 1, outlet 3, outlet 5, outlet 6, and outlet 9 were calculated to be approximately 1%, 2%, 0.3%, 0.4%, and 0.3%, respectively, between the medium and fine meshes. Between the coarse and medium meshes the percent differences for these same outlets were approximately 3%, 9%, 2%, 3%, and 1%, respectively. Thus, the results between the medium and fine meshes are in close agreement and, therefore, we chose the medium mesh for the final simulations of both the normal and stroke conditions.

Figure 6 illustrates pressure contours and velocity profiles in the cerebrovascular model from CFD for the normal condition. As shown, higher pressures are observed in the aorta compared to the cerebral arteries due to the fact that most of the pressure drop occurs in the smaller cerebral arteries. As the aortic root is attached with a smaller diameter inlet tube, there is some unsteadiness and recirculating flow in the downstream ascending aorta. Generally, the highest velocities are observed in the inlet tube. Flow speeds in the aortic arch are also much higher compared to the more distal downstream arteries. Additionally, it is interesting that the simulation revealed that the flow in the left common carotid artery has a higher velocity than that in the right common carotid.

Quantitative values of volumetric flow rate and pressure at all of the outlets from the CFD simulation at the normal condition are summarized in Figure 3B. The flow distribution in the axillary, external, and combined middle and anterior arteries are equal to 9.62%, 6.87%, and 5.68%, respectively. Because outlet boundary conditions were assigned to match the experimental flow rate measurement through each artery outlet to within ±10%, we validate the simulations by comparing the resultant outlet pressures from CFD with the experimental pressure measurements. As summarized in Tables 2, 3, all of the arterial outlet pressures from CFD are close to the experimental values to within ±7%, with many of the CFD outlet pressures within the uncertainty of the experimental measurement.

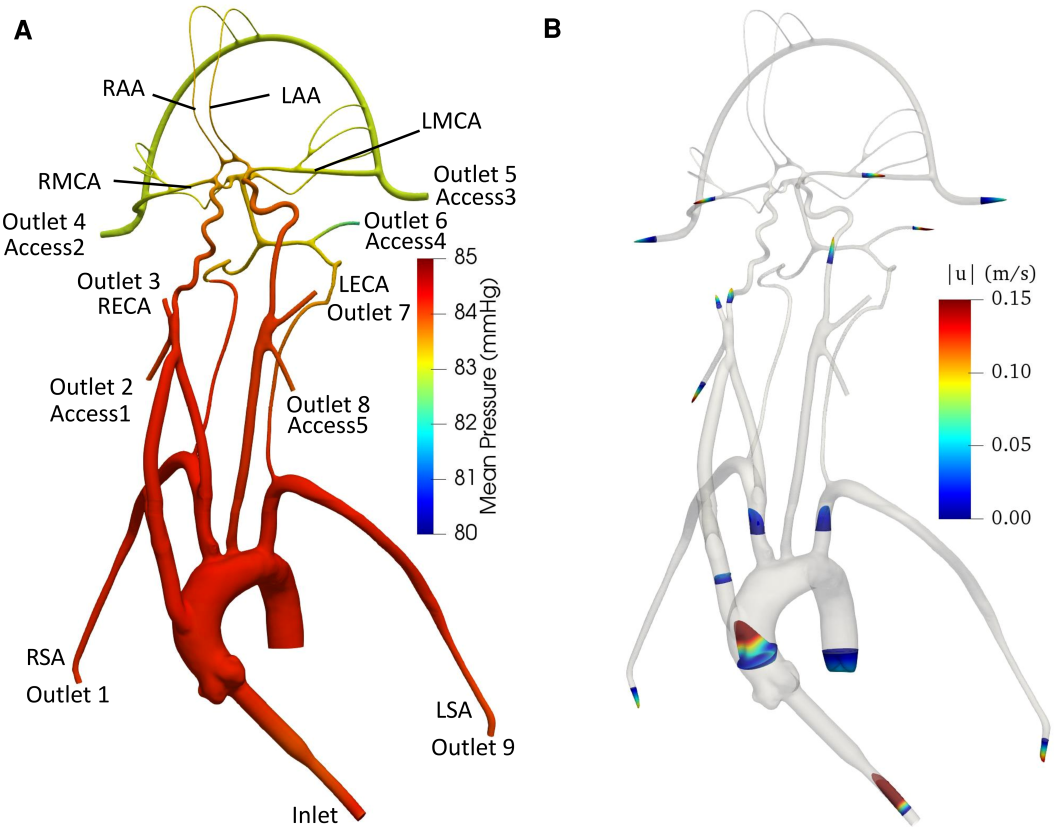

FIGURE 6
(A) Mean pressure contours and (B) profiles of mean velocity at various sections in the anatomical cerebrovascular model from CFD for the normal condition.

TABLE 2 Mean pressure (mmHg) obtained from *in vitro* experiments and CFD at various inlet and outlets for the normal condition. The experimental values are reported as mean ± standard deviation (SD) from three experiments.

Location	*In vitro* pressure (mmHg)	CFD pressure (mmHg)	% Difference
Inlet	84.91 ± 0.90	84.61	−0.35
Outlet 1 (RSA)	83.84 ± 0.67	84.08	0.28
Outlet 2 (Access1)	82.56 ± 0.32	83.94	1.67
Outlet 3 (RECA)	83.93 ± 0.37	84.07	0.17
Outlet 4 (Access2)	82.11 ± 1.5	82.84	0.90
Outlet 5 (Access3)	83.43 ± 1.8	82.88	−0.66
Outlet 6 (Access4)	83.51 ± 1.27	82.19	−1.58
Outlet 7 (LECA)	83.90 ± 1.30	83.88	−0.02
Outlet 8 (Access5)	83.83 ± 0.44	83.82	−0.01
Outlet 9 (LSA)	80.31 ± 1.04	83.95	4.53

TABLE 3 Mean pressure (mmHg) obtained from *in vitro* experiments and CFD at the inlet and outlets for the stroke condition. The experimental values are reported as mean ± standard deviation (SD) from three experiments.

Location	*In vitro* pressure (mmHg)	CFD pressure (mmHg)	% Difference
Inlet	84.25 ± 0.79	84.64	0.46
Outlet 1 (RSA)	83.04 ± 0.85	84.09	1.26
Outlet 2 (Access1)	81.01 ± 0.72	83.84	3.49
Outlet 3 (RECA)	82.02 ± 0.67	84.04	2.46
Outlet 4 (Access2)	–	–	–
Outlet 5 (Access3)	80.04 ± 1.2	83.13	3.86
Outlet 6 (Access4)	78.83 ± 1.7	82.19	4.26
Outlet 7 (LECA)	80.40 ± 1.19	83.96	4.42
Outlet 8 (Access5)	79.55 ± 0.96	83.89	5.45
Outlet 9 (LSA)	78.74 ± 1.56	83.94	6.60

4. Discussion

The objective of this study is to establish a realistic *in vitro* experimental model and a corresponding computational model of the cerebral vasculature that can be used to investigate flow and embolus migration and lodging in the brain. Measurements of pressure and flow rate were acquired and corresponding CFD simulations were performed and compared with the experiments to validate the flow predictions. Overall, the CFD predictions were in relatively close agreement with the experiments, to within ±7% of the mean experimental pressure measurements with many of the CFD predictions within the uncertainty of the experimental measurement.

The *in vitro* model developed in this study represents a realistic anatomical model of the cerebrovasculature and the upstream arteries that produce a realistic flow distribution. The measurements of the flow distribution are in close agreement with the range of clinical values reported in the literature (30, 31). Compared with other *in vitro* cerebrovascular models, the present model consists of the major cerebral vasculature and the aorta. In contrast, previous work (e.g. 10, 36, 37), used models that did not incorporate all of the vasculature that is considered in the present study.

The present CFD simulations closely correspond with the *in vitro* experimental measurements of pressure in the various arterial outlets of the model. Interestingly, as found in previous studies (38, 39), we observed that the regional flow distribution in the cerebrovascular model was highly sensitive to the prescribed outlet pressures. In an exploratory sensitivity study, it was observed that small variations in the prescribed outlet pressures within the range of the uncertainty of the experimental pressure measurements yielded extremely large variations in the regional flow distribution in the model. Also, the flow pattern in the aortic arch in the current investigation generally agrees with that reported in the computational study of Numata et al. (40). The transient flow field found in the aortic arch in the present work has also been reported in other studies (41–44).

Finally, there are several limitations of the present study that should be addressed in future work. First, only flow is measured and simulated in the model; we do not consider embolus migration and lodging, which is a topic of ongoing research. Additionally, steady flow is considered in this study, whereas the physiological flow in the aorta and cerebrovascular is pulsatile in nature. The objective of the current research, however, is to provide a tiered validation data set for systematically validating computational simulations, the first step of which is to validate by comparing with steady flow. Also, the working fluid used in this study is Newtonian. The non-Newtonian rheology of blood is planned to be included in future work. Finally, the CFD simulations in this study assume that the walls of the vascular model are rigid, which is a reasonable assumption for steady flow through the model. Future work investigating pulsatile flow, however, could also consider the influence of vessel wall motion due to fluid-structure interaction and its influence on the flow and migration of emboli.

Data availability statement

The raw data supporting the conclusions of this article will be made available by the authors, without undue reservation.

Ethics statement

Ethical review and approval was not required for this study in accordance with the local legislation and institutional requirements.

Author contributions

SB, BAC, KBM: study design and methodology. SB and BAC: simulations and analysis. SB, BAC, KBM, and JES: validation experiments. SB, BAC, and KBM: writing original draft. SB, BAC, KBM, FC, SDS, JES: revision and editing. All authors contributed to the article and approved the submitted version.

Funding

This work was partially supported by the United States National Institutes of Health (NHLBI) through Grant HL146921.

The NIH did not have any involvement in the study design, in the collection, analysis and interpretation of data; in the writing of the manuscript; and in the decision to submit the manuscript for publication. The findings and conclusions in this article have not been formally disseminated by the United States. FDA and should not be construed to represent any agency determination or policy. The mention of commercial products, their sources, or their use in connection with material reported herein is not to be construed as either an actual or implied endorsement of such products by the Department of Health and Human Services.

Acknowledgments

We thank Kenneth Aycock for reviewing the manuscript.

Conflict of interest

The authors declare that the research was conducted in the absence of any commercial or financial relationships that could be construed as a potential conflict of interest.

Publisher's note

All claims expressed in this article are solely those of the authors and do not necessarily represent those of their affiliated organizations, or those of the publisher, the editors and the reviewers. Any product that may be evaluated in this article, or claim that may be made by its manufacturer, is not guaranteed or endorsed by the publisher.

References

1. Benjamin EJ, Blaha MJ, Chiuve SE, Cushman M, Das SR, Deo R, et al. Heart disease and stroke statistics-2017 update: a report from the American heart association. *Circulation*. (2017) 135(10):e146–603. doi: 10.1161/CIR.0000000000000485

2. Go AS, Mozaffarian D, Roger VL, Benjamin EJ, Berry JD, Blaha MJ, et al. Heart disease and stroke statistics-2014 update: a report from the American heart association. *Circulation*. (2014) 129(3):e28–e292. doi: 10.1161/01.cir.0000441139.02102.80

3. Giller CA, Purdy P, Lindstrom WW. Effects of inhaled stable Xenon on cerebral blood flow velocity. *AJNR: Am J Neuroradio*. (1990) 11:177–82.

4. Gur D, WolfsonJr SK, Yonas H, Good WF, Shabason L, Latchaw RE, et al. Progress in cerebrovascular disease: local cerebral blood flow by Xenon enhanced CT. *Stroke*. (1982) 13:750–8. doi: 10.1161/01.STR.13.6.750

5. Gur D, Yonas H, Jackson DL, Wolfson SK Jr, Rockette H, Good WF, et al. Simultaneous measurement of cerebral blood flow by the Xenon/CT method and the microsphere method. *In Vest Radiol*. (1985) 20:672–7. doi: 10.1097/00004424-198510000-00004

6. Ito M, Lammertsma AA, Wise RJS, Bernardi S, Frackowiak RSJ, Heather JD, et al. Measurement of regional cerebral blood flow and oxygen utilisation in patients with cerebral tumours using ^{15}O and positron emission tomography: analytical techniques and preliminary results. *Neuroradiology*. (1982) 23:63–74. doi: 10.1007/BF00367239

7. Norrving B, Nilsson B, Risberg J. rCBF in patients with carotid occlusion. Resting and hypercapnic flow related to collateral pattern. *Stroke*. (1982) 13:155–62. doi: 10.1161/01.STR.13.2.155

8. Uemura K, Kanno I, Miura Y, Miura S, Tominaga S. Tomographic study of regional cerebral blood flow in ischemic cerebrovascular disease by 81mKr intraarterial infusion and HEADTOME. *J Comput Assist Tomogr*. (1982) 6(4):677–82. doi: 10.1097/00004728-198208000-00003

9. Yonas H, Wolfson SK Jr, Gur D, Latchaw RE, Good WF, Leanza R, et al. Clinical experience with the use of xenon-enhanced CT blood flow mapping in cerebral vascular disease. *Stroke*. (1984) 15:443–50. doi: 10.1161/01.STR.15.3.443

10. Chung EML, Hague JP, Chanrion MA, Ramnarine KV, Katsogridakis E, Evans DH. Embolus trajectory through a physical replica of the major cerebral arteries. *Stroke*. (2010) 41(4):647–52. doi: 10.1161/STROKEAHA.109.574400

11. Carr IA, Nemoto N, Schwartz RS, Shadden SC. Size-dependent predilections of cardiogenic embolic transport. *Am J Physiol Heart Circ Physiol*. (2013) 305(5):H732–739. doi: 10.1152/ajpheart.00320.2013

12. Mukherjee D, Jani ND, Selvaganesan K, Weng CL, Shadden SC. Computational assessment of the relation between embolism source and embolus distribution to the circle of willis for improved understanding of stroke etiology. *J Biomech Eng*. (2016) 138(8):081008 (13 p.). doi: 10.1115/1.4033986

13. Nogles TE, Galuska MA. Middle cerebral artery stroke. In: *Statpearls*. Treasure island (FL): StatPearls Publishing (2022)

14. Rapp JH, Hollenbeck K, Pan XM. An experimental model of lacunar infarction: embolization ofmicrothrombi. *J. Vasc.Surg*. (2008) 48(1):196–200. doi: 10.1016/j.jvs.2008.01.038

15. Pollanen MS. Behaviour of suspended particles at bifurcations: implications for embolism. *Phys Med Biol*. (1991) 36:397–401. doi: 10.1088/0031-9155/36/3/008

16. Bushi D, Grad Y, Einav S, Yodfat O, Nishri B, Tanne D. Hemodynamic evaluation of embolic trajectory in an arterial bifurcation: an in-vitro experimental model. *Stroke*. (2005) 36(12):2696–700. doi: 10.1161/01.STR.0000190097.08862.9a

17. Taylor CA, Figueroa CA. Patient-specific model of cardiovascular mechanics. *Annu Rev Biomed Eng*. (2009) 11:109–34. doi: 10.1146/annurev.bioeng.10.061807.160521

18. Cebral JR, Castro MA, Burgess JE, Pergolizzi RS, Sheridan MJ, Putman CM. Characterization of cerebral aneurysms for assessing risk of rupture by using patient-specific computational hemodynamics models. *AJNR Am J Neuroradiol*. (2005) 26(10):2550–9.

19. Gijsen FJ, Wentzel JJ, Thury A, Mastik F, Schaar JA, Schuurbiers JC, et al. Strain distribution over plaques in human coronary arteries relates to shear stress. *Am J Physiol Heart Circ Physiol*. (2008) 295(4):H1608–1614. doi: 10.1152/ajpheart.01081.2007

20. Berry JL, Santamarina A, Moore JE Jr, Roychowdhury S, Routh WD. Experimental and computational flow evaluation of coronary stents. *Ann Biomed Eng*. (2000) 28(4):386–98. doi: 10.1114/1.276

21. Li Z, Kleinstreuer C. Blood flow and structure interactions in a stented abdominal aortic aneurysm model. *Med Eng Phys*. (2005) 27(5):369–82. doi: 10.1016/j.medengphy.2004.12.003

22. Migliavacca F, Balossino R, Pennati G, Dubini G, Hsia TY, de Leval MR, et al. Multiscale modelling in biofluidynamics: application to reconstructive paediatric cardiac surgery. *J Biomech*. (2006) 39(6):1010–20. doi: 10.1016/j.jbiomech.2005.02.021

23. Taylor CA, Draney MT, Ku JP, Parker D, Steele BN, Wang K, et al. Predictive medicine: computational techniques in therapeutic decision-making. *Comput Aided Surg*. (1999) 4(5):231–47. doi: 10.3109/10929089909148176

24. Malinauskas RA, Hariharan P, Day SW, Herbertson LH, Buesen M, Steinseifer U, et al. FDA Benchmark medical device flow models for CFD validation. *ASAIO Journal*. (2017) 63(2):150–60. doi: 10.1097/MAT.0000000000000499

25. Craven BA, Aycock KI, Manning KB. Steady flow in a patient-averaged Inferior vena Cava— part II: computational fluid dynamics verification and validation. *Cardiovasc Eng Tech*. (2018) 9:654–73. doi: 10.1007/s13239-018-00392-0

26. Riley JM, Price NS, Saaid HM, Good BC, Aycock KI, Craven BA, et al. In vitro clot trapping efficiency of the FDA generic Inferior vena Cava filter in an anatomical model: an experimental fluid-structure interaction benchmark. *Cardiovasc Eng Technol*. (2021) 12(3):339–52. doi: 10.1007/s13239-021-00524-z

27. Hariharan P, Aycock KI, Buesen M, Day SW, Good BC, Herbertson LH, et al. Inter-laboratory characterization of the velocity field in the FDA blood pump model using particle image velocimetry (PIV). *Cardiovasc Eng Technol*. (2018) 9:623–40. doi: 10.1007/s13239-018-00378-y

28. Aycock KI, Hariharan P, Craven BA. Particle image velocimetry measurements in an anatomical vascular model fabricated using inkjet 3D printing. *Exp Fluids*. (2017) 58:154. doi: 10.1007/s00348-017-2403-1

29. Gallagher MB, Aycock KI, Craven BA, Manning KB. Steady flow in a patient-averaged inferior vena cava—part I: particle image velocimetry measurements at rest and exercise conditions. *Cardiovasc Eng Technol*. (2018) 9:641–53. doi: 10.1007/s13239-018-00390-2

30. Lantz BMT, Foerster JM, Link DP, Holcroft JW. Regional distribution of cardiac output: normal values in man determined by video dilution technique. *AJR Am J Roentgenol*. (1981) 137(5):903–7. doi: 10.2214/ajr.137.5.903

31. Hunter G, Palmaz JC, Carson SN, Lantz BMT. Surgically induced carotid subclavian steal syndrome. Diagnosis by video dilution technique. *Arch Surg*. (1983) 118(11):1325–9. doi: 10.1001/archsurg.1983.01390110071015

32. Menter F, Kuntz M, Langtry R. Ten years of industrial experience with the SST turbulence model. Turbulence. *Heat and Mass Transfer*. (2003) 4:625–32.

33. Menter FR. Two-Equation eddy-viscosity turbulence models for engineering applications. *AIAA Journal*. (1994) 32:1598–605. doi: 10.2514/3.12149

34. Zhang Z, Kleinstreuer C. Low-Reynolds-Number turbulent flows in locally constricted conduits: a comparison study. *AIAA Journal*. (2003) 41(5):831–40. doi: 10.2514/2.2044

35. Mantegazza A, Tobin N, Manning KB, Craven BA. Examining the universality of the hemolysis power law model from simulations of the FDA nozzle using calibrated model coefficients. *Biomech Model Mechanobiol*. (2022. doi: 10.1007/s10237-022-01655-5

36. Bouillot P, Brina O, Chnafa C, Cancelliere NM, Vargas MI, Radovanovic I, et al. Robust cerebrovascular blood velocity and flow rate estimation from 4D-CTA. *Med Phys*. (2019) 46(5):2126–36. doi: 10.1002/mp.13454

37. Yu H, Huang GP, Ludwig BR, Yang Z. An in-vitro flow study using an artificial circle of willis model for validation of an existing one-dimensional numerical model. *Ann Biomed Eng*. (2019) 47(4):1023–37. doi: 10.1007/s10439-019-02211-6

38. Kempley ST, Gamsu HR. Arterial blood pressure and blood flow velocity in major cerebral and visceral arteries. I. Interindividual Differences. *Early Hum Dev*. (1993) 34(3):227–32. doi: 10.1016/0378-3782(93)90180-3

39. Brindle RC, Ginty AT, Whittaker AC, Carroll D, Lucas SJE. Assessment of the cerebral pressure- flow relationship using psychological stress to manipulate blood pressure. *Psychophysiology*. (2018) 55(12):e13265. doi: 10.1111/psyp.13265

40. Numata S, Itatani K, Kanda K, Doi K, Yamazaki S, Morimoto K. Blood flow analysis of the aortic arch using computational fluid dynamics. *Eur J Cardio-Thorac Surg*. (2016) 49(6):ezv459. doi: 10.1093/ejcts/ezv459

41. Cheng Z, Juli C, Wood NB, Gibbs RG, Xu XY. Predicting flow in aortic dissection: comparison of computational model with PC-MRI velocity measurements. *Med Eng Phys*. (2014) 36(9):1176–84. doi: 10.1016/j.medengphy.2014.07.006

42. Miyazaki S, Itatani K, Furusawa T, Nishino T, Sugiyama M, Takehara Y, et al. Validation of numerical simulation methods in aortic arch using 4D flow MRI. *Heart Vessels*. (2017) 32(8):1032–44. doi: 10.1007/s00380-017-0979-2

43. Vinoth R, Kumar D, Adhikari A, Vijayapradeep S, Geetha K, Ilavarasi R. Steady and transient flow CFD simulations in an aorta model of normal and aortic aneurysm subjects. *The Proceedings of the Int Conf on Sensing and Imaging*. (2017) 506:29–43. doi: 10.1007/978-3-319-91659-0_3

44. Eslami P, Seo JH, Lardo AC, Chen MY, Mittal R. Flow dynamics in the aortic arch and its effect on the arterial input function in cardiac computed tomography. *J Biomech Eng*. (2019) 141(10):1045011–018. doi: 10.1115/1.4043076

frontiers | Frontiers in Medical Technology

TYPE Original Research
PUBLISHED 23 February 2023
DOI 10.3389/fmedt.2023.1096289

OPEN ACCESS

EDITED BY
Selene Pirola,
Delft University of Technology, Netherlands

REVIEWED BY
Nitesh Bhatia,
Imperial College London, United Kingdom
Catriona Stokes,
University College London, United Kingdom
Marc Horner,
Ansys, United States

*CORRESPONDENCE
John F. LaDisa
jladisa@mcw.edu

SPECIALTY SECTION
This article was submitted to Cardiovascular Medtech, a section of the journal Frontiers in Medical Technology

RECEIVED 11 November 2022
ACCEPTED 26 January 2023
PUBLISHED 23 February 2023

CITATION
Venn J, Larkee CE, Garcia GJM, Rayz VL and LaDisa JF Jr (2023) A workflow for viewing biomedical computational fluid dynamics results and corresponding data within virtual and augmented reality environments.
Front. Med. Technol. 5:1096289.
doi: 10.3389/fmedt.2023.1096289

A workflow for viewing biomedical computational fluid dynamics results and corresponding data within virtual and augmented reality environments

John Venn[1], Christopher E. Larkee[2], Guilherme J. M. Garcia[1], Vitaliy L. Rayz[1,3] and John F. LaDisa Jr[1,4]*

[1]Department of Biomedical Engineering, Marquette University and Medical College of Wisconsin, Milwaukee, WI, United States, [2]Opus College of Engineering, Marquette University, Milwaukee, WI, United States, [3]Weldon School of Biomedical Engineering, Purdue University, West Lafayette, IN, United States, [4]Department of Pediatrics - Division of Cardiology, Herma Heart Institute, Children's Wisconsin and the Medical College of Wisconsin, Milwaukee, WI, United States

Researchers conducting computational fluid dynamics (CFD) modeling can spend weeks obtaining imaging data, determining boundary conditions, running simulations and post-processing files. However, results are typically viewed on a 2D display and often at one point in time thus reducing the dynamic and inherently three-dimensional data to a static image. Results from different pathologic states or cases are rarely compared in real-time, and supplementary data are seldom included. Therefore, only a fraction of CFD results are typically studied in detail, and associations between mechanical stimuli and biological response may be overlooked. Virtual and augmented reality facilitate stereoscopic viewing that may foster extraction of more information from CFD results by taking advantage of improved depth cues, as well as custom content development and interactivity, all within an immersive approach. Our objective was to develop a straightforward, semi-automated workflow for enhanced viewing of CFD results and associated data in an immersive virtual environment (IVE). The workflow supports common CFD software and has been successfully completed by novice users in about an hour, demonstrating its ease of use. Moreover, its utility is demonstrated across clinical research areas and IVE platforms spanning a range of cost and development considerations. We are optimistic that this advancement, which decreases and simplifies the steps to facilitate more widespread use of immersive CFD viewing, will foster more efficient collaboration between engineers and clinicians. Initial clinical feedback is presented, and instructional videos, manuals, templates and sample data are provided online to facilitate adoption by the community.

KEYWORDS

simulation - computers, Extended reality (XR), hemodynamics, fluid structure interaction and CFD, patient-specific 3D model

1. Introduction

Predicting the impact of fluid flow in biomedical applications is time consuming and mathematically complex without computational tools. Computational fluid dynamics (CFD) is a method of simulating fluid passing through or around an object, in the case of arteries and vessels for the current applications, by replacing partial differential equations governing the flow with algebraic equations that can be solved numerically using digital computers. Biomedical CFD therefore yields spatial and temporal patterns of fluid flow that are difficult

to measure experimentally, costly to obtain routinely, and potentially intractable due to non-existent clinical methods or the emergent state of a given pathologic situation (1, 2).

CFD researchers with a biomedical focus can spend weeks or months creating realistic geometric models, determining appropriate boundary conditions, running numerical simulations, and post-processing results (3). The results are typically viewed on a 2D display at one point in time, or by slowly progressing through sequential time steps without the aid of supplementary data. Issues with this traditional approach are that only a fraction of the available CFD results are being studied in detail, and potentially inefficiently. For example, a common approach in one co-authors lab is to run simulations for 3–8 cardiac cycles with ~2,500 to >25,000 time steps per cycle (4), depending on CFL number. Historically, such simulations have taken days to months of physical time to complete. Results that are generated include scalar and vector quantities mentioned below that are then used to calculate additional indices believed to be of clinical and/or biological importance (e.g., wall shear stress) at each element for vessel geometries discretized into tetrahedral meshes of up to 8 million elements (5). Rather than viewing results at each time step and element location, 50 time-steps have traditionally been extracted from simulation results for corresponding videos (~50 frames-per-second). Results were also traditionally used to construct temporal waveforms at inlet or outlet services, and indices of interest were viewed side-by-side at specific time points (3). Another large limitation with traditional approaches to CFD is that resulting associations from related data can go unnoticed since they are not often viewed in concert with other available data. This is an important point because biomedical CFD simulations are often conducted to better appreciate the relationship between mechanical stimuli and biological response, which can be complex and challenging to visualize without access to complementary information easily viewed in the local proximity of a vessel. Immersive visualization through tools like virtual reality (VR) and augmented reality (AR) can, in theory, alleviate many of these issues by taking advantage of improved depth cues, custom interactivity and development to simultaneously view many sources of related data using an immersive approach that can create a sense of presence within the data for a CFD researcher (6).

The first known attempt to view biomedical CFD results immersively was documented in 2000 when a coronary artery graft was viewed in an IVE to better uncover approaches aimed at reducing failure rates (7). Feedback was mostly positive, but it was noted that "significant time" was put toward reformatting the simulation results before they could be viewed immersively. A common issue presenting when preparing CFD results for immersive viewing is that there is a paucity of approaches that store 3D geometry and vertex magnitude in a format that is natively compatible with related software. A 2010 study aided the process of viewing CFD results in a IVE by developing a semi-automatic workflow that used MATLAB (The MathWorks; Natick, MA) as an intermediary tool to convert select CFD results into files that were compatible with a specific software platform used within an IVE (6). The workflow imitated pulsatile flow in arteries by using time-varying velocity vectors. Velocity vectors for each time step had the same coordinates, but their colors and lengths changed depending on the speed at each location for a particular time step. Blood flow within the featured arteries therefore appeared as though it was pulsating when time steps were displayed rapidly in succession. The tools developed for this application lacked accessibility given the software used to display the results in VR were specific to the IVE within the facility where it was used. Consequently, more advanced functionality was difficult to test and implement. More specifically, preparation of the CFD results featured in the IVE was conducted on in-house computer software packages and using scripts where only the individuals who built the models, ran the simulations, and prepared the visualizations could advance resulting data to the point of use within the specified IVE. In 2015, a study outside of biomedical research viewed CFD results for urban planning using Unity (Unity Technologies; San Francisco, CA) (8). Unity is a multipurpose game engine that is compatible with many immersive systems from head mounted displays (HMD) to large-scale IVEs. Using an approachable and well-documented toolset like Unity may allow more users and labs to create and view their simulation results immersively, potentially alleviating many of the limitations experienced previously with CFD results visualization.

The objective of the current work was to develop a rapid, easy to use, semi-automatic workflow that combines biomedical CFD results and subsequent supplementary data for immersive viewing and use as a collaborative tool between engineers and clinicians by more easily and rapidly being able to view all available data. The presentation below is similar to prior work advancing methods for CFD related to boundary condition developments (9, 10) in that the utility of the method is presented first in a simple example, and then extended to several specific applications. Application of the workflow is demonstrated across clinical research areas including: the aorta with application to congenital cardiovascular disease, the Circle of Willis with respect to cerebral aneurysms, and the nasal airway for surgical treatment planning. The resulting workflow also aimed to permit viewing across platforms spanning a range of cost and development considerations including a large-scale CAVE-type (CAVE Automatic Virtual Environment) (11, 12) (~$1.5 million clustered approach), stereoscopic projector (~$5,000 single processor approach) and HMD (~$500 mobile approach).

2. Materials and methods

The methods below describe steps in the workflow for use with hardware capable of generating and interacting with objects within a virtual environment. All data featured were obtained following Institutional Animal Care and Use Committee (IACUC) approval from the Medical College of Wisconsin and Marquette University (Application 1), and Institutional Review Board (IRB) approval from the University of California San Francisco (Application 2) or the Medical College of Wisconsin (Application 3).

2.1. Platforms for immersive viewing

Viewing CFD results immersively requires access to specific hardware. Common types of devices used in the current work

included several HMD, a large-scale IVE, and standalone stereoscopic projectors. A HMD includes equipment that is worn by a user to display content directly in front of the eyes. The first HMD was developed in 1968 and subsequent upgrades continued over the next five decades. However, in many cases the devices either lacked functionality, quality and or were too costly (13). Beginning in the 2010's, companies like Samsung and Oculus (now Meta Quest) helped revitalize interest in immersive visualization and VR with HMD product lines that were less expensive, more accessible and provided a higher quality that had been possible previously. All data analysis is precomputed for the current workflow, which enables the visualization to run on low end HMDs such as the Gear VR or Oculus Go, as well as the Oculus Rift on moderately powerful desktop PCs.

Large-scale IVEs can offer advantages over HMDs. For example, large-scale IVEs often facilitate simultaneous experiences with other end users. Large-scale IVEs range in shape and size, each designed for unique purposes (14). Examples include projection-based cylindrical or dome structures, 4–6 walled CAVE-type systems and panel-based system with narrow bezels (15). Wearing system-specific glasses within such IVEs allows for stereoscopic viewing of content. One example is the MARquette Visualization Laboratory (MARVL) within the Opus College of Engineering at Marquette University (16). MARVL is a $1.2 million, 1,700 ft^2 facility with hardware and software that aims to create a sense of presence within content through stereoscopic viewing for improved depth cues, surround sound, and motion tracking. MARVL has space for over 30 people to view content that has been filmed, reconstructed or created computationally.

Standalone stereoscopic projectors can also serve as virtual environments. This hardware offers a less expensive alternative to large-scale IVEs, while still offering stereoscopic and collaborative viewing (17). Depending on the installation, standalone stereoscopic projectors may not generate as large of a projection as multi-display systems so a user looking directly at the screen from some distance may naturally conclude they are in the real world (18) based on cues noted in his or her peripheral vision.

2.2. Workflow requirements

The workflow described here to display and interact with CFD simulation results within immersive environments has five steps (Figure 1): (1) format, (2) convert, (3) reorganize, (4) customize, and (5) arrange. The workflow is compatible with a variety of CFD software packages and uses open source packages once the CFD results are obtained. For a standard multi-time step CFD simulation resulting in scalars such as pressure, time-average wall shear stress (TAWSS), oscillatory shear index (OSI) as well as animated vector information in the form of streamlines or glyphs (i.e., 3D arrows originating from data points that are colored based on scalar values), the workflow is almost fully automated with the user only needing to complete small tasks and run scripts for each step.

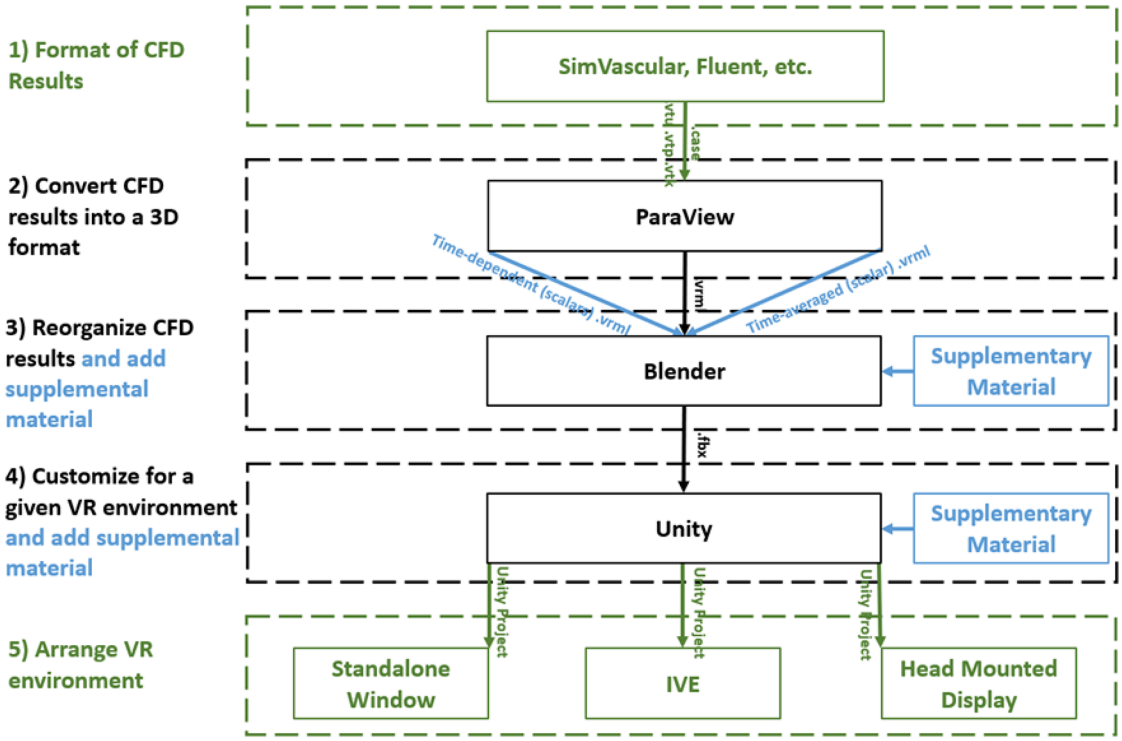

FIGURE 1
Diagram of the immersive visualization workflow after a CFD simulation is complete. CFD results in a (1) format of the simulation software are (2) converted into .vrml files (type of 3D geometry) before being (3) reorganized in Blender where supplementary material can be added. Simulation results and supplementary material are (4) customized within Unity for the given application and then (5) arranged for a given immersive virtual environment. black = necessary steps, blue = optional steps, green = user selects one of the options.

Requirements for the workflow presented above were determined based on the simulation and visualization needs of investigators within the Department of Biomedical Engineering at Marquette University/Medical College of Wisconsin and collaborating clinical divisions, while keeping potential derivative projects in mind. Based on programs and input from associated researchers, the workflow was designed to facilitate viewing of CFD results using a diverse set of hardware including HMDs, IVEs and standalone stereoscopic projectors. For automation purposes, the main Unity template used in part 5 of the workflow is geared to work on systems using the Oculus software development kit (SDK). SDK are libraries of code and examples that help aid the developers in building an application for a specific HMD or IVE. For this workflow, modest alterations can be made to the template to address variances in a platform's SDK if a particular CFD simulation is to be viewed using an IVE or other type of HMD such as the Microsoft HoloLens. To date, the workflow has been successfully tested on VR-based HMD's (e.g., Samsung Gear VR and Oculus Rift), the AR-based Microsoft HoloLens, as well as a large-scale IVE and standalone stereoscopic projector within MARVL.

2.3. Format of CFD results

The workflow was designed to accommodate common CFD software packages such as the commercial software Fluent (ANSYS Inc; Canonsburg, PA) and open source software SimVascular (simtk.org). These software packages yield results that can be saved in formats such as .vtk, .vtu, .vtm or .cas files. Given the potential interchangeability and capability of geometry, mesh and simulation results files, it is possible the workflow could also work for other software packages that can be saved, or converted into, one of these formats. The aforementioned files facilitate viewing CFD results on a 2D display but are not natively compatible with IVEs. The steps within the workflow are designed to use supporting software packages that are common within academic, engineering and digital design facilities. **Table 1** lists the supporting packages that are required by the workflow, along with the function being performed by each package.

As an initial test case, we present methods associated with the workflow based on a CFD simulation run using a cylinder phantom. These data are from a microfocal x-ray CT scan of PE-240 tubing as discussed in detail elsewhere (19). For the current work, the imaging data was segmented, lofted into a 3D model, meshed, and an associated simulation was run using SimVascular. The pulsatile inflow waveform used for the simulation was from prior literature of a similarly sized vessel (20). The walls were considered rigid and a 3-element-Windkessel model was applied to the outlet thereby allowing pressure within the cylinder to range between the normal diastolic and systolic values of 80 and 120 mmHg typically measured in a healthy adult. Simulation results were output as a series of 20 .vtu files. The following figures in the methods section were generated from these results for the initial test case.

TABLE 1 Programs used in the current workflow and their function in immersively viewing CFD results.

	Function
ParaView	Convert CFD results into a 3D format compatible with immersive visualization
Blender	Reorganize 3D format files and add supplementary data
Unity	Animation, custom interaction, add supplementary data and application used to view CFD results immersively

2.4. Convert CFD results into a 3D format

The majority of CFD simulations display flow patterns over some duration of physical time that often represents one cycle of the event being studied (e.g., one heartbeat or one breathing cycle). Velocity results are commonly shown using streamlines or glyphs. To view the streamlines or glyphs in an immersive environment, the CFD results need to be converted into a form that stores 3D geometry, vertex magnitude, and is compatible with the selected 3D gaming engine. The number of glyphs or streamlines to be implemented is a balance between end user preference of aesthetics and ensuring the visualization is not so complex that it is no longer performant enough for the associated hardware. Some guidance on specific details implemented previously can be found elsewhere (6). For the workflow's purpose, streamlines and glyphs for each time step are converted into .vrml files using ParaView version 5.4.2 (Kitware, Inc; Clifton Park, NY). ParaView is an open source software package for scientific and interactive visualization. It was chosen for its ease of use in monoscopically visualizing CFD results before their conversion and because it also has excellent utility as a file conversion tool. ParaView does support stereoscopic viewing, but with several limitations. For example, it may require a special build on some IVE's (16), and may not be available natively with some HMDs to date. Moreover, there is often a lag when viewing consecutive time steps and the viewer is unable to easily view supplementary data sources. The current workflow uses a custom Python script, within ParaView (version 5.4.2), to save each time step as a .vrml file.

2.5. Reorganize CFD results

Blender, (Blender Foundation; Amsterdam, Netherlands) is an open-source graphics program used to rectify the import and export formats between ParaView and Unity. ParaView's exportable 3D formats are .x3d or .vrml. In contrast, Unity's suitable importable 3D formats are .fbx, dao, .3ds, .dxf, .obj and .skp. For the current workflow, Blender takes .vrml files exported from ParaView and ultimately exports the entire CFD simulation as a .fbx file for import into Unity. Within Blender all model objects are set to have a consistent scale and default orientation, and their origin is established in a sensible position near an object's center of gravity. All the objects and vertex colors ultimately used during an animation for immersive viewing are created in one Blender project (**Figure 2**).

When preparing CFD simulations that have multiple time steps, it is important for the workflow that each time step is uploaded in the

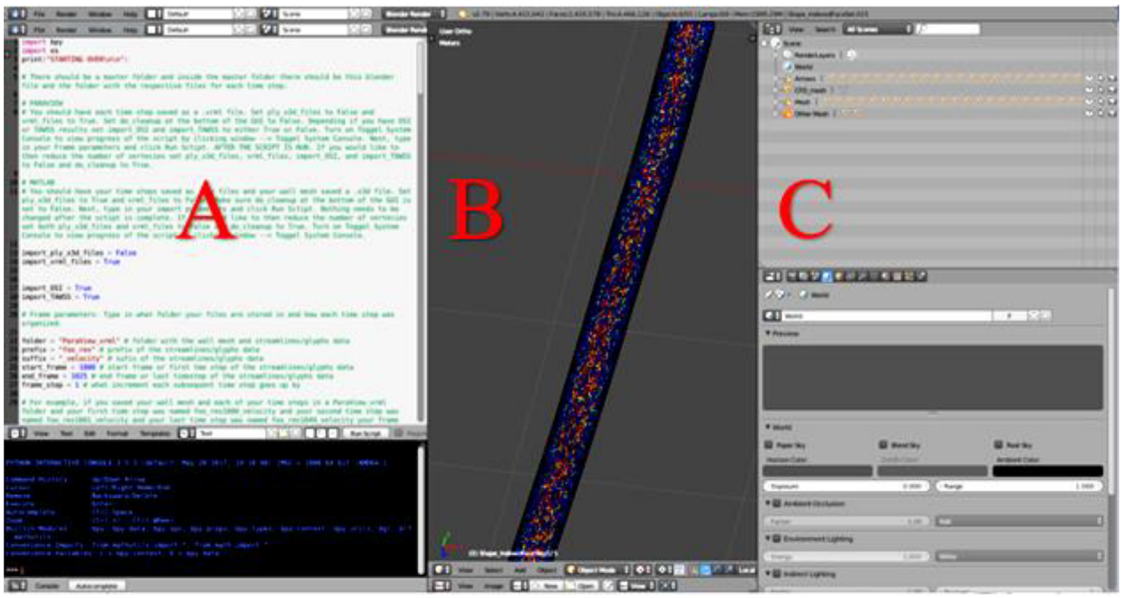

FIGURE 2
Screenshot of Blender's interface depicting CFD simulation details from a cylinder phantom. (A) Blender's Text Editor where a Python script is used to reorganize the simulation details and reduce the number of vertices. (B) Blender's 3D View which displays every object of the simulation. Objects will be turned on or off within Unity as part of a later step, and (C) Blender's Outliner of parent-child relationships where each object may be edited.

correct 3D space. To ensure proper object positioning, a Python script was written for implementation in Blender's text editor. The script re-creates the original CFD simulation, sequencing the 3D-geometry-time-steps inside the wall mesh and creates proper parent-child relationships that are necessary when the Blender project is loaded into Unity. At the top of the Python script, shown in Figure 2A, is a set of instructions. In addition to re-creating and organizing the simulation, the Python script also creates a wire-frame wall-mesh game object, UV maps the wall mesh (technique used to wrap a 2D texture on a 3D model), and deletes unnecessary cameras and lamps that are rooted in the .vrml files.

It is common for a CFD model's mesh to have duplicate structures (i.e., a double-sided mesh). When viewing CFD results immersively, an excessive number of vertices can slow down the frame rate of the Unity project, which can contribute to simulator sickness (21, 22) [i.e., motion sickness thought to result when sensory cues receive conflicting inputs from visual vs. vestibular systems (23, 24)]. If the wall mesh is visible in the 3D view without glyphs or streamlines, this indicates a secondary script in the workflow should be run to remove duplicate structures and consequently reduce the number of vertices. The secondary script may also be run regardless of whether the wall mesh is double-sided if the user would like to reduce the number of vertices. Lastly, the Blender file is exported as an .fbx file and loaded into Unity.

The ability to add related supplementary data sources to the viewing of CFD simulation results is one of the main reasons why our CFD researchers and collaborators created the current workflow for immersive visualization. Importantly, supplementary data such as medical imaging can provide valuable information on surrounding structures and tissues, thus combining anatomical and functional results for comprehensive analysis. Depending on the type of data the user wishes to display as supplementary material, it can be added in either the Blender project or Unity template. For example, in the current workflow and template, volumetric imaging data (i.e., CT, MRI) used to create a CFD model and consisting of a stack of slices are imported in Blender while a flow waveform created in a program such as Excel (Microsoft; Redmond, Washington) is added later in Unity.

2.6. Customize for the application

The Unity game engine is used in the workflow for its speed, flexibility and ability to integrate data from multiple sources. The combination of Blender and Unity have become the basis for all projects conducted in MARVL to date (16). After the models are prepared in Blender, it is a straightforward procedure to import them into Unity. An environment is created to house models, the models are positioned in the scene, lighting is established, and supplementary features or data are added as needed for a particular application.

For the current workflow, a pre-programed automated Unity template was created for viewing of CFD results immersively using a standalone stereoscopic projector (e.g., Gear VR or Oculus Rift). If the user prefers to view their content using a different HMD or a large-scale IVE, changes to the Unity scene, scripts, and/or custom packages are required. As seen in Table 2, the prefabricated automated Unity template has minimum and optional outputs with additional functionality. The Unity template, *via* automated code, animates the streamlines/glyphs, animates/changes the wall mesh texture for scalar quantities (i.e., pressure, TAWSS, OSI), and toggles through volumetric imaging data. The

TABLE 2 Minimum and optional output, along with additional functionality, of the unity template. Italicized text indicates the user must manually alter the data into the unity prefabricated template.

Minimum Output	Optional Output	Additional Functionality
Animated streamlines or glyphs with *legends*	Toggle between surface (i.e. wall) scalars including pressure, TAWSS, and OSI	*View complementary data such as medical imaging data, data patient, and local structural (e.g. histology) or functional (i.e. myography)*
Fly throughout simulation results	*Animate inlet boundary condition waveform*	*Toggle view between multiple cases or instances (e.g. pre/post treatment)*
Transparent map of current location within the immersive space	Toggle through volumetric imaging data	*Fly down set track*

template also includes a basic environmental audio system containing prerecorded ultrasound samples from several locations within the blood flow domain over a cardiac cycle that have been synchronized to the expected animation. Importing and animating a flow waveform and assigning proper scales (e.g., ranges and units) to the legends for indices being visualized are not automated. However, the approach is straightforward and can be accomplished quickly while not requiring alteration to any code. If the user does not have a full set of supplementary data, the Unity template still works. The initial script to set up the CFD visualization, called an editor script, recognizes how little or how much information is rooted in the .fbx file created in Blender.

Three tasks are required to complete the automation portion of the Unity template: (1) import the .fbx file created in Blender, (2) scale, rotate, and reposition the simulation assets to a convenient location, and (3) run the pre-written editor script that recognizes the type of information in the .fbx file. This script then tags and assigns game objects. Once a user manually sets up data such as the flow waveform and legends for each index, the Unity scene should appear similar to Figure 3 (top), which displays assets consistent with the maximum output listed in Table 2. Figure 3 (bottom) is a screenshot of the Unity scene when data in Figure 3 (top) is in "Play mode".

2.7. Arrange for a given IVE

When in the virtual environment, interaction is achieved *via* selected buttons included in the Unity scene. For example, if the user includes the optional output and function for the Unity template (Table 2), the clickable buttons and scales are displayed as in Figure 3B. In the absence of volumetric imaging data within the .fbx file, for example, the imaging up and down arrow buttons would not appear in the Unity scene after the editor script was run.

Different HMDs use their corresponding interaction devices to foster movement and selection (Figure 4). For the Gear VR and Oculus Rift, the trackable controller is viewed as an orange wand virtually in the visualization. When the user positions the wand over one of the buttons, it turns yellow to indicate an ability to be selected. When the user selects the button, the corresponding action is applied to the simulation. The current workflow has designated the gaming pad to conduct movement for the Gear VR, while the Oculus Rift uses the right analog stick for movement. Steering is achieved by the user's head rotation for both the Gear VR and Oculus Rift. For interaction, movement and steering within MARVL's large-scale IVE, the Unity template was altered to use the FlyStick2 wireless interaction device (Advanced Realtime Tracking; Weilheim, Germany). The current template uses standard mouse and keyboard controls when viewing CFD results using a standalone stereoscopic projector.

3. Results

The workflow discussed above was tested with three different clinical case studies from CFD researchers at our institution who had an interest in expanding viewing of CFD results in immersive environments with complementary data. The case studies aim to demonstrate its potential utility of the workflow across clinical research areas and using virtual environments spanning a range of cost and development considerations (Table 3). As discussed in more detail below, these include hemodynamics imparted on the thoracic aorta with respect to a congenital cardiovascular disease, cerebral vasculature with application to aneurysm progression, and nasal airflow with application to virtual surgery planning. All data featured in the current work was accessed following applicable Institutional Animal Care and Use Committee or Institutional Review Board approvals.

The thoracic aorta simulation featured here leverages data, methods and results discussed in detail elsewhere (25, 26, 27, 28). Briefly, the simulation focuses on coarctation of the aorta (CoA), one of the most common congenital cardiovascular defects (29). It most often presents as a narrowing just downstream of the left subclavian artery. CoA is associated with decreased life expectancy, and hypertension presents in most patients despite treatment (30). Mechanically induced structural and functional vascular changes are implicated in CoA, but the mechanisms by which stimuli lead to vascular changes such as altered smooth muscle phenotypic expression and endothelial dysfunction ultimately resulting in hypertension are not fully understood. Using a clinically representative rabbit model of the untreated (i.e., CoA) and treated (i.e., Corrected) conditions as compared to Controls, simulation results provide detailed mechanical stimuli and vascular alterations from a 20 mmHg blood pressure (BP) gradient, which is the current putative treatment threshold implemented clinically. Available data specifically includes blood flow velocity, pressure, TAWSS, OSI, magnetic resonance angiography (MRA), and blood flow waveforms from associated CFD simulations. The impact of mechanical stimuli on the expression of key proteins impacting vascular remodeling, relaxation, and stiffness is also available for locations above and below the coarctation in each group. This includes Verhoeff-Van Gieson (VVG) and immunohistochemical (IHC) images, as well as

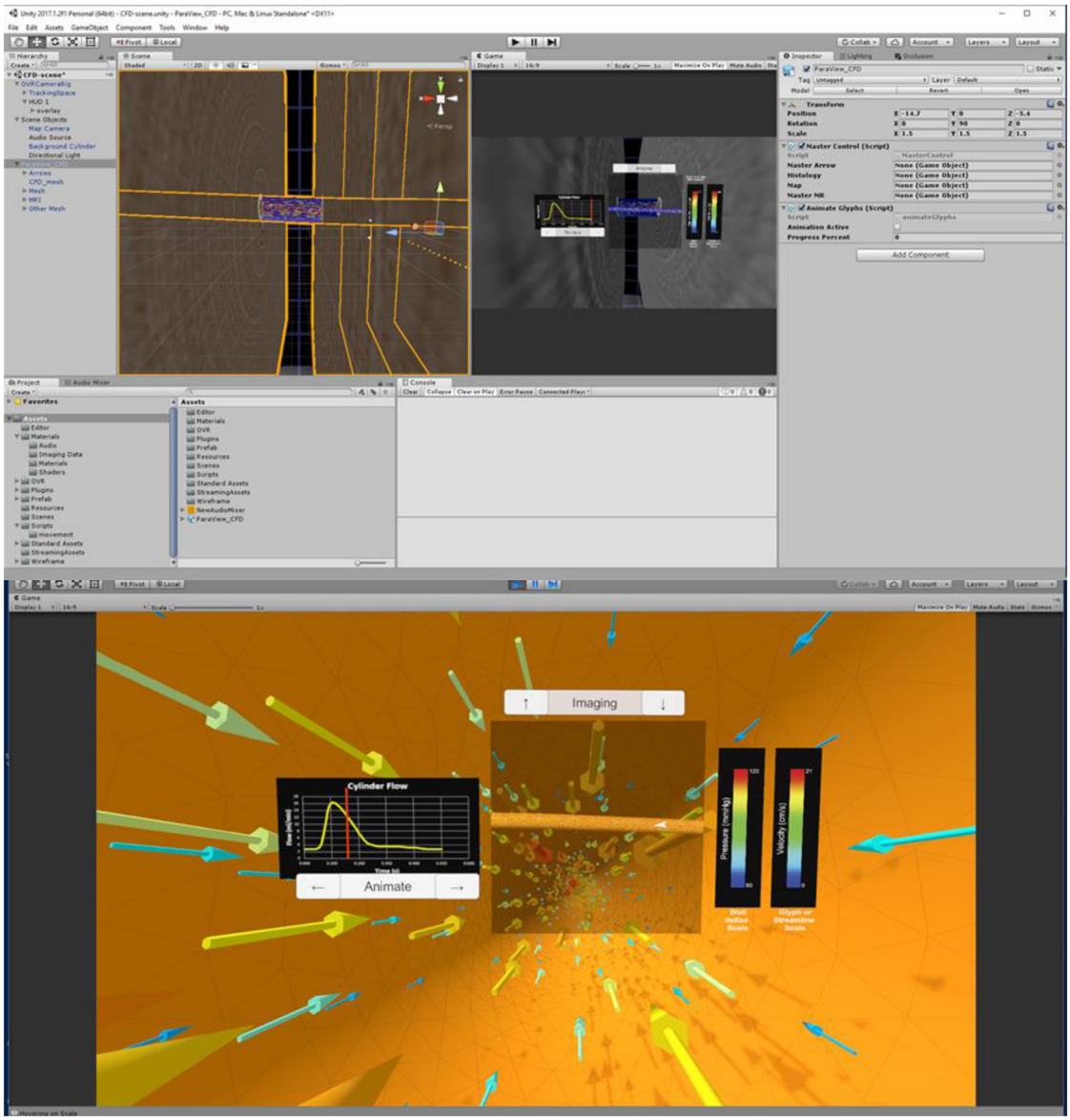

FIGURE 3
Screenshots of Unity's interface upon completing the steps described for the cylinder CFD simulation. "Play mode" is shown in the top panel with a standalone stereoscopic projector output shown in the bottom panel.

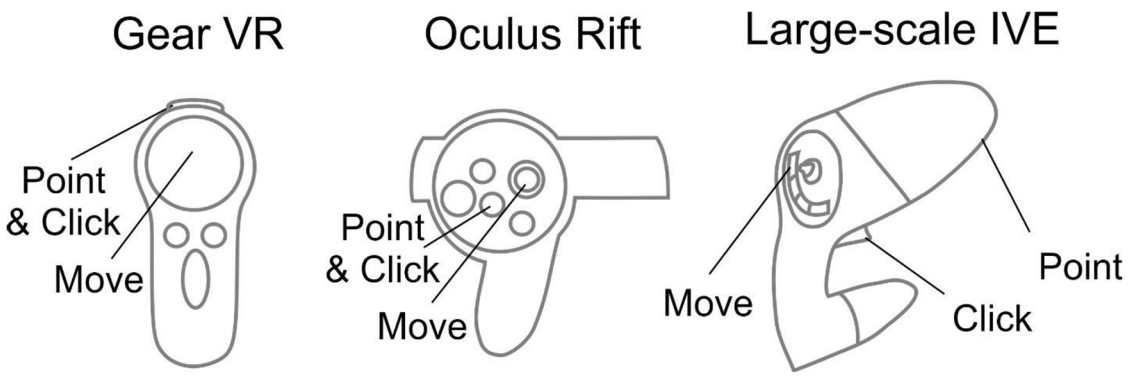

FIGURE 4
Controls implemented in the workflow. Controls for the Gear VR (left), Oculus Rift (middle), and large-scale immersive virtual environment *via* FlyStick 2 (right) are shown. The trackable controllers are viewed as an orange beam in the Unity Scene. The user positions the controller in space to point the beam at a portion of the results to be viewed and then make a selection *via* the buttons shown.

TABLE 3 Portions of workflow implemented in the three featured CFD application examples.

	Coarctation of the Aorta	Cerebral Aneurysm	Nasal Airway
CFD Software	SimVascular	Fluent	Fluent
Velocity Visualization	Glyphs	Streamlines	Streamlines
Unity template	Optional (CFD results, legends, inflow waveform, imaging data) plus additions for group/treatment viewing	Minimum (CFD results and legend)	Minimum (CFD results and legend) plus additions for pre/post treatment viewing

myography data of vascular function in response to contractile or relaxation agents (27). Our objective with these data as a case study in the current work was to immersively and simultaneously compare CFD and experimental results. Examples from rabbits in each group (i.e., CoA, Corrected, and Control) used the same methods outlined above to create versions of the results for immersive viewing within available virtual environments.

A second clinical application area in the current work features data from the Circle of Willis, which is a common area of cerebral aneurysm formation. Local hemodynamic forces play an important role in aneurysm growth and rupture (31); therefore, obtaining patient-specific flow metrics can help in diagnostics and treatment planning. In this case, flow simulations were conducted for an aneurysm of the basilar artery. In addition to a pulsatile CFD simulation, available data include time-resolved, three-directional phase-contrast MRI (4D flow MRI) velocity measurements (32, 33). While both CFD and 4D flow MRI provide valuable information on complex flow patterns in aneurysms, both approaches have limitations and advantages. The accuracy of 4D flow MRI is affected by limited spatiotemporal resolution, dynamic range of velocities, and image noise. CFD modeling, while providing superior accuracy, relies on modeling assumptions, e.g., laminar or turbulent flow regime, blood properties, and boundary conditions that may be not physiologically representative. Hence, there is potential utility in interacting with detailed spatiotemporal data to compare CFD simulation and *in vivo* 4D flow MRI measurements for the same aneurysm using an immersive approach. The end goal of these data as a case study in the current work was to view the cerebral aneurysm in its natural anatomical orientation and observe the complex intra-aneurysmal flow patterns obtained from the imaging and modeling modalities.

A third case study below features CFD simulations of nasal airflow designed to effectively communicate virtual surgery modeling predictions and help surgeons determine which approach may be optimal for patients with nasal airway obstruction (34). Two CFD simulations were used. The first simulation shows the nasal airflow patterns in a patient with nasal obstruction due to deviated septum (pre-surgery). The second simulation was from the same patient, but after virtual surgery to correct the obstruction (i.e., post-surgery). Both CFD simulations included pressure and velocity information from steady simulations appropriate for this portion of the anatomy. The end goal of this data was to immersively travel through the nasal cavity while being able to compare the pre and post-surgery states instantaneously. A representative surface model from a scan of a human head and x, y, and z coordinates that would be later used to create a set animation track were also available from collaborating researchers.

3.1. Application 1 - arterial hemodynamics with application to coarctation of the aorta

3.1.1. Format of CFD results

MRA imaging data from the thoracic aorta of representative rabbits in each group (Control, CoA, and Corrected) were obtained using GE Healthcare's 3-T Sigma Excite MRI scanner at the Medical College of Wisconsin. Computational models were created from this data using SimVascular as discussed elsewhere (27, 28). Corresponding CFD results from each simulation were represented as twenty-five .vtu files representing instantaneous results at regular intervals spanning the duration of a single cardiac cycle. Two .vtk files were also created from this instantaneous data, one each for TAWSS and OSI. Simulation results from representative rabbits in each group all used the same workflow above as discussed in more detail below.

3.1.2. Convert CFD results into 3D format

Collaborating researchers for this case study desired to view instantaneous pressure, along with the scalars of TAWSS and OSI, and velocity results as vector representations. The glyph workflow was therefore used to implement the following details. First, each .vtu file was loaded into ParaView. Next, pressure was assigned to display on the aortic wall for each time step. Glyphs were then added using ParaView's glyph tool at each time step. The Python script was run, during which each .vtu file was saved as a .vrml file containing velocity (glyphs) and pressure (wall) information, respectively. OSI and TAWSS .vtk files were then separately loaded into ParaView and exported as .vrml files.

3.1.3. Reorganize CFD results and add supplementary data

The provided Blender template was opened, instructions were completed, and the script was run. Each time step took approximately fifteen seconds to load.

After the CFD simulation was reorganized in Blender, the Blender scene was altered to display supplementary data. First, image slices representing volumetric MRA data were overlapped on the wall mesh. Then, the aorta was conceptually divided into two regions within the immersive space: (1) a proximal region above the spatial location of the coarctation and (2) a region distal to the coarctation location. Within Blender, the scene was then saved and exported as a .fbx file. The inflow waveform was then created in a readily available graphics program (e.g., Microsoft Excel, SigmaPlot, or similar) and saved as a .png

image. A .png image was also created that included a montage representation of the VVG, IHC, and myography data taken from the proximal and distal regions of the aorta. Finally, each MRA imaging slice, flow waveform PNG image, regional PNG images, and .fbx file were then copied into the Unity template.

3.1.4. Customize for CoA data

The Unity template refreshed upon opening, which allowed each PNG image and the .fbx file (now a prefab) to appear. Next, the CFD simulation prefab was dropped into the hierarchy where it was properly scaled and repositioned. The editor script to set up the scene was run to properly tag glyphs, the wall mesh, and volumetric image slices. The flow waveform and legends for each indices (i.e., pressure, TAWSS, OSI) of interest were then set up.

3.1.5. Arrange for a given IVE

The Unity template was slightly altered to display the montage of structure and function data from locations above and below the coarctation. The alterations allowed these montages to switch if a user was originally in the proximal end of the CoA and then flew through the CoA into the distal end, or vice versa. These data have also been subsequently viewed immersively on the Gear VR, Microsoft HoloLens and large-scale IVE within MARVL. The final versions of each thoracic aortic simulation using the Oculus Rift and HoloLens are shown in Figure 5.

3.2. Application 2 - cerebral vasculature hemodynamics for aneurysm progression

3.2.1. Format of CFD results

This case study utilized contrast-enhanced MRA and three-directional phase-contrast MR velocimetry (4D flow MRI) datasets obtained for a basilar tip aneurysm patient at the University of California San Francisco. Patient-specific vascular geometries were obtained from the MRA data using in-house segmentation tools. The region of interest was then defined, noise was reduced, and the surfaces were converted into IGES format using a 3D modeling software Geomagic Design (3D systems; Rock Hill, South Carolina). The computational mesh on the domain was created using Hypermesh (Altair; Troy, Michigan) and the transient, incompressible Navier-Stokes equations were solved using a finite volume solver Fluent (ANSYS Inc; Canonsburg, PA) (32). The inflow and outflow boundary conditions were obtained from the 4D flow MRI data and used to prescribe time-dependent waveforms for the CFD solver. The simulation data were then exported into VTK format for data visualization. *In vivo* 4D flow MRI data containing velocity components through the cardiac cycle were processed using ParaView and EnSight (ANSYS Inc; Canonsburg, PA) (33). Both the CFD simulation and 4D flow MRI data were presented to MARVL as .cas files from Fluent, only including velocity information. The CFD simulation had sixty-six files representing instantaneous results at regular intervals spanning the duration of a single cardiac cycle and the 4D flow MRI simulation had twenty files over the same duration.

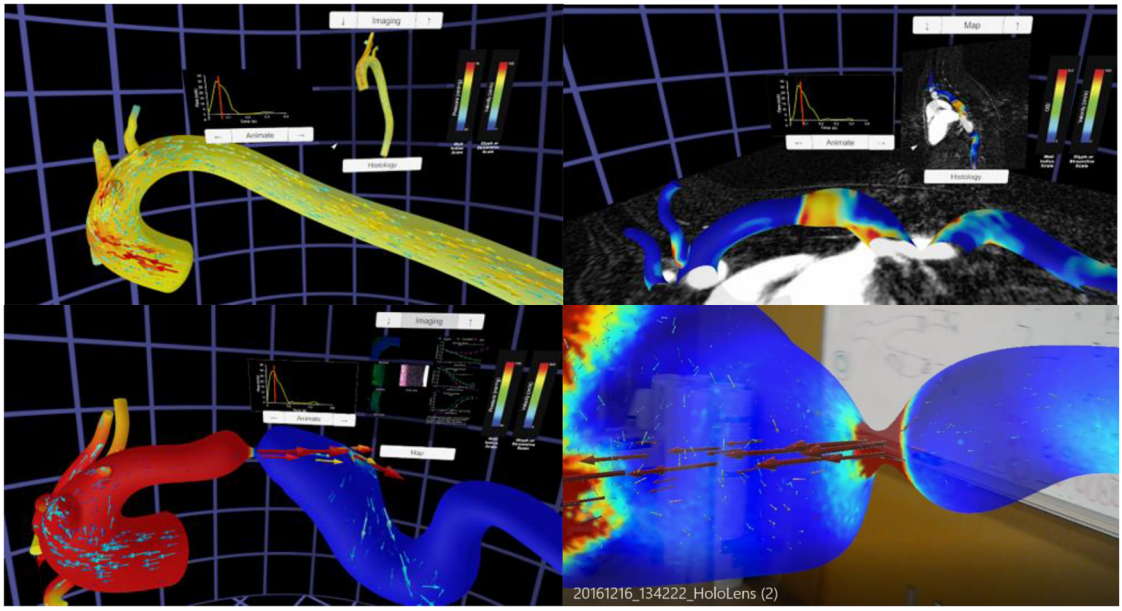

FIGURE 5
Screenshots from immersive viewing of a thoracic aorta data with application to coarctation of the aorta (CoA). Results shown using the Oculus Rift include those from a user simultaneously viewing instantaneous velocity vectors and pressure from a simulation in the Control group (top left), peak systolic pressure and velocity from a simulation in the CoA group (bottom left) together with local immunohistochemistry (i.e., structure) and myography (i.e., function) data, and oscillatory shear index and corresponding imaging data from a simulation of the Corrected group (top right). All results have a marker on associated inflow waveforms that indicate current time during the cardiac cycle. The current viewing location within the geometry and legends for each index are also present in each panel shown. The bottom right image shows a HoloLens after processing data from this application through the workflow and viewing in augmented reality within a research laboratory setting.

3.2.2. Convert CFD results into 3D format

The streamline workflow was used for this case study at the request of the collaborator. First, the CFD .cas file was loaded into ParaView. Tube-based streamlines were then added at each file using ParaView's stream tracer tool and tube filter. Finally, each of the sixty-six files in the cardiac cycle were saved as .vrml files using the custom Python script. The same process was performed for the 4D flow MRI .cas file, where each of the twenty files representing the cardiac cycle were saved as .vrml files. The corresponding geometry data was not extracted from the 4D flow MRI data due to the limited spatial resolution of the images. Therefore, the wall mesh from CFD data was manually overlaid on the MRI velocity data in Unity to provide a frame of reference for the 4D flow data.

3.2.3. Reorganize CFD results

The following steps were implemented with data from CFD and 4D flow MRI. First, the Blender template was opened, and the associated script was run. Each time step took approximately twelve seconds to load. After the CFD simulation was created, it was noted that its wall mesh was double-sided, and each time step had a large number of vertices. Therefore, the secondary Blender Python script was run to remove duplicate mesh structures and decrease the vertex count. After the 4D flow data was processed, slight alterations were made to the Blender scene to account for the lack of an associated all wall mesh, which was later added in Unity. Finally, the Blender project was exported as a .fbx file.

3.2.4. Customize for cerebral aneurysm data

Collaborating researchers did not request viewing of any supplementary data with the CFD and 4D flow MRI results. The results were therefore prepared for the immersive environment by opening and refreshing the Unity template, causing the .fbx file (now a prefab) to appear. Next, the prefab was added into the hierarchy where it was properly scaled and repositioned within the virtual world so that its presentation was at a desired scale and elements such as the background, cameras, and user interface were located in reasonable positions for the experience. The wall mesh was originally solid white, which was thought to be suboptimal. Instead, a red material was created and applied to the wall mesh to better represent its classic association with arteries. To add the CFD wall mesh to the 4D flow data, the wall mesh of the CFD simulation was manually overlaid on the 4D flow MRI data. Next, the editor script was run allowing the wall mesh and streamlines to be tagged, and scripts were assigned to the various game objects. Finally, the velocity legend was labeled using scales consistent across the types of data.

3.2.5. Arrange for a given IVE

Standard interaction was sufficient for this case study. The resulting versions of the CFD simulation and 4D flow data visualized using the Oculus Rift are displayed in Figure 6. These data have also subsequently been viewed immersively in MARVL's large-scale IVE.

3.3. Application 3 - nasal airflow for virtual treatment planning

3.3.1. Format of CFD results

The two nasal airflow simulations originated from the same obstructed nasal cavity CT scan obtained at the Medical College of Wisconsin. Using Mimics (Materialise; Leuven, Belgium), CT data was segmented to create a 3D model representing the nasal passage prior to surgery (i.e., pre-surgery). A virtual septoplasty (i.e., post-surgery) model was also created in Mimics to represent the surgical outcome after the septal deviation was corrected. Both 3D models were then meshed using ICEM-CFD (ANSYS Inc; Canonsburg, PA) and steady CFD simulations were conducted using Fluent. Resulting CFD simulation results were available as separate .cas files for each simulation. To foster the collaborators vision of comparatively viewing pre and post-operative results while traveling through the airway, an .stl file was provided that represented a rendered surface model from a scan of a representative human head. Additional steps were required with the current workflow to further achieve the collaborator's vision for immersive visualization of results. These additional steps are discussed in more detail below.

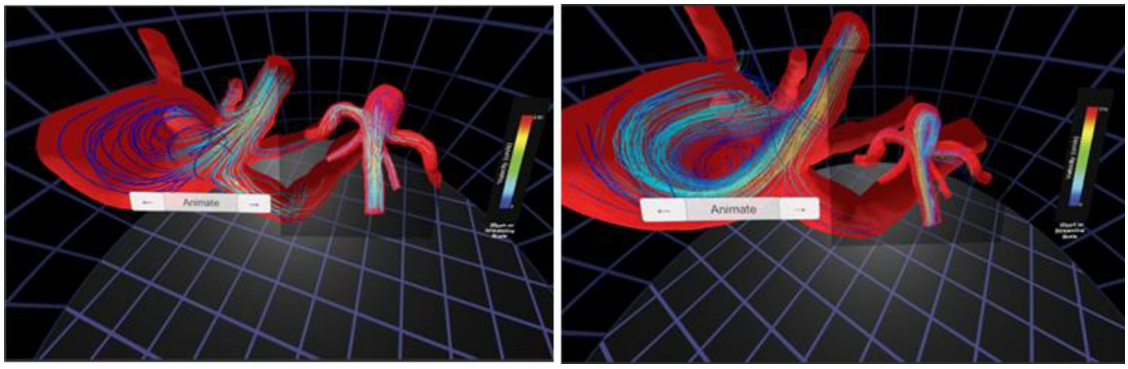

FIGURE 6
Screenshots from immersive viewing of cerebral vascular data with application to characterization of aneurysmal hemodynamics using the Oculus Rift. Streamlines of velocity from CFD simulation results (left) are shown alongside those from 4D flow (right). The current viewing location within the geometry and legends for velocity are also present in each panel shown.

3.3.2. Convert CFD results into 3D format

The workflow was used with the streamlines option to visualize changes in velocity and pressure from the pre- to virtual post-surgery states. First, the respective .cas files (simulations) and .stl files (anatomy) were loaded into ParaView. A set of tubed-streamlines were applied to the pre-surgery and post-surgery data using ParaView's stream tracer tool and tube filter. Both indexes were selected so clinicians could switch between velocity and pressure information as discussed below. Seven .vrml files were exported representing: (1) anatomical wall mesh of a head, (2) pre-surgery and (3) post-surgery nasal cavity mesh, (4) pre-surgery and (5) post-surgery streamlines colored by velocity magnitude, and (6) pre-surgery and (7) post-surgery streamlines colored by pressure magnitude.

3.3.3. Reorganize CFD results

As with the prior case studies discussed above, the Blender template was opened, and the associated scripts were run. Each .vrml file took about fifteen seconds to load. The wall mesh for both the pre- and post-surgery models included additional geometry at the top of the nasal cavity that was unnecessary for the collaborators' viewing objectives. This unnecessary geometry was therefore manually deleted using Blender.

3.3.4. Customize for nasal airflow data

Supplementary data for this case comprised of x, y, and z coordinates that clinical collaborators desired to use as a specific track for a camera within the immersive space to move along (i.e., virtual endoscope). The coordinates were provided as two .txt files, corresponding to the right and left nasal cavities. After the project was reorganized in Blender, the scene was altered to add coordinates for vertex points along each track using Blender's text editor. The vertices were parented to two cameras, one for the left nasal cavity and one for the right nasal cavity. The Blender scene was then exported as an .fbx file. The Unity template was then opened and refreshed, causing the .fbx file (now considered a prefab) to appear in the Unity template. Next, the prefab was added into the hierarchy where it was properly scaled and repositioned.

3.3.5. Arrange for a given IVE

This project was slightly different from the two reviewed above and therefore required modest alteration. First, the Unity camera head node was parented to the Blender camera. Next, scripts were written to (1) toggle between the pre and post-surgery results, (2) toggle between velocity and pressure streamlines, and (3) start and switch the camera animation created in Blender. Finally, legends were added to optimize on the range of values for pressure and velocity in each simulation. The resulting Unity scene, in play mode, initially appears as **Figure 7**. The figure also shows the view inside the left or right nasal cavity when the user toggles between pre and post-surgery CFD simulation results, observing the changes in geometry, velocity, and pressure information using the Oculus Rift.

4. Discussion

Researchers using CFD for biomedical applications can spend weeks or months creating realistic geometric models, determining appropriate boundary conditions, running simulations, and post-processing results (3). In most cases, only a fraction of the simulation results are studied in detail, and results are typically viewed on a 2D display, presented at one timepoint from a single viewing angle, or at several timepoints. Currently available software tools allow for viewing of a CFD model with its corresponding imaging data and resulting simulation indices. However, spatiotemporal relationships between hemodynamic indices of interest from CFD and important data concerning structure or function are rarely shown together. This shortcoming in concurrent viewing of data may limit our ability to make associations between mechanical stimuli and biological response for a given pathology. VR and AR may alleviate many of these issues through the use of improved depth cues, custom interactivity, and an immersive approach that can create a sense of presence within the data by a researcher (6). Motivated by recent work using Unity to view CFD results for another discipline (8), we sought to develop a rapid, easy to use, semi-automatic workflow that combines biomedical CFD results and supplementary data to be viewed in a wide range of systems. As outlined above, we present methods associated with the workflow using data from a cylinder phantom imaged *via* microfocal x-ray CT (19). Three case studies with different input and output specifications were then presented for several clinical applications viewed across platforms spanning a range of cost and implementation considerations (e.g., size of full-scale IVE vs. HMD).

Our intention is for the workflow to be used as a collaborative tool between CFD researchers and clinicians by more easily and quickly being able to view available data. Data scientists may also find the tool useful. However, our perspective during development of the current workflow was as CFD researchers who needed a set of tools that were not available at the time. Many CFD researchers are students gaining credentials toward careers in industry or academia. With this in mind, ease of use for the current workflow was confirmed by one graduate and one undergraduate student at our institution. While the graduate student had some prior experience running CFD simulations and using ParaView, neither student was familiar with Blender, Unity or methods implemented to view results immersively in VR or AR. Students were presented with a PNG flow waveform and 20 .vtu files previously generated using SimVascular. Thus, the students were presented with the minimum output along with an animated flow waveform, which is part of the Optional Output portion of **Table 2**. The immersive visualization workflow was successfully completed by the graduate student in one hour and seven minutes. This completion time included processing such as running the Python script in ParaView, running the Python script in Blender, opening Unity, and reloading the .fbx file into the Unity scene. The undergraduate student was then presented with the same data. After study personnel trained the undergraduate student on how to use ParaView, the workflow was successfully completed in fifty-nine minutes, which also included the processing time for each step. As a frame of reference, a user who was proficient in ParaView,

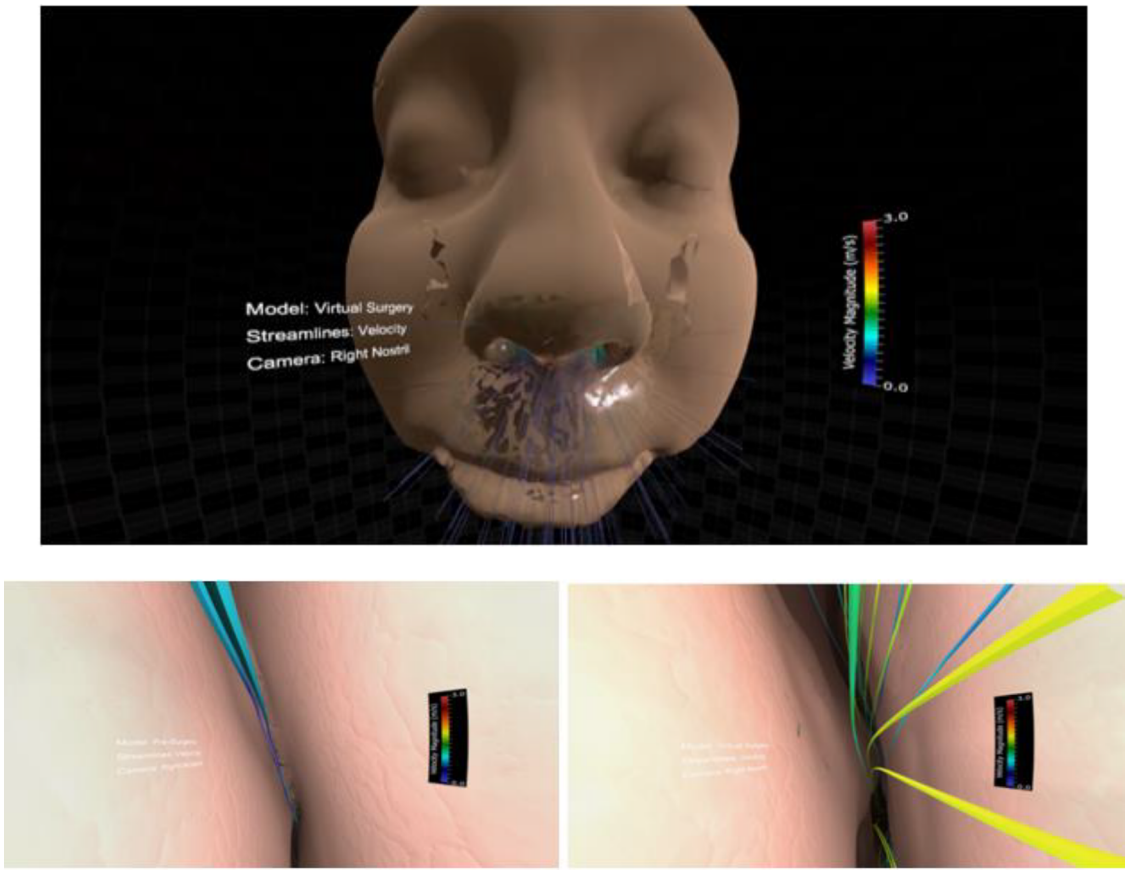

FIGURE 7
Screenshots from immersive viewing of nasal airway data with application to virtual treatment planning using the Oculus Rift. Initial view of the scene using a representative geometry (top) along with views of velocity streamlines from inside the right nasal cavity pre-surgery (lower left) and post-surgery (lower right). Note the increase in velocity post-surgery following removal of the obstructed region resulting in increased regional flow.

Blender and Unity was able to prepare the same data set for immersive viewing in eighteen minutes, including the processing time for each step. Overall, study personnel were satisfied with this result. While this initial and informal feedback does not represent a rigorous usability study, it does suggest the workflow presented here can be used by others in the field as novice researchers with no prior knowledge of Blender or Unity could not likely have easily viewed their simulation results immersively in this short amount of time previously (i.e., ~1 h).

The current methods and applications highlighted should be interpreted relative to several potential limitations. The aortic coarctation and cerebral aneurysm applications were implemented in a way that allows the vasculature to disappear as the virtual camera nears the location a vessel. In contrast, our collaborators for the nasal airway for surgical treatment planning application requested a perspective consistent with endoscopy using the proposed methods. This highlights the utility of the tools presented to address the needs of collaborators for a given application. It may be possible to script extraction of flow waveforms from ParaView within regions of interest *a priori*. The user could leverage the Python window (for example) to code steps to set a cut plane and engage a filter to integrate velocity for points within the plane. Results could then be implemented in the current workflow as was done for inflow waveforms. Setting the location of imaging data, planes and complementary data is done in Unity as described above. Hence, the workflow may take additional time to implement with multiple imaging data sets if their co-ordinate systems are not aligned with the CFD geometry. The workflow is currently limited to volumetric imaging data from which CFD models were created and data from those modalities from which data can be viewed on a plane positioned within Unity. Immersive visualization of CFD results can be misleading depending on the users viewing angle, which is an important consideration related to the use and applicability of the current workflow. One approach to mitigating this issue within MARVL discussed in detail elsewhere (16) has been to limit the use of head-tracking to situations where a single user is in the IVE. However, for collaborative settings such as those for which the current workflow was developed, we set a virtual camera at a position and orientation representative of a seated person in the center of the room. The stereo axis of each screen is then aligned to the face normal of each screen thereby allowing the audience to visualize a stereo image on all screens, albeit with more pronounced screen boundaries. The CAVE-type implementation within MARVL uses the VR toolkit MiddleVR to supplement some features missing from Unity for use in the CAVE. Like Unity, MiddleVR is not open-source, but both are available under a generous license for educational use and the future may bring fully open-source alternatives. Although Unity is

not open source, the project files and resources that rely on it can be shared under an open-source license.

The goal of the current work was to present and disseminate a new tool for enhanced viewing of CFD results and associated data in an IVE. As has been previously recounted to our team, an IVE offers the potential for more real estate with fewer distractions. The approach employed in describing our methods is similar to prior work advancing methods for CFD related to boundary condition developments (9, 10) in that the utility of the method is presented first in a simple example, and then extended to several specific applications. Future work applying the current advancements will strive to quantitatively assess the ability of the methods presented here provide measurable insights, likely using established measures and relative to current trends and challenges (35, 36). It is also important to note that although the workflow has been tested with additional users from our lab having some familiarity with CFD methods, an extensive usability evaluation using the System Usability Scale (SUS) or similar measure has not been conducted to date. As a result, statistical evaluation of data generated by researchers using the workflow is not available to date. Including such information from collaborating labs would be an extensive undertaking involving the coordination of multiple investigators that is beyond the funding, personnel resources and scope of work for our research at the current time. We acknowledge that as a major limitation of the current work, but are optimistic that such feedback and associated data will be obtained intrinsically following the dissemination of the workflow.

The workflow featured requires some processing of CFD simulation results as discussed before immersive versions of the results can be created for viewing. The user can then interact with the perspectives and orientations of these immersive versions, but the current version of the workflow does not allow for additional operations with the simulation results to be performed in real-time. Such interaction is available in other programs (e.g., ParaView), but to our knowledge these programs do not easily allow for inclusion of complementary data. Interestingly, related work has recently been conducted in this area for visualization of CFD simulation results of intracranial arteriovenous malformations (AVM) (37) in which users can interactively block arteries supplying an AVM in VR. Similar to the current workflow, the AVM study also leverages pre-computed CFD simulation results. The inclusion of real-time manipulation of native simulation results immersively *via* user interaction represents a potential area of development for the current workflow moving forward.

The data format from our simulations was in the form of vertex colors, and the UV maps were generated in order to allow those data to be more easily processed. UV maps were generated by baking vertex colors onto 2D image files, not mapping 2D images onto 3D faces, so the UV unwrapping distortion was avoidable by using a large number of UV patches. Swapping image files seemed to be robust and performant, but there are several ways to achieve multiple color maps. For example, alternative methods such as using custom shaders and multiple vertex colors could also likely work with additional scripting.

There are many file formats and software tools that are used for CFD. The choice of file formats implemented here are consistent with those common to researchers using SimVascular, FLUENT and ParaView. The use of other files formats may allow for the elimination of steps presented to date in future iterations of the workflow, or by those researchers starting from a different file format. It is also worth noting that the specific devices featured in the current work may undergo iterations. Hence, the workflow may need to be revisited on a case-by-case basis as new devices become commercially available. Nonetheless, the workflow was also implemented so that immersive visualization of CFD simulation results could be used as a collaborative tool between engineers and clinicians. For example, study personnel have been in meetings with clinical colleagues who have a firm understanding of principles governing fluid flow and their current putative relationships to pathology. In a specific prior meeting with one of these clinical collaborators, study personnel were asked to show time-varying pressure, followed by velocity and then TAWSS using a conventional visualization software. This took a substantial amount of time as the resulting indices from each time step were loaded into memory and rendered. Depending on the availability, proximities and schedules of collaborators, this may be a barrier to collaboration and translation. Implementation of the approaches described results in hardware memory requirements that are far lower than other visualization methods because our results are included in the visualization of objects instead of computed (called and rendered). This is what allows the current methods to run on mobile platforms effectively. The drawback at present is that this approach is less flexible in general. As compared to traditional approaches, rapid and immersive presentation of CFD and complementary data may facilitate mutual understanding between the engineering and clinical collaborators reviewing a case. To underscore results presented for the aortic coarctation study, all related forms of data were presented concurrently using the workflow presented. MRI slices could be toggled on and the user could move through each plane relative to the subject-specific geometry created and associate hemodynamics indices. Similarly, corresponding structural IHC and myography function data from above as compared to below the coarctation were triggered to present based on the location of the virtual camera, and multiple states analogous to control, preoperative and postoperative were available to the user at runtime. To date, no other tool allows for such holistic visualization of results. Having all these data present through such an analysis tool, we believe, is more likely to result in a better understanding between data types and be hypothesis-generating related to future study of the pathology. Study personnel are therefore optimistic that the current workflow will have distinct clinical utility beyond conventional viewing of CFD results. The following informal feedback was obtained by collaborators for each of the case studies presented.

This would be a valuable education tool for our patients with CoA, which can present very early in life, but also older kids who come in with hypertension. This tool could help them understand the condition better. The VR simulations are a unique, innovative sharing tool I think would increase patient and family engagement. A great way to visually see surgical changes.

I see this as a first step in using flow dynamics to predict which aneurysms are more likely to rupture and therefore need to be surgically treated. First we need to visualize the problem, which can be done using the 3D VR model to objectify what is bad and what is good.

The nasal airflow visualization was very impressive. The general feedback from those who experienced it was that this would be a very useful educational tool in this context and many other surgical contexts as a way to see the 3D relationships between structures. The addition of the two simulations on top of each other was a great way to visually see surgical changes. Surgery is a very visual field, and this was very helpful. As one becomes more familiar with the CFD information, having this information to visually see in the model was more impressive to surgeons than just seeing the simulations in 2D.

5. Conclusions

Immersive tools offer one approach to extracting more details from biomedical CFD simulation results. However, it is imperative to decrease and simplify associated processing steps to facilitate more widespread use of immersive CFD viewing. The workflow described herein can be used by novice researchers within ~1 h, demonstrating the ease of the workflow for an audience who may not be familiar with the specific tools used in VR and AR. The workflow is capable of combining biomedical CFD results from a range of pathologies with supplementary clinical data to be viewed in a wide range of immersive environments including an IVE, HMD, and standalone stereoscopic projector. As of the time of publishing, video tutorials for the steps outlined above are provided on YouTube and the workflow is available for download in GitHub. Exploration of these resources can also mitigate the inherent issue present here of trying to replicate multimodal data visualization through print and text-based media. We anticipate that future work will allow for deformable walls and associated imaging data from fluid-structure interaction simulations and additional indices of interest.

Data availability statement

Details related to the original contributions presented in the study are included in the article. Further inquiries can be directed to the corresponding author/s.

Ethics statement

All data featured were obtained following Institutional Review Board (IRB) approval from the University of California San Francisco and the Medical College of Wisconsin. Written informed consent to participate was provided by the participants' legal guardian. All animal data featured were obtained following Institutional Animal Care and Use Committee (IACUC) approval from the Medical College of Wisconsin and Marquette University.

Author contributions

All authors contributed to the conceptualization of the manuscript, analysis of data and interpretation of results. All authors also contributed to the writing and editing of the associated manuscript. All authors contributed to the article and approved the submitted version.

Funding

Research reported in this publication was partially supported by the American Heart Association under award number 15GRNT25700042 (JFL) as well as the National Institutes of Health - National Heart, Lung, and Blood Institute under award numbers R01HL142955 (JFL) and R15HL096096 (JFL) and the National Center for Advancing Translational Sciences under award number UL1TR001436. The content is solely the responsibility of the authors and does not necessarily represent the official views of the National Institutes of Health or the American Heart Association.

Acknowledgments

The authors gratefully acknowledge our clinical collaborators and end users who provided feedback on the workflow.

Conflict of interest

The authors declare that the research was conducted in the absence of any commercial or financial relationships that could be construed as a potential conflict of interest.

Publisher's note

References

1. Lee BK. Computational fluid dynamics in cardiovascular disease. *Korean Circ J.* (2011) 41:423–30. doi: 10.4070/kcj.2011.41.8.423

2. Samyn MM, LaDisa JF Jr. Novel applications of cardiovascular magnetic resonance imaging-based computational fluid dynamics modeling in pediatric cardiovascular and congenital heart disease. In: C Constantinides, editors. *Assessment of cellular and organ function and dysfunction using direct and derived MRI methodologies*. London: Intech (2016). p. 27–56.

3. LaDisa JF Jr, Bowers M, Harmann L, Prost R, Doppalapudi AV, Mohyuddin T, et al. Time-efficient patient-specific quantification of regional carotid artery fluid dynamics and spatial correlation with plaque burden. *Med Phys.* (2010) 37:784–92. doi: 10.1118/1.3292631

4. LaDisa JF Jr, Alberto Figueroa C, Vignon-Clementel IE, Kim HJ, Xiao N, Ellwein LM, et al. Computational simulations for aortic coarctation: representative results from a sampling of patients. *J Biomech Eng*. (2011) 133:091008. doi: 10.1115/1.4004996

5. Kwon S, Feinstein JA, Dholakia RJ Jr, LaDisa JF. Quantification of local hemodynamic alterations caused by virtual implantation of three commercially available stents for the treatment of aortic coarctation. *Pediatr Cardiol*. (2014) 35:732–40. doi: 10.1007/s00246-013-0845-7

6. Quam DJ, Gundert TJ, Ellwein L, Larkee CE, Hayden P, Migrino RQ, et al. Immersive visualization for enhanced computational fluid dynamics analysis. *J Biomech Eng*. (2015) 137(3):0310041–03100412. doi: 10.1115/1.4029017

7. Forsberg AS, Laidlaw DH, Van Dam A, Kirby RM, Kafniadakis GE, Elion JL. Immersive virtual reality for visualizing flow through an artery. *Proceedings Visualization 2000. VIS 2000 (Cat. No.00CH37145)*. (2000):457–60. doi: 10.1109/VISUAL.2000.885731

8. Berger M, Cristie V. CFD post-processing in unity3D. *Procedia Comput Sci*. (2015) 51:2913–22. doi: 10.1016/j.procs.2015.05.476

9. Figueroa CA, Vignon-Clementel IE, Jansen KE, Hughes TJR, Taylor CA. A coupled momentum method for modeling blood flow in three-dimensional deformable arteries. *Comput Methods Appl Mech*. (2006) 195:5685–706. doi: 10.1016/j.cma.2005.11.011

10. Vignon-Clementel IE, Figueroa CA, Jansen KE, Taylor CA. Outflow boundary conditions for three-dimensional finite element modeling of blood flow and pressure in arteries. *Comput Methods Appl Mech Eng*. (2006) 195:3776–96. doi: 10.1016/j.cma.2005.04.014

11. Cruz-Neira C, Sandin DJ, DeFantin TA, Kenyon RV, Hart JC. The CAVE: audio visual experience automatic virtual environment. *Commun ACM*. (1992) 35:64–72. doi: 10.1145/129888.129892

12. *Plato, allegory of the cave, republic*. Harmondsworth: Penguin (1974). 240–48.

13. Patterson R, Winterbottom MD, Pierce BJ. Perceptual issues in the use of head-mounted visual displays. *Hum Factors*. (2006) 48:555–73. doi: 10.1518/001872006778606877

14. Sherman WR, Craig AB. *Understanding virtual reality: Interface, application, and design*. San Francisco: Morgan Kaufmann Publishers Inc. (2003).

15. Febretti A, Nishimoto A, Thigpen T, Talandis J, Long L, Pirtle JD, et al. CAVE2: a hybrid reality environment for immersive simulation and information analysis. *Proceedings of SPIE, The Eng Reality of Virtual Reality*. (2013) 2013:8649. doi: 10.1117/12.2005484

16. LaDisa JF Jr, Larkee CE. The MARquette visualization lab (MARVL): an immersive virtual environment for research, teaching and collaboration. *Front Educ*. (2020) 5:38. doi: 10.3389/feduc.2020.00038

17. Sharples S, Cobb S, Moody A, Wilson JR. Virtual reality induced symptoms and effects (VRISE): comparison of head mounted display (HMD), desktop and projection display systems. *Displays*. (2008) 29:58–69. doi: 10.1016/j.displa.2007.09.005

18. Alfano PL, Michel GF. Restricting the field of view - perceptual and performance effects. *Percept Motor Skill*. (1990) 70:35–45. doi: 10.2466/pms.1990.70.1.35

19. LaDisa JF Jr, Olson LE, Ropella KM, Molthen RC, Haworth ST, Kersten JR, et al. Microfocal x-ray computed tomography post-processing operations for optimizing reconstruction volumes of stented arteries during 3D computational fluid dynamics modeling. *Comput Methods Programs Biomed*. (2005) 79:121–34. doi: 10.1016/j.cmpb.2005.03.005

20. LaDisa JF Jr, Olson LE, Molthen RC, Hettrick DA, Pratt PF, Hardel MD, et al. Alterations in wall shear stress predict sites of neointimal hyperplasia after stent implantation in rabbit iliac arteries. *Am J Physiol Heart Circ Physiol*. (2005) 288:H2465–75. doi: 10.1152/ajpheart.01107.2004

21. Won J, Kim YS. A new approach for reducing virtual reality sickness in real time: design and validation study. *JMIR Serious Games*. (2022) 10:e36397. doi: 10.2196/36397

22. So RH, Lo WT, Ho AT. Effects of navigation speed on motion sickness caused by an immersive virtual environment. *Hum Factors*. (2001) 43:452–61. doi: 10.1518/001872001775898223

23. Yeo SS, Kwon JW, Park SY. EEG-based analysis of various sensory stimulation effects to reduce visually induced motion sickness in virtual reality. *Sci Rep*. (2022) 12(1):18043. doi: 10.1038/s41598-022-21307-z

24. Saredakis D, Szpak A, Birckhead B, Keage HAD, Rizzo A, Loetscher T. Factors associated with virtual reality sickness in head-mounted displays: a systematic review and meta-analysis. *Front Hum Neurosci*. (2020) 14:96. doi: 10.3389/fnhum.2020.00096

25. LaDisa JF Jr, Bozdag S, Olson J, Ramchandran R, Kersten JR, Eddinger TJ. Gene expression in experimental aortic coarctation and repair: candidate genes for therapeutic intervention? *PLoS One*. (2015) 10:e0133356. doi: 10.1371/journal.pone.0133356

26. LaDisa JF Jr, Tomita-Mitchell A, Stamm K, Bazan K, Mahnke DK, Goetsch MA, et al. Human genotyping and an experimental model reveal NPR-C as a possible contributor to morbidity in coarctation of the aorta. *Physiol Genomics*. (2019) 51:177–85. doi: 10.1152/physiolgenomics.00049.2018

27. Menon A, Eddinger TJ, Wang H, Wendell DC, Toth JM, LaDisa JF Jr. Altered hemodynamics, endothelial function, and protein expression occur with aortic coarctation and persist after repair. *A J Physiol*. (2012) 303:H1304–18. doi: 10.1152/ajpheart.00420.2012

28. Menon A, Wendell DC, Wang H, Eddinger TJ, Toth JM, Dholakia RJ, et al. A coupled experimental and computational approach to quantify deleterious hemodynamics, vascular alterations, and mechanisms of long-term morbidity in response to aortic coarctation. *J Pharmacol Toxicol Methods*. (2012) 65:18–28. doi: 10.1016/j.vascn.2011.10.003

29. Ferencz C, Rubin JD, McCarter RJ, Brenner JI, Neill CA, Perry LW, et al. Congenital heart disease: prevalence at livebirth. The Baltimore-Washington infant study. *Am J Epidemiol*. (1985) 12:31–6. doi: 10.1093/oxfordjournals.aje.a113979

30. Cohen M, Fuster V, Steele PM, Driscoll D, McGoon DC. Coarctation of the aorta. Long-term follow-up and prediction of outcome after surgical correction. *Circulation*. (1989) 80:840–5. doi: 10.1161/01.CIR.80.4.840

31. Detmer FJ, Chung BJ, Mut F, Slawski M, Hamzei-Sichani F, Putman C, et al. Development and internal validation of an aneurysm rupture probability model based on patient characteristics and aneurysm location, morphology, and hemodynamics. *Int J Comput Assist Radiol Surg*. (2018) 13:1767–79. doi: 10.1007/s11548-018-1837-0

32. Rayz VL, Abla A, Boussel L, Leach JR, Acevedo-Bolton G, Saloner D, et al. Computational modeling of flow-altering surgeries in basilar aneurysms. *Ann Biomed Eng*. (2015) 43:1210–22. doi: 10.1007/s10439-014-1170-x

33. Liu J, Koskas L, Faraji F, Kao E, Wang Y, Haraldsson H, et al. Highly accelerated intracranial 4D flow MRI: evaluation of healthy volunteers and patients with intracranial aneurysms. *Magma*. (2018) 31:295–307. doi: 10.1007/s10334-017-0646-8

34. Vanhille DL, Garcia GJM, Asan O, Borojeni AAT, Frank-Ito DO, Kimbell JS, et al. Virtual surgery for the nasal airway: a preliminary report on decision support and technology acceptance. *JAMA Facial Plast Surg*. (2018) 20:63–9. doi: 10.1001/jamafacial.2017.1554

35. Slater M. Measuring presence: a response to the witmer and singer presence questionnaire. *Presence*. (1999) 8:560–5. doi: 10.1162/105474699566477

36. Oeltze-Jafra S, Meuschke M, Neugebauer M, Saalfeld S, Lawonn K, Janiga G, et al. Generation and visual exploration of medical flow data: survey, research trends and future challenges. *Comput Graph Forum*. (2018) 38:87–125. doi: 10.1111/cgf.13394

37. Sprengel U, Saalfeld P, Stahl J, Mittenentzwei S, Drittel M, Behrendt B, et al. Virtual embolization for treatment support of intracranial AVMs using an interactive desktop and VR application. *Int J Comput Assist Radiol Surg*. (2021) 16:2119–27. doi: 10.1007/s11548-021-02532-9

frontiers | Frontiers in Bioengineering and Biotechnology

TYPE Original Research
PUBLISHED 28 February 2023
DOI 10.3389/fbioe.2023.1127855

OPEN ACCESS

EDITED BY
Francesco Sturla,
IRCCS San Donato Polyclinic, Italy

REVIEWED BY
Alberto Cesare Luigi Redaelli,
Politecnico di Milano, Italy
Chloe Armour,
Imperial College London,
United Kingdom

*CORRESPONDENCE
Yong He,
yong.he@surgery.ufl.edu

†PRESENT ADDRESS
Rosamaria Tricarico,
Medtronic Inc., Structural Heart & Aorta, Cardiovascular Group, Santa Rosa, CA, United States

SPECIALTY SECTION
This article was submitted to Biomechanics, a section of the journal Frontiers in Bioengineering and Biotechnology

RECEIVED 20 December 2022
ACCEPTED 17 February 2023
PUBLISHED 28 February 2023

CITATION
Tricarico R, Berceli SA, Tran-Son-Tay R and He Y (2023), Non-invasive estimation of the parameters of a three-element windkessel model of aortic arch arteries in patients undergoing thoracic endovascular aortic repair.
Front. Bioeng. Biotechnol. 11:1127855.
doi: 10.3389/fbioe.2023.1127855

Non-invasive estimation of the parameters of a three-element windkessel model of aortic arch arteries in patients undergoing thoracic endovascular aortic repair

Rosamaria Tricarico[1†], Scott A. Berceli[2,3], Roger Tran-Son-Tay[1,4] and Yong He[2*]

[1]Department of Biomedical Engineering, University of Florida, Gainesville, FL, United States, [2]Division of Vascular Surgery and Endovascular Therapy, Department of Surgery, University of Florida, Gainesville, FL, United States, [3]North Florida/South Georgia Veterans Health System, Gainesville, FL, United States, [4]Department of Mechanical and Aerospace Engineering, University of Florida, Gainesville, FL, United States

Background: Image-based computational hemodynamic modeling and simulations are important for personalized diagnosis and treatment of cardiovascular diseases. However, the required patient-specific boundary conditions are often not available and need to be estimated.

Methods: We propose a pipeline for estimating the parameters of the popular three-element Windkessel (WK3) models (a proximal resistor in series with a parallel combination of a distal resistor and a capacitor) of the aortic arch arteries in patients receiving thoracic endovascular aortic repair of aneurysms. Pre-operative and post-operative 1-week duplex ultrasound scans were performed to obtain blood flow rates, and intra-operative pressure measurements were also performed invasively using a pressure transducer pre- and post-stent graft deployment in arch arteries. The patient-specific WK3 model parameters were derived from the flow rate and pressure waveforms using an optimization algorithm reducing the error between simulated and measured pressure data. The resistors were normalized by total resistance, and the capacitor was normalized by total resistance and heart rate. The normalized WK3 parameters can be combined with readily available vessel diameter, brachial blood pressure, and heart rate data to estimate WK3 parameters of other patients non-invasively.

Results: Ten patients were studied. The medians (interquartile range) of the normalized proximal resistor, distal resistor, and capacitor parameters are 0.10 (0.07–0.15), 0.90 (0.84–0.93), and 0.46 (0.33–0.58), respectively, for common carotid artery; 0.03 (0.02–0.04), 0.97 (0.96–0.98), and 1.91 (1.63–2.26) for subclavian artery; 0.18 (0.08–0.41), 0.82 (0.59–0.92), and 0.47 (0.32–0.85) for vertebral artery. The estimated pressure showed fairly high tolerance to patient-specific inlet flow rate waveforms using the WK3 parameters estimated from the medians of the normalized parameters.

Conclusion: When patient-specific outflow boundary conditions are not available, our proposed pipeline can be used to estimate the WK3 parameters of arch arteries.

KEYWORDS

image-based computational fluid dynamics, thoracic endovascular aortic repair, three-element windkessel model, boundary conditions, personalized cardiovascular medicine

1 Introduction

Thoracic endovascular aortic repair (TEVAR) has been increasingly used to treat aortic arch pathologies (Wallen et al., 2018; Brown et al., 2021). However, in contrast to other locations along the aortic tree, aortic arch endografts are subjected to more severe biomechanical forces that can lead to post-operative complications (Scali et al., 2012; Pecoraro et al., 2017; Voskresensky et al., 2017). In this perspective, computational fluid-dynamics (CFD) simulations have contributed to the investigation of the mechanisms of aortic stent graft complications following TEVAR (Gallo et al., 2016; Madhavan and Kemmerling, 2018; van Bakel et al., 2018; Tricarico et al., 2020b; Hu et al., 2022). Since its first biomedical applications at the end of the 20th century (Stergiopulos et al., 1992), eased by the evolution and better accessibility of medical imaging tools and computational resources, computational modeling has been widely utilized to investigate hemodynamic characteristics that are difficult to measure *in vivo* (Sengupta et al., 2022). The ongoing optimization of these tools and their regulation aim to their safe integration into the biomedical device investigation for personalized treatment, which will be fundamental to the development of next-generation cardiovascular devices.

However, among the major challenges of patient-specific computational modeling is obtaining the patient-specific input data, which directly influence result accuracy, but often are not available (Morris et al., 2016; Gray and Pathmanathan, 2018; Madhavan and Kemmerling, 2018; He et al., 2022). In the absence of patient-specific measurements, the state of the art of boundary condition estimation for CFD analysis is using data from healthy subjects reported in the literature (Lantz et al., 1981; Taylor et al., 1998; Olufsen et al., 2000) and often integrated into lumped parameter Windkessel models (Armour et al., 2022). The Windkessel model (Westerhof et al., 2009) uses electrical analogues to describe a hydraulic system, where pressure (P) and flow (Q) are analogous to voltage and current respectively (Garber et al., 2022). When patient-specific flow rate and/or pressure waveforms are not available, a Windkessel model is a common strategy to impose vascular outlet boundary conditions; it has the advantage of allowing for interdependent time-varying flow rate and pressure distributions. The most popular Windkessel model has three elements, a proximal resistor (R_1) in series with a parallel combination of a distal resistor (R_2) and a capacitor (C). These parameters represent the total resistances (R_{tot}, $R_1 + R_2$) and compliances distal to the artery of interest, receiving the arterial flow rate under a specific pressure. Previous studies have demonstrated that, compared with zero-pressure assumption at the outlets, a three-element Windkessel (WK3) model achieves a better overall performance in terms of matching the inflow data and producing physiological pressure waveforms (Morbiducci et al., 2010; Pirola et al., 2017).

In this study, we analyzed ultrasound-derived patient-specific flow rate and intra-operatively measured pressure waveforms to build a set of algorithms for first-degree estimation of the parameters of the WK3 model that can be utilized when patient-specific flow rate and pressure waveforms are not available. The WK3 parameters can be estimated using more readily available patient-specific data, such as vessel diameter that can be extracted from computed tomography angiography (CTA) and brachial artery pressure that can be measured non-invasively by a cuff.

2 Materials and methods

2.1 Parameter estimation pipeline

We propose a pipeline for estimating the parameters of the WK3 model of the aortic arch branch arteries when the artery-specific flow rate and pressure waveforms are not available (Figure 1). The goal is to use the artery-specific total resistance (R_{tot}) and cardiac period (T) to scale the population-averaged, artery-specific normalized R_1, C, and R_2 values (R_{1nom}, C_{norm}, and R_{2norm}) to estimate the non-normalized parameters as:

$$R_1 = R_{1norm} \cdot R_{tot}; \quad R_2 = R_{2norm} \cdot R_{tot}; \quad C = \frac{C_{norm} \cdot T}{R_{tot}} \tag{1}$$

To encompass the patient-to-patient variability of mean flow rates and pressures, normalized R_1, C, and R_2 parameters are used and defined as:

$$R_{1norm} = \frac{R_1}{R_{tot}}; \quad R_{2norm} = \frac{R_2}{R_{tot}} = 1 - R_{1norm}; \quad C_{norm} = R_{tot} \cdot \frac{C}{T} \tag{2}$$

T_{tot} is calculate from mean pressure ($\bar{P}$) and mean flow rate ($\bar{Q}$) as described in Eq. 3.

$$R_{tot} = R_1 + R_2 = \frac{\bar{P}}{\bar{Q}}; \tag{3}$$

The mean arterial pressure can be estimated from the non-invasively measured systolic (SBP) and diastolic (DBP) brachial blood pressures *via* a commonly used equation

$$\bar{P} = \frac{1}{3}(SBP - DBP) + DBP \tag{4}$$

assuming systole is one-third of the cardiac cycle (Sesso et al., 2000). Mean flow rate can be measured by Doppler ultrasound if available or estimated from the previously published flow rate-diameter relationships based on the diameter extracted from CTA images, such as those reported by us (Tricarico et al., 2020a). CTA is routinely performed for diagnosis and treatment planning of aortic pathologies and is often used in clinical research to extract three dimensional arterial models. Cardiac period can be calculated

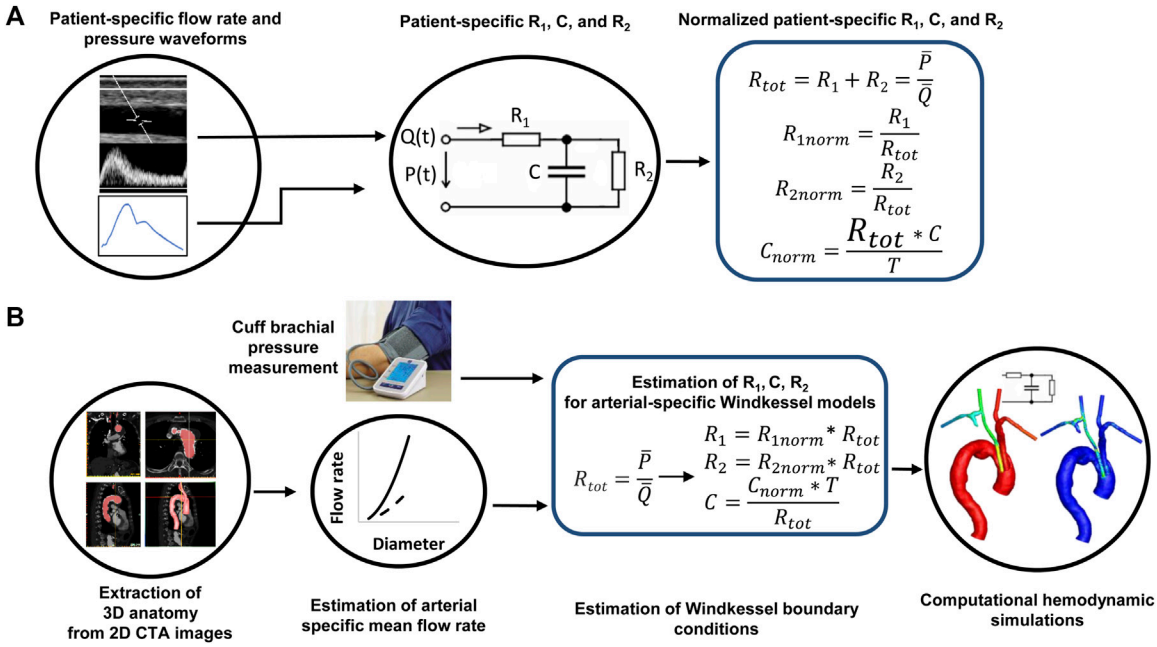

FIGURE 1
The pipeline of patient-specific estimation of the parameters of a three-element Windkessel model when lacking patient-specific flow rate and pressure waveforms. **(A)** Derivation of normalized Windkessel model parameters from patient-specific flow rate and pressure waveforms. **(B)** Estimation of Windkessel model parameters informed by non-invasive vascular imaging and pressure data. R_{tot}: the sum of the two resistances; T: the cardiac period.

from heart rate. Furthermore, by defining the normalized flow rate, pressure, and time as each variable divided by its mean (flow rate, pressure) and T, respectively, the differential equation governing the relation between flow rate and pressure in the WK3 model is maintained (Supplementary Material). The population-averaged, artery-specific R_{1norm}, C_{norm}, and R_{2norm} values can be extracted from measured flow rate and pressure data. We describe the extraction and assessment of the combinations of normalized parameters in the next sections.

2.2 Patient-specific flow rate and pressure data acquisition and processing

We developed a prospective study to measure patient-specific waveforms of flow rate and pressure data in aortic arch branch arteries in 10 patients suffering aortic aneurysms or dissections, undergoing TEVAR. The protocol for this prospective study was approved by the University of Florida College of Medicine Institutional Review Board (Gainesville, FL, United States), and informed consent was signed by every patient. Duplex ultrasound measurements were acquired under resting conditions (with awake patients in supine position) using a Philips iU22 system. Measurements were collected on multiple locations of bilateral common carotid (proximal, middle, and distal), subclavian (distal to the vertebral artery, thyrocervical and costocervical trunks, and internal thoracic artery), and vertebral arteries at pre-operative and 1-week post-operative time in the vascular laboratory. We did not take intra-operative flow rate measurements as this would interrupt the standard TEVAR procedure. Arterial diameters and flow rates were extracted from ultrasound images. Details on the methodology of flow rate calculation have been described in our previous work (Tricarico et al., 2020a).

Intra-operative pressure measurements were performed invasively using a TruWave disposable pressure transducer (Edwards Lifesciences, Irvine, CA, United States) before and after stent graft deployment in brachiocephalic artery, left common carotid, and left subclavian arteries, all carried out after catheter flushing. All pressure waveforms were traced and smoothed in Matlab R2017b (Mathworks Inc., Natick, MA, United States) using the heart rate extracted from ultrasound images, due to patient sedation at the time of the intra-operative pressure measurements. In addition, non-invasive brachial artery pressures were collected by a cuff at the time of the ultrasound imaging and mean arterial pressure was estimated using Eq. 4.

2.3 Patient-specific R_1, C, and R_2 identification

We identified the non-normalized R_1, C, and R_2 values for each artery (common carotid, subclavian, and vertebral arteries) of the patients to obtain the average of each parameter for this patient cohort using the Simulink Design Optimization toolbox (Mathworks Inc.), where the WK3 model was built, and the governing equation of the WK3 model is embedded into the block diagram (additional details in Supplementary Figure S1). Measured patient-specific, pre-operative flow and pre-deployment pressure waveforms (referred to as training dataset in Section 2.5) were used as imposed input and expected output of the model,

respectively. Since there were no intra-operative pressure measurements in the right common carotid artery and subclavian artery, pressure waveforms measured at the corresponding left side arteries were utilized for simulations on the right vasculature. In addition, subclavian artery pressures were used for vertebral artery simulations, due to invasiveness and risks of intra-deployment measurements in vertebral arteries.

Because $R_{tot} = R_1+R_2$, there are only two independent parameters in the WK3 model that need to be identified. The mean flow rate and mean pressure used to calculate R_{tot}, were obtained from the corresponding waveforms. The Runge-Kutta method was chosen as the solver with a fixed time step of 10^{-4} s to maximize the accuracy of pressure waveform calculation iteratively. A non-linear least square method and trust-region-reflective algorithm were utilized with both parameter tolerance and function tolerance of 0.001. The sum of squared error (SSE) between measured and simulated pressure of the WK3 model was chosen as the cost function for the optimization problem. At each iteration, the cost function quantified the quality of the pressure matching, and at the end of the optimization process, the optimized R_1, C, and R_2 combination was collected. Additionally, the L^2-norm of the relative error for pressure estimation in time was calculated as in Eq. 5 and collected for each R_1, C, and R_2 combination on each artery.

$$||e||_{L^2} = \sqrt{\frac{\sum_{k=1}^{N}\left|P_{simul}(t_k) - P_{exp}(t_k)\right|^2}{\sum_{k=1}^{N}P_{exp}(t_k)^2}} * 100 \quad (5)$$

where P_{simul} and P_{exp} are simulated and experimentally measured pressures, respectively; N is the number of time steps in a cardiac period. Additional details of the parameter estimation process are given in Supplementary Figure S2. After obtaining the optimized, non-normalized R_1, C, and R_2 values for each artery, the corresponding normalized R_1, C, and R_2 values were calculated as Eq. 2.

2.4 Sensitivity analysis of the predicted pressure waveform on normalized R_1, C, and R_2 parameters

A Monte Carlo method was performed in the Simulink Design Optimization Toolbox to examine the sensitivity of predicted pressure to the parameters of the WK3 model. For purposes of comparison, all flow rate and pressure waveforms were normalized to their means in Matlab. In addition, time-normalization by the cardiac period and interpolation (every 0.01) were performed. For each type of artery, the averages of the normalized pre-operative flow rate and pre-deployment pressure waveforms were imposed respectively as input and expected output of the WK3 model. Accordingly, normalized WK3 model parameters were used as the input. 1500 sets of the two independent parameters (R_{1norm} and C_{norm}) were randomly generated under the hypothesis of a uniform distribution for the three arterial-specific Monte Carlo analyses. The simulation ran until a minimum cost function was achieved.

TABLE 1 Percentage of patients with comorbidities.

Hypertension (HTN)	80 (%)
Active/former tobacco users	60%
Hyperlipidemia (HDL)	50%
Previous aneurysm interventions	40%
Congestive heart failure (CHF)	20%
Cerebral artery disease	20%
Arrhythmia	20%
Chronic obstructive pulmonary disease (COPD)	10%
Gastroesophageal reflux disease (GERD)	10%
Carotid artery disease	10%
Sleep apnea	10%
Arthritis	10%

2.5 Assessment of the normalized R_1, C, and R_2

The normalized R_1, C, and R_2 values obtained from pre-operative flow and pre-deployment pressure data (Section 2.3, training dataset) were assessed using the post-operative flow at 1 week and post-deployment pressure data (testing dataset) for the left arteries of all patients. Specifically, the medians of the normalized R_1, C, and R_2 obtained from the training dataset were scaled to each R_{tot} and T to estimate the patient-specific, non-normalized R_1, C, and R_2 parameters of each artery, as detailed in Eq. 1. R_{tot} was calculated from the mean flow rate and pressure calculated from the measured waveforms of the testing dataset. Each estimated R_1, C, and R_2 and patient-specific (non-normalized) input flow rate were used in the Winkessel model to estimate pressure waveforms using Simulink Design Optimization toolbox. Relative errors between estimated and measured artery-specific pressure waveforms were calculated. Additionally, the estimated R_1, C, and R_2 values were tested on the Windkessel model, imposing non-normalized pressure waveforms as input and flow rate waveforms as expected output, to quantify relative errors between estimated and measured flow rate waveforms. Simulated pressure and flow rate waveforms are presented in normalized form for comparison purposes.

2.6 Statistical analysis

Both non-normalized and normalized parameter values are presented as artery-specific median and 25th-75th percentiles (interquartile range, IQR). Other data were presented as mean ± standard deviation. T-tests or Mann-Whitney rank sum tests were performed to detect statistical differences in flow rate and pressure means. Statistical analyses were performed in Sigmaplot (SYSTAT Software Inc., Chicago, IL, United States). A p-value <0.05 was considered statistically different.

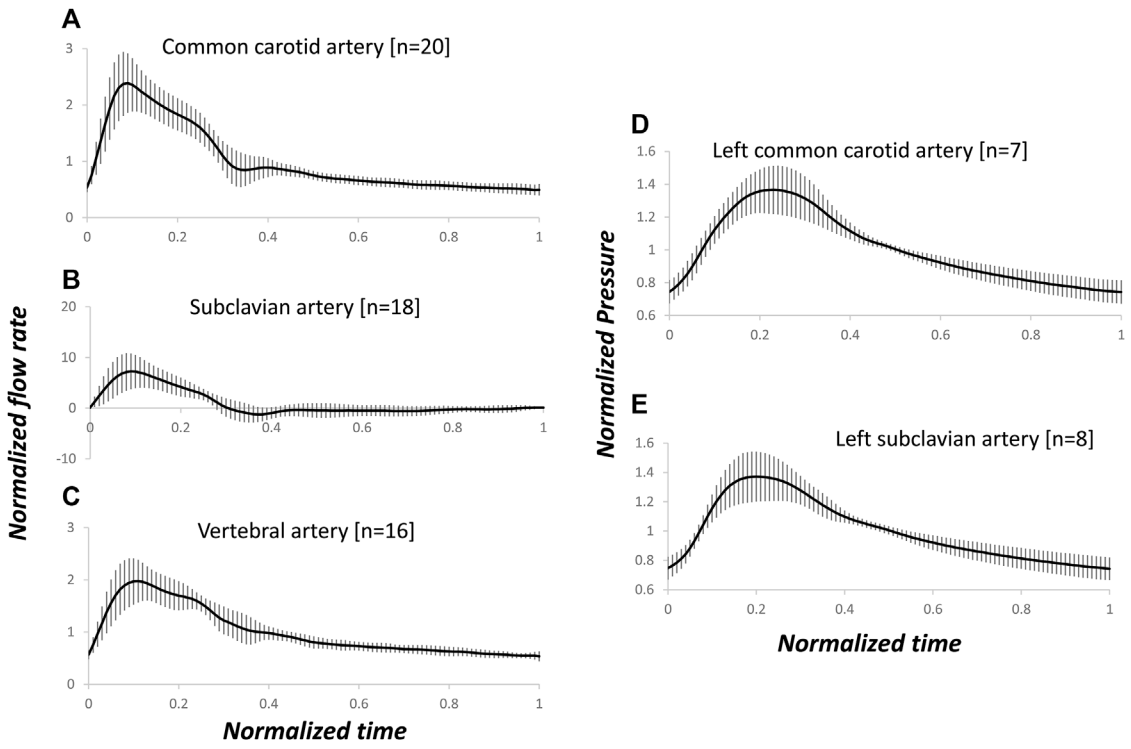

FIGURE 2
Arterial-specific, pre-operative, normalized flow rate and pre-deployment, normalized pressure waveforms. The flow rate and pressure were normalized by the corresponding mean of each waveform. Average and standard deviation of flow rates in common carotid **(A)**, subclavian **(B)** and vertebral **(C)** arteries, and pressure in left common carotid **(D)** and subclavian **(E)** arteries. The number of measured blood vessels, n, is also shown.

3 Results

3.1 Patient cohort

The analyzed population, 10 patients with age 64 ± 3 (range, 40–82) years and body surface area 2.0 ± 0.3 (range, 1.6–2.3) m^2, was 50% male. Four of ten patients underwent percutaneous transluminal repair only, either with TEVAR isolated to the descending thoracic aorta or TEVAR with a fenestrated branch to the left subclavian artery. The remaining six patients underwent a hybrid TEVAR procedure, which involved left subclavian artery coverage and a left common carotid artery-left subclavian artery bypass. The average heart rate for these patients was 63 ± 10 beats per minute (range, 47–76 beats per minute). The most common comorbidities for this set of subjects are listed in Table 1. The majority of subjects suffered hypertension (80%) and were active or former tobacco users (60%).

3.2 Flow rate and pressure data

No statistically significant difference of the mean flow rate was observed between the right and left sides. Therefore, the main results are presented on left and right arteries combined hereafter. The mean flow rates of the pre-operative dataset for common carotid artery (458 ± 139 mL/min), subclavian artery (185 ± 116 mL/min) and vertebral artery (90 ± 59 mL/min) were not statistically different from the means of the post-operative 1 week dataset (428 ± 147, 228 ± 116, and 92 ± 48 mL/min for common carotid, subclavian, and vertebral arteries, respectively). No significant differences of the mean pressures between left common carotid artery and subclavian artery of the pre-deployment (83 ± 11 vs. 85 ± 12 mmHg for common carotid artery and subclavian artery, respectively) or post-deployment (89 ± 13 vs. 88 ± 10 mmHg for common carotid and subclavian arteries, respectively) dataset were observed, neither between pre- and post-deployment mean pressures in each artery.

Figures 2A–C present the patient-specific normalized arterial flow rate waveforms for the pre-operative dataset. Notably, the subclavian artery showed systolic high peak and reversal flow at early diastole (Zhang et al., 2022), not present in the mono-phasic waveforms of common carotid artery and vertebral artery. Figures 2D, E present the normalized, pre-deployment pressure waveforms in the left common carotid artery and subclavian artery.

3.3 Patient-specific R_1, C, and R_2 parameters

When the patient-specific optimized R_1, C, and R_2 parameters were obtained from the WK3 simulation (as described in Section 2.3), the relative errors on the pressure waveform matching were small and 4 (3–4) %, 4 (3–6) %, and 3

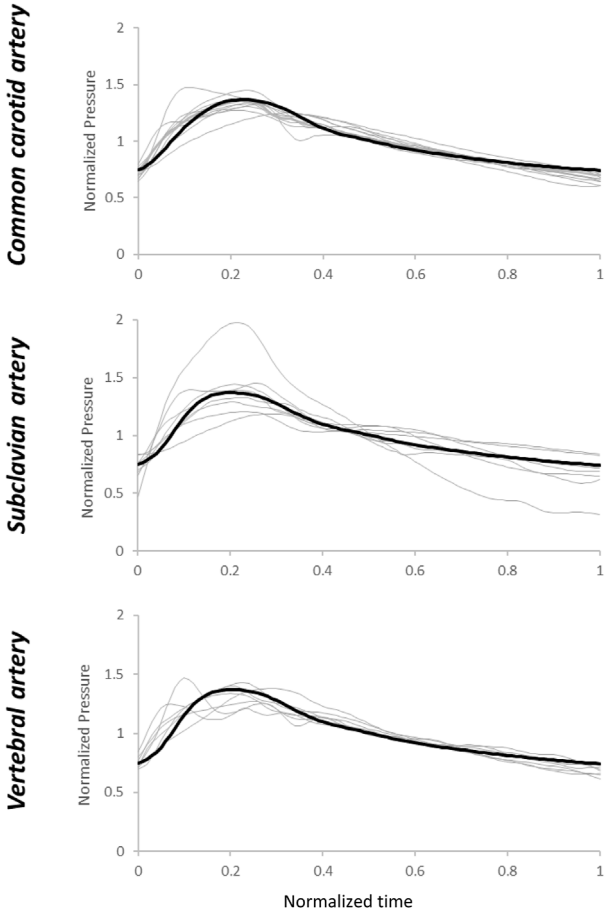

FIGURE 3
Estimated pressure waveforms using patient-specific, pre-operative input flow rate waveforms. The black line represents the average of the measured waveforms. Normalization has been performed post-simulation for comparison purposes.

(3–5) % for common carotid, subclavian, and vertebral arteries, respectively (example of pressure waveform matching and corresponding relative error in Supplementary Figure S3). The individual estimated and average of measured pressure waveforms are shown in Figure 3. The patient-specific non-normalized and normalized parameters of the WK3 model for each type of artery are shown in Table 2.

The normalized WK3 model parameters are also shown in Figure 4 as boxplots. The fairly large ranges of normalized resistances and compliance on each artery can be related to the apparent variation of the normalized waveform profiles among patients (Figure 2).

3.4 Sensitivity analysis

The Monte Carlo analysis provided information on the sensitivity of the pressure waveform to the variation of the R_1, C, and R_2 parameters for each type of artery. From the contour plots describing the output quality (minimized values) with different parameter combinations, we can see that the sensitivity of the pressure output to the WK3 parameters varies with different combinations of these parameters (Figure 5). For example, when C equals 0.5, the common carotid artery pressure is more sensitive to R_1 when R_1 is small ($R_1 < 0.05$), and less sensitive when R_1 is larger (Figure 5A). The combination of the medians of normalized R_1 and C parameters obtained from WK3 simulations for both common carotid artery and subclavian artery falls into the area of minimized value equal to 0.1, indicating good matching between expected and simulated pressure waveform (Figures 5A, B). The combination of the medians of normalized parameters for the vertebral artery falls into the area of minimized value equal to 0.3, suggesting the existence of alternative R_1 and C combinations which could better represent the pressure outlet waveform (Figure 5C). For all three arteries, the pressure output is more sensitive to variations of R_1 than C (smaller R_1 ranges than C ranges). Around the medians of the normalized parameters, the common carotid artery pressure is not sensitive to relatively small deviations of R_1 and C. The pressure of subclavian artery is even more tolerable to deviations of C from their corresponding medians (Figure 5B). The contour plot of vertebral artery is similar to that of carotid artery (Figure 5C), although with different axes' ranges. Around the medians of the normalized parameters, the vertebral artery pressure is more sensitive to small deviations of R_1 and C for smaller R_1 and larger C. Plots of the normalized pressure waveforms under some minimized values are shown for common carotid, subclavian, and vertebral arteries (Figures 5D–F). Note that the simulated pressure waveform may be different for the same minimized value although the overall differences are the same.

TABLE 2 Arterial-specific normalized and non-normalized R_1, C, and R_2 parameters of common carotid, subclavian, and vertebral arteries from the ten analyzed patients.

Artery	*Non-Normalized Results*			*Normalized Results*		
	R_1	R_2	C	Normalized R_1	Normalized R_2	Normalized C
	[mmHg sec/mL]	[mmHg sec/mL]	[mL/mmHg]			
Carotid arteries	1.14 (0.72; 1.85)	10.35 (7.79; 12.45)	0.04 (0.02; 0.06)	0.10 (0.07; 0.15)	0.90 (0.84; 0.93)	0.46 (0.33; 0.58)
Subclavian arteries	0.96 (0.81; 1.42)	33.10 (18.99; 68.19)	0.06 (0.03; 0.11)	0.03 (0.02; 0.04)	0.97 (0.96; 0.98)	1.91 (1.63; 2.26)
Vertebral arteries	8.93 (6.71; 20.33)	37.79 (21.47; 92.04)	0.01 (0.00; 0.02)	0.18 (0.08; 0.41)	0.82 (0.59; 0.92)	0.47 (0.32; 0.85)

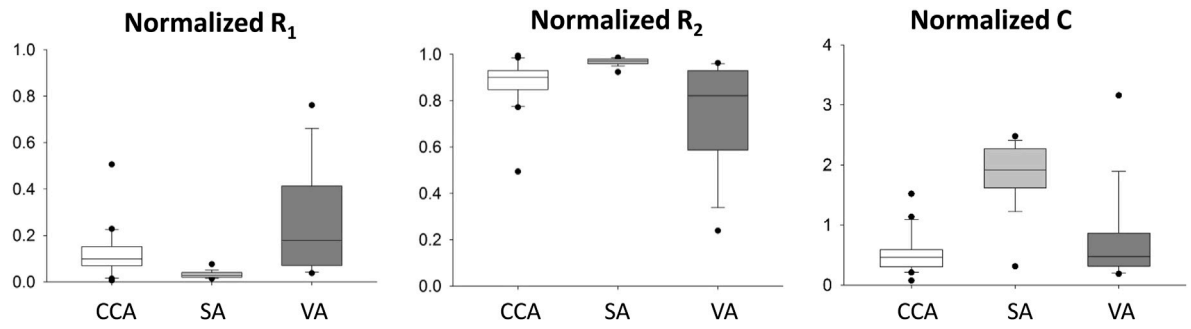

FIGURE 4
Distribution of patient-specific, normalized R_1, C, and R_2 parameters for common carotid (CCA), subclavian (SA), and vertebral (VA) arteries. In these plots, the minimum represents the data point with the lowest value above the first quartile minus 1.5 times of the interquartile range, and the maximum represents the data point with the highest value below the third quartile plus 1.5 times of the interquartile range. The lower vertical line connects the minimum to the first quartile; the upper vertical line connects the third quartile to the maximum.

3.5 Assessment of the normalized R_1, C, and R_2 parameters

First, the individual flow rate waveform was used as the testing input, and the average flow rate waveform of the testing dataset for each type of artery is reported in Figure 6. The estimated pressure showed fairly high tolerance to patient-specific inlet flow rate waveforms using the estimated R_1, C, and R_2 parameters. Relative errors of pressure output of the testing dataset were: 13 (9–15) % for common carotid artery, 16 (10–17) % for subclavian artery, and 12 (11–16) % for vertebral artery. The estimated pressure waveforms are shown in Figure 7. Compared with the average of the measured waveforms, only two subclavian arteries presented largely out-of-range estimated pressure waveforms at the systolic peaks. An example of the measured and corresponding estimated pressure waveforms is shown in Supplementary Figure S4. These resulted from flow rate waveforms with very high peak systolic and large reversal diastolic flow. Using the pressure waveform as input, the relative errors of estimated flow rate waveform matching were higher: 34 (29–43) % for common carotid artery, 94 (74–116) % for subclavian artery, 30 (23–31) % for vertebral artery (Figure 8). One example of the measured and estimated flow rate waveforms of a subclavian artery using the measured pressure waveform as the input is shown in Supplementary Figure S5.

4 Discussion

When physiological pressure in the flow field is desired, the Windkessel model is one of the most commonly used methods for specifying the outlet boundary condition if the pressure waveforms at the outlets are not available. Based on patient-specific flow rate and pressure waveform measurements, we obtained the R_1, C, and R_2 parameters of the three elements of the Windkessel model of aortic arch arteries in patients undergoing thoracic endovascular aortic repair. These parameters were then normalized. The normalized parameters can be used to estimate the patient-informed, non-normalized parameters when only limited but common clinical data of the cohort of these patients are available. We have demonstrated that a reasonable pressure waveform could be obtained using estimated parameters of the Windkessel model.

The patient-specific R_1, C, and R_2 values of the arch arteries obtained in our study are in the order of magnitude of most R_1, C, and R_2 values of previously published studies (Table 3) (Alimohammadi et al., 2014; van Bakel et al., 2018; Bonfanti et al., 2019; Pirola et al., 2019; Armour et al., 2022). Differences in ranges are related to flow rate and pressure averages as well as Windkessel model settings, such as the steady-state conditions on the definition of R_{tot}, which is not always imposed on the Windkessel model allowing larger ranges for the two, therefore independent, resistances. To the best of our knowledge, our study is the only one that uses artery-specific flow rate and pressure waveforms to identify the R_1, C, and R_2 values. Restricted by the setup in the operating room, recording pressure waveform requires additional dedicated devices, which might be the reason of only minimal and maximal pressure data were available in some studies (Alimohammadi et al., 2014; Bonfanti et al., 2019).

A few strategies have been applied to estimate the parameters of Windkessel model when the flow rate and/or pressure waveforms are not available. When the flow rate waveform was available, but the pressure waveform was not available, a method was proposed to scale a baseline pressure waveform from the literature using the measured brachial mean and pulse pressures (Romarowski et al., 2018). They have demonstrated that a multivariable optimization approach based on available patient-specific phase-contrast magnetic resonant imaging (PC-MRI) data of flow rate waveform, similar to our patient-specific estimation of R_1, C, and R_2, provides the most similar results to patient-specific PC-MRI-observed hemodynamics. When none of the waveforms was available, iterative CFD simulations of dissected aorta were performed to minimize the differences between invasively measured minimal and maximal pressure values and the respective simulated values at the outlets by tuning R_1, C, and R_2. This process is time consuming and can take 8 h (Alimohammadi et al., 2014). In a later report by the same group, a fixed ratio of R_1 to R_{tot} was set at the arch arteries, and the compliance attributed to all the outlets was distributed

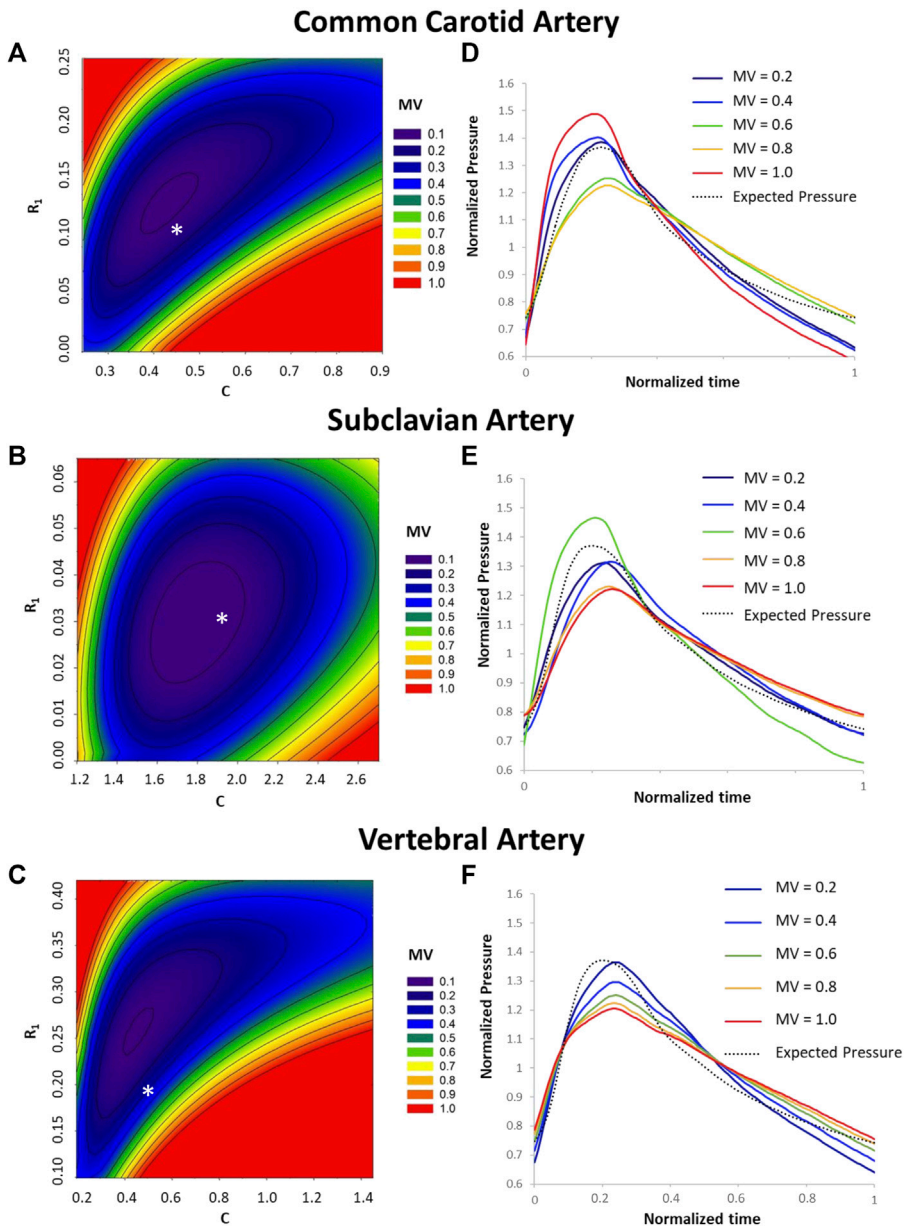

FIGURE 5
Sensitivity analysis of predicted pressure on variations of R_1, C, and R_2. Contour plot of minimized values (MV) under different combinations of the R_1 and C values are shown for common carotid artery **(A)**, subclavian artery **(B)**, and vertebral artery **(C)**. For reference, the medians of normalized R_1 and C values for each type of artery (Table 2) are shown by an * in A, B, and **(C)**. The minimized value is one of the outputs from the Optimization toolbox and quantifies the difference between the predicted and expected pressure values under a set of R_1, C, and R_2 values. A smaller minimized value corresponds to a better overall match between predicted and expected pressures. Plots of the normalized pressure waveforms under some minimized values are shown for common carotid artery **(D)**, subclavian artery **(E)** and vertebral artery **(F)**.

proportionally to the mean flow at each outlet (Bonfanti et al., 2019). Even though the pressure waveforms seem to be recorded, they were not used; instead, mean pressure values and MRI-derived flow spits at the branches were used to calibrate the Windkessel model parameters (Armour et al., 2022). R_1 has been estimated using the artery lumen area and pulse wave velocity, which is also related to the arterial radius (Pirola et al., 2017). Another notable example of deriving the Windkessel model parameters when only the geometry is available is to use impedance in the frequency domain (Xu et al., 2018). The flow rate waveform at the branch was obtained by scaling the inlet flow rate waveform per Murray's law of an empirical exponent in the range 2–3. Combining the pressure waveform obtained from the literature, Fourier transform of the flow rate and pressure waveforms was used to obtain the impedance. The parameters R_1, R_2, and C were calibrated to match the landmark values of the impedance. The advantage of this strategy is that an iterative optimization process is not needed once the flow rate and pressure waveforms are available. A recent study did not use any

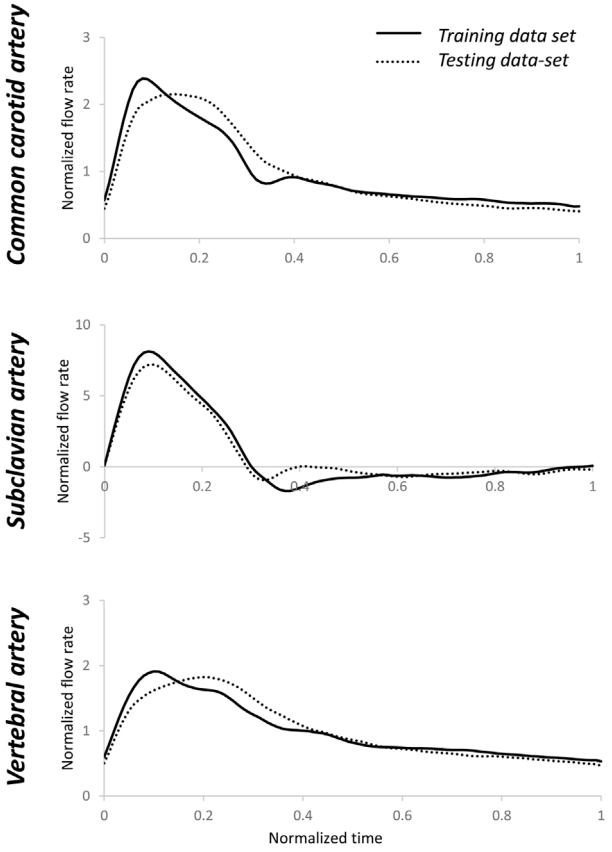

FIGURE 6
Averages of normalized testing flow rate waveforms for common carotid, subclavian, and vertebral arteries. The averages of the training flow rate waveforms that were used in section 2.3 are also shown. There were visible differences between the training and testing flow rate waveforms. Normalization was performed post-simulation for comparison purposes.

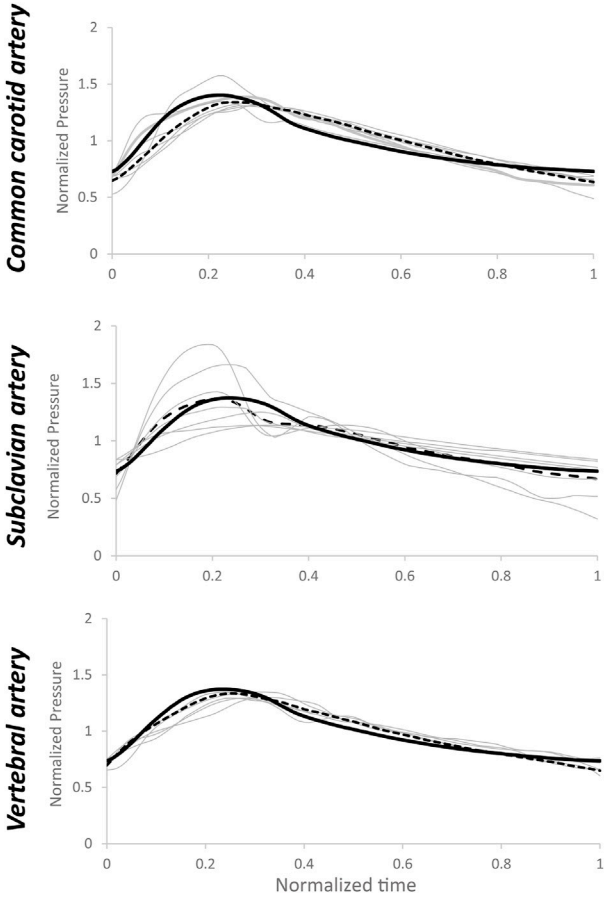

FIGURE 7
Estimated pressure waveforms (grey lines) using patient-specific inputs of flow rate data and estimated R_1, C, and R_2 values based on medians of arterial-specific parameters. Dotted lines represent the average of estimated pressure, while the black line represents the average value of measured pressure. Normalization has been performed post-simulation for comparison purposes.

patient-specific information to estimate the parameters (Fatma et al., 2022). Instead, a pressure waveform was obtained from the literature; a series of CFD simulations were performed to update the flow rate and pressure waveforms at the outlets, which were then used to optimize the Windkessel model parameters in Matlab. Different from our current study using the whole pressure waveform, the sum of the differences in maximal, mean, and minimal pressures between expected and computed values was used as the objective function in the genetic optimization algorithm.

We did not obtain flow and pressure data at the inlet of ascending aorta and the outlet of descending aorta. When patient-specific data are not available, a few approaches have been developed to apply these boundary conditions. It is common to use an MRI-measured flow rate waveform from the literature but interpolate to the heart rate of the patient (Alimohammadi et al., 2014). A more complicated way considers the compliance of the aorta by introducing a capacitor before the aortic inlet of the 3D model. The flow rate entering the 3D model is determined by a lumped parameter model that receives a flow rate waveform obtained from the literature but adopted by the patient-specific hemodynamic data (cardiac output, heart rate, and systolic-to-diastolic duration ratio extracted from Doppler ultrasonography) (Bonfanti et al., 2019). The distal outlets use WK3 models (van Bakel et al., 2018; Bonfanti et al., 2019).

A Windkessel model represents the impedance of the distal vascular bed to blood flow (Westerhof et al., 2009). Cardiac output has been estimated from invasively or non-invasively measured peripheral pressure pulses using a WK3 model at the ascending aorta (De Wilde et al., 2007; Bogert et al., 2010). In this method, only the systolic portion of the arterial pressure curve was used, avoiding the issue of reversed flow during the diastole. We also tested the normalized R_1, C, and R_2 parameters using the pressure waveform as input. The relative errors of estimated flow rate waveform matching were higher than the relative errors of estimated pressure waveform matching when the flow rate waveform was the input, especially for the subclavian artery, which might have a very high peak systolic flow and a high reversed flow during diastole. However, as shown in Figures 2D, E, the normalized pressure waveforms of the left common carotid artery and left subclavian artery are hardly distinguishable although the flow waveforms of these two arteries are clearly different (Figures 2A, B). Therefore, flow rate waveforms

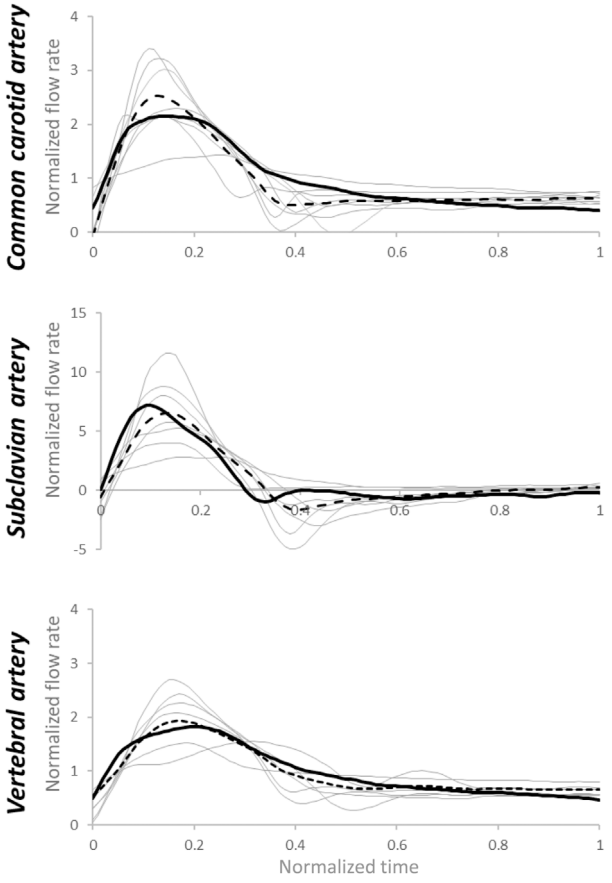

FIGURE 8
Estimated flow rate waveforms (grey lines) using patient-specific inputs of pressure data and estimated R_1, C, and R_2values based on medians of arterial-specific parameters. Dotted lines represent the average of estimated flow rates, while the black continuous line represents the average of measured flow rates. Normalization has been performed post-simulation for comparison purposes.

are more informative than the pressure waveforms. These flow rate waveforms with a higher complexity cannot be adequately reproduced in detail from pressure waveforms by a simple WK3 model. A more complex model, such as a four-element WK model with an inertance term, might be able to capture more details of the waveforms and reduce the errors between measured and predicted flow rates (Stergiopulos et al., 1999). However, since the inertance is difficult to be estimated (Westerhof et al., 2009), we recommend the use of pressure waveform as the input to the WK3 model.

We suggest that when measured mean flow rate is not available, it can be estimated from published flow rate-diameter relationships. Different power laws have described the relationship between flow rate and diameter at various arterial levels (Murray, 1926; Cheng et al., 2007; Cebral et al., 2008; Revellin et al., 2009; Chnafa et al., 2017). We investigated the flow rate and diameter relationships of the arch branch arteries in the TEVAR patients using ultrasound-measured flow rates and CTA-measured lumen diameters (Tricarico et al., 2020a). The power values of the best fit flow rate-diameter relationships are between 1.6 and 2.4. However, for subclavian artery, the R^2 of the flow rate-diameter fit was only 0.20 due to the wide scatter of the flow rate-diameter points. This is actually not accidental because these TEVAR patients commonly have a pathological subclavian artery with a wide arrange of diameter sizes. A larger study is needed to define the flow rate-diameter relationships according to the patient and arterial pathological characteristics.

The medians of normalized R1 and C values for each type of artery (Table 2) did not fall in the exact minimum of the minimized value space (indicated with an *, Figure 5). In the sensitivity analysis, the averages of the normalized pre-operative flow rate and pre-deployment pressure were used. To fully evaluate the sensitivity of the estimated pressure on the WK3 parameters, we intentionally used a wide range of combinations of random WK3 parameters. Therefore, it is not a surprise to see that the medians of the patient-specific normalized parameters did not locate at the position with a minimum minimized

TABLE 3 The R_1, C, and R_2 parameters extracted from the literature.

References	R_1 (mmHg sec/mL)	R_2 (mmHg sec/mL)	C (mL/mmHg)
Common carotid artery			
Alimohammadi et al. (2014)	0.110	14.590	0.085
Bonfanti et al. (2019)	0.728–1.793	12.271–30.221	0.017–0.065
Pirola et al. (2019)	2.176	34.884	0.040
Armour et al. (2022)	0.675–3.301	10.353–21.005	0.080–0.147
Subclavian artery			
Alimohammadi et al. (2014)	0.150	11.410	0.110
van Bakel et al. (2018)	1.388	17.108	0.020
Bonfanti et al. (2019)	0.556–1.038	9.379–20.406	0.029–0.052
Pirola et al. (2019)	0.900	21.005	0.080
Armour et al. (2022)	0.450–0.975	3.451–12.453	0.133–0.427
Vertebral artery			
van Bakel et al. (2018)	3.713	40.615	0.01

value for certain artery, such as vertebral artery. But even for vertebral artery, the medians of the normalized parameters were at a position with a small minimized value.

There are limitations to the current study. We have demonstrated that a physiological pressure waveform can be generated from input flow rate waveform. The relative errors are due to a multitude of factors, including the reduction of patient-specific waveform variability to one artery-specific waveform profile, the simplistic nature of the lumped element model, and the small patient dataset. The availability of other information, such as the flow rate waveform of the internal carotid artery considering the patient gender, age, and cardiovascular disease state (Durka et al., 2018), will help reduce the relative error. The assumption of pressure symmetry was theoretically supported by the arterial connection at the cerebrovascular level (Circle of Willis) and confirmed by the small pressure difference on bilateral measurements of one patient (data not shown). However, it may not be valid for pathological cases and/or patients with interrupted circle of Willis (observed in 4%–16% of analyzed populations (Fawcett and Blachford, 1905; Iqbal, 2013; Klimek-Piotrowska et al., 2016). Moreover, subclavian artery pressures were used for vertebral artery simulations. We believe that such differences are minor to the scope of the study. Negative systolic peaks (reversal flow rates) such as those that occur in cases of subclavian steal syndrome, cannot be reproduced with the provided R_1, C, and R_2 parameters. Last, differences generated by the proposed framework and other methodology for boundary condition estimation for CFD applications have not been investigated. For these reasons, this methodology is of consideration for first-degree approximation of clinically-relevant hemodynamic waveforms.

In conclusion, based on the analysis of flow rate and pressure measurements in ten patients undergoing TEVAR procedures, we provided the R_1, C, and R_2 values of the arch arteries, which can be used directly in other CFD simulations when there are not any patient-specific data available. We also propose a pipeline to estimate R_1, C, and R_2 parameters for common carotid, subclavian, and vertebral arteries, based on brachial pressure values and mean flow rate estimated from arterial diameter, in case of lacking flow rate and/or pressure waveforms. In our pipeline, approximation of resistances (R_1 and R_2) and compliance (C) of a WK3 model is realized by multiplying and dividing, respectively, the provided values of normalized resistances and compliances parameters to the value of R_{tot}. We also provide the variations of the WK3 model parameters, which can be used to quantify unavoidable uncertainties in hemodynamics when assumptions are made. This pilot study deserves future developments. A larger patient cohort is needed for a better population stratification (separating males from females, young from elderly, *etc.*). The flow rate-diameter relationship of these arteries, especially subclavian artery, can also be improved by larger studies.

Data availability statement

The raw data supporting the conclusions of this article will be made available by the authors, without undue reservation.

Ethics statement

The studies involving human participants were reviewed and approved by the University of Florida College of Medicine Institutional Review Board (Gainesville, FL). The patients/participants provided their written informed consent to participate in this study.

Author contributions

RT, SB, RT-S-T, YH: study conceptualization, methodology; RT, YH: data collection; RT, SA-B, RT-S-T, YH: data analysis; RT, YH: original draft; RT-S-T, SAB: review and editing; RT-S-T, SB: funding acquisition; Final approval of the article: RT, SB, YH, RT-S-T Overall responsibility: YH.

Funding

This study was supported by CyBHOR (Cyber-Physical System for the Hospital Operating Room), an Industry/University Cooperative Research Center (1266260) funded by the National Science Foundation of the United States.

Conflict of interest

The authors declare that the research was conducted in the absence of any commercial or financial relationships that could be construed as a potential conflict of interest.

Publisher's note

Supplementary material

The Supplementary Material for this article can be found online at: https://www.frontiersin.org/articles/10.3389/fbioe.2023.1127855/full#supplementary-material

References

Alimohammadi, M., Agu, O., Balabani, S., and Diaz-Zuccarini, V. (2014). Development of a patient-specific simulation tool to analyse aortic dissections: Assessment of mixed patient-specific flow and pressure boundary conditions. *Med. Eng. Phys.* 36 (3), 275–284. doi:10.1016/j.medengphy.2013.11.003

Armour, C. H., Guo, B., Saitta, S., Pirola, S., Liu, Y., Dong, Z., et al. (2022). Evaluation and verification of patient-specific modelling of type B aortic dissection. *Comput. Biol. Med.* 140, 105053. doi:10.1016/j.compbiomed.2021.105053

Bogert, L. W. J., Wesseling, K. H., Schraa, O., Van Lieshout, E. J., De Mol, B. A. J. M., Van Goudoever, J., et al. (2010). Pulse contour cardiac output derived from non-invasive arterial pressure in cardiovascular disease. *Anaesthesia* 65 (11), 1119–1125. doi:10.1111/j.1365-2044.2010.06511.x

Bonfanti, M., Franzetti, G., Maritati, G., Homer-Vanniasinkam, S., Balabani, S., and Díaz-Zuccarini, V. (2019). Patient-specific haemodynamic simulations of complex aortic dissections informed by commonly available clinical datasets. *Med. Eng. Phys.* 71, 45–55. doi:10.1016/j.medengphy.2019.06.012

Brown, J. A., Arnaoutakis, G. J., Szeto, W. Y., Serna-Gallegos, D., and Sultan, I. (2021). Endovascular repair of the aortic arch: State of the art. *J. Cardiac Surg.* 36 (11), 4292–4300. doi:10.1111/jocs.15920

Cebral, J. R., Castro, M. A., Putman, C. M., and Alperin, N. (2008). Flow-area relationship in internal carotid and vertebral arteries. *Physiol. Meas.* 29 (5), 585–594. doi:10.1088/0967-3334/29/5/005

Cheng, C., Helderman, F., Tempel, D., Segers, D., Hierck, B., Poelmann, R., et al. (2007). Large variations in absolute wall shear stress levels within one species and between species. *Atherosclerosis* 195 (2), 225–235. doi:10.1016/j.atherosclerosis.2006.11.019

Chnafa, C., Bouillot, P., Brina, O., Delattre, B. M. A., Vargas, M. I., Lovblad, K. O., et al. (2017). Vessel calibre and flow splitting relationships at the internal carotid artery terminal bifurcation. *Physiol. Meas.* 38 (11), 2044–2057. doi:10.1088/1361-6579/aa92bf

De Wilde, R. B. P., Schreuder, J. J., Van Den Berg, P. C. M., and Jansen, J. R. C. (2007). An evaluation of cardiac output by five arterial pulse contour techniques during cardiac surgery. *Anaesthesia* 62 (8), 760–768. doi:10.1111/j.1365-2044.2007.05135.x

Durka, M. J., Wong, I. H., Kallmes, D. F., Pasalic, D., Mut, F., Jagani, M., et al. (2018). A data-driven approach for addressing the lack of flow waveform data in studies of cerebral arterial flow in older adults. *Physiol. Meas.* 39 (1), 015006. doi:10.1088/1361-6579/aa9f46

Fatma, K., Carine, G.-C., Marine, G., Philippe, P., and Valérie, D. (2022). Numerical modeling of residual type B aortic dissection: Longitudinal analysis of favorable and unfavorable evolution. *Med. Biol. Eng. Comput.* 60 (3), 769–783. doi:10.1007/s11517-021-02480-1

Fawcett, E., and Blachford, J. V. (1905). The circle of willis: An examination of 700 specimens. *J. Anat. physiology* 40 (1), 63–70.

Gallo, D., Lefieux, A., Morganti, S., Veneziani, A., Reali, A., Auricchio, F., et al. (2016). A patient-specific follow up study of the impact of thoracic endovascular repair (TEVAR) on aortic anatomy and on post-operative hemodynamics. *Comput. Fluids* 141, 54–61. doi:10.1016/j.compfluid.2016.04.025

Garber, L., Khodaei, S., and Keshavarz-Motamed, Z. (2022). The critical role of lumped parameter models in patient-specific cardiovascular simulations. *Archives Comput. Methods Eng.* 29 (5), 2977–3000. doi:10.1007/s11831-021-09685-5

Gray, R. A., and Pathmanathan, P. (2018). Patient-specific cardiovascular computational modeling: Diversity of personalization and challenges. *J. Cardiovasc. Transl. Res.* 11 (2), 80–88. doi:10.1007/s12265-018-9792-2

He, Y., Northrup, H., Le, H., Cheung, A. K., Berceli, S. A., and Shiu, Y. T. (2022). Medical image-based computational fluid dynamics and fluid-structure interaction analysis in vascular diseases. *Front. Bioeng. Biotechnol.* 10, 855791. doi:10.3389/fbioe.2022.855791

Hu, J., Li, F., Qiu, P., Wu, X., Pu, H., Zhao, Z., et al. (2022). Clinical validation of the impact of branch stent extension on hemodynamics in ISF-TEVAR involving LSA reconstruction. *Front. Cardiovasc. Med.* 1448, 911934. doi:10.3389/fcvm.2022.911934

Iqbal, S. (2013). A comprehensive study of the anatomical variations of the circle of willis in adult human brains. *J. Clin. diagnostic Res. JCDR* 7 (11), 2423–2427. doi:10.7860/jcdr/2013/6580.3563

Klimek-Piotrowska, W., Rybicka, M., Wojnarska, A., Wojtowicz, A., Koziej, M., and Holda, M. K. (2016). A multitude of variations in the configuration of the circle of willis: An autopsy study. *Anatomical Sci. Int.* 91 (4), 325–333. doi:10.1007/s12565-015-0301-2

Lantz, B. M., Foerster, J. M., Link, D. P., and Holcroft, J. W. (1981). Regional distribution of cardiac output: Normal values in man determined by video dilution technique. *AJR. Am. J. Roentgenol.* 137 (5), 903–907. doi:10.2214/ajr.137.5.903

Madhavan, S., and Kemmerling, E. M. C. (2018). The effect of inlet and outlet boundary conditions in image-based CFD modeling of aortic flow. *Biomed. Eng. online* 17 (1), 66. doi:10.1186/s12938-018-0497-1

Morbiducci, U., Gallo, D., Massai, D., Consolo, F., Ponzini, R., Antiga, L., et al. (2010). Outflow conditions for image-based hemodynamic models of the carotid bifurcation: Implications for indicators of abnormal flow. *J. Biomech. Eng.* 132 (9), 091005. doi:10.1115/1.4001886

Morris, P. D., Narracott, A., von Tengg-Kobligk, H., Silva Soto, D. A., Hsiao, S., Lungu, A., et al. (2016). Computational fluid dynamics modelling in cardiovascular medicine. *Heart (British Card. Soc.* 102 (1), 18–28. doi:10.1136/heartjnl-2015-308044

Murray, C. D. (1926). The physiological principle of minimum work: I. The vascular system and the cost of blood volume. *Proc. Natl. Acad. Sci. U. S. A.* 12 (3), 207–214. doi:10.1073/pnas.12.3.207

Olufsen, M., Peskin, S., Kim, W., Pedersen, E., Nadim, A., and Larsen, J. (2000). Numerical simulation and experimental validation of blood flow in arteries with structured-tree outflow conditions. *Ann. Biomed. Eng.* 28, 1281–1299. doi:10.1114/1.1326031

Pecoraro, F., Lachat, M., Cayne, N. S., Pakeliani, D., Rancic, Z., Puippe, G., et al. (2017). Mid-term results of chimney and periscope grafts in supra-aortic branches in high risk patients. *Eur. J. Vasc. Endovascular Surg.* 54 (3), 295–302. doi:10.1016/j.ejvs.2017.06.014

Pirola, S., Cheng, Z., Jarral, O. A., O'Regan, D. P., Pepper, J. R., Athanasiou, T., et al. (2017). On the choice of outlet boundary conditions for patient-specific analysis of aortic flow using computational fluid dynamics. *J. Biomech.* 60, 15–21. doi:10.1016/j.jbiomech.2017.06.005

Pirola, S., Guo, B. L., Menichini, C., Saitta, S., Fu, W. G., Dong, Z. H., et al. (2019). 4-D flow MRI-based computational analysis of blood flow in patient-specific aortic dissection. *IEEE Trans. Biomed. Eng.* 66 (12), 3411–3419. doi:10.1109/Tbme.2019.2904885

Revellin, R., Rousset, F., Baud, D., and Bonjour, J. (2009). Extension of Murray's law using a non-Newtonian model of blood flow. *Theor. Biol. Med. Model.* 6 (1), 7. doi:10.1186/1742-4682-6-7

Romarowski, R. M., Lefieux, A., Morganti, S., Veneziani, A., and Auricchio, F. (2018). Patient-specific CFD modelling in the thoracic aorta with PC-MRI–based boundary conditions: A least-square three-element windkessel approach. *Int. J. Numer. Method Biomed. Eng.* 34 (11), e3134. doi:10.1002/cnm.3134

Scali, S. T., Chang, C. K., Feezor, R. J., Hess, P. J., Jr., Beaver, T. M., Martin, T. D., et al. (2012). Preoperative prediction of mortality within 1 year after elective thoracic endovascular aortic aneurysm repair. *J. Vasc. Surg.* 56 (5), 1266–1273. doi:10.1016/j.jvs.2012.04.018

Sengupta, S., Hamady, M., and Xu, X.-Y. (2022). Haemodynamic analysis of branched endografts for complex aortic arch repair. *Bioengineering* 9 (2), 45. doi:10.3390/bioengineering9020045

Sesso, H. D., Stampfer, M. J., Rosner, B., Hennekens, C. H., Gaziano, J. M., Manson, J. E., et al. (2000). Systolic and diastolic blood pressure, pulse pressure, and mean arterial pressure as predictors of cardiovascular disease risk in men. *Hypertension* 36(5): 801–807. doi:10.1161/01.HYP.36.5.801

Stergiopulos, N., Westerhof, B. E., and Westerhof, N. (1999). Total arterial inertance as the fourth element of the windkessel model. *Am. J. Physiol.* 276 (1-2), H81–H88. doi:10.1152/ajpheart.1999.276.1.h81

Stergiopulos, N., Young, D. F., and Rogge, T. R. (1992). Computer simulation of arterial flow with applications to arterial and aortic stenoses. *J. Biomechanics* 25 (12), 1477–1488. doi:10.1016/0021-9290(92)90060-E

Taylor, C. A., Hughes, T. J., and Zarins, C. K. (1998). Finite element modeling of three-dimensional pulsatile flow in the abdominal aorta: Relevance to atherosclerosis. *Ann. Biomed. Eng.* 26 (6), 975–987. doi:10.1114/1.140

Tricarico, R., Laquian, L., Allen, M. B., Tran-Son-Tay, R., Scali, S. T., Lee, T. C., et al. (2020a). Temporal analysis of arch artery diameter and flow rate in patients undergoing aortic arch endograft procedures. *Physiol. Meas.* 41 (3), 035004. doi:10.1088/1361-6579/ab7b40

Tricarico, R., Tran-Son-Tay, R., Laquian, L., Scali, S. T., Lee, T. C., Beck, A. W., et al. (2020b). Haemodynamics of different configurations of a left subclavian artery stent graft for thoracic endovascular aortic repair. *Eur. J. Vasc. Endovasc. Surg.* 59 (1), 7–15. doi:10.1016/j.ejvs.2019.06.028

van Bakel, T. M., Arthurs, C. J., van Herwaarden, J. A., Moll, F. L., Eagle, K. A., Patel, H. J., et al. (2018). A computational analysis of different endograft designs for Zone 0 aortic arch repair. *Eur. J. Cardiothorac. Surg.* 54 (2), 389–396. doi:10.1093/ejcts/ezy068

Voskresensky, I., Scali, S. T., Feezor, R. J., Fatima, J., Giles, K. A., Tricarico, R., et al. (2017). Outcomes of thoracic endovascular aortic repair using aortic arch chimney stents in high-risk patients. *J. Vasc. Surg.* 66 (1), 9–20.e3. doi:10.1016/j.jvs.2016.11.063

Wallen, T. J., Bavaria, J. E., and Vallabhajosyula, P. (2018). Hybrid arch surgery challenges other forms of arch treatment. *J. Cardiovasc. Surg.* 59, 554–558. doi:10.23736/s0021-9509.18.10516-7

Westerhof, N., Lankhaar, J. W., and Westerhof, B. E. (2009). The arterial Windkessel. *Med. Biol. Eng. Comput.* 47 (2), 131–141. doi:10.1007/s11517-008-0359-2

Xu, H., Piccinelli, M., Leshnower, B. G., Lefieux, A., Taylor, W. R., and Veneziani, A. (2018). Coupled morphological–hemodynamic computational analysis of type B aortic dissection: A longitudinal study. *Ann. Biomed. Eng.* 46 (7), 927–939. doi:10.1007/s10439-018-2012-z

Zhang, J., Wang, L., Chen, Y., Wang, S., Xing, Y., and Cui, L. (2022). Color Doppler ultrasonography for the evaluation of subclavian artery stenosis. *Front. Neurology* 13, 804039. doi:10.3389/fneur.2022.804039

frontiers | Frontiers in Bioengineering and Biotechnology

TYPE Original Research
PUBLISHED 30 March 2023
DOI 10.3389/fbioe.2023.1103905

OPEN ACCESS

EDITED BY
Amirhossein Arzani,
The University of Utah, United States

REVIEWED BY
Leonid Goubergrits,
Charité Universitätsmedizin Berlin, Germany
Giuseppe De Nisco,
Polytechnic University of Turin, Italy

*CORRESPONDENCE
Yun Shi,
shi.yun@zs-hospital.sh.cn
Shengzhang Wang,
szwang@fudan.edu.cn

†These authors have contributed equally to this work

SPECIALTY SECTION
This article was submitted to Biomechanics, a section of the journal Frontiers in Bioengineering and Biotechnology

RECEIVED 21 November 2022
ACCEPTED 15 March 2023
PUBLISHED 30 March 2023

CITATION
Peng C, He W, Huang X, Ma J, Yuan T, Shi Y and Wang S (2023), The study on the impact of AAA wall motion on the hemodynamics based on 4D CT image data.
Front. Bioeng. Biotechnol. 11:1103905.
doi: 10.3389/fbioe.2023.1103905

The study on the impact of AAA wall motion on the hemodynamics based on 4D CT image data

Chen Peng[1†], Wei He[2†], Xingsheng Huang[3], Jun Ma[3], Tong Yuan[2], Yun Shi[2,4,5]* and Shengzhang Wang[1,6,7]*

[1]Department of Aeronautics and Astronautics, Institute of Biomechanics, Fudan University, Shanghai, China, [2]Department of Vascular Surgery, Zhongshan Hospital, Fudan University, Shanghai, China, [3]Shenzhen Raysight Intelligent Medical Technology Corporation, Shenzhen, Guangdong, China, [4]Institute of Vascular Surgery, Fudan University, Shanghai, China, [5]National Clinical Research Center for Interventional Medicine, Fudan University, Shanghai, China, [6]Institute of Biomedical Engineering Technology, Academy for Engineering and Technology, Fudan University, Shanghai, China, [7]Yiwu Research Institute, Fudan University, Yiwu, Zhejiang, China

Purpose: To analyze the effect of the physiological deformation of the vessel wall on the hemodynamics in the abdominal aortic aneurysm (AAA), this paper compared the hemodynamics in AAA based on the moving boundary (MB) simulation and the rigid wall (RW) simulation.

Method: Patient-specific models were reconstructed to generate mesh based on four-dimensional computed tomography angiography (4D CT) data. The dynamic mesh technique was used to achieve deformation of the vessel wall, surface mesh and volume mesh of the fluid domain were successively remeshed at each time step. Besides, another rigid wall simulation was performed. Hemodynamics obtained from these two simulations were compared.

Results: Flow field and wall shear stress (WSS) distribution are similar. When using the moving boundary method (MBM), mean time-averaged wall shear stress (TAWSS) is lower, mean oscillatory shear index (OSI) and mean relative residence time (RRT) are higher. When using the 10th and 20th percentile values for TAWSS and 80th and 90th percentile values for RRT, the ratios of areas with low TAWSS, high OSI and high RRT to the entire vessel wall are higher than those assuming the vessel as rigid. In addition, one overlapping region of low TAWSS, high OSI and high RRT by using the MBM is consistent with the location of thrombus obtained from the follow-up imaging data.

Conclusion: The hemodynamics results by using the MBM reflect a higher blood retention effect. This paper presents a potential tool to assess the risk of intraluminal thrombus (ILT) formation based on the MBM.

KEYWORDS

four-dimensional computed tomography angiography (4D CT), computational fluid dynamics (CFD), moving boundary method (MBM), abdominal aortic aneurysm (AAA), intraluminal thrombus (ILT)

1 Introduction

Abdominal aortic aneurysm (AAA) is defined as permanent and irreversible local dilation of the abdominal aorta (Chen et al., 2014). At present, the pathogenesis of AAAs is not completely clear, but a large number of studies have shown that the occurrence of AAAs is related to degeneration in the media layer of the aorta (Salman et al., 2019). Loss of elastin, deposition and remodeling of collagen fibers lead to the formation and growth of AAAs (Gasser et al., 2006; Valentin et al., 2013). AAAs rupture when the stress acting on the vessel wall exceeds the strength of the vessel wall, and the mortality rate for ruptured AAAs patients can be 65%–85% in China (Canchi et al., 2018).

Recent studies have shown that hemodynamics plays an important role in the progression of AAAs (Tanweer et al., 2014; Boyd et al., 2016). The non-invasive method for hemodynamics simulation, which combined the clinical medical image data with the computational fluid dynamics (CFD) is needed. Notably, the hemodynamics of AAA is considered to be a key factor in the formation and growth of intraluminal thrombosis (ILT), for the ILT could prevent rupture of the AAA by reducing the stresses acting directly on the vessel wall (Arzani et al., 2014), and the prediction of ILT formation in AAAs is important.

Zambrano et al. (2016) and Gharahi et al. (2015) collected CT image data from different cases and analyzed the relationship between wall shear stress (WSS) and thrombus aggregation and AAAs growth based on the computational fluid dynamics (CFD) simulation. Doyle et al. followed up a patient for up to 2.5 years and analyzed the hemodynamics of AAA, they found that long-term low time average wall shear stress (TAWSS) promoted the AAA wall dilation and thrombus formation (Doyle et al., 2014). Suh et al. (2011a) and Suh et al. (2011b) simulated the progression of AAAs, calculated the oscillatory shear index (OSI) and particle retention time (PRT) to quantify the recirculation effects of blood in aneurysms, and found that platelet activation induced by stagnant blood flow can induce thrombus formation. However, these studies assumed the aorta as rigid and ignored the *in vivo* deformation of aorta (which is caused by blood flow, peri-arterial tissue, respiration, heartbeat, etc.)

To overcome the above shortcomings, the fluid-structure interaction (FSI) method was applied in the hemodynamics simulation in AAAs. Bluestein et al. (2009) used the FSI method to simulate the hemodynamics of two patients, with varied AAA geometries and ILT structures and compare the AAA rupture risk. Ong et al. (2018) presented evidence for one type of flow dynamics within the aneurysm sac. They performed CTA image-based patient-specific FSI modeling of three cases of aortic aneurysms, their study showed that the formation of the ILT is associated with vortex, and recirculation flow within the aneurysm sac may lead to the formation of ILT. Drewe et al. (2017) aimed to perform FSI simulations of an ideal AAA geometry to determine the influence of proximal neck and iliac bifurcation angles on AAA wall stress. They found that AAAs can expand and rupture in areas with low WSS, and large iliac bifurcation angles imply less likelihood of thrombus development.

In the above studies, the settings of the material parameters of the vessel wall were based on the previous studies that have been used by Shi et al. (2021), Shang et al. (2013), and Di Martino et al. (2001), respectively. However, for patients of different ages, the material parameters such as the thickness and elastic modulus in different regions (such as ascending aorta and abdominal aorta) are quite different (Xiong et al., 2011). Therefore, hemodynamics simulated by the FSI method may differ from physiological conditions.

The moving boundary method (MBM) can reflect the effect of the *in vivo* deformation of aorta on the hemodynamics without setting specific material parameters. Some researchers have used this method to calculate vessel wall stiffness, WSS, etc. They demonstrated the potential of MBM for clinical application (Piccinelli et al., 2013; Farzaneh et al., 2019). Danilov et al. (2017) and Lozovskiy et al. (2018) developed a stabilized finite element method and performed simulation based on 4D-CT and collected hemodynamics results of the left/right ventricle, the method of these studies is proven to be stable and robust when deformation is large, and without needing interpolation. Their work extended the application of 4D CT in hemodynamics studies. However, using the MBM to assess ILT formation risk in AAA was rarely been reported.

In this study, 4D CT image data of one AAA patient at 21 cardiac instants in one cardiac cycle were used to reconstruct the patient-specific instantaneous geometries. After mesh generation, the coordinates of each node at different time-instants were calculated. Then the user-defined function (UDF) in Fluent was used to control the movement of each node for achieving the deformation of the vessel wall, surface mesh and volume mesh of fluid domain at each time step were remeshed. After that, the hemodynamics in AAA using the MBM combined with CFD simulation were obtained.

In addition, we also reconstructed the rigid model and performed the rigid wall simulation, the size of the rigid model was set to be equal to the mean size of the models at 21-time points. We analyzed the differences between the hemodynamics results by performing these two simulations. In general, this paper explored the influence of *in vivo* deformation of the abdominal aorta on hemodynamics and evaluated the formation risk of thrombosis in AAA.

2 Materials and methods

2.1 Image data acquisition

A 61-year-old male patient with a maximum AAA diameter of 32.99 mm was selected for the acquisition of 4D CT image data. All imaging data were obtained from the Department of Vascular Surgery, Zhongshan Hospital, Fudan University, and permission were obtained from the ethics committee.

The CTA data was obtained by using a 320-row multidetector CT scanner (Aquilion ONE, Toshiba Medical Systems, Irvine, CA, United States). The view field ranged from at least 5 cm proximal to the celiac trunk and the femoral artery bifurcation for each set of CTA data, as shown in Figure 1A.

When scanning the patient, the slice thickness of CTA was 1.0 mm, and the patient was scanned every 5% cardiac cycle, as

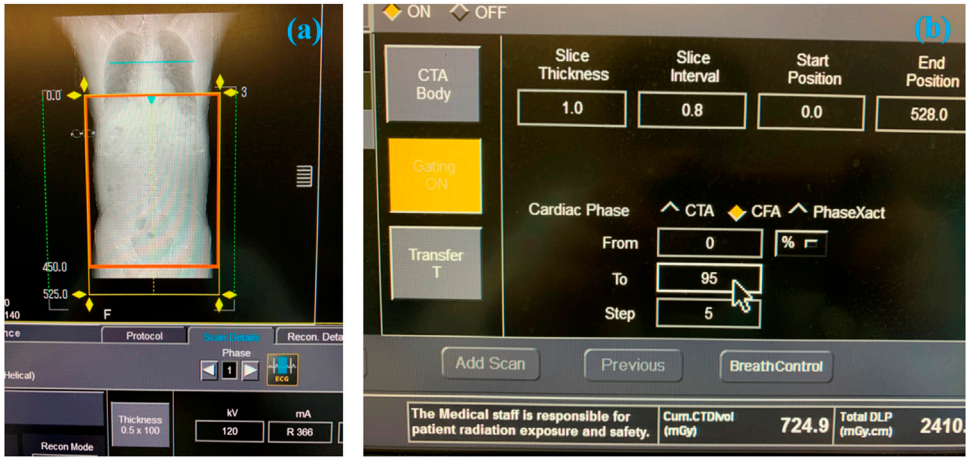

FIGURE 1
The process of obtaining the 4D CT image data. **(A)** The selected scanning range of AAA. **(B)** Parameters setting during scanning.

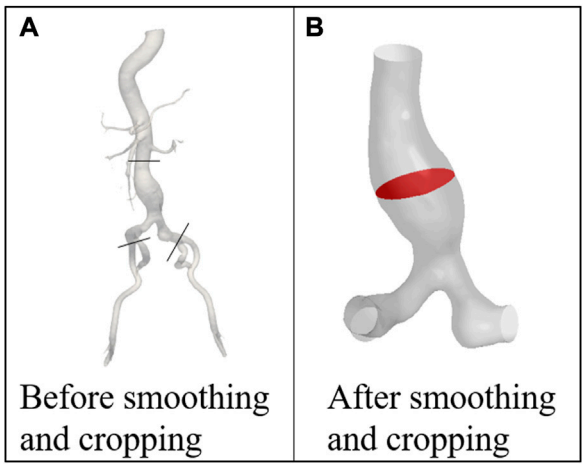

FIGURE 2
Models of the patient **(A)** before and **(B)** after smoothing and cropping. POI is marked with red color.

shown in Figure 1B. The original in-plane resolution matrixes were 512 × 512 (the spatial resolution was 1.12 mm × 1.12 mm), which was low and cannot be used for model reconstruction. By using the B-Spline algorithm, which can be used to interpolate and sharpen the original image data, we obtained the 1024 × 1024 (the spatial resolution was 0.56 mm × 0.56 mm) in-plane resolution matrixes at 21-time points. The deep learning method based on the U-net technique was used for automatic segmentation and to suppress the signal corresponding to the tissue surrounding the aorta (Supported by Shenzhen Rui Xin Intelligent Medical Technology Co., Ltd.). The image of 21 time-instants in one cardiac cycle was stored in DICOM format, which was described in Module 1 of the Supplementary Material.

TABLE 1 The difference between the maximum and minimum POI area in one cardiac cycle before and after smoothing.

	$A_{max}(mm^2)$	$A_{min}(mm^2)$	Ratio (%)
Before smoothing	910.32	887.32	2.53
After smoothing	901.43	876.37	2.78
Difference (%)	0.98	1.23	0.25

2.2 Model reconstruction

The 4D CT image data was imported into the open-source software: SimVascular 2018 (Stanford University, United States) for preliminary smoothing (Lan et al., 2018), as shown in Figure 2A. Since AAAs tend to occur in the infrarenal (IR) abdominal aorta region (Amirbekian et al., 2009), the abdominal aorta and iliac arteries under the renal arteries was selected as the computational domain (Qiu et al., 2018), as shown in Figure 2B. Models at 21-time points were smoothed and cropped in Geomagic Studio 2013 (Raindrop Corporation, United States). The model of the first phase was chosen as the model of the initial moment when using the MBM.

The surface with the largest cross-sectional area perpendicular to the centerline of the AAA was chosen as the plane of interest (POI), which was marked with red color, as shown in Figure 2B.

The effect of the area change ratio due to vessel wall deformation (Eq. 1), the differences between the maximum and minimum areas of POI before and after smoothing (Eq. 2), and the difference in the area change ratio due to the smoothing treatment (Eq. 3) were calculated to check whether the errors caused by smoothing affect the accuracy of simulation and the results are summarized in Table 1.

$$\text{ratio} = \frac{A_{max} - A_{min}}{A_{max}} * 100\% \quad (1)$$

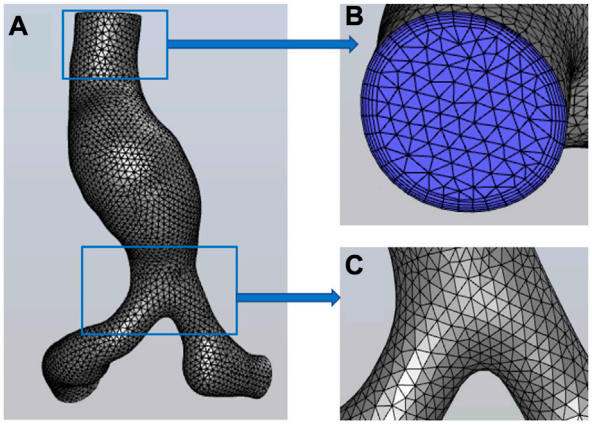

FIGURE 3
Mesh information. **(A)** the global mesh information, **(B)** the mesh at the inlet and the boundary layer mesh, **(C)** the mesh at the bifurcation of iliac arteries.

$$\text{Difference}_A = \frac{A_{original} - A_{smoothed}}{A_{original}} * 100\% \quad (2)$$

$$\text{Difference}_{ratio} = \left\{\text{ratio}_{smoothed}(max.min) - \text{ratio}_{original}(max, min)\right\} * 100\% \quad (3)$$

where the A_{max}, A_{min} represent the maximum and minimum areas of POI, $A_{original}$ and $A_{smoothed}$ represent the POI area values of the original and the smoothed models.

As shown in Table 1, the differences between the maximum and minimum areas of POI are both less than 3%. The differences in area change are less than 1.5% and the area change rate is only 0.25% before and after smoothing. It indicates that the error caused by the smooth operation is small and would not affect the numerical simulation accuracy.

2.3 Mesh generation

The tetrahedral mesh was generated in HyperMesh 14.0 (Altair, United States). The global mesh size of the model at the initial time was set as 0.3 cm, and the wedge-shaped boundary layer mesh was generated in the fluid domain. After the grid independence test (the process is described in Module 2 of the Supplementary Material), the mesh of the initial model is shown in Figure 3. The node number and elements of the fluid mesh, and node number of the surface mesh of the vessel wall at the initial moment were 30,750, 89,022, and 4,917, respectively.

Global mesh densification was performed on models at other 20 time-instants, with the mesh size set as 0.02 cm. The node number of the vessel wall for the subsequent 20 time-instants was 144,650 ± 10,025 (mean ± SD). The process was described detailed in Module 3 of the Supplementary Material. Note that these surface meshes are not involved in computational fluid dynamics simulations, but only store coordinate information of surface nodes at different time points.

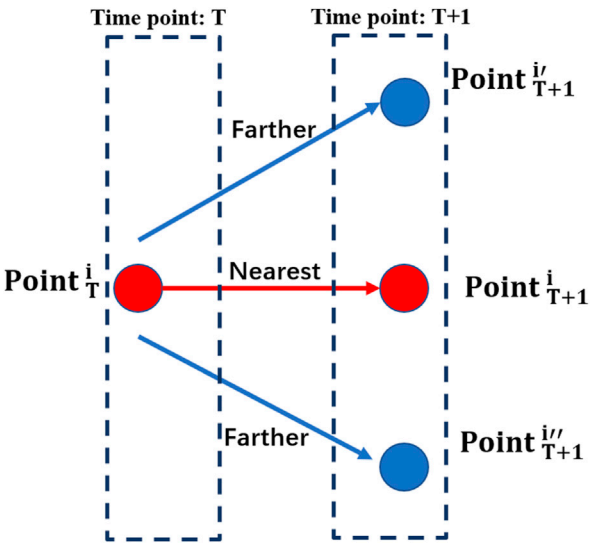

FIGURE 4
Node displacement calculation between two adjacent time-instants.

2.4 Calculation of nodal displacement at different time-instants

As described in Section 2.3, the surface mesh of models was densified at the next 20 time-instants to provide more optional nodes for the grid nodes to move from the current time point to the next (as shown in Figure 4), which can ensure that each node at the current moment could move to its nearest node at the next moment.

As shown in Figure 4, $Point_T^i$ represents the ith node at the current moment, $Point_{T+1,}^i$ $Point_{T+1}^{i'}$ and $Point_{T+1}^{i''}$ represent the nodes that could be chosen for $Point_T^i$ at next moment. It is obvious that $Point_{T+1}^i$ is closest to $Point_T^i$, and other nodes which are not selected will be deleted.

Matlab R2020b (MathWorks, United States) was used to calculate the coordinate information of nodes at different time-instants. As shown in Figure 4, the nodes' displacements at different time-instants were calculated according to the minimum distance principle (Vahidkhah et al., 2017). For two adjacent time-instants, the distance of different nodes and the coordinates at the next moment were expressed as Eqs 4, 5:

$$d^i = min\left|\mathbf{X}_{T+1}^N - \mathbf{X}_T^i\right| \quad (4)$$

$$\begin{cases} x_{T+1}^i = x_T^i + dx^i \\ y_{T+1}^i = y_T^i + dy^i \\ z_{T+1}^i = z_T^i + dz^i \end{cases} \quad (5)$$

where $\mathbf{X}_T^i$ represents the coordinate of the ith node at time point T, $\mathbf{X}_{T+1}^N$ represent the coordinates of all nodes at the moment T+1, and d^i represents the minimum distance value between the ith grid node at moment T and all grid nodes at time phase T+1. Eq. 5 indicates that the coordinates of the next moment in three directions are obtained by adding the coordinates of the current moment to the corresponding distances moved in each of the three directions.

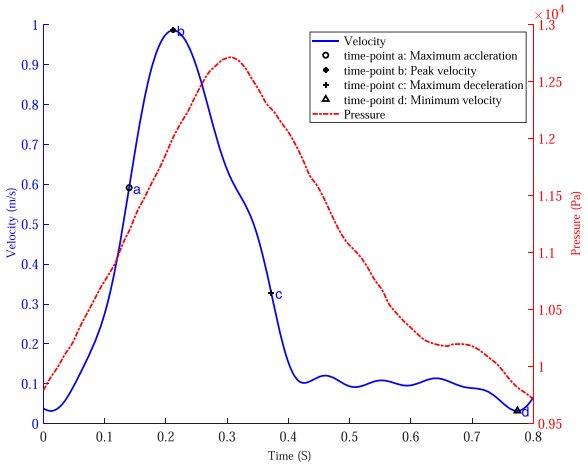

FIGURE 5
The velocity waveform at the inlet of the abdominal aorta and the pressure waveform at the outlets of the iliac arteries and four specific time points were marked on the velocity profile.

Afterward, the grid node coordinates were interpolated for 21 time-instants [so that the Courant number was less than 1 (Khalafvand et al., 2017)], and 80-time steps were generated for each interval of the 21-time-instants, resulting in 1600 (=20 0180) time steps for one cardiac cycle of computation. The generated coordinate files of each grid node were invoked by the user-defined function (UDF) in Fluent 2019 R3 (ANSYS, Canonsburg, PA, United States). To avoid non-convergence of calculation due to excessive mesh distortion, a remeshing technique was used in Fluent to regenerate new surface mesh as well as meshes in the fluid domain when the maximum mesh skewness was greater than 0.7, the process of performing the MB simulation was also described detailed in Module 4 of the Supplementary Material.

2.5 Boundary conditions

The boundary conditions were all derived from another volunteer, the velocity waveform at the inlet of the IR aorta was measured by 2D phase-contrast magnetic resonance imaging (PC-MRI, and the magnetic resonance System is 3.0 T Discovery MR750, GE Medical System, United States) technique, and the pressure waveform at the outlets of the iliac arteries was measured by the pressure guidewire, as shown in Figure 5.

The UDF function in Fluent was used to specify the velocity of each node at the aorta inlet and specify the pressure waveform of the iliac artery outlets.

Based on the maximum velocity waveform at the inlet of the IR aorta, four specific time points were selected to analyze the hemodynamics in AAA: time of maximum acceleration of velocity (time-point a, 0.14 s), time of maximum deceleration of velocity (time-point c, 0.37 s), time of maximum velocity (time-point b, 0.21 s) and time of minimum velocity (time-point d, 0.78 s).

2.6 Solving settings

In the numerical simulation based on MBM, Arbitrary Lagrangian-Eulerian (ALE) method was used to solve the continuity and momentum equation, as shown in Eqs 6, 7:

$$\frac{\partial}{\partial t}\int_V \rho dV + \int_S \rho\left(\vec{v} - \vec{v}_b\right)\cdot\vec{n}dS = 0 \quad (6)$$

$$\int_V \frac{\partial}{\partial t}\left(\rho\vec{v}\right)dV + \int_S \rho\left(\vec{v} - \vec{v}_b\right)\cdot\vec{n}dS = -\int_S p\mathbf{I}\cdot\vec{n}dS + \int_S \boldsymbol{\tau}\cdot\vec{n}dS \quad (7)$$

where $\vec{v}$ represents the velocity vector of blood, $\vec{v}_b$ represents the velocity vector of the grid nodes of the vessel wall, $\vec{n}$ represents the normal vector, ρ represents the blood density, p represents the pressure, $\mathbf{I}$ represents the unit tensor, and $\boldsymbol{\tau}$ represents the viscous stress tensor. When assuming the vessel wall as rigid, the continuity equation and the Navier-Stokes equation could be simplified into Eqs 8, 9:

$$\frac{\partial}{\partial t}\int_V \rho dV + \int_S \rho\left(\vec{v}\right)\cdot\vec{n}dS = 0 \quad (8)$$

$$\int_V \frac{\partial}{\partial t}\left(\rho\vec{v}\right)dV + \int_S \rho\left(\vec{v}\right)\cdot\vec{n}dS = -\int_S p\mathbf{I}\cdot\vec{n}dS + \int_S \boldsymbol{\tau}\cdot\vec{n}dS \quad (9)$$

The blood was assumed as an incompressible Newtonian fluid with a density of 1060 kg/m^3, and the viscosity was set as 0.0035Pa · s. No-slip and no-flux conditions were applied at the vessel wall. The pressure implicit with the splitting of operators (PISO) algorithm was used to solve the continuity and the momentum equations to obtain velocity and pressure. The second-order upwind scheme was used to discrete the control equations at grid nodes of the fluid domain (Khalafvand et al., 2017), the laminar solver was used for the Reynolds number is small and fluid in the lumen of the vessel does not develop turbulence (Peng et al., 2022). The cardiac cycle was0.8 s, the time step size was 0.0005 s, at the end of each time step, the surface mesh and the volume mesh of the fluid domain were remeshed. The residual of continuity and velocity in three directions were set as 1e-4 and each time step is iterated 50 times to ensure that

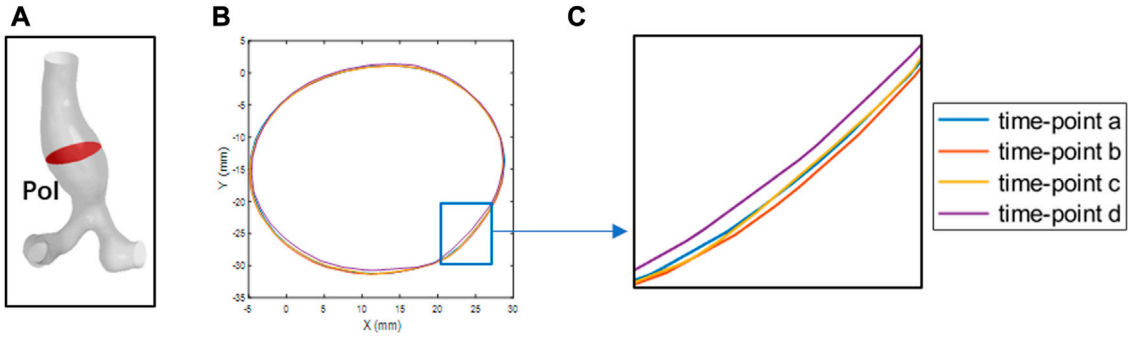

FIGURE 6
The POI at four-time points is outlined. **(A)** the POI of abdominal aortic aneurysms. **(B)** the boundary contours at the four specific time points **(C)** local magnification of **(B)**.

the results converge. The numerical simulations were performed for cardiac cycles. The workstation AMD Ryzen Thread Ripper 3990X 64-core Processor was used. The time requirement was 36 h when performing the MB simulation and 4 h when performing the RW simulation, it should be noted that the size of the rigid model was set to be equal to the mean size of the models at 21-time points so that the comparison could more clearly demonstrate the effects of wall deformation. The TAWSS, OSI, and relative residence time (RRT) were calculated and compared based on the WSS obtained from the simulation results, as shown in Eq. 10 (Peng et al., 2022):

$$\begin{cases} \mathrm{TAWSS} = \dfrac{1}{T}\displaystyle\int |wss| dt \\ \mathrm{OSI} = \dfrac{1}{2}\left\{1 - \dfrac{\left|\displaystyle\int_0^T wss dt\right|}{\displaystyle\int_0^t |wss| dt}\right\} \\ \mathrm{RRT} = \dfrac{1}{\dfrac{1}{T}\left|\displaystyle\int_0^T wss dt\right|} \end{cases} \tag{10}$$

3 Results

The simulation results of the last cardiac cycle obtained using both methods were post-processed in CFD Post 2019 R3 (ANSYS, Canonsburg, PA, United States).

3.1 Verification of boundary continuity

To verify the boundary continuity when performing the MB simulation, the coordinate information of the POI nodes at four specific time points (time point a to time point d) was derived. Matlab was used to extract the edge contours of the POI for observation, as shown in Figure 6. As shown in Figures 6B, C, the POI contours are continuous and undistorted at four specific time points, indicating that the vessel wall of the abdominal aorta is free of malformed bulges and depressions during the simulation, in line with the requirements for computational quality.

In addition, the overall deformation information was shown in AAA.gif of the Supplementary Material.

3.2 Flow fields

The results of the flow field simulated by these two methods are visualized in Figure 7. We narrowed the range of color bar (change the upper limit of velocity into 0–0.5 m/s, i.e.) to make the colors of streamlines more distinct. Overall, the spatial distributions of the flow field at the four specific time points are consistent.

As the blood flow accelerated from time point a to time point b, the flow field within the vessel is stable and no vortex is formed. During this process, the viscous force effect of the blood has little influence on the flow field, while the effect of inertial force is relatively significant. The acceleration effect of the flow is greater than the convective deceleration effect caused by the widening of the aorta. The flow field manifests itself mainly as an ordered laminar flow. However, during the deceleration of the blood at the inlet, the viscous effect of the blood is obvious. The flow state of the blood in AAA gradually becomes disordered. At time point d, the blood flow attaches to the bulging aneurysm wall, and the vortex and secondary flow form within the AAA. In the area near the AAA wall, the recirculation region appears.

3.3 Wall shear stress

The distribution of the WSS on the vessel wall is shown in Figure 8. Overall, the WSS distributions at the four corresponding specific time points are consistent using these two methods. In the region close to the POI, the low WSS values (20th percentile values) appear and indicated a weak shearing effect of blood on the AAA. As the inlet blood velocity increases, the high WSS values(80th percentile values) gradually appears at the bifurcation of the abdominal aorta and iliac arteries, which may lead to endothelial cell damage and destruction (Liu et al., 2014). As the inlet blood flow velocity decreases, the regions with high WSS values gradually reduce. At time point c, the high WSS based on MB simulation is concentrated in the abdominal aortic

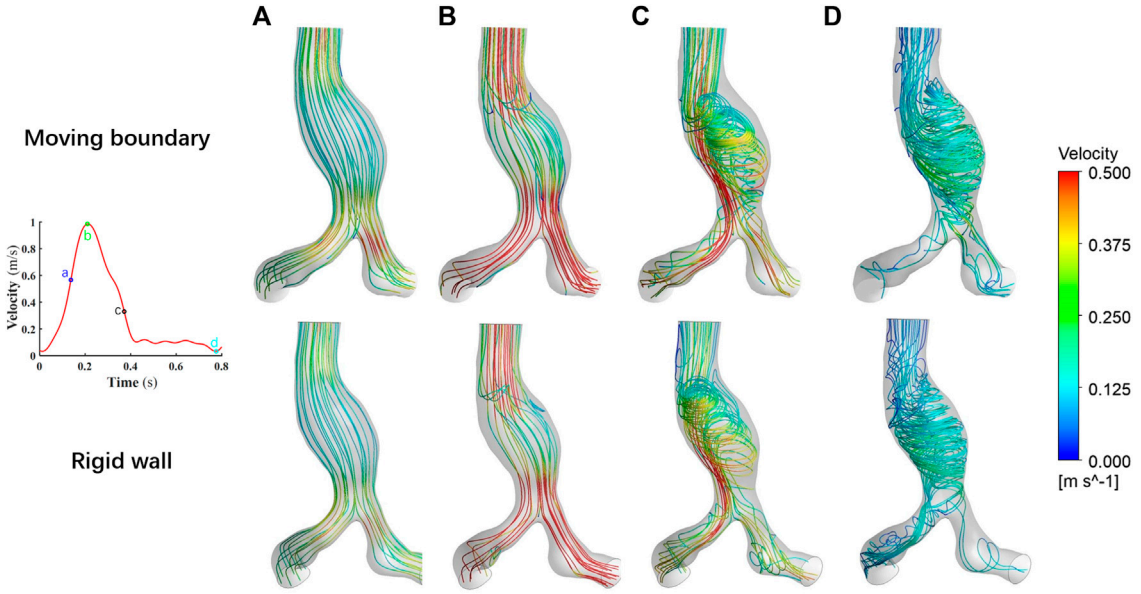

FIGURE 7
Comparison of the flow fields at four specific time points by using two methods. **(A)** Time moment of maximum acceleration of velocity, **(B)** Time moment of maximum velocity, **(C)** Time moment of maximum deceleration of velocity and **(D)** Time moment of minimum velocity.

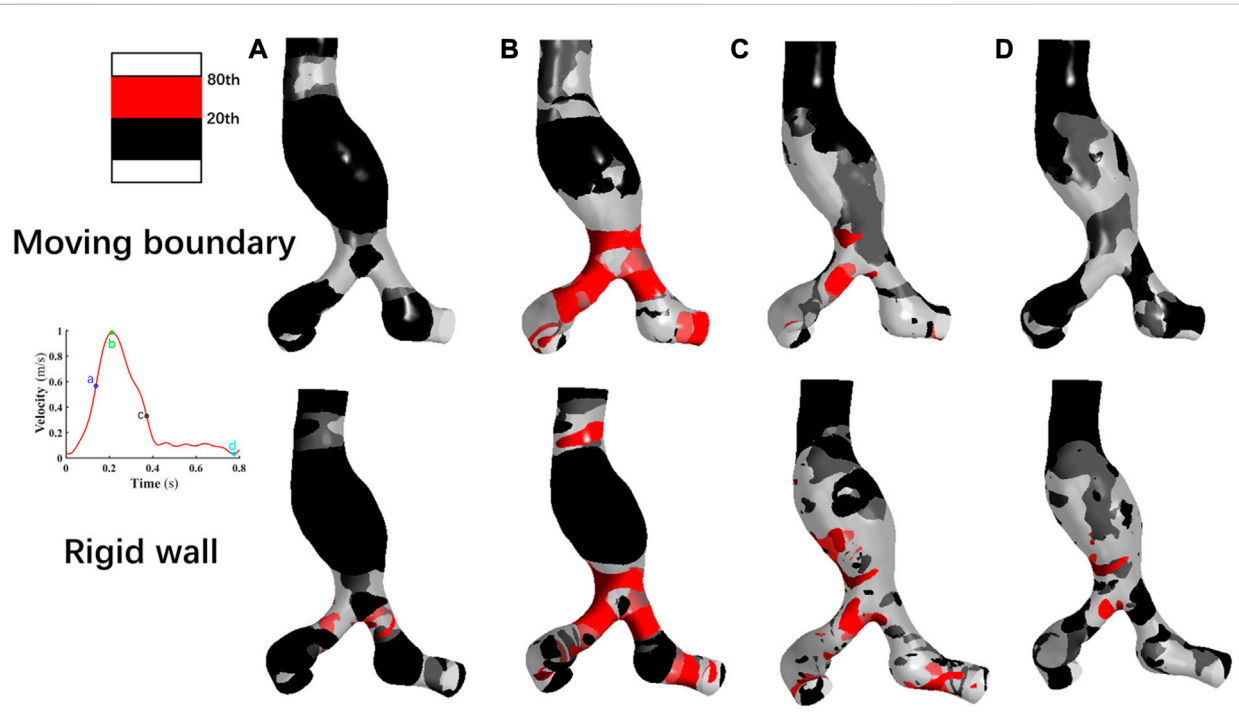

FIGURE 8
Comparison of the wall shear stress distribution at four specific time points by using two methods. **(A)**: Time moment of maximum acceleration of velocity, **(B)**: Time moment of maximum velocity, **(C)**: Time moment of maximum deceleration of velocity and **(D)**: Time moment of minimum velocity.

bifurcation and the iliac arteries, and the high WSS obtained by assuming the vessel wall as rigid occurs in these locations as well as in localized regions of the aneurysm wall. At time point d, most of the WSS values obtained by using the MBM were lower than 20th percentile values. When performing the RW simulation, a small number of high WSS values still appears in parts of the

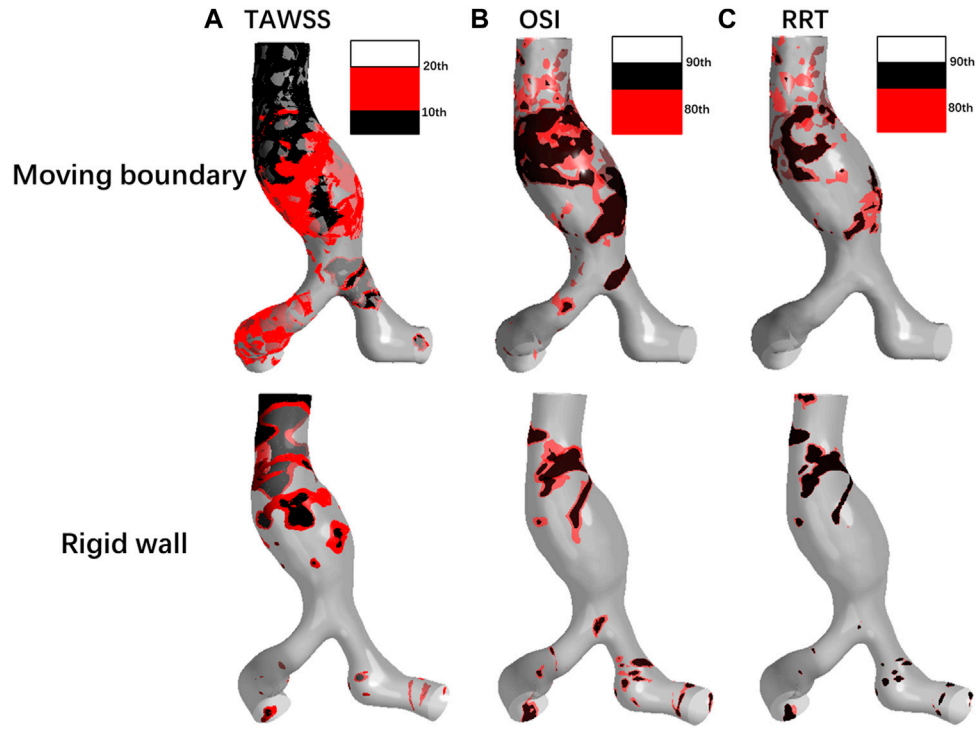

FIGURE 9
Comparison of **(A)** TAWSS, **(B)** OSI, and **(C)** RRT distributions by using two methods.

abdominal aortic bifurcation, in the region where the iliac arteries join the AAA and in the distal neck of the AAA.

Notably, the distribution region of high WSS obtained by assuming the vessel wall as rigid is more extensive than that of MBM. The ratios of high WSS area to the whole vessel wall are 0.54%, 14.33%, 8.57%, and 0.15% at four specific time points by using MBM, and these ratios obtained from the RW simulation are 2.41%, 28.62%, 15.32%, and 2.18%, respectively.

3.4 TAWSS, OSI, RRT

TAWSS, OSI and RRT were calculated using Eq. 10 to assess the blood stagnation status and to further predict the risk of thrombus formation.

As shown in Figure 9A, the TAWSS simulated by using MBM fluctuates slightly throughout the vessel wall, with distribution in most regions of less than 10th percentile values. In contrast, the TAWSS obtained from the RW simulation differs significantly across regions. Low TAWSS is mainly concentrated on the aneurysm wall, but in the downstream region of the AAA neck and the iliac artery bifurcation, TAWSS are larger than 20th values.

Besides, the ratios of the area where the low TAWSS located to the entire vessel wall area are 37.85% and 11.71% by using MBM and assuming the vessel wall as rigid, respectively.

As shown in Figure 9B, the high OSI (larger than 80th percentile values) obtained by using MB simulation is distributed over most of the aneurysm wall, AAA's neck, and the iliac arteries, whereas the higher OSI obtained by assuming rigid vessel wall is relatively concentrated in the proximal neck of AAA and the bifurcation of the iliac arteries. In general, the region of high OSI obtained by using MBM is more widespread. Moreover, the percentage of the area with high OSI to the whole vessel wall obtained by using MBM is higher than that obtained from the RW simulation (69.32% and 21.72%, respectively). It implies the direction of the shear stress has a faster change frequency when using the MBM, since the direction of the blood velocity near the aorta changes constantly when applying the no-slip conditions. High OSI produces an oscillatory effect on the vessel wall and reflects a higher risk of damage to aorta compared to the rigid wall.

RRT obtained using the two methods are shown in Figure 9C. The high RRT (larger than 80th percentile values) obtained using MBM are distributed in the region of the proximal neck of AAA and adjacent to the POI. For results obtained from RW simulation, high RRT are relatively concentrated in the region of aneurysms' proximal neck. High RRT obtained by using MBM spreads more widely on the vessel wall than those obtained from RW simulation. The ratios of the area of the region where high RRT locates to the whole vessel wall area obtained from these two methods are 24.12% and 6.37%, respectively. Moreover, the distribution regions with high RRT are generally consistent with the distribution regions of high OSI.

Furthermore, when comparing the flow field and RRT distribution obtained by using MBM, high RRT tends to be concentrated near the recirculation region of the

TABLE 2 Comparison of the mean value of three parameters on the vessel wall by using two methods.

Methods	TAWSS(Pa)	OSI	RRT(Pa^{-1})
Moving Boundary	1.35	0.26	2.24
Rigid wall	1.65	0.15	1.98

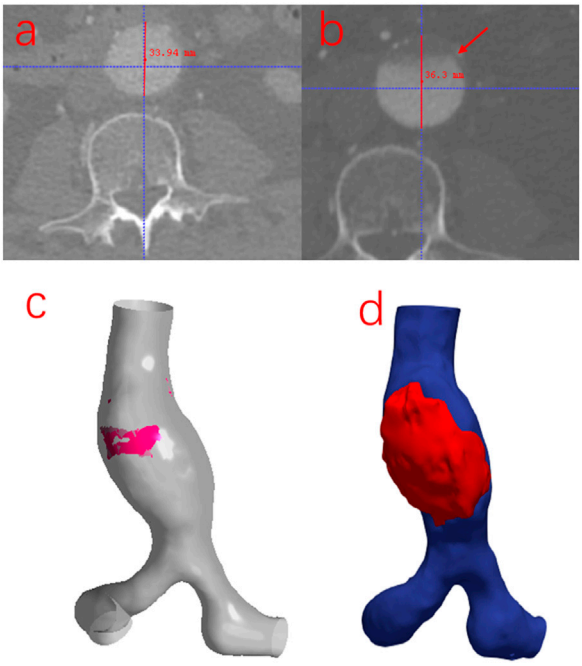

FIGURE 10
(A) The initial cross-section of the maximum diameter of AAA. **(B)** The cross-section of the maximum diameter of AAA was obtained from the follow-up image data. **(C)** The overlapping region of low TAWSS, high OSI, and high RRT obtained from the MB simulation: is marked in red color. **(D)** The location of the thrombus was reconstructed from the follow-up image data.

flow field. When the blood flow velocity is low and the streamline takes on a spiral shape, the substances in the blood may stagnate for a long time near the aneurysm wall. Leukocytes, platelets and other substances may have stronger migration and adhesion effects in such a hemodynamic environment. This suggests that the effect of prolonged high RRT and recirculation region may increase the risk of thrombosis near the AAA.

To quantitatively compare the TAWSS, OSI, and RRT of each case simulated by these two methods, the mean values of the three parameters on the vessel wall were calculated, which are summarized in Table 2. The mean value of TAWSS obtained from the RW simulation is 18.18% higher, while the mean OSI value and mean RRT value are 42.31% and 11.61% lower than the results obtained from the MB simulation, respectively. It may indicate that results obtained from the MBM reflect a higher effect of blood stagnation.

3.5 The comparison between the MB simulation results and follow-up image data

To investigate whether there is an association between the simulation results when using the MBM and the risk of thrombosis and the growth of AAA, the follow-up data from the same patient was collected after 2 years in this study. As shown in Figure 10, the ILT forms in the region near the POI but the maximum diameter of the AAA increases by only 2.36 mm. There is an overlapping region with low TAWSS, high OSI and high RRT when using the MBM. (Notably, there is no overlapping region when performing the RW simulation.) Although the ratio of the area of the overlapping region to the entire vessel wall is only 4.92%, the thrombus almost occupies the anterior wall of the aneurysm near the overlapping region after 2 years. It indicates a higher likelihood of thrombosis when all three factors (low TAWSS, high OSI and high RRT) mentioned above work together, and the ILT may prevent the further growth of AAA.

4 Discussion

The combination of CFD and medical imaging data has been widely used for hemodynamics simulation in the clinical assessment of cardiovascular disease in patients. However, the traditional RW simulation does not consider the deformation of the vessel wall, which does not conform to the actual physiological conditions (Vergara et al., 2017). Although the FSI method can simulate the interaction of the vessel wall with blood, the results may differ from the real hemodynamics due to the difficulty of obtaining patient-specific vessel wall material parameters quickly and accurately (Shamloo et al., 2020).

In this paper, the 21-time phases models in one cardiac cycle of one AAA patient were reconstructed and the mesh was generated. After that, the spatial coordinates of each mesh node at different time-instants were calculated, then the UDF was used to control the displacement of each node without considering the material properties of the vessel wall. We also assumed the vessel wall as rigid for another simulation, and the differences between the results of these two simulations were compared to analyze the influence of the vessel wall deformation on hemodynamics in AAA.

The spatial distribution of flow fields simulated by using the MBM and assuming the vessel wall as rigid is similar. Notably, at time-point d, the flow field near the AAA is very disorganized with a large number of vortexes. It may indicate that aneurysm formation may have undesirable effects on laminar flow patterns of blood, which has the potential to damage the endothelial cells (Hsu et al., 2001).

The TAWSS was calculated as the tangential component of traction on the vessel wall through the cardiac cycle. Zambrano et al. (2016) found that the ILT accumulated in areas of low TAWSS. Once ILT initially gathered near the lumen wall, it enhanced the effect of aggregation of new thrombus at regions where TAWSS was low. In regions of low TAWSS, red blood cells, platelets, and other substances within the blood were transported in a smaller area near the wall, which indicated a stronger stagnation effect in the near-wall region (Bilgi and Atalık, 2019).

The results of OSI, and RRT distribution on the vessel wall are quite different using these two methods. We speculated these parameters related to WSS strongly correlated with the deformation of the vessel wall, according to Gallo et al., we selected the 10th and 20th percentile for TAWSS, 80th and 90th values for OSI and RRT, which can provide a more complete and proper analysis of the difference between the rigid wall and moving boundary simulations.

High OSI indicates that during the movement of the blood vessel wall, the direction changes the frequency of the shear stress near the vessel wall is fast. This may be because when using the no-slip boundary condition, the blood flow velocity at the near-wall surface changes continuously during the cardiac cycle, as does the vessel wall. High OSI damage to the endothelial cells is serious. Prolonged high OSI may exacerbate changes in the orientation of endothelial cell alignment in these regions (Bilgi and Atalık, 2019), cause inflammation in the intima layer of the vessel wall and degeneration of elastin in the media layer of aorta, and lead to an increased risk of thrombus formation (Meng et al., 2014; Soldozy et al., 2019).

Besides, the high/low OSI is usually accompanied by high/low RRT (Liu et al., 2021). Since high OSI causes damage to the endothelium, which is accompanied by the release of clotting factors, platelets, lipids and other substances, the blood undergoes a deposition effect and adheres to the vessel wall (Chen et al., 2018). A high RRT indicates the blood stays in the low-velocity recirculation region of the aneurysm for a long time, prolongs the contact time between blood substances and the low-velocity layer near the vessel wall, and creates conditions for the migration and aggregation of platelet white blood cells and coagulation factors into the aneurysm wall (Zambrano et al., 2016; Kelsey et al., 2017; Yeow and Leo, 2018).

In general, the ILT formation is associated with low TAWSS, high OSI, and high RRT, which may cause damage to the intima of the vessel wall in AAA, promote the inflammatory reaction on the vessel wall, and release the coagulation factors and lead to the formation and growth of thrombus.

The diameter of the maximum cross-section of AAA only increases by 2.36 mm, while there is a large amount of ILT formation in the anterior wall of the AAA. The ILT effectively reduced wall stress in AAAs, which provided AAAs from rupture (Lindquist Liljeqvist et al., 2020). A large strain constitutive relation into patient-specific AAA simulations and demonstrated that the presence of the ILT can significantly reduce wall stress by up to 38% (Piechota-Polanczyk et al., 2015). Our results also suggested to some extent that ILT could prevent AAA growth and rupture, so that the diameter of the AAA does not increase significantly.

There is still considerable potential for improvements in this study. We used the physiological data of the previous volunteer as the boundary conditions for numerical simulation. The PCMRI and ultrasound techniques can be used to set individual boundary conditions for each patient (Peng et al., 2022). In addition, due to the limitation of spatial resolution, it is difficult to accurately obtain the deformation information of the visceral arteries. Therefore, this paper only selected the AAA and iliac arteries to reconstruct patient-specific models. The visceral arteries (such as the renal arteries, and the trunk celiac artery) also needed to be considered in the numerical simulation. Assuming the blood as Newtonian fluid and ignored its viscoelastic was also the limitation of our study. We also consider collecting 4D CT image data of more AAA patients for MB simulation.

In general, this paper has demonstrated the feasibility of applying the MBM to the hemodynamics simulation within AAA. It could describe the vessel wall deformation, and provide effective reference information for clinical evaluation of the ILT formation risk in AAA.

5 Conclusion

We simulated the hemodynamics in this paper under the *in vivo* deformation of vessel wall based on 4D CT medical image data, proved the feasibility of the MBM, and compared the simulation results with those assuming a rigid vessel wall. The overall spatial distributions of flow fields and WSS by using the MBM and assuming a rigid vessel wall are similar. Besides, deformation of the vessel wall leads to the lower TAWSS, higher OSI and higher RRT distributions. The simulation results obtained from the MBM reflect a higher blood stagnation effect in AAA. And the combination of the MBM with 4D CT image data may provide a new idea for the clinical prediction of the ILT formation risk in AAA.

Data availability statement

The original contributions presented in the study are included in the article/Supplementary Material, further inquiries can be directed to the corresponding authors.

Ethics statement

The studies involving human participants were reviewed and approved by the Ethics committee of Zhongshan Hospital, Fudan University. The patients/participants provided their written informed consent to participate in this study. Written informed consent was obtained from the individual(s) for the publication of any potentially identifiable images or data included in this article.

Author contributions

CP, WH, YS, and SW: conception and design of the work, numerical simulation, data processine, manusctipt writing. XH, JM, and TY: medical image data collection and post-process. All authors analysis and interpretation of data, critical review of manuscript for important intellectual content, and final approval of manuscript.

Funding

This study is supported by the National Natural Science Foundation of China (No. 32071310).

Conflict of interest

Authors XH and JM were employed by the company Shenzhen Raysight Intelligent Medical Technology Corporation.

The remaining authors declare that the research was conducted in the absence of any commercial or financial relationships that could be construed as a potential conflict of interest.

Publisher's note

All claims expressed in this article are solely those of the authors and do not necessarily represent those of their affiliated organizations, or those of the publisher, the editors and the reviewers. Any product that may be evaluated in this article, or claim that may be made by its manufacturer, is not guaranteed or endorsed by the publisher.

Supplementary material

The Supplementary Material for this article can be found online at: https://www.frontiersin.org/articles/10.3389/fbioe.2023.1103905/full#supplementary-material

References

Amirbekian, S., Long, R. C., Jr, Consolini, M. A., Suo, J., Willett, N. J., Fielden, S. W., et al. (2009). *In vivo* assessment of blood flow patterns in abdominal aorta of mice with mri: Implications for aaa localization. *Am. J. Physiology-Heart Circulatory Physiology* 297, H1290–H1295. doi:10.1152/ajpheart.00889.2008

Arzani, A., Suh, G.-Y., Dalman, R. L., and Shadden, S. C. (2014). A longitudinal comparison of hemodynamics and intraluminal thrombus deposition in abdominal aortic aneurysms. *Am. J. Physiology-Heart Circulatory Physiology* 307, H1786–H1795. doi:10.1152/ajpheart.00461.2014

Bilgi, C., and Atalık, K. (2019). Numerical investigation of the effects of blood rheology and wall elasticity in abdominal aortic aneurysm under pulsatile flow conditions. *Biorheology* 56, 51–71. doi:10.3233/bir-180202

Bluestein, D., Dumont, K., De Beule, M., Ricotta, J., Impellizzeri, P., Verhegghe, B., et al. (2009). Intraluminal thrombus and risk of rupture in patient specific abdominal aortic aneurysm–fsi modelling. *Comput. methods biomechanics Biomed. Eng.* 12, 73–81. doi:10.1080/10255840802176396

Boyd, A. J., Kuhn, D. C., Lozowy, R. J., and Kulbisky, G. P. (2016). Low wall shear stress predominates at sites of abdominal aortic aneurysm rupture. *J. Vasc. Surg.* 63, 1613–1619. doi:10.1016/j.jvs.2015.01.040

Canchi, T., Saxena, A., Ng, E., Pwee, E. C., and Narayanan, S. (2018). Application of fluid–structure interaction methods to estimate the mechanics of rupture in Asian abdominal aortic aneurysms. *Bionanoscience* 8, 1035–1044. doi:10.1007/s12668-018-0554-z

Chen, C.-Y., Antón, R., Hung, M.-y., Menon, P., Finol, E. A., and Pekkan, K. (2014). Effects of intraluminal thrombus on patient-specific abdominal aortic aneurysm hemodynamics via stereoscopic particle image velocity and computational fluid dynamics modeling. *J. biomechanical Eng.* 136, 031001. doi:10.1115/1.4026160

Chen, H., Bi, Y., Ju, S., Gu, L., Zhu, X., and Han, X. (2018). Hemodynamics and pathology of an enlarging abdominal aortic aneurysm model in rabbits. *PloS one* 13, e0205366. doi:10.1371/journal.pone.0205366

Danilov, A., Lozovskiy, A., Olshanskii, M., and Vassilevski, Y. (2017). A finite element method for the Navier-Stokes equations in moving domain with application to hemodynamics of the left ventricle. *Russ. J. Numer. Analysis Math. Model.* 32, 225–236. doi:10.1515/rnam-2017-0021

Di Martino, E. S., Guadagni, G., Fumero, A., Ballerini, G., Spirito, R., Biglioli, P., et al. (2001). Fluid–structure interaction within realistic three-dimensional models of the aneurysmatic aorta as a guidance to assess the risk of rupture of the aneurysm. *Med. Eng. Phys.* 23, 647–655. doi:10.1016/s1350-4533(01)00093-5

Doyle, B. J., McGloughlin, T. M., Kavanagh, E. G., and Hoskins, P. R. (2014). "From detection to rupture: A serial computational fluid dynamics case study of a rapidly expanding, patient-specific, ruptured abdominal aortic aneurysm," in *Computational biomechanics for medicine* (New York, NY: Springer), 53–68.

Drewe, C. J., Parker, L. P., Kelsey, L. J., Norman, P. E., Powell, J. T., and Doyle, B. J. (2017). Haemodynamics and stresses in abdominal aortic aneurysms: A fluid-structure interaction study into the effect of proximal neck and iliac bifurcation angle. *J. biomechanics* 60, 150–156. doi:10.1016/j.jbiomech.2017.06.029

Farzaneh, S., Trabelsi, O., and Avril, S. (2019). Inverse identification of local stiffness across ascending thoracic aortic aneurysms. *Biomechanics Model. Mechanobiol.* 18, 137–153. doi:10.1007/s10237-018-1073-0

Gasser, T. C., Ogden, R. W., and Holzapfel, G. A. (2006). Hyperelastic modelling of arterial layers with distributed collagen fibre orientations. *J. R. Soc. interface* 3, 15–35. doi:10.1098/rsif.2005.0073

Gharahi, H., Zambrano, B., Lim, C., Choi, J., Lee, W., and Baek, S. (2015). On growth measurements of abdominal aortic aneurysms using maximally inscribed spheres. *Med. Eng. Phys.* 37, 683–691. doi:10.1016/j.medengphy.2015.04.011

Hsu, P.-P., Li, S., Li, Y.-S., Usami, S., Ratcliffe, A., Wang, X., et al. (2001). Effects of flow patterns on endothelial cell migration into a zone of mechanical denudation. *Biochem. biophysical Res. Commun.* 285, 751–759. doi:10.1006/bbrc.2001.5221

Kelsey, L. J., Powell, J. T., Norman, P. E., Miller, K., and Doyle, B. J. (2017). A comparison of hemodynamic metrics and intraluminal thrombus burden in a common iliac artery aneurysm. *Int. J. Numer. methods Biomed. Eng.* 33, e2821. doi:10.1002/cnm.2821

Khalafvand, S. S., Ng, E. Y.-K., Zhong, L., and Hung, T.-K. (2017). Three-dimensional diastolic blood flow in the left ventricle. *J. biomechanics* 50, 71–76. doi:10.1016/j.jbiomech.2016.11.032

Lan, H., Updegrove, A., Wilson, N. M., Maher, G. D., Shadden, S. C., and Marsden, A. L. (2018). A re-engineered software interface and workflow for the open-source simvascular cardiovascular modeling package. *J. biomechanical Eng.* 140, 0245011. doi:10.1115/1.4038751

Lindquist Liljeqvist, M., Hultgren, R., Bergman, O., Villard, C., Kronqvist, M., Eriksson, P., et al. (2020). Tunica-specific transcriptome of abdominal aortic aneurysm and the effect of intraluminal thrombus, smoking, and diameter growth rate. *Arteriosclerosis, Thrombosis, Vasc. Biol.* 40, 2700–2713. doi:10.1161/atvbaha.120.314264

Liu, G., Wu, J., Huang, W., Wu, W., Zhang, H., Wong, K. K., et al. (2014). Numerical simulation of flow in curved coronary arteries with progressive amounts of stenosis using fluid-structure interaction modelling. *J. Med. Imaging Health Inf.* 4, 605–611. doi:10.1166/jmihi.2014.1301

Liu, M.-Y., Jiao, Y., Liu, J., Zhang, S., and Li, W. (2021). Hemodynamic parameters predict in-stent thrombosis after multibranched endovascular repair of complex abdominal aortic aneurysms: A retrospective study of branched stent-graft thrombosis. *Front. Cardiovasc. Med.* 299, 654412. doi:10.3389/fcvm.2021.654412

Lozovskiy, A., Olshanskii, M. A., and Vassilevski, Y. V. (2018). A quasi-Lagrangian finite element method for the Navier–Stokes equations in a time-dependent domain. *Comput. Methods Appl. Mech. Eng.* 333, 55–73. doi:10.1016/j.cma.2018.01.024

Meng, H., Tutino, V., Xiang, J., and Siddiqui, A. (2014). High wss or low wss? Complex interactions of hemodynamics with intracranial aneurysm initiation, growth, and rupture: Toward a unifying hypothesis. *Am. J. Neuroradiol.* 35, 1254–1262. doi:10.3174/ajnr.a3558

Ong, C. W., Yap, C. H., Kabinejadian, F., Nguyen, Y. N., Cui, F., Chua, K. J., et al. (2018). Association of hemodynamic behavior in the thoracic aortic aneurysm to the intraluminal thrombus prediction: A two-way fluid structure coupling investigation. *Int. J. Appl. Mech.* 10, 1850035. doi:10.1142/s1758825118500357

Peng, C., Liu, J., He, W., Qin, W., Yuan, T., Kan, Y., et al. (2022). Numerical simulation in the abdominal aorta and the visceral arteries with or without stenosis based on 2d pcmri. *Int. J. Numer. Methods Biomed. Eng.* 38, e3569. doi:10.1002/cnm.3569

Piccinelli, M., Vergara, C., Antiga, L., Forzenigo, L., Biondetti, P., and Domanin, M. (2013). Impact of hemodynamics on lumen boundary displacements in abdominal aortic aneurysms by means of dynamic computed tomography and computational fluid dynamics. *Biomechanics Model. Mechanobiol.* 12, 1263–1276. doi:10.1007/s10237-013-0480-5

Piechota-Polanczyk, A., Jozkowicz, A., Nowak, W., Eilenberg, W., Neumayer, C., Malinski, T., et al. (2015). The abdominal aortic aneurysm and intraluminal thrombus: Current concepts of development and treatment. *Front. Cardiovasc. Med.* 2, 19. doi:10.3389/fcvm.2015.00019

Qiu, Y., Yuan, D., Wen, J., Fan, Y., and Zheng, T. (2018). Numerical identification of the rupture locations in patient-specific abdominal aortic aneurysmsusing hemodynamic parameters. *Comput. methods biomechanics Biomed. Eng.* 21, 1–12. doi:10.1080/10255842.2017.1410796

Salman, H. E., Ramazanli, B., Yavuz, M. M., and Yalcin, H. C. (2019). Biomechanical investigation of disturbed hemodynamics-induced tissue degeneration in abdominal aortic aneurysms using computational and experimental techniques. *Front. Bioeng. Biotechnol.* 7, 111. doi:10.3389/fbioe.2019.00111

Shamloo, A., Ebrahimi, S., Amani, A., and Fallah, F. (2020). Targeted drug delivery of microbubble to arrest abdominal aortic aneurysm development: A simulation study

towards optimized microbubble design. *Sci. Rep.* 10, 5393–5417. doi:10.1038/s41598-020-62410-3

Shang, E. K., Nathan, D. P., Sprinkle, S. R., Vigmostad, S. C., Fairman, R. M., Bavaria, J. E., et al. (2013). Peak wall stress predicts expansion rate in descending thoracic aortic aneurysms. *Ann. Thorac. Surg.* 95, 593–598. doi:10.1016/j.athoracsur.2012.10.025

Shi, Y., Peng, C., Liu, J., Lan, H., Li, C., Qin, W., et al. (2021). A modified method of computed fluid dynamics simulation in abdominal aorta and visceral arteries. *Comput. Methods Biomechanics Biomed. Eng.* 24, 1718–1729. doi:10.1080/10255842.2021.1912742

Soldozy, S., Norat, P., Elsarrag, M., Chatrath, A., Costello, J. S., Sokolowski, J. D., et al. (2019). The biophysical role of hemodynamics in the pathogenesis of cerebral aneurysm formation and rupture. *Neurosurg. focus* 47, E11. doi:10.3171/2019.4.focus19232

Suh, G.-Y., Les, A. S., Tenforde, A. S., Shadden, S. C., Spilker, R. L., Yeung, J. J., et al. (2011a). Hemodynamic changes quantified in abdominal aortic aneurysms with increasing exercise intensity using mr exercise imaging and image-based computational fluid dynamics. *Ann. Biomed. Eng.* 39, 2186–2202. doi:10.1007/s10439-011-0313-6

Suh, G.-Y., Les, A. S., Tenforde, A. S., Shadden, S. C., Spilker, R. L., Yeung, J. J., et al. (2011b). Quantification of particle residence time in abdominal aortic aneurysms using magnetic resonance imaging and computational fluid dynamics. *Ann. Biomed. Eng.* 39, 864–883. doi:10.1007/s10439-010-0202-4

Tanweer, O., Wilson, T. A., Metaxa, E., Riina, H. A., and Meng, H. (2014). A comparative review of the hemodynamics and pathogenesis of cerebral and abdominal aortic aneurysms: Lessons to learn from each other. *J. Cerebrovasc. endovascular Neurosurg.* 16, 335–349. doi:10.7461/jcen.2014.16.4.335

Vahidkhah, K., Barakat, M., Abbasi, M., Javani, S., Azadani, P. N., Tandar, A., et al. (2017). Valve thrombosis following transcatheter aortic valve replacement: Significance of blood stasis on the leaflets. *Eur. J. Cardio-Thoracic Surg.* 51, 927–935. doi:10.1093/ejcts/ezw407

Valentin, A., Humphrey, J. D., and Holzapfel, G. A. (2013). A finite element-based constrained mixture implementation for arterial growth, remodeling, and adaptation: Theory and numerical verification. *Int. J. Numer. methods Biomed. Eng.* 29, 822–849. doi:10.1002/cnm.2555

Vergara, C., Le Van, D., Quadrio, M., Formaggia, L., and Domanin, M. (2017). Large eddy simulations of blood dynamics in abdominal aortic aneurysms. *Med. Eng. Phys.* 47, 38–46. doi:10.1016/j.medengphy.2017.06.030

Xiong, G., Figueroa, C. A., Xiao, N., and Taylor, C. A. (2011). Simulation of blood flow in deformable vessels using subject-specific geometry and spatially varying wall properties. *Int. J. Numer. methods Biomed. Eng.* 27, 1000–1016. doi:10.1002/cnm.1404

Yeow, S. L., and Leo, H. L. (2018). Is multiple overlapping uncovered stents technique suitable for aortic aneurysm repair? *Artif. organs* 42, 174–183. doi:10.1111/aor.12993

Zambrano, B. A., Gharahi, H., Lim, C., Jaberi, F. A., Choi, J., Lee, W., et al. (2016). Association of intraluminal thrombus, hemodynamic forces, and abdominal aortic aneurysm expansion using longitudinal ct images. *Ann. Biomed. Eng.* 44, 1502–1514. doi:10.1007/s10439-015-1461-x

Frontiers in
Medical Technology

Explores innovative solutions to global healthcare challenges

An innovative journal that explores technologies which can maintain healthy lives and contribute to the global bioeconomy by addressing key medical and healthcare needs.

Discover the latest Research Topics

See more →

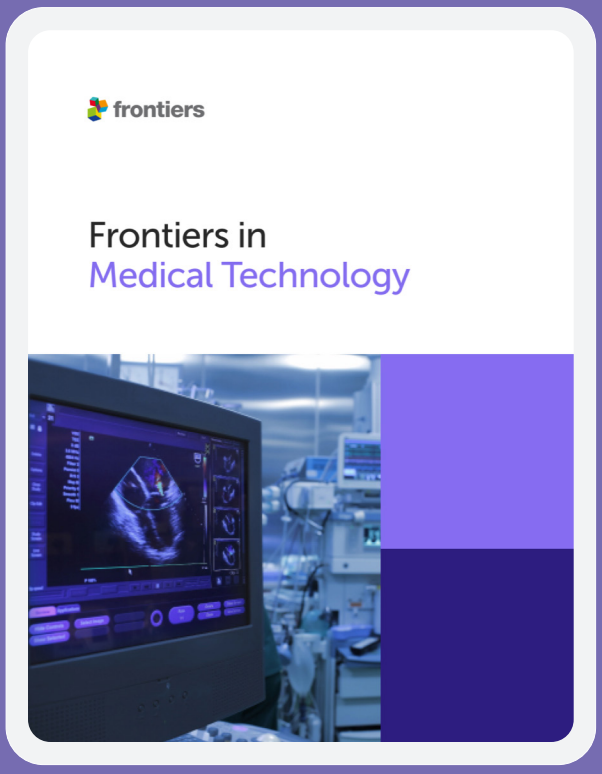

Frontiers

Avenue du Tribunal-Fédéral 34
1005 Lausanne, Switzerland
frontiersin.org

Contact us

+41 (0)21 510 17 00
frontiersin.org/about/contact